Department of Physics and Astronomy

X-ray and Observational Astronomy Group

Using Gamma-Ray Bursts' Pulses for Large-Scale Population Analysis.

Alexander Amaral-Rogers

Submitted in accordance with the requirements for the degree of Doctor of Philosophy.

Under the supervision of Richard Willingale at the University of Leicester.

April 19, 2017

The candidate confirms that the work submitted is his own and that appropriate credit has been given where reference has been made to the work of others.

Using Gamma-Ray Bursts' Pulses for Large-Scale Population Analysis.

Alexander Amaral-Rogers

Abstract

The current paradigm of GRB lightcurves is that the totality of the gamma-ray prompt emission can be modelled by the presence of either a single pulse, or by a series of convolved pulses, which rapidly decay before the onset of an X-ray afterglow. These pulses are well studied; but are popularly modelled by empirical functions which do not relate the spectral and temporal properties of the pulse as a unified whole. In this thesis we utilise a physically motivated model of pulse emission, that incorporates both spectral and temporal behaviour, to fit the lightcurves of a significant proportion of all Swift observed GRBs with known associated redshifts; the X-ray afterglows observed by the Swift X-Ray Telescope are also fitted, using an empirical model, resulting in GRB lightcurves which are completely parameterised. We produce, with this data, an exhaustive GRB pulse and afterglow catalogue, and investigate some of the most commonly observed relationships between the fundamental GRB parameters.

In Chapter 3 of this thesis we investigate the GRB luminosity distribution, utilising the large GRB pulse dataset of Chapter 2, in order to significantly improve our GRB population statistics. We produce, instead, a GRB pulse luminosity function for which the traditional GRB luminosity function can be considered as the high-luminosity tail. Given that the GRB luminosity distribution has been well studied, and has lead to assertions of evolution in observed GRB characteristics over cosmological timescales, we evaluate many of these models using our expanded dataset, and constrain more tightly the aforementioned luminosity function parameters. This, in turn, has allowed us to investigate some of the more common GRB progenitor model theories, and to indicate which models are more favourable in reproducing the observed behaviour of GRBs.

Acknowledgements

I'd like to thank my supervisor, Richard Willingale, without whom, this thesis would not have been possible. With his patient explanation of GRB phenomena, and useful insights into good coding practise, Dick was the epitome of the approachable PhD supervisor.

My thanks also go to my colleagues, officemates, and fellow PhD students, whom have kept me entertained and optimistic for the entirety of my PhD.

Finally, and most importantly, I'd like to thank my girlfriend Ellie, and my son Piran; they gave me the impetus to get through the most tedious parts of writing up a thesis, and are a constant inspiration to me, every day.

Contents

List of Figures

List of Tables

List of Abbreviations

BACODINE	BATSE Co-ordinates Distribution Network
BAT	Burst Alert Telescope
BAT6	BAT 6-Year Survey
BATSE	Burst And Transient Source Experiment
BH	Blackhole
BPL	Broken Power-Law
CALET	Calorimeter Electron Telescope
CCD	Charge Coupled Device
CGRO	Compton Gamma-Ray Observatory
COMPTEL	Imaging Compton Telescope
EE GRB	Extended Emission Gamma-Ray burst
EGRET	Energetic Gamma-Ray Experiment Telescope
ESA	European Space Agency
FRED	Fast Rise Exponential Decay
FREGATE	French Gamma-ray Telescope
FOV	Field Of View
FWHM	Full Width Half Maximum
GBM	Gamma-ray Burst Monitor
GCN	Gamma-ray burst Co-ordinates Network
GRB	Gamma-Ray Burst
GRBM	Gamma-Ray Burst Monitor
GROND	Gamma-Ray Burst Optical/Near-Infrared Detector

GSC	Gas Slit Camera
GTC	Gran Telescopio Canarias
HEAO-1	High Energy Astrophysics Observatory 1
HEASARC	High Energy Astrophysics Science Archive Research Centre
HEB	High Energy Bands
HETE-2	High Energy Transient Explorer 2
HL GRB	High Luminosity GRBs
HPGSPC	High Pressure Gas Scintillator Proportional Counter
HXD	Hard X-ray Detector
IBIS	Imager on Board the Integral Satellite
IC	Inverse Compton
IGC	Induced Gravitational collapse
IM	Imaging Mode
IMP-6	Interplanetary Monitering Platform 6
INTEGRAL	International Gamma-Ray Astrophysics Laboratory
IPN 1/2	Interplanetary Network
ISEE-3	International Sun-Earth Explorer 3
ISM	Interstellar Medium
ISS	International Space Station
JAXA	Japanese Aerospace Exploration Agency
JEM-X	Joint European X-ray Monitor
LAT	Large Area Telescope
LEB	Low Energy Bands
LECS	Low Energy Concentrator Spectrometer
LIGO	Laser Interferometric Gravitational Observatory
LGRB	Long Gamma-Ray Bursts
LL GRB	Low Luminosity Gamma Ray Burst
LMC	Large Magellanic Cloud
MAXI	Monitor of All-sky X-ray Image

MECS	Medium Energy Concentrator Spectrometer
MIR	Mid Infrared
NASA	National Aeronautical and Space Agency
NFI	Narrow Field Instruments
NIR	Near Infrared
NS	Neutron Star
OGBD	Orbiter Gamma Burst Detector
OSO-7	Orbiting Solar Observatory 7
OSSE	Oriented Scintillation Spectrometer Experiment
P60	Palomar 60 Inch Telescope
PAITITEL	Peters Automates Infrared Telescope
PC	Photon Counting
PD	Photon Diode
PDS	Phoswich Detection System
PL	Power Law
PLEC	Power law with Exponential Cutoff
PSF	Point Spread Function
PVO	Pioneer Venus Orbiter
ROTSE	Robotic Optical Transient Search Experiment
RXTE	Rossi X-ray Timing Explorer
SFR	Star Formation rates
SGRB	Short Gamma-ray burst
SHOALS	Swift Gamma-Ray Burst Host Galaxy Legacy Survey
SN(e)	Supernova(e)
SPI	Spectrometer on Integral
SXC	Soft X-ray Camera
TAN	Transient Astronomy Network
TDE	Tidal Distuption Event
TDRS	Tracking and Data Relay Satellites

TGRS	Transient Gamma-Ray Spectrometer
TNG	Telescopio Nazionale Galileo
TOUGH	The Optically Unbiased GRB Host Survey
UKSA	United Kingdom Space Agency
ULGRB	Ultra Long Gamma Ray Burst
UV	Ultraviolet
UVOT	Ultraviolet and Optical Telescope
VLT	Very Large Telescope
WAM	Wide Band All Sky Monitor
WD	White Dwarf
WFC	Wide Field Cameras
WHT	William Herschel Telescope
WR	Wolf Rayet star
WT	Window Timing
WXM	Wide field X-ray Monitor
XIS	X-ray Imaging Spectrometers
XRF	X-ray Flashes
XRS	X-Ray Spectrometer
XRT	X-Ray Telescope

Publications

The work contained within Chapter 2 is currently pending complete translation into a paper submission, with future digital release of the data included.

The work contained within Chapter 3 has been published as:

Title: The Pulse Luminosity Function of Swift Gamma-Ray Bursts

Authors: Amaral-Rogers, A.; Willingale, R.; and O'Brien, P.T.

Publication: Monthly Notices of the Royal Astronomical Society, Volume 464, Issue 2, p.2000-2017

DOI: 10.1083/mnras/stw2394

Published: 01/2017

Chapter 1

Introduction

1.1 Initial Discovery

Ironically, the most energetic events in the universe was first discovered via a satellite system designed to detect man-made nuclear weapons detonation. Launched on the 17^{th} October 1963, the Vela satellite system [1] provided full sky coverage, each with a payload of separate X-ray scintillation, Gamma-ray, and neutron detectors. On the 2^{nd} of July 1967 a pulse of Gamma-ray photons, in the energy range $0.2 - 1.5$ MeV, was detected by the then two satellite constellation, lasting approximately 10 seconds. This event, later known as Gamma-Ray Burst (GRB) 670702, was to be the first of many such pulses and was notable due to the lack of simultaneous observation by the X-ray, and neutron detectors. Given its unusual nature, entirely dissimilar to that of a nuclear explosion, the event was considered an oddity and was filed away.

It was not until the prediction of Gamma-ray emission during the early stages of supernovae initiation by Colgate (1968), and the encouragement by Colgate, that Ray Kelbesadel and his team decided to painstakingly trawl through the vast amount of data that Vela had produced. Whilst no pulses were detected at times coincidental with that of observed supernovae, many of the unusual bursts were discovered,

[1] Initially a pair of satellites, the Vela constellation grew to incorporate 6 Vela Hotel, and 6 Advanced Vela satellites over the years, from 1963-1970, and detected Gamma-ray bursts up until 1979.

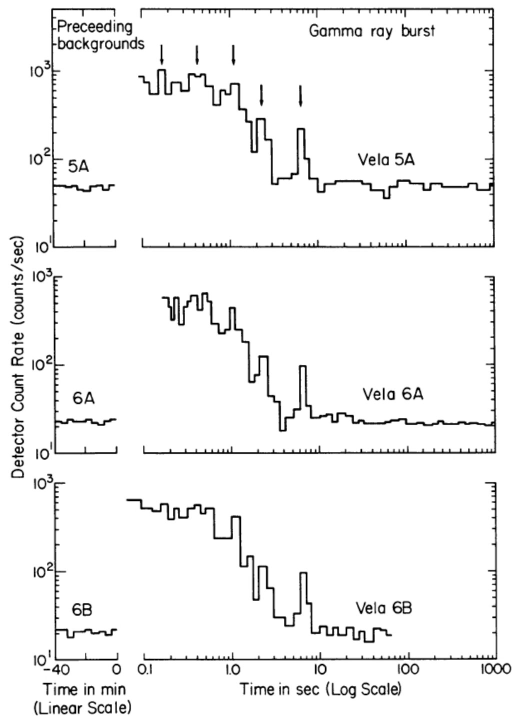

Figure 1.1: *Figure taken from Klebesadel, Strong & Olson (1973) showing the lightcurves of GRB 700822 observed by three of the Vela constellation spacecraft. Background counts preceding the bursts are shown before the main period of the burst, whilst notable structures observed by the three simulatenous detections are highlighted by the arrows.*

with sixteen such bursts detected between July 1969 and July 1972. Like GRB 670702, these bursts were detected by multiple spacecraft almost simultaneously, and likewise, only by the onboard Gamma-ray instruments; durations of the bursts ranged from less than one second to approximately 30 seconds; and time-integrated flux densities varied from $\sim 10^{-5}$ to $\sim 10^{-4}$ ergs cm^{-2}. Other variations in the characteristics of the bursts were seen, however, it was clear that the sources were not man-made due to the general shape of the bursts, the lack of multi-messenger detections, and triangulation from time-delays between spacecraft ruling out near-Earth origin. The first published GRB lightcurve of GRB 700822, shown in Figure 1.1, displayed five noteable features and was an example of the significant temporal variation observed within pulse structures.

Although first, Vela was not the only system to detect Gamma-ray bursts; some of the events documented by Klebesadel, Strong & Olson (1973) were simultaneously observed by NASA's Orbiting Solar Observatory (OSO-7), and Interplanetary

Monitering Platforms (IMP-6) (Cline et al., 1973; Wheaton et al., 1973), and by the Soviets' Kosmos 461 satellite (Mazets, Golenetskii & Il'Inskii, 1974). By the 7^{th} Texas Symposium on Relativistic Astrophysics, held in 1974, Gamma-ray bursts were a popular and controversial topic; the symposium's review paper alone outlined approximately 150 different progenitor models ranging from the prosaic to the exotic (Ruderman, 1975). Given the serendipitous nature of GRB discovery, missions in the early 1960s and 1970s were not specifically designed to observe GRBs. The wealth of early data collected was predominantely spectral, and temporal in nature, whilst precise on-sky positioning remained unavailable.

Subsequent Gamma-ray missions were designed specifically to study this new phenomenon, and were soon being launched from the late 1970s; since then there has been continous Gamma-ray coverage by both general Gamma-ray missions, and dedicated, space-based, GRB missions including: Apollo 16 (Metzger et al., 1974), Venera 11 & 12 (Mazets et al., 1979), Prognoz 7 (Barat et al., 1981b), Ginga (Murakami et al., 1989), the International Sun-Earth Explorer (ISEE, Anderson et al., 1978), the High Energy Astrophysics Observatory (HEAO-1, Knight, Matteson & Peterson, 1981), Helios 2 (Cline et al., 1979), the Pioneer Venus Orbiter (PVO, Klebesadel et al., 1980), Granat (Paul et al., 1991), Ulysses (Hurley et al., 1992), the Compton Gamma-Ray Observatory (CGRO, Gehrels, Chipman & Kniffen, 1993), BeppoSAX (Boella et al., 1997), the High Energy Transient Explorer (HETE-2, Ricker et al., 2003), Fermi (Atwood et al., 2009; Meegan et al., 2009), Wind (Aptekar et al., 1995), the INTErnational Gamma-Ray Astrophysics Laboratory (INTEGRAL, Winkler, Pace & Volonté, 1993), the Monitor of All-sky X-ray Image (MAXI, Matsuoka et al., 2009), the Rossi X-Ray Timing Explorer (RXTE, Bradt, Rothschild & Swank, 1993), Suzaku (Mitsuda et al., 2007), and Swift (Gehrels et al., 2004) (see Figure 1.2).

1.2 Major Gamma-Ray Burst Missions

The following discussion on major Gamma-ray burst missions, both active and inactive, is not to be considered exhaustive and only focuses on the few missions that are of direct importance to this thesis; details on other missions however can be found in NASA's High Energy Astrophysics Science Archive Research Centre, given in Appendix I; online repositories for the various GRB mission catalogues, which are generally more up to date than published catalogues, are also available there.

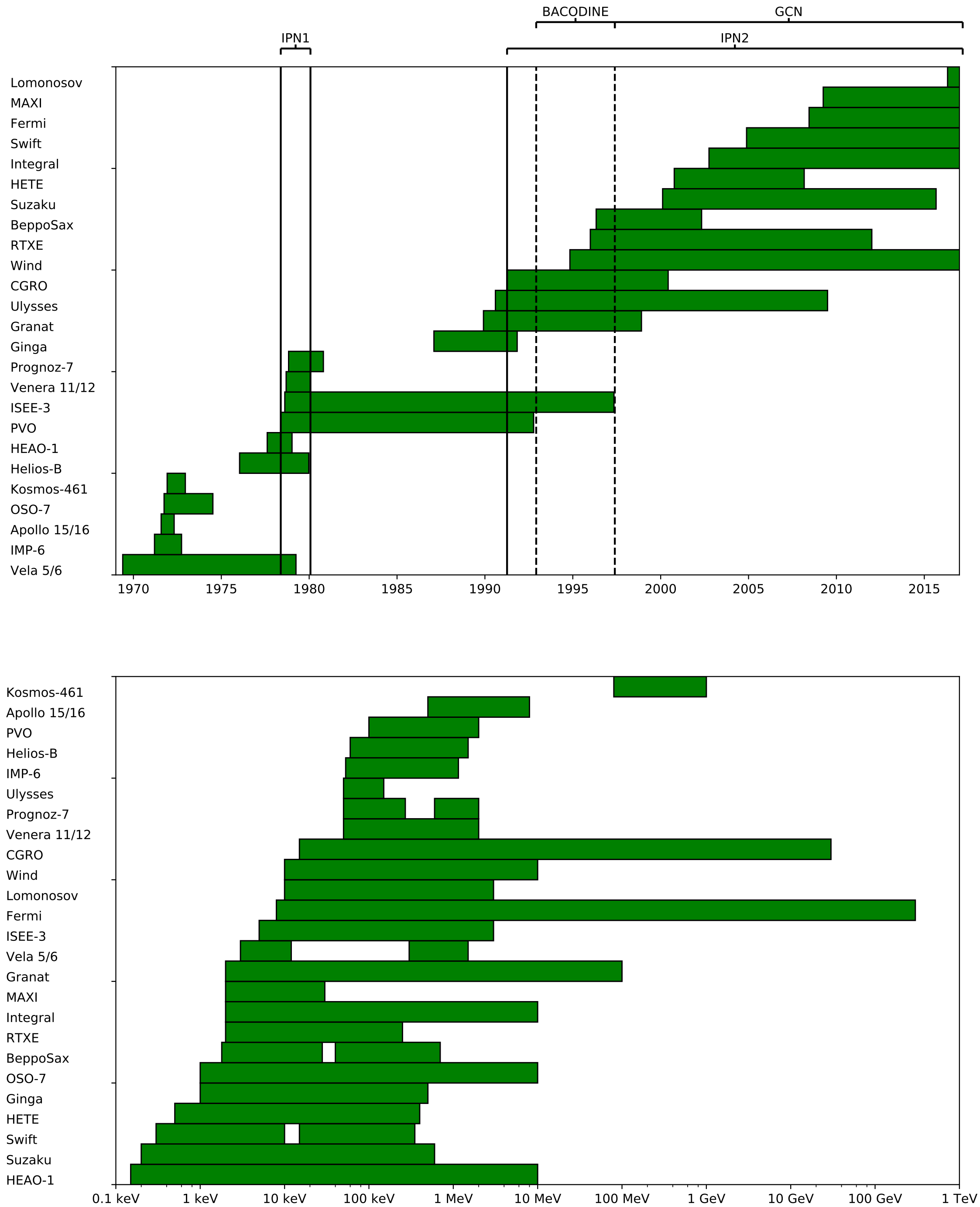

Figure 1.2: *The lifetimes of major Gamma-ray, and X-ray missions that detected GRBs from 1969 to present day (top); and the corresponding energy ranges of the onboard detectors (bottom). IPN 1, IPN 2, BACODINE, and GCN brackets denote durations in which the InterPlanetary Networks (IPN 1/2), BAtse COordinates DIstribution NEtwork (BACODINE), and the later Gamma-ray burst Coordinates Network (GCN), were in operation; a description of these missions are available in Section 1.4.2; Mission data taken from NASA's HEASARC website, given in Appendix I.*

As the principal mission from which this thesis has been built upon, the Swift satellite instruments are given greater description than all other missions, and is instead covered in Section 1.3.

1.2.1 The Pioneer Venus Orbiter

Launched on the 20^{th} of May, 1978, NASA's Pioneer Venus Orbiter carried onboard the Orbiter Gamma Burst Detector (Klebesadel et al., 1980). Designed to record spectral, and temporal GRB data spanning from 100 keV to 2 MeV, the PVO continued operating until 1992, whereby it had detected 228 GRBs (Chuang, 1990; Chuang et al., 1992).

1.2.2 The Compton Gamma-Ray Observatory

On the 5^{th} of April 1991, NASA launched the Compton Gamma-Ray Observatory (CGRO) carrying four major experiments including a specifically designed gamma-ray burst monitor. The Burst And Transient Source Experiment (BATSE) (Fishman et al., 1985) consisted of eight modules, each containing: an uncollimated, large-area, flat NaI crystal scintillation detector covering the energy range from 30 keV to 1.9 MeV; and a NaI(Tl) spectroscopic scintillation detector with 100 μs time resolution, covering 15 keV to 110 MeV, and directional precision of a few degrees (Fishman et al., 1989). These detectors provided half-sky coverage [2] over the duration of the 9 year mission, during which BATSE detected over 2,700 GRBs (Paciesas et al., 1999). The other instruments on-board the CGRO were the Oriented Scintillation Spectrometer Experiment (OSSE), the Imaging Compton Telescope (COMPTEL), and the Energetic Gamma-Ray Experiment Telescope (EGRET). Providing photon energy coverage from 20 MeV up to 30 GeV (Dingus, 1995b), EGRET provided high energy data for five BATSE detected GRBs (Dingus, 1995a; Schneid et al., 1992).

1.2.3 BeppoSAX

The Dutch/Italian satellite BeppoSAX was launched on the 30^{th} of April 1996 and carried 3 major experiments observing in the Gamma-ray and X-ray energy

[2] Whilst the distribution of the eight modules allowed for simultaneous isotropic observation, the CGRO was deployed in low-Earth orbit, severely limiting the field of view.

regimes: the Gamma-Ray Burst Monitor (GRBM, Feroci et al., 1997) consisted of four CsI(Na) slabs with temporal resolution of 0.48 ms, covering 40 - 700 keV; the Wide Field Cameras (WFC, Jager et al., 1997), two coded mask X-ray cameras with a 20° field of view (FOV), and angular resolution of 5 arcminutes, observing photons of between 1.8 - 28 keV; and the Narrow Field Instruments (NFI), in reality four separate instruments including the Low/Medium Energy Concentrator Spectrometers (LECS, MECS Parmar et al., 1997; Sacco et al., 1997), the High Pressure Gas Scintillator Proportional Counter (HPGSPC, Segreto et al., 1997), and the Phoswich Detection System (PDS, Frontera et al., 1997). BeppoSAX continued to operate for a further 6 years during which it observed 1082 GRBs (Frontera et al., 2009).

1.2.4 Other Major Missions

Wind

Launched on the 1^{st} of November, 1994, NASA's Wind satellite carries on-board the dedicated Gamma-ray burst experiment, Konus (Aptekar et al., 1995), and the Transient Gamma-Ray Spectrometer (TGRS, Owens et al., 1995). Konus is a Russian built instrument similar to those placed on the Kosmos, and Venera satellites and observes between 10 kev - 770 keV. The position of Wind between the Earth and Sun allows Konus omni-directional coverage, a feat that is impossible for low-Earth orbiting spacecraft. The TGRS observes between 15 keV and 10 MeV with an energy resolution of 2 keV at 1 MeV. Both instruments are still in operation with Konus and the TGRS detecting 2,219 GRBs from 1995 to 2012 (Cline et al., 2003).

The High Energy Transient Explorer 2

An international collaboration from institutes in the U.S., Japan, and Europe lead to the development and launch of the High Energy Transient Explorer on the 9^{th} of October, 2000. On board HETE-2 were a Gamma-ray, and two X-ray instruments: the Soft X-ray Camera (SXC, Villasenor et al. 2003), the Wide field X-ray Monitor (WXM, Shirasaki et al. 2000), and the FREnch GAmma-ray TElescope (FREGATE Atteia et al. 1995). The SXC consisted of two coded mask X-ray CCDs, observing from 0.5 keV to 14 keV, with a FOV of $\sim$ 0.9 steradians and resolution of 30 arcseconds. The WXM was made of two orthogonally orientated coded mask X-ray detectors observing from 2 keV to 25 keV and spatial resolution of 10 arcminutes. FREGATE consisted of four Gamma-ray detectors with a FOV of $\sim$ 3 steradians observing from 6 keV to 400 keV. The three instruments had limited overlap between the FOVs such that $\sim$ 1.5 steradians were being observed simultaneously. From mission launch to March 2008, the WXM, and FREGATE instruments detected 84 GRBs. Many of the algorithms developed for burst detection by HETE would be later incorporated into the Swift Burst Alert Telescope's burst trigger chain.

Suzaku

Suzaku was a Japanese X-ray mission with involvement from the US and was launched on the 10^{th} of July, 2005 and remained operational until the 2^{nd} of September, 2015. On board were three instruments: the X-Ray Spectrometer [3] (XRS, Kelley et al., 2007), the X-ray Imaging Spectrometers (XIS, Koyama et al., 2007), and the Hard X-ray Detector (HXD, Takahashi et al., 2007). The XIS consisted of four co-aligned X-ray telescopes, each focussing onto an X-ray CCD with energy range of 0.2 to 12 keV; combined, the XIS instruments had a FOV of 0.1 steradians. The HXD observed between 10 keV to 600 keV. Whilst the HXD has a narrow FOV of 0.006 steradians, the anti-coincidence shield component (the Wide band All-sky Monitor, WAM) used as background rejection for the rest of the HXD components, was sensitive to photons outside of the FOV. As such the HXD-WAM could act as a limited all-sky GRB monitor (Ohno et al., 2005; Yamaoka et al., 2005) and over the first six years, detected over 850 GRBs (Ohno et al., 2012).

The International Gamma-Ray Astrophysics Laboratory

Three of the four instruments onboard ESA's INTEGRAL mission are related to Gamma-ray, and X-ray observation: the Spectrometer on Integral (SPI, Vedrenne et al., 2003), the Imager on Board the Integral Satellite (IBIS, Ubertini et al., 2003), and the Joint European X-Ray Monitor (JEM-X, Lund et al., 2003). SPI observes with a coded FOV of $\sim$ 0.1 steradians from 2 kev to 8 MeV with energy resolution of 2.2 keV at 1.33 MeV; IBIS has a coded FOV of 0.02 steradians and covers 15 keV to 10 MeV; whilst JEM-X has a FOV of $\sim$ 0.004 steradians, detects 3 keV to

[3] Sadly the XRS lost all coolant before any scientific data was recorded, rendering the instrument inoperable.

35 keV X-ray photons, and can localise sources to within 1 arcminute. Launched in October 2002, INTEGRAL is still in operation, with 388 GRBs collected in the first SPI GRB catalogue (Rau et al., 2005).

Fermi

Fermi, the joint American, and European mission, was launched on the 11^{th} of June, 2008, to low-Earth orbit and carried on-board two Gamma-ray instruments. The Gamma-ray Burst Monitor (GBM, Meegan et al., 2009), consists of low, and high energy detecters observing between 8 keV to 1 MeV, and 150 keV to 40 MeV respectively. GBM's large FOV of ~ 9.5 steradians allows for a GRB detection rate of 0.5 GRBs day^{-1} and, as of February 2017, has observed 2,022 GRBs (Gruber et al., 2014; von Kienlin et al., 2014), however the extremely poor localisation accuracies of $> 10°$ results in Fermi GBM bursts generally having little follow-up unless detected by other, more precise, missions. The Large Area Telescope (LAT, Atwood et al., 2009) observes between 20 MeV to 300 GeV with a FOV of 2.4 steradians. The LAT's localisation accuracy is related to the square-root inverse of the burst's fluence [4] such that brighter bursts are harder to localise. As of February 2017, the LAT has observed 124 GRBs (Ackermann et al., 2013).

The Monitor of All-Sky X-Ray Image

The X-ray mission, MAXI, is attached to the Japanese Experimental Module on-board the International Space Station (ISS) and began operation in August 2009. The Gas Slit Camera (GSC, Mihara et al., 2011) observes over an energy range of 2 keV to 30 keV, with a FOV of 0.25 steradians. Up to August 2016, MAXI has observed 84 GRBs (Serino et al., 2014, 2013).

1.3 Swift

The desire to combine multi-wavelength observation, highly accurate GRB positional data, and fast upload time resulted in the design of the Swift satellite: a medium-class, joint NASA, UK, and Italian Space Agency mission. Launched on the 20^{th}

[4] Fluence is the time-integrated radiant energy per unit area; for GRBs, fluence is typically quoted in units of ergs s^{-1}.

of September 2004, Swift carries on board 3 co-aligned instruments observing in the Gamma-ray, X-ray, and Ultraviolet/Optical regimes: the Burst Alert Telescope (BAT, Barthelmy et al., 2005a); the X-Ray Telescope (XRT, Burrows et al., 2005a); and the Ultraviolet and Optical Telescope (UVOT, Roming et al., 2005). For this thesis we analyse only the GRB data recorded by the BAT and XRT, despite the UVOT also observing many of the XRT afterglows. The UVOT does, however, provide a subtle role in this thesis: providing a more precise on-sky localisation than that which is available from utilising solely the XRT data; such precise localisation can limit the position of the GRB afterglow, or host galaxy, for later spectroscopic or photometric observations.

1.3.1 The Burst Alert Telescope

Utilising the technique of coded apeture imaging (see Caroli et al. 1987 for details) for producing Gamma-ray images, the Burst Alert Telescope (BAT) consists of a large coded apeture mask situated above the plane of the BAT detector array, and surrounded by graded shielding to protect from diffuse isotropic cosmic emissions and anisotropic emission from the Earth. The D-shaped coded aperture mask, situated 1 metre above the BAT instrument, consists of $\sim 54,000$ lead tiles in a random 50% open, 50% closed pattern, with a total area of 2.7 m^2 yielding a field of view (FOV) of 1.4 steradians. The BAT detectors consist of $\sim 33,000$ CdZnTe solid-state detectors constructed into 16 blocks of 8 modules, with each module consisting of two arrays of 128 pixels; this hierarchical structure can tolerate the loss of pixels, modules, and blocks without compromising burst detection and localisation. The combination of the 4x4 mm CdZnTe pixels, 5x5 mm mask tiles, and 1 metre separation results in the BAT instrument having an angular resolution of 20 arcmin full width half maximum (FWHM), and centroiding precision of typically 4 arcmin.

The CdZnTe detectors operate between 10 and 500 keV, and are typically binned temporally over 64 ms. The effective area of the BAT, nominally greater than 1000 cm^2, drops off above approximately 150 keV with GRB emission at greater energies contributing little to overall fluences given the general shape of GRB spectra; typical BAT observations are therefore binned into four passbands: 15 - 25 keV, 25 - 50 keV, 50 - 100 keV, and 100 - 350 keV.

The BAT has an adjustable table of dozens of criteria for triggering, with typical event rate trigger thresholds ranging from 4 to 11 σ above background noise[5]. Once an event has passed these criteria, on-board software evaluates the gamma-ray image to determine if the source is point-like. Should the event pass (ruling out variation in bright galactic sources, and magnetospheric particle events) the event is reclassified as a burst. In some cases the GRB lightcurve is long, and smooth and does not satisfy the criteria for a rate trigger. Such a burst, however, may be detected by the image trigger, whereby gamma-ray sources within an image are compared to an on-board catalog. New sources, or sources with high temporal variability are labelled as transients, and are treated in the same manner as rate triggered bursts. Given the fast slew rate (typically $\sim$ 1 min), and the overlapping FOVs of the BAT, XRT, and UVOT, once the initial burst has been localised by the BAT, the satellite slews the XRT on target [6]; late-time observations, therefore, are not limited to a single instrument but instead consist of simultaneous observation by all three instruments.

1.3.2 The X-Ray Telescope

The high energies of X-ray photons precipitated the need for grazing incidence optics to focus incoming X-rays onto the XRT CCD, given the propensity of high energy photons to transmit through conventional reflective optics. Using a Wolter 1 X-ray telescope, consisting of 12 concentric nested mirrors with a combined effective area of 110 cm^{-2} and focal length of 3.5 metres, the XRT has a FOV of 23.6 x 23.6 arcmin, and resolution of 18 arcseconds. The XRT CCD consists of 600 x 600 pixels that can operate in 3 different modes of observation: imaging (IM), window timing (WT), and photon counting (PC)[7]. Imaging mode observations suffer greatly from pile-up, in which 1 photon arriving at a pixel whilst it is in the process of being read out is indistinguishable from several photons of lesser energies; as such, imaging mode provides no spectral information and is instead utilised for on-sky localisation providing centroiding precision of $\sim$ 5 arcseconds.

GRB observations by the XRT autonomously switch between WT, and PC modes depending on the flux at that time. Window timing collapses the XRT data down

[5]With a background count rate of 0.3 counts s^{-1}, the fluence sensitivity of the BAT is $\sim 10^{-8}$ ergs s^{-1} cm^{-2} between 15 - 150 keV.

[6]Slewing can be restricted to a later time if the burst occured within zones of avoidance, centred on the Sun, the Moon, and the Earth.

[7]A fourth mode, photon diode (PD) was rendered inoperable due to a micrometeorite impact shortly after reaching orbit.

into a 1D image, reducing the readout time[8] and prevents saturation when the source is very bright. The PC mode, in contrast, reads out all pixel values which provides the opportunity for pile-up if the source is bright; as such the PC mode is utilised to observe source fluxes ranging from the sensitivity limit of 2×10^{-14} to 9×10^{-10} ergs s^{-1} cm^{-2}, whilst the WT operates up to three orders of magnitude brighter than the PC flux limit.

The XRT CCDs observe between 0.1 and 10 keV with a steady rise in effective area up to 1.5 keV, a plateau at approximately 100 cm^2, and a sharp turn off at approximately 6 keV; the effective area below 0.3 keV peaks at 10 cm^{-2} and contributes little to overall observations. Like the BAT, detections are binned into multiple energy passbands: 0.3 - 1.5 keV, and 1.5 - 10 keV. Spectral resolution of the XRT was $\sim$ 140 eV at 6 keV although degradation would have occured in the 10 years of operation in a hostile environment.

1.3.3 The Ultraviolet and Optical Telescope

Observing between 170-650 nm (1.91 - 7.29 eV), the UVOT is a modified Ritchey-Chretien telescope with a 30 cm, diffraction limited, primary mirror, and focal length of 3.81 metres; coupled to the CCD is a microchannel plate, intensifying the incoming signal through a stimulated cascade of electrons. The 11-positional UVOT filter provides low-resolution grism spectra, magnification, and broadband UV/Optical photometry capabilities. With a FOV of 17 x 17 arcmin and a point spread function (PSF) of 2.5 arcseconds, the UVOT is able to produce a finding chart with 0.3 arcsecond precision relative to the background stars in the field of view. When combined with the XRT positional data, the UVOT can produce a refined XRT position of typically 1-2 arcseconds (Goad et al., 2007).

[8]The time resolution of the window timing mode is 1.8 ms, compared to the photon counting mode's 2.5 s temporal resolution.

1.4 Future Missions

1.4.1 The Space-Based Multiband Astronomical Variable Objects Monitor

The Space-based multiband astronomical Variable Objects Monitor (SVOM) is a joint venture between the Chinese National Space Agency (CNSA), the Chinese Academy of Science (CAS), and the French Space Agency (CNES); and like NASA's Swift, is a multi-wavelength observatory, carrying four instruments that observe over gamma-ray, X-ray, and optical passbands. ECLAIRS (Barret et al., 2001; Schanne et al., 2015) is a wide FOV (2 sr), coded-mask gamma-ray imager, with a detector plane consisting of an 80×80 pixels Schottky CdTe CCD. ECLAIRs has an energy range spanning from 4 keV to 150 keV, and above 20 keV, is more sensitivite than the Swift Burst Alert Telescope. With localisation capabilities better than 16 arcminutes, ECLAIRs is predicted to observe 70 - 80 GRBs yr^{-1}. The fast response and localisation times of ECLAIRs has led to the aim of observing 50% of all GRB redshifts, an improvement on the $\sim$ 33% achieved by Swift (Lien et al., 2016a). The Gamma-Ray Monitor (GRM; Dong et al. 2010) consists of three observing modules with a combined FOV of 2 sr, made of NaI scintillating crystals in front of photomultipliers. The energy range of the GRM extends from 15 keV to 5 MeV, and is expected to observe 90 - 100 GRBs yr^{-1}. The Micro-channel X-ray Telescope (MXT; Götz et al. 2014) utilises micropore optics in a lobster-eye geometry with a FOV of 64 $\times$ 64 arcminutes, and a point spread function (PSF) of 3.7 arcminutes. The energy range of the XMT is 0.2 keV to 10 keV with a 5σ sensitivity of 2×10^{-12} ergs s^{-1} cm^{-2} in 10 ks. The Visible Telescope (VT) is a Ritchey-Chretien telescope, with a dichroic beam-splitter that produces two energy channels: 0.4 μm - 0.65 μm (blue channel), and 0.65 μm - 1 μm (red channel), which are each focused on a 2k $\times$ 2k pixels CCD. Both channels have spatial resolution of 0.77 arcseconds, and are capable of observing down to a magnitude of 22.5 (M_V) in 100 s. Both the MXT and VT have been designed with matching sensitivites such that the majority of SVOM detected GRB afterglows should be observable with both instruments.

In addition to the onboard systems, the Ground-based Wide-Angle optical Camera (GWAC) will simultaneously observe 63% of the FOV of the ECLAIRs instruments in real-time. Consisting of 36 wide angle cameras, each is made up of 4k $\times$ 4k pixel CCDs with sensitivity in the 500 nm - 800 nm wavelength regime. GWAC will have its own trigger system, capable of sending out alerts via the Gamma-Ray Co-ordinates Network.

1.4.2 POLAR

POLAR (Produit et al., 2005) is a Joint European-Chinese space-based Compton Calorimeter, dedicated to observing the polarisation of GRB prompt emission. Potentially attached to the Chinese Tiangong 2 space station, POLAR carries the OBOX polarisation detector consisting of 25 detector modules, each of 64 units of low-Z plastic scintillators. Observing between 50 keV - 500 keV, POLAR will have a $70^\circ \times 70^\circ$ FOV (4.14 sr, $\sim$ 1/3 of the sky), and is predicted to observe $\sim$ 50 GRBs per year. The POLAR instrument is attached to the Chinese space-station Tiangong 2, and was launched on the 15th September, 2016; having passed the final calibration stage, POLAR has observed several GRBs which were simultaneously detected by other space-based observatories (Kole et al., 2016).

1.5 Gamma-Ray Burst Follow-up

To constrain models on Gamma-ray burst progenitors, their emission mechanisms, and the central engines powering them, both the aquisition of accurate GRB positional data, and the fast dissemination of the aforementioned data is required in order to allow other experiments to observe the rapidly fading phenomena (Fishman & Meegan, 1995). Direct observational data of GRB afterglows in lower energy regimes are not directly pertinent to this thesis however the determination of GRB redshifts by ground-based observatories allows for the correction of dust absorption on X-ray spectra, as well conversion of the observer-frame flux into rest-frame luminosities.

1.5.1 GRB Localisation

The Interplanetary Network

Constrained by its inability to focus Gamma-rays, the Vela satellite system utilised time delays between various spacecraft's signal detections to localise Gamma-ray emission to a series of annuli on the sky; combining all baseline annuli would produce an overlapped region to which the emission was localised. It was through this method that solar activity and near Earth sources were ruled out as origins of the first Gamma-ray bursts (Klebesadel, Strong & Olson, 1973) despite the large size of the error box. Assuming the distance between spacecraft was well-known, the width of each annulus was dependent on the distance of the baseline, the uncertainty in time-delay measurement, and the sine of the angle; with a high Earth, geocentric orbit of $\sim 120,000$ km, Vela's localisation errors were dominated by the short baselines. With the launch of later, dedicated, GRB missions (Helios-2, the PVO, Venera 11 & 12, Prognoz-7, and HEAO-2) significantly longer baselines were formed along the Earth-Venus-Sun triangle and the InterPlanetary Network (IPN) was formed. From initiation in 1978 to network degradation in 1980, the IPN detected and localised 84 Gamma-ray bursts with error boxes ranging from less than a square arcminute to over 1000 square degrees.

In 1990, the Ulysses spacecraft joined with the PVO, the only original member of the first IPN to still be in operation, and the IPN was reformed. This second iteration of the IPN has, to date, not broken temporal coverage as new missions such as the CGRO, Wind, RXTE, and BeppoSAX joined whilst original members were being decommissioned. Given the improvement in timing analysis and the large baselines available, the second iteration of the IPN typically localises GRBs to error boxes on the order of 1 square arcminute to 100 square degrees, depending on the number of spacecraft detections and the brightness of the burst (Hurley et al., 2013). Whilst in many cases the region is small enough that follow-up observation could have a high likelihood of detecting a GRB counterpart, the localisation analysis can be extremely time intensive; as such, few IPN GRBs have follow-up observations by ground-based observatories.

Contemporary GRB Localisation

Unlike Gamma-ray missions in the 1970s-1980s, later spacecraft were able to localise Gamma-ray emission through either: the deconvolution of a pre-known coded mask from the observed Gamma-ray image (IBIS/SPI, INTEGRAL; BAT, Swift); scintillation of incoming Gamma-ray photons and observation of the scattered photons (GBM, Fermi); and the utilisation of scintillating, or particle tracking, anticoincident devices (GRBM, BeppoSAX; WAM, Suzaku; LAT, Fermi) [9].

Point source localisation is determined by the combination of effective area, FOV, photon directional errors, exposure, source characteristics (brightness, background, and source spectrum), and spacecraft pointing precision. However, combining data from wide-field and narrow field instruments can improve precision. Swift, the most sophisticated GRB localisation platform currently in orbit, generally sees a reduction in the radius of a GRB error box from a few arcminutes to a few arcseconds by utilising the imaging mode of the Swift XRT, and the UVOT finding chart. This improvement sees a ground-based FOV crowded by potential host galaxies or uncataloged sources reduced to one that contains a few objects, significantly increasing the likelihood of finding a GRB counterpart. In a few cases there are several probable host galaxies after a refined position was distributed, highlighting the challenges involved with determining the redshift of GRBs (Levan et al., 2007).

1.5.2 The Gamma-Ray Co-ordinates Network

Like many space-based observatories, local storage on-board the CGRO was to be utilised before periodic information uploads to ground stations were required. On the order of days, this delay would have limited the ability of ground-based follow-up campaigns to detect GRB counterparts in other energy regimes. It was early into the mission however that the tape storage devices failed, resulting in the requirement of continuous real-time transmission of data from the CGRO to the ground via NASA's Tracking and Data Relay Satellites (TDRS). This failure led to an opportunity to develop a system to rapidly disseminate GRB positional notifications to other observatories, eventually leading to the creation of the BAtse COordinates DIstribution NEtwork (BACODINE). The delay from burst detection by BATSE to general notification was at most 5.5 seconds, allowing for follow-up observations whilst the GRB was still visibly bursting. Fast GRB localisation uploads were not limited to BATSE however; BeppoSAX, with it's ability to tightly localise GRBs to error boxes of a few square arcminutes, would upload data once per orbit, giving a reponse time of a few hours. Soon many ground-based observatories, keen to do optical follow-ups on GRBs, joined the network and BACODINE was renamed the

[9] For references to the instruments, see the mission descriptions in Sections 1.2, and 1.3; for references to the techniques, see Bloser et al., 2014; Caroli et al., 1987; Fenimore & Cannon, 1978; Garson et al., 2006; Johansson et al., 1980; Peterson, 1975; Poulsen et al., 2000; Renaud et al., 2006; Siegmund et al., 1981.

Gamma-ray burst Coordinates Network (GCN) in 1997.

The modern GCN consists of: several Gamma-ray and X-ray missions including the IPN, WIND (Konus instrument), INTEGRAL, Swift, AGILE, Fermi, MAXI, and CALET; as well as missions subscribing to the Transient Astronomy Network (TAN) including neutrino and gravitational wave detectors such as the IceCube neutrino observatory, and the Laser Interferometer Gravitational Observatory (LIGO). This combined network is able to disseminate positional, and observational data on GRBs (and other transient phenomena) in real-time (and near real-time) to subscribers of the network; for example, the median time delay between burst detection and optical follow-up for Swift, HETE-2, and BeppoSax were 15 minutes, 3.5 h, and 14 h respectively (Fiore et al., 2007). Follow-up by ground-based observatories are encouraged and their results are likewise posted via GCNs[10].

1.5.3 Ground-Based Observatories

Many ground-based observatories regularly perform follow up on the GRB trigger notices distributed via the GCN. These include: the large ($\geq$ 10 m) Keck, and Gran Telescopio Canarias (GTC) observatories; the medium-large ($\leq$ 10 m) Gemini North/South, Very Large Telescope (VLT), and Subaru observatories; the medium ($\leq$ 5 m) William Herschel Telescope (WHT), and Telescope Nazionale Galileo (TNG) observatories; and the small ($\leq$ 3 m) Nordic Optical Telescope (NOT), Faulkes North/South, and Liverpool robotic observatories. These telescopes are situated in both the northern, and southern hemispheres and are capable of performing deep photometry and spectroscopy in ultraviolet, optical, and near infrared regimes.

Photometric redshifts are often accompanied by large uncertainties unless significant features, such as the onset of a Lyman-α forest [11]. For the majority of GRBs with an observed optical afterglow, or a clear host galaxy, the redshift is determined via spectroscopy (see Figure 1.3 for the bandwidths of major GRB follow-up spectrom-

[10] GCNs come in two flavours: notices and circulars. Notices are posted when space-craft are observing GRBs (or other transients) whilst the object is active; circulars are follow-up observations of notices, and can originate from ground-based, as well as space-based, observatories

[11] The Lyman-α line arises from electron transition from the n=1 to n=2 energy level of a neutral hydrogen atom. If the emission from a source traverses numerous intervening clouds of neutral hydrogen before arriving at the observer-frame, an absorption line component from each individual cloud is observed, building up into a forest of redshifted Lyman-α lines.

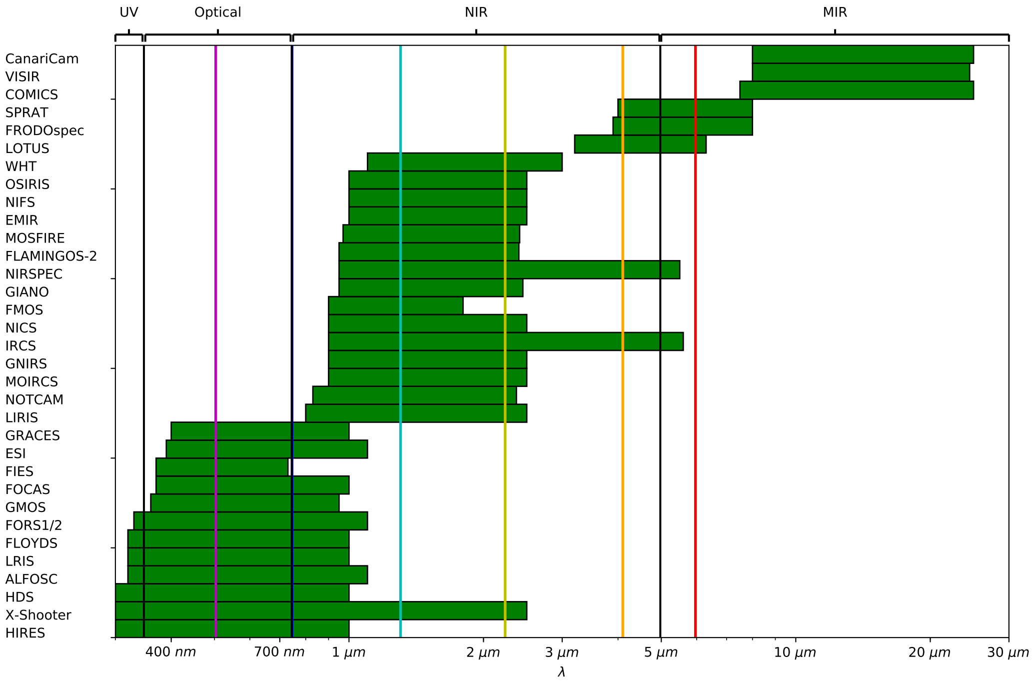

Figure 1.3: *The wavelength ranges of spectroscopic and photometric instruments (left labels) attached to major ground-based observatories (right labels) that regularly perform follow-up of GRB notifications. The coloured lines denotes the O[II]* 3727Å *line (a common, bright line seen in GRB afterglows, and host galaxies) redshifted to* $z = 0.35$ *(magenta),* $z = 1.0$ *(blue),* $z = 2.5$ *(cyan),* $z = 5$ *(yellow),* $z = 10$ *(orange), and* $z = 15$ *(red).*

eters; links to the major ground-based observatories are listed in Appendix I). In most cases where the resolving power of the spectrometers are high [12], and numerous spectral features are observed with high statistical significance, the derived redshifts are considered reliable. In some cases however, few spectral features are seen and redshifts derived from such spectra are taken with a hint of scepticism.

[12] The resolving power of the spectrometers, $R = \lambda/\Delta\lambda$, ranges from $R = 260$ (FORS1/2, VLT) to $R = 160,000$ (HDS, Subaru), where a larger resolving power allows for better definined spectral features; this however, often comes with the cost of reduced wavelength coverage.

1.6 The History of GRB Observation

1.6.1 Temporal, and Spectral Properties of GRBs

Fast spectral variability, and correlation between spectral hardness and intensity was observed by the Soviets' Venera-11, and Venera-12 satellites (Mazets et al., 1983), whilst hard-to-soft evolution of the GRB pulse spectrum was seen by Prognoz-7 (Barat et al., 1981a; Boer et al., 1986). The Japanese Aerospace Exploration Agency's (JAXA) Ginga satellite found soft X-ray emission at late times (Yoshida et al., 1989) whilst ISEE-3, Venera 11/12, HEAO-1, and Ginga found controversial evidence of spectral cyclotron, and annihiliation lines in the gamma-ray continuum (Barat et al., 1984; Fenimore et al., 1988; Hueter, 1984; Klebesadel, Evans & Laros, 1981; Mazets et al., 1981; Murakami et al., 1988; Teegarden & Cline, 1981). Temporally, millisecond time variability was observed by Vela (Klebesadel, Strong & Olson, 1973), and NASA's HEAO-1 (Knight, Matteson & Peterson, 1981); combined with the finite speed of information transfer, this provided an estimation on the size of the gamma-ray emission region, suggesting that GRBs originate from compact sources with radii of a few hundreds of kilometres [13], such as blackholes or neutron stars (Schmidt, 1978). It was further suggested, from observations by Venera, that there existed multiple sub-classes of GRBs: long duration, single pulsed; long duration, multiple pulses; and short duration single pulsed bursts (Mazets & Golenetskii, 1981).

Like earlier missions, BATSE observed incredible variability in the temporal profiles of GRB lightcurves. Four temporal profile classes were suggested, independant of burst duration: single pulse; single or multiple pulses with smooth, well defined peaks; bursts exhibiting distinct, separate espisodes of emission; and very erratic, chaotic and sharp bursts (Fishman, 1993). Initially only those bursts with a single peak were determined to have a Fast Rise Exponential Decay (FRED) pulse shape with hard-to-soft evolution of the spectrum (Bhat et al., 1994), however later studies showed that multi-peaked, messy lightcurves were made up of many pulses, often overlapping each other to a significant degree (Norris et al., 1996) and each exhibiting the same hard-to-soft evolution seen in the single pulsed classes, as well as a correlation between the pulse's peak energy, and its flux (Crider et al., 1999a,b).

[13] A time variability of $\Delta t = 1$ ms gives an upper limit to the radius of the source region, R, of 300 km where $R \leq c\Delta t$.

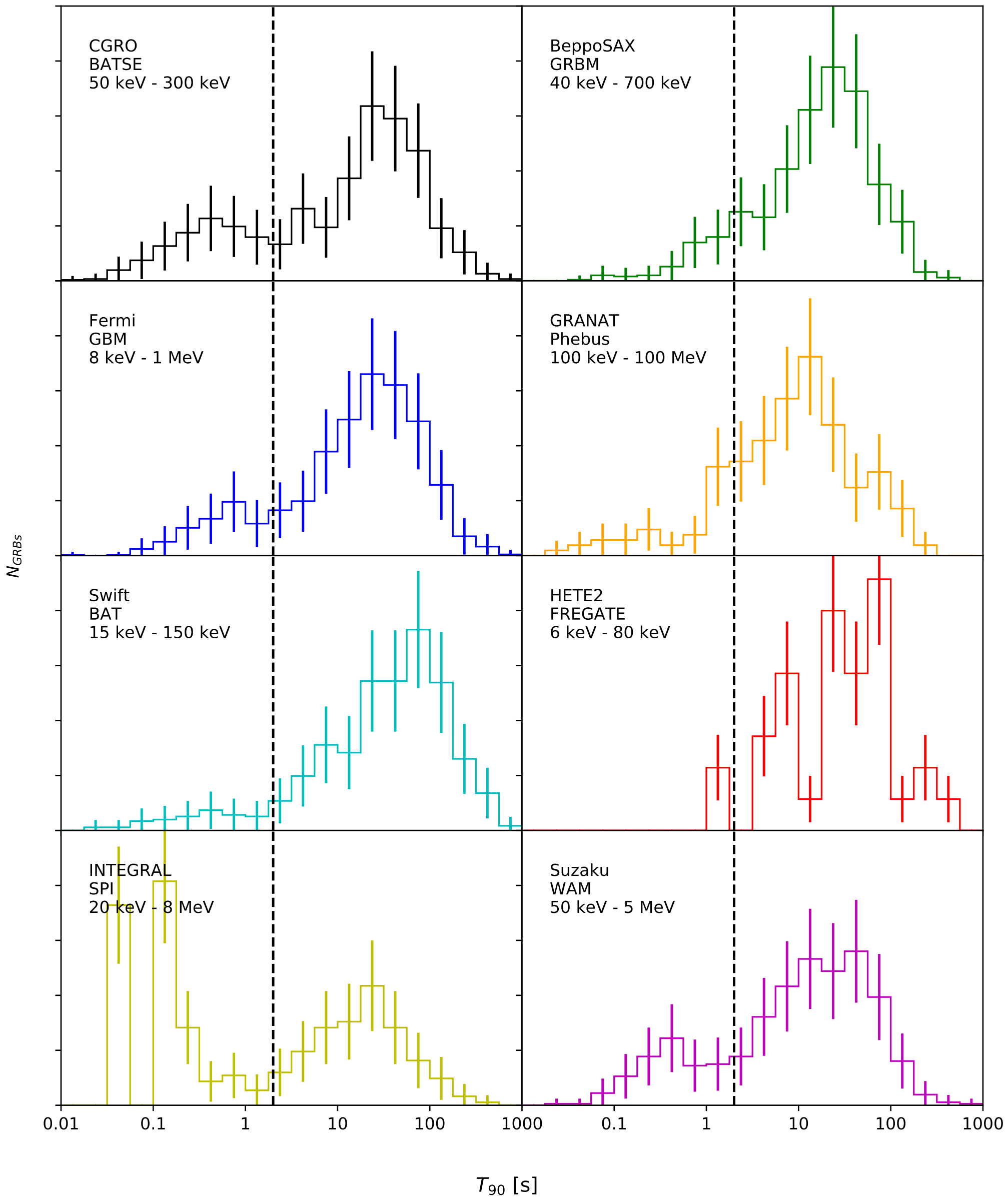

Figure 1.4: *The T_{90} distributions from CGRO/BATSE (black, Paciesas et al., 1999), BeppoSAX/GRBM (green, Frontera et al., 2009), Fermi/GBM (blue, Gruber et al., 2014; von Kienlin et al., 2014), Granat/Phebus (orange, Terekbov et al., 1995; Terekhov et al., 1994; Tkachenko et al., 2002, 1998), Swift/BAT (cyan, Donato et al., 2012), HETE-2/FREGATE (red, Barraud et al., 2003), INTEGRAL/SPI (yellow, Rau et al., 2005), and Suzaku (magenta, `http://www.astro.isas.jaxa.jp/suzaku/HXD-WAM/WAM-GRB/`). A bimodal population is clearly seen in several instruments with a delimiter at $T_{90} = 2$ seconds (dashed black line), with some overlap between (Kouveliotou et al., 1993). Histograms are normalised for ease of comparison between missions with quoted errors representing bin counting errors and do not take into account the intrinsic measurement errors.*

From data released in the first BATSE GRB catalogue (1B) (Fishman et al., 1994), a new definition for GRB duration, T_{90} [14], was calculated by Kouveliotou et al. (1993). Using the distribution of T_{90}, in combination with the spectral hardness [15], Kouveliotou et al. (1993) showed the presence of a bimodal GRB population of spectrally hard, short GRBs ($T_{90} \leq 2$ seconds); and spectrally soft, long GRBs ($T_{90} \geq 2$ seconds, see Figures 1.4 & 1.6). A third group of spectrally soft, intermediate brightness, and duration GRBs has also been proposed (Horváth, 1998; Mukherjee et al., 1998) however this was more controversial than the bi-modal model. The strong overlap between the two distributions (see Qin et al., 2013) lead to the suggestion that the current T_{90} descriminator is imprecise, leading to contamination of samples by the tails of the other distribution (Bromberg et al., 2013; Lü et al., 2014); such alternatives have however made little traction into replacing the current paradigm.

The T_{90} distributions of instruments like BATSE showed a clear bimodality, with approximately 25% of BATSE GRBs being classified as short; a phenomena also seen in other broadband missions such as Suzaku, and INTEGRAL (see Figure 1.4). The softness of Swift's BAT passbands (15 keV - 150 keV) in comparison to BATSE's (50 keV - 300 keV), coupled to the inverse relationship between the image trigger of the BAT and the fluence of the burst (short GRBs are typically fainter than long GRBs), lead to a smaller percentage of Swift GRBs being classified as short ($\sim$ 10%). The 'short, hard' and 'long, soft' distributions seen in the BATSE duration vs. hardness diagram are arguably present in those of Swift (see Figure 1.6), however the softness of the Konus Wind, Fermi, and Swift SGRB samples suggests that the observed hardnesses of BATSE SGRBs are a detector selection effect (Sakamoto et al., 2006, 2011b), with Swift LGRBs initially having the same hardness as SGRBs in the first 1 s before softening (Ghirlanda, Ghisellini & Celotti, 2004).

The time integrated spectra of BATSE GRBs showed a distinct, non-thermal, profile with few features [16], and little variation in shape between bursts and were well fitted

[14]The duration T_{90} covers 90% of the cumulative counts detected starting from 5% and finishing at 95%. The more rarely mentioned duration, T_{50}, follows the same procedure but starts at 25% and terminates at 75%.

[15]Spectral hardness for BATSE was defined as the ratio of the fluence in the 100-300 keV over 50-100 keV passbands

[16]The presence of spectral lines, as observed by ISEE-3, Venera 11/12, HEAO-1, and Ginga, in the Gamma-ray spectra of GRBs were not conclusively proven by BATSE; some observations suggested spectral line detection (Palmer et al., 1994), whilst others found no evidence for it (Briggs et al., 1998).

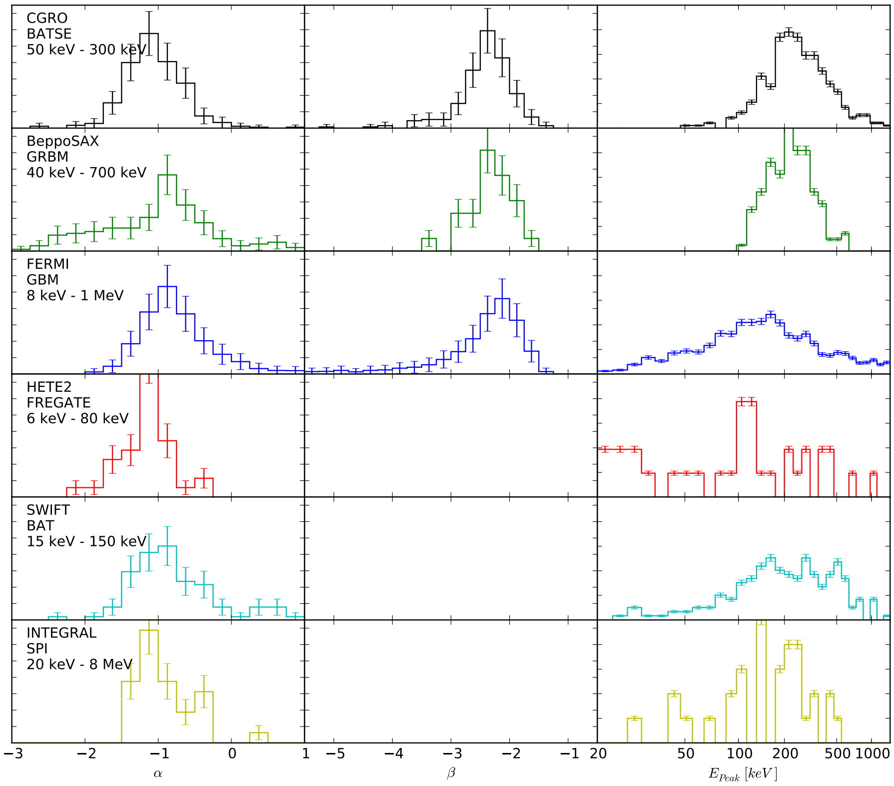

Figure 1.5: *The distributions of the best fit spectral parameters for CGRO/BATSE (black, Kaneko et al., 2006; Preece et al., 2000), BeppoSAX/GRBM (green, Guidorzi et al., 2011), Fermi/GBM (blue, Gruber et al., 2014; von Kienlin et al., 2014), HETE-2/FREGATE (red, Barraud et al., 2003), Swift/BAT (cyan, Donato et al., 2012), and INTEGRAL/SPI (yellow, Bošnjak et al., 2014). Several models are fitted including the Band function, a single power-law, a smoothed broken power-law, and a Comptonised model, depending on the passband of the instrument and optimum model selection.* α*, and* β *represent the low, and high energy indexes respectively with* E_{Peak} *repesenting the peak of the* νF_ν $(E^2N(E))$ *spectrum. The CGRO/BATSE spectral parameters quoted are for 350 of the bightest BATSE GRBs, whilst all other instrument's fitted spectra have no such selection bias. Histograms are normalised for ease of comparison between missions with quoted errors representing bin counting errors and do not take into account the intrinsic measurement errors.*

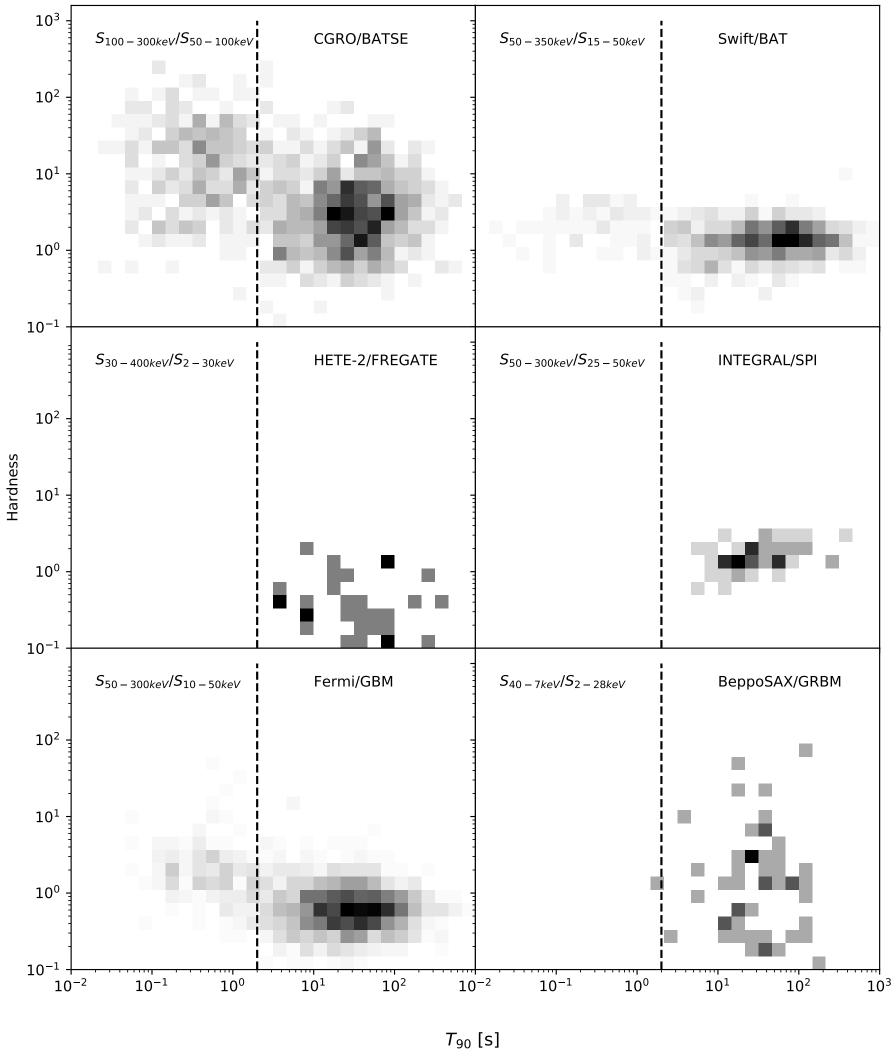

Figure 1.6: *The observed T_{90} vs. spectral hardness (defined as the ratio of the fluences of the high-energy and low-energy passbands) distributions for the CGRO/BATSE (top-left), Swift/BAT (top-right), HETE-2/FREGATE (middle-left), INTEGRAL/SPI (middle-right), Fermi/GBM (bottom-left), and BeppoSAX/GRBM (bottom-right) instruments; the T_{90} data is taken from references in Figure 1.4, and is binned for a 2D histogram in an arbitrary 1/6 dex. A bimodal GRB population is seen of 'short, hard' (short GRBs, SGRBs), and 'long, soft' (long GRBs, LGRBs) bursts, delimited at a T_{90} of 2 seconds (dashed line, Kouveliotou et al., 1993), by BATSE; however such a clear separation is not seen by the other instruments/missions.*

by the empirical Band model (Band et al., 1993); in some cases single power-laws, smoothed power-laws, and Comptonised models were also appropriate and optimum models were selected based on improvements to various statistical measures. For the Band model, the number of photons per energy bin, $N(E)$, is given by:

$$N(E) = A \begin{cases} \left(\frac{E}{100keV}\right)^{\alpha} \exp\left(-\frac{E}{E_0}\right) & E \leq E_0(\alpha-\beta), \\ \left(\frac{E}{100keV}\right)^{\beta} \exp(\beta-\alpha) \left[\frac{E_0(\alpha-\beta)}{100keV}\right]^{\alpha-\beta} & E \geq E_0(\alpha-\beta); \end{cases} \tag{1.1}$$

where α, and β are the low, and high energy indexes respectively, and E_0 is the pivotal, or turnover energy. The break energy is given by $E_{Break} = E_0(\alpha - \beta)$ whilst the peak energy of the νF_ν [17] ($E^2N(E)$) spectrum is given by $E_{Peak} = E_0(2+\alpha)$. Typical fitted spectral parameters for the brightest BATSE bursts were of: $\alpha \sim -1.1$, $\beta \sim -2.2$, $E_{Break} \sim 246$ keV, and $E_{Peak} \sim 281$ keV (Kaneko et al., 2006; Preece et al., 2000). A subgroup of GRBs were observed by BATSE, BeppoSAX, and HETE-2 with lower peak energies in their ($E^2N(E)$) spectrum (Barraud et al., 2003; Heise et al., 2001; Kippen et al., 2003; Sakamoto et al., 2005). Initially considered a separate population, and termed as X-Ray Flashes (XRFs), these particular bursts showed similarity to the more energetic, classical GRB; with no clear difference between their characteristics, it is however, suggestive of a single population of GRBs with a continuum of parameters wider than initially thought (Granot, Ramirez-Ruiz & Perna, 2005).

1.6.2 Spatial Properties of GRBs

Whilst there was a wealth of highly precise spectral and temporal data, early GRB missions lacked gamma-ray imaging capabilities and therefore were unable to precisely localise the source of gamma-ray emission on-sky. Using triangulation techniques (see Section 1.5.1), a 2-satellite constellation could localise the source of Gamma-ray emission to a large circle on the celestial sphere; the addition of more satellites to the network would reduce this area to a series of overlapping annuli, albeit with large uncertainties. This poor, early localisation, coupled to a small sample size, initially lead to the assertion that gamma-ray bursts were galactic in origin, otherwise the energy budget required would be unprecedented (Fishman et al., 1978;

[17] F_ν is the spectral flux density, and is given in units of energy per unit time per unit area over a certain passband.

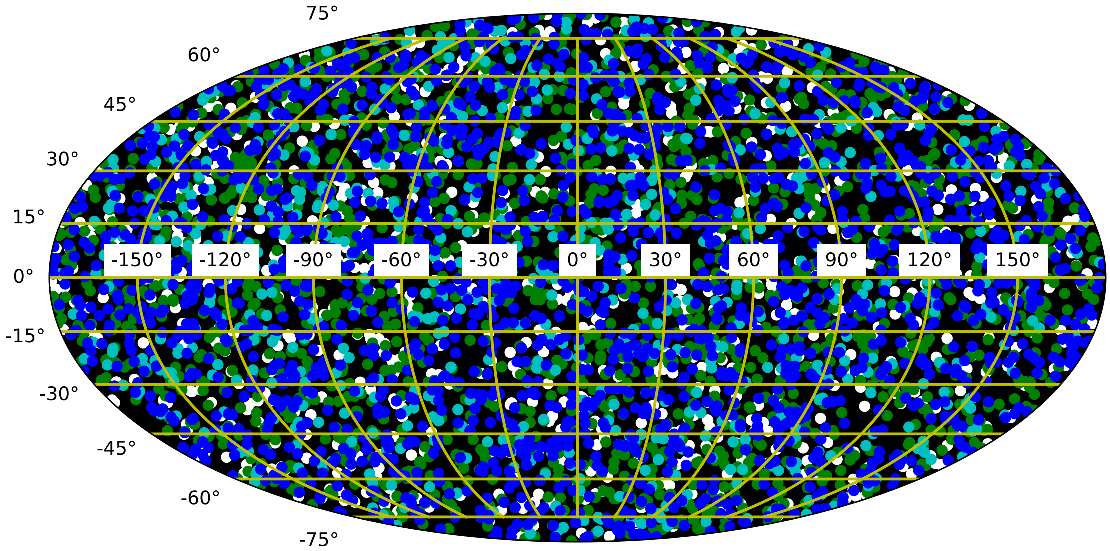

Figure 1.7: *The all-sky distribution of 1,637 BATSE GRBs (white, Paciesas et al., 1999), 1,082 BeppoSAX GRBs (green, Frontera et al., 2009), 872 Swift GRBs (cyan, Donato et al., 2012), and 1818 Fermi GRBs (blue, Gruber et al., 2014; von Kienlin et al., 2014) shown on a Mollweide projection with Galactic co-ordinates.*

Schmidt, 1978). This theory was corroborated by data from the Soviets' Venera satellites (Mazets & Golenetskii, 1981), however observations by NASA's Helios-2 satellite instead found that the spatial distribution of gamma-ray bursts suggested either an extremely close by, or extra-galactic isotropic source distribution (Cline et al., 1979).

It was NASA's PVO that first found a counterpart object to a gamma-ray burst: that of supernova remnant N49 in the Large Magellanic Cloud (LMC) with GRB 790305 (Evans et al., 1981). After many subsequent GRBs were localised to the same source, that of pulsar PSR B0525-66, it was reclassified as a soft gamma-ray repeater and not a gamma-ray burst. During this time Paczynski (1986) proposed a cosmological origin for gamma-ray bursts, requiring an isotropic energy release on the order of 10^{51} ergs s^{-1}: similar to the energy released during a supernova, but on shorter timescales. The astounding energy requirements for Paczynski's theory lead many to prefer the galactic origin theory and soon it was suggested that the GRB formation rate was consistent with that of a galactic population of neutron stars at distances between 0.15 and 2 kpc (Hartmann, Woosley & Epstein, 1990).

It was apparent almost immediately from analysis of the first 153 GRBs detected by

BATSE that the angular distribution of GRBs was isotropic, or very near isotropic (Meegan et al., 1992). By the inception of the BATSE 4B catalogue (Paciesas et al., 1999) there was visually little or no deviation from isotropy. As more GRBs were observed however, separate statistical analysis of short, intermediate, and long GRBs indicated that short and intermediate GRBs were distributed anisotropically (Balazs, Meszaros & Horvath, 1998; Balázs et al., 1999; Litvin et al., 2001; Magliocchetti, Ghirlanda & Celotti, 2003; Mészáros et al., 2000; Vavrek et al., 2008) whilst long GRBs, which made up the majority of BATSE bursts, were consistent with a random distribution (Balazs, Meszaros & Horvath, 1998; Balázs et al., 1999; Vavrek et al., 2008). Although short and intermediate GRBs had an element of anisotropy, they were not consistent with a distribution expected were the sources Galactic in origin; a near-Sol System or Galactic halo origin however were not entirely ruled out. The precise angular localisations of GRBs observed by Swift, BeppoSAX, and Fermi showed clear isotropy (see Figure 1.7), supporting the evidence provided by BATSE, and Helios-2 that GRBs were cosmological in origin, rather than Galactic; a question which had been answered by the first measured redshift of a GRB afterglow (see Section 1.5.3).

Although a significant improvement over the capabilities of early missions, the $\sim 1.5 - 13°$ (Meegan et al., 1993) angular precision BATSE could achieve severely limited the ability of ground-based follow-up observations to measure distances to the sources. Despite uncertainty as to the true spatial distribution of GRBs, the deviation from homogeneity could be evaluated; a spatial distribution that was truely uniform in the local, Euclidian, Universe would produce a relationship between the integrated number of bursts, N, and the peak flux, P, such that $N(P) \propto P^{-3/2}$. The BATSE log(N)-log(P) distribution, spanning 5×10^{-8} to 1×10^{-3} ergs s^{-1} cm^{-2}, showed that the brightest GRBs followed a power-law with index of $-3/2$, consistent with the data from the PVO (see Figure 1.8). There was significant deviation from homogeneity by the faintest, and therefore furthest, gamma-ray bursts (Fenimore et al., 1993): an outcome consistent with that of the Galactic origin theory. Statistical analysis into the homogeneity of the flux distribution using the V/V_{max} metric (Schmidt, 1968) revealed that for all missions, and GRB types (long or short) the distribution was non-homogeneous ($\langle V/V_{max}\rangle \leq 1/2$) (Guetta & Piran, 2005; Guetta, Piran & Waxman, 2005; Terekhov et al., 1994). The angular distribution of the weakest [18], and the brightest GRBs, showed angular isotropy in

[18] GRBs with peak flux below the break in the BATSE log(N)-log(P) distribution.

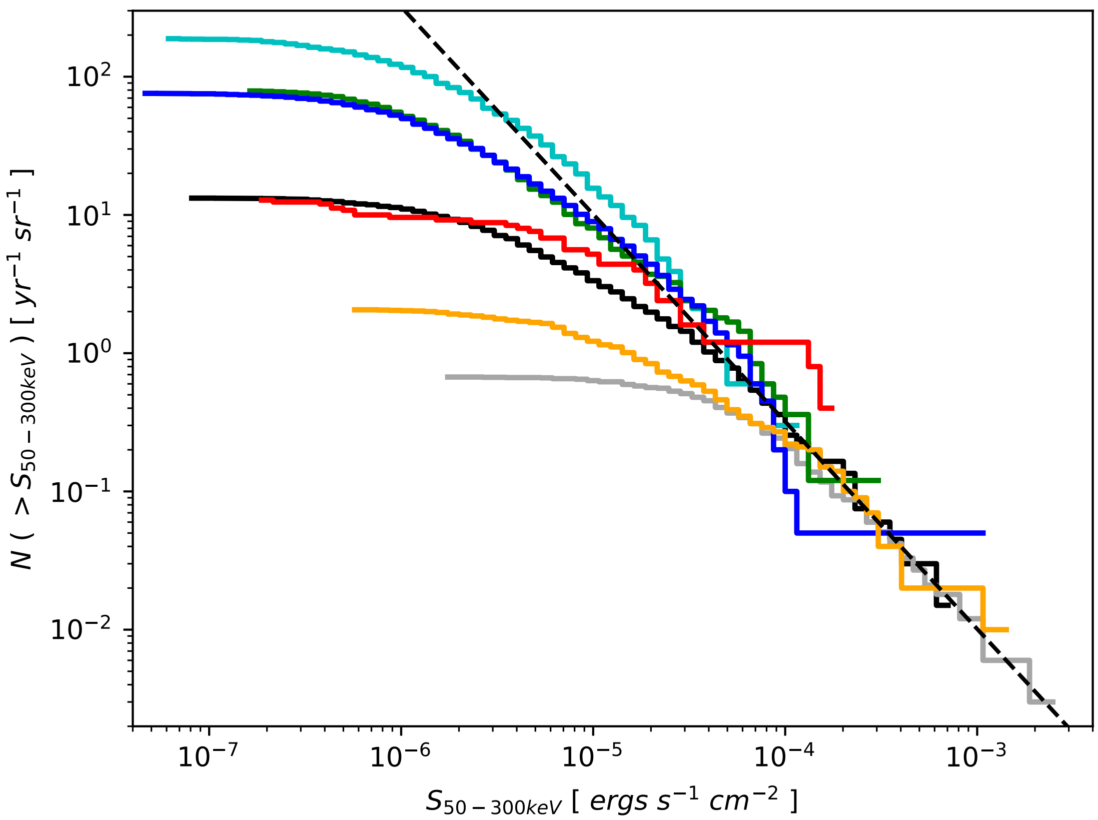

Figure 1.8: *The log(N)-log(S) distribution of long GRBs detected by CGRO/BATSE (black), GBM/Fermi (blue), BAT/Swift (cyan), OGBD/PVO (grey), GRBM/BeppoSAX (green), Phebus/Granat (orange), and FREGATE/HETE-2 (red). The non-BATSE log(N)-log(S) distributions have been normalised to the BATSE high-fluence tail for ease of comparison. The dashed line denote the expected power-law relation of index* $-3/2$.

contradiction to Galaxy disk models (Mao & Paczynski, 1992), in agreement with those models invoking cosmological origin.

1.6.3 Afterglow, and Redshift Properties of GRBs

In order to determine the progenitors of gamma-ray bursts, astrophysicists sought to detect X-ray, or optical counterparts to the observed gamma-ray emission. On the 28^{th} February, 1997, BeppoSAX detected a rapidly fading counterpart to GRB 970228 (Costa et al., 1997) after slewing to the source within a few hours of detection by the GRBM; this fading X-ray "afterglow" followed a power-law temporal decay in the observed flux with $F(t) \propto t^{-1.3\pm0.1}$ (Costa et al., 1997). The rapid dissemination of precise on-sky coordinates allowed for ground-based observation that soon lead to the discovery of an optical afterglow counterpart (van Paradijs et al., 1997), and a few days later, the appearance of a bump in the optical and near infra-red (NIR) spectrum, intepreted as an underlying supernova [19] (Galama et al., 2000). The first evidence of the GRB-supernova relationship was provided by the observation of supernova 1998bw in the errorbox of GRB 980425 (Galama et al., 1998a); the spectral features of 1998bw suggested a extremely bright supernova whilst the isotropic luminosity of the GRB was orders of magnitude fainter than the majority of long GRBs (Frail et al., 2001). Other evidence of the GRB-SN connection was seen with a supernova bump in the late time optical afterglow of GRB 980326 (Bloom et al., 1999), and the discovery of supernova 2003dh after the bright optical afterglow of GRB 030329 had faded (Hjorth et al., 2003; Stanek et al., 2003). The optical lightcurves of supernova 2003dh suggested that the GRB progenitor was a main sequence star of mass $25 \leq M_{\odot} \leq 40$ (Deng et al., 2005). GRBs were later found to have optical emission during the prompt phase (GRB 990123, Akerlof et al., 1999), whilst the detection of a radio afterglow component of GRB 970508 (Frail et al., 1997), in combination with X-ray, optical, and NIR detections, supported the theory that GRB afterglow emission was driven by synchrotron emission from electrons in a relativistically expanding outflow (Frail et al., 1997; Galama et al., 1998b; Goodman, 1997). Further associations of GRBs and supernovae include: GRB 031203, SN 2003lw (Malesani et al., 2004); GRB 060218, SN 2006aj (Campana et al., 2006a); GRB 100316D, SN 2010bh (Starling et al., 2011); GRB 120422A, SN 2012bz (Melandri et al., 2012; Wiersema et al., 2012); and GRB 130702A, SN 2013dx (D'Elia et al., 2015; Toy et al., 2016).

With the rapid acquisition of GRBs after the BAT trigger by the XRT, the relationship between the prompt Gamma-ray emission and the X-ray afterglow was revealed. The early X-ray decay phase of Swift GRBs (see Figure 1.9) was shown to be the fading X-ray component of the prompt emission before the X-ray afterglow began to dominate (Barthelmy et al., 2005b; O'Brien, 2006). The discovery of X-ray flares within XRT lightcurves raised questions as to how long the underlying central engine remained active. Correlations between the brightness of the BAT prompt emission and XRT flares indicated a common origin for the two pulse types (Margutti et al., 2010); whilst all X-ray flares could be explained via prolonged in-

[19] GRB 970228 was not the first burst with which a supernova signal was detected but was chronologically the earliest.

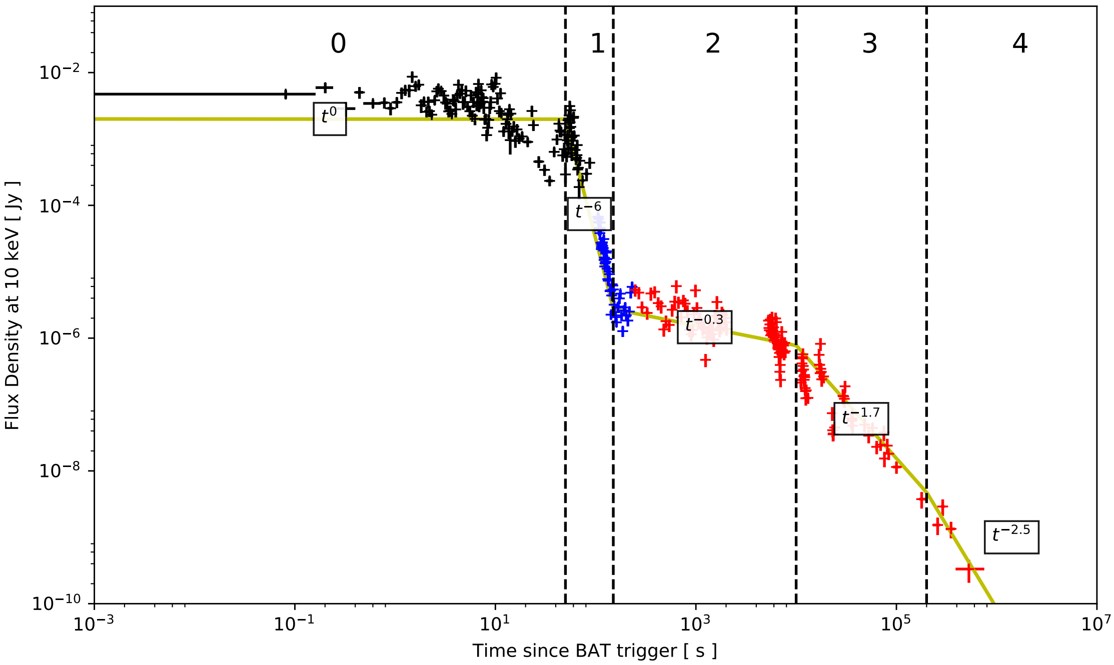

Figure 1.9: *The lightcurve of GRB 070420 (z=3.01, derived from photometric observations of UVOT images; Oates et al., 2009), overlaid by power-laws highlighting the slopes of the various canononical stages of the 0) GRB prompt emission; and afterglow phase: 1) the steep decay phase arising from the X-ray tail of the BAT prompt emission; 2) the plateau phase; 3) the normal decay phase; and 4) a post jet-break phase (Nousek et al., 2006). Whilst the afterglow is believed to have arisen from external shocks, the central engine may still be active over longer durations; some X-ray flaring can be seen in all stages of the X-ray afterglow (for example see GRB 061121 Page et al. 2007), that is consistent with the internal shock model, albeit at lower energies (see for example bottom left panel, Figure 1.12; GRBs 121027A, and 060218. The post jet-break phase is not always evident in GRB lightcurves, and occurs when the beaming angle, σ_{beam} becomes larger than the jet collimation angle σ_{jet}. Colours represent BAT data (black), XRT window timing data (blue), and XRT photon counting data (red).*

ternal engine activity, a significant proportion could also be explained via refreshed, internal, shocks (Chincarini et al., 2010, 2007).

The breakthrough moment in the cosmological vs. galactic origin argument arrived with the observation of long duration burst 970508. Like GRB 970228, it was found to have an optical afterglow; with absorption lines of Fe II, and Mg II it was placed at a redshift of $0.835 \leq z \leq 2.3$ [20] (Metzger et al., 1997) and was

[20] A redshift of $0.835 \leq z \leq 2.3$ equates to the progenitor explosion occuring between 10.836 to 11.549 Gyrs ago, with a lower limit on the isotropic energy release in Gamma-rays as $E_{iso} = 7\times10^{51}$ ergs s^{-1}.

clearly cosmological in origin. When the optical afterglow faded, a host galaxy was observed with redshifted emission lines of O II, and Ne III at $z = 0.835$ (Bloom et al., 1998). The short duration burst 050709, observed by HETE-2 (Butler et al., 2005), and Chandra (Frail, 2004), was found to have a redshift of $z = 0.16$ (Price, Roth & Fox, 2005) and was associated with a irregular star-forming galaxy; given the low rate of star formation in the host galaxy, young stellar progenitors for short GRBs were ruled out, suggesting that degenerate binaries were the preferred central engines (Fox et al., 2005; Villasenor et al., 2005). By the end of the BeppoSAX era, 90% of GRBs showed the presence of clear X-ray afterglows; however only in 50% of GRBs were optical afterglows seen (De Pasquale et al., 2003; Vedrenne & Atteia, 2009): so called 'dark' bursts. The vivacity of classifying a GRB using the long/short paradigm has been called into question since the determination of GRB redshifts; the duration in the observer-frame of a GRB is not trivially linked to an intrinsic GRB property, and due to cosmological time-dilation, will be different to the duration in the source rest-frame (e.g. GRB 090429B, $z = 9.4$, $T_{90}^{obs} = 5.5$ s, $T_{90}^{rest} = 0.53$ s). Evidence suggests that up to a certain redshift, the T_{90} duration of Swift GRBs increases in line with the $z + 1$ time-dilation relation; however for bursts with $z > 6$ such a relation is no longer true, with the population appearing to have a shorter rest-frame duration than expected (Littlejohns et al., 2013).

The rapid dissemination of precise on-sky co-ordinates to ground-based observatories lead to a significant proportion of Swift GRBs having an associated redshift. From mission launch to the 17^{th} of April, 2016, there have been 1,043 GRBs observed by Swift; 328 of which have a redshift measure (see Figure 1.10), leading to a redshift completeness of $\sim 1/3$. The pre-Swift distribution of redshifts peaked at significantly lower redshifts than their Swift contemporaries, with the average pre-Swift burst occuring at $\bar{z} \sim 1.3$ (Bagoly et al., 2006a,b; Jakobsson et al., 2006b). Of the 328 Swift GRBs, 21 have been SGRBs ($\bar{z}_{SGRB} = 0.76$); whilst the remaining 307 LGRBs are, on average, at a higher redshift of $\bar{z}_{LGRB} = 2.14$. This significant discrepency between the average redshift of pre-Swift and Swift GRBs arises from the greater sensitivity of the Swift BAT over instruments onboard HETE-2, and BeppoSAX (Gehrels, Ramirez-Ruiz & Fox, 2009).

The utilisation of GRBs as indicators of cosmic evolution in star-formation rates and metallicity, or as probes of cosmological parameters, comes with the understanding that an unbiased redshift dataset, representative of the true GRB population, is required. Many studies apply parameter cuts to the detected GRB population to

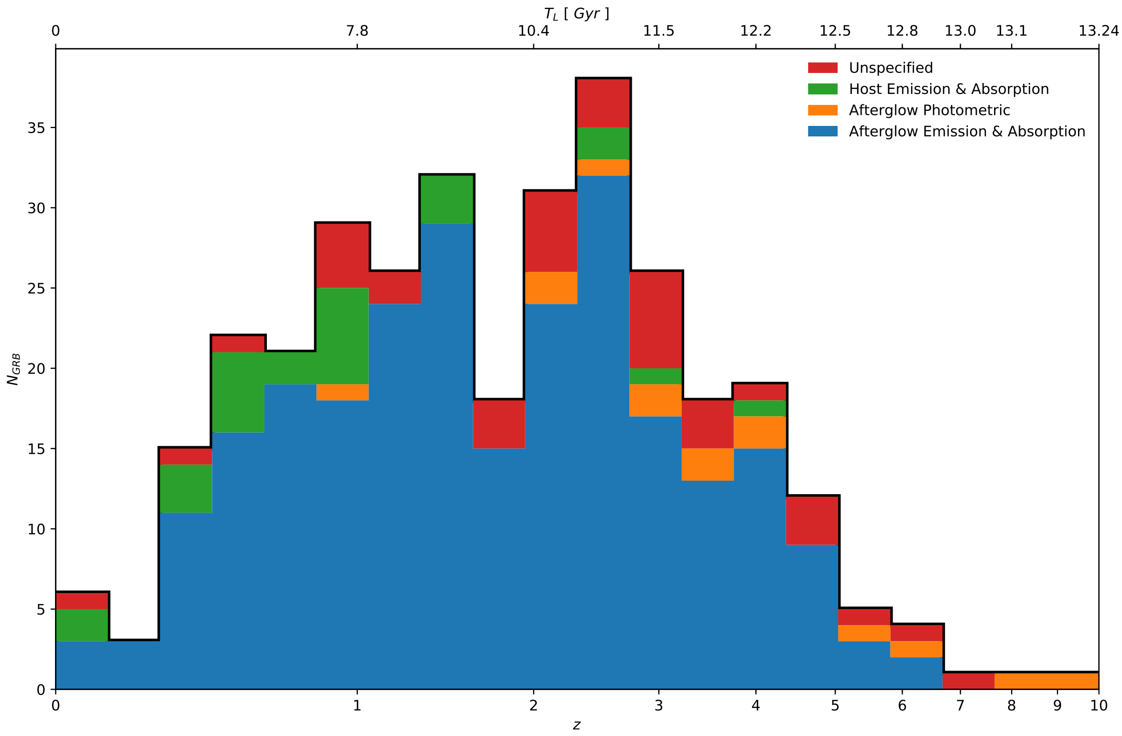

Figure 1.10: *The redshift distribution of 328 Swift observed GRBs with colours representing the method of redshift determination (see Appendix I for links to data). The solid black line traces the total number of GRBs per redshift bin. The current record holder for highest redshift GRB belongs to 090429B (*$9.06 \leq z \leq 9.52$*, Cucchiara et al., 2011), whilst the closest GRB is the non-Swift burst 980425 (*$z = 0.0085$*, Tinney et al., 1998).* T_L *is the light travel time, and is calculated assuming a flat* ΛCDM *with* $H_0 = 69.9$ *km* s^{-1} *Mpc*$^{-1}$*, and* $\Omega_m = 0.286$*.*

obtain smaller datasets which can be said to represent the unbiased GRB parent population to a greater level of completeness. The application of a T_{90} cut is an example of bias control at its most simplistic: short GRBs occur at lower redshifts than long GRBs and the progenitor channels differ. More sophisticated models may include peak flux cuts, or incorporate optimum ground-based follow-up observing conditions (see for example Jakobsson et al. 2006a). The BAT 6 year survey (BAT6; Salvaterra et al. 2012), Swift Gamma-Ray Burst Host Galaxy Legacy Survey (SHOALS; Perley et al. 2016a), and The Optically Unbiased GRB Host Survey (TOUGH; Hjorth et al. 2012) are examples of bias correction at its most complex, involving over a dozen GRB parameters that reduce the parent population of several hundred GRBs with observed redshifts down to a (mostly) unbiased sample of ~ 50 GRBs (see Figure 1.11).

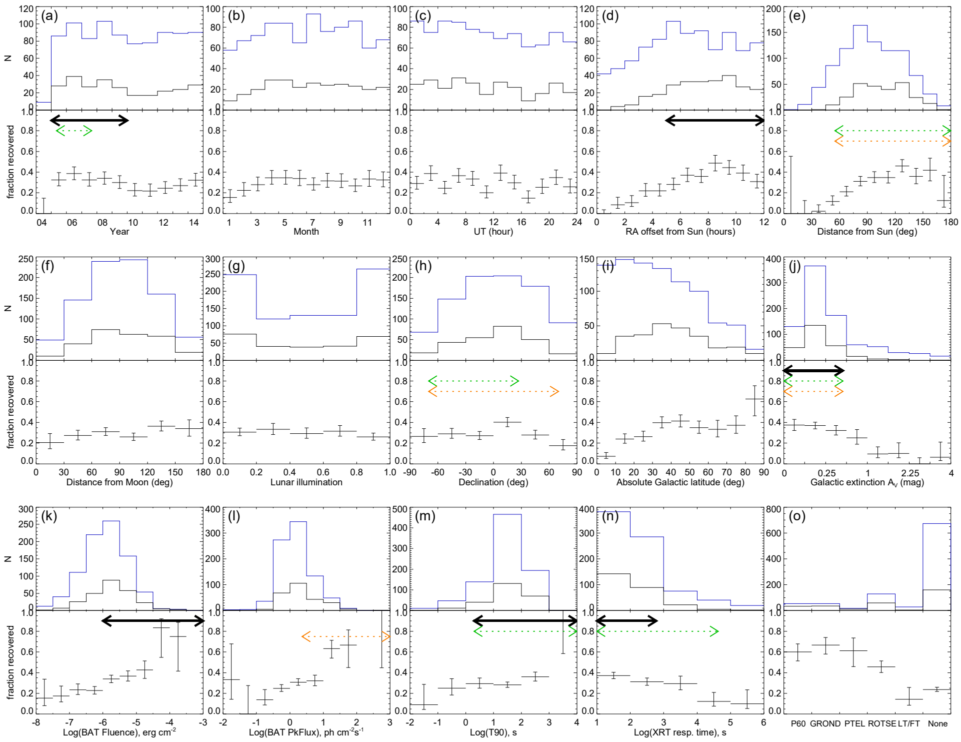

Figure 1.11: *Redshift recovery numbers and fractions for GRBs as a function of various observational parameters. Redshifts quoted are from GRB afterglows with rapidly observed spectroscopic redshifts rather than late time host galaxy surveys. Blue, and black histograms indicate all triggered Swift GRBs, and Swift GRBs with a known redshift respectively; the lower panels show the ratio of the two. Observational parameters are: (a) year, (b) month, and (c) hour of burst; (d) RA, and (e) angular offsets from the sun; (f) angular distance from Moon; (g) Lunar illumination; (h) declination, and (i) Galactic latitude; (j) Galactic extinction; (k) BAT fluence; (l) BAT peak flux; (m) burst* T_{90}*; (n) XRT response time; and (o) recovery rate of ground-based GRB follow-up (the Palomar 60-inch telescope, P60; the Gamma-Ray Burst Optical/Near-infrared Detector, GROND; the Peters Automated Infrared Telescope, PAIRITEL; the Robotic Optical Transient Search Experiment, ROTSE-III; and the Faulkes/Liverpool telescopes). Observational parameter cuts employed by SHOALS (black arrows), TOUGH (green arrows), and the BAT6 (orange arrows) surveys are indicated. Figure is taken from Perley et al. 2016a.*

1.6.4 Host Galaxy Properties of GRBs

The conjecture that short GRBs were related to galaxies or regions with low star-formation were verified by observations of short GRBs 050509B (Bloom et al., 2006; Gehrels et al., 2005; Hjorth et al., 2005), and 050724 (Barthelmy et al., 2005c; Berger et al., 2005) occuring in similar galaxy types to that of GRB 050709. Long GRBs were shown however to belong to galaxies or regions with active star-formation [21] and low-metallicity (Bloom et al., 1998; Bloom, Kulkarni & Djorgovski, 2002; Christensen, Hjorth & Gorosabel, 2004; Djorgovski et al., 1998; Fruchter et al., 2006, 1999; Graham & Fruchter, 2013; Svensson et al., 2010), with some LGRBs found in high-metallicity environments (Levesque et al., 2010a,b). Typically short GRBs are found to be at large offset from the centre of the host galaxy, ranging from 1 kpc to 75 kpc (Berger, 2010; Fong, Berger & Fox, 2010); although it has been proposed that there exists a population of SGRB progenitors that have been kicked from the host galaxy (Bloom, Sigurdsson & Pols, 1999; Grindlay, Portegies Zwart & McMillan, 2006; Tunnicliffe et al., 2014). Long GRBs, in contrast, appear to have a small offset of up to 7 kpc (Bloom, Kulkarni & Djorgovski, 2002), with 90% of LGRBs occuring within 5 kpc of the centre, correlating to the brightest regions of host galaxies (Blanchard, Berger & Fong, 2016). Given the more massive host galaxies in which SGRBs occur, translating the physical offset into a distribution normalised by the size of the host galaxy produces nearly identical distributions.

1.7 The Current Paradigms of Gamma-Ray Bursts

Taken individually, the features observed within the prompt emission may appear as part of a smooth continuum despite having arisen from GRBs with very different progenitor models. The presence of multiple classes of GRBs (see Figure 1.12 for example lightcurves), as discussed in the previous section, become clear however when comparisons are made between other instrinsic qualities of the lightcurves. The "short-hard"/"long-soft" correlation observed by Kouveliotou et al. (1993) is the first example of such a relationship, and is still popular as the primary discriminator of GRB classes to date. The discovery of GRBs that exhibit properties that diverge noticibly from the norm of the parent population, and/or share properties from both

[21] Typical LGRB host galaxies were shown to have star-formation rates an order of magnitude greater than host galaxies of SGRBs (Berger, 2009).

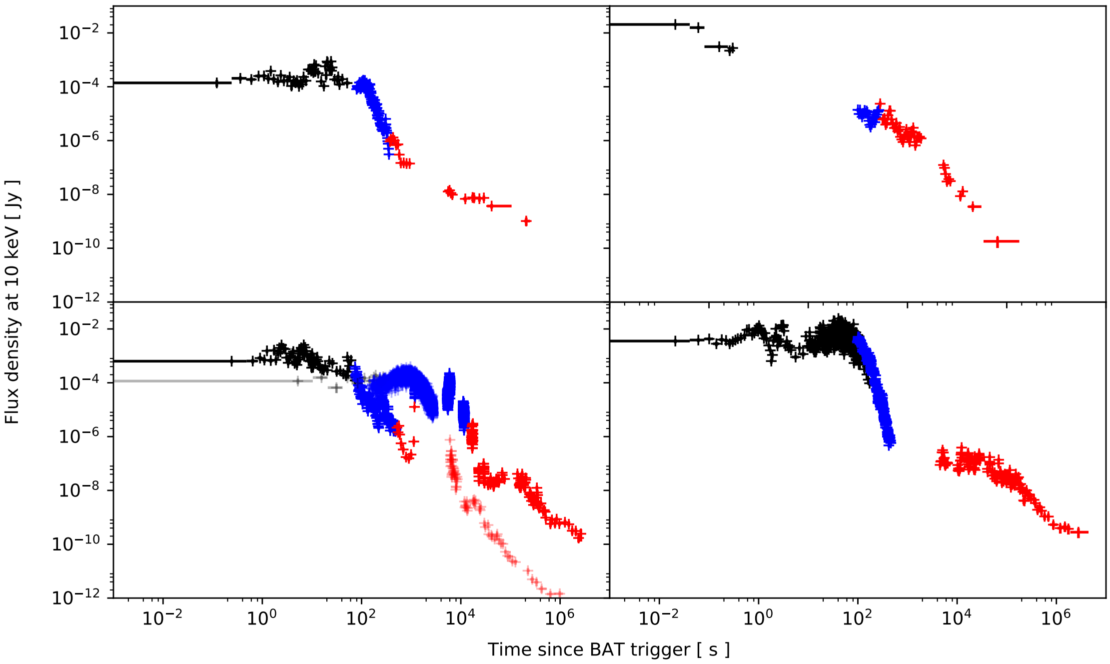

Figure 1.12: *Swift detected lightcurves from the various taxonomies of GRBs. Example GRBs include a classically long GRB (GRB 151111A; top left; z=3.35); a classically short GRB (GRB 090510; top right; z=0.903); a low-luminosity long GRB (GRB 060218; bottom left; high-transpacency data; z=0.0334); a ultra-long GRB (GRB 121027A; bottom left; low-transpacency data; z=1.773); and an extended emission short GRB (GRB 060614; bottom right; z=0.1257). Colours represent BAT data (black), XRT window timing data (blue), and XRT photon counting data (red).*

major GRB classes has, however, led to the requirement of classification systems with greater finesse; GRBs are now predominantly classified depending on a wide variety of prompt, afterglow, and host galaxy parameters rather than by duration alone. A formal classification system has been proposed, that of Type I, and Type II GRBs [22] (Gehrels et al., 2006; Zhang, 2006); however, such a system requires a great deal more information than the easily observable T_{90}-hardness distribution and has seen a generally slow uptake in usage.

The correlations shown in Figure 1.13 are an example of some of the most commonly discussed relationships observed in GRB prompt emission. Outside of GRB classification, such relationships are useful tools into the determination of the true energetics of such phenomena. In relationships where a measurable parameter in the

[22] Type I GRB: catastrophic destruction of compact star/s and no associated SN. Type II GRB: Core collapse of a massive star, an associated SN, and a star-forming host galaxy.

GRB category	Number of bursts (percentage)
Short	90 (8.95%)
Short with EE	12 (1.19%)
Long	850 (84.49%)
Ultra-Long	16 (1.59%)
Un-constrained	66 (6.56%)

Table 1.1: *The population of GRB categories detected by Swift BAT over 11 years up to GRB 151027B (Table 2, Lien et al. 2016b).*

observer-frame can be linked to an energetics-related parameter in the rest-frame, the measured parameter can be utilised as a proxy for redshift measurements in situations where one was not observed. Such correlation-based GRB analysis was especially common in the pre-Swift era when redshift data was sparce (see for example Firmani et al. 2004; Salvaterra & Chincarini 2007; Yonetoku et al. 2004). Of these correlations, the most commonly utilised included: the source-frame peak energy, E_{peak}, of the νF_{ν} spectrum vs. the source-frame isotropic energy, E_{iso} (Amati relation; Amati 2006; Amati et al. 2002; Lloyd-Ronning, Fryer & Ramirez-Ruiz 2002), or the source-frame collimation-corrected energy of the burst, E_{Γ} (Ghirlanda relation; Ghirlanda, Ghisellini & Lazzati 2004); the lag-luminosity relationship between the spectral lag and the source-frame peak luminosity, L_{peak} (Gehrels et al., 2006; Norris & Bonnell, 2006); and the variability-energy relationship between the "spikiness" of a GRB lightcurve, and its source-frame isotropic energy (Fenimore & Ramirez-Ruiz, 2000; Reichart et al., 2001; Schaefer, 2006). The intrinsic scatter in these correlations and, in some cases, the inclusion of an extra, unknowable, $z + 1$ parameter introduces significant uncertainty into the derived energetics of a burst and therefore the vivacity of this technique has been called into question (Butler et al., 2007; Hakkila et al., 2008).

1.7.1 Long/Type II

Long GRBs, of durations greater than 2 seconds, are seen over a wide range of redshifts, with an average Swift LGRB redshift of $\bar{z}_{LGRB} = 2.14$ (Lien et al., 2016a). The spectra of long GRBs, fitted with the Band function (see Equation 1.1), have low, and high energy indices ranging from $-1.85 < \alpha < -0.72$, and $-3.59 < \beta < -2.19$, with peak energies of 26 keV $< E_{peak} <$ 3.835 MeV (Nava et al., 2012). The

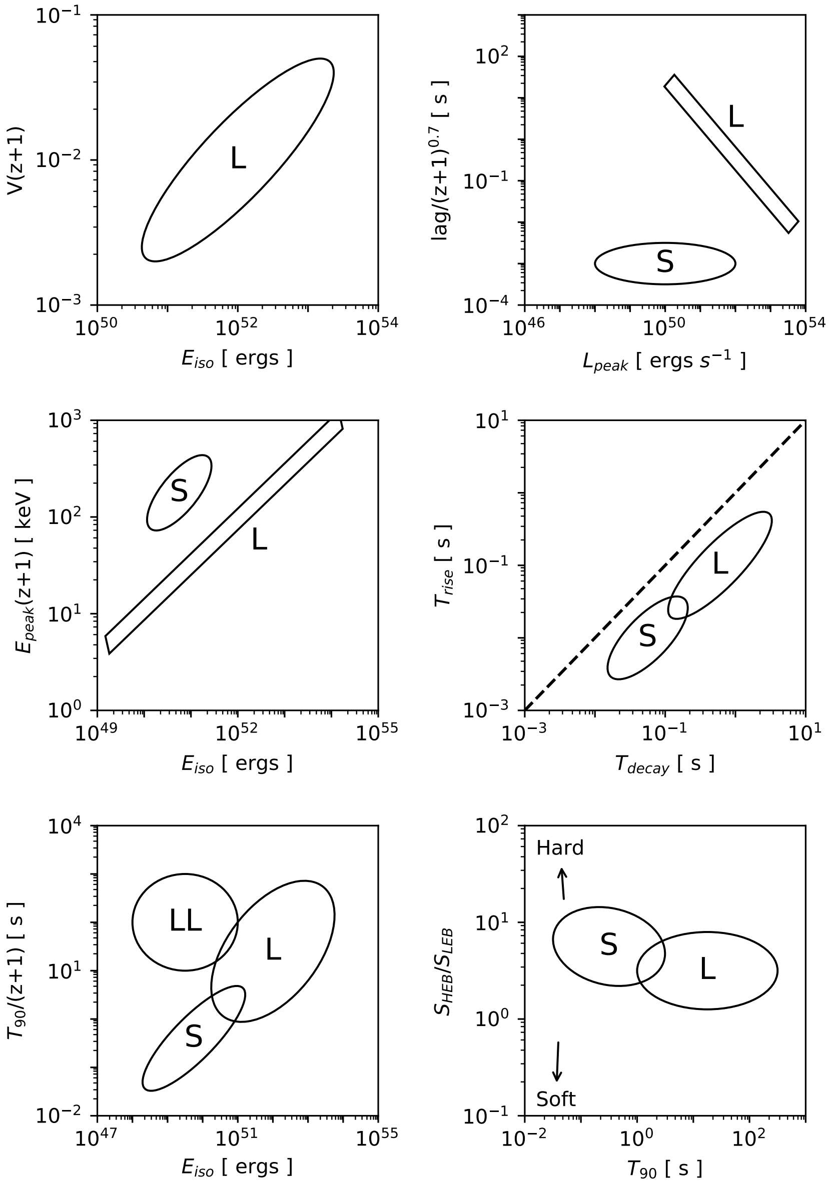

Figure 1.13: *Schematic diagram illustrating some of the most discussed correlations between various prompt emission properties for short (S), long (L), and low-luminosity (LL) GRBs; figure adapted from Gehrels, Ramirez-Ruiz & Fox (2009). The variability, V, vs. the burst-frame isotropic energy, E_{iso} (top left); the variability is the measure of the lightcurve's "spikiness", and is defined as the mean square of the time signal post processing of the low-frequencies. The burst-frame spectral lag vs. the observer-frame peak luminosity, L_{peak} (top right). The burst-frame E_{peak} of the νF_ν spectrum vs. the burst-frame isotropic energy, E_{iso} (the Amati relation; middle left). The pulse rise time, T_{rise}, vs. the pulse decay time, T_{decay} (middle right; Norris et al. 1996) The burst-frame duration, T_{90}, vs. the burst-frame isotropic energy, E_{iso} (bottom left). The hardness ratio vs. the observer-frame burst duration. The hardness ratio is defined as the ratio of the fluences in the high (HEB), and low (LEB) energy bands (bottom right; Kouveliotou et al. 1993).*

spectral lag of Long GRBs [23] is > 0 s (spectral lag can also vary within bursts, e.g. from 0.004s to 0.85 s Hakkila et al., 2008) and in extreme cases, can be on the order of a few seconds (e.g. GRB 130514A, Kawakubo et al., 2015).

Some classically long GRBs have been linked spacially and spectroscopically with hydrogen-deficient supernova signatures (SNe Ib/c, Chornock et al., 2010; Galama et al., 2000, 1998a; Malesani et al., 2004; Melandri et al., 2012; Pian et al., 2006; Starling et al., 2011; Wiersema et al., 2012). This lead to the assertion that long GRBs are associated with massive stars, and was bourne out by observations of long GRBs originating from the brightest star-forming regions of their host galaxies (Chary, Becklin & Armus, 2002; Fruchter et al., 2006; Hogg & Fruchter, 1999; Le Floc'h et al., 2003; Savaglio, 2008); typically these regions exhibited large star-formation rates, with $0.7 < \mathrm{SFR} < 270$ $\mathrm{M}_{\odot}$ yr^{-1} (Levesque et al., 2010a). Long GRB host galaxies tend to have lower metallicities than expected, with $7.9 < [12 + \log(O/H)] < 8.4$ [24] (Stanek et al., 2006), although some LGRBs have been found at higher metallicities (e.g. GRB 020819, $[12 + \log(O/H)] = 9.0 \pm 0.1$; GRB 050826, $[12 + \log(O/H)] = 8.83 \pm 0.1$; Levesque et al., 2010a,b; Perley et al., 2016b).

The constraining of long duration GRBs to high star-forming regions, along with the observation of associated supernova remnants, suggests that the progenitor star is high-mass, and subsequently short-lived; furthermore, the Hydrogen deficient SN spectra indicates that the star shed its Hydrogen envelop prior to core-collapse. These observational constraints are satisfied by Wolf-Rayet type stars; however, Wolf-Rayet stars have predominantely strong stellar winds in which a significant amount of angular momentum may be lost, a hindrance to the formation of jets. The progenitors of GRBs are therefore a subset of Wolf-Rayet stars with weak stellar winds, such as those with sub-solar metallicities (Georgy et al., 2009; Gräfener et al., 2012; MacFadyen & Woosley, 1999; Petrovic et al., 2005; Woosley, 1993b; Woosley & Heger, 2005; Yoon & Langer, 2005).

Low-Luminosity

The gamma-ray burst 980425, notable for being the first GRB associated with a supernova (SN 1998bw), was also notable for its underluminous gamma-ray emission.

[23] Spectral lag is the time delay between the arrival of high-energy, and low-energy photons (Cheng et al., 1995; Norris et al., 1996).

[24] For the Sun, $[12 + \log(O/H)] = 8.66 \pm 0.05$ (Asplund, Grevesse & Sauval, 2005).

At several orders of magnitude fainter than the average emission of high-luminosity (HL) GRBs at an equivalent redshift, GRB 980425 was initially considered an oddity; additional GRBs were soon detected with similar characteristics however, many concurrent with supernovae (GRB 031203/SN 2003lw, Malesani et al. (2004); GRB 030329/SN 2003dh, Stanek et al. (2003); GRB 060218/ SN 2006aj, Campana et al. (2006a); GRB 100316D/SN 2010bh, Starling et al. (2011)). Given the clear association of these low luminosity (LL) GRBs with the same hydrogen/helium deficient supernovae as their more luminous cousins, it was suggested that the processes of emission differed: with low-luminosity emission proposed to have arisen from shock breakout of the parent star (Bromberg, Nakar & Piran, 2011; Nakar, 2015; Nakar & Sari, 2012), rather than from an emerging jet normally seen in HL GRBs (Campana et al., 2006b; Colgate & McKee, 1969; Kulkarni et al., 1998; Soderberg et al., 2006a). This differing emission process appears to produce significantly lower beaming factors (< 14; Liang et al. 2007; Soderberg et al. 2006b) than HL GRBs (~ 100; Frail et al. 2001; Guetta, Piran & Waxman 2005; Zhang et al. 2004), leading to wider beam opening angles ($\theta_j >\sim 31°$ vs. $\theta_j \sim 10°$; Cenko et al. 2010; Piran 2004). Typically LL GRBs exhibit single peaks which display little temporal variability, are spectrally softer than HL GRBs (2.7 keV $< E_{peak} <$ 190 keV), and exhibit spectral lags on the same order as HL LGRBs.

Because of their faintness, LL GRBs are detected infrequently (approx. once every 3 years) despite their formation rate, which ranges from 10-1000 times higher than that of HL GRBs (Chapman et al., 2007b; Guetta & Della Valle, 2007; Liang et al., 2007; Pian et al., 2006; Virgili, Liang & Zhang, 2009). The handful of LL GRBs, that have an associated redshift, lie extremely closeby ($0.0085 < z < 0.251$) in host galaxies very similar to those of brighter LGRBs: actively star-forming, small, galaxies of either spiral, or irregular, morphologies (Christensen et al., 2008; Levesque et al., 2011; Margutti et al., 2007; Prochaska et al., 2004). The host galaxies of LL GRBs are generally metal-poor [25] - a pre-requisite for Wolf-Rayet stars to produce jet-emission; the LL GRB 020819 however is a notable outlier, having occured in a galaxy with super-solar metallicity (Levesque et al., 2010b). It is still not clear as to whether low-luminosity GRBs are indeed a separate class of LGRBs however, or if they are simply outliers of a wider distribution; such a distinction would require a significantly larger sample-size to determine, and an instrument far more sensitive than those currently available.

[25] Gamma-ray bursts are also found in metal-poor regions of higher-metallicity galaxies.

Ultra-Long

The discovery of long GRBs, like GRB 101225A (Thöne et al., 2011), with durations greater than 10^3 s and unusual X-ray/optical lightcurves, lead to the determination of a new subgroup of long GRBs: so called 'ultra-longs' (Evans et al., 2014; Levan et al., 2014). They exhibit strong hard-to-soft evolution of their spectra, with photon indexes [26] consistent with those of classical long GRBs [27]. Currently a small subgroup (GRBs 091024A, 101225A, 111209A, 121027A, and potentially 130925A), ultra-long GRBs have been detected at $0.35 < z < 1.77$ in compact, highly star-forming dwarf galaxies; these host galaxies are notable for being smaller, and less luminous than the hosts of their LGRB contemporaries but are not unusual for field galaxies in their redshift range (Evans et al., 2014; Levan et al., 2014). To date, only the host galaxy metallicity of GRB 111209 has been determined and, with $[12 + \log(O/H)] = 8.3 \pm 0.3$, is not unusually low for a long GRB. Several very different progenitor models have been proposed: a tidal disruption event (TDE) of a star onto an accreting black hole; the induced gravitational collapse (IGC) of a neutron star accreting material from a massive companion in its SN phase (Podsiadlowski et al., 2010; Ruffini et al., 2001); or a hydrogen-rich supernova like SN2005cs (SNe II-P) (Gendre et al., 2013; Nakauchi et al., 2013). A very luminous supernova has been associated with ultra-long GRB 111209A, with an unusual low-metallicity content compared to type Ib/c supernova; this is suggestive of a differing central engine, possible a strongly magnetised neutron star (magnetar, Gompertz & Fruchter, 2017; Greiner et al., 2015).

1.7.2 Short/Type I

Short GRBs, of durations less than 2 seconds, are seen over a narrower range of redshifts than their longer duration cousins. Detected with $0.1218 < z < 2.609$ (Berger, 2009; Levesque et al., 2009; Rowlinson et al., 2010), the average Swift SGRB redshift is at $\bar{z}_{SGRB} = 0.4$ (Berger, 2009); this however may be due to a variety of selection effects, including: the spectral hardness of the burst, the Swift image trigger, the rapid decay of the optical afterglow, and the observation bias of $z \sim 1$ SGRBs due to faint afterglows (Fong, Berger & Fox, 2010). The spectra

[26] The photon index, Γ, denotes a spectra that is fit by a power-law of slope $-\Gamma$.

[27] In cases where the spectra has been fitted by a Band function, or cutoff power-law, the values of E_{peak} was found to reside at the low-energy tail of the classic long GRB E_{peak} distribution.

of short GRBs exhibit a wider range range of photon indexes ($-2.18 < \Gamma < 0.14$) than those of long GRBs but are consistent, whilst peak energies of the $E^2N(E)$ distribution are typically harder than long GRBs, with 59 keV $< E_{peak} <$ 7.5 MeV (Kann et al., 2011); the spectral lag of short GRBs is significantly less than long GRBs and is typically within 0 ± 20 ms.

Short GRBs have been associated with old elliptical galaxies, star-forming galaxies, and galaxy clusters (Barthelmy et al., 2005c; Berger et al., 2005; Bloom et al., 2006; Bloom, Sigurdsson & Pols, 1999; Gehrels et al., 2005; Grindlay, Portegies Zwart & McMillan, 2006; Hjorth et al., 2005; Tunnicliffe et al., 2014), and can exhibit significant offset from the host galaxy's core (1 - 75 kpc, Berger, 2010; Berger et al., 2005; Church et al., 2011; Fong, Berger & Fox, 2010; Fox et al., 2005; Troja et al., 2008). Although in cases of star-forming galaxies SGRBs were not associated with star forming regions (Fox et al., 2005), there is some evidence that short GRBs trace the star-formation rate, albeit with a different mechanism than that of long GRBs, and with significant time delay (Leibler & Berger, 2010; Virgili et al., 2011b); short GRB host galaxies however display noticibly less star-formation than long GRBs, with typical star formation rates of $0.2 < \mathrm{SFR} < 6.1\ M_{\odot}\ \mathrm{yr}^{-1}$ (Berger, 2014). The metallicities of short GRB host galaxies are higher than those of long GRBs, with $8.5 < [12 + \log(O/H)] < 8.9$; they are, however, in line with the metallicities of field galaxies at $0.3 < z < 1$, and are excellent agreement with the luminosity-metallicity relation (Berger, 2009) as the host galaxies of short GRBs tend to be more massive than those of long GRBs (Wainwright, Berger & Penprase, 2007).

The favoured progenitor type of short GRBs is therefore the merger of two compact stellar objects: either a neutron star-neutron star (NS-NS), or a black hole - neutron star (BH-NS) coalescing binary (Belczynski et al., 2006; Blinnikov et al., 1984; Chapman et al., 2007a; Eichler et al., 1989; Paczynski, 1986; Rosswog & Ramirez-Ruiz, 2003). The formation time of the compact binary system, and the long merger time (up to 10^{10} years) can explain the time delay between burst and star-formation, whilst the kick velocity received in neutron star formation can explain the large offsets of short bursts from their host galaxies, or the lack of an associated host (Bloom, Sigurdsson & Pols, 1999; Grindlay, Portegies Zwart & McMillan, 2006). In the final few seconds of merger prior to the formation of short GRBs, the predominant avenue of energy emission is via graviational waves; the detection of such a signal concurrent with the detection of a short GRB would be as significant a discovery as that of the long GRB-SN link. The first discovery of gravitational waves by the

Advanced Laser Interferometric Gravitational Observatory (Advanced LIGO; Abbott et al., 2016) has not however been linked to any new transients by Swift (Evans et al., 2016).

Extended-Emission

The discovery of short GRBs that exhibited late time rebrightening which did not resemble the typical prompt emission from long GRBs lead to the determination of a separate subgroup of short GRBs (Norris & Bonnell, 2006). The total fluence from the rebrightened phase, although less bright than the prompt emission component, was comparable due to the long duration of rebrightened emission (Perley et al., 2009). As the rebrightening was a significant component of emission, the corresponding T_{90} of the burst was found to be greater than the traditional 2 second descriminator and as such was generally considered as long GRBs. Many so called 'extended emission' GRBs exhibited similarities with short GRBs: a lack of associated supernova remnant, negligible spectral lag (060505, Fynbo et al., 2006; McBreen et al., 2008; 060614, Fynbo et al., 2006; Gal-Yam et al., 2006; Gehrels et al., 2006; 080503, Perley et al., 2009), and associated elliptical host galaxies (050509B, Gehrels et al., 2005; 050724, Barthelmy et al., 2005c; Berger et al., 2005; 060614, Fynbo et al., 2006). A component of extended emission was found in approximately 25% of the Swift short GRB sample, with the longer than usual afterglow suggesting a differing progenitor type to that of the classical short GRB (Norris, Gehrels & Scargle, 2010).

The current preferred progenitor for extended emission GRBs is that of a NS-NS coalescing binary where the outcome of merger is a stable, or unstable neutron star with intense magnetic fields: a magnetar (Dai & Lu, 1998; Dai et al., 2006; Gompertz, O'Brien & Wynn, 2014; Metzger et al., 2011; Rowlinson et al., 2013; Ruderman, Tao & Kluźniak, 2000). White dwarf binaries have also been suggested to contribute towards the population of extended emission GRBs but would not be the primary channel for formation (Chapman et al., 2007a; Metzger, Quataert & Thompson, 2008).

1.8 The Fireball Model of GRB Emission

Whilst the progenitors of GRBs outlined in Section 1.6.1, and 1.6.2 differ greatly, it is commonly believed that the mechanisms which leads to the production of the prompt emission, and afterglow, are broadly similar (Piran, 1999). The fireball model (Goodman, 1986; Paczynski, 1986; Rees & Meszaros, 1992, 1994) is a phenomenologically motivated model which has proven to reproduce the GRB prompt and afterglow emission with a great deal of success and is extensively reviewed (Gehrels, Ramirez-Ruiz & Fox, 2009; Mészáros, 2002, 2006; Piran, 1999; Zhang & Mészáros, 2004).

1.8.1 The Initial Fireball

The final evolutionary stages of GRB progenitors inexorably lead towards the formation of an accreting compact object: for long GRB progeniters, the cessation of fusion in the inner layers of the star cuts off the radiation pressure holding up the outer layers, resulting in a catastrophic collapse of the star into a blackhole (Paczyński, 1998b; Woosley, 1993a); for a compact binary system, the two bodies coalesce into a blackhole as angular momentum is lost in the form of gravitational waves [28] (Eichler et al., 1989; Paczynski, 1986). The resulting, rapidly rotating, compact central object of several solar masses is surrounded by a toroidal debris disk partially held up by the high angular momentum imparted during collapse of the initial system. During the process of collapse, or merger, a large amount of gravitational energy is released in an extremely small volume, over millisecond timescales. The liberated energy (typically on the order of a solar rest-mass) is augmented over longer timescales, and larger volumes, with comparable energies derived from episodic infall of material onto the blackhole from either the central parts of the progenitor star, or debris from the compact star merger. This initial release of energy is predominantly emitted via gravitational waves (near 10^2 - 10^3 Hz in frequency; Narayan, Paczynski & Piran, 1992), and thermal $\nu_e\bar{\nu}_e$ pairs (approximately 10 - 30 MeV in temperature; Goodman, Dar & Nussinov, 1987; Meszaros & Rees, 1993b), with these two regimes emitting comparable amounts of energy (nominally several $\times 10^{53}$ ergs).

[28] In the progenitor model for extended emission GRBs it is possible for the intermediate, or final stages, prior to GRB jet formation to form a (quasi)stable magnetar (Ruderman, Tao & Kluźniak, 2000; Spruit, 1999; Thompson, 1994; Usov, 1992).

Situated above and below the accretion disk, on the rotational axis, are regions of low density into which the neutrino emission is free to self-annihilate and form a cascade of particles: from high-energy γ-ray photons; through $e^{\pm}$ pairs; to protons and other, more exotic, baryons (Kumar & Panaitescu, 2008; Shemi & Piran, 1990). This process is highly inefficient, and only a small fraction of the neutrino energy (0.1% - 1%; 10^{50} - 10^{52} ergs) [29] goes into producing the high-temperature fireball ($kT >$MeV). The optically thick fireball is transparent to gravitational waves, which propagate freely; theoretically, a component of the gravitational wave emission is detectable with current laser interferometer technologies, however to date no such emission has been observed from a gamma-ray burst. The short duration of fireball production, and massive energy conversion, infers a photon luminosity many orders of magnitude greater than the Eddington luminosity (Equation 1.2); above which, hydrostatic equilibrium between self-gravity and radiation pressure no longer applies, and the fireball expands along the rotational axis, from an initial radius, r_0 ($\sim 10^6 - 10^7$ cm), in tightly collimated jets (Frail et al., 1997, 2001; Harrison et al., 1999; Panaitescu & Kumar, 2001; Popham, Woosley & Fryer, 1999; Racusin et al., 2009; Rhoads, 1997; Soderberg et al., 2006a). The Eddington luminosity, L_E, is given by:

$$L_E = \frac{4\pi GMc}{\kappa} = 1.26 \times 10^{38} \left(\frac{M}{M_\odot}\right) \text{ergs } s^{-1}, \tag{1.2}$$

and is derived from the gravitational constant, G, the fireball mass, M, the speed of light, c, and the opacity, κ. For purely ionised hydrogen the opacity is given by $\kappa = \sigma_T/m_p$, where σ_T is the Thompson scattering cross-section, and m_p is the proton rest-mass. The expansion of the fireball is therefore intrinsically linked to its particle makeup: in reality the Eddington luminosity is higher for a fireball with a greater baryon load (Paczynski, 1990), and therefore the final expansion velocity is lower, although still highly relativistic (Cavallo & Rees, 1978; Goodman, 1986; Paczynski, 1986; Shemi & Piran, 1990).

The photon luminosity driving the adiabatic expansion of the fireball is converted into the kinetic energy of the constituent matter; as the co-moving temperature, T' is inversely proportional to the co-moving radius of the outflow, r', the temperature of

[29] In some cases there is an equal, or greater, amount of energy stored in the co-moving magnetic field of the fireball.

the fireball drops [30]. The optical depth of the fireball is dominated by the scattering of the $e^{\pm}$ pairs, and as the fireball cools below a co-moving temperature of $T' \sim 17$ keV, the electrons recombine and the fireball becomes optically thin to its own thermal electrons (Goodman, 1986; Paczynski, 1986; Shemi & Piran, 1990); at this point the surface of the fireball, termed the "photosphere", is observable with a radius of $r_{ph} \sim 10^{12} - 10^{13}$ cm. The relativistic Doppler effect produced from the high Γ factors results in the radiation escaping from the spherically expanding photosphere to appear, to a distant observer, as having being emitted from a tightly beamed spheroid with a light cone opening angle of $\theta_{beam} \propto 1/\Gamma$; in the early stages of fireball emission the beaming angle, θ_{beam}, is less than the jet collimation angle, θ_{jet}, and the outflow cannot be distinguished from an isotropically expanding shell. As the expansion of the fireball comes at the expense of the co-moving internal energy, the bulk Lorentz factor [31] cannot increase above $\Gamma_{max} \sim E_0/M_0c^2$ (typically 100-1000, Ghirlanda et al. 2012; Lithwick & Sari 2001; Tang et al. 2015; Zou, Fan & Piran 2011; Zou & Piran 2010), where E_0 is the initial energy imparted to the fireball of mass M_0. The radius at which the fireball reaches its maximum Lorentz factor is termed the "saturation radius", $r_s \sim r_0\Gamma_{max}$ ($r_s \sim 3 \times 10^{10} t\Gamma_{max}$ cm), beyond which the fireball enters its coasting phase of expansion (Goodman, 1986; Paczynski, 1986, 1991; Shemi & Piran, 1990). The radius of the photosphere may be above, or below the saturation radius, and is dependant on the initial radius and luminosity of the fireball (Mészáros & Rees, 2000).

Were the ejected fireball to expand uncontested, an observer would determine the prompt emission to be thermal with some inverse Compton upscattering of the highest energy photons (Goodman, 1986; Paczynski, 1986; Shemi & Piran, 1990); the observed spectra of GRBs are distinctly non-thermal however, suggesting an additional, intermediary stage. An effective solution is via a collisionless [32] shock whereby a second relativistic outflow collides with slower moving material in the local environment (Daigne & Mochkovitch, 2000; Kobayashi, Piran & Sari, 1997; Paczynski & Xu, 1994; Rees & Meszaros, 1994). This material can originate from

[30] The radiation pressure dominated adiabatic index is $\gamma_a = 4/3$. The co-moving temperature, T', evolves with the co-moving volume, V', such that $T' \propto V'^{1-\gamma_a}$; as V' is $\propto r'^3$, the the co-moving temperature evolves as $T' \propto r'^{-1}$.

[31] The Lorentz factor, Γ, is given by $\Gamma = 1/\sqrt{1 - v^2/c^2}$ where v is the relative velocity of the outflow, and c is the speed of light.

[32] The dominant interactions in collisionless shocks are mediated via chaotic electric and magnetic fields as the collisional mean free path is greater than the thickness of the impacting shells (Piran, 2004).

previous, low-Γ, accretion outflows, and are termed "internal" shocks [33]. Emission from the on-axis expanding shock will appear blue-shifted in the observer-frame by a factor of 2Γ, decreasing to a factor Γ at the boundary of the lightcone $\theta \propto 1/\Gamma$; at angles greater than the lightcone opening angle, the emission is redshifted with respect to the observer (see Figure 1.14). Due to the curvature of the emitting shock in the observer-frame, photons originating from higher latitudes must traverse a greater distance than those emitted from on-axis; this time delay produces the spectral lags observed in GRB spectra. Radiation efficiency is moderate for bolometric models, typically on the order of 5-20%; widely differing Lorentz factors can increase the radiation efficiency to between 30-50% (Beloborodov, 2000; Kobayashi & Sari, 2001; Lazzati, Morsony & Begelman, 2009; Spada, Panaitescu & Mészáros, 2000), however doing so would produce significantly varying spectral peak energies within a burst, which is not observed.

Such internal shocks occur above the photospheric, and saturation radii, at the dissipation radius, $r_{dis} \sim ct_v\Delta\Gamma^2$; where t_v is the temporal variation of the central engine, and $\Delta\Gamma$ is the difference in the ejected shell's Lorentz factors. With the shortest variation timescale on the order of $t_{v,min} > 10^{-4}$ s, such variability is capable of reproducing the complicated GRB lightcurves observed by instruments such as BATSE and BAT (Doi, Takami & Yamazaki, 2007; Giannios & Spruit, 2007; Kobayashi, Piran & Sari, 1997; Panaitescu & Mészáros, 1999; Sari & Piran, 1997).

An external shock is generated when the fireball runs into a medium which did not originate from the central engine; i.e. when the fireball slams into the interstellar medium (ISM), or wind pre-ejected from the progenitor star prior to collapse. These external shocks consist of two parts: the forward propagating shock, and a reversely propagating shock that acts to retard the fireball (Meszaros & Rees, 1993a). For a coasting fireball of total energy, E_0, colliding with the external medium of particle density, n_{ext}, the deceleration radius of the external shock is $r_{dec} \sim (3E_0/4\pi n_{ext} m_p c^2 \Gamma^2_{max})^{1/3}$ cm; at this radius the fireball has swept up a fraction of the fireball mass and the initial bulk Lorentz factor has decreased to half of its initial value. The timescale over which such a deceleration to occur is generally $t_{dec} \sim r_{dec}/2c\Gamma_{max}$ s, and is in good agreement with the observed timescales of external shocks. The gradual sweeping up of matter leads to the luminosity of the

[33] A gamma-ray burst can consist of many separate outflow events, each producing a propagating shock front; this is seen in GRB lightcurves as multiple FRED pulses (Fishman & Meegan, 1995; Norris et al., 1996).

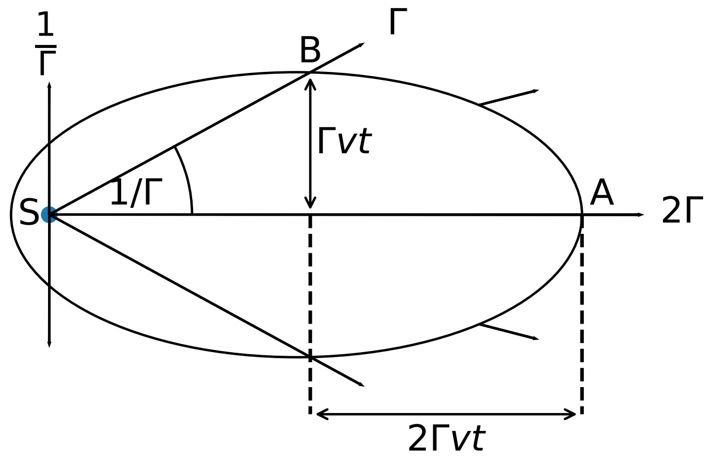

Figure 1.14: *A spherically expanding shell from point S, with* $\Gamma \gg 1$*, will appear as a spheroid in an observer-frame located to the right. On axis emission from the shell (point A) will appear to be Doppler blue-shifted by a factor of* 2Γ *with the boosting effect dropping to a factor of* Γ *at the edge of the lightcone (point B); outside of the lightcone emission is redshifted. A photon from point B will arrive after a photon from point A, due to the extra distance travelled, and is termed "high-latitude" emission. This produces both the classic fast-rise exponential decay (FRED) profile seen in GRB lightcurves, and the spectral lag. The apparent transverse, and semi-major axis radii of the ellipsoid are* $r_{\perp} = \Gamma vt$*, and* $r_{\parallel} = 2\Gamma vt$*, where* v *is the relativistic velocity of the shell (*$v/c \sim 1$*), and* t *is the observer time. Figure is adapted from Rees (1966, 1967).*

shock increasing, with $L \propto t^2$, eventually peaking at r_{dec}, before proceeding to decay as $L \propto t^{-1}$ for an adiabatically cooling shock (Rees & Meszaros 1992, although can cool more steeply if cooling regime is radiative). As the shock is decelerated, the opening angle of the jet begins to widen, until the jet angle is greater than the collimation angle; this produces an achromatic break observed in many late time X-ray lightcurves (e.g. region 4 of Figure 1.9), as the jet continues to expand laterally (Daigne, 2004).

1.8.2 Shock Spectra

Within shocks, particles are accelerated via the Fermi process to ultra-relativistic energies by turbulent magnetic fields (Achterberg et al., 2001; Blandford & Eichler, 1987; Ellison & Double, 2002; Lemoine & Pelletier, 2003; Spitkovsky, 2008). The kinetic energy of the fireball of is dominated by protons, of mass m_p, with the constituent electrons, of mass m_e, containing $\sim (m_e/m_p)$ less energy (Meszaros & Rees, 1993a; Meszaros, Rees & Papathanassiou, 1994). The collisionless nature of the shocks redistributes some of the proton energy to the electrons, up to some fraction, η_e (typically ~ 0.1; Wu, Dai & Liang 2004), of the thermal energy equipartition value; if a fraction, $\zeta_e \leq 1$, of all the shocked thermal electrons are able to achieve this initial η_e equipartition value, then the minimum co-moving Lorentz factor of electrons injected into the Fermi acceleration process, $\gamma_{e,min}$, is given by:

$$\gamma_{e,min} = \left(\frac{m_p}{m_e}\right)\left(\frac{\eta_e}{\zeta_e}\right)\frac{(p-2)}{(p-1)}\Gamma; \tag{1.3}$$

where Γ is the bulk Lorentz factor of the shock (Blandford & McKee, 1976; Bykov & Meszaros, 1996). Above this energy the Fermi acceleration process produces a power-law distribution of electron energies, with $N(\gamma_e) \propto \gamma_e^{-p}$ for $\gamma_e > \gamma_{e,min}$, where γ_e is the electron's Lorentz factor, and p is typically ≥ 2 (Fermi, 1949) [34]. The accelerated $e^{\pm}$ distribution produces non-thermal radiation via the synchrotron emission process, such that, for a relativistic electron with energy, γ_e, the observer-frame frequency of photons emitted is given by

$$\nu(\gamma_e) = \Gamma\gamma_e^2\frac{eB}{2\pi m_e c}; \tag{1.4}$$

where B is the co-moving magnetic field strength, e is the electron charge, and c is the speed of light (Rybicki & Lightman, 1979; Sari, Piran & Narayan, 1998). The associated frequency emitted by electrons with energy $\gamma_{e,min}$ is therefore:

$$\nu_m \equiv \nu(\gamma_e) = \Gamma\gamma_{e,min}^2\frac{eB}{2\pi m_e c} = \frac{\Gamma^3 eBm_p^2}{2\pi m_e^3 c}\left(\frac{\eta_e}{\zeta_e}\right)^2\left(\frac{p-2}{p-1}\right)^2, \tag{1.5}$$

and for an optically thin shock, with small radiative losses (Rybicki & Lightman, 1979), the synchrotron spectrum is:

[34] Fireball models for a Fermi distribution of photons with $1 < p < 2$ have been calculated by Bhattacharya (2001); Dai & Cheng (2001), and requires a maximum electron injection energy of $\gamma_{e,max} \sim 4 \times 10^7 B^{-1/2}$; this modifies the minimum electron injection energy to $\gamma_{e,min} = \left[\left(\frac{2-p}{p-1}\right)\left(\frac{m_p}{m_e}\right)\eta_e\Gamma\gamma_{e,max}^2\right]^{1/(p-1)}$, and is utilised identically as the original $\gamma_{e,min}$.

$$F_\nu \propto \begin{cases} \nu^{1/3} & \nu < \nu_m \\ \nu^{-(p-1)/2} & \nu > \nu_m \end{cases} \tag{1.6}$$

Synchrotron Cooling

The energy loss from electrons via photon emission, known as "synchrotron cooling", occurs over a timescale of $t_c = \gamma_e m_e c^2/P(\gamma_e)$, where $P(\gamma_e)$ is the emitted power in the observer-frame, given by $P(\gamma_e) = \sigma_T \Gamma c B^2 \gamma_e^2/6\pi$ (Sari, Piran & Narayan, 1998). If the synchrotron cooling time is less than the dynamical time, $t_d \sim r/2c\Gamma$, the electrons cool down to $\gamma_c = 6\pi m_e c/\sigma_T \Gamma B^2 t_c$, which produces a cooling break frequency at

$$\nu_c \equiv \nu(\gamma_c) = \frac{12\pi m_e ce}{\sigma_T^2 \Gamma B^3 t_c^2}, \tag{1.7}$$

with $F_\nu \propto \nu^{-1/2}$ for $\nu > \nu_c$ (Ghisellini & Celotti, 1999; Sari, Piran & Narayan, 1998). The shape of the distribution of electron energies results in the majority of electrons occupying the regime near the minimum injection energy, γ_m. If the cooling energy, γ_c is less than γ_m, then the entire population of electrons will cool rapidly: a "fast-cooling" regime; if the cooling energy is greater than the minimum injection energy however ($\gamma_c > \gamma_m$), then most electrons are unable to lose energy rapidly: a "slow-cooling" regime. The highest energy electrons will always cool rapidly however and with energies $\propto \gamma_e^{(2-p)}$, the upmost part of the spectrum will satisfy $F_\nu \propto \nu^{-p/2}$ for $\nu > \nu_m$ if $\nu_m > \nu_c$, or $\nu > \nu_c$ if $\nu_m < \nu_c$.

Synchrotron Self-Absorption

At the lowest energy regimes of the synchrotron spectrum, the frequency of photons emitted are low enough that they are effectively thermalised with the emitting relativistic electrons; this produces a syncrotron self-absorption spectrum below a characteristic frequency, ν_a, of $F_\nu \propto \nu^{5/2}$ or $F_\nu \propto \nu^2$ (Granot, Piran & Sari, 1999; Katz, 1994; Katz & Piran, 1997; Meszaros & Rees, 1993a; Meszaros, Rees & Papathanassiou, 1994). By definition, the self-absorption frequency occurs when the optical depth, τ, satisfies:

$$\tau_a \equiv 1 \sim \frac{r_s}{\Gamma}\frac{p+2}{8\pi m_e \nu_a^2}\int_{\gamma_{e,min}}^{\infty} P(\gamma_e)\frac{N(\gamma_e)}{\gamma_e}d\gamma_e, \tag{1.8}$$

where r_s is the radius of the expanding shock (Granot, Piran & Sari, 1999; Wijers & Galama, 1999); this produces a self-absorption frequency of:

$$\nu_a \sim \frac{B(p+2)^{1/2}}{4\pi}\left(\frac{r_s \sigma_T c}{3m_e}\right)^{1/2}\left[\int_{\gamma_{e,min}}^{\infty} \gamma_e N(\gamma_e) d\gamma_e\right]^{1/2}. \tag{1.9}$$

The index of the synchrotron self-absorption spectrum is dependant on the population of electrons that are emitting and absorbing photons; the electron distribution within the shocks are assumed to be homogenous, which for a slow-cooling electron distribution ($\nu_m < \nu_c$) is a good assumption. For fast-cooling spectra ($\nu_c < \nu_m$), the electron energy distribution is not homogenous, as the outermost part of the shock consists of hot electrons whilst those deeper in the shock have cooled considerably. These two electron populations reach an optical depth of unity at different frequencies, producing an additional break, ν_{ac}, below the synchrotron self-absorbtion frequency, ν_a. Where $\nu_{ac} < \nu < \nu_a$, F_ν is $\propto \nu^{11/8}$; below ν_{ac} the spectrum follows the traditional $F_\nu \propto \nu^2$ relationship (Granot, Piran & Sari, 2000).

Inverse Compton

An additional component of very high-energy photons are produced from upscattering by relativistic electrons: the inverse Compton (IC) process [35]. The energy of photons are boosted by a factor of γ_e^2 which modifies the observer-frame frequency relationship shown in Equation 1.4 to $\nu(\gamma_e) \propto \gamma_e^4$, with the component thought to be typically in the GeV-TeV ($4 \times 10^{24} - 4 \times 10^{27}$ Hz) range (Böttcher & Dermer, 1998; Vietri, 1997). Each photon is upscattered only once as the high energy photon will appear in the electron's rest frame with an energy greater than the Klein-Nishina threshold of $m_e c^2 = 0.511$ MeV, and the decreased interaction cross-section makes a second upscattering event highly unlikely.

[35] As the upscattering electrons are the source of the initial synchrotron emission, the inverse Compton process in this case is an example of syncrotron self-Compton emission (Ghisellini & Celotti, 1999; Waxman, 1997).

Evolution of Shock Breaks

Given the dynamic nature of the shock mechanisms, it is natural that the spectrum will evolve with time as the energy of the electrons is radiated away. The rate of such evolution is given by:

$$\frac{d\gamma_e}{dt} = -\frac{\sigma_T B^2}{6\pi m_e c}\gamma_e^2 + \frac{\gamma_e}{3n}\frac{dn}{dt} \tag{1.10}$$

where n is the electron number density; the first term on the right hand side represents radiative losses, and the second term arises from adiabatic cooling (Granot & Sari, 2002). As the energies of the electrons decreases, so too must there be temporal evolution of ν_m, ν_c, and ν_a. This evolution, which occurs with differing magnitudes for the spectral breaks, can see a fast-cooling shock evolving into a slow-cooling shock. Such evolution is present in the prompt emission, giving rise to the classic hard-to-soft evolution. In external shocks however, the duration of emission is significantly longer and so the evolution of the spectrum is more pronounced; eventually this leads to the spectrum peaking in the radio-bands months, or years, later.

The Synchrotron Spectrum

The resulting shock sychrotron spectra displayed in Figure 1.15 are shown as photon counts vs. frequency [36], rather than flux vs. frequency, for ease of comparison with the observed prompt emission parameters. The slopes of each power-law segment are within the yellow boxes, denoting the relationship with $N(\nu)$, and F_ν respectively. The examples shown are representative of external shock spectra however the processes are identical for internal shocks. It is the properties of the shocked matter that determines the position of the spectral breaks; for internal shocks, the peak of the νF_ν ($E^2 N(E)$) spectrum is sometimes observable towards the high-energy part of the Swift BAT. The indexes on either side of the break directly correspond to the α, β, indexes of the Band function of Equation 1.1, and are in good agreement with the distribution of parameters observed (Yu et al. 2015b, although Preece et al. 2002; Shen & Zhang 2009). In cases where $p > 2$, the high energy slope of the prompt emission is in good agreement with observed distributions of GRB prompt

[36] The photon count spectrum, $N(\nu)$ is related to the flux, F_ν by $dN(\nu)/d\nu = dF(\nu)/d\nu - 1$.

spectral indexes, with $\beta > 2$ (see Figure 1.5). Although the observed lower-energy index of Swift spectra can often be flat ($F_\nu \propto \nu^0$), assuming parameters that are inhomogenous (e.g. magnetic fields within the shock) will reproduce the observed distribution of low-energy indexes.

The temporal evolution in the spectral breaks of synchrotron emission are shown in Figure 1.15 with the arrows denoting the direction, and the magnitude. These rates are taken from Granot & Sari (2002) and are based on a radiative, and hydrodynamic solution to shocks expanding into the ISM (top magnitude), or pre-ejected wind from a massive progenitor star (bottom magnitude); these two cases are particularly relevant to the afterglow phase of GRB emission, however similar evolution occurs in the prompt phase.

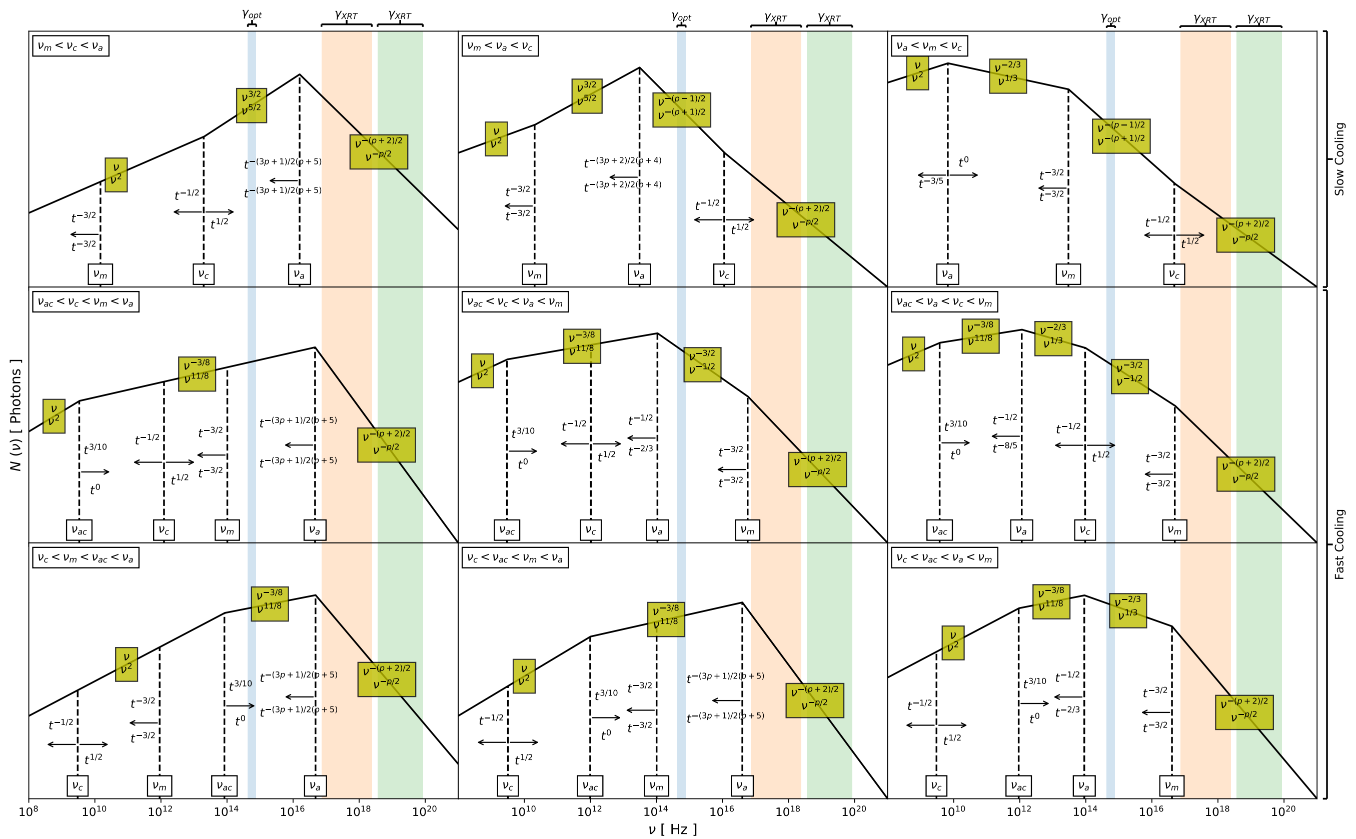

Figure 1.15: *Schematics of the various synchrotron emission profiles of shocks for "fast cooling" ($\nu_m < \nu_c$; bottom six) and "slow cooling" ($\nu_c < \nu_m$; top three) spectra (solid lines). The characteristic spectral breaks denoted arise from: syncrotron self-absorbion, ν_a; an electron cooling frequency, ν_c; the minimum injection frequency of the relativistic electrons, ν_m; and the absorption due to fast cooling electrons, ν_{ac} (dashed lines). Shaded regions denote the passbands for: optical, $\gamma_{\rm opt}$; Swift XRT, γ_{XRT}; and BAT, γ_{BAT}. Yellow boxes denote both the slope of the photon distribution (top), and the gradient of the spectra as a function of frequency (bottom). The parameter p is the index of the power-law distribution of electron energies arising from Fermi acceleration: $N(\gamma_e) \propto \gamma_e^{-p}$, where γ_e is the electron co-moving Lorentz factor. Arrows denote the direction of the temporal evolution in the spectral breaks for the external ISM (top), or pre-ejected wind (bottom). Figure is adapted from work by Granot & Sari 2002; Shen & Zhang 2009; Yu et al. 2015b.*

1.9 Monte-Carlo Methods in Astronomy

The Monte-Carlo (MC) method is a commonly used technique for parameter estimation utilising random sampling to examine the desired parameter space of a given model, for some observed dataset. Given the ubiquitous usage of such methods in this thesis, a short description on the basics, in particular the sub-branches of MCs and the MC diagnostic tools used, are provided in this section.

Under the umbrella of statistical analysis, there are two major schools of thought regarding parameter inference: the Bayesian and frequentist methods. These two schools differ in how they treat the observed data, and model parameters, leading to subtle differences in the interpretations of the resulting analysis. In frequentist analysis, the data is assumed to have been taken from a repeatable random sample of infinite size, whilst the underlying model parameters are taken to be fixed; for Bayesian analysis, the observed data is taken from a realised sample (in essence the data is not repeatable), whilst a probability distribution can be ascribed to the underlying model parameters. As the desired outcome of any statistical inference is the ability to characterise the model parameters, a confidence interval is often quoted alongside the parameter estimates; this interval denotes a range of values, within which the true parameter value is likely to lie.

The differences between these two axioms, however, leads to two different interpretations of the confidence intervals of the model parameters. In frequentist analysis, an $n\%$ confidence interval indicates that after a sufficiently large number of repeat experiments, the resulting intervals would cover the true parameter value in $n\%$ of cases. In Bayesian analysis, the confidence (also referred to as credible) interval for the model posterior indicates that there is a $n\%$ probability that the parameter value lies within that region, given the data and any prior information. Although the philosophical differences between the definitions of confidence/credibility intervals are significant, both schools provide equally powerful tools in statistical analysis; the challenge is therefore applying the more appropriate method of data analysis to the situation at hand. Due to the transient nature of GRBs, Bayesian analysis was deemed the more appropriate inference technique, and is used throughout this thesis; a brief overview of Bayesian anaylsis is therefore included.

1.9.1 The Bayesics

We have a model, $M = F_{model}(\theta_{true})$, for some particular process or relation, in which we wish to compare to some observed data, D (which consists of F_{obs}, and an associated error, e_{obs}), in order to determine the true parameters of the model, θ_{true}. In Bayesian analysis, statistical inference on the model parameters is achieved through determining the probability, or posterior, distribution function (PDF), $P(\theta_{true}|D, M)$, to which statements on the probability that the true value of the parameter lies within a certain range can be made. The posterior distribution is attained through the application of Bayes Theorem, which states that

$$P(\theta_{true}|D, M) = \frac{P(\theta_{true}|M)P(D|\theta_{true}, M)}{P(D|M)}, \tag{1.11}$$

where $P(\theta_{true}|M)$ is defined as the parameter prior, $P(D|\theta_{true}, M)$ is the likelihood, and $P(D|M)$ is the evidence; the best estimate is subsequently the peak of the posterior, and confidence intervals can be quoted for regions in which the user believes the values of the true parameters lie. Care must be taken when reporting the posterior: in the ideal case, the posterior is single-modal, and so the mode/mean provides the information required; where the posterior is multi-modal however, the mode or mean may lie in a valley of improbability between two probable peaks, and so preferrably the whole posterior is presented.

The Likelihood

The likelihood function, $P(D|\theta_{true}, M)$ (also commonly denoted by $\mathcal{L}$), is the probability of the data given the model, and is therefore the product of the convolved probabilities of each data point:

$$\mathcal{L}(D|\theta_{true}, M) = \prod_{i=1}^{N} P(D_i|F_{model}); \tag{1.12}$$

it is the most instinctive component of Bayes theorem, and is likewise often utilised in Frequentist analysis; indeed, in cases where the priors are a uniform probability distribution, then the peak of the posterior and the likelihood function are the same, which is the outcome of Frequentist analysis. In the likelihood function, the probability distribution of a single observation, $D_i = (F_{obs,i}, e_{obs,i})$, is compared to a given F_{model} by assuming that the PDF takes some form; for example, a Gaussian PDF:

$$P(D_i|F_{model}) = \frac{1}{(2\pi e_{obs,i}^2)^{1/2}} \exp\left(\frac{-[F_{obs,i} - F_{model}]^2}{2e_{obs,i}^2}\right). \tag{1.13}$$

Other functional forms, such as the Poisson distribution, are also common, and the user is not restricted to one model assumption per dataset. Multiple PDF forms can be used in conjunction to differing data regimes, e.g. where photon count rates are extremely small a Poissonian is more correct, however a Gaussian PDF is applicable when the count rates are very high.

It is often more convenient to refer to the log-likelihood, rather than the likelihood, when deriving the posterior, due to the finite computational precision of very small, or very large, numbers. For example, a Gaussian PDF log-likelihood is derived by combining Equations 1.12 and 1.13 and taking the logarithm:

$$\log(\mathcal{L}) = -\frac{1}{2}\sum_{i=1}^{N}\left(\log(2\pi e_i^2) + \frac{-[F_{obs,i} - F_{model}]^2}{e_i^2}\right). \tag{1.14}$$

The (log)likelihood is a powerful technique for statistical inference, as it can be tailored to be as complicated as a user desires for the given task at hand; as likelihood functions can be significantly affected by outliers, a common addition is that of nuisance parameters which model the behaviour of the outliers. Although this adds extra complication to the model, they can be marginalised out in the processing phase, leaving the desired parameters behind. Further care is required when modelling the effect of measurement errors on the model; in the above example the only component of error was in the observed data; however in reality this error component will propagate through the model, and can have a subtle effect on the results (e.g. D'Agostini 2005).

The Prior

The prior is the probability distribution of a parameter before any evidence from the experiment is taken into account, and is often the most subjective component of Bayesian analysis. In more complex models with > 1 input parameters, $\theta_{true} = \{\theta_{1,true}, \theta_{2,true}, ..., \theta_{k,true}\}$, the prior, $P(\theta_{true}|M)$, denotes the product of all the constituent priors, such that

$$P(\theta_{true}|M) = \prod_{k=1}^{N} P(\theta_{k,true}|M), \tag{1.15}$$

where each component prior can take a different functional form to reflect the information already known. An observer may choose an uninformative prior, such as the uniform distribution, or determine an informative prior (e.g. a Gaussian) based on intuition, or evidence from previous experiments. Whilst prior selection can be controversial, especially in the frequentist vs Bayesian argument, it can be shown that by increasing the data, the likelihood gets narrower and the influence of the prior is diminished.

In more complicated Bayesian analysis cases where a prior, $P(\theta|M)$, is dependent on a parameter, ψ, that is not part of the likelihood function, $P(D|\theta, M)$, then the prior must be replaced by a likelihood, $P(\theta|\psi, M)$, and the prior, $P(\psi|M)$, such that $P(\theta|M) = P(\theta|\psi, M)P(\psi|M)$. This is an example of Hierarchical Bayesian analysis, and can be repeated for an arbitrary number of iterations until the highest order priors are totally independent of any other parameters.

The Evidence

The model evidence, or model likelihood, is the likelihood function which has been marginalised over all the model parameters such that

$$P(D|M) = \sum_{k} P(D|\theta_{true,k}, M)P(\theta_{true,k}|M) = \int P(D|\theta_{true}, M)P(\theta_{true}|M)d\theta. \tag{1.16}$$

Although an important component of Bayesian analysis, in essence the evidence normalises the posterior and produces a true probability distribution. If the user requires the full probability distribution for model testing (i.e. when comparing $P(D|M)$ to $P(D|M')$) then the evidence can be calculated directly if the functional form of the likelihood and prior are known; in cases where the likelihood is unknown then the evidence can be derived using a Monte-Carlo method. For parameter estimation, the evidence can be ignored, which results in the posterior distribution being proportional to the prior information convolved with the likelihood function, i.e. $P\theta_{true}|D, M) \propto P(\theta_{true}|M)\mathcal{L}(D|\theta_{true}, M)$.

1.9.2 Monte-Carlo Methods

Markov Chains

The particular type of MC method used thoughout this thesis for parameter estimation are that of the Markov Chain family of Monte Carlo methods, or more specifically a Metropolis-Hastings Markov Chain Monte Carlo (M-H MCMC) method (Hastings, 1970; Metropolis et al., 1953). Utilised because of their resistance to the "curse of dimensionality" [37], these methods rely on producing an ordered, random-walk, sequence of parameter datapoints, $\{\theta_s\} = \{\theta_1, \theta_2, \theta_3, ..., \theta_{N_s}\}$, in which the position of the s^{th} point, θ_s, is dependent only on θ_{s-1}; the s^{th} point is therefore drawn from the proposal probability distribution, $P(\theta_s|\theta_{s-1})$.

An M-H MCMC is typically initiated at a random start point, unless the user has some information on where to start; multiple chains are often set to operate from differing start points to ensure that convergence is at a global, rather than local, region. The next element of the M-H Markov Chain is generated by a three step procedure:

1. Draw a trial point from the proposal probability distribution $P(\theta_{trial}|\theta_{s-1})$; the proposal probability density function must be symmetric, such that $P(\theta_{trial}|\theta_{s-1}) = P(\theta_{s-1}|\theta_{trial})$. An example of this is a uniform distribution centred on point θ_{s-1}, with a search width of S_w, such that $P(\theta_{trial}|\theta_{s-1}) = \frac{1}{S_w}$ for $\theta_{s-1} - S_w/2 \leq \theta_{s-1} \leq \theta_{s-1} + S_w/2$; a Gaussian distribution symmetric around θ_{s-1} is also popular, and lets larger steps to be made (although such steps are far less probable than smaller steps). If the search width is particularly narrow, every new step may be accepted and subsequently the Metropolis-Hastings method may take a long time to converge to the target distribution; likewise, if the search width is too large then the majority of steps are rejected and convergence is delayed. The search width is therefore fine-tuned such that more steps are rejected than accepted, with the target total acceptance ratio within the chain of ~ 0.4.

[37] The curse of dimensionality is where the data-space becomes more sparsely sampled as the parameter space increases, requiring a significantly greater number of steps to reach the same fidelity as a lower-dimensional problem.

2. Accept a trial point with an acceptance probability $P(\text{accept}|\theta_{trial}, \theta_{s-1}) = \min\left[\frac{P(\theta_{trial})}{P(\theta_{s-1})}, 1\right]$; if the new point is more probable, then the trial point is always accepted. If the new point is less probable, there is still a possibility that the new point is accepted; this is an important component of M-H routines as it allows for the random walk to sample the target distribution correctly by escaping local regions of high density to find the global target density. In Bayesian analysis, $P(\theta_{trial})/P(\theta_{s-1})$ equates to the ratio of the two likelihood functions evaluated at those points.

3. If the trial point is accepted then set $\theta_s = \theta_{trial}$, elsewise set $\theta_s = \theta_{s-1}$.

This procedure is repeated on the order of $10^4 - 10^8$ times to build up a large set of samples that represent the target distribution [38]; which, in this case, is the same as the Bayesian posterior distribution. The proposal distribution, $P(\theta_s|\theta_{s-1})$, is not clearly related to to the posterior, $P(\theta|D)$; however at a limit of high s, then the s^{th} element is drawn from $P(\theta|D)$ if the proposal and acceptance probabilities achieve detailed balance:

$$\frac{P(\theta_s|\theta_{s-1})}{P(\theta_{s-1}|\theta_s)} \frac{P(\text{accept}|\theta_s, \theta_{s-1})}{P(\text{accept}|\theta_{s-1}, \theta_s)} = \frac{P(\theta_s)}{P(\theta_{s-1})}; \tag{1.17}$$

the Metropolis-Hastings Monte-Carlo routine satisfies this requirement, independent of the form of $P(\theta_{trial}|\theta_{s-1})$.

1.9.3 Post-Processing of Monte Carlo Chains

Burn-In

Burn-in occurs when the starting position of Markov chains are situated far from the high-density regions of the target proposal distribution, which then proceed to propagate towards the high-density region of the proposal distribution. Burn-in indicates a lack of understanding as to the shape and location of the target distribution but is generally of little import; if some prior information is known as to the position of the maximum of the posterior distribution, then this may be

[38] It is important to note that Metropolis-Hastings MCMCs severely struggles to sample from a target distribution that is periodic in nature (e.g. a cosine function); in these cases, alternative MCMC routines, such as Nested sampling Monte Carlo routines (Feroz et al., 2013; Skilling, 2004), are more suitable.

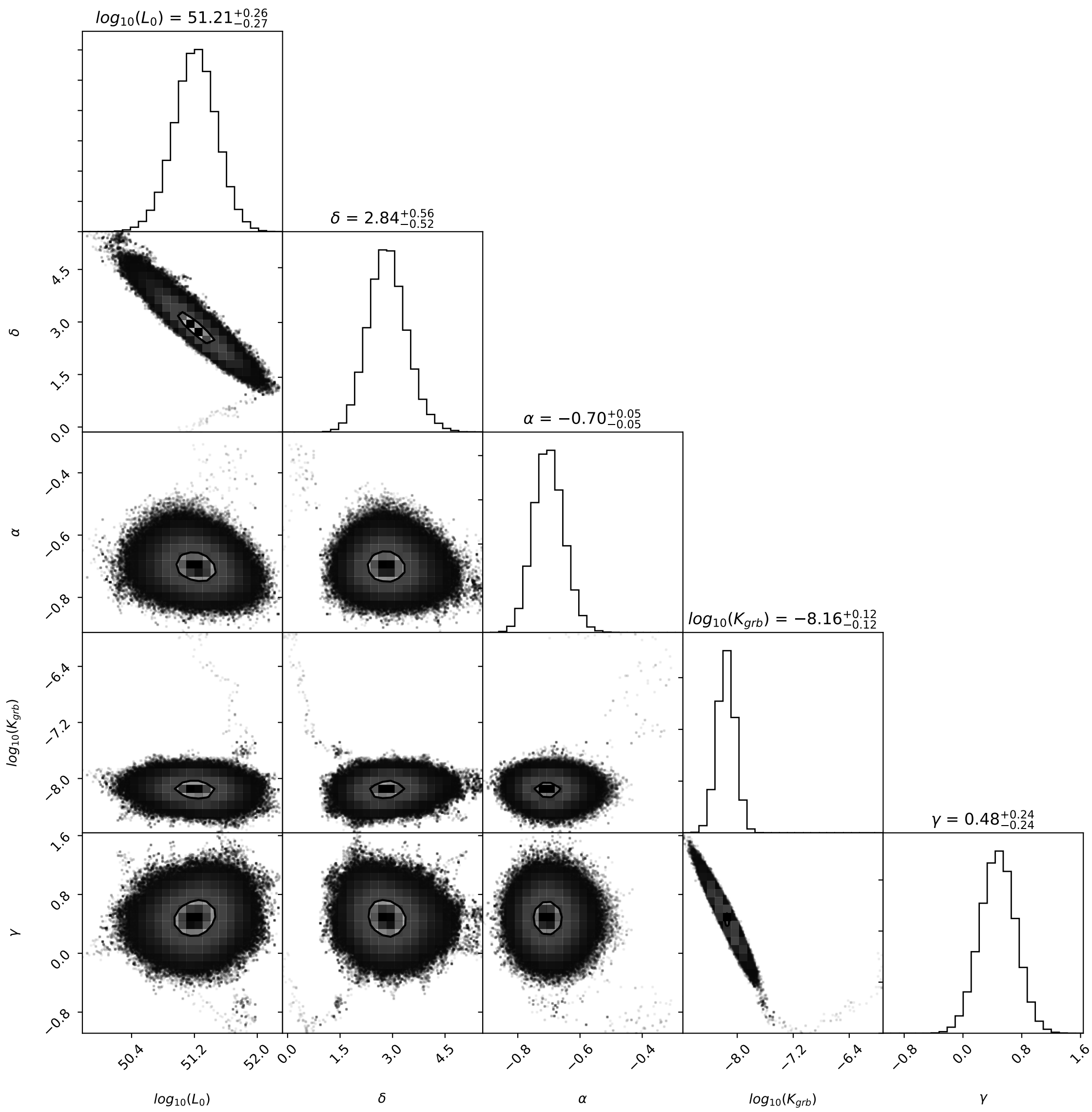

Figure 1.16: *Example posterior distributions of a GRB luminosity function modelled by a power-law with an exponential cutoff, and derived using a Metropolis-Hastings MCMC.* α *is the power-law index of the PLEC, and the luminosity cutoff at a given redshift is modelled by* $L_c(z) = L_0(z+1)^\delta$ *ergs* s^{-1}*; the normalisation factor at a given redshift is also given by* $K_{Norm}(z) = K_{GRB}(z+1)^\gamma$ *GRBs* $M_\odot^{-1}$*. The MCMC chain consists of* 2×10^7 *correlated samples (gray transparent points), with 2D binning in the highest density central regions of the posterior; contour lines denote regions of 0.5, 1, 1.5, and 2* σ *confidence, with a "burn-in" phase also seen. Quoted figures are the mean parameter values of the posterior distribution and are marginalised over all other parameters; also quoted are the inter-quartile range denoted as the sub/super scripts, and highlighted with the dashed lines in the parameter histograms. Figure produced using the Corner routine developed by Foreman-Mackey (2013) for the Python programming language.*

utilised as the initial point of the chain and no burn-in is observed. Burn-in samples are typically found in low-density regions which may not normally be sampled, and for a short Markov chain the burn-in is effectively producing an oversampling of those regions; where the sample size is small, it is often convenient to simply cut the burn-in phase which removes their effect. If the sample size is extremely large, and the the burn-in phase very short, then no post-processing is really required as the effect is marginal.

Convergence Tests

To ensure that a MCMC chain converges on a global, rather than local, high-density region, multiple chains can be run from differing initial positions; these chains should converge on the same target distribution if the parameter space has been well-sampled. The heuristic convergence test developed by Gelman & Rubin (1992), is a commonly utilised method to evaluate the magnitude of the convergence; however it is not a panacea: failure to pass confirms lack of convergence, but passing does not guarantee that convergence occurs. It is, however, useful when used in combination with density plots of the parameter chains.

For a number of chains, N_c, each of length, N_s, the Gelman and Rubin convergence test is derived by producing the mean and variance of each chain:

$$\bar{\theta}_{chain} = \tfrac{1}{N_s}\textstyle\sum_{s=1}^{N_s}\theta_{s,chain}; \quad \sigma^2_{chain} = \tfrac{1}{N_s-1}\textstyle\sum_{s=1}^{N_s}(\theta_{s,chain} - \bar{\theta}_{chain})^2. \tag{1.18}$$

The mean of the chain means, the mean of the chain variances, and the variance of the chain means, are then calculated:

$$\bar{\theta}_{all} = \tfrac{1}{N_c}\textstyle\sum_{c=1}^{N_c}\bar{\theta}_{chain}; \quad \bar{\sigma}^2_{all} = \tfrac{1}{N_c}\textstyle\sum_{c=1}^{N_c}\sigma^2_{chain}; \quad \sigma^2_{\bar{\theta}_{chain}} = \tfrac{1}{N_c-1}\textstyle\sum_{c=1}^{N_c}(\bar{\theta}_{chain} - \bar{\theta}_{all})^2. \tag{1.19}$$

Finally, the Gelman and Rubin test is calculated:

$$G = \frac{\frac{N_c-1}{N_c}\sigma^2_{chain} + \frac{1}{N_c}\sigma^2_{\bar{x}_{chain}}}{\sigma^2_{chain}}. \tag{1.20}$$

In the case where all the Markov chains well-sample the posterior distribution, the average inter-chain variance, $\sigma^2_{\bar{\theta}_{chain}}$, and the variance of the chain means, $\sigma^2_{\hat{\theta}_{chain}}$, are roughly equal and $G \sim 1$. If the chains do not converge on a unique solution then $G > 1$; as the Gelman and Rubin test produces a continuum, typically convergence is agreed when $G < 1.1$.

Chain Correlation and Thinning

A Metropolis-Hastings MC method will produce a Markov chain that consists of correlated samples from the target probability density. The magnitude of this correlation may be evaluated by deriving the chain auto-correlation function. For a single-parameter chain, of length, N_s, and equally weighted samples, the auto-correlation function is defined for step lags of $\Delta = 1, 2, ..., N_s - 1$:

$$\hat{C}_\Delta = \frac{1}{N_s - \Delta} \sum_{s=1}^{N_s - \Delta} \frac{(\theta_s - \hat{\theta})(\theta_{s+\Delta} - \hat{\theta})}{\hat{C}^2}, \tag{1.21}$$

where $\hat{\theta}$ is the sample mean of the chain, and $\hat{C}$ is the sample variance. By definition, $\hat{C}_{\Delta=0} = 1$, which will drop to zero as Δ increases; whilst a naturally uncorrelated chain will have $\hat{C}_\Delta = 0$ for $\Delta \geq 1$. An uncorrelated chain can be produced from a correlated chain by defining a correlation threshold that requires a minimum lag to reach, Δ_{min}. In a process called "thinning", the Δ^{th}_{min} elements of the chain are extracted, with the rest of the data discarded, resulting in a nominally uncorrelated sample with size of $\sim N_s/\Delta_{min}$. The process of thinning to improve the quality of data is generally considered pointless however as any correlations are averaged out by a suitably large initial chain (Link & Eaton, 2012); thinning to aid any computational analysis is however commonly used (Owen, 2015).

1.10 This Thesis

This thesis focusses on the global properties of Swift detected GRB pulses by applying the physically motivated pulse model by Genet & Granot (2009b), and the empirical afterglow model by Willingale et al. (2007), to the majority of GRBs observed by Swift, with known redshifts, in the X-ray and gamma-ray regimes; the results of this large scale population analysis is combined into a GRB lightcurve component catalogue in Chapter 2. The relationships between the characterising parameters of the models are also compared, both within, and between, the differing burst types; whilst common correlations, such as the Amati E_{peak} - E_{iso} relation, are evaluated on an individual pulse level, rather than from the time-averaged lightcurve behaviour.

In Chapter 3, the bolometric luminosities of long duration GRB pulses, fitted in Chapter 2, are utilised alongside the GRB redshift distribution to produce an LGRB pulse luminosity function that tests many of the more popular LGRB progenitor models. Evolution in the LGRB formation rate, and/or luminosity evolution in the GRB luminosity function, are explored; the presence of a bimodal population of long GRBs is also investigated. The GRB pulse formation rates, derived in this work, are compared to the observed cosmic star-formation rate density and against existing GRB formation rate models.

The final chapter of this thesis summarises the conclusions of the individual science chapters, and discusses the avenues of possible progression down which the results from this study may be taken in the future.

Chapter 2

The Swift GRB Pulse and Afterglow Catalogue

2.1 Chapter Overview

The current paradigm of GRB lightcurves is that the totality of the prompt emission can be modelled by the presence of either a single pulse, or by a series of convolved pulses. These pulses are well studied, but in many papers, they are modelled by empirical functions which do not relate the spectral and temporal properties of the pulse. In this chapter we utilise a physically motivated model of pulse emission, that incorporates both spectral and temporal behaviour, to fit a significant proportion of all Swift observed GRBs with associated redshifts. We furthermore fit an empirical afterglow component to the model, and produce an exhaustive catalogue of all the fitted parameters.

2.2 Introduction

With their highly transient nature and large fluence, GRBs have been of great interest to the astrophysics community since their initial discovery. The extreme physics of the progenitors are of great importance to star-formation theory, and the large distances involved ($z > 8$) allow for such models to be tested on a cosmological scale;

however, such analysis is stymied by the lengthy accumulation time of a statistically significant population, and the disconnection between the high-energy phenomena to the star-formation rate, or other host-galaxy properties. Over time, large-scale GRB missions have overcome the first issue; thousands of GRBs have been detected by BATSE (5B catalogue, with 2,145 GRBs, Goldstein et al. 2013), Fermi (4-year catalogue, with 1818 GRBs, Gruber et al. 2014; von Kienlin et al. 2014), and Swift (1st catalogue, 237 GRBs, Sakamoto et al. 2008a; 2nd catalogue, 476 GRBs, Sakamoto et al. 2011b; and 3rd catalogue, 1034 GRBs, Lien et al. 2016b), with new bursts detected on an almost daily basis. These catalogues have collated a vast amount of temporal and spectral data, which in turn has revealed the presence of separate long duration ($T_{90} > 2$ s), and short duration ($T_{90} < 2$ s) GRBs (Kouveliotou et al., 1993), which were later associated with the death of massive stars (LGRBs, Fryer et al. 2007; MacFadyen & Woosley 1999; Woosley & Heger 2005, 2006), and the coalescing of two compact objects (SGRBs, Eichler et al. 1989; Fryer, Woosley & Hartmann 1999; Nakar 2007). Intriguing correlations between spectral and temporal parameters have also been revealed (e.g. the Amati relation, Amati 2006; Amati et al. 2002; the Ghirlanda relation Ghirlanda, Ghisellini & Lazzati 2004; and the lag-luminosity relation Norris 2002; Norris, Marani & Bonnell 2000), which have been used to test the progenitor models of the various GRB types, and in some cases, to derive pseudo-redshifts for bursts where suitable ground-based observation was unavailable.

Given its unique ability to rapidly respond to GRB triggers, and the various energy ranges of the onboard instruments, Swift has provided the most redshift complete sample to date; approximately 1/3 (397 GRBs, Lien et al. 2016b) of all Swift detected GRBs have well constrained redshifts, derived from spectroscopic or photometric observations of the host-galaxy, or the GRB afterglow itself. Because of this, a large number of GRB studies incorporate Swift data to produce smaller surveys (typically < 70 GRBs) which account for ground-based observing bias, and consist of a high level of redshift completeness; including BAT6 (Salvaterra et al., 2012), SHOALS (Perley et al., 2016a), and TOUGH (Hjorth et al., 2012). Given the vast distances over which bursts are observable, these surveys have been utilised to great effect in determining the luminosity functions of long GRBs (e.g. Jakobsson et al. 2012; Salvaterra et al. 2012; Salvaterra & Chincarini 2007); deriving the cosmic star-formation rates at high-redshift (e.g. Kistler et al. 2009); or calculating the observation rates of gravitational waves (Ghirlanda et al., 2016).

The major shortfall in such studies, however, has been the tendency to determine the behaviour of GRBs from time-averaged characteristics. The morphology of GRB lightcurves, in reality, displays remarkable temporal and spectral variance, with no two bursts showing the same behaviour (Nemiroff et al., 1993). Many GRB lightcurves exhibit temporal features that conform to that of a rapid rise in burst intensity followed by a gradual decay, termed a FRED, either singularly or as part of a greater continuum (Fishman, 1993; Fishman et al., 1994). These features, or pulses, overlap to a greater or lesser degree, which makes the separation of characteristics of the pulses difficult to achieve; comprehending the specific relationships between pulse characteristics is important however, as it is a finer measure of the mechanisms behind GRB prompt emission. Observations by BATSE (Fishman et al., 1985) have shown that pulses display interesting behaviour, including: spectral hard-to-soft evolution, the cause of which was unknown for over a decade (Bhat et al., 1994; Hurley, 1991; Norris, 1983; Norris et al., 1986); the lagging in the arrival time of low-energy photons compared to those of higher energies (Chen et al., 2005; Gruber et al., 1992; Norris, Scargle & Bonnell, 2001; Shen, Song & Li, 2005; Wu & Fenimore, 2000); and significant asymmetry between the rise, and fall times of the pulses, regardless of their duration (Link, Epstein & Priedhorsky, 1993; Nemiroff et al., 1994; Norris et al., 1996). Further studies, utilising Swift data, has confimed the existence of separate distributions in the lag timescales of short, and long GRBs, consistent with the BATSE data (Bernardini et al., 2015; Hakkila & Preece, 2011); and although the evidence for a lag-luminosity relation in Swift GRBs has weakened, a lag-luminosity correlation has been observed in Swift X-ray flares (Margutti et al., 2010). Swift studies of the Amati, and Ghirlanda correlations of GRB pulses has also shown there to be no evolution with redshift of the relations (Basak & Rao, 2013), in agreement with the behaviour seen in the time-averaged lightcurves.

Pulse analysis has since expanded into modelling the prompt emission in order to extract maximal information from the observed data. Some models, such as that of Norris et al. (1996), lack physical motivation and consider the spectral and temporal components as independent from each other (e.g. GRB 970717; Figure 2.2, Norris et al. 1996). Whilst far from sophisticated, these models have revealed a correlation between the rise, and decay times of the pulses, with short, and long GRBs occupying the lower, and higher timescales of the correlation respectively (Chincarini et al., 2007; Hakkila & Preece, 2011; Norris et al., 2005, 1996). Other models, such as the Internal Collision induced Magnetic Reconnection and Turbulence (ICMART) model

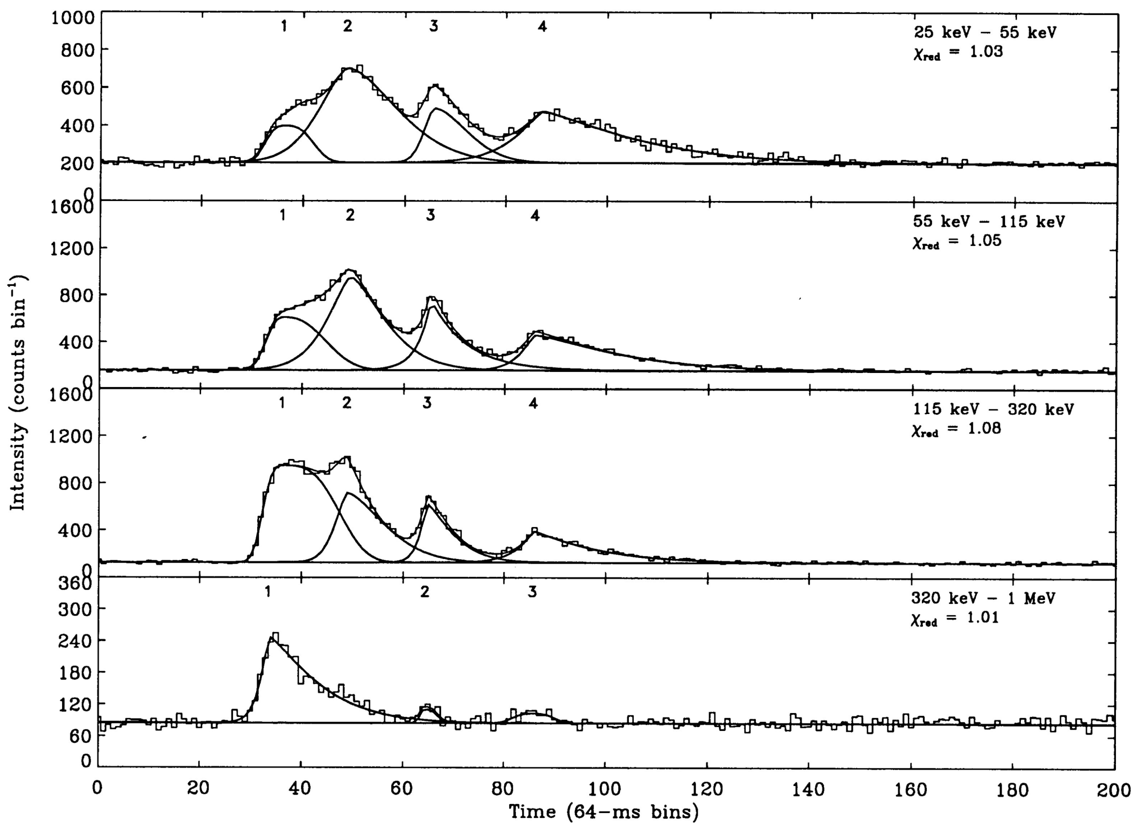

Figure 2.1: *The lightcurves of BATSE GRB 970717 (BATSE trigger 543), fitted by Norris et al. (1996) using their empirical model for GRB pulses. Each pulse is fitted only over time, leading to the parameters of pulse 4 in the 115 keV - 320 keV passband being independent to those of pulse 4 in the 25 keV - 55 keV passband.*

(Zhang & Yan, 2011) attempted to model pulse emission originating from magnetic reconnection; whilst the emission from the pulse model by Genet & Granot (2009b) (referred to as the G&G model) originates from internal shocks [1].

In this chapter, we expand on the work by Willingale et al. (2010) and apply the phenomenologically motivated model of Genet & Granot (2009b) to the entire Swift population of GRBs to produce an extensive catalogue of parameterised pulses and afterglows that together form the entirety of the observed GRB emission. We outline the physical reasoning behind the pulse model in Section 2.3, alongside the empirical afterglow model; whilst the selection criteria for our GRB sample, and the fitting

[1] The G&G model can be modified to simulate magnetic reconnection, rather than internal shock emission mechanisms, and has shown that the luminosity-variability and luminosity-peak frequency are natural outcomes of the physical model, and can reproduce the observed distribution of spectral lags, and pulse asymmetry (Beniamini & Granot, 2016).

procedures are discussed in Section 2.4. The global properties of our GRB catalogue (e.g. redshift, burst type, and fit statistics) are discussed in Section 2.5, with the pulse and afterglow results discussed in Section 2.6. We finally conclude our findings in Section 2.7.

2.3 The GRB Lightcurve Model

With the launch of the Swift satellite (Gehrels et al., 2004), the detection of GRBs in the Swift XRT passbands revealed a new regime, that of a steep, or rapid, decay phase (SDP, or RDP; see Figure 1.9 for example), which was observed in the majority of GRBs with early-time X-ray follow-up (Campana et al., 2005; Chincarini et al., 2005; Tagliaferri et al., 2005; Yamazaki et al., 2006). This new regime, when combined with the previously observed plateau and post-plateau decay phases, produced a profile that was well characterised by a series of breaks in an extended power-law (see Barthelmy et al. 2005b; Tagliaferri et al. 2005); an additional late-time break attributed to the jet break of the burst, was also seen in a few rare cases (Burrows et al., 2006). Superimposed on top of the numerous underlying X-ray regimes, were X-ray flares: these flares can be extremely bright, in some cases similar in peak flux, or fluence, to pulses observed in the prompt emission, and generally occur in the first few phases of the XRT lightcurves (Burrows et al., 2005b; Falcone et al., 2006, 2007; Krimm et al., 2007).

It was soon suggested that the rapid decay phase was an artifact of the prompt emission decaying into the X-ray passbands, given that it exhibited a smooth continuation of the prompt behaviour, both spectrally [2] and temporally (O'Brien et al., 2006). Although a great deal of models have attempted to explain the origins of this emission (e.g. Mészáros & Rees 2001; Nousek et al. 2006; Ramirez-Ruiz, Celotti & Rees 2002; Tagliaferri et al. 2005), the most popular has been that of high-latitude emission (HLE; Kumar & Panaitescu 2000). In this model a spherically expanding shell will emit over a finite range of radii; when the lowest-latitude component of the shell passes beyond the emission radius, only the higher-latitude components relative to the line-of-sight continue to emit. In order to reconcile the prompt emission, rapid decay phase, and the theory of high-latitude emission, a phenomenological model for

[2] The rapid decay phase also displayed hard-to-soft evolution over its duration, similar in behaviour to that of the pulses within the early gamma-ray prompt emission (Zhang, Liang & Zhang, 2007).

the prompt emission was needed that could be extended to lower-energies, and later times. Numerous, simplified, models have been utilised to investigate these relationships (e.g. see Hascoët, Daigne & Mochkovitch 2012; Liang et al. 2006; Nousek et al. 2006; Zhang et al. 2008), however many of the assumptions used to create these models were considered arbitrary or inappropriate. A more realistic model was required that combined the pulse profile on timescales that included covering the HLE, was capable of explaining observed spectral evolution, and could be combined with other pulses to reproduce the totality of the rapid decay phase. This lead to the development to the phenomenologically driven GRB pulse model by Genet & Granot (2009a,b); Willingale et al. (2010), described in Section 2.3.1, which was based largely on work by Granot (2005); Granot, Cohen-Tanugi & Silva (2008); Sari, Piran & Narayan (1998).

2.3.1 The Pulse Model

The model by Genet & Granot (2009b), referred to as the G&G model, is a simplified toy version of the Fireball model, whereby the observed gamma-ray emission arises from a relativistically expanding shell (where Lorentz factor, $\Gamma \gg 1$), of radius, R, that is extremely thin ($\Delta R_{shell} \ll R/\Gamma^2$) [3]. The Lorentz factor of the shell is taken to evolve with radius as $\Gamma^2 = \Gamma_0^2(R/R_0)^{-m}$, where $\Gamma_0 \equiv \Gamma|_{R_0}$. In their work, Genet & Granot derived both the specific case of a shell in its coasting phase of expansion ($m = 0$), and a more general case where m is a user defined input. In the work of Willingale et al. (2010), the limiting case of $m = 0$ was used throughout [4]; as this chapter is an extension of that work, we adopt the same model. Emission from a shell is modelled as having arisen over a finite range of radii, $R_0 < R < R_f$ (red curves, Figure 2.2), where the component of the shell outside of this region is inert. At a radius, $R = R_0$, the leading edge of the shock enters the emission zone, and immediately turns on; progressively higher-latitude regions of the shell begin to emit as they, too, begin to traverse the emitting region until eventually the flux peaks at $R = R_f$. Beyond this radius, emission from the shell terminates and the pulse

[3] The emitting electrons of internal shocks are expected to be fast-cooling, such that energy is radiated on a shorter timescale than the shell-crossing time. This leads to a thin, cooling layer of emitting electrons behind the shock.

[4] The Fireball model suggests that the majority of internal shocks occur when the two colliding shells are in their coasting phases. Whilst internal shocks rely on two colliding shells, the proceeding shell must be at a lower Lorentz factor for collision to occur; a single shell toy model for the shock is therefore valid, as the higher-Lorentz shell would dominate the observed emission.

decays away as the trailing higher-latitudes continue to emit.

During this brief period of emission, the shell is assumed to be emitting in a uniform and isotropic manner, such that the co-moving luminosity, L' at co-moving frequency, ν', is dependent only on the radius of the shell ($L'_{\nu'} = L'_{\nu'}(R)$). The co-moving luminosity of the shell, over this range of radii, is therefore given by:

$$L'_{\nu'}(R) = L'_0 \left(\frac{R}{R_0}\right)^a S\left(\frac{\nu'}{\nu'_p}\right), \tag{2.1}$$

where the peak of the $\nu' L'_{\nu'}(R)$ spectrum occurs at a frequency $\nu'_p(R) \equiv \nu'_0(R/R_0)^d$, and $\nu'_0 \equiv \nu'_0|_{R_0}$; the model also assumes that the peak luminosity evolves with radius as $L'_{\nu'_p} = L'_0(R/R_0)^a$, with $L'_0 \equiv L'_{\nu'_p}|_{R_0}$. The factors a, and d are therefore the evolutionary indices of the co-moving frequency, and the co-moving luminosity respectively. The spectrum, $S(\nu'/\nu'_p)$, is given the Band functional form to replicate the observed prompt spectrum of the majority of GRBs [5].

For fast-cooling electrons in a shock with an internal magnetic field, B, the peak frequency of the νF_ν spectrum, ν_p, for a Fermi distribution of electrons with energies, γ_e, greater than the minimum injection energy, $\gamma_{e,min}$ ($\gamma_{e,min} \propto \Gamma$; see Equation 1.3), is given by $\nu_p = \nu_m$ ($\nu_m \propto \gamma^2_{e,min}\Gamma B$; see Equation 1.5), where ν_m is defined as the photon frequency emitted by an electron with energy $\gamma_{e,min}$. For uniform colliding shells, the relative Lorentz factor of the upstream and downstream shells, and therefore $\gamma_{e,min}$, are roughly constant; this leads to $\nu'_p \propto B'$. For the coasting phase ($m = 0$), the co-moving magnetic field is expected to be normal to the radial direction, such that $B' \propto B/\Gamma$; as we also expect $B \propto R^{-1}$, this leads to $\nu'_p \propto R^{-1}$ and $d = -1$. These shells, expanding with a constant Γ, have a shell-crossing photon flux, and an average energy per particle, which are independent of radius. This leads to the assertion that the energy generation rate, dE'/dt', and the total co-moving luminosity, $L' \sim \nu'_p L'_{\nu'_p}$ are constant (i.e. $\propto R^0$). As $\nu'_p \propto R^d$, $L'_{\nu'_p} \propto R^a$, and $d + a = 0$, then for $d = -1$, $a = 1$. These assertions are true for many different emission mechanisms in the fast-cooling phase, include synchrotron emission; the formulation used through this work is therefore based upon the limiting case of $m = 0$, $d = -1$, and $a = 1$.

[5] There is evidence, in some rare cases, of an underlying thermal component within the prompt emission spectra of GRBs (see Guiriec et al. (2011) for example), however it is not required to model the vast majority of GRB pulses.

A photon emitted from the source at time $T = t_{ej}$, concurrent to the ejection of a shell, will reach an observer (at redshift, z) at time $T = T_{ej}$. The forwardmost part of the expanding shell (assuming the observer is on-axis, this region corresponds to a latitude of $\theta = 0°$), will begin to emit as it passes through $R = R_0$ at time $T = t_0$. The arrival time of the first photon emitted by this shell will appear, with respect to the observer, to arrive at time $T = T_{ej} + T_0$ where T_0 is given by:

$$T_0 = \frac{(z+1)R_0}{2c\Gamma_0^2}. \tag{2.2}$$

The shell continues to emit at greater latitudes as it expands through the emission region, before the on-axis front of the shell abruptly ceases to emit as it passes beyond $R = R_f$ [6]; the time at which this occurs in the observer-frame is given by $T = T_{ej} + T_f$, where T_f is:

$$T_f = \frac{(z+1)R_f}{2c\Gamma_0^2} = T_0\left(1.0 - \frac{\Delta R}{R_0}\right), \tag{2.3}$$

and $\Delta R = R_f - R_0$. We furthermore define two normalised times:

$$\bar{T} \equiv \tfrac{T-T_{ej}}{T_f} \quad \text{and} \quad \bar{T}_f \equiv \tfrac{T_0}{T_f}, \tag{2.4}$$

for which $\bar{T} = 1$ corresponds to the peak time of the pulse. Integrating the luminosity over the whole equal arrival time surface produces a flux, in terms of the number of photons, N, per unit energy, E, per unit area, A, per unit time T, of:

$$\frac{dN}{dEdAdT}(E, T \geq T_0 + T_{ej}) = P(\bar{T}, \bar{T}_f)B\left(\frac{E}{E_f}\bar{T}\right) \tag{2.5}$$

where $B(E\bar{T}/E_f)$ is the notation for a Band function spectrum. It is important to note that only for a coasting shell of $m = 0$, and $d = -1$, does the observed flux function have the same form as the assumed Band function spectrum:

[6]For $R_0 < R < R_f$, the maximum latitude, from which photons reach the observer, is given by $\theta^2_{max} = [(T - T_{ej})/T_0 - 1.0]/\Gamma^2$. Where the shell has expanded beyond $R = R_f$, the emission comes from a range of latitudes, $\theta_{min} < \theta < \theta_{max}$, where $\theta^2_{min} = \bar{T}/\Gamma^2$.

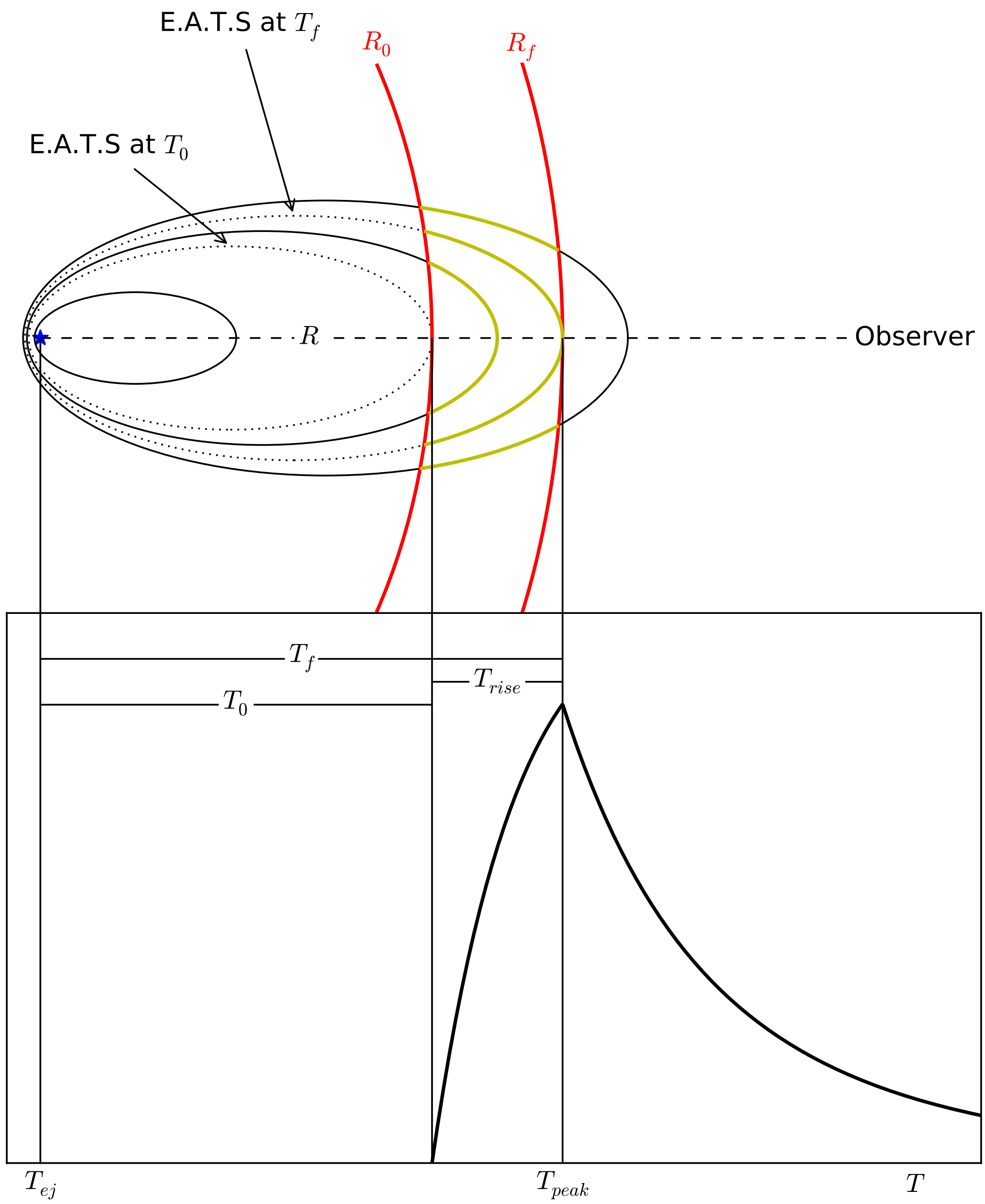

Figure 2.2: *Schematic of the equal arrival time surfaces (EATS) of a spherically expanding shell in a coasting phase ($m = 0$). The surface will appear as an ellipsoid when the expansion is at a high Lorentz factor, with the ratio of the major to minor axis of $\Gamma = 3$ set for illustration purposes (Rees, 1966). The coasting shell, emitted at time $T = T_{ej}$ (blue star), is quiescent for $R < R_0$, until it enters the emitting region ($R_0 < R < R_f$) at time $T = T_0 + T_{ej}$. The emission from the part of the expanding shell traversing the emitting region (yellow lines) will increase as more of the shell enters and begins to radiate, before reaching a peak at $T = T_f + T_{ej} = T_{peak}$. Beyond a radius, R_f, the forwardmost region of the shell is no longer emitting, resulting in a sharp drop in flux as the emission contribution comes from increasingly greater latitudes (HLE emission).*

$$B\left(\frac{E}{E_f}\bar{T}\right) = B_n \begin{cases} \left(\frac{E}{E_f}\bar{T}\right)^{\alpha} \exp\left(-\frac{E}{E_f}\bar{T}\right) & E\bar{T} \leq E_f(\alpha-\beta) \\ \left(\frac{E}{E_f}\bar{T}\right)^{\beta} (\beta-\alpha)^{\beta-\alpha} \exp(\beta-\alpha) & E\bar{T} > E_f(\alpha-\beta) \end{cases} \tag{2.6}$$

for a pulse with brightness B_n. The cutoff energy of the Band function, E_c decays with respect to time as $E_c(T) = E_f\bar{T}^{-1}$, where $E_f \equiv E_c|_{T=T_{ej}+Tf}$, and the peak of the νF_ν spectrum at $T = T_{peak}$ is $E_{peak} = (\alpha+2)E_f$.

In the original model by Genet & Granot, the formulation for the pulse flux is such that the normalising time is set from the point at which the shell begins to emit, (i.e. $T = T_0$). In performing fits of real GRB lightcurves, Willingale et al. instead chose to set this normalising time at $T = T_{peak}$, where the spectral data available for each pulse was maximal. As we, too, are fitting observed GRB lightcurves, the pulse profile in this chapter, $P(\bar{T}, \bar{T}_f)$, is given by:

$$P(\bar{T}, \bar{T}_f) = \bar{T}^{-1}[\min(\bar{T}, 1)^{a+2} - \bar{T}_f^{a+2}](1 - \bar{T}_f^{a+2})^{-1}, \tag{2.7}$$

and for $T = T_{ej} + T_f$, the value of $P(\bar{T}, \bar{T}_f)$ is 1 (see Figure 2.2 for pulse schematic). Although in most cases the model peaks at T_{peak}, in some combinations of model parameters (most notably for very large values of T_f, or for a hard spectrum), the pulse may have a rounded peak which begins to decay before $T = T_f$. In many cases this pulse form is suitable for the observed pulse, however in other cases, the pulse has a rounded, rather than sharp, peak. This can be explained by the fading of emission past $R = R_f$ from the lowest-latitude parts of the shell, rather than by a sudden cessation of emission. The effect upon the observed pulse peak is relatively small however, and in the interests of utilising a simple model, we ignore continued pulse emission.

The totality of the prompt emission is often a combination of two or more of these pulses, with the observed rapid decay phase (RDP) in the early-time X-ray lightcurves of the XRT consisting of the superposition of all the preceding tails of the prompt pulses. Each pulse can have a different spectral (E_f, α, and β), temporal (T_{rise}, and T_f), and brightness (B_n) characteristics; the specific combination of these pulses can reproduce the complicated time-averaged spectra seen in the GRB prompt emission. It should also be noted that late-time X-ray flares can be explained by either a central engine that is active for longer, or via refreshed shocks

(Chincarini et al., 2010, 2007); therefore the pulse model described above is also suited to fitting these flares.

2.3.2 The GRB Afterglow

Unlike the pulse model by Genet & Granot, the model for the afterglow component of Swift GRBs is based on empirical fits to the observed X-ray afterglows by the XRT. The decay phase of 40 XRT lightcurves displayed a common temporal profile: that of an early, exponential decay, $\propto \exp(-T_{fall}/T)$, followed by a turnover into a power-law decay, $\propto T^{-\alpha}$; the transition point of which occured at time $T = T_{fall}$, where the gradient, and the flux, of the two functions are equal (O'Brien et al., 2006) [7]. In most lightcurves, but not all, this early component was then followed by the classic late-time afterglow "hump" with durations typically on the order of a few hours. As the initial rise of the afterglow was hidden by the, far more dominant, prompt emission component, the afterglow is observed as a plateau in the decay phase, which likewise evolves into a final power-law decay [8]. These simple lightcurves were further complicated by the addition, in some cases, of superimposed X-ray flares, similar in shape to those observed in the prompt emission.

It was shown that for both the RDP phase, and the afterglow components, c, the temporal behaviour, $A_c(T)$, could be modelled by the same empirical function, given by:

$$A_c(T) = A_{n,c} \begin{cases} \exp\left(\alpha_c - \frac{T\alpha_c}{T_{c,fall}}\right) \exp\left(\frac{-T_{c,rise}}{T}\right) & T < T_{c,fall} \\ \left(\frac{T}{T_{c,fall}}\right)^{\alpha_c} \exp\left(\frac{-T_{c,rise}}{T}\right) & T \geq T_{c,fall} \end{cases} \tag{2.8}$$

where $A_{n,c}$ is the normalisation of the afterglow component, c; the turn-on, and turn-over times occurs at $T = T_{c,rise}$, and $T = T_{c,fall}$ respectively; and the decay index at late-times is denoted by α_c (Willingale et al., 2007). This function reaches a maximum at time $T_{c,max} = (T_{c,rise}T_{c,fall}/\alpha_c)^{1/2}$ with flux:

[7] This modelled the rapid decay phase solely as an X-ray phenomena, as tying the RDP to the gamma-ray prompt emission would come a few years later.

[8] An additional break was sometimes seen at very late times of the X-ray afterglow, which was indicative of an achromatic burst jet-break (Bloom, Frail & Kulkarni, 2003; Frail et al., 2001; Rhoads, 1997, 1999)

$$A_{c,max} = A_{n,c} \exp\left(\alpha_c - 2\left(\frac{\alpha_c T_{c,rise}}{T_{c,fall}}\right)^{1/2}\right). \tag{2.9}$$

The totality of the Swift XRT temporal lightcurve was then produced by the co-adding of the prompt decay and afterglow components (see Figure 2.3). In the work of Willingale et al., and in this chapter, the prompt emission component is no longer fitted by this model, and is instead the X-ray tail of the totality of the prompt emission pulses, in agreement with the current understanding as to the origins of the rapid decay phase. To this end we also remove the need for subscripts on the rise and fall times, as well as the decay indices.

Like the pulse profile, the afterglow is convolved to a spectrum to produce the observed flux , in numbers of photons, N, per unit energy, E, per unit area A, per unit time, T, of:

$$\frac{dN}{dEdAdT}(E,T) = A(T)B\left(\frac{E}{E_f T_{fall}}T\right). \tag{2.10}$$

As the emission process for GRB afterglows, like that of internal shocks, arise from synchrotron processes as the shell ploughs into the external medium, the cutoff energy of the Band function, E_c, evolves with respect to time as $E_c(T) = E_f(T/T_{fall})^d = E_f(T/T_{fall})^{-1}$, where $E_f \equiv E_c|_{T=T_{fall}}$.

2.3.3 Raw Data

For each particular burst, the BAT 4-channel (15 - 25 keV, 25 - 50 keV, 50 - 100 keV, and 100 - 350 keV passbands) 64 ms binned lightcurve data file is downloaded from `http://gcn.gsfc.nasa.gov/swift_gnd_ana.html`. This file is passed through a minimum significance binning routine which iteratively loops through the data, extracting the bins which are above the user defined threshold, re-binning the remainder, and repeating until completion (see Section 2.1, Evans et al. (2010) for a more in-depth discussion of the routine). The XRT lightcurve data is extracted from the hardness ratio ascii file downloaded from the Swift XRT lightcurve repository (Evans et al., 2009, 2007), and contains the data for the hard (1.51 - 10 keV), and soft (0.3 - 1.5 keV) XRT passbands; as the XRT lightcurves are already processed, no further processing on our part is required.

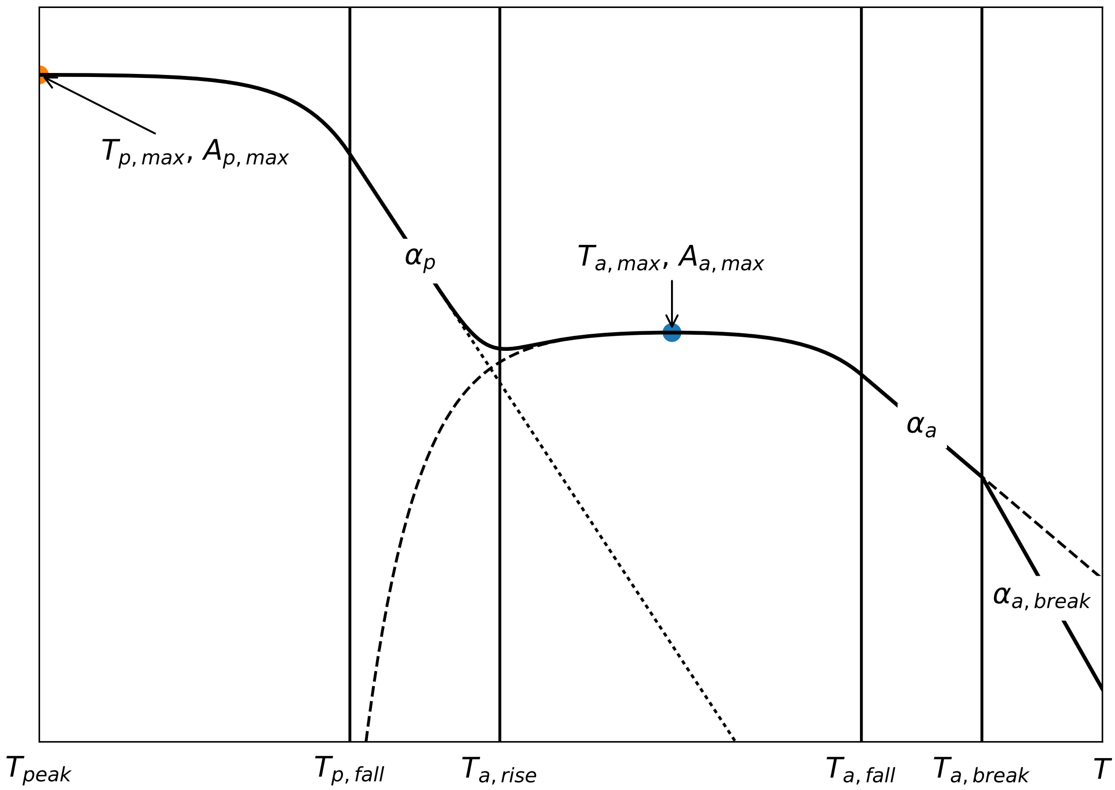

Figure 2.3: *Log-log schematics of the pulse decay phase (dotted profile; denoted by the subscript, p), and afterglow phase (dashed profile; denoted by the subscript, a) utilised by Willingale et al. to fit Swift XRT afterglows. The combined XRT profile is the superposition of the two components,* $A_p(T) + A_a(T)$*, and is shown by the solid black line. Peaks of the two profiles are annotated, and the relevant timescales, and decay indices are highlighted. The afterglow component includes a jet-break at time* $T = T_{a,break}$*, with a new, post-break, decay index of* $\alpha_{a,break}$*. The peak of the RDP component is set at a time* $T = T_{peak}$*, to highlight that the decay begins from the peak of a prompt emission pulse.*

Spectra Count Rates

The count rates of the various energy bands were calculated using XSPEC version 12.9.0 (Arnaud, 1996) for the prompt and afterglow phases of the GRB lightcurves. The XSPEC compatable data files required include: the unbinned XRT window timing, and photon counting spectral data (.pi files); and the BAT spectral files (.pha files); and are available to download from the Swift Burst Analyser site, `http://www.swift.ac.uk/burst_analyser/`, as a .tar file. The ancillary response files used by XSPEC for a particular time interval, and observing mode, are burst dependent, and are also contained within the aforementioned .tar file; along with the BAT response files (.rsp). The response matrix files are dependent on the epoch of observation [9], and must be downloaded separately.

The typical length of the Markov Chains used to fit the pulses, is of the order of 10^4, and as such is prohibitively time consuming (> several hours) when trying to run XSPEC over each iteration. Instead, a 3D lookup table (α, $\alpha - \beta$, and $\log_{10}[E_c]$) is calculated for each burst, assuming a Band function spectral profile. A $20 \times 20 \times 20$ grid will take approximately 15 minutes to generate, whilst linear interpolation onto the grid takes fractions of a second per MCMC iteration. The count rates of the soft XRT passband are sensitive to absorption by the intervening dust column, and was corrected for by fixing the Galactic, and intrinsic column densities (using the early-time NH_{Gal}, and NH_{Int} data available from the XRT spectra page of the Swift Burst Analyser page) and running the XSPEC WABS (or ZWABS if the dust column was fit with a particular redshift) routine. It was also found that the XSPEC Band function model was hard-coded to be unable to generate a spectra with $E_c < 1$ keV; and as late-time pulse spectra often drops below this threshold, a custom XSPEC Band function was created to overcome this particular barrier.

2.3.4 Data Fitting

For each particular pulse, T_{rise}, and T_{peak} are clear observables in the GRB lightcurves and are defined by the user before fitting commences. The value of T_{rise} was initially allowed to float, in order to find the optimum position, before being fixed for all subsequent fitting. To avoid unphysical rise times, T_{rise} is fitted as a fraction of T_f, such that $T_{rise} = F_r T_f$ where $0 < F_r < 1$. In a few cases where the rise time is poorly constrained by a few datapoints, the rise time is fixed over all MCMC iterations; however, for the majority of all fitted pulses, the MCMC routines are able to find a global minimum (see Figure 2.4 for example posterior distributions of GRB 110715A). In many bursts, significant emission is seen before the trigger and some of the first pulses in such cases will have a large negative T_{rise}. This is corrected for by converting the zeropoint of all GRB lightcurves to the start of the rise of the first pulse, i.e. $T_{zero} = T_{peak,1} - T_{rise,1}$; with all subsequent pulse peak times within the lightcurve updated such that $T_{peak,n} \rightarrow T_{peak,n} - T_{zero}$.

For all pulses, the low-energy index of the Band function was fit from an initial point

[9] The required response matrix files for a particular epoch are shown in `http://www.swift.ac.uk/analysis/xrt/files/SWIFT-XRT-CALDB-09_v20.pdf`.

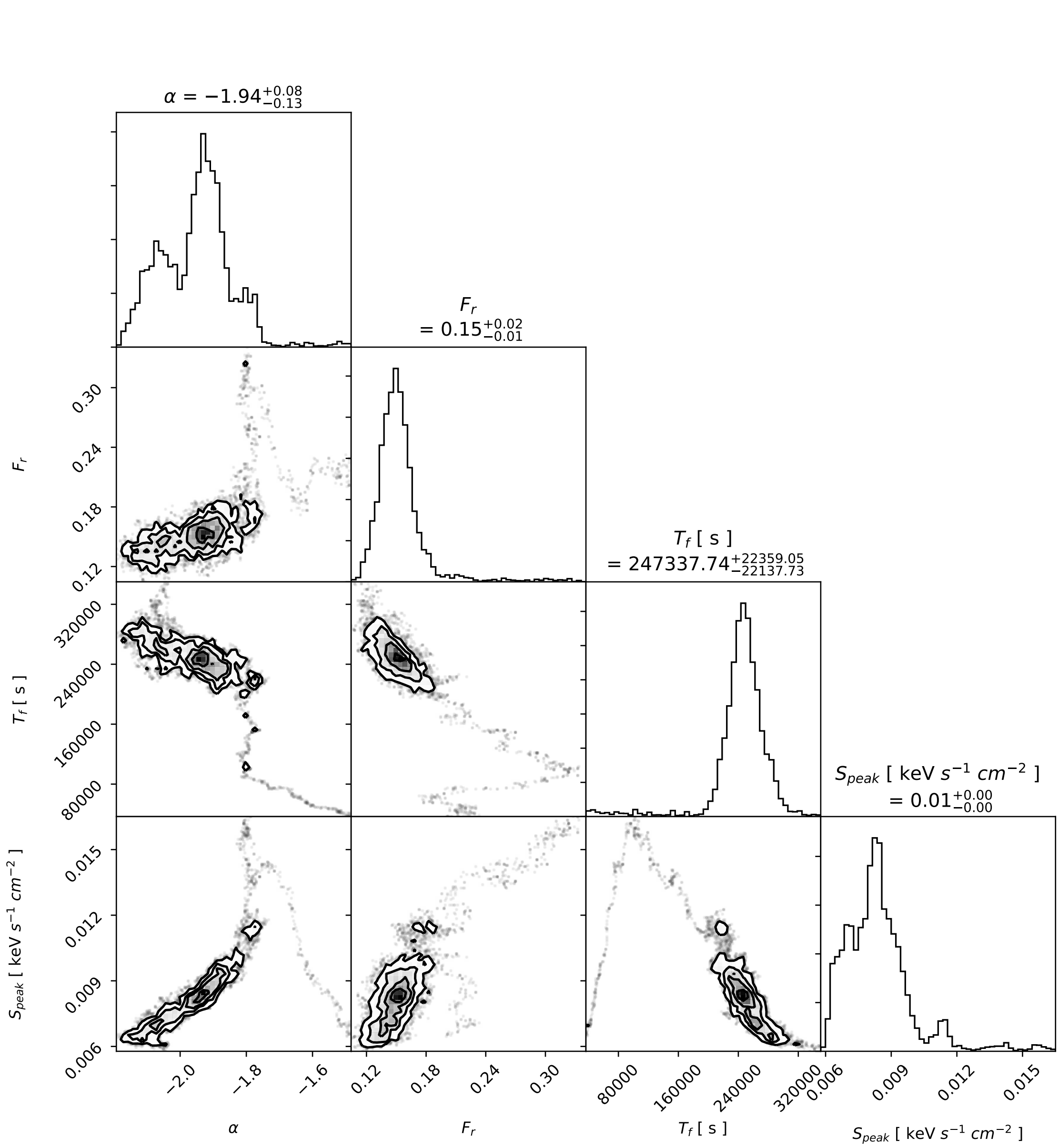

Figure 2.4: *Example posterior distributions of the pulse fitting of the 7^{th} pulse of GRB 110715A, derived using a Metropolis-Hastings MCMC routine, and a chi-squared likelihood function. α, and E_f are the low-energy index, and cutoff energy $E_f = E_c|_{T=T_{peak}}$ of the Band function respectively. T_f, is the arrival time of the last emitted photon of the shell; F_r, is the arrival time of the first photon as a fraction of the arrival time of the last photon of the pulse ($T_{rise} = F_r T_f$); and S_{peak} is the flux at time T_{peak}. The MCMC chain consists of 10^4 correlated samples (grey transparent points), with 2D binning in the highest density central regions of the posterior; contour lines denote regions of 0.5, 1, 1.5, and 2 σ confidence, with a "burn-in" phase also seen. Quoted figures are the mean parameter values of the posterior distribution and are marginalised over all other parameters; also quoted are the inter-quartile range denoted as the sub/super scripts.*

at $\alpha = -1.5$, whilst the difference between the low and high spectral indicies was fixed at $\alpha - \beta = 10$. This effectively reduces the Band function to a simpler power-law with an exponential cut-off. Because of the relatively soft energy bandwidth of the Swift BAT, and the signal to noise of the measured light-curves, a power-law with exponential cutoff produces a comparable fit quality to that of a Band function, without being so computationally demanding. For a few pulses the count rate in the higher energy channels was effectively zero and the spectral index was very poorly determined. In such cases the lower spectral index was therefore constrained to $\alpha > 2.5$. For the majority of GRB pulses the cut-off energy of the Band function lies outside the passband of the BAT; in such cases we fix the cutoff energy of the Band function at T_{peak} at $E_{f,z} = 500$ keV in the source frame of the burst, corresponding to $E_f = 500/(z+1)$ keV in the observer frame, similar to the fixed cutoff energies utilised by other studies, e.g. Firmani et al. (2004); Natarajan et al. (2005). For some pulses however, with good statistics and energy coverage (including both the BAT and XRT data), it was possible to constrain E_f by the fitting to some other value (usually a lower energy).

In work by Willingale et al. (2010), degeneracy was observed between the fitted temporal parameters, such as T_{rise}, and the emission process index, a, whereby a fast rise can be achieved when $a = 1$, and T_{rise} is fast; or $a > 1$, and T_{rise} is on longer timescales. Whilst observing any deviation from pure synchrotron emission in the shell is of great interest for studies of the fireball model, in most cases the pulses are not well defined enough to simultaneously fit both parameters and so a is constrained throughout this Chapter at $a = 1$. In a few cases, features in the GRB lightcurves are not well reproduced by the pulse model; plots of these GRBs, and a discussion of their peculiarities, are outlined in the following section.

2.4 The Swift GRB Catalogue

Collating the vast amount of temporal, spectral, positional, and morphological data available for Swift GRBs is extremely time consuming. Many online catalogues and tables are available for the various GRB parameters, including (but not limited to): the first, and second Swift burst catalogue (Sakamoto et al., 2008a, 2011b); the NASA maintained Swift GRB table (for the url, see Appendix I.1), and the Swift Burst Analyser maintained by Phil Evans (where we extract our raw lightcurve data; Evans et al. 2009, 2007). To reduce the extremely large number of citations inevitibly required, we use the data collected in the comprehensive Third Swift BAT GRB Catalogue by Lien et al. (The 3rdS catalogue; references therein), which consists of all Swift BAT observed GRB data from mission launch, through to GRB 160716A. When referring to a particular GRB parameter (e.g. T_{90}), we cite the table identifier in that work, from which we extract the data, for ease of comparison.

We have attempted to fit the 397 redshift observed Swift BAT and XRT GRB lightcurves of the 3rdS catalogue with the G&G pulse model, and empirical afterglow model, described in Section 2.3. To ensure a good quality of fits, several observation criteria are applied: 1) bursts must have clear evidence of a minimum of one pulse in the BAT passbands; 2) the observed pulse within the BAT must have a suitable level of statistics, typically $\geq 5\sigma$, to ensure that such an event is real; 3) early XRT data must be available to allow constraining of the rapid decay phase from the combined BAT pulses; and 4) the lightcurves must not have broken observations of pulses and flares due to orbit breaks, which complicates the determination of the true pulse parameters. GRBs can fail multiple criteria, and we highlight the number of GRBs rejected by each criterion, and morphology type, in Figure 2.5. Out of a possible 397 GRBs, we were able to fit a total of 182 bursts, rejecting 219 GRBs, to produce a completeness of 46%. For GRBs classed as ultra-long, short with extended emission, or are of unconstrained duration, we suffer from small number statistics and can therefore not determine, with any degree of certainty, whether the redshift distributions of the GRBs fitted in this chapter are truely representative of the parent population. For long and short duration bursts, the redshift distributions consist of much larger sample sizes, and are representative of the parent redshift distributions. The full list of rejected GRBs, their redshifts, types, durations, and failcodes is available in Table 1 of Appendix II; whilst the full list of fitted GRBs, their redshifts, types, durations, column densities, and χ^2_r values are available in Table II of Appendix II.

The monthly observation rate of Swift GRBs is highlighted in Figure 2.6 and shows that the percentage of GRBs with an observed redshift has dropped from a high of 57% in 2006, down to 22.4% (for a partial year) in 2016. It has been suggested that this significant drop in redshift completeness is, in part, due to the initial excitement of rapid burst followup being replaced with the tedium of routine observation (Perley et al., 2016a). As a significant fraction of GRB redshifts are derived from long-term observations of the host galaxy, more recent years will see a drop in redshift

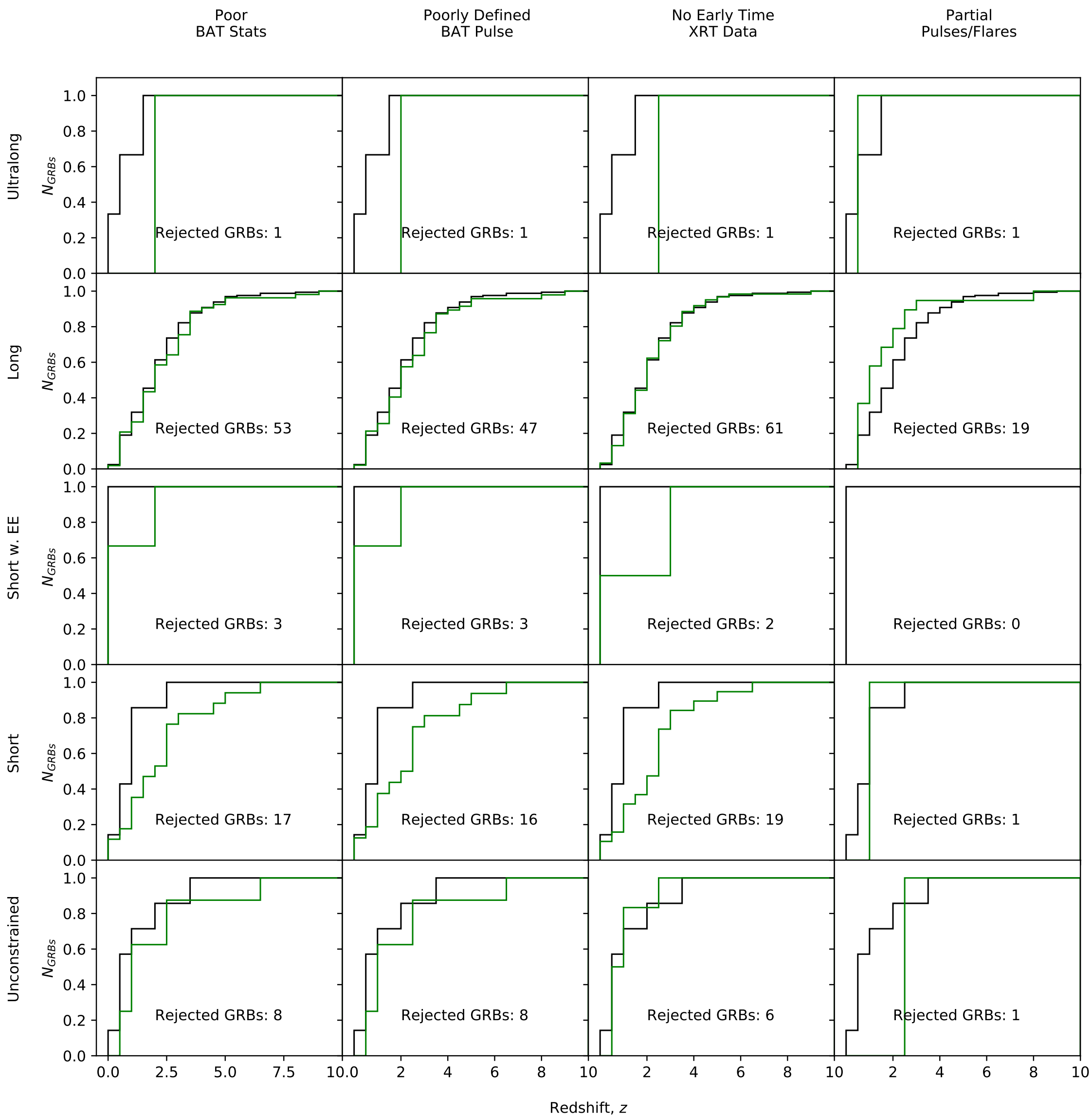

Figure 2.5: *The cumulative redshift distribution of GRBs that failed the various suitability criteria (green) vs the distribution of GRBs which we were able to fit (black). Bursts are separated into their morphologies depending on the scheme outlined in Lien et al. (2016b); however the unconstrained bursts group is a combination of all the bursts in Lien et al. to which there was uncertainty as to the type.*

completeness until such surveys are complete. These later years are subsequently dominated by redshift observations taken within days, or weeks, of the initial burst; for these reasons, catalogues that aim to produce unbiased samples, such as the TOUGH (Hjorth et al., 2012), and SHOALS (Perley et al., 2016a) surveys, often extract the first 4-5 years of observational data (2005 - 2009) because of their high level of completeness. It has been reported that a seasonality effect on the redshift completeness exists, with the January - March period seeing a completeness of 26% compared to a 35% completeness for the rest of the year; however, this effect is seen for both northern, and southern, hemisphere bursts (Perley et al., 2016a); as we are not attempting to produce a redshift unbiased GRB catalogue, we do not quantify such an effect.

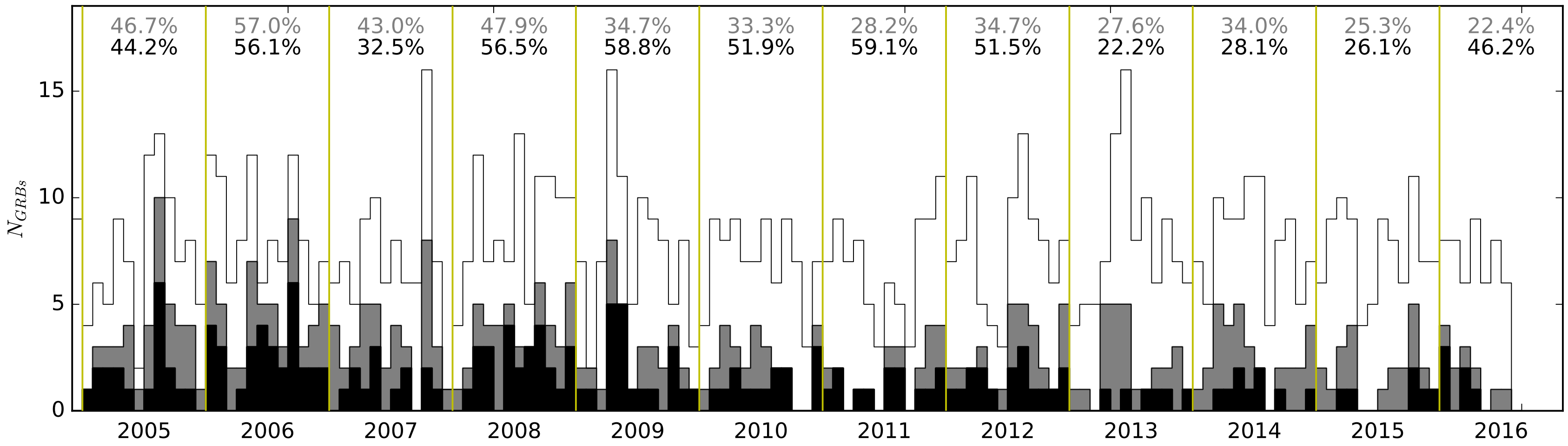

Figure 2.6: *A histogram of the number of GRBs detected per month in the 3rdS Catalogue, for all GRBs (white histogram), GRBs with observed redshifts (grey histogram), and GRBs which we were able to fit (black histogram). The percentages at the top denote the percentage of all GRBs with observed redshift for that particular year (grey text), and the percentage of all GRBs with observed redshift that we were able to fit (black text). Yellow lines are the boundaries for each year.*

GRB Category	No of bursts	No of bursts w. redshift	No of bursts w. redshift fitted
Short	88	28	7
Short w. EE	12	6	2
Long	889	332	163
Ultralong	10	9	3
Unconstrained	75	22	7
Total	1074	397	182

Table 2.1: *Summary of the number of GRBs in each catagory. The first two columns are derived from data in the 3rdS Catalogue, as are the GRB types of our fitted population of GRBs.*

In the early years (2005 - 2012), we are fairly consistent in our ability to fit the GRB lightcurves with our pulse model; however if simpler, more routine bursts, are not having their redshifts reported, then our completeness decreases as we attempt to fit a population dominated by more complex lightcurves. It has been shown that the fraction of time that the BAT is slewing, was fairly steady over the 2005 - 2011 period, at approximately 0.10; however, this has marginally increased from 2012 onwards to $\sim$ 0.14 (Lien et al., 2016b). As the number of GRBs detected has remained steady, this translates as a slightly longer slew time per burst; as we require good, early-time XRT data, in order to fit the rapid decay phase of the XRT afterglow, this increased slew time could have a subtle effect on our ability to fit the later GRB lightcurves.

We see significant variation between the different methods of redshift measurement, and our ability to fit the GRB lightcurves (see Figure 2.7). Typically observation of the burst afterglow will see a higher level of fit completion than that of the GRB population with redshifts derived from observations of the host galaxy. GRBs with photometric redshifts are also more difficult to fit when compared to GRBs with spectroscopically derived redshifts; however, only in the case of GRB 160703A is this is due to the photometric redshift only providing an upper limit to the redshift, which we consider to be too poor quality to fit.

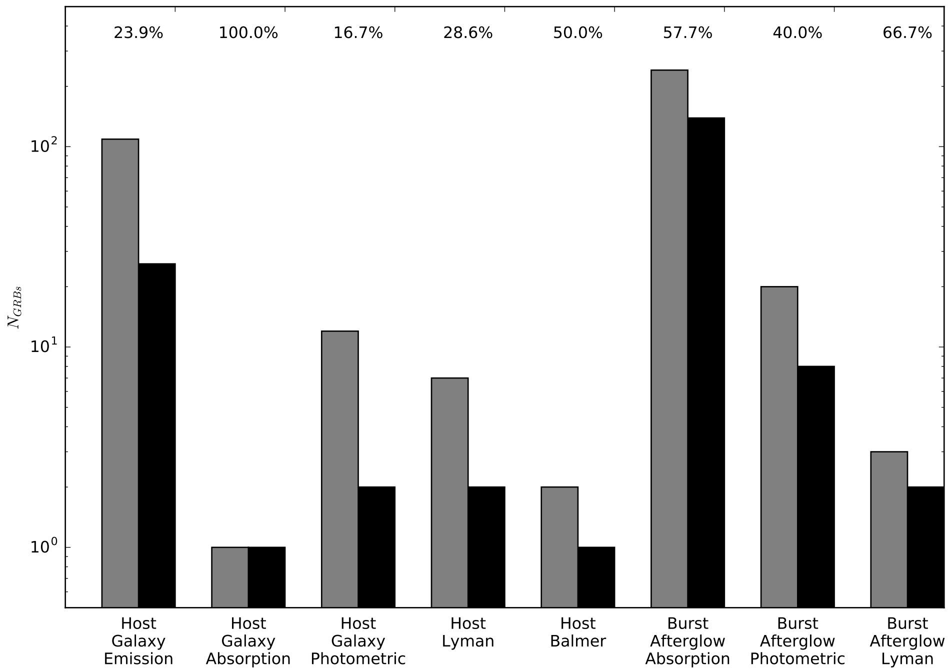

Figure 2.7: *A histogram of the various redshift measurement types from the 3rdS Catalogue (grey bars), and the GRBs fit in this Chapter (black bars). The percentage of each measurement type we were able to fit is denoted at the top in black text.*

2.4.1 GRB Morphology

The number of bursts of each of the common types (short, short with extended emission, long, ultralong [10], and unconstrained) are summarised in Table 2.1, and are taken from Table 2 of the 3rdS Catalogue. Table 3 of the 3rdS Catalogue lists all the bursts confidently defined as short bursts with extended emission; whilst Table 4 lists bursts which are potentially short bursts with extended emission. Bursts from Table 4, which we were able to fit, are also classified as unconstrained. Some differences are seen between the numbers reported in Table 2.1, to those reported in the source, as the numbers quoted therein include bursts which are potentially of that class (i.e. there is uncertainty to their type); in this Chapter, we redefine those bursts whose class is uncertain, as unconstrained. The distribution of BAT T_{90} durations are shown in Figure 2.8 for all GRBs with observed redshifts, and the bursts which we were able to fit. For bursts that lie on either side of the 2 s T_{90}

[10]Ultralong bursts in the 3rdS Catalogue are defined as bursts with $T_{90} > 1000$ s.

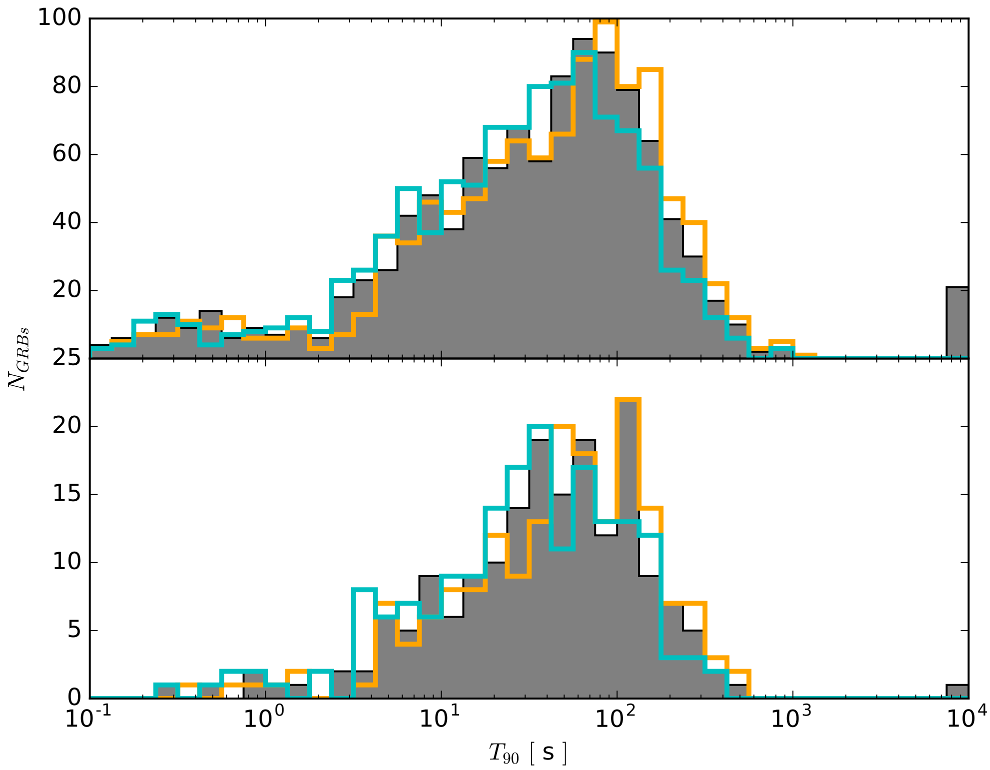

Figure 2.8: T_{90} *distributions (grey) for the BAT detected GRBs with observed redshift (top), and the fitted GRBs in our sample (bottom); also shown are the respective lower bound (cyan), and upper bound (orange) distributions.*

descriminator of Kouveliotou et al. (1993), if the uncertainty of the T_{90} value is large enough to allow the burst to potentially lie in the other category then we consider the burst type to be unconstrained; this equates to 10 bursts for our fitted sample, and 52 bursts for all GRBs with observed redshift in the 3rdS Catalogue.

The bar plot of Figure 2.9 (data taken from Table 2.1) displays the population of each GRB category. We find that short bursts, and short bursts with extended emission, are the most difficult for us to fit; this is due to the lack of early-time XRT data, however poor statistics in the BAT, and the lack of clear pulses are also of similar importance (see Figure 2.5).

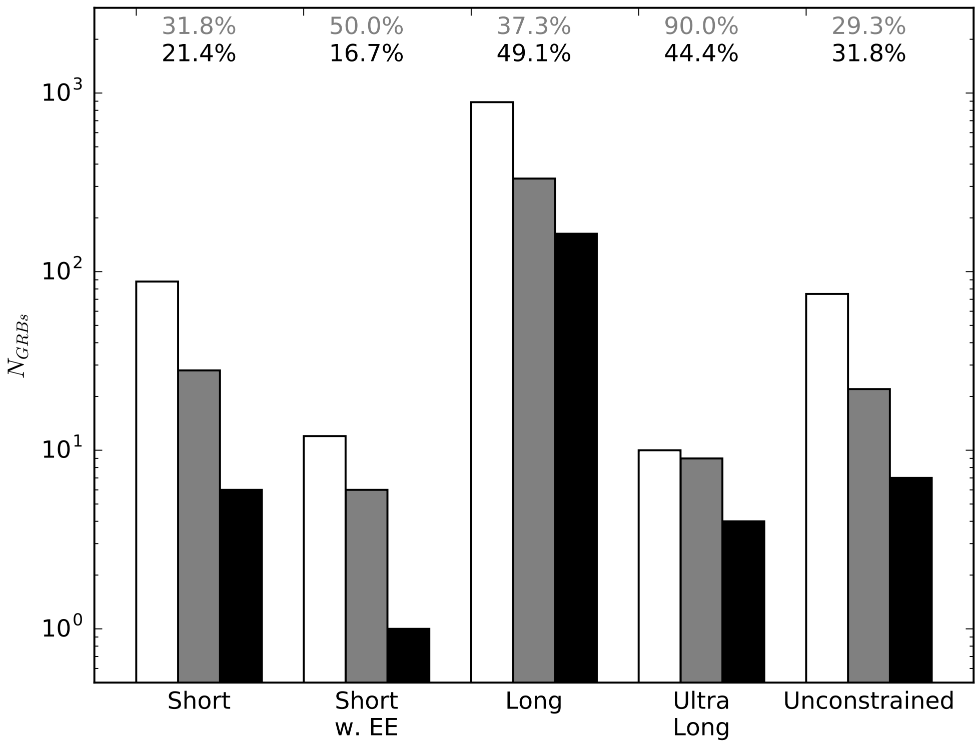

Figure 2.9: *The population of each GRB category for all Swift detected GRBs (white bars), GRBs with observed redshifts (grey bars), and our fitted GRB lightcurves (black bars). The figures at the top denote the percentage of all GRBs with observed redshift for that particular category (grey text), and the percentage of all GRBs with observed redshift that we were able to fit within that group (black text).*

2.4.2 Absorption Columns

As the count rate of the soft XRT passband is sensitive to absorption by the intervening dust column, we collate the early-time NH_{Gal}, and NH_{Int} data from the XRT spectra pages of the Swift Burst Analyser in order to produce dust-corrected count rates in the XRT passbands. These are produced automatically by deriving the Galactic column densities from the Galactic HI maps of Kalberla et al. (2005) using the element abundances of Anders & Grevesse (1989), and fitting the excess absorption (see Section 2.1.1, Evans et al. 2009, for details). The sky distribution of our fitted bursts are shown in Figure 2.10, for both the Galactic, and intrinsic dust columns, with larger circles denoting GRBs at higher redshift. Unsurprisingly, we see that higher Galactic dust columns are observed closer to the plane of the Galaxy, where the density of GRBs with observed redshifts are also lowest. This is reflected in the distribution of NH_{Gal}, which shows that there is no obvious bias between GRBs with observed redshift, and our own fitted GRBs; however for GRBs with high NH_{Gal} ($> 3 \times 10^{21}$ cm^{-3}), the fraction of GRBs with observed redshift drops dramatically. Due to extinction by the thicker dust column closer to the Galactic plane, the ability to observe the optical afterglow is inhibited, although other observational constrains, such as source confusion, are also contributing factors.

The NH_{Int} column density is derived by separating the total dust column density into Galactic dust, and excess components (see for example, Willingale et al. 2013); and for bursts where NH_{Gal} is high, the sensitivity to NH_{Int} will be much reduced. As the redshift completeness of high NH_{Gal} bursts decreases, this effect is rotated onto the NH_{Int} column density distribution, and produces the appearance of a slight bias in favour of observing the GRB redshift when the NH_{Int} column density is higher. In order to improve their redshift completeness, and reduce bias, surveys such as TOUGH, SHOALS, and BAT6 introduce foreground extinction cuts ($A_V <$ 0.5 mag, which corresponds to $NH_{Gal} = 10^{21}$ cm^{-3} using the $A_V - N_H$ relation of Predehl & Schmitt 1995), which essentially removes most bursts within 20° of the Galactic plane (for reference, $NH_{Gal} = 10^{21}$ cm^{-3} corresponds to an average Galactic latitude of $-13°$ in the South, and $+22°$ in the North; Willingale et al. 2013). Such studies do not, however, distinguish between the various causes of the extinction.

The intrinsic X-ray column density of our fitted GRBs shows strong correlation with the redshift of the burst (see Figure 2.11), in agreement with other studies that utilise fitted spectral data from Swift (e.g. Campana et al. 2012, 2010; Starling et al. 2013; Watson & Jakobsson 2012). Initially, this correlation was assumed to have arisen from the mapping of the excess absorption at $z = 0$, to the intrinsic column density in the burst frame [11] (Galama & Wijers, 2001). Numerous, alternate, suggestions as to the cause of this correlation have been put forward, including photoelectric absorption from the intergalactic medium (Behar et al., 2011); contributions from intervening systems in the line-of-sight, (Campana et al., 2012); or absorption arising from a diffuse, warm-hot, intergalactic medium, (Starling et al., 2013).

[11] If the intrinsic absorption column density is located entirely, or at least significantly, at the host, then the effect of an absorbing column of gas upon X-ray photons is expected to decrease with redshift. As one approaches the source frame of the observed X-ray photons, the photon energy range is blueshifted, and so the cross-section of the intervening column is reduced.

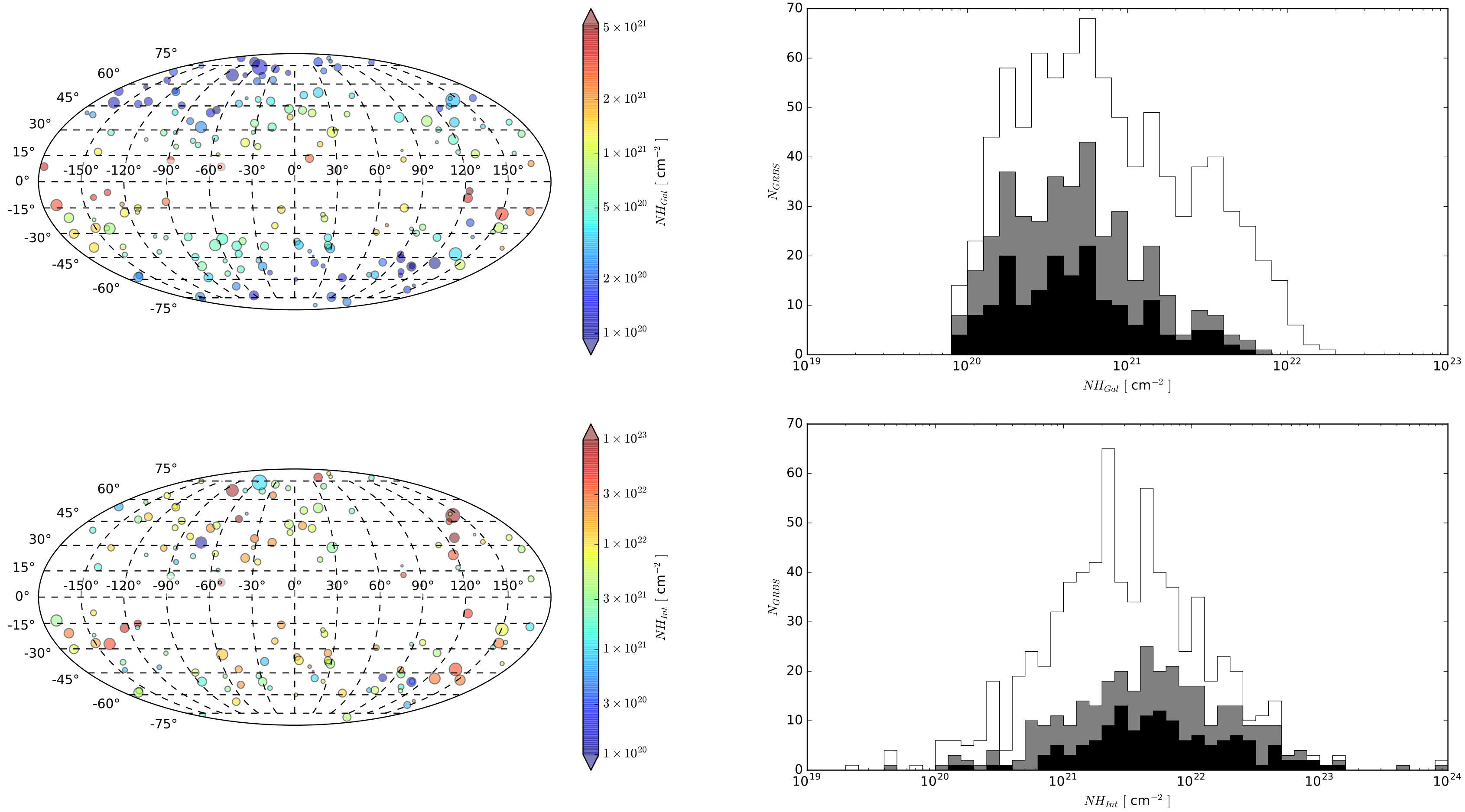

Figure 2.10: *Sky maps (left; in Galactic co-ordinates) and histograms (right), of the Galactic absorption column,* NH_{Gal} *(top row), and the intrinsic absorption column,* NH_{int} *(bottom row). The larger diameter circles denote GRBs at higher redshift. The* NH_{Gal}*, and* NH_{int} *histograms for the entire 3rdS Catalogue are shown (white histograms), along with the distributions for the redshift observed 3rdS GRBs (grey histograms), and the GRBs fit in this Chapter (black histograms).*

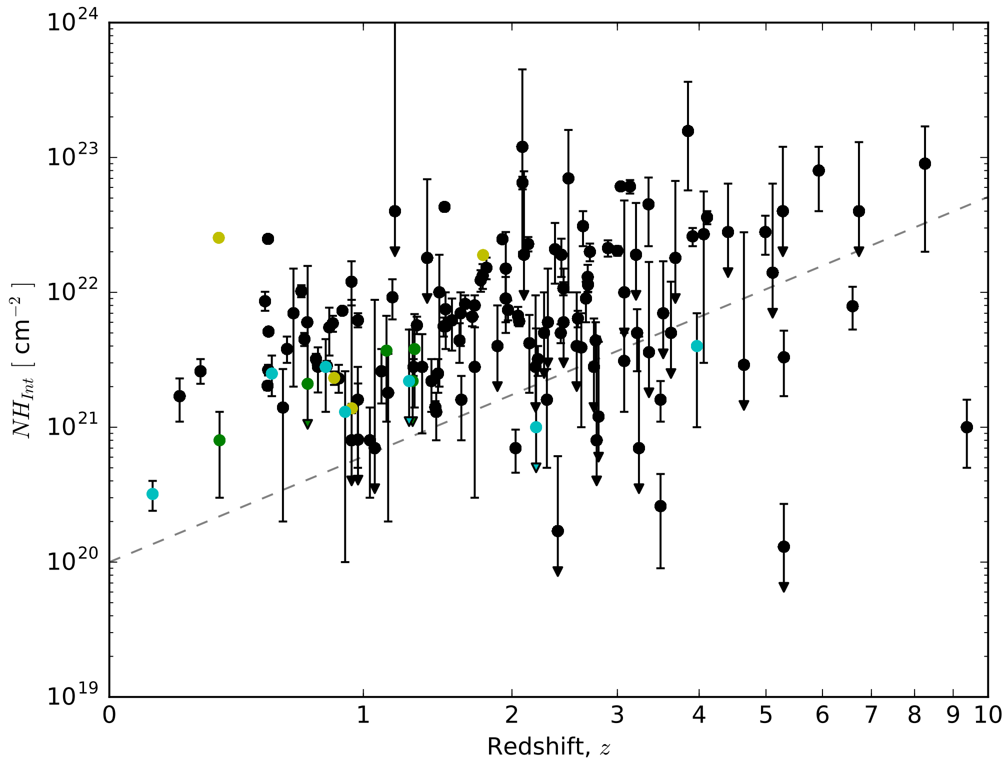

Figure 2.11: *The intrinsic X-ray column density, NH_{int}, as a function of redshift for ultralong (yellow), long (black), short (green), and unconstrained duration (cyan) GRBs, with the errorbars denoting the 90% confidence interval; downwards facing arrows denote unconstrained lower limits. The $(z+1)^{2.6}$ mapping relation of the excess absorption at $z = 0$, to the intrinsic column density in the burst frame (Galama & Wijers, 2001), is shown by the dashed grey line.*

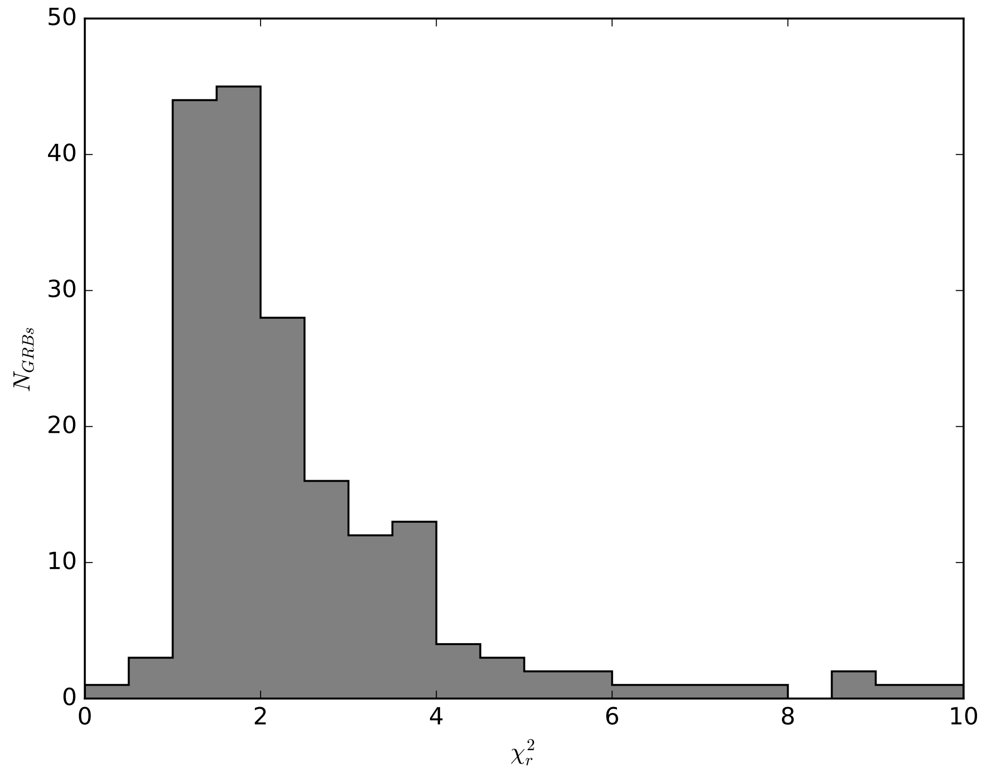

Figure 2.12: *The distribution of fitted GRB lightcurve* χ_r^2 *values, using the pulse model of Genet & Granot (2009b), and the afterglow model of Willingale et al. (2007).*

2.4.3 Fit Quality

The entire list of fitted pulses are shown in Table 3 of Appendix II, with the sequence of pulses within the burst numbered in temporal order. Where parameters were free to float during the fitting process, the 90% confidence intervals are displayed as sub/super scripts. In Table 3, T_{peak} is the normalised time, with the origin equating to the start of the first fitted pulse within the burst; because of this, the rise time, T_{rise}, and the peak time are always equal for the first pulse of each burst. T_{peak} is not to be confused with the time of peak flux, which can occur later; it is the time of the start of the pulse decay after the final shell is ejected at time T_{ej}.

The low-energy spectral index of the Band function, α, and the cutoff energy at time $T = T_{peak}$, E_f are also given. The original notation in Willingale et al. (2010) quotes values of b_1, for the low-energy spectral index of the Band function; however both values are not equivalent, as the formulation of the Band function in that work

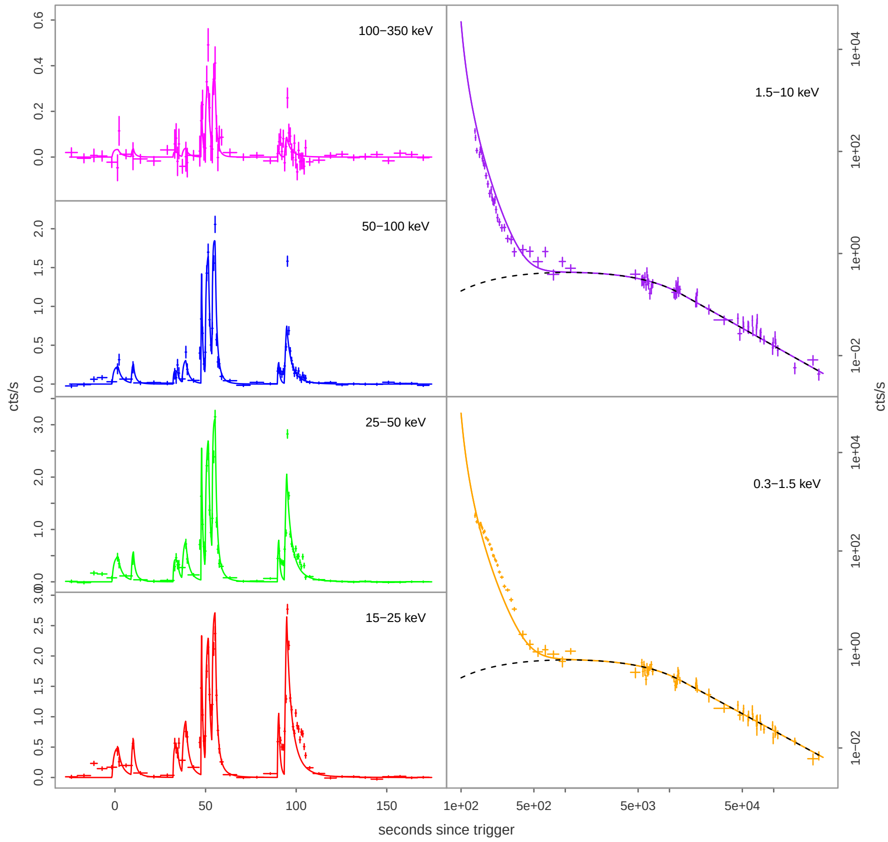

Figure 2.13: *Pulse, and afterglow fitted lightcurves of GRB 111228A.*

is such that $\alpha = b_1 - 1$. The fluxes of the Band function, F_f, at T_{peak}, observed over the combined Swift BAT, and XRT passbands (0.3 - 350 keV) are given, along with the bolometrically corrected isotropic peak luminosities, L_f. Conversion from flux to luminosity requires calculation of the cosmological luminosity distance, which we derive assuming a flat ΛCDM cosmology, with $H_0 = 71$ km s^{-1} Mpc^{-1}, $\Omega_m = 0.27$, and $\Omega_\Lambda = 0.73$ (Larson et al., 2011).

The entire list of afterglow components are shown in Tables 4, and 5 of Appendix II, with Table 4 containing the temporal parameters of the afterglow, and Table 5 containing the spectral components. The rise time of the afterglow plateau, T_{rise}, is typically set at around $T = 100$ s, between the end of the BAT, and the start of the XRT lightcurves; however for a few bursts (e.g. GRB 080319B, 081222), an earlier rise time is adopted. The time at which the afterglow decay evolves into a power-law, T_{fall}, is freely fitted, along with the decay index, α_c.

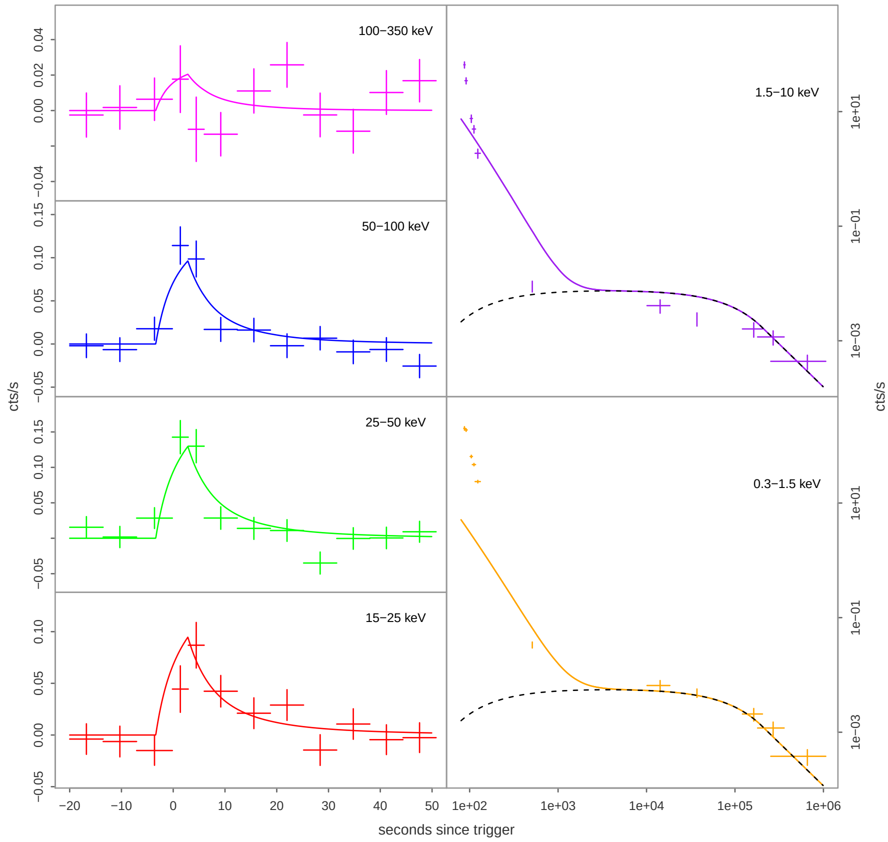

Figure 2.14: *Pulse, and afterglow fitted lightcurves of GRB 120422A.*

For a few bursts (e.g. GRB 061021, 150403A) an additional late-time break, T_{break} is observed, and is included in the model fits with the post-break decay index, α_{break}. The low-energy index of the Band function at $T = T_{fall}$, α_{fall}, and the cutoff energy, $E_{c,fall}$, are tabulated in Table 5, with the fluxes of the Band function, F_{aft}, observed over the bolometric passband (1 keV - 1 MeV). The bolometrically corrected peak luminosity of the afterglow plateau, L_{aft}, is also provided; along with the isotropic energy, and the T_{90} duration of the afterglow.

The distribution of fitted χ_r^2 values for the 182 GRBs, and afterglows, fitted in this catalogue are shown in Figure 2.12 with a median (and inter-quartile range) of $\chi_r^2 = 1.96^{+1.01}_{-0.51}$. Given the scale of the Swift Pulse, and Afterglow catalogue, we do not attempt a burst by burst description, and instead choose to highlight a few of our fits for which unusual behaviour can be seen, and which produces a significant contribution to the overall χ^2 of that particular burst. The poorest fit to a GRB

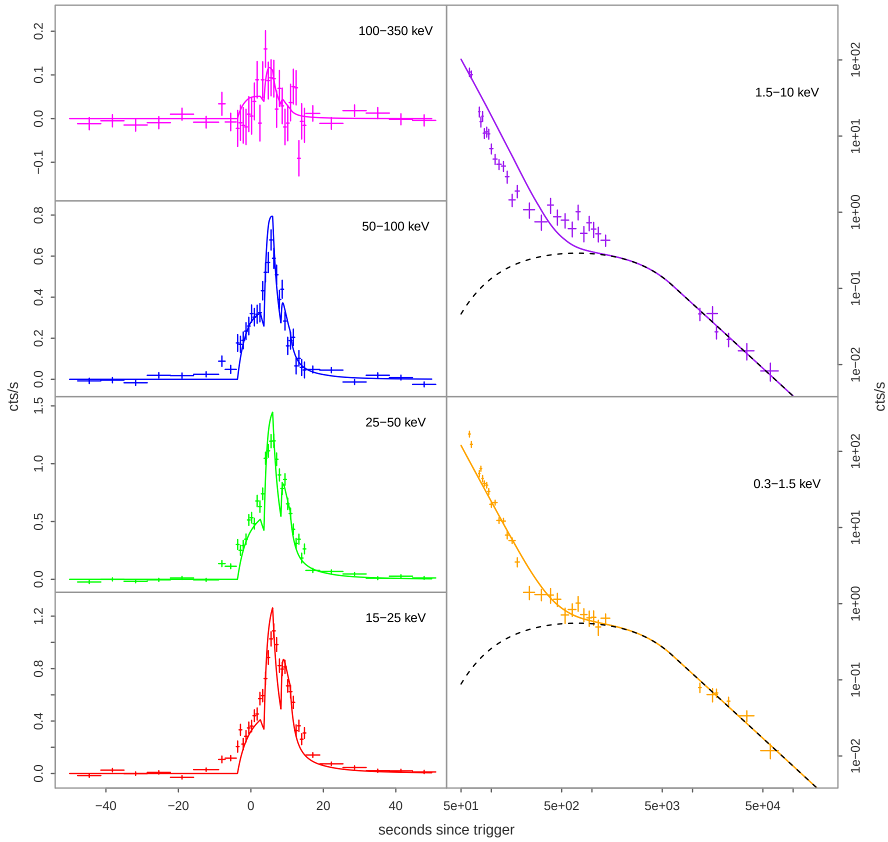

Figure 2.15: *Pulse, and afterglow fitted lightcurves of GRB 120811C.*

lightcurve in this work, is shown in Figure 2.13 for GRB 111228A. Although some of the poor χ^2 statistics come from poorly constraining the rapid decay phase in the XRT passbands, the significant proportion of the overall fit discrepencies come from the 9^{th} pulse, which is extremely narrow, and bright. As this pulse is the dominant contributer to the flux during the RPD phase, this pulse cannot be of an arbitrary narrowness in order to replicate the observed peakedness. A convolution of a very narrow, bright pulse, and a fainter, wider, and softer pulse would produce a better fit to the data; however, visually there is not strong evidence of a secondary pulse shape.

For both GRB 120422A (see Figure 2.14), and 120811C (see Figure 2.15), we are able to reproduce the totality of the BAT emission across all passbands, and fit the afterglow plateau and steady decay phases. Both these bursts, however, are examples of where the decay from the combined emission of the BAT pulses does

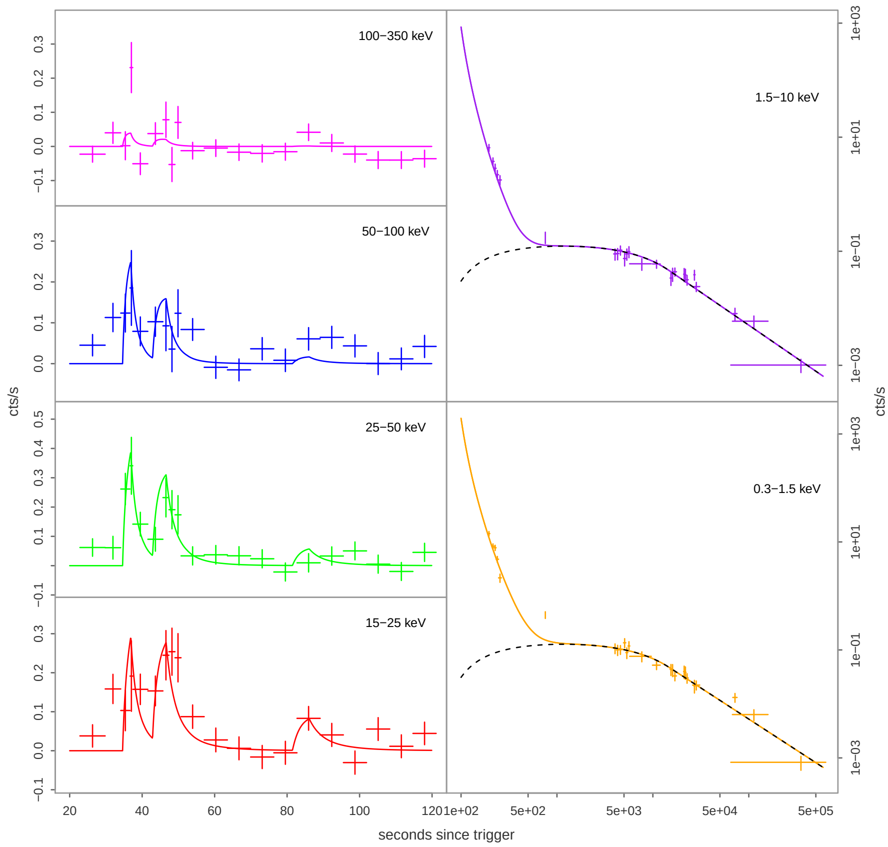

Figure 2.16: *Pulse, and afterglow fitted lightcurves of GRB 151027B.*

not map well to the observed rapid decay phase in the XRT passbands. For GRB 120422A, the observed RDP is at a significantly steeper gradient than that which we were able to fit. Underestimation of the RPD in the early times of the XRT lightcurve would suggest that some later, softer pulse were required; however there is clearly no evidence of this in the BAT passbands. For GRB 120811C, although the decay index of the RPD appears to reproduce the observed decay rate, the rapid decay phase in the harder XRT passband appears to lag behind that of the softer XRT passband. Both lagging of the RPD, and underestimation of the decay index, dominate the χ^2 distributions of those particular bursts, and produce some of the largest χ_r^2 errors in this work. Such discrepencies between the model fits, and the observed RDP, can also be indicative of unusal pulse behaviour (e.g. emission is non-synchrotron in nature); for a non-synchrotron emission process, the evolution in the spectral break is not constrained to $E_c \propto T^{-1}$ decay. Given that few bursts

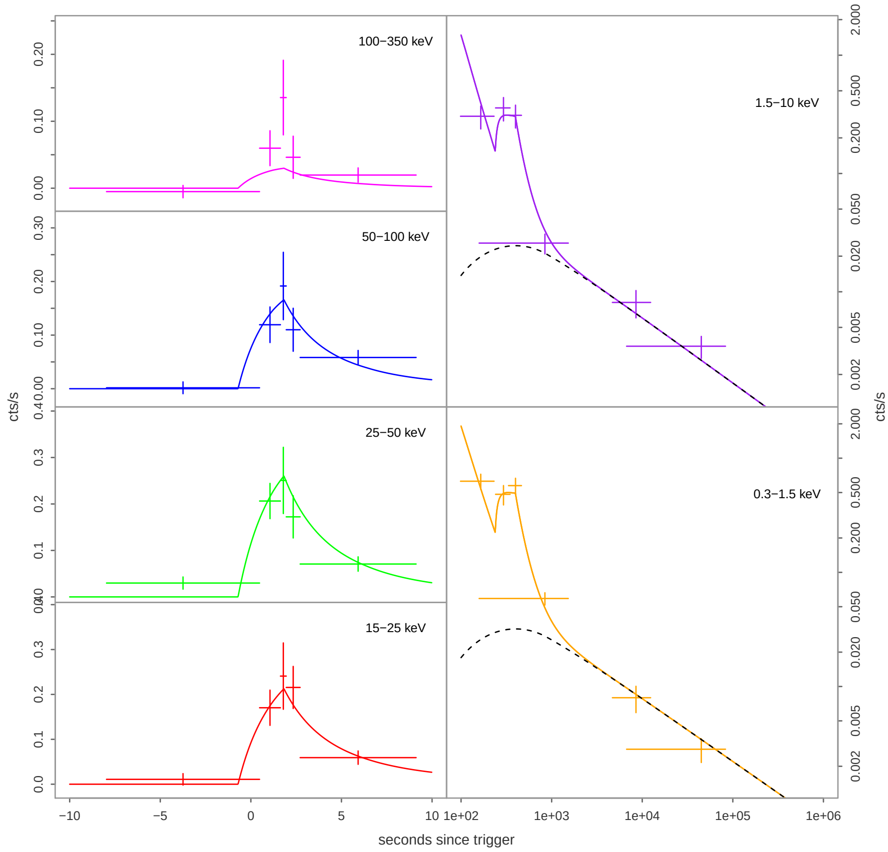

Figure 2.17: *Pulse, and afterglow fitted lightcurves of GRB 160314A.*

exhibit such differences, it is possible that the burst is special; however, in this work we have not examined if variable pulse evolution is a viable solution, given that the model still reproduces the observed prompt emission.

For a few GRBs, such as 151027B (see Figure 2.16) and 160314A (see Figure 2.17), the model reproduces the count rates in all but the highest energy passband of the BAT. This suggests that for a few cases, the cutoff energies of the Band function are too high; or the high-energy component of the spectrum is observable, and the $\beta = \alpha - 10$ restriction we place is unrealistic. For softer pulses (e.g. pulse 2, GRB 151027B), that peak in the lower-energy BAT passbands, this produces a lesser effect on the quality of fits, whilst harder pulses (e.g. pulse 1, GRB 151027B; and pulse 1, GRB 160314A) produce a greater contribution of error. Opening up the Monte-Carlo fitting routines to account for this, is problematic; for pulses with so few datapoints, this would produce poorly constrained parameters. Where XRT pulse data is also available, better constraints are possible, and the spectral break may be fitted.

When fitting the GRB lightcurves, model residuals can indicate the presence of an additional pulse, or flare. One has to be careful in such cases, however, as it is possible to over-fit a lightcurve by attributing a pulse to any significant variations. If a model is simple, the inclusion of a secondary component can be analysed by comparing the two posterior distributions (in such cases, the evidence must be included in posterior estimation), and determining if the addition of the secondary component is more probable. However, given the complexities of the lightcurves present, and the sophistication of the pulse models, we do not calculate whether the addition of a new pulse produces a statistically significant improvement in the quality of fits. We rely, instead, on selecting pulses that appear to have the 'traditional' fast-rise and exponential decay, and typically have more than one datapoint in high flux regions of the pulse. For extremely narrow, and faint pulses where the significance binning was required to be high, this can lead to some uncertainty and for such cases we err on the side of caution; however, in situations where a single temporal datapoint is of extremely high flux compared to the surrounding time bins, we may chose to fit a pulse.

2.5 Discussion

In this work we have produced a catalogue of 182 fitted GRBs, covering January 2005 to April 2016, and consisting of 862 pulses and 182 afterglow components. Throughout this section, we calculate the relations between the various fundamental parameters using a standard data reduction routine: the application of a Metropolis-Hastings MCMC, with a likelihood function derived from the methodology outlined in D'Agostini (2005). All fitted parameters are accompanied by values for the 50% confidence intervals of the fit posterior distributions. When discussing pulses in this section, we are not differentiating between pulses that occur in the BAT, or are late-time X-ray flares; in such cases where we discuss X-ray flares, such differences are expressly made.

2.5.1 Pulses

We find that the average number of pulses required to reproduce the entirety of a GRB lightcurve varies between each GRB type (see Figure 2.18). Unsurprisingly, given their significantly shorter duration, short bursts are typically fit with only one pulse, whilst short bursts with extended emission typically requires four pulses. Long GRBs were also fitted by a median of 4 pulses, although the variation is wider than that of short bursts with extended emission. Ultralong GRBs, such as GRB 130925A, require the greatest number of pulses to reproduce the totality of the gamma-ray and X-ray emission; typically around 17 pulses, but in some cases requiring up to 38 pulses, this highlights the enormous variability observed within the lightcurves of these particular types of GRBs. There are some GRBs classified as long, or unconstrained, which have a comparable number of pulses as those found in ultra-long GRBs; however, this could be either a natural outlier, or may indicate that the 1000 s delimiter in the 3rdS catalogue is incorrect. Furthermore, given that the number of GRBs fitted which do not belong to the long duration category is < 10 for each group, the importance of the differences in these distributions should not be over-estimated.

The spectra of the different GRB types display a great deal of similarity regarding the distributions of the low-energy spectral index; however given that many pulses were fitted with a fixed $500/(z+1)$ keV spectral break, the distributions of E_f are less informative and, in the most part, indicate the redshift distribution of the GRBs rather than the true GRB pulse break energy distribution.

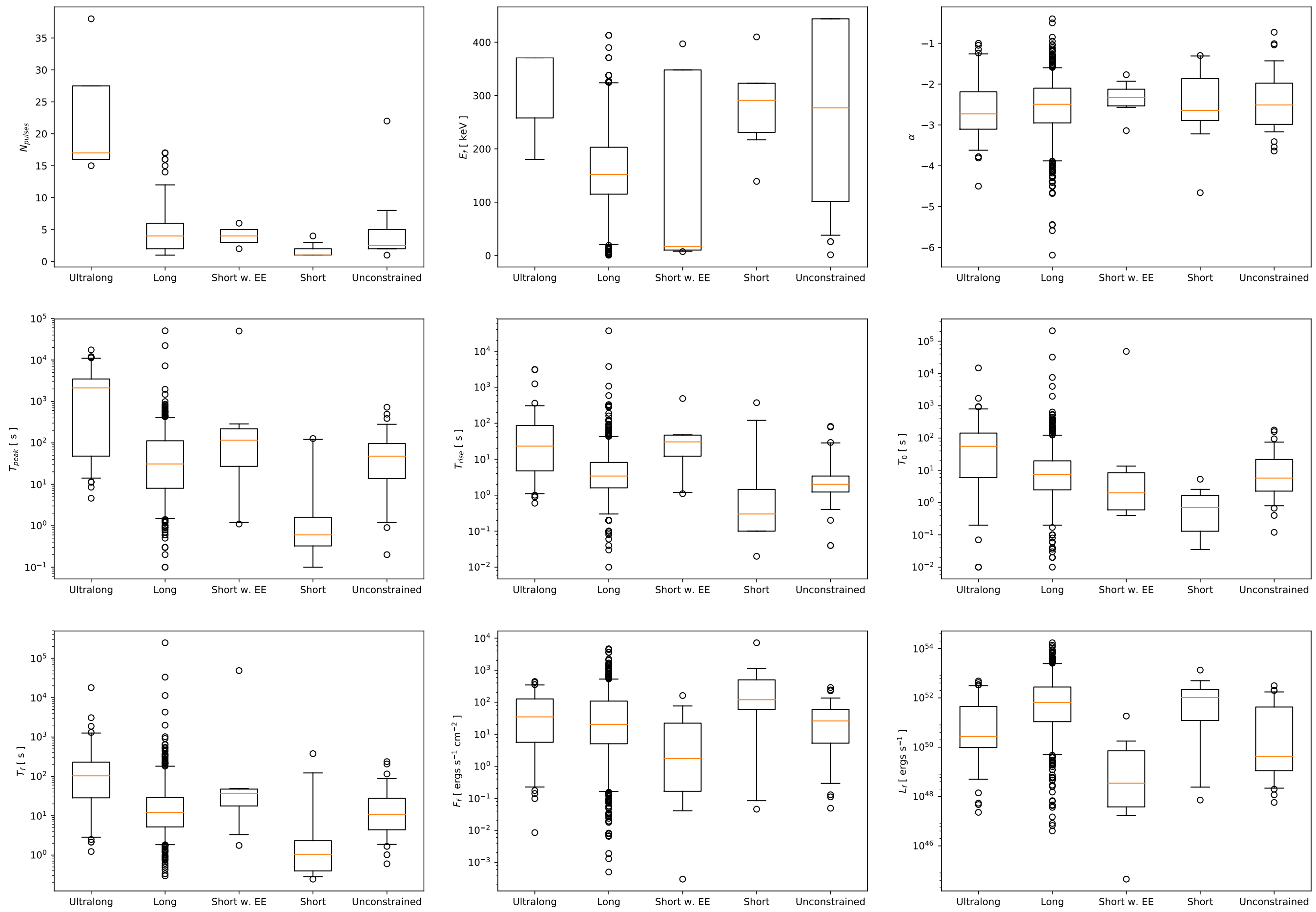

Figure 2.18: *A whisker boxplot for the fitted pulse parameters of each GRB type. Shown are: the number of pulses, N_{pulse}, required to be fit in order to reproduce the GRB lightcurve; the temporal parameters of the pulses, T_{peak}, T_{rise}, and T_f; the cutoff energy of the Band function at $T = T_{peak}$, E_f; the low-energy spectral index, α; the flux at time $T = T_{peak}$, observed over the 0.3 - 350 keV passband, F_f; and the bolometrically corrected peak luminosity, L_f. The orange line denotes the median values for each GRB category with the boxes spanning the interquartile range. The whiskers describe the 5^{th} and 95^{th} percentiles, and the circles denote values that lie ouside this range. See Appendix II, Table 6 for the median, and interquartile range data.*

The timescale, T_0, which is the time between shell ejection, and the beginning of the emission of the pulse, acts as a proxy for the radius of the shell when it begins to emit. Although we do not have a measure for the Lorentz factor of the shell, if we assume that the shells are emitted with the same velocity, regardless of GRB type, then the variation in the emission radius is of several orders of magnitude between short and ultralong GRBs. The rise time of the pulse emission, T_{rise}, like that of T_0, can also act as a measure of the radius of the emitting region, and indicates that short duration GRBs have a narrower emission region than that of ultralong, long, or short GRBs with extended emission. The shorter timescales of short GRB pulses does not, however, translate to a luminosity distribution which is, on average, fainter than those of other GRB types; indeed the distribution is consistent with that of long GRB pulses, although of significantly narrower spread. The luminosity of pulses observed within the lightcurves of short GRBs with extended emission are significantly fainter than any other GRB type, however given that almost as much of the total emission is observed in the X-ray regime as is seen in gamma-rays, a significant number of the pulses are late-time X-ray flares, and therefore skew the luminosity distribution towards fainter pulses.

Pulse correlations

A strong, positive correlation is seen between the rise time of the pulse, T_{rise}, and the arrival time of the last photon emitted, T_f (Figure 2.19); and the peak time of the pulse, T_{peak}, with T_f (Figure 2.20). For the $T_{rise} - T_f$ relation, little variation is observed, between the fitted parameters of the correlation, for the various GRB categories. The $T_{peak} - T_f$ relation, however, sees similar distributions for long, short with extended emission, and unconstrained duration bursts; whilst ultralong and short bursts see a shallower correlation. The presence of the correlation has been observed before, with a weak correlation present in the work of Willingale et al. (2010) for 12 GRBs; however in that work, there was not enough data to separate into burst types. Studies utilising the pulse model of Norris et al. (1996), where the temporal profile of the pulse follows a two-component exponential function with different time constants, also shows evidence of a positive correlation between their pulse rise, and decay times (Chincarini et al., 2010; Norris et al., 1996); and their peak, and decay times (Norris et al., 2005). It is important to note, however, that the decay time reported in those works are not strictly equivalent to the T_f

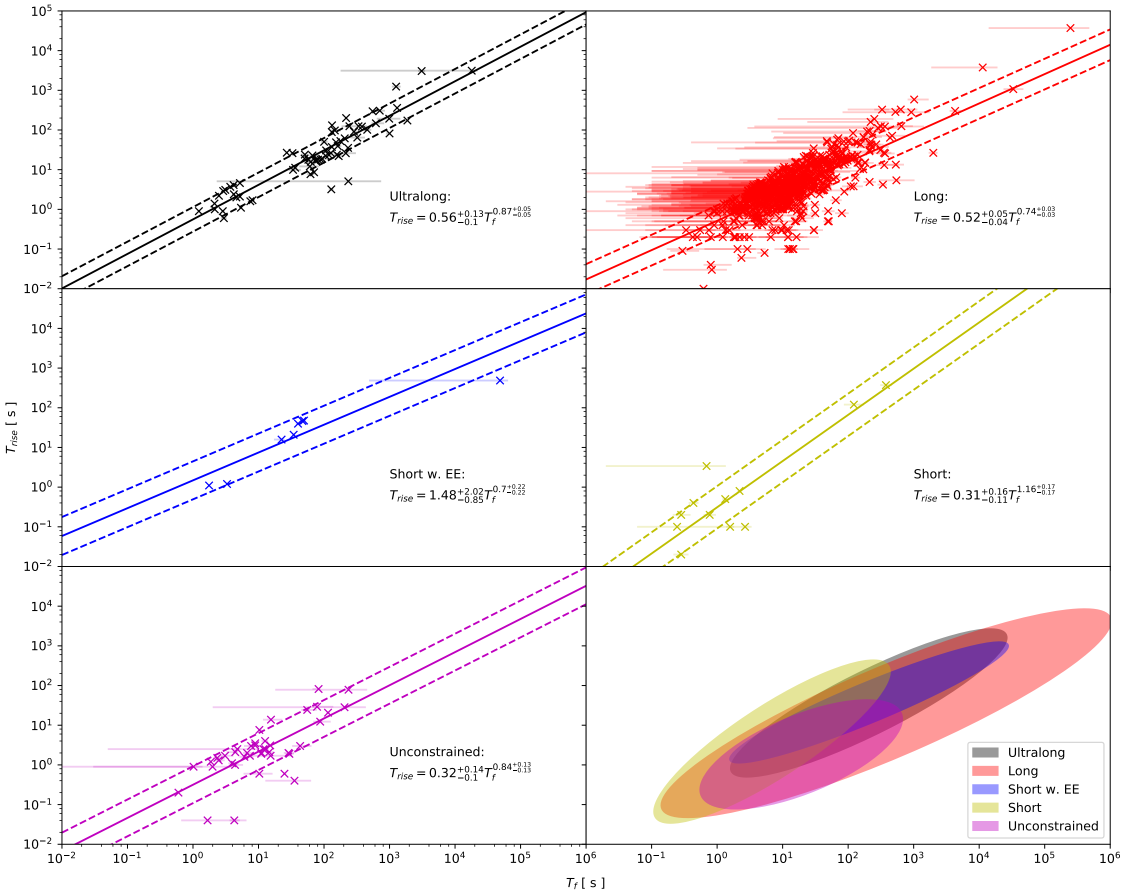

Figure 2.19: *Distributions of the pulse rise time, T_{rise}, against T_f. Shown are the fitted pulse data for ultralong (black), long (red), short with extended emission (blue), short (yellow), and unconstrained bursts (magenta). The text in the figures show the fitted relations between the distribution parameters, for each burst type, with uncertainties quoted at the 1σ confidence interval. The solid line denotes the maximum likelihood model, with the dashed lines denoting the 1σ limit of the intrinsic scatter in the data. The ellipses in the bottom right figure approximately encircle the regions in which the distributions of T_{rise}, T_f extends, for each burst type.*

parameter of this work.

There is a strong anti-correlation between the distribution of pulse T_f values, and the observed flux, F_f, over the 0.3 - 350 keV passband, at $T = T_{peak}$ (see Figure 2.21). Given the strong positive correlations between T_f, T_{rise}, and T_{peak}, this equates to slow rising, late-time X-ray flares producing the faintest of observed fluxes. This is supported by the work of Chincarini et al. (2007), in which Gaussian approximations of Swift X-ray flares showed a strong anti-correlation between the peak time, and the peak intensity; and by Lazzati, Perna & Begelman (2008), where they quantified

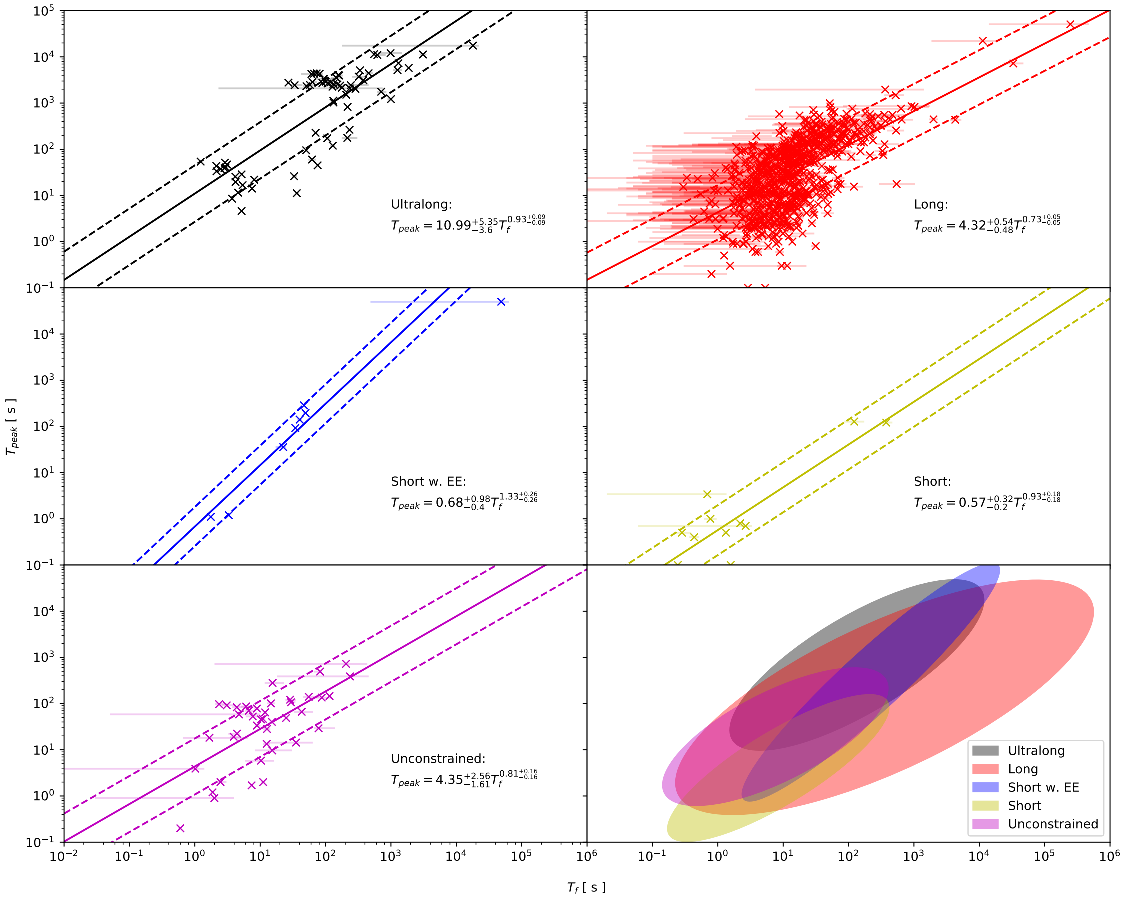

Figure 2.20: *Distributions of the pulse rise time, T_{peak}, against T_f. Shown are the fitted pulse data for ultralong (black), long (red), short with extended emission (blue), short (yellow), and unconstrained bursts (magenta). The text in the figures show the fitted relations between the distribution parameters, for each burst type, with uncertainties quoted at the 1σ confidence interval. The solid line denotes the maximum likelihood model, with the dashed lines denoting the 1σ limit of the intrinsic scatter in the data. The ellipses in the bottom right figure approximately encircle the regions in which the distributions of T_{peak}, T_f extends, for each burst type.*

the relation with an index of -0.56 ± 0.08. In later work by Chincarini et al. (2010), the relation between the peak time, and flux of X-ray flares was shown with an index of -0.7 ± 0.01; as a check, we also calculate this relation and find that for long GRBs the relation between T_{peak} and F_f has an index of $-0.45^{+0.07}_{-0.07}$.

As shown in Figure 2.22, there is a strong negative correlation with the bolometrically corrected peak luminosity, L_f, and the burst-frame T_f, regardless of the GRB type. For long duration bursts, a linear fit in logspace produces a relation between L_f, and T_f of $L_f = 3.16^{+6.19}_{-2.09} 10^{52} [T_f/(z+1)]^{-1.35 \pm 0.17}$ ergs s^{-1}. We find that the re-

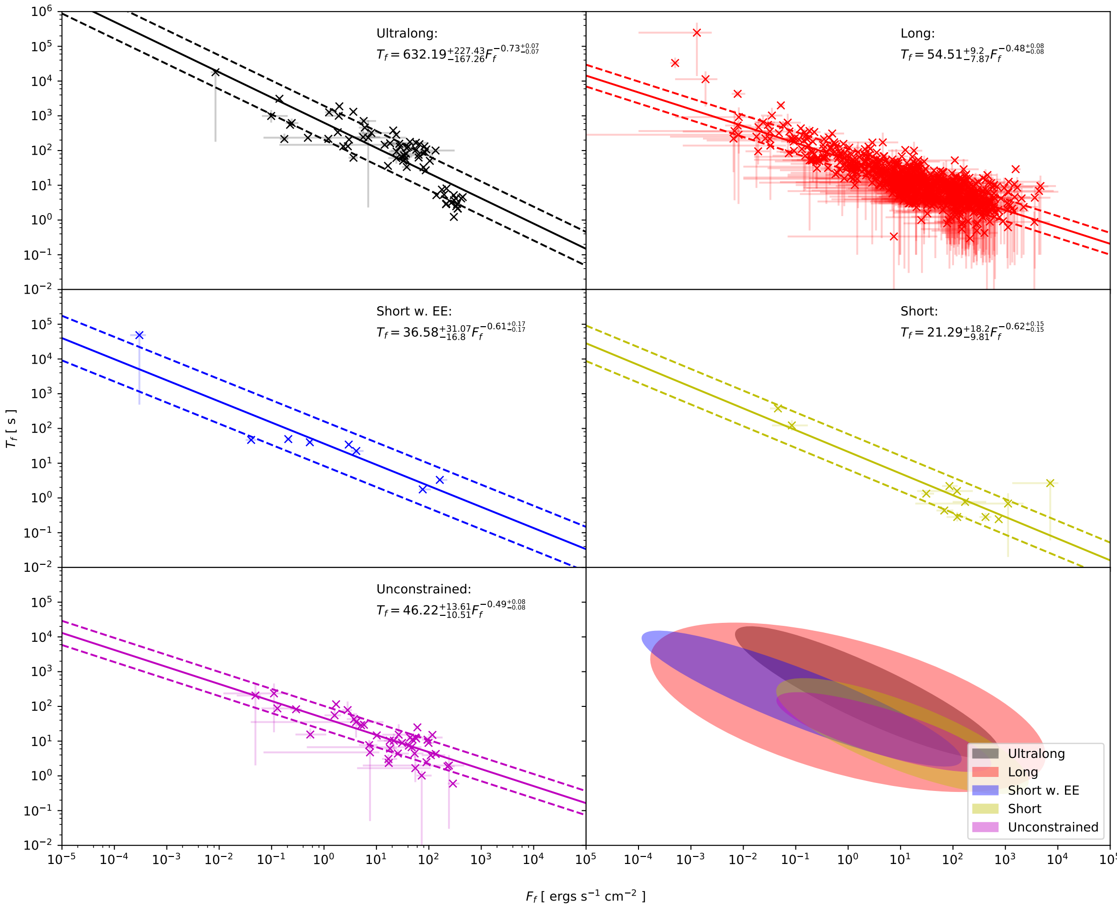

Figure 2.21: *Distribution of T_f against observed flux, F_f, over the 0.3 - 350 keV passband, at $T = T_{peak}$. Shown are the fitted pulse data for ultralong (black), long (red), short with extended emission (blue), short (yellow), and unconstrained bursts (magenta). The text in the figures show the fitted relations between the distribution parameters, for each burst type, with uncertainties quoted at the 1σ confidence interval. The solid line denotes the maximum likelihood model, with the dashed lines denoting the 1σ limit of the intrinsic scatter in the data. The ellipses in the bottom right figure approximately encircle the regions in which the distributions of T_f, and F_f extends, for each burst type.*

lations between the two parameters are stronger for short bursts, short bursts with extended emission, and the unconstrained bursts in our sample when compared to that of the long, and ultralong bursts. A similar correlation was found in Willingale et al. (2010), with an index of, -2.0 ± 0.2; whilst the larger study of Dainotti et al. (2015) produced a similar relation to our own work, with a derived best fit index of $-1.52^{+0.13}_{-0.11}$ [12]. Studies of the average flare luminosity as a function of time since

[12] Such a result is unsurprising, given that both these studies utilise the same models, and analysis techniques, that we adopt in this work.

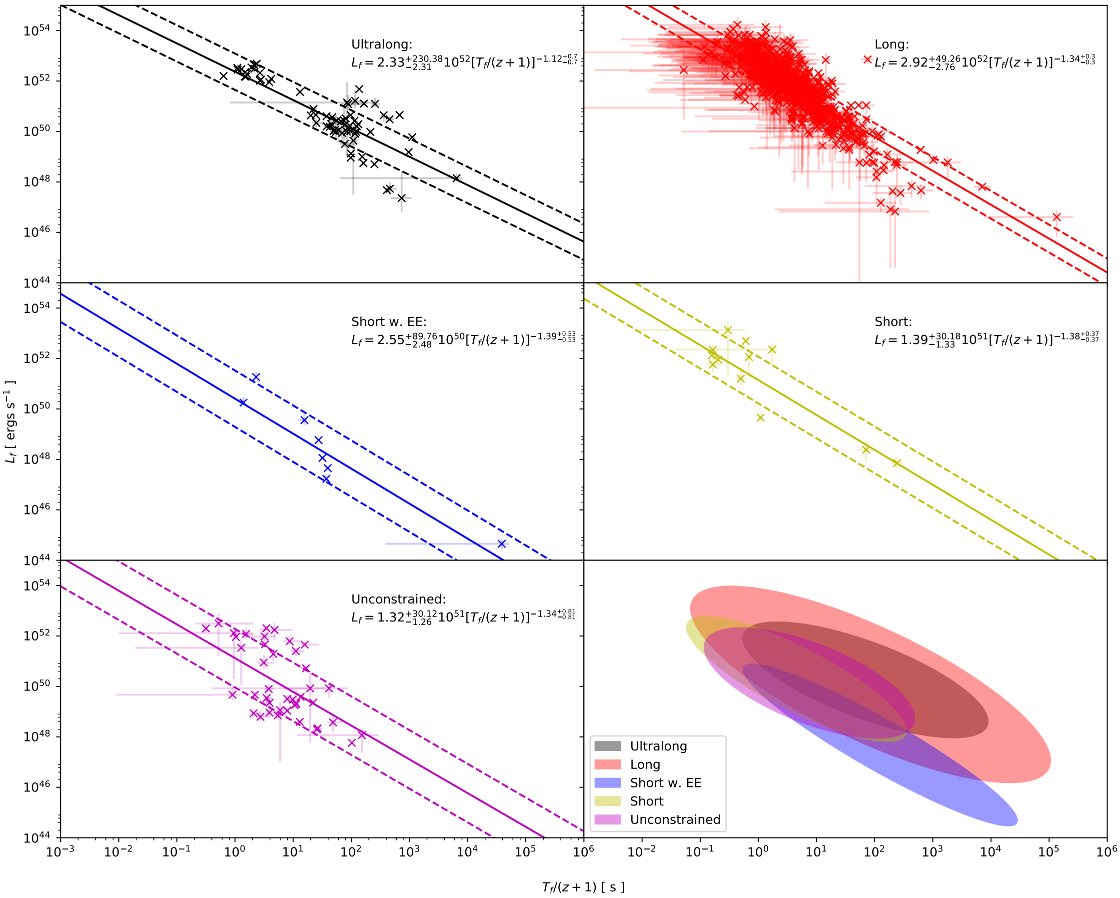

Figure 2.22: *Distribution of L_f vs. the burst frame T_f. Shown are the fitted pulse data for ultralong (black), long (red), short with extended emission (blue), short (yellow), and unconstrained bursts (magenta). The text in the figures show the fitted relations between the distribution parameters, for each burst type, with uncertainties quoted at the 1σ confidence interval. The solid line denotes the maximum likelihood model, with the dashed lines denoting the 1σ limit of the intrinsic scatter in the data. The ellipses in the bottom left figure approximately encircle the regions in which the distributions of T_f, and L_f extends, for each burst type.*

burst trigger, have also shown a relation of similar magnitude, with an index of -1.5 ± 0.16 (Lazzati, Perna & Begelman, 2008).

Out of 862 pulses, 162 have a spectral index of $\alpha > -2.0$, which we require for calculating the peak of the νF_ν ($E^2N(E)$) spectrum, as $E_{peak} = (\alpha + 2.0)E_f$; softer pulses, with $\alpha \leq -2.0$, subsequently do not have a peak energy in this framework. We plot the relation between the burst-frame $E_{peak}(z+1)$, and the bolometric peak luminosity in the burst-frame, L_f, in Figure 2.23. Given the smaller sample size to which we fit the E_{peak} relations, we do not seperate bursts into their respective populations, and instead fit to the combined data. We derive the L_f-E_{peak} relation of $L_f = 5.03^{+8.41}_{-3.15} 10^{51} [E_{peak}(z+1)]^{0.56 \pm 0.14}$ ergs s^{-1}, for the combined pulse and X-ray flare data. This relationship differs significantly from the derived L_f-E_{peak} relation of Willingale et al. (2010), with their index noticeably steeper at 1.83 ± 0.16, and their normalisation factor five orders of magnitude lower than our own. This steeper correlation index is also seen other studies of the L_f-E_{peak} correlation, with many finding a relation index of > 2 (Ghirlanda et al., 2009; Nava et al., 2008; Yonetoku et al., 2004); however these studies are fitting to a extremely small sample sizes, or investigate the time-averaged properties of the burst (Nava et al., 2008; Yonetoku et al., 2004).

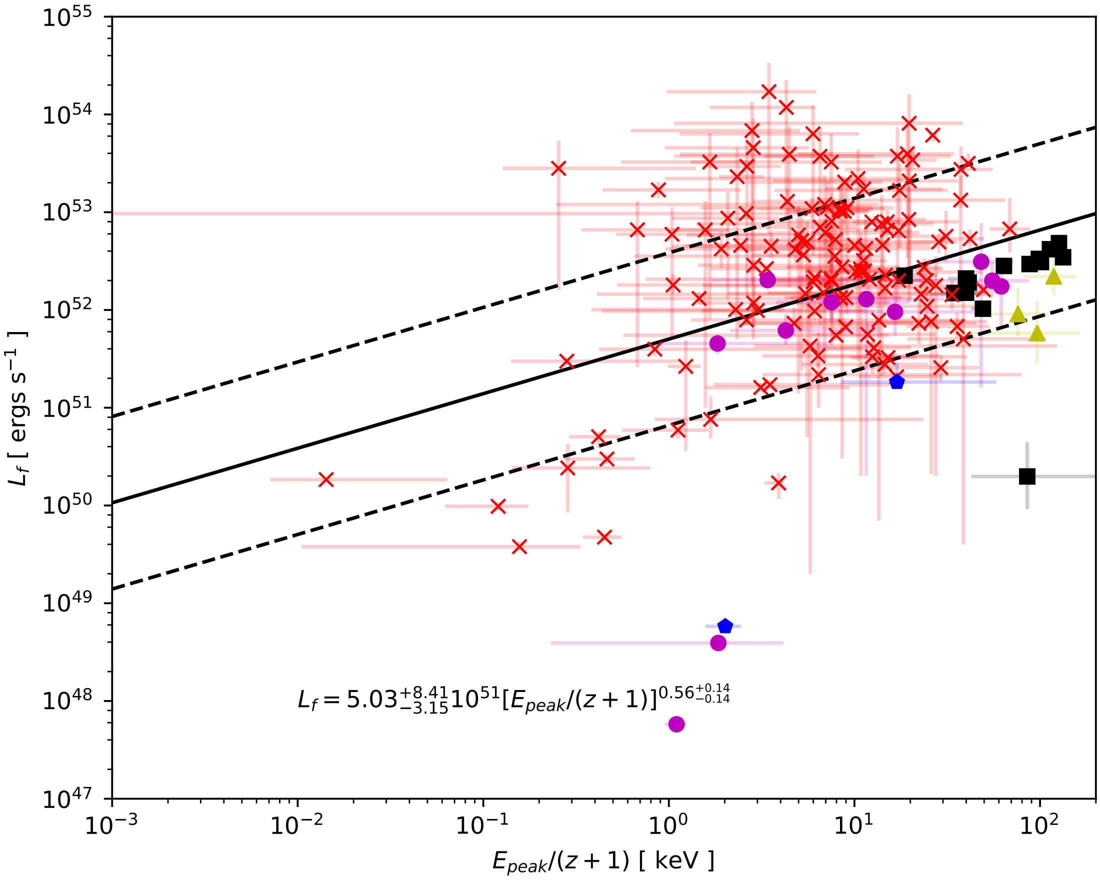

Figure 2.23: *Distribution of L_f vs. the observer-frame E_{peak}. Shown are the fitted pulse data for ultralong (black squares), long (red crosses), short with extended emission (blue pentagons), short (yellow triangles), and unconstrained bursts (magenta circles). The text in the figure show the fitted relation between L_f and E_{peak}, with uncertainties quoted at the 1σ confidence interval. The solid line denotes the maximum likelihood model, with the dashed lines denoting the 1σ limit of the intrinsic scatter in the data.*

2.5.2 Afterglows

We present the GRB afterglow data collated in Tables 4, and 5, of the Appendix; with the distributions of the fitted afterglow parameters shown in Figure 2.24. We find a strong correlation between the peak luminosity of the afterglow plateau, L_{aft}, and the length of time of the plateau, given by T_{fall}. We derive an L_{aft}-T_{fall} relation of $L_{aft} = 2.35^{+3095}_{-2.34} 10^{50}\ T_{fall}^{-0.58 \pm 0.17}$, (see Figure 2.25), in good agreement with work by Dainotti et al. (2015, 2010), who find a T_{fall} index of -0.9 ± 0.2. The equivalent relation for prompt emission pulses is also shown in that figure. Unsurprisingly, we also see a strong correlation between the brightness of the afterglow plateau, and that of the brightest peak in the GRB prompt emission, with the relation quantified by $L_{aft} = 1.86^{+13631}_{-1.54} 10^{-1}\ L_{f,peak}^{0.94 \pm 0.07}$.

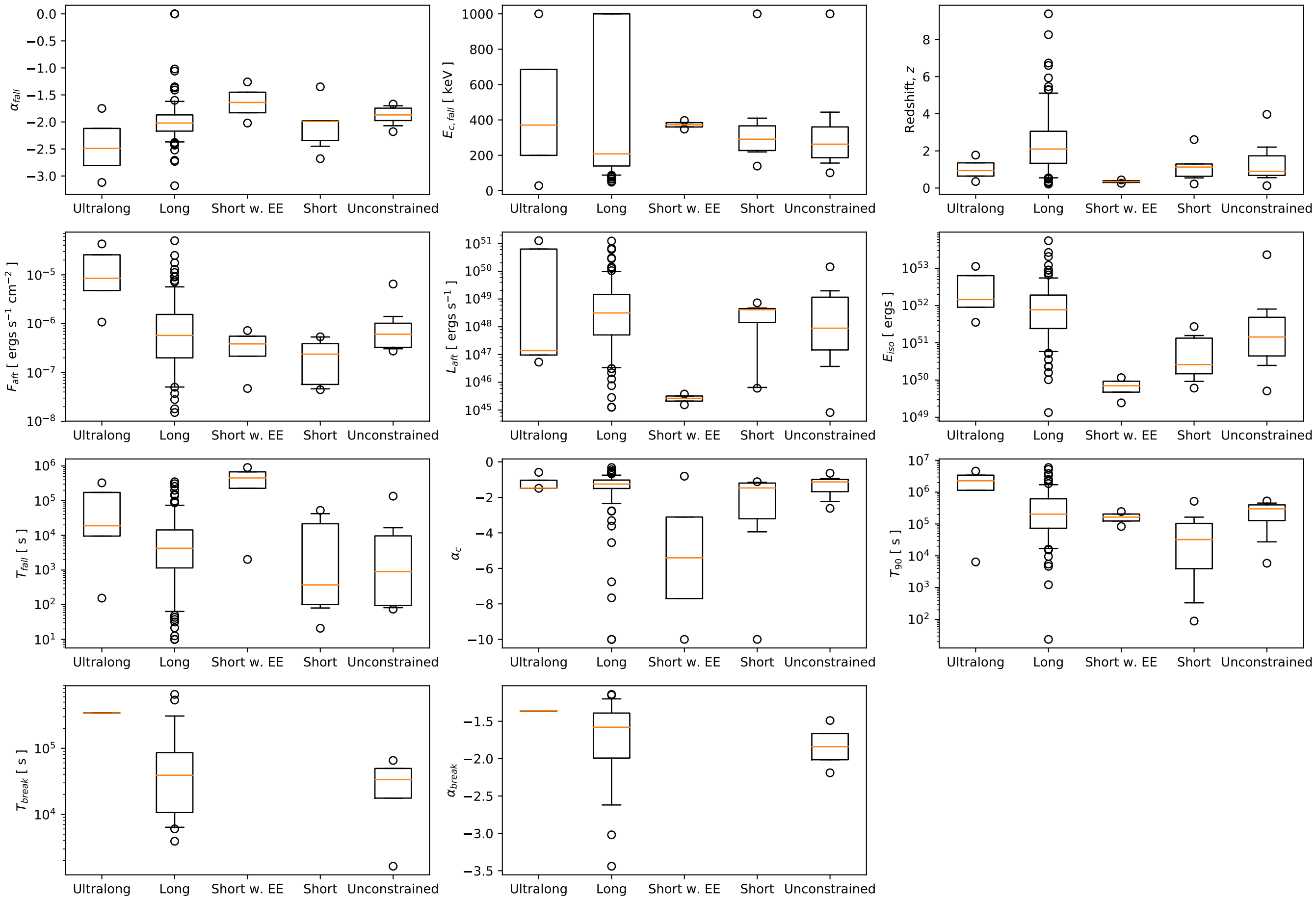

Figure 2.24: *A whisker boxplot for the fitted afterglow parameters of each GRB type. Shown are: the low-energy spectral index at time* $T = T_{fall}$, α_{fall}*; the cutoff energy of the Band function at* $T = T_{fall}$, $E_{c,fall}$*; the redshift,* z*; the peak flux of the afterglow observed over the 0.3 - 350 keV passband,* F_{aft}*; the bolometrically corrected afterglow peak luminosity,* L_{aft}*; the isotropic energy,* E_{iso}*; the end time of the afterglow plateau,* T_{fall}*; the post-plateau temporal decay index,* α_c*; the* T_{90} *duration of the afterglow; and in cases where a late-time jet break is observed, the time of the jet break,* T_{break}*, and the post-jetbreak temporal index,* α_{break}*. The orange line denotes the median values for each GRB category with the boxes spanning the interquartile range. The whiskers describe the* 5^{th} *and* 95^{th} *percentiles, and the circles denote values that lie ouside this range. See Appendix II, Table 7 for the median, and interquartile range data.*

2.6 Conclusions

To summarise the work in this Chapter, we have fitted the spectral, and temporal pulse models of Genet & Granot (2009a) to 182 GRBs of all types, and have produced an exhaustive catalogue of 862 pulses. These pulses are modelled using a simple profile derived from the synchrotron emission of internally shocking colliding, coasting, shells in the fast cooling regime. These pulses, when combined with the fitted afterglow models of Willingale et al. (2007), are able to reproduce the totality of emission seen from the early-time BAT, to late-time XRT regimes. We find that the pulse models are able to reproduce all burst types with equal ability, suggesting that the emission processes are the same. We find that pulses, and X-ray flares exist as a continuum; however, this work is unable to determine whether late-time X-ray flares arise from refreshening of earlier shocks, or from prolonged activity of the central engine.

We find strong anti-correlations in the L_f-$T_f/(z+1)$ relation, such that brighter pulses occur when the ejection time is small; this is consistent with other work in the literature, and in good agreement with their derived parameterisations. We also find strong correlations in the L_f-$E_{peak}(z+1)$ relation, such that harder pulses (which E_{peak} is a measure of) are more luminous; however, this relation is typically of a weaker nature than other available studies. Furthermore, evidence of strong correlations between the afterglow and prompt emission components of GRB lightcurves, are observed.

Future modelling will look at introducing an interdependence of the pulse parameters; the pulse model at the moment treats each event as an independent event, which is clearly not realistic. In reality, slower shells must be being re-energised by the collisions of later, more energetic shells which overtake them at later times. These shells may continue to sweep up matter from the intersteller region, or from pre-ejected winds, and may lose energy in a non-synchroton emission process that may be revealed when opening up the initial constraints we placed on the pulse model.

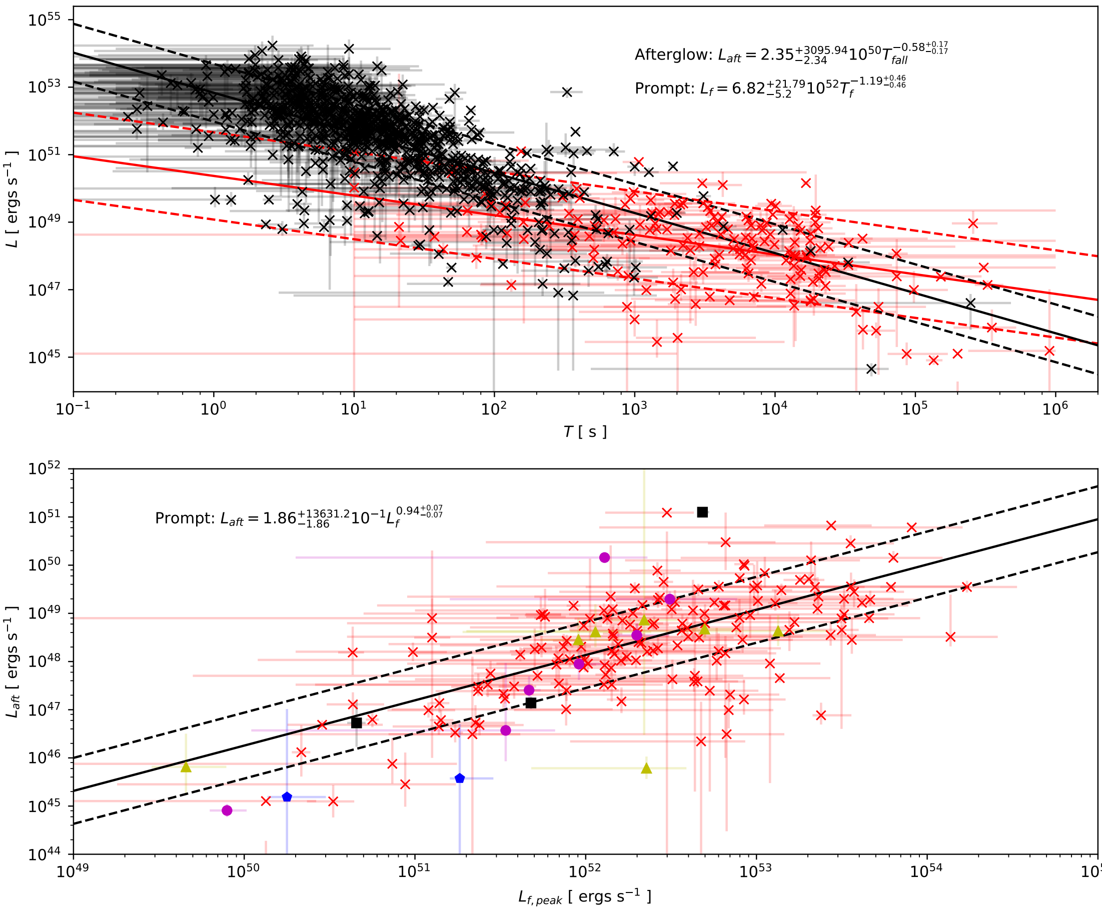

Figure 2.25: *The distribution of the peak luminosities of the GRB afterglow plateaus (red data), vs. the time at which the afterglow turns over to a power-law decay, T_{fall} (top panel); also shown are the peak luminosity of the GRB prompt emission pulses (black data), against T_f. The distribution of the peak luminosity of the afterglow, L_{aft}, vs. the luminosity of the brightest pulse within the GRB lightcurve, $L_{f,peak}$, is also shown (bottom panel), for ultralong (black squares), long (red crosses), short with extended emission (blue pentagons), short (yellow triangles), and unconstrained GRBs (magenta circles). Solid lines highlight the best-fit relationship between the luminosity and temporal parameters, with dashed lines denoting the 1σ confidence intervals; the text in the figures show the fitted relations between the distribution parameters, with uncertainties also quoted at the 1σ confidence interval.*

Chapter 3

The GRB Pulse Luminosity Function

3.1 Chapter Overview

The GRB luminosity distribution has been well studied; however, given the relatively small number of GRBs with measured redshifts, the uncertainties in the observed behaviour of the GRB luminosity function (LF) are large. In an effort to improve GRB population statistics, and subsequently to constrain more tightly the parameters of the GRB LF, we utilise the vast amount of pulse luminosity data collated in Chapter 2 to model the GRB pulse luminosity function and to test some of the more common GRB progenitor model theories.

We begin this chapter by presenting a background to the early GRB luminosity function research which utilised GRB data predominantely from the CRGO's BATSE, and Swift's BAT. We proceed to determine a suitable dataset of GRBs extracted from the GRB components catalogue fitted using the methodology of Willingale et al. (2010), and outlined in Chapter 2. Treating each pulse as an individual event, we produce the GRB pulse LF under a variety of different progenitor models and compare the resulting luminosity functions derived in this work with those found in the wider literature. We end by discussing the merits of each model, and the impact they have on cosmic star-formation rates.

3.2 Introduction

The luminosity function is a powerful tool for population analysis. When applied to Gamma-ray bursts, they can be used to verify theoretical models of the physical processes that go into forming GRBs and as a benchmark for deriving observation rates of future GRB missions, and gravitational wave detection likelihoods. The luminosity function does however require a precise measure of the distance to the GRB in order to convert from the observed flux to the rest-frame luminosity. Prior to the launch of Swift (Gehrels et al., 2004), the number of long Gamma-Ray Bursts (LGRBs) localised to a suitably fine error circle on the sky such that follow-up observation could find an associated host galaxy or afterglow was small; out of some 2704 GRBs detected by BATSE (Goldstein et al., 2013) only a handful had a measured redshift, made possible only due to simultaneous detection of the burst by other Gamma-ray missions with greater localisation abilities.

The earliest population analysis of GRBs utilised either the V/V_{max} method (Schmidt, 1968) whereby a GRB was placed at the furthest distance, within a spherical volume, V_{max}, at which it could be observable (Guetta, Piran & Waxman, 2005; Piran, 1992; Schmidt, 1999, 2001); or the $N(> P) \propto P^{-3/2}$ isotropic distribution discussed in Section 1.5.2 (Cohen & Piran, 1995; Fenimore & Bloom, 1995), where $N(> P)$ is the number of GRBs with fluence greater than P. Alternatively, given the lack of real redshifts, many authors instead sought to derive pseudo-redshifts using properties of the LGRB lightcurves in order to derive a LGRB luminosity function; the most popular of which included the lag-luminosity relationship (Kocevski & Liang, 2006; Norris, Marani & Bonnell, 2000), the variability-luminosity relationship (Fenimore & Ramirez-Ruiz, 2000; Lloyd-Ronning, Fryer & Ramirez-Ruiz, 2002; Reichart et al., 2001; Wei & Gao, 2003); and the Amati relationship (Amati et al., 2002; Atteia, 2003; Firmani et al., 2004; Salvaterra & Chincarini, 2007; Salvaterra et al., 2009; Yonetoku et al., 2004). The large intrinsic scatter within these relationships produces however a redshift distribution that, whilst arguably represents that of the true LGRB redshift distribution, also shows significant uncertainty in the fitted parameters. These early studies found large discrepencies between the observed distribution of GRBs and the assumed models of GRB formation, most notably that the rate of GRB formation was greater at high-redshift than the corresponding star-formation rate would have implied. Physical solutions, like the propensity for GRBs to occur in low-metallicity environments, were popular (Salvaterra & Chincarini, 2007; Salvaterra et al., 2009); empirical solutions, like the evolution in GRB brightness toward more luminous, distant bursts or or the inclusion of an additional rate evolution parameter, also saw frequent useage (Firmani et al., 2004; Kocevski & Liang, 2006; Salvaterra & Chincarini, 2007; Salvaterra et al., 2009; Yonetoku et al., 2004).

With the launch of the Swift mission, with its fast slew rate and accurate on-sky localisation, suddenly a large proportion of GRBs being detected had associated photometric and/or spectroscopic redshifts of either the host galaxy or the GRB's X-ray afterglow, often within a day or two from the initial trigger. Early Swift GRB LF papers continued to develop the LGRB luminosity function by utilising either small numbers of LGRBs with measured redshifts (Kistler et al., 2008; Li, 2008), with poor constraints on fitted parameters; or by artificially boosting the LGRB redshift sample by combining real and pseudo redshift data from Swift and BATSE (Butler, Bloom & Poznanski, 2010; Salvaterra et al., 2012). Over time, the sample size of GRBs with observed redshifts has increased[1], with populations including ever further, and fainter bursts. Contemporary GRB LF studies utilise larger datasets of several hundred GRBs with observed redshifts (for example Cao et al. 2011; Dainotti et al. 2014; Deng et al. 2016; Howell & Coward 2013; Pescalli et al. 2015; Petrosian, Kitanidis & Kocevski 2015; Robertson & Ellis 2012; Wanderman & Piran 2010; Yu et al. 2015a) however, these luminosity functions are still built upon relatively small sample sizes when compared to those found in other branches of astrophysics.

Throughout these earlier studies the emphasis has been on trying to extract information about the average behaviour of the LGRB as a whole; in general, characterising the luminosity of a GRB using the flux of the single brightest peak in the lightcurve binned in 1 second bins (see for example Yonetoku et al. (2004)), or by using the brightest part of the time-averaged lightcurve (Lloyd-Ronning & Ramirez-Ruiz, 2002). In some cases where there is little, or no, variation in the lightcurve such an approach is acceptable. The majority of BATSE and Swift GRBs however, show significant variation in the complexity of their lightcurves, with multiple peaks in the early prompt and late-time emission that, in some cases, are of comparable brightness to the most luminous part of the GRB lightcurve. The luminosity and total energy output of GRBs spans many orders of magnitude. Whilst some bursts consist of a single Fast Rise Exponential Decay (FRED) profile, others have mul-

[1] As of January 2016 over 1000 GRBs have been observed by Swift with 295 GRBs having associated redshifts.

tiple peaks; some are very spikey with rapid variations while others have a much smoother profile. Many lightcurves display astonishing chaotic time-variability, continually varying between bright, short peaks and low troughs where in some cases the flux drops below the detection threshold for a while before flaring up again. The current paradigm therefore is that the totality of the prompt emission is constructed of simple pulses (Norris et al., 2005; Willingale et al., 2010); lasting from fractions of a second, to minutes in duration, these pulses are independent of each other but with many overlapping to some degree to produce the incredible lightcurve variation observed. Late-time X-ray flares (Chincarini et al., 2007; Falcone et al., 2007) seen above the afterglow emission hundreds, and in some cases thousands of seconds, after the initial trigger appear to mostly follow the same mechanism as the prompt emission pulses: internal shocks from a reactivated central engine; essentially the lower energy tail of a unimodal pulse energy distribution [2].

In this chapter we follow a different approach; using the fitted GRB data from Chapter 2, based on a physically motivated model for the prompt and high-latitude emission from GRBs (Genet & Granot, 2009b; Willingale et al., 2010), we extract a subset of 118 long Gamma-ray bursts to produce a total of 607 individual Gamma-ray pulses and X-ray flares. The wealth of information stored within these other, less-luminous, pulses are utilised to produce a GRB pulse luminosity function; of which the more conventional LGRB LF can be considered as a high-luminosity subset. Instead of the single data point extracted by more conventional GRB luminosity function studies, our GRBs contain on average 5 pulses; the more variable lightcurves contain pulses numbering in the tens, significantly increasing our sample size over single pulse studies. Using the measured redshift, the peak flux, and spectrum we derive the rest-frame bolometric luminosity for each pulse, and use the totality of our data to construct and evaluate various GRB pulse luminosity functions.

The structure of this chapter is therefore as follows: we discuss the selection criteria for our GRB sample in Section 4.3. We outline the various methods for constructing a luminosity function in Section 4.4; and in Section 4.5 we discuss the Markov Chain Monte Carlo routine utilised to fit our luminosity function model parameters. Sections 4.6, 4.7, and 4.8 are discussions on the results from models convolved to the cosmic star formation rate density with either: a single population of GRB

[2] Many early-time X-ray flares have an observable Gamma-ray counterpart in the BAT however the majority of late-time X-ray flares would have Gamma-ray fluxes well below the BAT detection limit.

progenitors (Type I models), or two separate populations of high, and low luminosity GRBs (Type II models); and GRB formation rate models that rely on no prior assumptions on progenitor mechanisms (Type III models). Section 4.9 compares the LGRB formation rates with the observed cosmic star formation rate density and we finally conclude our findings in Section 4.10.

3.3 The Long GRB Dataset

From the data summarised in Table II of Chapter 2, we extract a subset of fitted GRBs based solely on the $T_{90} > 2$ s descriminator found by Kouveliotou et al. (1993). Although the use of such a crude measure could potentially lead to the inclusion of so called "extended emission" (EE) type bursts (GRBs which exhibit the same characteristics as traditional short GRBs, save for the total duration which is typically greater than 2 s; Gompertz, O'Brien & Wynn 2014; Norris & Bonnell 2006), only EE SGRBs 050724, and 061006 were fitted in Chapter 2. As EE SGRBs follow different progenitor channels to LGRBs, and typically occur at lower redshifts than their longer lasting cousins (D'Avanzo et al., 2014), we exclude these two bursts from our sample. The rejection criteria for a GRB's suitability to being fitted, outlined in Chapter 2, is reiterated below, along with the T_{90} descriminator; the number of GRBs which fail each criterion is highlighted within the brackets [3], and the redshift distributions of the GRBs which fail each criterion are shown in Figure 3.1:

- the GRB has an observed redshift and a $T_{90} > 2$ s (13 GRBs rejected);
- is not a known short GRB with extended emission (2 GRBs rejected);
- sufficient statistics in the BAT lightcurve to define at least 1 pulse profile (30 GRBs rejected);
- a BAT lightcurve in which pulses are reasonably well defined (23 GRBs rejected);
- early data from the XRT so that the decay of the pulses is well constrained (29 GRBs rejected); and

[3] A GRB may fail multiple selection criteria, which is reflected in the denoted numbers.

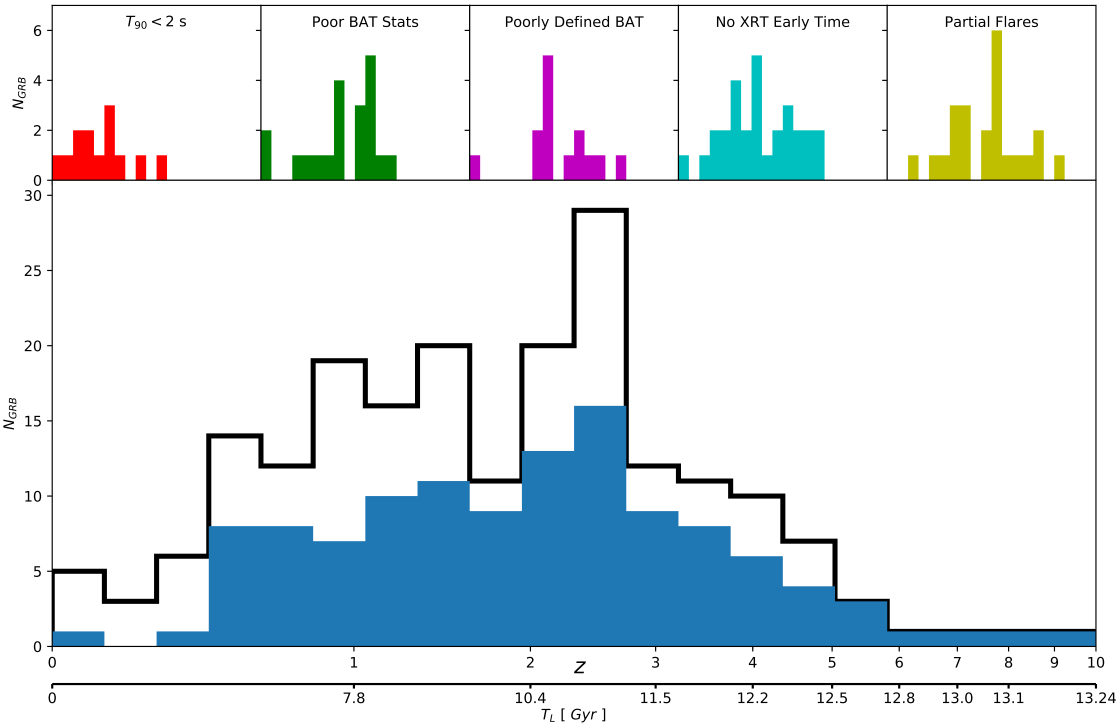

Figure 3.1: *The redshift distribution of all Swift bursts, with an associated redshift, spanning GRB 050126 to GRB 110503A (solid black line). The redshift distribution of GRBs rejected for model fitting are shown in the top row: a T_{90} of less than 2 seconds (red); insufficient statistics for a single BAT pulse (green); poorly defined BAT pulses (magenta); no early-time XRT data which covers the rapid decay phase (cyan); and poor coverage of late-time X-ray flaring due to orbit breaks etc. (yellow). The resulting distribution of GRBs, in both redshift and lookback time, that pass all selection criteria is shown as the blue histogram. Data is taken from Table 1.*

- XRT data which provide good definition of X-ray flares, avoiding flares for which profiles are incomplete or broken by orbit gaps etc.. (23 GRBs rejected)

We evaluate any redshift bias that the various rejection criteria may accidentally introduce into our LGRB dataset by computing the 2-sample Anderson-Darling (AD) statistic (Anderson & Darling, 1952; Darling, 1957; T. W. Anderson, 1954) [4] on the redshift distributions of accepted GRBs and of GRBs which failed the rejection criteria, under the null hypothesis that both are drawn from the same population. The Anderson-Darling 2-sample statistic is given by:

[4]The Anderson-Darling test statistic is a modified Kolmogorov-Smirnov test statistic, and is preferred due to its greater sensitivity to differences in the tails of distributions, and its ability to sense differences between very large datasets.

$$A^2_{mn} = \frac{mn}{m+n} \int_{-\infty}^{\infty} \frac{\{F_m(x) - G_n(x)\}^2}{H_{m+n}(x)\{1 - H_{m+n}(x)\}} dH_{m+n}(x) \tag{3.1}$$

where $F_m(x)$, and $G_n(x)$, are independent empirical distribution functions of m, and n number of samples and $H_{m+n} = \{mF_m(x) + nG_n(x)\}/(m+n)$. As we are calculating the likelihood of two distributions being drawn from the same parent distribution, no assumptions are required for the shape of the parent; this is not the case were we calculating a one-sample test. We utilise the k-sample (k=2 produces Equation 3.1) Anderson-Darling test codified in the SciPy stats package (Jones, Oliphant & Peterson, 2001), which is based on the work by Scholz & Stephens (1987). The critical significance values are modelled as a third order polynomial, and interpolated over a percentile grid of [0.75, 0.90, 0.95, 0.975, 0.99]; outside of this range, the P-values are extrapolated and, as such, come with large uncertainties the further away one gets. We therefore quote the calculated AD statistic and the appropriate significance level at which the null hypothesis may be rejected.

The threshold for rejection of the null hypothesis is often given at the arbitrary P-value of > 0.95; given this, we can reject the null hypothesis that the redshift distribution of GRBs with a $T_{90} < 2$ s is drawn from the same distribution as LGRBs, as the AD statistic of 11.377 corresponds to a significance level of $P > 0.99$. As short and long GRBs have different progenitors, which follow different evolutionary paths, it is expected that the two populations should differ in their redshift distributions. We also choose to accept the null hypothesis for both the rejection criteria of early XRT data, and complete XRT flares, having been drawn from the same parent population as our sample of LGRBs: the AD statistics are 0.825, and -0.875 respectively, which corresponds to P-values of $P = 0.85$ and $P \ll 0.75$. The criteria for a minimum of one pulse in the BAT, and a well defined BAT pulse are, like the T_{90} criterion, both rejected with P-values of > 0.99. Out of those GRBs which fail these two criteria, 9 are short GRBs ($0.089 < z < 0.915$), and 1 is a short GRB with extended emission ($z = 0.41$); excluding these GRBs from the rejected sample, we find that the new AD statistics correspond to $P = 0.83$, and $P = 0.38$ respectively and therefore we do not see any significant bias to our LGRB sample.

In summary, out of 187 LGRBs with associated redshifts covering the 76 month period from GRB 050126 to GRB 110503A with $T_{90} > 2$ s, 118 GRB (see Table 3.1 for GRBs) lightcurves were deemed suitable and fitted with 607 pulses: a completeness of $\sim 63\%$. As a comparison study, Salvaterra et al. (2012) utilised GRBs spanning an almost identical time period as our own and, after applying their selection criteria, drew a population of 58 LGRBs of which 52 have measured redshifts: a completeness of $\sim 39\%$ [5].

3.3.1 Spectral Data

The conversion of an observer-frame photon flux to a burst-frame luminosity requires an understanding of the spectral profile of the pulse, in order to derive a K-correction factor, K_{corr} (derivation shown in Appendix III). The GRB pulse fitting of Chapter 2 includes the automatic derivation of the K-correction for each individual pulse, such that the luminosities quoted are in the bolometric burst-frame. For some pulses, with good statistics and energy coverage (including both the BAT and XRT data), it was possible to constrain the burst-frame cutoff energy of the spectra, E_c, by direct fitting. For the majority of GRB pulses however, the cut-off energy of the Band function [6] lies outside the passband of the BAT; in such cases the cutoff energy of the Band function at the peak of the pulse was set at $E_{cz} = 500$ keV in the source frame of the burst, corresponding to $E_c = 500/(z+1)$ keV in the observer frame, similar to the fixed cutoff energies utilised by other studies (e.g. Firmani et al. 2004; Natarajan et al. 2005). This naturally leads to questions on the vivacity of the K-correction and, by extent, on the derived bolometric luminosities. Joint analysis of the spectra of GRB pulses observed simultaneously by Swift and other satellites such as Fermi (GBM; 8 keV - 40 MeV), Suzaku (WAM; 50 keV - 5 MeV), and Wind (Konus; 10 keV - 10 MeV) are rare and are often based on a few GRBs (see for example Krimm et al. 2009) and therefore we cannot directly compare spectral fits on a pulse-by-pulse basis for the majority of our 607 pulses. We instead compare the spectral characteristics of each prompt emission pulses utilised within this chapter with the time-averaged spectral parameters observed by other space-based gamma-ray, and X-ray observatories with wider energy passbands than

[5]The Salvaterra et al. (2012) completeness is derived from the 132 available redshifts that were available at the time of that paper's writing. Whilst the majority of GRB redshifts are released within a few days of initial observation, some are derived, or updated, only after extended follow up observations months, or years, after the initial burst; in all cases we endeavour to obtain the most up to date redshift information available.

[6]In this section we refer to the parameters of the Band function as b_1, b_2, and E_c, rather than the α, β, and E_0 of Equation 1.1, so as to not get confused with the α, and β labels commonly used for the GRB luminosity function.

GRB	z	GRB	z	GRB	z	GRB	z
050126	1.29	050315	1.949	050319	3.24	050401	2.9
050416A	0.654	050525A	0.606	050730	3.97	050801	1.56
050802	1.71	050814	5.3	050820A	2.612	050908	3.35
050922C	2.198	051016B	0.936	051109A	2.346	060108	2.03
060115	3.53	060116	6.6	060124	2.297	060206	4.05
060210	3.91	060223A	4.41	060418	1.489	060502A	1.51
060522	5.11	060526	3.21	060604	2.68	060605	3.8
060607A	3.082	060614	0.125	060707	3.43	060714	2.71
060729	0.54	060801	1.13	060814	0.84	060904B	0.703
060906	3.685	060908	1.884	060912A	0.937	060926	3.208
060927	5.6	061021	0.346	061110A	0.758	061121	1.314
061222A	2.088	061222B	3.36	070208	1.17	070306	1.496
070318	0.84	070419A	0.97	070506	2.31	070521	0.553
070529	2.5	070721B	3.626	070802	2.45	070810A	2.17
071020	2.412	071031	2.692	071122	1.14	080210	2.641
080310	2.427	080319B	0.937	080319C	1.95	080413A	2.433
080413B	1.1	080430	0.767	080603B	2.69	080604	1.416
080605	1.64	080607	3.036	080707	1.23	080721	2.6
080804	2.2	080805	1.505	080810	3.35	080905B	2.374
080913	6.7	080916A	0.689	080928	1.692	081007	0.53
081008	1.967	081118	2.58	081203A	2.1	081222	2.77
081230	2.03	090102	1.547	090205	4.65	090418A	1.608
090423	8.26	090424	0.544	090429B	9.4	090516	4.109
090519	3.85	090530	1.3	090618	0.54	090715B	3.0
090812	2.452	091018	0.971	091020	1.71	091029	2.752
091109A	3.076	091208B	1.063	100219A	4.667	100316B	1.18
100418A	0.623	100425A	1.755	100513A	4.772	100621A	0.542
100814A	1.44	100816A	0.805	100901A	1.408	100906A	1.727
101219B	0.55	110106B	0.618	110205A	2.22	110213A	1.46
100422A	1.770	110503A	1.613				

Table 3.1: *The fitted long gamma-ray bursts, and their associated redshifts, from Chapter 2, spanning the period from January 2005, to May 2011, are utilised in this chapter to derive the GRB pulse luminosity function.*

the Swift BAT. Although not strictly equivalent, given that the totality of the GRB prompt emission is a convolution of many constituent pulses and that GRB pulses have the propensity to evolve from being spectrally hard to spectrally soft, such a comparison can reveal if there are any significant deviations between the parameters of the two spectra.

Out of 118 GRBs from our dataset, 51 were observed by other missions, totalling 183 prompt-phase pulses; the spectral parameters of which, assuming a power-law with exponential cutoff form, are shown in Figure 3.2. We define a deviation metric for the ith spectral parameters P_i such that $\Delta P_i = |P_{i,Swift} - P_{i,other}|/\sigma_{i,combined}$ where $\sigma_{i,combined}$ is the resulting uncertainty of the two measurements combined in quadrature ($\sigma^2_{i,combined} = \sigma^2_{i,Swift} + \sigma^2_{i,other}$), and a $\Delta P_i < 1$ denotes a parameter that is within the combined 1σ uncertainties. We find good agreement between our pulse spectral parameters and those of the time-averaged GRB spectra, with the median deviation in the spectral indexes, and peak energies of $\Delta b_1 = 1.25^{+1.89}_{-0.70}$, and $\Delta E_{peak} = 0.70^{+0.52}_{-0.35}$; where the subscripts/superscripts denote the 25^{th} and 75^{th} percentiles respectively. We calculate and compare the K-corrections one would derive utilising both spectra and observe a median deviation between the two broadband observations on the scale of $\Delta K_{corr} = 0.28^{+0.24}_{-0.15}$; we therefore conclude that for the majority of GRB spectra, the effect of introducing a fixed cutoff energy is negligible on the bolometric burst-frame luminosities, and is consistent with the intrinsic uncertainties of the fitted parameters.

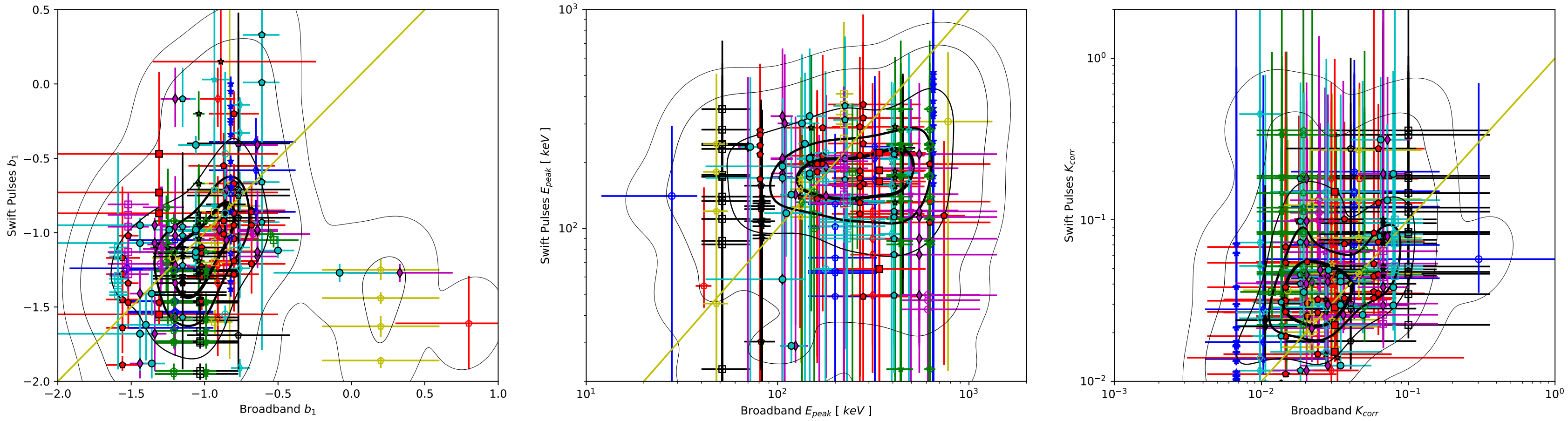

Figure 3.2: *The fitted Swift GRB pulse spectral parameters, b_1 (left), and E_{peak} (middle) vs. the corresponding time-average spectral parameters derived from observations by higher-energy missions; the resulting pulse K-corrections, K_{corr}, and broadband K_{corr} are also shown (right). The diagonal yellow line denotes where a GRB's pulse parameters and the broadband time-averaged parameters are equal. Black contours encircle regions which contain 8% (thickest), 38%, 68%, 95%, and 99.5% (thinnest) of the data, whilst errorbars denote 1σ uncertainty. Filled data points denote GRBs in which the spectrum of is a joint fitting of Swift and broadband mission data, whilst empty points are based on broadband mission spectra only. References for data points is found in Appendix III.*

3.4 Modelling the GRB Pulse Luminosity Function

We note that the nomenclature of "luminosity function" in reference to GRBs refers specifically to the GRB luminosity probability density function (PDF); to obtain what is in general analogous to the LFs found in other areas of astrophysics one must convolve the GRB luminosity PDF with the cosmic GRB formation rates. Any subsequent reference to the GRB luminosity function in this chapter will follow this convention and refer to the GRB luminosity PDF. Throughout this chapter we used the formulation of comoving distance, volume and luminosity distance given by Hogg (1999) utilising the seven-year WMAP cosmological parameters of $H_0 = 71$ km s^{-1} Mpc^{-1}, $\Omega_m = 0.27$, $\Omega_k = 0$ and $\Omega_\Lambda = 0.73$ (Larson et al., 2011). All errors quoted in this chapter are the 1σ confidence intervals, in line with the majority of GRB LF literature.

Throughout this chapter we discuss reproducing the GRB pulse luminosity function through a variety of models which, in some cases, include various sub-models. Type I models invoke a cosmic star-formation rate coupled to a single population of GRB progenitors (Section 4.4.2); Type II models are similar to Type I save for the separation of GRB progenitors into low, and high-luminosity populations (Section 4.4.1); whilst Type III models are direct fits to GRB formation rates and exclude a-priori assumptions about the nature of GRB progenitors (Section 4.4.2). Models I, and III are further explored through the inclusion of various extra evolutionary effects (see Section 4.4.6) and are summarised as:

Type I-1: no evolution in either the break of the pulse LF, L_{break} ($\delta = 0$), or the GRB formation rate, K_{GRB} ($\gamma = 0$ or $Z/Z_\odot = \infty$);

Type I-2: evolution of only the GRB formation rate, K_{GRB} ($\gamma \neq 0$);

Type I-3: evolution of only the break, or cutoff, of the luminosity function, L_{break} ($\delta \neq 0$);

Type I-4: evolution of the GRB formation rate through the presence of metallicity density evolution ($Z/Z_\odot \neq \infty$);

Type I-5: both L_{break} and K_{GRB} are free to evolve (δ & $\gamma \neq 0$).

Type III-1: no evolution in the break of the pulse LF, L_{break} ($\delta = 0$);

Type III-2: evolution in the break of the pulse LF, L_{break} ($\delta \neq 0$);

The observed distribution of pulse bolometric luminosities, $N(L, z)$, by definition spanning the energy band of 1 - 10000 keV [7], is displayed in Figure 3.3. Pulses for which the peak only appears in the BAT or XRT lightcurves are shown as circles and stars respectively, whilst pulses observed simultaneously by both instruments are denoted by triangles. The $N(L, z)$ distribution displays a wide range of brightnesses for prompt emission pulses, and late time X-ray flares; and whilst the very brightest of pulses ($L_{1-10000keV} > 1 \times 10^{53}$ ergs s^{-1}) are exclusively from the prompt emission, the X-ray flares and prompt emission pulse luminosity distributions are indistinguishable from each other.

The standard procedure for relating the observed distribution of LGRBs to the comoving burst formation rate (see for example Butler, Bloom & Poznanski (2010); Fenimore & Ramirez-Ruiz (2000); Lloyd-Ronning, Fryer & Ramirez-Ruiz (2002); Salvaterra et al. (2012); Salvaterra & Chincarini (2007)) is given by:

$$N(L, z)dzdL = \phi(L, z) \left[D(L, z) \frac{\Delta\Omega\Delta T \Psi_*(z)}{(z+1)} \frac{dV_c(z)}{dz} \right] dzdL \tag{3.2}$$

where the observed distribution of LGRB bursts, $N(L, z)$, is a convolution of the comoving burst formation rate, $\Psi_*(z)$, the comoving volume element, $dV_c(z)/dz$, a detection probability profile, $D(L, z)$, and the GRB luminosity probability density function, $\phi(L, z)$. The factor of $1/(z + 1)$ corrects for cosmological time dilation whilst $\Delta\Omega$ and ΔT are the terms correcting for the field of view of the BAT and the total duration our GRB sample covers.

3.4.1 Luminosity Function

The functional forms for LGRB LFs represented in the Swift literature are predominantly that of a broken power-law (sometimes with a smoothed transition between low and high luminosity regions) (Butler, Bloom & Poznanski, 2010; Cao et al., 2011; Liang et al., 2007; Lloyd-Ronning, Fryer & Ramirez-Ruiz, 2002; Salvaterra

[7] The bolometric luminosity of each individual pulse is derived from applying a K-correction to the pulse flux using the spectrum at peak time as a fiducial spectrum.

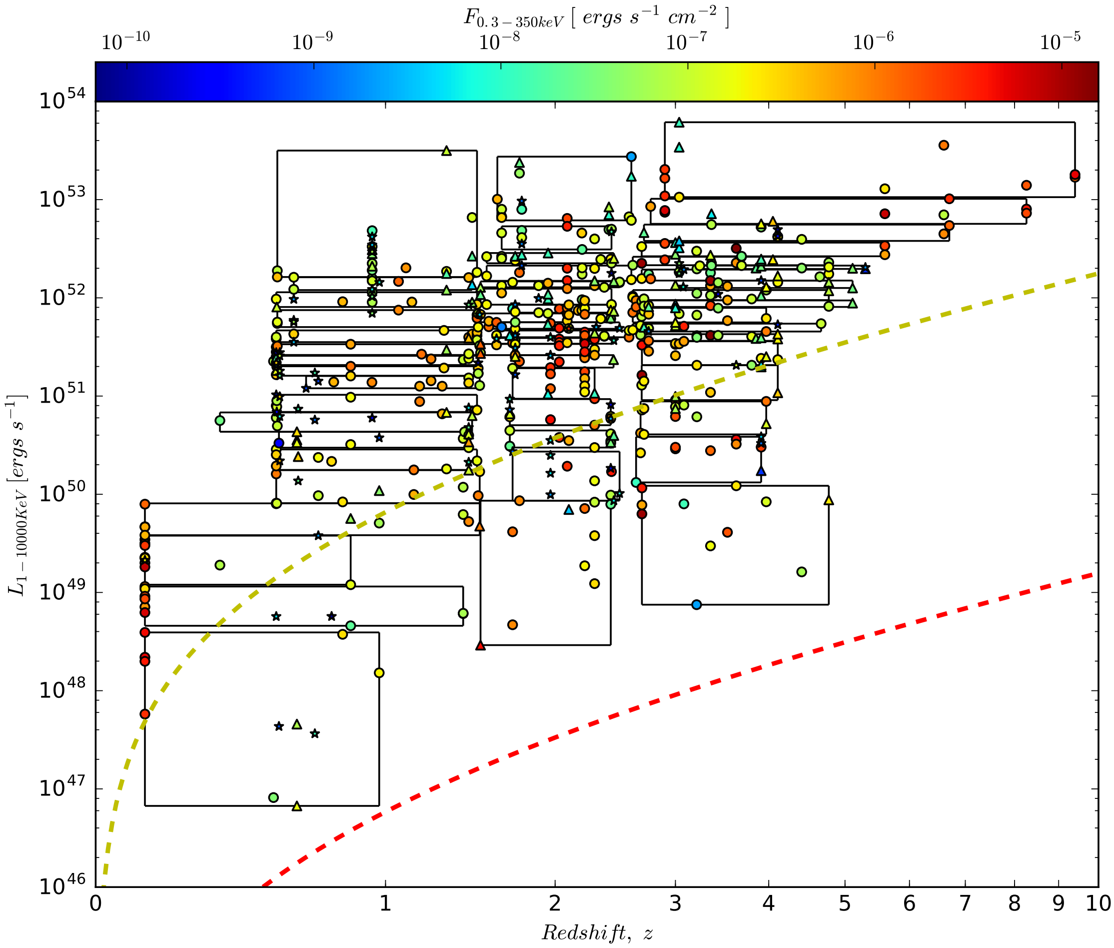

Figure 3.3: *The distribution of peak luminosities as a function of redshift, $N(L, z)$. The circles and stars indicate pulses detected only with the BAT or XRT instruments respectively with triangles denoting pulses detected by both instruments simultaneously. BAT observed pulses are visible below the BAT detection limit as fainter pulses co-added to prior, brighter pulses can be "boosted" into the detection range. Pulse colours denote the integrated peak flux in the observed 0.3 - 350 keV passband. The overlain boxes show the corresponding J_i sets used to determine each bin's limits with an explanation to the derivation of set limits outlined in Section 4.5. The yellow dashed and red dashed lines show the detection threshold of the bolometric luminosity as a function of redshift, with a burst detection threshold in the BAT (15-350 keV) of 0.1 photons cm^{-2} s^{-1}, equivalent to 8×10^{-9} ergs cm^{-2} s^{-1} (Sakamoto et al., 2008a) and an approximate XRT (0.3-10 keV) pulse/flare detection limit of 3×10^{-12} ergs cm^{-2} s^{-1}. In practice the XRT detection limit depends on the brightness of the afterglow component and the time since trigger, so the lower detection threshold can vary by up to 3.5 dex from burst to burst (Burrows et al., 2005a). Few pulses are seen near the XRT threshold and the detection likelihood of pulses is discussed in Section 4.4.5. The K-correction to convert the BAT & XRT flux detection limits to that of bolometric luminosities utilises the average spectral parameters of the Band function derived from our dataset of 607 pulses with $b_1 = -1.57$, $b_2 = -11.60$ and $E_c = 183$ keV.*

et al., 2012), or a power-law with an exponential cutoff (Cao et al., 2011; Salvaterra et al., 2012; Salvaterra & Chincarini, 2007; Salvaterra et al., 2009). In this chapter, to ensure completeness, we utilise both a broken power-law (BPL),

$$\phi(L,z) = L_n \begin{cases} \left(\frac{L}{L_{break}}\right)^{\alpha} & L \leq L_{break} \\ \left(\frac{L}{L_{break}}\right)^{\beta} & L > L_{break} \end{cases} ; \tag{3.3}$$

and a power-law with exponential cutoff (PLEC),

$$\phi(L,z) = L_n \left(\frac{L}{L_{break}}\right)^{\alpha} \exp\left[\left(\frac{-L}{L_{break}}\right)\right]; \tag{3.4}$$

to model our pulse luminosity function. α and β (BPL only) are the low & high luminosity indexes; L_{break} is the break luminosity; and L_n is the normalisation of the LF, which is given by the reciprocal of the LF integral. The normalisation factor is sensitive to the limits of integration and can have an effect on the derived efficiency parameter, K_{GRB}, up to a factor of 2. The limits of integration are therefore chosen by various authors depending on the constraints that they place on their data sets, bias controls, or calculation methods [8]; the variation in normalisation is small however when compared to the intrinsic uncertainties in the CSFRD, IMF evolution, metallicity density, etc.. We adopt the faintest, and brightest pulse luminosities as the limits of integration, which in this chapter spans 1×10^{46} to 1×10^{54} ergs s^{-1}.

A Separate Low-Luminosity GRB Population

Although LGRB studies generally prefer utilising luminosity functions that assume a single population of LGRBs, a small group of LGRBs appear to exist with particularly low luminosities (LL, $L < 10^{50}$ ergs s^{-1}) that are poorly fitted by these single population models (Chapman et al., 2007b; Howell & Coward, 2013; Liang et al., 2007; Qin et al., 2010; Virgili, Liang & Zhang, 2009). Typically these LL LGRBs are assumed to trace the same progenitor models as those of higher luminosity LGRBs whilst convolved to a separate luminosity function. Such luminosity functions pro-

[8] The brightest subsection of low-z GRBs are often utilised as the subsample avoids Malmquist bias, and is less succeptible to other intrinsic biases such as redshift detectability, and uncertainty in the CSFRD at high-z (Cao et al., 2011); utilising the least/most luminous pulses (Firmani et al., 2006; Salvaterra et al., 2012), or integrating over infinity, especially for PLEC LF models (Campisi, Li & Jakobsson, 2010), is also common.

duce markedly differing normalisation rates for the two types of LGRBs; the local formation rates of LL LGRBs are suggested to be several orders of magitude greater than those of more luminous LGRBs.

With the incorporation of bright prompt emission pulses, and late time, faint X-ray flares, 72 of 607 pulses fall into the luminosity regime typically associated with LL LGRBs. In this chapter we evaluate the performance of bimodal LF models (denoted as Type II models) compared to single population LGRB models (Type I models). Following a similar procedure set out by Liang et al. (2007), we produce a bimodal luminosity function by combining two luminosity functions, $\phi_{LL}(L)$ and $\phi_{HL}(L)$ such that:

$$\phi(L) = \phi_{LL}(L)K_{LL-GRB} + \phi_{HL}(L)K_{HL-GRB}, \tag{3.5}$$

where the LGRB formation rate efficiencies, K_{LL-GRB} and K_{HL-GRB} are included in the LF to allow for different formation efficiencies of the two GRB types, and are analogous to the ρ_0^{LL} and ρ_0^{HL} parameters found in Liang et al. (2007). Both $\phi_{LL}(L)$ and $\phi_{HL}(L)$ follow the same shape as Equations 3.3 and 3.4 and each population is fitted separately to ensure that the LL and HL parameters are independent of each other. Normalisation limits for the bimodal LFs, as that of the single population model, are set at 1×10^{46} to 1×10^{54} ergs s^{-1}.

3.4.2 LGRB Co-moving Pulse Rate

We model the comoving burst rate, $\Psi_*(z)$, or more specifically the comoving pulse formation rate (pulses yr^{-1} Mpc^{-3}) using two diametrically opposed models:

$$\Psi_*(z) = K_{pulse} \begin{cases} K_{GRB}\psi_*(z)\iota(z)F(z) & \text{Type I} \\ \psi_{GRB}(z) & \text{Type III} \end{cases} . \tag{3.6}$$

Type I models assume a functional form for the cosmic star formation rate density (CSFRD), $\psi_*(z)$ ($M_\odot$ yr^{-1} Mpc^{-3}), which are coupled to: an evolving fraction of high-mass stars that are capable of forming GRBs at a given redshift, $F(z)$; an additional rate density evolution parameter, $\iota(z)$, capable of boosting GRB formation rates above CSFRD levels, and conversion factors K_{pulse}, and K_{GRB} which describe the average number of pulses per GRB, and the number of GRBs formed per solar mass of stars respectively. Included amongst the Type I models is a non-evolving GRB luminosity function derived when $\iota(z)$ is constant, and the break luminosity index, $\delta = 0$. Type III models are a common alternative to Type I models where direct fitting of a simple functional form to $\Psi_*(z)$, in this chapter taken to be a triple broken power-law, allows for ease of comparison between cosmic star formation rate density models without the need for refitting of GRB luminosity functions.

All the parameters used in modelling the comoving pulse formation rate are functions of redshift with the exception of K_{pulse}: the number of pulses per GRB shows no correlation with redshift; having removed the effect of the BAT rest-frame duration, $T_{90}/(z+1)$, we derive a Spearman's partial rank correlation coefficient of $\rho_s = -0.045$, implying that K_{pulse} is redshift-independent.

3.4.3 Cosmic Star Formation Rate Density

The comoving burst formation rate is dependant on the properties of the central engines that power GRBs; for LGRBs the preferred mechanism is that of a collapsar: massive stars that undergo catastrophic core collapse into blackholes (MacFadyen & Woosley, 1999; Paczyński, 1998a; Woosley, 1993b), favoured because of the observed association with Type Ib/c supernovae (Galama et al., 1998a; Stanek et al., 2003) with Wolf-Rayet stars the favoured progenitor type. With their high mass ($M > 25M_\odot$), and subsequently short main-sequence lifespans, Wolf-Rayet stars closely trace the local star formation rate; as such, for type I/II models, we take the Cole (Cole et al., 2001) functional form for the CSFRD:

$$\psi_*(z) = \frac{(a_1 + a_2 z)h}{1 + (z/a_3)^{a_4}}, \tag{3.7}$$

in units of $M_\odot$ yr^{-1} Mpc^{-3}; and use the best fit parameters: $a_1 = 0.0389$, $a_2 = 0.0545$, $a_3 = 2.973$, and $a_4 = 3.655$ derived by Kobayashi, Inoue & Inoue (2013) (see Figure 3.4). These values are based on corrections to the work by Hopkins & Beacom (2006) where overestimations in the CSFRD were found to have arisen due to uncertainties in the correction for dust-obscuration and the conversion from UV luminosity to intrinsic star formation rates. These coefficients produce a cosmic star formation rate that has an almost flat profile, in log-space, to a redshift of $z = 2$ and approximately an order of magnitude greater formation rate at $z = 0$ than that produced from using Hopkins and Beacom's fitted parameters.

3.4.4 The Cosmic IMF

A contributing second-order effect from an evolving population of high-mass stars is considered by some authors either explicitly in the modelling of derived GRB luminosity functions (Lloyd-Ronning, Fryer & Ramirez-Ruiz, 2002) or as an explanation to the observed evolution in luminosity or rate parameters (Cao et al., 2011; Kistler et al., 2008). The CSFRD is, by definition, the total star formation rate at a given redshift and, for completeness, in this chapter we explicitly convert the CSFRD to a formation rate density of stars capable of undergoing catastrophic core collapse and forming GRBs (i.e. with mass greater than $25M_{\odot}$) by deriving the fractional mass of stars greater than a "GRB ignition mass", $F(z)$, given by $F(z) = \int_{25M_{\odot}}^{120M_{\odot}} M\Phi(M,z)dM / \int_{0.01M_{\odot}}^{120M_{\odot}} M\Phi(M,z)dM$. In our derivation of the fraction of high-mass stars we assume an IMF, $\Phi(M,z)$, which is top-heavy at high redshift as logically in the metal-poor early universe the Eddington limit, and subsequently the population of high mass stars, was much greater than more recent epochs. Studies into extra-galactic star formation history indicates an evolving IMF (Davé, 2008; van Dokkum, 2008; Wilkins, Trentham & Hopkins, 2008) up to $z \sim 2$ and as such we adopt the redshift-dependent IMF model of Davé (2008) where the IMF takes the form of a broken power-law (Kroupa, 2001):

$$\Phi(M,z) = \begin{cases} \left(\frac{M}{\hat{M}}\right)^{-1.3} & M \leq \hat{M} \\ \left(\frac{M}{\hat{M}}\right)^{-2.3} & M > \hat{M} \end{cases} \tag{3.8}$$

with the characteristic break mass evolving with redshift: $\hat{M} = 0.5(z+1)^2 M_{\odot}$, which we naively extrapolate up to $z = 10$. The effect of the evolving IMF on the distribution of stellar masses is subtle; in the current epoch, approx. 9.6% of all stellar mass formed per year is locked up within stars of $M > 25M_{\odot}$, increasing to approx. 62.5% at $z = 10$ (see Figure 3.4).

3.4.5 The Swift Detection Likelihood

It is common, in previous studies of the Swift GRB luminosity function, where only the defining pulse luminosities (i.e. the brightest) were utilised, to set the likelihood of detection by the BAT within its field of view to be at unity. In deriving a GRB pulse luminosity function incorporating data from the XRT we include pulses up to

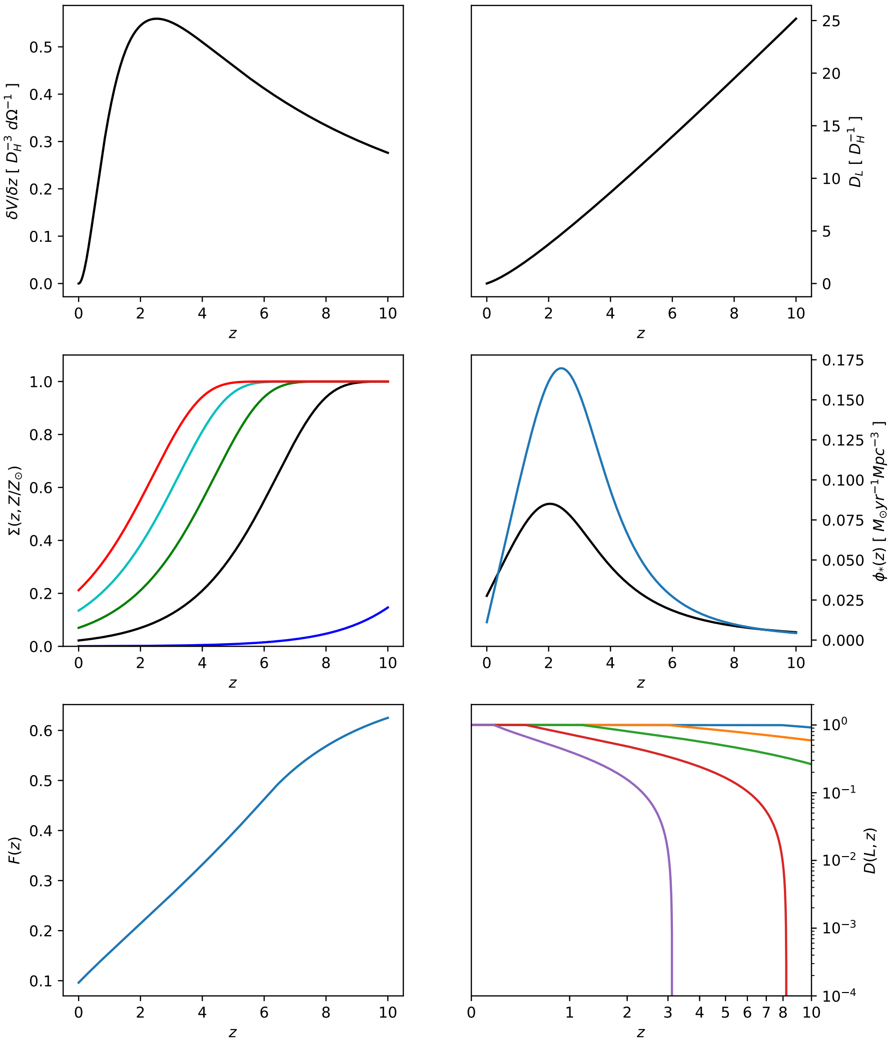

Figure 3.4: *The co-moving volume element, D_V/D_z (top left panel), and luminosity distance, D_L (top right panel), are derived from the formula in Hogg (1999), and using the cosmology parameters outlined at the start of Section 3. The metallicity density evolutionary parameter of Langer & Norman (2006), $\Sigma(z, Z/Z_{\odot})$ (middle left panel), is shown at metallicity thresholds of $Z = 0.01$ (blue), $Z = 0.1$ (black), $Z = 0.2$ (green), $Z = 0.3$ (cyan), and $Z = 0.4$ (red). The cosmic star formation rate models (middle right panel) parameterised by Hopkins & Beacom (2006) (blue), and Kobayashi, Inoue & Inoue (2013) (black), are shown; with the high mass star formation rate efficiency parameter, $F(z)$ (bottom left panel). The likelihood of detection by Swift is shown for GRBs with a luminosity of 10^{48} (magenta), 10^{49} (cyan), 10^{50} (red), 10^{51} (green), and 10^{52} (blue) ergs s^{-1}.*

three orders of magnitude less luminous than the detection threshold of the BAT. We produce a model of the Swift detection profile, $D(L, z)$, assuming total detection likelihood above the BAT detection threshold which scales to zero at an effective XRT detection threshold of 3×10^{-12} ergs s^{-1} cm^{-2} as a power-law of index $\sim -1/3$ (see Figure 3.4). This is, of course, a naive model of Swift's detection profile: each pulse is treated as an individual event and assuming unity down to the XRT detection threshold is inappropriate; each pulse detected by the XRT was because the burst was detected by the BAT, and the XRT detection threshold varies considerably from burst to burst depending on the brightness of the afterglow component, and the time between XRT detection and BAT trigger. Furthermore, as there is often significant overlap between pulses, fainter pulses may be seen when an earlier, significantly brighter pulse is present. Modelling the combined detection profile of Swift is highly complicated and, as such, the results are somewhat subjective. Our detection profile convolved to the CSFRD, metallicity density, and constant $\phi(L, z)$, produces a distribution of pulses that closely traces the observed distribution up to approximately 10^{51} ergs s^{-1} (solid line, Figure 3.5). Setting the detection profile to unity above either the XRT or BAT detection thresholds produces the dotted and dashed distributions which tends to overestimate the population of low luminosity pulses (>XRT = unity) or underestimates the population of sub-peak luminosities (<BAT = 0) requiring, respectively, a luminosity function that is more positively or negatively tilted to compensate.

3.4.6 Redshift Evolution Models

For a Type I GRB LF model, the basic method of taking a CSFRD convolved to a luminosity function, detection profile, and cosmological volume element produces a distribution of LGRBs that under-represents the observed high-redshift, high-luminosity population. The solution is to provide an extra evolutionary effect in the modelling and allow it to float when fitting the model parameters. In this chapter we look at three of the most common evolutionary effects: evolution of the break, or cutoff, of the luminosity function; a metallicity density evolution such that LGRBs trace low metallicity star forming regions; and a more generic rate density evolution on top of the CSFRD as solutions to differences between the observered and Type I pulse distribution functions.

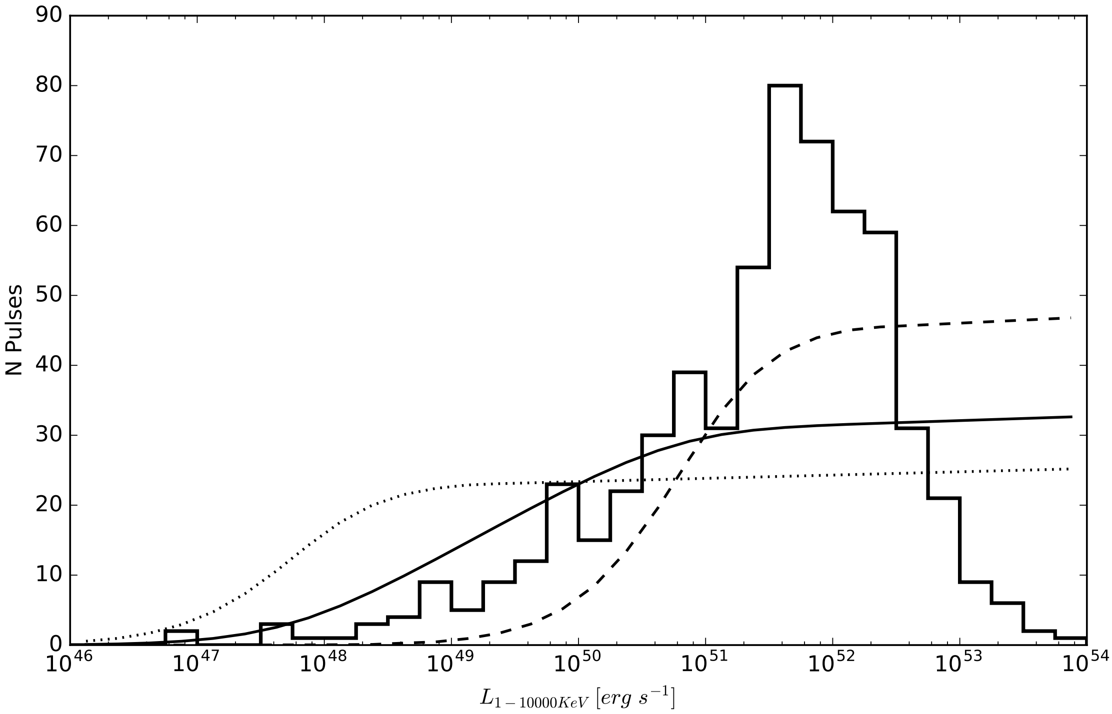

Figure 3.5: *The observed distribution of pulse luminosities for a type I model with rate evolution of $\gamma = 0$ where the luminosity function is assumed to be constant. The solid curve is the expected distribution resulting from integrating Equation 3.2 whilst assuming a detection profile, $D(L, z)$, that varies from unity at the BAT threshold down to non-detection at the approximate XRT threshold. The dotted curve is the expected distribution assuming $D(L, z)$ is unity down to the XRT sensitivity limit and the dashed curve arises when setting the BAT detection threshold as the lower limit of detection.*

Break Luminosity

Evolution in the break, or cutoff, luminosity is of the form $L_{break}(z) = L_0(z+1)^{\delta}$, where L_0 is the break in the LF at $z = 0$ and δ is the index of LF evolution (Campisi, Li & Jakobsson, 2010; Firmani et al., 2004; Kocevski & Liang, 2006; Lloyd-Ronning, Fryer & Ramirez-Ruiz, 2002; Petrosian, Kitanidis & Kocevski, 2015; Salvaterra et al., 2012; Salvaterra & Chincarini, 2007; Salvaterra et al., 2009; Virgili et al., 2011a; Yonetoku et al., 2004; Yu et al., 2015a). This has the further effect that the normalisation parameter, L_n, becomes $L_n(z)$. In this chapter the break luminosity evolution can be applied to both the Type I and Type III LGRB pulse formation rate models. In principle, luminosity break evolution can be incorporated into Type II models such that either one, or both, GRB populations see their own luminosity evolution. Given the large number of free parameters, and the small population of low-luminosity pulses, however, we believe that we do not yet have the statistics to draw meaningful conclusions from such a model.

Metallicity Density

Extreme mass-loss through stellar winds, a characteristic of high-mass stars, will prevent the formation of a GRB; if, however, the progenitor has low metallicity ($Z < 0.1Z_{\odot}$) then the mass-loss rate is severely dampened and a GRB is able to form (Fryer, Woosley & Hartmann, 1999; Mészáros, 2006). LGRB progenitors should therefore preferentially form in low-metallicity galaxies at any given redshift. A model of fractional mass densities belonging to metallicities below metallicity Z at redshift z, $\Sigma(z)$ has been derived by Langer & Norman (2006) from the Schechter distribution function of galaxy masses and the mass-metallicity relationship determined from SDSS surveys. The functional form of $\Sigma(z)$ is given by:

$$\Sigma(z) = \frac{\hat{\gamma}[0.84, (Z/Z_{\odot})^2 10^{0.3z}]}{\Gamma(0.84)} \tag{3.9}$$

where $\hat{\gamma}$ and Γ are the lower incomplete and complete gamma functions respectively. The metallicity density will always boost high-redshift GRB formation rates, with the metallicity threshold determining how rapidly this rate increases; a higher metallicity threshold will produce a smaller increase in GRB formation with redshift, tending towards no evolution when $Z/Z_{\odot} \to \infty$ (Qin et al., 2010; Salvaterra et al., 2012; Salvaterra & Chincarini, 2007; Virgili et al., 2011a).

Rate Density

Metallicity density evolution acts as a physical explanation to observed evolution in GRB formation rates, however the formulation of the model relies on no scatter in the mass-metallicity relationship, and no redshift evolution in the faint end of the Schechter galaxy mass function and the rate at which the average galactic metallicity evolves. One may instead use a simple $(z+1)^{\gamma}$ factor to produce the same effect as metallicity density evolution with the advantage that rate density also allows for a dampening of GRB formation rates at high-z, something that is impossible for the formulation of metallicity density to achieve (Cao et al., 2011; Kistler et al., 2008; Kocevski & Liang, 2006; Petrosian, Kitanidis & Kocevski, 2015; Qin et al., 2010;

Robertson & Ellis, 2012; Salvaterra et al., 2012, 2009; Virgili et al., 2011a). This factor is however purely empirical, which frustrates interpretations of the results. Both the metallicity density and rate density evolution are incorporated into the Type I GRB formation rate model, $\Psi_*(z)$, through the $\iota(z)$ term in Equation 3.6, either singularly or in combination with each other (Qin et al., 2010).

Combined Break Luminosity & Rate Density

Evolution either in rate density, or break luminosity has been utilised as a solution to discrepencies between theoretical, and observed LGRB luminosity functions. Little study has however been made on the performance of more complex evolutionary models involving evolution in both rate and break luminosity. In this chapter we evaluate the performance of a Type I combined rate/break evolutionary model and compare this model's performance with the more common univariate Type I evolutionary models.

3.5 The MCMC Simulation

We bin the observed distribution, $N(L, z)$, by splitting the 607 GRB pulses into equipopulous redshift bins: $0.125 < z \leq 1.505$, $1.51 < z \leq 2.6$, and $2.612 < z \leq 9.4$; we furthermore bin over luminosity to improve statistics at the high and low luminosity tails of the GRB pulse distribution such that the ith bin is the associated set $J_i \equiv \{j|L_i^{min} < L < L_i^{max}, z_i^{min} < z < z_i^{max}\}$, with $n(J_i)$ as the total number of pulses in J_i, set at a minimum of 11 pulses: a tradeoff between maximising the total number of bins, and reducing the fractional Poissonian error component of each bin. The lower and upper redshift and luminosity limits of each bin are subsequently trimmed to remove excess "padding" of empty data space with the resulting bins shown in Figure 3.3. For a non-trivial model with parameters, $\hat{\theta}$, a Gaussian minus log-likelihood function can be constructed using methods outlined by D'Agostini (2005), giving:

$$-\log(\mathcal{L}[\hat{\theta}|n(J_i)]) = \sum_{i=1}^{N} \frac{\log(2\pi\sigma_i^2)}{2} + \sum_{i=1}^{N} \frac{[n(J_i) - \int_{L_i^{min}}^{L_i^{max}} \int_{z_i^{min}}^{z_i^{max}} \eta(L, z; \hat{\theta}) dL dz]^2}{2\sigma_i^2} \tag{3.10}$$

where $\eta(L,z;\hat{\theta})$ is equivalent to the R.H.S of Equation 3.2 and the associated squared error of the ith bin is given by $\sigma_i^2 = \sigma_{n(J_i)}^2 + \sigma_{L_i}^2 + \sigma_{z_i}^2$. The error in $n(J_i)$, $\sigma_{n(J_i)}$ is naively taken as the standard deviation of a Poissonian distribution with mean, $n(J_i)$, giving $\sigma_{n(J_i)} = \sqrt{n(J_i)}$. The errors, σ_{L_i}, and σ_{z_i} are defined as uncertainties in the limits of integration for each bin. As the bin edges are defined only by the minimal/maximal pulse luminosities and redshifts contained therein, assuming a 10% uncertainty in the limits of integration gives:

$$\sigma_{L_i} = \int_{0.9L_i^{min}}^{1.1L_i^{max}} \int_{z_i^{min}}^{z_i^{max}} \eta(L,z;\hat{\theta})dLdz - \int_{L_i^{min}}^{L_i^{max}} \int_{z_i^{min}}^{z_i^{max}} \eta(L,z;\hat{\theta})dLdz; \tag{3.11}$$

$$\sigma_{z_i} = \int_{L_i^{min}}^{L_i^{max}} \int_{0.9z_i^{min}}^{1.1z_i^{max}} \eta(L,z;\hat{\theta})dLdz - \int_{L_i^{min}}^{L_i^{max}} \int_{z_i^{min}}^{z_i^{max}} \eta(L,z;\hat{\theta})dLdz. \tag{3.12}$$

A Metropolis-Hastings Markov Chain Monte Carlo method is preferred for the maximisation of the minus log-likelihood due to the high dimensionality of the fitting, as well as being able to return the confidence regions of all fitted parameters. Assuming uniform priors for the indexes: α, β, γ, and δ; and logarithmic priors for K_{GRB} and L_0, we run MCMCs with chain lengths of 1×10^6 with typical "burn in" taking around 2×10^3 iterations. To ensure that the MCMC program is finding the global, rather than local, maximum we evaluate the MCMC convergence success by running multiple MCMCs from random starting points and deriving the Gelman & Rubin (Gelman & Rubin, 1992) potential scale reduction factors (PSRFs). An example posterior distribution, of a single MCMC chain, is shown in Figure 3.6 for a fully evolving BPL model, whilst an example of a converging series of MCMC chains is shown for the fully evolving PLEC model, allowing GRB rate and break luminosity evolution, in Figure 3.7.

For the Type I models our results are discussed in Section 3.6 and tabulated in Table 3.2; the results derived using the Type II bimodal low-luminosity and high-luminosity functions are discussed in Section 3.7 and displayed in Table 3.3; and the results for a Type III LF independent of formation rate models are discussed in Section 3.8 and shown in Table 3.4. The χ_r^2 quoted are derived from the 54 bins shown in Figure 3.3, the associated error of the ith bin, σ_i, and the number of fit parameters of the model. For a set of n data points, fitted by a model, m, with k free parameters, the Akaike Information Criterion (AIC, AIC$_c$; Akaike 1974) is related to the log-likelihood function by:

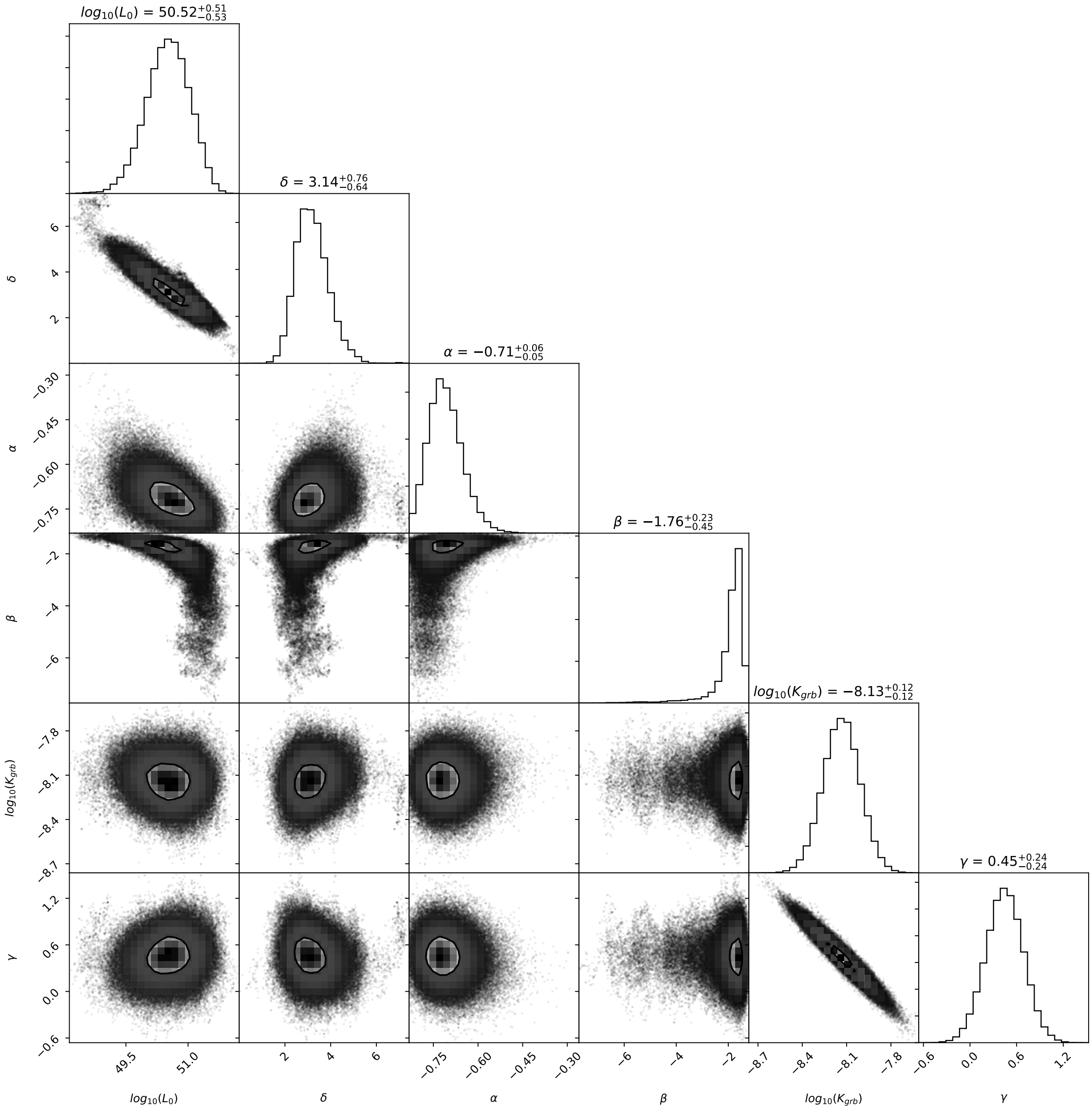

Figure 3.6: *Example posterior distributions of a GRB luminosity function modelled by a broken power-law, and derived using a Metropolis-Hastings MCMC.* α*, and beta, are the power-law indices, and the luminosity cutoff at a given redshift is modelled by* $L_c(z) = L_0(z+1)^{\delta}$ *ergs* s^{-1}*; the normalisation factor at a given redshift is also given by* $K_{Norm}(z) = K_{GRB}(z+1)^{\gamma}$ *GRBs* $M_{\odot}^{-1}$*. The MCMC chain consists of* 2×10^7 *correlated samples (gray transparent points), with 2D binning in the highest density central regions of the posterior; contour lines denote regions of 0.5, 1, 1.5, and 2* σ *confidence, with a "burn-in" phase also seen. Quoted figures are the mean parameter values of the posterior distribution and are marginalised over all other parameters; also quoted are the inter-quartile range denoted as the sub/super scripts, and highlighted with the dashed lines in the parameter histograms. Figure produced using the Corner routine developed by Foreman-Mackey (2013) for the Python programming language.*

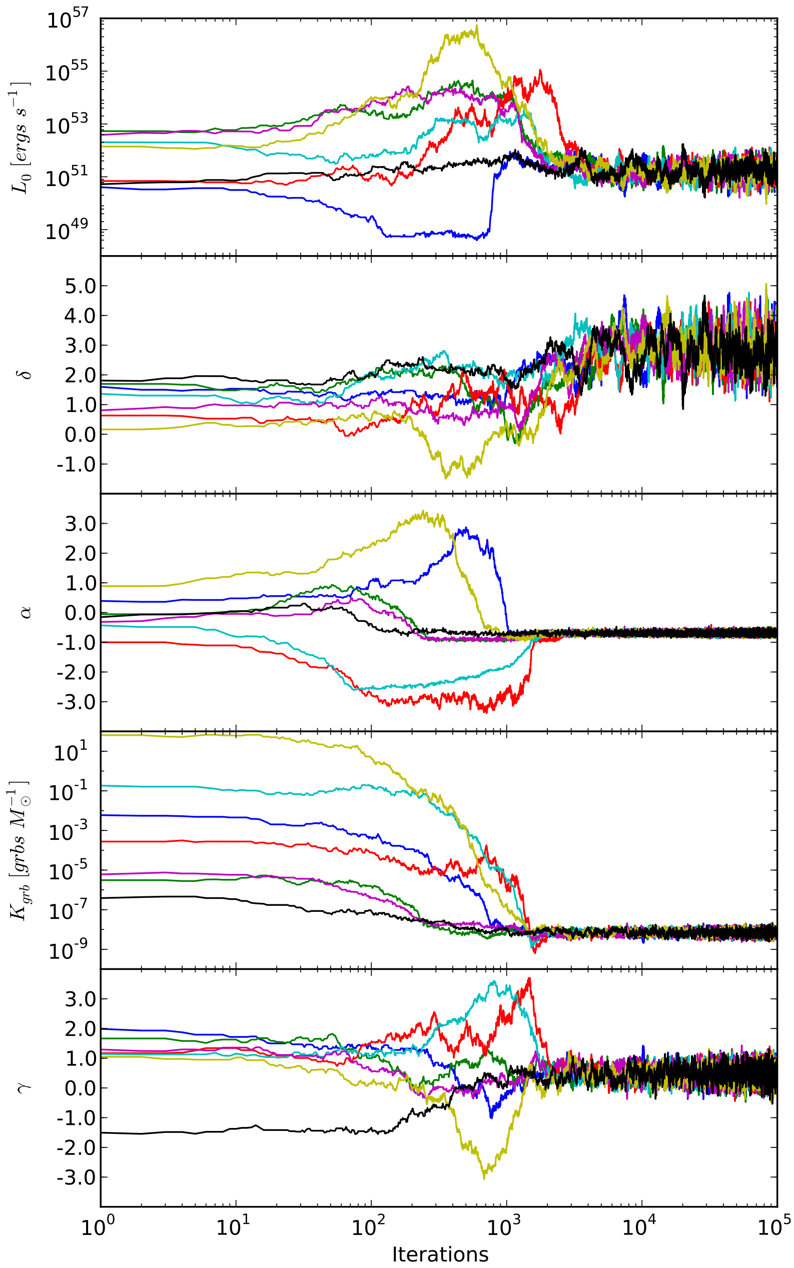

Figure 3.7: *7 MCMC chains for the Type I GRB pulse LF PLEC model convolved with the CSFRD, and the fractional population of high mass stars. The parameters for the break luminosity,* L_0*; luminosity break evolution,* δ*; low-luminosity index,* α*; GRB formation rate,* K_{grb}*; and GRB formation rate evolution,* γ*, were allowed to evolve from random start points and converge to a unique solution typically around* $\sim 2 \times 10^3$ *iterations. Gelman & Rubin PSRFs statistics for each of the parameters were derived with* $\sigma_{PSRF} = 1.0051, 1.0073, 1.0058, 1.0022, 1.0052$ *for* L_0*,* δ*,* α*,* K_{grb}*, and* γ *respectively.*

$$\mathrm{AIC}_c = 2k - 2\log\mathcal{L} + \frac{2k(k+1)}{n-k-1} \tag{3.13}$$

The AIC_c is used rather than the AIC, as the third term on the R.H.S adjusts for the bias that a finite sample size can contain, and penalises models with larger numbers of free parameters. In comparing between all sets of models, M, we utilise the Akaike weights, $w_m(\mathrm{AIC}_c)$:

$$w_m(\mathrm{AIC}_c) = \frac{\exp^{\{-\Delta(\mathrm{AIC}_c)_m/2\}}}{\sum_m^M \exp^{\{-\Delta(\mathrm{AIC}_c)_m/2\}}} \tag{3.14}$$

where $\Delta(\mathrm{AIC}_c)_m = (\mathrm{AIC}_c)_m - \min(\mathrm{AIC}_c)_M$; the Akaike weights can be considered as the probability that model m is the best amongst all the chosen models, M.

3.6 Type I GRB Pulse LF Models

3.6.1 No Evolution Model (Type I-1)

We find that the scenario in which there is no inclusion of evolutionary models: luminosity break, rate density, or metallicity, produces a fit of $\chi_r^2 = [1.81, 1.83]$ for the BPL and PLEC models respectively. This model produces a distribution of GRB pulses that underestimates the extrema of the observed pulse luminosity distribution (see column 1, Figure 3.8). The cumulative luminosity probabilities are marginally overestimated for the lowest redshift bin, especially at higher luminosities; however the discrepencies become significant at the higher redshift bins, with chronic underestimation at all luminosities (see column 1, Figure 3.9). The derived normalised Akaike information criterion weights, $w_m(\mathrm{AIC}_c)$ for the BPL and PLEC LF models are $\sim \times 10^{-7}$, making these models highly unlikely, compared to the fully evolving LF and GRB rate type I-5 models, to minimise the Kullback-Leibler discrepancy and as such we can reject this model. This finding is in agreement with single pulse studies utilising the brightest prompt emission pulses (Daigne, Rossi & Mochkovitch, 2006; Qin et al., 2010; Salvaterra et al., 2012; Salvaterra & Chincarini, 2007; Salvaterra et al., 2009; Virgili et al., 2011a; Wanderman & Piran, 2010).

3.6.2 Rate Density Model (Type I-2)

The addition of a simple $(z+1)^{\gamma}$ rate evolution produced a best fit to the observed pulse distribution of $\gamma = 0.51 \pm 0.30$ for the BPL and PLEC models. This shifts the peak of the CSFRD to higher redshifts, boosting the GRB pulse formation rate at high-z whilst reducing low-z formation rates, producing broadly the same deficiencies as the non-evolving Type I-1 model with regards to reproducing the observed population of LGRBs at the extrema (see column 3, Figure 3.8), and the inability to replicate the cumulative luminosity probabilities in the higher redshift bins (see column 3, Figure 3.9). A marginal improvement in the fits of $\chi^2_r = [1.78, 1.78]$ is seen and the addition of the extra evolutionary parameter makes this model approximately twice as likely as the non-evolving Type I-1 model to produce our observed GRB pulse distribution according to Akaike weighting. This is however still approximately 10^6 times less likely than the fully evolving Type I-5 model, making this model highly unlikely and as such we reject it as a solution to the observed evolution in the GRB pulse distribution.

Our derived γ values are consistent with those derived in single pulse GRB LF studies, albeit towards the lower end of the distribution ($0.5 < \gamma < 1.93$, Cao et al. 2011; Dainotti et al. 2014; Kistler et al. 2008; Qin et al. 2010; Robertson & Ellis 2012; Salvaterra et al. 2012; Virgili et al. 2011a). This diversity, in part, reflects the diversity of GRB formation models used, most notably the CSFRD, and the selection methods of suitable GRBs preferred by the authors. Furthermore, excluding the evolving formation rate efficiency of high-mass stars, $F(z)$, which itself produces a weak rate evolution, would result in a greater derived γ value as such effects are ignored in other papers. Direct comparisons between studies are difficult given the variation in methods, and data utilised, however the common result is that inclusion of a rate density parameter improves the performance of the fit but is less effective than other evolutionary models (see Salvaterra et al. 2012 for example).

BPL	$Z/Z_\odot$	K_{GRB} [10^8 GRBs $M_\odot^{-1}$]	γ	L_0 [10^{52} ergs s^{-1}]	δ	α	β	χ_r^2	$w_m(\mathrm{AIC}_c)$
I-1)	-	$1.18^{+0.10}_{-0.09}$	-	$1.69^{+1.29}_{-0.73}$	-	$-0.79^{+0.04}_{-0.04}$	$-1.91^{+2.04}_{-2.04}$	1.81	1.4×10^{-7}
I-2)	-	$0.67^{+0.28}_{-0.20}$	$0.51^{+0.30}_{-0.30}$	$1.70^{+1.22}_{-0.71}$	-	$-0.78^{+0.04}_{-0.04}$	$-1.88^{+1.12}_{-1.12}$	1.78	2.6×10^{-7}
I-3)	-	$1.20^{+0.10}_{-0.09}$	-	$0.02^{+0.05}_{-0.02}$	$3.35^{+0.74}_{-0.74}$	$-0.70^{+0.06}_{-0.06}$	$-1.69^{+0.56}_{-0.56}$	1.05	0.0961
I-4)	0.01	$653.0^{+66.7}_{-65.6}$	-	$1.21^{+0.77}_{-0.47}$	-	$-0.75^{+0.06}_{-0.06}$	$-1.69^{+0.23}_{-0.23}$	1.67	5.1×10^{-6}
	0.1	$14.3^{+1.2}_{-1.1}$	-	$1.05^{+0.74}_{-0.43}$	-	$-0.75^{+0.06}_{-0.06}$	$-1.59^{+0.22}_{-0.22}$	1.69	4.6×10^{-6}
	0.2	$4.91^{+0.43}_{-0.39}$	-	$1.05^{+0.77}_{-0.45}$	-	$-0.75^{+0.06}_{-0.06}$	$-1.55^{+0.27}_{-0.27}$	1.71	4.5×10^{-6}
	0.3	$2.87^{+0.25}_{-0.23}$	-	$1.26^{+0.92}_{-0.53}$	-	$-0.76^{+0.05}_{-0.05}$	$-1.60^{+0.43}_{-0.43}$	1.71	4.7×10^{-6}
	0.4	$2.07^{+0.18}_{-0.17}$	-	$1.46^{+1.00}_{-0.60}$	-	$-0.77^{+0.04}_{-0.04}$	$-1.70^{+0.48}_{-0.48}$	1.71	5.6×10^{-6}
	0.5	$1.67^{+0.15}_{-0.14}$	-	$1.67^{+1.04}_{-0.64}$	-	$-0.77^{+0.04}_{-0.04}$	$-1.83^{+0.55}_{-0.55}$	1.70	6.3×10^{-6}
	0.6	$1.47^{+0.13}_{-0.12}$	-	$1.70^{+1.86}_{-0.89}$	-	$-0.77^{+0.04}_{-0.04}$	$-1.89^{+4.33}_{-4.33}$	1.71	5.4×10^{-6}
I-5)	-	$0.69^{+0.24}_{-0.18}$	$0.49^{+0.25}_{-0.25}$	$0.02^{+0.06}_{-0.02}$	$3.26^{+0.72}_{-0.72}$	$-0.70^{+0.06}_{-0.06}$	$-1.67^{+0.72}_{-0.72}$	1.00	0.3029

PLEC	$Z/Z_\odot$	K_{GRB} [10^8 GRBs $M_\odot^{-1}$]	γ	L_0 [10^{52} ergs s^{-1}]	δ	α		χ_r^2	$w_m(\mathrm{AIC}_c)$
I-1)	-	$1.13^{+0.10}_{-0.10}$	-	$4.31^{+1.18}_{-0.92}$	-	$-0.75^{+0.05}_{-0.05}$	-	1.83	2.0×10^{-7}
I-2)	-	$0.65^{+0.25}_{-0.18}$	$0.51^{+0.28}_{-0.28}$	$4.55^{+1.32}_{-1.02}$	-	$-0.75^{+0.05}_{-0.05}$	-	1.78	4.8×10^{-7}
I-3)	-	$1.19^{+0.10}_{-0.10}$	-	$0.15^{+0.12}_{-0.07}$	$2.92^{+0.54}_{-0.54}$	$-0.70^{+0.05}_{-0.05}$	-	1.08	0.0999
I-4)	0.01	$642.4^{+58.7}_{-53.8}$	-	$5.35^{+1.50}_{-1.17}$	-	$-0.76^{+0.05}_{-0.05}$	-	1.79	6.2×10^{-7}
	0.1	$13.9^{+1.3}_{-1.2}$	-	$5.34^{+1.65}_{-1.26}$	-	$-0.76^{+0.05}_{-0.05}$	-	1.80	5.2×10^{-7}
	0.2	$4.77^{+0.44}_{-0.40}$	-	$5.25^{+1.72}_{-1.29}$	-	$-0.76^{+0.05}_{-0.05}$	-	1.79	9.0×10^{-7}
	0.3	$2.76^{+0.26}_{-0.23}$	-	$5.02^{+1.58}_{-1.20}$	-	$-0.75^{+0.05}_{-0.05}$	-	1.75	2.1×10^{-6}
	0.4	$1.98^{+0.18}_{-0.17}$	-	$4.74^{+1.42}_{-1.09}$	-	$-0.75^{+0.05}_{-0.05}$	-	1.73	3.8×10^{-6}
	0.5	$1.62^{+0.15}_{-0.14}$	-	$4.56^{+1.30}_{-1.01}$	-	$-0.74^{+0.05}_{-0.05}$	-	1.72	4.1×10^{-6}
	0.6	$1.42^{+0.13}_{-0.12}$	-	$4.38^{+1.22}_{-0.95}$	-	$-0.74^{+0.05}_{-0.05}$	-	1.72	3.7×10^{-6}
I-5)	-	$0.68^{+0.23}_{-0.07}$	$0.49^{+0.24}_{-0.24}$	$0.17^{+0.14}_{-0.08}$	$2.83^{+0.55}_{-0.55}$	$-0.70^{+0.05}_{-0.05}$	-	1.04	0.5010

Table 3.2: *Fitted results for Type I models, where the GRB pulse formation rate function, $\Psi_*(z)$, incorporates a Cole CSFRD parameterised by Kobayashi, Inoue & Inoue (2013). The best fit parameters for the BPL and PLEC LF models are shown for the scenarios of I-1) where there is no extra evolutionary parameter ($\iota(z) = 1$); I-2) there is evolution in the GRB formation rate ($\iota(z) \propto (z+1)^\gamma$); I-3) there is evolution in the break luminosity ($L_{break} \propto (z+1)^\delta$); I-4) there is present a metallicity density evolution ($\iota(z) = \Sigma(z)$ and $\Sigma(z) = \hat{\Gamma}[0.84, (Z/Z_\odot)^2 10^{0.3z}]/\Gamma(0.84)$) and; I-5) there is simultaneously evolution of the rate density and break luminosity ($\iota(z) \propto (z+1)^\gamma$ and $L_{break} \propto (z+1)^\delta$).*

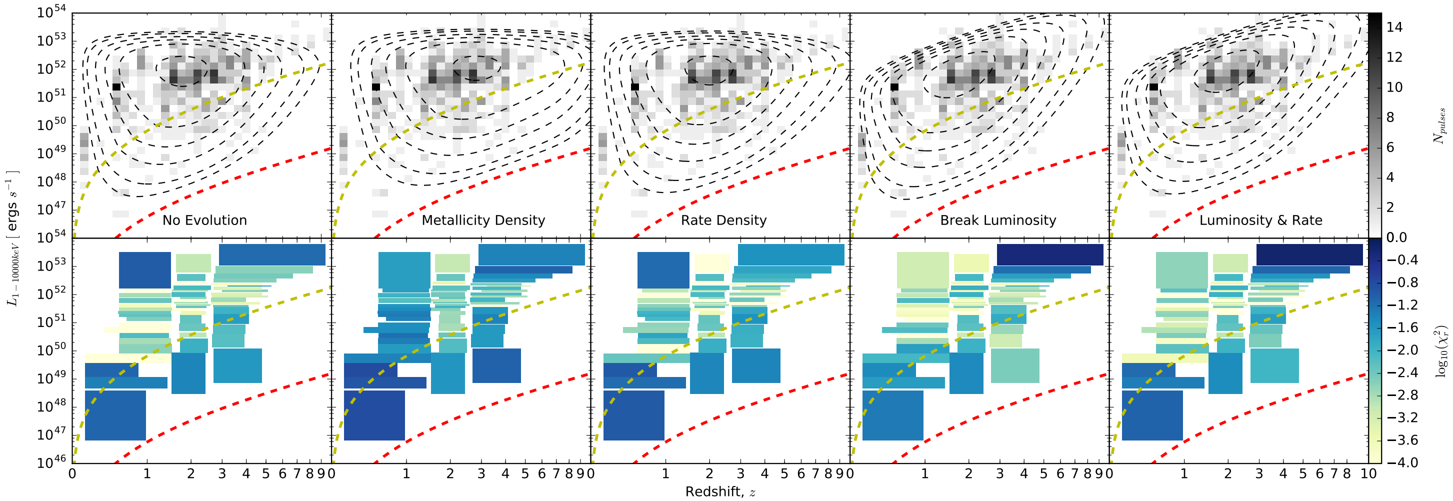

Figure 3.8: *The derived GRB pulse luminosity distribution for a Type I PLEC LF (dashed contours) overlaying the observed pulse distribution, binned to an arbitrary 1/4 dex in luminosity and 1/32 dex in redshift (top row). The five models shown corresponds to: a non-evolving, I-1, model (column 1); a metallicity density I-4 model with metallicity density threshold, $Z/Z_\odot$ (column 2); a rate density evolution I-2 model, incorporating an additional $(z+1)^\gamma$ evolutionary factor (column 3); a break luminosity I-3 model evolving as $L_b = L_0(z+1)^\delta$ (column 4); and a bivariate break, and rate evolution I-5 model (column 5). The corresponding logarithm of the reduced χ^2 of the fits are shown for the data bins (bottom row). The upper (yellow) and lower (red) dashed lines denote the detection thresholds of the BAT and XRT respectively. The equivalent figures for the broken power-law distributions are available in Appendix III.*

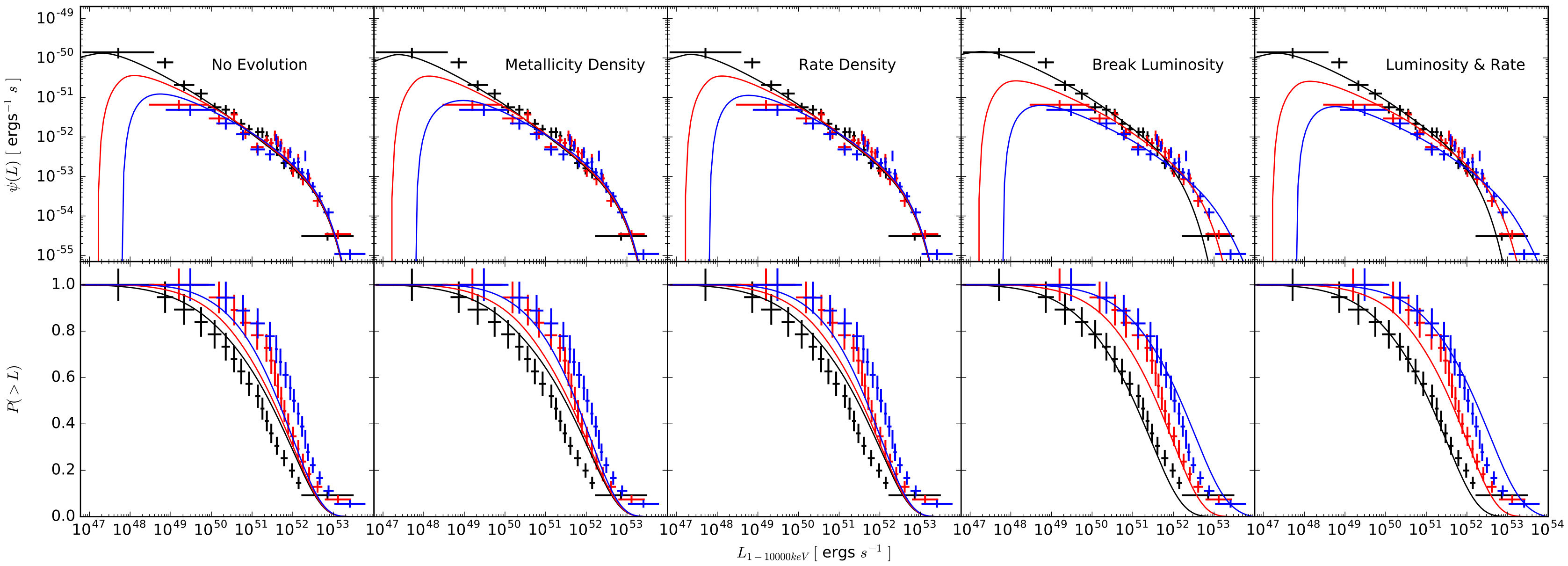

Figure 3.9: *The observed, and derived GRB pulse probability densities (top row) for the three redshift bins, and the equivalent cumulative probability densities (bottom row) for Type I GRB pulse formation models with a PLEC LPDF. The five models shown corresponds to: a non-evolving, I-1, model (column 1); a metallicity density I-4 model with metallicity density threshold, $Z/Z_\odot$ (column 2); a rate density evolution I-2 model, incorporating an additional $(z+1)^\gamma$ evolutionary factor (column 3); a break luminosity I-3 model evolving as $L_b = L_0(z+1)^\delta$ (column 4); and a bivariate break, and rate evolution I-5 model (column 5). Black data, and lines correspond to the* $0.125 < z \leq 1.505$ *redshift bin; whilst red, and blue data correspond to the* $1.51 < z \leq 2.6$ *and* $2.612 < z \leq 9.4$ *bins respectively. The turn-off at low luminosities is due to the convolution to the Swift detection profile. The equivalent figures for the broken power-law distributions are available in Appendix III.*

3.6.3 Metallicity Density Model (Type I-4)

Our attempts at fitting metallicity density evolution proved to be unsuccessful, with our MCMC code unable to converge on a unique solution, suggesting strong degeneracy between $Z/Z_\odot$ and other fitted parameters. We therefore chose to set six metallicity thresholds and fit our data, covering $0.01 < Z/Z_\odot < 0.6$. We find that degeneracy exists between the metallicity threshold, and all other fitted parameters, with this degeneracy arising from the unique shape of $\Sigma(z)$. The functional form of $\Sigma(z)$ can be crudely considered as a linear rise in z connecting two plateaus at $\Sigma(z) \approx 0$ and $\Sigma(z) \approx 1$. The metallicity density threshold acts to shift $\Sigma(z)$ in z, whereby a greater $Z/Z_\odot$ shifts the start of the linear rise to lower-z. For $Z/Z_\odot = 0.01$, this shift is strong enough that the majority of $\Sigma(z)$ is at the first plateau, resulting in a significantly higher K_{GRB} to compensate. As $Z/Z_\odot$ increases, more of $\Sigma(z)$ occupies the upper plateau and K_{GRB} tends towards values found for Type I models excluding metallicity density evolution. Further degeneracy between $Z/Z_\odot$ and L_0, α, and β arises when convolving $\Sigma(z)$ to the Swift detection profile, $D(L, z)$. As the detection thresholds of the BAT and XRT effectively bisects the $L-z$ plane, changes to the size of the plateau that $\Sigma(z)$ produces is rotated onto the L dimension by $D(L, z)$, and is counterbalanced by variation of the LF parameters.

Despite the range of metallicity density thresholds fitted, our Type I-4 models produces broadly similar quality of fits, with small variations as displayed by the χ^2_r and Akaike weights in Table 3.2. Across all $Z/Z_\odot$ in both the BPL and PLEC we see a general improvement in the quality of fits as compared to both the non-evolving Type I-1 model and Type I-2 rate density model. An example distribution, with a metallicity density threshold of $Z/Z_\odot = 0.1$, is shown in column 2, Figures 3.8 & 3.9, and shows similar deficiencies of models that instill a rate evolution on the cumulative luminosity probability function. The combined Akaike weights make the Type I-4 metallicity density model 153 times more likely than the non-evolving Type I-1 model and 70 times more likely than the Type I-2 rate density model whilst the evolving Type I-3 LF break model is 3.7×10^3 more likely. These values strongly suggests that either the metallicity density evolution is not a suitable explanation for the observed distribution of GRB pulses, or that assumptions made in the derivation of $\Sigma(z)$ are not entirely appropriate. The derivation of the metallicity density evolution by Langer & Norman (2006) does not, for example, consider scatter in the mass-metallicity relationship, redshift evolution of the faint end of the SGMF, or the rate at which the average galactic metallicity evolves with redshift.

Although the degeneracies of the metallicity density prevents suitable convergence in the metallicity density threshold, our results are broadly similar to studies utilising a GRB's brightest pulse: Salvaterra et al. (2012) finds that metallicity density evolution is more likely than rate density evolution and less likely than evolution in the break to minimise information loss, although to a much less significant degree than we find; Qin et al. (2010) finds that a GRB formation rate that is proportional to both CSFRD and metallicity density (with $Z/Z_{\odot} = 0.1$) only barely reproduces the z distribution; whilst Virgili et al. (2011a) find such models fail to reproduce observations to enough significance to pass the author's criteria.

3.6.4 Break Luminosity Evolution (Type I-3)

Evolution in the break, or cutoff, of the LF model is the most common explanation for the observed evolution in the GRB luminosity-redshift distribution. We find that the inclusion of break evolution produces an evolutionary factor δ of $3.35^{+0.74}_{-0.74}$ and $2.92^{+0.54}_{-0.54}$ for the BPL and PLEC models with corresponding χ^2_r values of 1.05 and 1.08.

As seen in column 4 of Figure 3.8, the evolution in the break acts to boost the GRB pulse distribution at the extrema, significantly improving the fit statistics. This becomes clearer when observing the cumulative luminosity probability function (column 4, Figure 3.9): non-evolving, or rate density evolving models consistently over estimate the distribution of low-redshift, high-luminosity pulses, whilst underestimating the luminosity distributions of higher redshift pulses. Evolution in the break luminosity dramatically improves the quality of fits such that there is marginal overestimation of low-luminosity intermediate-redshift, and high-redshift, high-luminosity pulses. Combined Akaike weights, $w_m(AIC_C)$ of 0.196, for the evolving LF break model shows that this model is 3×10^3 times more likely than Type I-4 metallicity density models, and 2.8×10^5 times more likely than Type I-2 rate density models to minimise information loss; luminosity evolution in the GRB LF, excluding or including all secondary GRB pulses, is preferred over all over forms of Type I univariate evolutionary models (Salvaterra et al., 2012; Salvaterra & Chincarini, 2007).

Our derived values for the LF break evolution parameter are consistent with GRB

LF studies that utilise Swift data ($2.1 < \delta < 3.5$, Campisi, Li & Jakobsson (2010); Pescalli et al. (2015); Petrosian, Kitanidis & Kocevski (2015); Salvaterra et al. (2012); Yonetoku et al. (2004); Yu et al. (2015a)), whilst studies that incorporate BATSE data display weaker luminosity evolution ($1.0 < \delta < 2.0$. Firmani et al. (2004); Kocevski & Liang (2006); Lloyd-Ronning, Fryer & Ramirez-Ruiz (2002); Salvaterra & Chincarini (2007); Salvaterra et al. (2009)). The BPL and PLEC LF parameters of α, $\beta = [-0.70^{+0.06}_{-0.06}, -1.69^{+0.56}_{-0.56}]$ and $L_0 = [2.0 \times 10^{50}, 1.5 \times 10^{51}]$ ergs s^{-1} are likewise in concordance with those found in the literature, with shallower low-luminosity gradients generally derived by studies that incorporate the fainter bursts/pulses detectable by Swift.

3.6.5 Evolving LF and Rate Density (Type I-5)

We derive values of $\gamma = 0.49^{+0.25}_{-0.25}$ for both LF model types and $\delta = [3.26^{+0.72}_{-0.72}, 2.83^{+0.55}_{-0.55}]$ for the BPL and PLEC, with a corresponding χ^2_r of 1.00, and 1.04 respectively, with the majority of this improvement seen in the very high redshift bins (see column 5, Figure 3.8). The derived evolutionary parameters are similar to those of Type I-2, I-3 univariate models, and suggests weak degeneracy between the rate density and break luminosity model parameters, with the evolution of the break performing the lion's share of log-likelihood optimisation; as such, the cumulative luminosity probability functions are near-identical for the Type I-3, and I-5 models (see column 5, Figure 3.9). The combined Akaike weights makes the Type I-5 bivariate evolving model more than 4 times as likely as the Type I-3 evolving LF break model despite the additional evolutionary parameters required. Although this suggests that a bivariate evolution model is preferred over a univariate evolution model, a model based solely on the evolution of the break luminosity cannot be ruled out entirely.

3.6.6 Redshift, Luminosity, and Flux Cuts

In all single population GRB pulse models the residuals of fitted GRB luminosity functions are greatest at the extrema of the GRB pulse $L - z$ distribution:

- non-evolving models underestimate the population of high-z, high-L pulses, whilst overestimating that of low-z, low-L pulses;

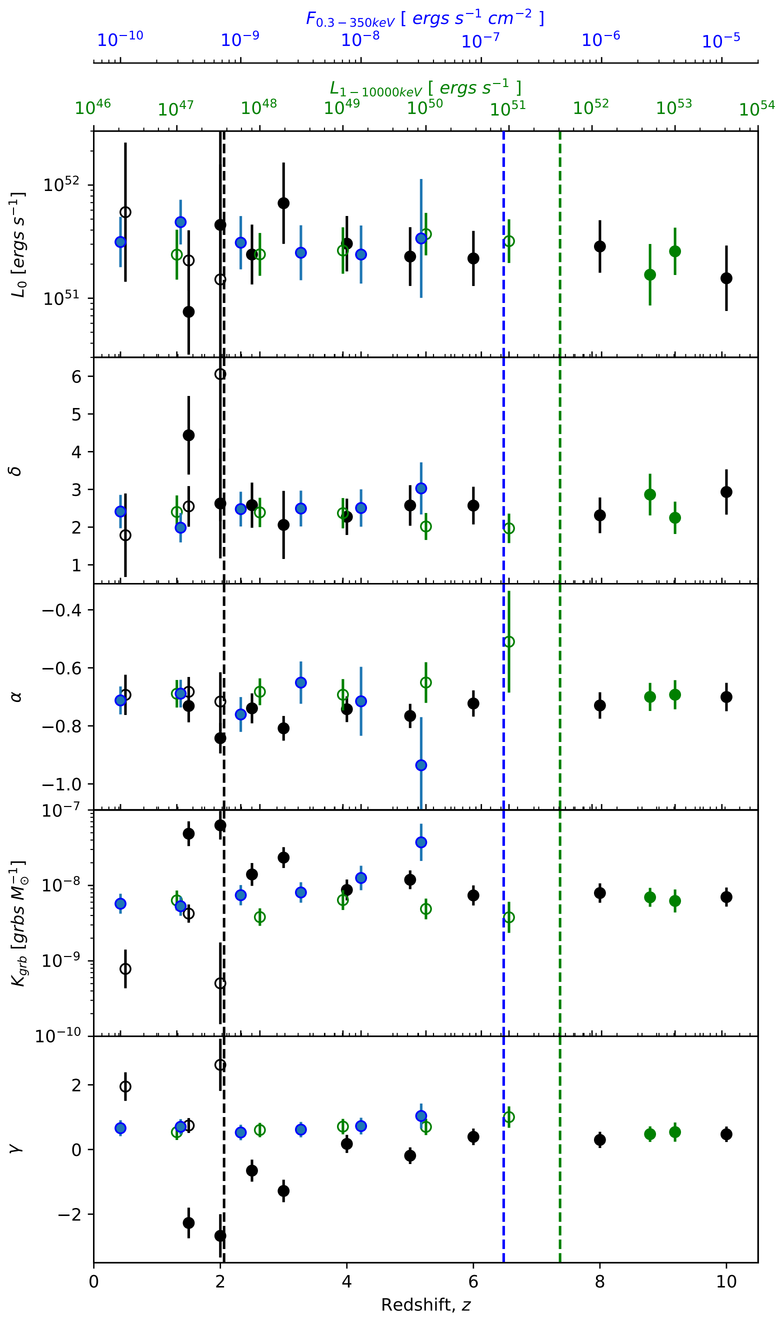

Figure 3.10: *Fitted MCMC parameters of a fully evolving Type I-5 PLEC LF model with successive redshift cuts (black axis), bolometric rest-frame luminosity cuts (green axis), or observer-frame integrated peak flux cuts (blue axis) to the GRB pulse data. Filled and empty circles denote the upper and lower cutoffs respectively for that particular dataset with 1σ uncertainties. Overlaid are the median redshift, luminosities, and fluxes of the pulse data (dashed lines).*

- rate density models overestimate the population of high-z, high-L pulses, whilst underestimating that of low-z, low-L pulses;
- both models that incorporate break luminosity overestimate the high-z, high-L GRB pulse populations but are consistent with their large associated uncertainties, contributing little to the log-likelihood function.

Discrepencies at the extrema may be due to parent GRBs that are significantly different from the bulk population, either through a separate GRB progenitor type (Pop III stars for high-z, high-L GRBs) or a via a more complex GRB luminosity function (LL & HL GRBs). Cutting away GRB pulses that lie in the extrema of the redshift, or luminosity distributions may produce noticeable changes in fitted parameters, suggestive of LGRB sub-populations. We find, however, that performing successive cuts in the data for the Type I-5 PLEC LF model (see Figure 3.10) of the high/low regions (filled/empty circles) of the z, or L distributions (black/green data) produces weak variations in the fitted parameters, which becomes more pronounced as the sample size decreases. Such variations in the fitted parameters are, however, small with good overlap of the 1σ confidence intervals. Whilst this suggests that the low-z/high-z, and low-L/high-L GRB pulses are part of a single population rather than belonging to unique sub-populations, we cannot rule out the possibility that the latter is true.

It is common in the data selection phase of GRB luminosity studies to apply a flux cut to the data, with authors arguing that the brightest GRBs in the observer-frame suffer the least from detection bias, and as such are more representative of the true population of GRBs. The study by Salvaterra et al. 2012, for example, utilises a flux cut of $P_{15-150keV} = 2.6$ photons s^{-1} cm^{-2} in the observer frame, equating to an integrated flux of $F_{15-150keV} \approx 1.21 \times 10^{-5}$ ergs s^{-1} cm^{-2} for a PLEC spectrum with $\alpha = -1.57$, $E_c = 183$ keV. The inclusion of a high flux limit has led to suggestions that the observed evolution seen in such studies arise from Malmquist bias, rather than being an intrinsic property of the GRB luminosity function (Howell & Coward, 2013). To this end, we vary the flux selection threshold on our GRB pulse data and re-run our MCMCs to refit the data. We find some variation in the GRB pulse luminosity fit parameters (see Figure 3.10, blue data) however such variation, like those of the redshift and luminosity thresholds, are consistent with the intrinsic uncertainties of the model fit parameters. Whilst the rate evolution parameter, γ, varies in direction such that it is not concrete that such evolution is real, the

BPL	Type I-1	Type II
K_{GRB}^{HL}	$1.18^{+0.10}_{-0.09} \times 10^{-8}$	$1.18^{+0.10}_{-0.09} \times 10^{-8}$
L_0^{HL}	$1.69^{+1.29}_{-0.73} \times 10^{52}$	$1.70^{+0.40}_{-0.32} \times 10^{52}$
α^{HL}	$-0.79^{+0.04}_{-0.04}$	-0.79
β^{HL}	$-1.94^{+2.04}_{-2.04}$	-1.94
K_{GRB}^{LL}	-	0.50×10^{-8}
L_0^{LL}	-	7.21×10^{46}
α^{LL}	-	-0.79
β^{LL}	-	-1.94
χ_r^2	1.81	1.91
$w_m(\text{AIC}_C)$	0.3587	0.0088
PLEC	Type I-1	Type II
K_{GRB}^{HL}	$1.13^{+0.10}_{-0.10} \times 10^{-8}$	$1.12^{+0.10}_{-0.09} \times 10^{-8}$
L_0^{HL}	$4.31^{+1.18}_{-0.92} \times 10^{52}$	$4.23^{+0.85}_{-0.71} \times 10^{52}$
α^{HL}	$-0.75^{+0.05}_{-0.05}$	-0.75
K_{GRB}^{LL}	-	1.11×10^{-8}
L_0^{LL}	-	1.10×10^{47}
α^{LL}	-	-0.75
χ_r^2	1.83	1.85
$w_m(\text{AIC}_C)$	0.5081	0.1244

Table 3.3: *The fitted Type I-1, non-evolving model GRB LF for a single population of GRBs (Table 3.2) and a Type II, bimodal population of high-luminosity ($L > 10^{50}$ ergs s^{-1}) and low-luminosity ($L < 10^{50}$ ergs s^{-1}) GRBs. K_{GRB} is given in units of GRBs $M_\odot^{-1}$ and L_0 is in units of ergs s^{-1}. Uncertainties in α and β for the bimodal population are not given as these parameters were fixed beforehand. The fitted LL GRB LF parameters are quoted without associated errors as they are unconstrained. The χ_r^2 values, and Akaike weights, $w_m(AIC_c)$, are derived from the bins shown in Figure 3.4.*

evolution in the break luminosity is strong and sees little variation when applying various data cuts.

3.7 The Type II GRB Pulse LF Models

To reduce the dimensionality of the bimodal LL & HL GRB LF model, we fix the indices of the two populations at the values derived for a Type I-1, non-evolving single population GRB LF, such that $\alpha = \alpha_{HL} = \alpha_{LL}$ (or $\beta = \beta_{HL} = \beta_{LL}$). We find little variation between the HL LF parameters and the single population Type I-1 LF parameters, unsurprising given the bulk of the GRB pulse population lies within the regime of HL GRBs. We find a local HL GRB formation rate density, ρ_0^{HL}

of $0.22^{+0.02}_{-0.02}$, $0.21^{+0.01}_{-0.02}$ GRBs Gpc^{-3} yr^{-1} for the PLEC and BPL LFs respectively, compared to the $0.09 < \rho_0^{HL} < 1.2$ GRBs Gpc^{-3} yr^{-1} range found by Howell & Coward (2013); Liang et al. (2007); Virgili, Liang & Zhang (2009) for their high luminosity GRBs. The secondary LL GRB pulse LF shows a break at $L_0^{LL} = 7.21 \times 10^{46}$, 1.10×10^{47} ergs s^{-1} for the BPL and PLEC LF models respectively, with a local GRB formation rate density of $\rho_0^{LL} = 0.09$, 0.21 GRBs Gpc^{-3} yr^{-1}. The ratio of low/high-luminosity GRB formation rate densities found in this chapter are approximately at unity, compared to the ratios of $50 - 200$ found in favour of LL GRBs (Howell & Coward, 2013; Liang et al., 2007; Virgili, Liang & Zhang, 2009); varying the limits of normalisation of the LFs has a small effect on the derived K_{GRB} efficiencies and is not a solution to the discrepency. Despite a sample of 72 GRB pulses, we are unable to constrain uncertainties in the fitted parameters.

The inclusion of a secondary LL LF marginally improves the fitting of the observed $L - z$ GRB pulse distribution at the lowest redshift bins (see column 3, Figure 3.11), reducing the χ_r^2 contribution of the low-L, low-z bins at the expense of twice the number of input parameters. Although reproducing the observed $L - z$ GRB pulse distribution, the overall combined Akaike weights for the Type II models ($w_m(\mathrm{AIC}_C) = 0.1332$), versus the non-evolving Type I-1 LF models ($w_m(\mathrm{AIC}_C) = 0.8668$) strongly suggests that a single, non-evolving population of GRB pulses is a better representation of the $L - z$ distribution. Like the non-evolving Type I-1 models, the bimodal GRB population significantly underestimates the observed cumulative pulse luminosity probability density at the higher redshift bins (see column 3, Figure 3.12) and is therefore not a suitable explanation for the observed evolution of the break luminosity. We do not rule out that LL GRB pulses are a separate subgroup; however our data does suggest that it is highly unlikely.

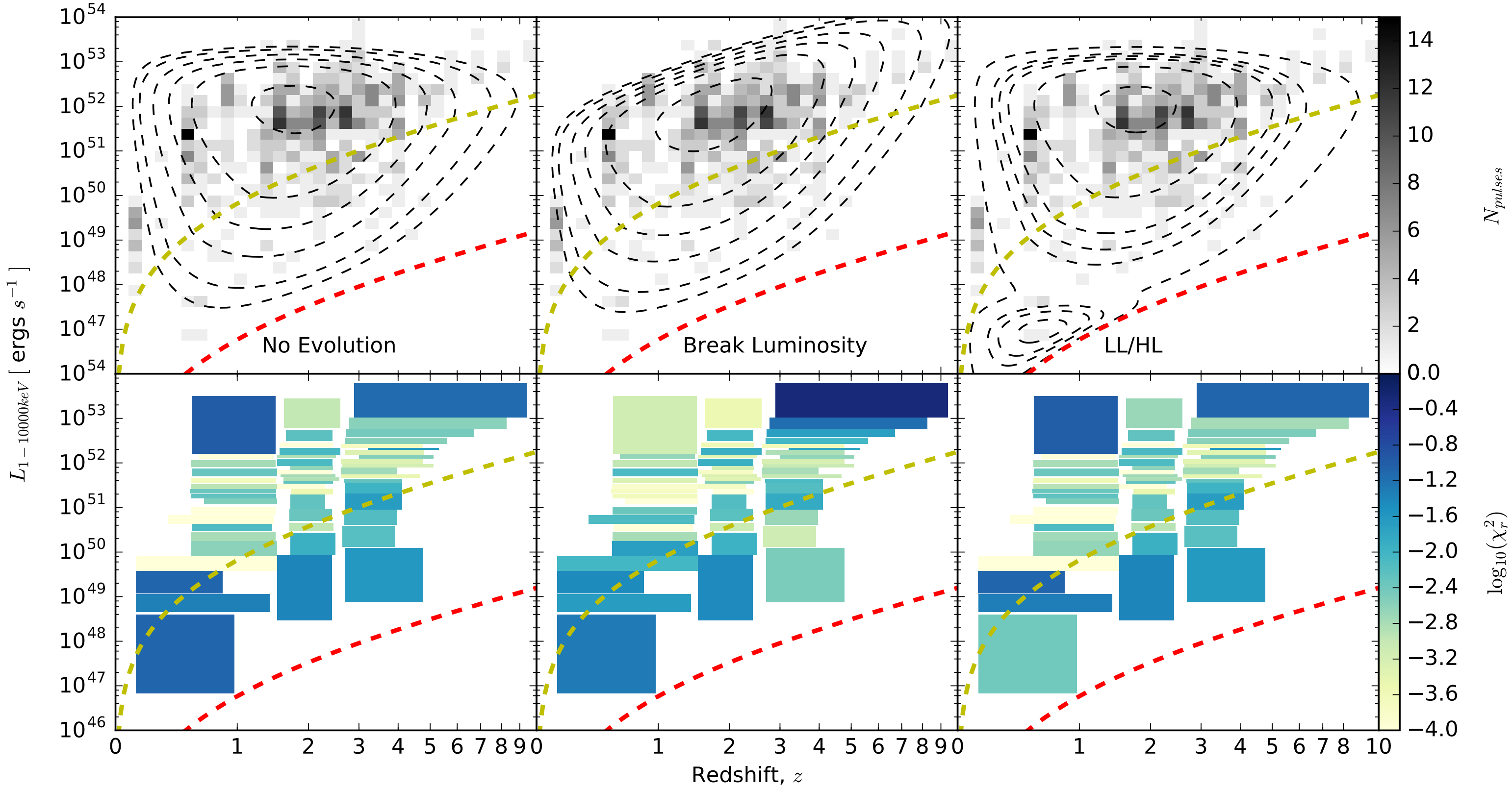

Figure 3.11: *The derived GRB pulse luminosity distribution for a Type II PLEC LF (dashed contours) overlaying the observed pulse distribution, binned to an arbitrary 1/4 dex in luminosity and 1/32 dex in redshift (top row). The three models shown corresponds to: the non-evolving, I-1, model (column 1); the break luminosity I-3 model evolving as $L_b = L_0(z+1)^\delta$ (column 2); and the bimodal low-luminosity/high-luminosity GRB population Type II model (column 3). The corresponding logarithm of the reduced χ^2 of the fits are shown for the data bins (bottom row). The upper (yellow) and lower (red) dashed lines denote the detection thresholds of the BAT and XRT respectively. The equivalent figures for the broken power-law distributions are available in Appendix III.*

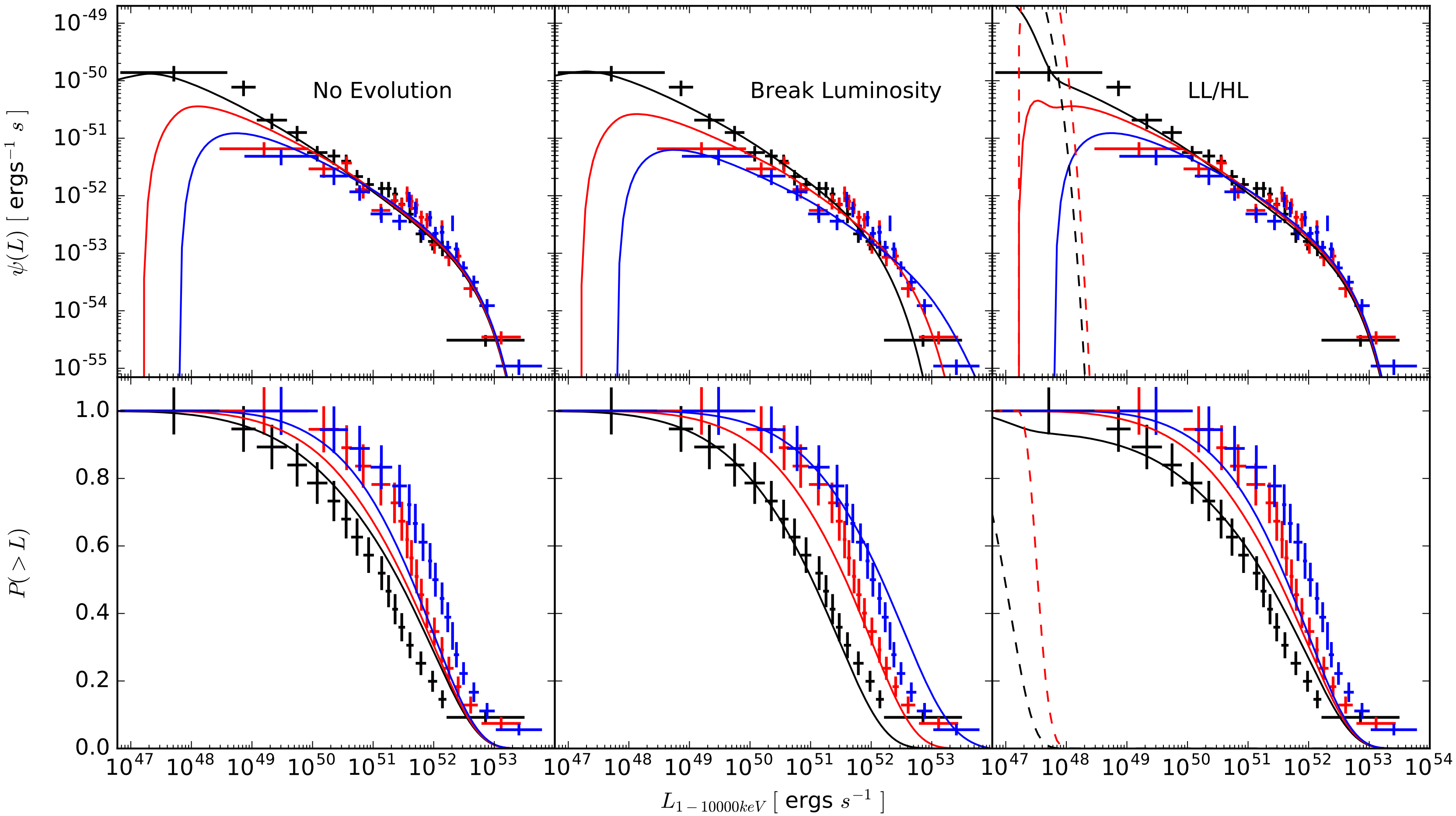

Figure 3.12: *The observed, and derived GRB pulse probability densities (top row) for the three redshift bins, and the equivalent cumulative probability densities (bottom row) for a Type II GRB pulse formation models with a PLEC LPDF. The three models shown corresponds to: the non-evolving, I-1, model (column 1); the break luminosity I-3 model evolving as* $L_b = L_0(z+1)^{\delta}$ *(column 2); and the bimodal low-luminosity/high-luminosity GRB population Type II model (column 3). Black data, and solid lines correspond to the high-luminosity component of the LPDF* $0.125 < z \leq 1.505$ *redshift bin; whilst red, and blue data correspond to the* $1.51 < z \leq 2.6$ *and* $2.612 < z \leq 9.4$ *bins respectively. The dashed line, only displayed in the lowest redshift bin, is the low-luminosity component of the Type II distribution. The turn-off at low luminosities is due to the convolution to the Swift detection profile. The equivalent figures for the broken power-law distributions are available in Appendix III.*

3.8 The Type III GRB Pulse LF Models

3.8.1 No Evolution Model (Type III-1)

We find that our fit utilising the Type III-1 GRB formation rate model, with χ_r^2 values of 2.14, and 2.13, produces a strong rise in GRB pulse formation rates from the current epoch, plateauing at $z = 1.5$, before decaying strongly away at $z = 2.6$. This follows a similar shape as the CSFRD and produces similar L_0, α, and β values as the equivalent Type I/II models fitted in Section 4.6, and 4.7. On initial inspection the Type III-1 model performs less well in fitting, as it requires more than twice the number of model parameters to achieve similar likelihoods, and suffers from the same inability to reproduce GRB pulse formation rates at the extrema of the $L - z$ pulse distribution as that of extra rate evolution for Type I-2 models (see column 1, Figure 3.13). Whilst this would lead to one assuming that a phemonenological model is better than an empirical one, it is important to note that the CSFRD models have significant uncertainties which are almost universally ignored when propagating errors, creating a false impression of greater quality; it is for this reason that we do not cast any favourable opinion on Type I over Type III models. The combined Akaike weight of $\text{AIC}_c = 5.61 \times 10^{-6}$ for both non-evolving Type III-1 LF models reinforces the conclusion that evolution in the break luminosity is required to reproduce the observed pulse $L - z$ distribution. This becomes more clear when looking at the probability, and cumulative density functions (Figure 3.14); the first column, corresponding to a non-evolving Type III-1 model, produces a CDF that fails to reproduce the clear luminosity evolution seen across the three redshift bins, with distinct underestimation of the luminosities of high-z pulses, and overestimation of the luminosities of low-z pulses.

Our pulse luminosity function is consistent with other studies that fit a triple power-law to the GRB formation rate. Although we utilise all pulses within a GRB lightcurve and our redshift breaks in the GRB formation rate differ, we find good agreement with the low-redshift, and high-redshift indexes of Butler, Bloom & Poznanski (2010) (BBP), and Wanderman & Piran (2010) (WP). We derive an α_1, and α_3 of $2.69^{+0.45}_{-0.45}$, $-1.83^{+1.01}_{-1.01}$ respectively, compared to: $3.35^{+0.74}_{-0.74}$, $-2.51^{+1.60}_{-2.25}$ (BBP); and $3.1^{+0.7}_{-0.7}$, $-2.9^{+1.6}_{-2.4}$ (WP) for their models that include GRBs with known redshifts. The intermediate-redshift indexes, α_2, derived by those studies ($1.32^{+0.58}_{-0.58}$, BBP; and $1.4^{+0.6}_{-0.6}$, WP) are significantly stronger than the $0.08^{+0.33}_{-0.33}$ we find, and can

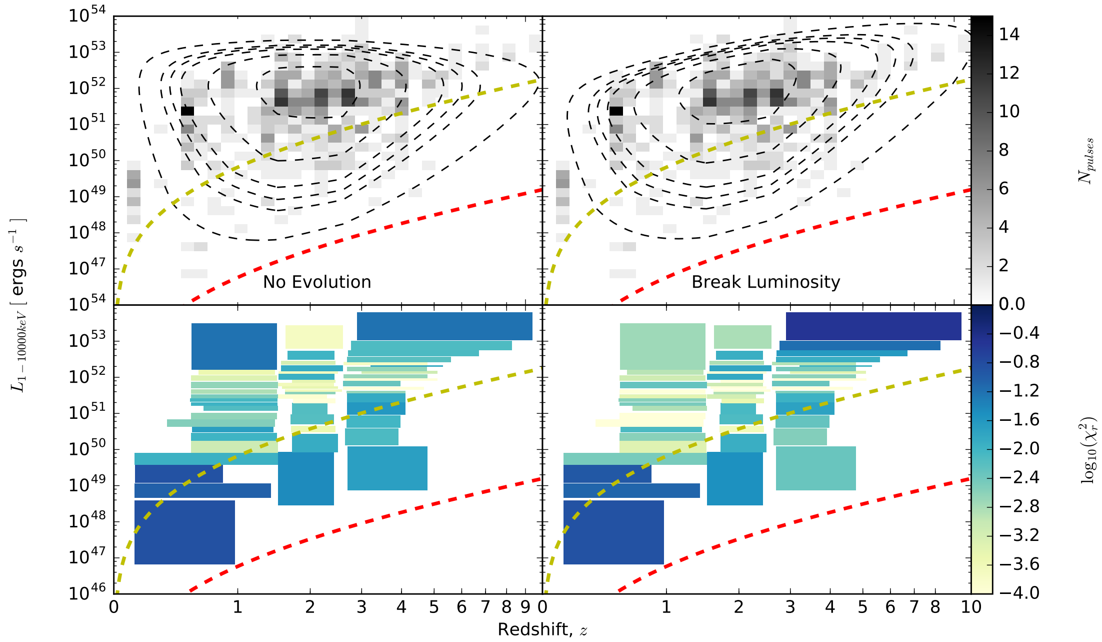

Figure 3.13: *The derived GRB pulse luminosity distribution for a Type III PLEC LF (dashed contours) overlaying the observed pulse distribution, binned to an arbitrary 1/4 dex in luminosity and 1/32 dex in redshift (top row). The two models shown corresponds to: a non-evolving, III-1, model (column 1); and a break luminosity III-2 model evolving as $L_b = L_0(z+1)^\delta$ (column 2). The corresponding logarithm of the reduced χ^2 of the fits are shown for the data bins (bottom row). The upper (yellow) and lower (red) dashed lines denote the detection thresholds of the BAT and XRT respectively. The equivalent figures for the broken power-law distributions are available in Appendix III.*

be explained by the difference in position of the first redshift break those authors utilise, who, like ourselves, do not set as a free parameter in their fitting.

Our luminosity functions produce a stronger low-luminosity index than these studies, possibly due to the large number of low-luminosity BAT and XRT pulses we incorporate, with $\alpha = -0.72^{+0.12}_{-0.12}$ compared to $-0.27^{+0.19}_{-0.19}$ (BBP), and $0.22^{+0.18}_{-0.31}$ (WP). Our low-luminosity index is however consistent both with our Type I and Type II models, and other studies that utilise a CSFRD. The high-luminosity index, β, derived by Butler, Bloom & Poznanski (2010) at $-3.46^{+1.53}_{-1.53}$ is significantly stronger than our own derived results of $-1.79^{+0.22}_{-0.22}$; however our results are consistent with $-1.4^{+0.3}_{-0.6}$ of Wanderman & Piran (2010) and is most likely due to both our studies utilising peak luminosities rather than the time-averaged luminosities used by Butler, Bloom & Poznanski (2010). The break luminosity, L_0, derived in this chapter at

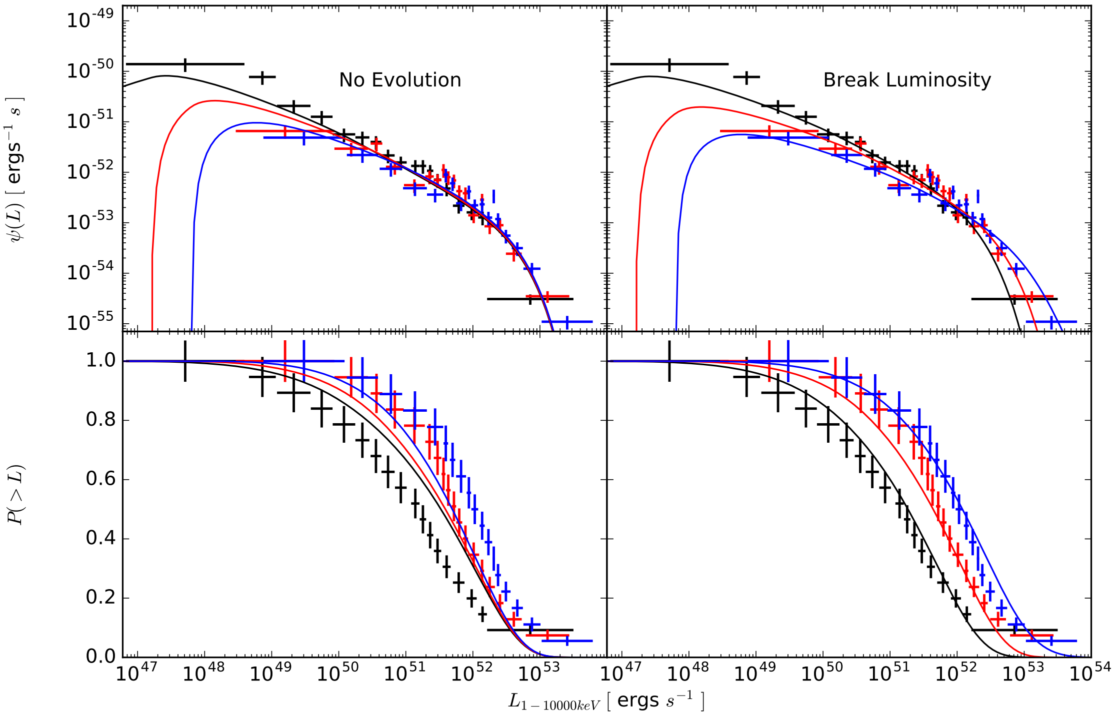

Figure 3.14: *The observed, and derived GRB pulse probability densities (top row) for the three redshift bins, and the equivalent cumulative probability densities (bottom row) for Type III GRB pulse formation models with a PLEC LPDF. The two models shown corresponds to: a non-evolving, III-1, model (column 1); and a break luminosity III-2 model evolving as* $L_b = L_0(z+1)^\delta$ *(column 2). Black data and lines correspond to the* $0.125 < z \leq 1.505$ *redshift bin; whilst red and blue data correspond to the* $1.51 < z \leq 2.6$ *and* $2.612 < z \leq 9.4$ *bins respectively. The turn-off at low luminosities is due to the convolution to the Swift detection profile. The equivalent figures for the broken power-law distributions are available in Appendix III.*

$10^{52.23^{+0.12}_{-0.12}}$ ergs s^{-1} is lower than either studies finds and is consistent with $10^{52.5^{+0.2}_{-0.2}}$ ergs s^{-1} (WP) but not with $10^{52.95^{+0.31}_{-0.31}}$ ergs s^{-1} (BBP).

3.8.2 Break Luminosity Evolution (Type III-2)

Like the Type I-3 model, inclusion of evolution in the break of the luminosity function significantly improves the quality of fits (χ^2_r = 1.43, 1.42 for the BPL, and PLEC respectively), with improvement at the high-L, high-z extrema of the pulse $L-z$ distribution (column 2, Figure 3.13). With a combined Akaike weight of $w_m(\mathrm{AIC}_C) \sim 1$ for the BPL, and PLEC models, the evolving Type III-2 luminosity functions are 1.7×10^5 times more likely than the non-evolving Type III-1 models to

BPL	Type III-1	Type III-2
a_1	$2.69^{+0.45}_{-0.45}$	$2.48^{+0.90}_{-0.90}$
z_1	1.5	1.5
a_2	$0.08^{+0.33}_{-0.33}$	$0.23^{+0.51}_{-0.51}$
z_2	2.6	2.6
a_3	$-1.83^{+1.01}_{-1.01}$	$-1.97^{+1.43}_{-1.43}$
ρ_0	$7.02^{+3.94}_{-2.52} \times 10^{-2}$	$8.29^{+8.13}_{-4.10} \times 10^{-2}$
L_0	$1.71^{+0.52}_{-0.39} \times 10^{52}$	$0.15^{+0.20}_{-0.09} \times 10^{52}$
δ	-	$2.04^{+0.45}_{-0.45}$
α	$-0.72^{+0.12}_{-0.12}$	$-0.69^{+0.09}_{-0.09}$
β	$-1.79^{+0.22}_{-0.22}$	$-1.88^{+0.25}_{-0.25}$
χ^2_r	2.14	1.43
$w_m(\mathrm{AIC}_C)$	1.1×10^{-7}	0.0415
PLEC	Type III-1	Type III-2
a_1	$2.23^{+1.32}_{-1.32}$	$2.39^{+1.25}_{-1.25}$
z_1	1.5	1.5
a_2	$0.73^{+0.38}_{-0.38}$	$0.85^{+0.44}_{-0.44}$
z_2	2.6	2.6
a_3	$-2.20^{+0.95}_{-0.95}$	$-2.27^{+0.82}_{-0.82}$
ρ_0	$7.98^{+15.19}_{-5.23} \times 10^{-2}$	$7.42^{+14.06}_{-4.86} \times 10^{-2}$
L_0	$4.02^{+1.25}_{-0.96} \times 10^{52}$	$0.36^{+0.48}_{-0.21} \times 10^{52}$
δ	-	$2.06^{+0.70}_{-0.70}$
α	$-0.71^{+0.07}_{-0.07}$	$-0.66^{+0.06}_{-0.06}$
χ^2_r	2.13	1.42
$w_m(\mathrm{AIC}_C)$	5.5×10^{-6}	0.9585

Table 3.4: *The fitted parameters for the Type III GRB LF models using a triple broken power-law function that is directly fitted to the GRB formation rate, either excluding (Type III-1) or including (Type III-2) evolution of the LF break. a_1, a_2, and a_3 are the gradients of the three power-laws; z_1, and z_2 are the redshift breaks, set at the bin edges discussed in Section 4.4; and ρ_0 is the GRB formation rate density at redshift $z = 0$. L_0 is given in units of ergs s^{-1}, and ρ_0 in units of GRBs Gpc^{-3} yr^{-1}.*

reproduce the observed pulse distribution. As shown in column 2, Figure 3.14, the CDF for a BPL LPDF model with break luminosity evolution is able to reproduce the observed CDFs for all redshift bins, within 1σ uncertainties. The evolutionary index of the break luminosity, at $\delta = 2.04^{+0.45}_{-0.45}$, and $2.06^{+0.7}_{-0.7}$ for the BPL, and PLEC models is weaker than that found using the fully evolving Type I-5 model but remains consistent with other Swift studies (see Section 4.6.4, 4.6.5 for references).

3.9 Long GRBs and the CSFRD

The fitted GRB formation rate densities for Type I-5 and Type III-1 models derived in this chapter are shown in Figure 3.15 overlain with observed cosmic star formation rate densities, the parameterised CSFRD model of Hopkins & Beacom (2006), and GRB formation rate models of Butler, Bloom & Poznanski (2010); Salvaterra et al. (2012); Wanderman & Piran (2010). Normalised to the CSFRD, our Type I-5 (including rate and luminosity evolution) and Type III-1 models trace the observed CSFRD well, especially at low/intermediate redshifts ($z < 5$), with up to a factor 2 deviation between derived high-z ($z > 5$) pulse rates and cosmic star formation rates for the Type III-1 model; suggestive of a redshift break at an earlier epoch than that which was assumed.

The parameterised model of Hopkins & Beacom (2006), common in the GRB literature as a model for CSFRD, traces the CSFRD at low redshifts, with noticeable drop-off at high-redshifts. Assuming that the GRB formation rate follows the CSFRD only, requires the addition of GRB formation rate evolution to the Type I-1 models to boost high-z GRB formation rates. This addition may, however, suggest that the parameterised CSFRD models are incorrect at high-z rather than implying the rate of GRB formation was greater at earlier epochs. Comparing the performance of our rate density evolving Type I-2 model, and the CSFRD as parameterised by Hopkins & Beacom (2006) to the observed CSFRD shows that our Type I-2 model with rate density produces a log-likelihood of 106.67 compared to a log-likelihood of -17.78 for Hopkins & Beacom (2006). The corresponding Akaike weights for the Type I-2 model is ~ 1.0[9], indicating that the GRB formation rate evolution seen is not real but is, instead, an artifact of utilising inappropriate CSFRD models. Utilising GRB formation rates as a probe of high-z star-formation is therefore highly speculative: conversion from GRB formation rates to star-formation rates are often cyclical; a star-formation rate and GRB evolution rate are assumed in order to derive a GRB formation rate, with which a star-formation rate is derived (Kistler et al., 2008; Robertson & Ellis, 2012); as such, careful consideration is required when attempting to derive CSFRD models using high-z burst rates.

[9]The log-likelihood for the Type I-2 model is calculated after the unknown conversion factor from GRB formation rate density to CSFRD is accounted for, and as such the comparison is with regards to the shape of the CSFRD.

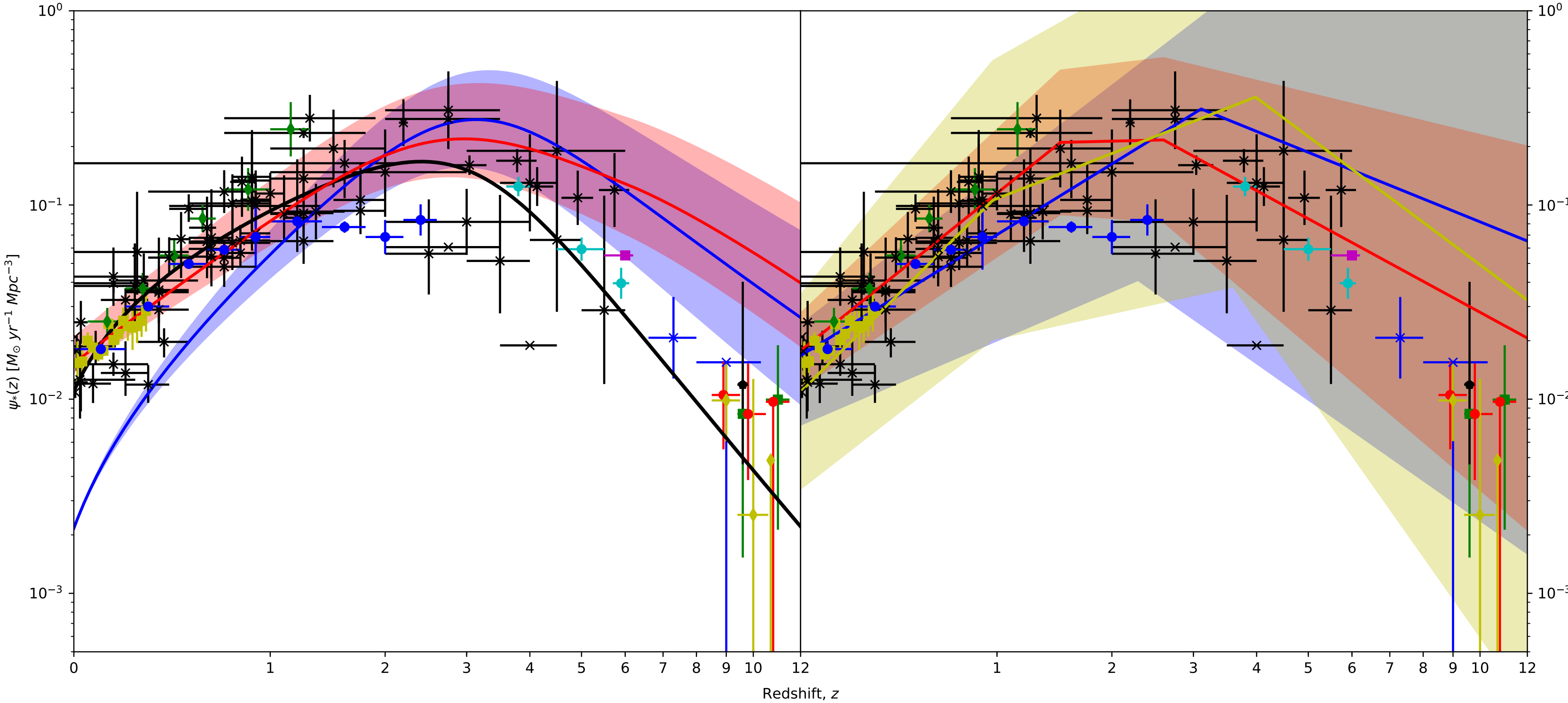

Figure 3.15: *Observed cosmic star formation rate densities normalised to the results collated by Hopkins & Beacom (2006) (solid black line best fit). Overplotted for comparison are the derived GRB formation rate densities using the rate evolution GRB LF models (top panel) of Salvaterra et al. (2012) (equivalent to a Type I-2 model; PLEC LF, blue line), and the rate & break luminosity evolution model derived in this work (Type I-5 model; PLEC LF, red line); and the direct GRB formation rate fitted LF models (bottom panel), equivalent to a Type III-1 model, of Butler, Bloom & Poznanski (2010) (yellow line), Wanderman & Piran (2010) (blue line), and the non-evolving Type III-1 model of this work (BPL LF, red line). Shaded regions denote* 1σ *uncertainties. All GRB formation rates are normalised to the observed star formation rates by maximising a minus log-likelihood function, producing normalisation constants, in units of* $M_\odot$ GRB^{-1}, *of* 6.56×10^9 *(Salvaterra et al., 2012), and* 0.17×10^9 *(this work, Type I-5 PLEC LF model with rate & break luminosity evolution); and* 2.74×10^9 *(Butler, Bloom & Poznanski, 2010),* 1.34×10^7 *(Wanderman & Piran, 2010), and* 2.53×10^8 *(this work, Type III-1 BPL LF model). Observed star-formation rate data is taken from Bouwens et al. (2003) (magenta squares), Hopkins & Beacom (2006) (black crosses), Baldry et al. (2005) (yellow squares), Pérez-González et al. (2005) (blue circles), Bouwens et al. (2007) (cyan circles), Bouwens et al. (2008) (blue crosses), Rujopakarn et al. (2010) (green diamonds), Zheng et al. (2012) (black pentagons), Coe et al. (2013) (green squares), Oesch et al. (2013) (yellow diamonds), and Ellis et al. (2013) (red circles).*

3.9.1 The Local GRB Formation rate

The GRB formation efficiency parameter, in combination with the star formation rate density at $z = 0$, produces the local GRB formation rate density, ρ_0. For the Type I models excluding rate density or metallicity density evolution (I-1, I-3), the formation efficiency, K_{GRB}, was derived to be $K_{GRB} = 1.18^{+0.10}_{-0.10} \times 10^{-8}$ GRBs $M_{\odot}^{-1}$, in good agreement with the values of $1.07 \pm 0.11 \times 10^{-8}$ and $1.05 \pm 0.05 \times 10^{-8}$ GRBs $M_{\odot}^{-1}$ (Salvaterra & Chincarini, 2007; Salvaterra et al., 2009). This equates to a local formation rate density of $\rho_0 = 0.22^{+0.02}_{-0.02}$ GRBs $Gpc^{-3}\ yr^{-1}$; for models including rate density (I-2, I-4) this drops to $\rho_0 = 0.12^{+0.05}_{-0.04}$ GRBs Gpc^{-3} yr^{-1}. For the Type III models, the local GRB formation rate is one of the model parameters, and for a non-evolving BPL LF model this produces a ρ_0 of $0.07^{+0.04}_{-0.03}$ GRBs Gpc^{-3} yr^{-1}, increasing to $0.083^{+0.08}_{-0.04}$ GRBs Gpc^{-3} yr^{-1} for a Type III-2 evolving BPL LF model. These values are towards the lower end of the distribution of values found in the literature for models excluding jet-beaming ($0.03 < \rho_0 < 7.3$ GRBs Gpc^{-3} yr^{-1}; Cao et al. (2011); Guetta, Piran & Waxman (2005); Porciani & Madau (2001); Salvaterra et al. (2012); Schmidt (2001); Wanderman & Piran (2010); Yu et al. (2015a)).

3.10 Conclusions

The lightcurves of Gamma-ray bursts exhibit wide variation in temporal fluctuations with some showing single, bright FRED-like profiles whilst others have multiple peaks, often with significant overlap. We extracted a subset of GRB pulses from Chapter 2, that had been fitted using the physically motivated model of Willingale et al. (2010) and which passed our particular selection criteria, to produce a total of 118 GRBs spanning from GRB 050126 to GRB 110503A, up to a redshift of $z = 9.4$. These Long GRBs contained 607 pulses spanning 8 decades of luminosity (10^{46} - 10^{54} ergs s^{-1}), and are observed from the early-time BAT down to late-time XRT regimes.

Traditionally, the brightest pulse of a GRB with known redshift is used as the defining luminosity of the burst. Such pulses however do not exhibit any other unique quality: they are often not the first pulse to trigger the BAT, nor do they solely occur within the prompt emission; they do not possess the hardest spectrum within a lightcurve, nor do they see the greatest hard-to-soft evolution of said spectrum; even their brightness is, in some cases, hardly unique as some bursts contain multiple pulses of comparable brightness. A great deal of information is therefore lost when utilising solely the brightest pulses, compounding the difficulties in population analysis for a relatively rare phenomenon which, until recently, was sparsely populated. We therefore choose to compute the GRB pulse luminosity function, of which the traditional GRB luminosity function can be considered as either a high-luminosity, or high-flux sub-population. We convolve a GRB pulse luminosity probability density function to a GRB formation rate model using three of the most popular GRB LF theories in the literature: Type I models that trace the cosmic star formation rate, convolved with various evolutionary effects such as break luminosity (I-3), rate density (I-2) and metallicity density evolution (I-4); Type II models that are bimodal in nature, allowing for distinct populations of low-luminosity and high-luminosity GRB pulses; and Type III models that are fitted directly to the GRB formation rate. We consider both PLEC, and BPL luminosity probability density functions which are, likewise, popular functional forms; our results however, suggest that they consistently produce similar quality of fits and therefore neither model is preferred in our conclusions.

We find that the inclusion of rate, and metallicity density evolution, which are popular solutions to the issue of underprediction in the GRB formation rate of high-z bursts, produces marginal improvement in our models however, when compared to other solutions, are entirely inadequate in explaining the observed evolution of GRB pulse luminosities. The derived GRB formation rate, either incorporating rate density evolution as a Type I-2 model, or as a Type III-1 model, traces the CSFRD up to high-z and suggests that the parameterisation of CSFRD models is poor at high redshift, rather than indicating an intrinsic evolution in the GRB formation rate on top of the CSFRD. We find that within Type I or Type III models, evolution in the break of the LPDF, as a function of $(z+1)^{\delta}$, is essential in order to reproduce the observed $L-z$ GRB pulse distribution, with δ exhibiting a strong (> 2), positive evolution, consistent with studies that utilise the single brightest GRB pulses. We evaluated the possibility that this evolution in the break luminosity was down to the presence of a bimodal population of low/high luminosity GRB pulses, however our results suggest that a single population of GRBs extending from the closest, least luminous to the brightest, and furthest GRBs is preferred. We observe that Type III models consistently produce poorer fits to the data than their Type I counterparts;

we conclude however, that this is an artifact of assuming that components of the Type I progenitor models are known with absolute precision, which is not the case for the CSFRD. To this end we do not attempt to determine the efficacy of one method over another.

We conclude that treating each GRB pulse as an independent event and utilising the entire GRB pulse population in GRB LF models produces parameters in excellent agreement to those derived using the single brightest pulse within a GRB's lightcurve; it is clear that there is no advantage to using solely the brightest GRB pulse as using all GRB pulses can dramatically improve the statistics of GRB luminosity functions, and may be extended to investigating the properties of other intrinsic GRB relationships. Whilst in reality each pulse cannot be truly independent from one another, as they are powered from a single central engine, the relationship between bright, and faint; late, and early pulses, is non-trivial.

Chapter 4

Conclusions

4.1 The GRB Pulse Catalogue

4.1.1 Conclusions

In prior work by Willingale et al. (2010), a physically motivated pulse model developed by Genet & Granot (2009a), and an empirical afterglow model formulated by Willingale et al. (2007), was applied to a few GRB lightcurves, and revealed the relationship between the prompt emission observed in the Swift BAT, and the rapid decay phase observed in early-time XRT data. These pulses, modelled by a simple fast-cooling synchrotron emission profile in internally shocked colliding shells, decay into the X-ray passbands before emission of the afterglow begins to dominate; combined, these two models were able to reproduce the totality of the observed gamma-ray and X-ray emission of those few bursts.

The most recent Swift GRB catalogue by Lien et al. (2016a) collated the entirety of Swift GRB data from late 2004 through to the middle of 2016, including approximately 400 bursts with an associated observed redshift. In Chapter 2, we analysed the entire population of Swift detected GRBs with measured redshifts, and extracted a sub-group of bursts, for which we were able to fit the totality of the BAT, and XRT lightcurves using the same pulse, and afterglow models utilised in the work of Willingale et al. (2010). Of 397 GRBs with redshifts, we were able to fit the lightcurves of 182 short, long, and ultralong GRBs with 862 pulses, and 182 afterglow components, and have produced an exhaustive catalogue with our results.

We find that the simplest pulse model by Genet & Granot (2009a) is capable of reproducing the pulse emission observed in all GRB types, suggesting that the colliding thin shell approximation is more than adequate to explain the emission process, without the need for more sophisticated models. These early-time prompt emission pulses in the gamma-ray regime, and late time X-ray flares observed by the XRT, appear to exist over a single continuum of energies, rather than belonging to two seperate populations. However, given that each pulse is modelled as an independent event, this work is unable to determine if there is a causal link between earlier pulses, and later flares: i.e. that X-ray flares arise from the refreshing of earlier shocks, or from prolonged activity in the central engine.

We find that some variation is observed between the pulse characteristics of the different burst types, most noteably in the timescales of the pulses, although this is hardly surprising given the large variation in duration of the burst types. Spectrally, these bursts appear broadly similar with regards to the distributions of the low-energy spectral indices; however, given that the BAT passband rarely extends above the spectral break, we are not able to determine if there is any statistically significant variation between the distributions of the E_{peak} parameter. Broadly speaking, the distribution of the brightnesses of pulses belonging to ultralong, long, and short GRBs are consistent, although we are suffering from small number statistics for the ultralong, and short GRB categories; however, short GRBs with extended emission appear to produce significantly fainter pulses than their contemporaries.

Strong, positive correlations are observed between the timescale parameters of the pulses, such that pulses that take a longer time to reach the emission region, will take a longer time to reach maximal emission. Furthermore, this relationship is seen across all the different GRB types, with the strength and spread of the relationships being broadly similar; however, given how few short, and ultralong GRBs we have in the pulse catalogue, we cannot determine if the consistency between those burst relations are real, or if by some chance the outliers of the smaller populations are unduly effecting the results. We find strong anti-correlations in the L_f-$T_f/(z+1)$ relation, such that brighter pulses occur when the time since ejection is short; this is consistent with other work in the literature, and in good agreement with their derived parameterisations. What is unique, in this work, is the ability to perform this analysis on each of the GRB types simultaneously. We again show broadly similar relations between L_f, and T_f, for all burst types, and although the pulses observed within short bursts with extended emission are typically an order of magnitude less luminous than other types of pulses, the relationship with the ejection times are still consistent. We also find evidence that there is a correlation between L_f, and E_{peak}, such that harder pulses (which E_{peak} is a measure of) are more luminous; however, this relation is typically of a weaker nature than other available studies, and, given our small population of observed E_{peak} values, is less statistically significant; if some of the pulses are outliers, then the observed relationship can easily disappear.

Like pulses, the fitted afterglow models show huge variation in durations, and energies between the burst types, and often between bursts of the same type. Spectrally, the afterglows of ultralong GRBs appear marginally softer than other types of GRBs, given their steeper low-energy index; however the distribution of the low-energy spectral indices of long GRBs also extends over this range. The rest-frame peak luminosities of the GRB afterglow plateaus are broadly consistent across all GRB types, save for short bursts with extended emission, which are typically several orders of magnitude fainter than those of other GRB types; subsequently, the isotropic energies of their afterglow components are also less energetic than those belonging to their contemporaries.

A strong anti-correlation is observed between the peak luminosity of the afterglow plateau, and the time at which the plateau ends; this relation extends over seven orders of magnitude in timescale, however the correlation isn't particularly narrow, with a standard deviation of over 1 decade. We also find a near one-to-one relationship between the luminosity of the brightest pulse within the GRB lightcurve, and the peak luminosity of the afterglow plateau; this indicates that the kinetic energy of the prompt emission pulses is, in part, transferred to the swept up matter from the interstellar medium, or pre-ejected winds, the emission from which is observed as the X-ray (and low energy photons) afterglow. Development of a physically model which relates the pulse and afterglow emission processes is therefore neccessary, and would provide a useful tool in measuring the characteristics of the local environment, and understanding how the local environment effects the observed GRB emission, and vice-versa.

4.1.2 Future Work

Pulse Modelling

The phenomenologically motivated model of Genet & Granot (2009b), described in Chapter 2, contains formulae describing the manifestation of an internal-shock driven pulse blast-wave, parameterised under both a fast-cooling, coasting, thin shell regime (all pulses fitted in Chapter 2 use this model); and a more general model, capable of modelling other synchrotron emission regimes and shell thicknesses. Many of the simplifying assumptions, such as isotropic emission by the pulse, dramatically effect the derived luminosities and are patently incorrect: in reality, jet emission is highly collimated, with more luminous GRB pulses having a smaller jet-beaming angle than those pulses which are less luminous (Ghirlanda et al., 2012). Other model shortcomings are more subtle: for example, a fast-cooling emission regime, may be inappropriate for modelling late-time X-ray flares; whilst collision of coasting shells may be inapplicable for very early pulses that form between the photospheric and the saturation radii, where the shells are still accelerating. Subsequently, these model assumptions allow for significant expansion in future work towards far more sophisticated models for pulse emission; the geometric effect of observing a pulse off-axis is a prime example of a more realistic correction (e.g. Miller, Marka & Bartos 2015; Salafia et al. 2016). Such models could shed light on more nuanced evolution within GRB lightcurves, test the efficacy of the fireball model, as well as potentially providing an alternate yardstick for differentiating between the various GRB morphologies.

Whilst the relationship between the prompt emission pulses and the rapid decay phase of the Swift XRT lightcurves have been shown, the link between the prompt emission and afterglow plateau is far less clear; it has been shown, however, that the luminosity of the prompt emission is correlated with the luminosity of the X-ray afterglow plateau (D'Avanzo et al., 2012). Having an extremely well parameterised prompt emission phase allows for future work to branch out from empirical afterglow models (e.g. Willingale et al. 2007), to more theoretical models that assume expansion of shells into the interstellar medium (Sari, Piran & Narayan, 1998) or pre-ejected stellar winds (Chevalier & Li, 2000), which will reveal more about the physical characteristics of the local GRB environment. Jet break models such as those by Rhoads (1999); Sari, Piran & Halpern (1999); Zhang et al. (2015) will also be incorporated into future afterglow models as upcoming missions, such as the POLAR gamma-ray observatory (see Section 1.4.2 for description), are designed specifically to observe the polarisation of GRB emission, and will reveal important insights into the geometrics of burst mechanics.

The spectra of the model used to fit the Swift GRB pulses takes the form of a Band function; more specifically it is a modified Band function whereby the high-energy index is set to a significantly steeper index than that of the low-energy index, essentially simplifying the Band function into a power-law with exponential cutoff. This is an acceptable method of modelling the spectra for non-thermal synchrotron emission over the relatively narrow BAT passbands, which often do not observe the spectral break in the Band function. Such assumptions become problematic, however, when looking at combining data from other high-energy missions (e.g. Fermi GBM, or MAXI GSC), which are often able to observe high-energy breaks in the spectra. Whilst freeing up the other Band function parameters to fitting is trivial, future work in combining data from other missions is a complicated affair, especially as one has to ensure correct cross-calibration of the instruments. Such a broadband approach to GRB pulse fitting has already been applied successfully to low-energy observations of the prompt emission of GRB 080310, by Littlejohns et al. (2012), for a synchrotron self-absorption modified Band function; which incorporated UV and optical data from the Swift UVOT, and numerous ground-based optical and NIR data (e.g. Faulkes North, ROTSE, REM, VLT, WHT, PAIRITEL, KAIT, Gemini, and others). Deviation from a purely non-thermal spectral shape is another avenue for future research: a growing subset of high-energy Fermi lightcurve spectra display a component of black-body thermal emission in addition to the more dominant non-thermal synchrotron emission (Burgess et al., 2014; Guiriec et al., 2011, 2015; Nappo et al., 2016; Zhang, 2014); in taking a more broadband approach to GRB pulse fitting, this additional component will need to be accounted for.

The launch of SVOM (see Section 1.4.1 for description) will be an important watershed moment for broad-band GRB pulse fitting. The ECLAIRS instrument (Barret et al., 2001) is similar in scope to that of the Swift BAT, but with greater sensitivities at energies greater than 20 keV, and a FOV of 2 sr; whilst the Gamma-Ray Monitor (GRM; Dong et al., 2010), which shares an overlapping FOV with ECLAIRS, will extend SVOM's gamma-ray observational capabilities up to 5 MeV. The Microchannel X-ray Telescope (MXT; Götz et al., 2014), and Visible Telescope (VT; Wu, Qiu & Cai, 2012) also share a FOV, which ensures that once SVOM has slewed on target, the rapid dissemination of sub-arcminute positional data to other ground-based observatories should ensure a higher redshift completeness than Swift ($\sim 75\%$; Paul et al., 2011); whilst the design of the VT and MXT instruments ensures that these instruments have a complimentary sensitivity to GRB afterglows. The SVOM mission is unique in regards to the inclusion of two ground-based instruments: the Ground-based Wide-Angle Camera (GWAC; Götz et al., 2014), and the Ground-based Follow-up Telescopes (GFTs; Götz et al., 2014). The GWAC will observe a fraction of the ECLAIRs FOV to search for the optical component of the prompt emission, and is predicted to detect 20% of SVOM GRBs (Paul et al., 2011); meanwhile, the GFTs will slew on target when ECLAIRs triggers on a GRB, and will follow up on targets with low significance (which are typically not disseminated to the wider GRB community).

It is this combination of high redshift completeness, and extremely wide EM coveraged, that will allow SVOM to constrain the E_{peak} spectral break observed within the prompt emission, and test the veracity of the Amati and Ghirlanda relations. The greater sensitivities of the SVOM instruments over their Swift counterparts, and rapid followup in optical and NIR regimes, will potentially see the population of very high redshift GRBs ($z > 6$) dramatically expanded, and may result in the indirect detection of population III stars (Paul et al., 2011). The pulse fitting methods utilised in this work can be adapted for SVOM data, although the challenge will be in combining data from the four space-based, and the two ground-based instruments; however, once complete, this will allow us to test the synchrotron emission internal shock models to a greater level of confidence.

The Pulse Catalogue

The Swift mission has now been in continous operation for almost 12 years, and given the strong science case still being made for continued financial support, it is expected to continue for many more years. Excluding any major incidents, the number of Swift triggered GRBs will continue to grow, and subsequently, the catalogue of GRB pulses fitted by the Genet & Granot (2009b) model will no doubt be expand. The large amount of data collated in Chapter 2 has barely been utilised; the derivation of a GRB pulse luminosity function is one example outcome of large scale population analysis from our data, and future work will inevitably involve simply analysing the vast amount of collated data for other, novel, research. Studies that look at combining prompt and X-ray afterglow data with large-scale spectroscopic surveys of the host galaxy (or optical/NIR afterglows) would also be of great interest, as they would help relate the characteristics of the observed GRBs to that of the local environment.

4.2 The GRB Pulse Luminosity Function

4.2.1 Conclusions

Although traditionally utilised as the characteristic luminosity of a GRB, the brightest pulse occupies no other particularly unique criteria which sets it apart from all the other pulses that are often present within GRB lightcurves. Although GRB pulses originate from a single central engine, there is a non-trivial relationship between all the pulses and flares; in essence, each GRB pulse appears as an independent event. A vast amount of information is therefore ignored when utilising only the brightest pulses, which compounds the difficulties in population analysis for a relatively sparsely populated phenomena. We therefore compute the GRB pulse luminosity function, of which the traditional GRB luminosity function can be considered as a high-flux (or high-luminosity) sub-population.

Taking the GRB pulse data from long duration GRBs, fitted in Chapter 2 using the phenomenologically motivated model of Willingale et al. (2010), we extra a subset of 118 GRBs up to a redshift of $z = 9.4$, spanning 607 early-time BAT, to late-time XRT pulses and flares. We convolve a GRB pulse luminosity probability density function to a GRB formation rate model using three of the most popular GRB LF theories in the literature: models that traces the cosmic star formation rate, convolved with various evolutionary effects such as break luminosity, rate density, and metallicity density evolution; bimodal models which allow for distinct populations of low-luminosity and high-luminosity GRB pulses; and models that are fitted directly to the GRB formation rate. We consider two of the more popular functional forms for the luminosity probability density; however, our results suggest that they consistently produce similar quality of fits and therefore neither model is preferred in our conclusions.

We find that the inclusion of rate, or metallicity density evolution, sees a marginal reduction in the discrepencies between observed and theoretical pulse distributions, in agreement with contemporary GRB studies; however these evolutionary effects are unable to explain the observed evolution of GRB pulse luminosities. Alternatively, we find that evolution in the break of the LPDF, as a function of $(z+1)^{\delta}$, is absolutely essential in reproducing the observed $L-z$ GRB pulse distribution, with δ exhibiting a very strong (> 2), positive evolution, consistent with studies that utilise the single brightest GRB pulses. We investigate the possibility that this evolution in the break luminosity can be explained by the presence of a bimodal population of low/high luminosity GRB pulses, however our results disagree with such a statement; instead preferring a single population of GRBs extending from the closest, least luminous to the brightest, and furthest GRBs.

We observe that models with no apriori assumptions, consistently produce poorer fits to the data than their star-formation convolved counterparts; this is, however, an artifact of assuming that input model components of the star-formation convolved progenitor models are known with absolute precision, which is clearly not the case. Because of this, we do not attempt to determine the efficacy of one method compared to another. The derived GRB formation rate, either incorporating rate density evolution or as a freely fitted model, traces the CSFRD up to high-z and suggests that the parameterisation of CSFRD models is poor at high redshift, rather than indicating an intrinsic evolution in the GRB formation rate on top of the CSFRD.

We conclude that treating each GRB pulse as an independent event and utilising the entire GRB pulse population in GRB LF models produces parameters in excellent agreement to those derived using the single brightest pulse within a GRB's lightcurve; there is no evidence that there is an advantage to using only the brightest GRB pulses, and incorporating all GRB pulses can dramatically improve the quality of the fit statistics of GRB luminosity functions.

4.2.2 Future Work

An extra 5 years worth of GRB pulse data is already available to incorporate with the existing GRB pulse dataset, almost doubling the sample size of long GRBs. Future work will inevitably involve updating the pulse luminosity function with the new data, allowing for a greater number of redshift bins, and tighter constraints on the derived model parameters. Further refinement may be made via the application of a multi-nest Monte-Carlo code; as a more sophisticated routine, multi-nest

MCMCs could potentially overcome the strong degeneracies observed between the parameters of the metallicity density evolution, and luminosity probability densities, and reveal if a preferred metallicity is an important component when modelling the GRB luminosity function.

In Chapter 2, we fitted 9 short/short w. EE GRBs falling within the timeframe bounded by GRBs 050126 and 160410A. Theoretically, short GRBs also trace the CSFRD, albeit with a significant time delay as the progenitor stars evolve off the main sequence, collapse into neutron stars, and in-spiral until coalescence. Although shorter in duration than long GRBs, some short GRBs show up to 4 pulses (e.g. GRB 051221A); whilst the short GRB with extended emission which we were able to fit displayed 6 pulses (GRB 050724). If an observer were interested in deriving cosmic star-formation rate densities, or total (long and short) GRB formation rates, then including data from short GRBs, in a similar manner to our utilisation of long GRB pulses, may be made (e.g. in a similar manner to Ando, 2004; Coward et al., 2012). Short GRB formation rates are of great interest to gravitational wave astronomers, given that the predicted GW frequencies produced are detectable with current technology; therefore, for a given GW detector like that of the Advanced-LIGO, SGRB formation rates give a measure of potential GW detection rates (Coward et al., 2012; D'Avanzo & Ghirlanda, 2016; Metzger & Berger, 2012; Sun, Zhang & Gao, 2017).

Both the current, and updated GRB pulse luminosity functions provide a useful tool for calculating the observed rates of high-z GRBs detected by future missions such as SVOM, or Theseus (a proposed gamma-ray burst observatory). Given the capability of SVOM to observe high redshift GRBs ($z > 6.5$) with the Visual Telescope, and the mission goal of achieving a 50% redshift completeness; in the future, the population of high-redshift bursts should see a dramatic increase, with a greater completeness across all redshifts. Applying the pulse fitting model to SVOM data, will therefore allow for extension of the GRB luminosity function up to very high redshifts, although SVOM will have to operate for approximately 3 years, with 50% redshift detection, to achieve the same level of statistics that the current Swift data allows.

Appendices

I Online Repositories, and Weblinks

NASA HEASARC Missions: https://heasarc.gsfc.nasa.gov/docs/heasarc/missions/

Swift GRB Table: http://swift.gsfc.nasa.gov/archive/grb_table/

I.1 GRB Online Repositories

OGBD; PVO

http://heasarc.gsfc.nasa.gov/W3Browse/gamma-ray-bursts/pvogrb.html

BATSE; CGRO

http://gammaray.nsstc.nasa.gov/batse/grb/catalog/current/index.html

GRBM; BeppoSAX

http://heasarc.gsfc.nasa.gov/W3Browse/gamma-ray-bursts/saxgrbmgrb.html

Konus; Wind

http://gcn.gsfc.nasa.gov/konus_grbs.html

WAM; Suzaku

http://www.astro.isas.jaxa.jp/suzaku/HXD-WAM/WAM-GRB/grb/trig/grb_table.html

SPI/IBIS; INTEGRAL

http://www.isdc.unige.ch/integral/science/grb#ISGRI

GBM; Fermi

http://heasarc.gsfc.nasa.gov/W3Browse/fermi/fermigbrst.html

LAT; Fermi

http://fermi.gsfc.nasa.gov/ssc/observations/types/grbs/lat_grbs/

GSC/SSC; MAXI

http://maxi.riken.jp/grbs/

FREGATE; HETE2

http://heasarc.gsfc.nasa.gov/w3browse/all/hete2grb.html

I.2 Major Ground-based GRB Follow-up Observatories

The Very Large Telescope (VLT)

`http://www.eso.org/public/unitedkingdom/teles-instr/vlt/vlt-instr/`

The Liverpool Telescope

`http://telescope.livjm.ac.uk/TelInst/Inst/`

The Faulkes North/South Telescopes

`http://lcogt.net/observatory/instruments/`

The Keck I/II Telescopes

`http://www2.keck.hawaii.edu/inst/`

The Gran Telescopio Canarias (GTC)

`http://www.gtc.iac.es/instruments/`

The Nordic Optical Telescope (NOT)

`http://www.not.iac.es/instruments/`

The Telescopio Nazionale Galileo (TNG)

`http://www.tng.iac.es/instruments/`

The Willian Herschel Telescope (WHT)

`http://www.ing.iac.es/Astronomy/instruments/`

The Gemini North/South Telescopes

`https://www.gemini.edu/sciops/instruments/`

The Subaru Telescope

`http://subarutelescope.org/Observing/Instruments/`

II GRB Pulse Catalogue Data

GRB	ID	T_{90} [s]	GRB Type	z	Failcode
050223	106709	$22.68^{+4.48}_{-4.48}$	Long	0.5915	3
050318	111529	$16.12^{+10.92}_{-10.92}$	Long	1.44	3
050406	113872	$5.776^{+1.393}_{-1.393}$	Long	2.44	1 2
050502B	116116	$17.72^{+1.9}_{-1.9}$	Long	5.2	4
050505	117504	$58.85^{+6.84}_{-6.84}$	Long	4.27	3
050509B	118749	$0.024^{+0.009}_{-0.009}$	Short	0.2249	1 2 3
050603	131560	$21.0^{+8.49}_{-8.49}$	Long	2.821	3
050714B	145994	$49.36^{+11.29}_{-11.29}$	Long	2.438	4
050724	147478	$98.68^{+8.56}_{-8.56}$	Short w. EE	0.257	1 2
050726	147788	$46.5^{+14.45}_{-14.45}$	Long	0.1646	1 2 3
050813	150139	$0.384^{+0.112}_{-0.112}$	Short	0.722	1 2 3 4
050819	151131	$37.72^{+7.33}_{-7.33}$	Long	2.5043	1
050824	151905	$25.01^{+5.55}_{-5.55}$	Long	0.83	1 2
050826	152113	$29.6^{+6.31}_{-6.31}$	Long	0.297	1 2
050915A	155242	$53.42^{+11.27}_{-11.27}$	Long	2.5273	4
050922B	156434	$157.0^{+94.5}_{-94.5}$	Long	4.5	4
051006	158593	$35.41^{+8.93}_{-8.93}$	Long	1.059	2
051008	158855	$12.41^{+1.36}_{-1.36}$	Long	2.77	3
051109B	163170	$15.7^{+4.12}_{-4.12}$	Long	0.08	1
051111	163438	$64.0^{+16.0}_{-16.0}$	Long	1.549	1 2 3
051117B	164279	$9.02^{+1.315}_{-1.315}$	Long	0.481	1
051221A	173780	$1.392^{+0.197}_{-0.197}$	Short	0.5464	3
060117	177666	$16.85^{+0.14}_{-0.14}$	Long	4.6	3
060123	020028	$16.85^{+0.14}_{-0.14}$	Unconstrained	1.099	1 2
060218	191157	$16.85^{+0.14}_{-0.14}$	Ultralong	0.0331	1 2
060319	202035	$10.29^{+1.72}_{-1.72}$	Long	1.172	3
060428B	207399	$96.0^{+50.6}_{-50.6}$	Long	0.348	1
060502B	208275	$0.144^{+0.051}_{-0.051}$	Short	0.287	3
060505	208654	$4.0^{+10000.0}_{-10000.0}$	Unconstrained	0.089	1 2
060512	209755	$8.4^{+1.728}_{-1.728}$	Long	0.4428	1 2
060602A	213180	$74.84^{+12.96}_{-12.96}$	Long	0.787	1 2 3
060805A	222683	$4.928^{+1.354}_{-1.354}$	Long	2.3633	1 2 3 4

GRB	ID	T_{90} [s]	GRB Type	z	Failcode
060923B	230702	$8.948^{+1.296}_{-1.296}$	Long	1.51	1 2 3
061110B	238174	$135.2^{+17.6}_{-17.6}$	Long	3.44	3
061201	241840	$0.776^{+0.095}_{-0.095}$	Short	0.0865	3
061210	243690	$85.23^{+13.09}_{-13.09}$	Short w. EE	0.41	1 2 3
061217	251634	$0.224^{+0.043}_{-0.043}$	Short	0.827	1 2 3
070125	020047	$0.224^{+0.043}_{-0.043}$	Unconstrained	1.5477	1 2
070224	261880	$48.0^{+35.78}_{-35.78}$	Long	1.99	1 2
070411	275087	$115.7^{+16.9}_{-16.9}$	Long	2.954	3
070429B	277582	$0.488^{+0.043}_{-0.043}$	Short	0.9023	1
070518	279592	$5.504^{+0.804}_{-0.804}$	Unconstrained	1.16	1 2 3
070611	282003	$13.18^{+3.47}_{-3.47}$	Long	2.04	1 2 3
070612A	282066	$365.3^{+51.7}_{-51.7}$	Long	0.617	3
070714A	284850	$3.0^{+1.414}_{-1.414}$	Unconstrained	1.58	3
070714B	284856	$65.64^{+9.51}_{-9.51}$	Short w. EE	0.92	3
070724A	285948	$0.432^{+0.086}_{-0.086}$	Short	0.4571	1 2 3
070809	287344	$1.28^{+0.373}_{-0.373}$	Short	0.2187	1 2 3
071003	292934	$148.4^{+4.6}_{-4.6}$	Long	1.1	3
071010A	293707	$6.324^{+1.866}_{-1.866}$	Long	0.98	1
071010B	293795	$36.12^{+2.28}_{-2.28}$	Long	0.947	3 4
071028B	295492	$51.2^{+1.6}_{-1.6}$	Long	0.94	1 2
071112C	296504	$44.8^{+1.6}_{-1.6}$	Long	0.823	1 2
071117	296805	$6.076^{+2.149}_{-2.149}$	Long	1.331	3
080129	301981	$50.18^{+9.17}_{-9.17}$	Long	4.349	1 2 3
080330	308041	$60.36^{+36.4}_{-36.4}$	Long	1.51	2
080411	309010	$56.33^{+0.92}_{-0.92}$	Long	1.03	3
080515	311658	$20.86^{+5.17}_{-5.17}$	Long	2.47	3
080516	311762	$5.764^{+0.223}_{-0.223}$	Long	3.2	1 2 3
080517	311874	$64.51^{+22.3}_{-22.3}$	Long	0.089	1 2
080520	312047	$3.324^{+0.862}_{-0.862}$	Long	1.545	1 2 3
080710	316534	$143.0^{+25.1}_{-25.1}$	Long	0.845	3
080905A	323870	$1.016^{+0.082}_{-0.082}$	Short	0.089	1 2 3
081029	332931	$275.1^{+49.0}_{-49.0}$	Long	3.8479	3
081121	335105	$17.52^{+2.01}_{-2.01}$	Long	2.512	3
081211B	000900530	$64.0^{+1.6}_{-1.6}$	Unconstrained	0.216	1 2

GRB	ID	T_{90} [s]	GRB Type	z	Failcode
081228	338338	$3.0^{+1.414}_{-1.414}$	Unconstrained	3.44	1 2 3
090201	341749	$74.26^{+1.68}_{-1.68}$	Long	2.1	3
090313	346386	$83.04^{+19.48}_{-19.48}$	Long	3.375	1 2 3
090407	348650	$315.5^{+55.9}_{-55.9}$	Long	1.4485	1 2
090726	358422	$56.68^{+12.17}_{-12.17}$	Long	2.71	3
090809A	359530	$8.868^{+2.875}_{-2.875}$	Long	2.737	4
090814A	359951	$78.06^{+7.98}_{-7.98}$	Long	0.696	1
090927	370846	$2.16^{+0.401}_{-0.401}$	Unconstrained	1.37	1 2 3
091024	373674	$112.3^{+13.8}_{-13.8}$	Long	1.092	3 4
091127	377179	$6.956^{+0.15}_{-0.15}$	Unconstrained	0.49	3
100117A	382941	$0.292^{+0.032}_{-0.032}$	Short	0.915	1 2 3
100213B	412220	$91.86^{+20.34}_{-20.34}$	Long	0.604	1
100316A	416076	$6.752^{+0.952}_{-0.952}$	Long	3.155	3
100316D	416135	$521.9^{+439.6}_{-439.6}$	Ultralong	0.014	3
100413A	419404	$192.6^{+12.1}_{-12.1}$	Long	3.9	4
100424A	420367	$104.0^{+14.6}_{-14.6}$	Long	2.465	1
100508A	421386	$49.26^{+7.43}_{-7.43}$	Long	0.5201	1 2
100625A	425647	$0.332^{+0.037}_{-0.037}$	Short	0.452	3
100628A	426114	$0.036^{+0.009}_{-0.009}$	Short	0.102	1 2 3
100704A	426722	$196.9^{+23.4}_{-23.4}$	Long	3.6	4
100728B	430172	$12.08^{+2.74}_{-2.74}$	Long	2.106	1
100902A	433160	$428.8^{+47.3}_{-47.3}$	Long	4.5	2
111005A	504779	$23.21^{+5.06}_{-5.06}$	Long	0.01326	1 2 3
111117A	507901	$0.464^{+0.054}_{-0.054}$	Short	1.3	3
111129A	508712	$8.476^{+1.278}_{-1.278}$	Long	1.0796	1 2 3
120224A	515976	$7.0^{+2.236}_{-2.236}$	Long	1.1	1 2 3
120401A	519043	$130.3^{+24.2}_{-24.2}$	Long	4.5	1 2
120624B	525068	$179.7^{+1.5}_{-1.5}$	Long	2.1974	3
120714B	526642	$157.3^{+24.0}_{-24.0}$	Long	0.3984	1 2
120722A	528195	$36.32^{+6.44}_{-6.44}$	Long	0.9586	1 2 3
120805A	530031	$48.0^{+22.63}_{-22.63}$	Long	3.1	1 2 4
120815A	531003	$7.232^{+2.517}_{-2.517}$	Long	2.3586	3
120909A	533060	$220.6^{+305.0}_{-305.0}$	Unconstrained	3.93	3 4
120923A	534402	$26.08^{+6.82}_{-6.82}$	Long	8.5	1 2 3

GRB	ID	T_{90} [s]	GRB Type	z	Failcode
121211A	541200	$182.7^{+38.7}_{-38.7}$	Long	1.023	4
121229A	544347	$111.5^{+41.3}_{-41.3}$	Long	2.707	1 2
130131B	547420	$4.3^{+0.257}_{-0.257}$	Long	2.539	1 2
130215A	548760	$66.22^{+10.66}_{-10.66}$	Long	0.579	3
130408A	553132	$4.24^{+0.681}_{-0.681}$	Long	3.758	3
130418A	553847	$274.9^{+39.3}_{-39.3}$	Long	1.218	1 2
130420A	553977	$121.1^{+11.7}_{-11.7}$	Long	1.297	3
130511A	555600	$2.74^{+0.398}_{-0.398}$	Long	1.3033	3
130518A	556113	$81.6^{+1.6}_{-1.6}$	Long	2.488	1 2
130528A	556870	$640.0^{+560.0}_{-560.0}$	Long	1.25	4
130603B	557310	$0.176^{+0.024}_{-0.024}$	Short	0.3565	1 2 3
130604A	557354	$76.28^{+29.76}_{-29.76}$	Long	1.06	1 2 3
130612A	557976	$4.0^{+1.414}_{-1.414}$	Unconstrained	2.006	1 2
130701A	559482	$4.38^{+0.253}_{-0.253}$	Long	1.155	3
131004A	573190	$1.536^{+0.326}_{-0.326}$	Short	0.717	1 2 3
131103A	576562	$15.21^{+3.03}_{-3.03}$	Long	0.5955	4
131117A	577968	$10.88^{+2.81}_{-2.81}$	Long	4.042	1 2 3
140213A	586569	$59.93^{+2.71}_{-2.71}$	Long	1.2076	3
140301A	589590	$27.8^{+8.39}_{-8.39}$	Long	1.416	1 2 3 4
140311A	591390	$70.48^{+7.59}_{-7.59}$	Long	4.954	3
140318A	592204	$7.604^{+1.276}_{-1.276}$	Long	1.02	4
140331A	594081	$209.7^{+32.8}_{-32.8}$	Long	4.65	1 2
140423A	596901	$134.1^{+23.1}_{-23.1}$	Long	3.26	3
140428A	597519	$17.42^{+5.9}_{-5.9}$	Long	4.7	2 3
140515A	599037	$23.42^{+2.04}_{-2.04}$	Long	6.33	4
140614A	601646	$77.39^{+15.89}_{-15.89}$	Long	4.233	1 2
140622A	602278	$0.132^{+0.036}_{-0.036}$	Short	0.959	1 2 3
140903A	611599	$0.296^{+0.034}_{-0.034}$	Short	0.351	1 2
140907A	611933	$80.0^{+35.78}_{-35.78}$	Long	1.21	1 2
141004A	614390	$3.924^{+1.112}_{-1.112}$	Long	0.573	3
141026A	616502	$139.5^{+14.8}_{-14.8}$	Long	3.35	1 2
141121A	619182	$481.0^{+38.1}_{-38.1}$	Ultralong	1.47	4
141212A	621229	$0.288^{+0.097}_{-0.097}$	Short	0.596	1 2 3
141220A	621915	$7.232^{+0.479}_{-0.479}$	Long	1.32	3

GRB	ID	T_{90} [s]	GRB Type	z	Failcode
141225A	622476	$86.15^{+45.22}_{-45.22}$	Long	0.915	1 2 3
150101B	000919640	$0.012^{+0.009}_{-0.009}$	Short	0.134	1 2
150120A	627137	$1.196^{+0.154}_{-0.154}$	Short	0.46	3
150206A	630019	$75.0^{+12.69}_{-12.69}$	Long	2.087	4
150413A	637899	$243.6^{+40.8}_{-40.8}$	Long	3.139	3
150423A	638808	$0.216^{+0.028}_{-0.028}$	Short	1.394	1 2 3
150424A	638946	$81.06^{+17.48}_{-17.48}$	Short w. EE	0.3	1 2
150727A	650530	$87.96^{+10.99}_{-10.99}$	Long	0.313	1 2
150915A	655721	$160.0^{+57.7}_{-57.7}$	Long	1.968	1 2
151029A	662086	$8.952^{+3.955}_{-3.955}$	Long	1.423	1 2 3
151031A	662330	$5.0^{+2.236}_{-2.236}$	Long	1.167	3
151112A	663179	$58.86^{+22.73}_{-22.73}$	Long	4.1	3
160131A	672236	$327.8^{+71.0}_{-71.0}$	Long	0.972	3
160303A	677495	$4.976^{+1.006}_{-1.006}$	Long	2.3	3
160410A	682269	$96.0^{+50.6}_{-50.6}$	Long	1.717	1
160425A	684098	$304.6^{+15.0}_{-15.0}$	Long	0.555	4
160624A	701288	$0.192^{+0.143}_{-0.143}$	Short	0.483	1 2
160703A	702699	$45.01^{+3.02}_{-3.02}$	Long	1.5	3

Table 1: The GRBs, with observed redshifts, rejected by the fitting criteria of Chapter 2. The redshift, ID, and duration data are extracted from Tables 39, and 9, respectively, of Lien et al. (2016b) (with references therein). The failcodes refer to the particular criterion failed: 1) bursts must have clear evidence of a minimum of one pulse in the BAT passbands; 2) the observed pulse within the BAT must have a suitable level of statistics to ensure that such an event is real; 3) early XRT data must be available to allow constraining of the rapid decay phase from the combined BAT pulses; and 4) the lightcurves must not have broken observations of pulses and flares due to orbit breaks, which complicates the determination of the true pulse parameters. Trigger IDs belonging to bursts 150101B, and 081211B do not share the same template as the rest of the bursts, and are due to being detected in ground-analysis, rather than by the onboard trigger.

GRB	ID	RA [°]	DEC [°]	T_{90} [s]	Type	z	NH_{Gal}	NH_{Int}	Z_{abs}	χ_r^2 (NDOF)
050126	103780	278.133	42.3941	$48.0^{+22.63}_{-22.63}$	Long	1.29	$5.5\ 10^{20}$	$0^{+1.3}_{-0}\ 10^{21}$	1.29	0.95 (60.0)
050215B	106107	174.4773	40.7924	$11.04^{+3.93}_{-3.93}$	Long	2.52	$1.96\ 10^{20}$	$0^{+1.5}_{-0}\ 10^{22}$	0.0	0.93 (128.0)
050219A	106415	166.4129	-40.6848	$23.81^{+2.26}_{-2.26}$	Long	0.2115	$1.42\ 10^{21}$	$1.7^{+0.6}_{-0.6}\ 10^{21}$	0.0	3.72 (176.0)
050315	111063	306.4795	-42.589	$95.4^{+13.96}_{-13.96}$	Long	1.95	$4.34\ 10^{20}$	$1.5^{+1.3}_{-1.0}\ 10^{22}$	1.949	1.89 (318.0)
050319	111622	154.1717	43.5797	$151.6^{+10.6}_{-10.6}$	Long	3.2425	$1.31\ 10^{20}$	$7^{+40.0}_{-7.0}\ 10^{20}$	3.24	1.36 (113.0)
050401	113120	247.8734	2.1866	$32.09^{+0.58}_{-0.58}$	Long	2.8983	$5.45\ 10^{20}$	$2.13^{+0.3}_{-0.29}\ 10^{22}$	2.9	1.42 (373.0)
050416A	114753	188.4769	21.0538	$6.668^{+3.422}_{-3.422}$	Long	0.6528	$2.69\ 10^{20}$	$7^{+8.0}_{-5.0}\ 10^{21}$	0.6535	1.23 (109.0)
050525A	130088	278.1381	26.3393	$8.836^{+0.071}_{-0.071}$	Long	0.606	$1.26\ 10^{21}$	$1.4^{+1.3}_{-1.2}\ 10^{21}$	0.606	8.59 (443.0)
050724	147478	246.1799	-27.5253	$98.68^{+8.56}_{-8.56}$	Short w. EE	0.257	$2.77\ 10^{21}$	$5.6^{+0.7}_{-0.6}\ 10^{21}$	0.257	3.28 (216.0)
050730	148225	212.0698	-3.7556	$154.6^{+18.6}_{-18.6}$	Unconst	3.9693	$3.51\ 10^{20}$	$4^{+3.0}_{-3.0}\ 10^{21}$	3.97	1.67 (594.0)
050801	148522	204.1443	-21.9332	$19.57^{+5.94}_{-5.94}$	Long	1.38	$8.51\ 10^{20}$	$0^{+2.45}_{-0}\ 10^{20}$	0.0	1.06 (74.0)
050802	148646	219.2851	27.7949	$27.46^{+8.16}_{-8.16}$	Long	1.7102	$1.96\ 10^{20}$	$2.8^{+2.7}_{-2.5}\ 10^{21}$	1.71	1.0 (230.0)
050803	148833	350.646	5.7877	$88.12^{+10.2}_{-10.2}$	Long	3.5	$6.4\ 10^{20}$	$1.6^{+0.6}_{-0.5}\ 10^{21}$	0.0	3.83 (312.0)
050814	150314	264.1959	46.3376	$142.9^{+41.7}_{-41.7}$	Long	5.3	$2.47\ 10^{20}$	$1.3^{+1.4}_{-1.3}\ 10^{20}$	0.0	1.56 (188.0)
050820A	151207	337.4166	19.5606	$240.8^{+11.5}_{-11.5}$	Long	2.6147	$5.22\ 10^{20}$	$0^{+7.78}_{-0}\ 10^{20}$	2.612	2.02 (557.0)
050822	151486	51.1032	-46.0289	$104.3^{+15.8}_{-15.8}$	Long	1.434	$1.47\ 10^{20}$	$1.41^{+0.15}_{-0.14}\ 10^{21}$	0.0	3.15 (340.0)
050908	154112	20.4669	-12.9538	$18.28^{+3.28}_{-3.28}$	Long	3.3467	$2.56\ 10^{20}$	$0^{+3.95}_{-0}\ 10^{21}$	3.35	1.97 (99.0)
050922C	156467	317.3872	-8.7625	$4.552^{+0.448}_{-0.448}$	Long	2.1995	$7.58\ 10^{20}$	$0^{+2}_{-0}\ 10^{21}$	2.198	2.53 (160.0)
051016B	159994	132.1151	13.6278	$4.0^{+0.448}_{-0.448}$	Long	0.9364	$3.54\ 10^{20}$	$1.2^{+0.5}_{-0.4}\ 10^{22}$	0.9364	1.78 (85.0)
051109A	163136	330.3209	40.8534	$37.2^{+6.07}_{-6.07}$	Long	2.346	$2.59\ 10^{21}$	$0^{+3.7}_{-0}\ 10^{21}$	2.346	1.22 (268.0)
051221A	173780	328.7125	16.8912	$1.392^{+0.197}_{-0.197}$	Short	0.5464	$7.52\ 10^{20}$	$1.3^{+1.2}_{-1.1}\ 10^{21}$	0.5465	3.9 (194.0)
060108	176453	147.0191	31.9314	$14.22^{+2.14}_{-2.14}$	Long	2.03	$1.89\ 10^{20}$	$0^{+2.09}_{-0}\ 10^{21}$	0.0	1.59 (63.0)

GRB	ID	RA [°]	DEC [°]	T_{90} [s]	Type	z	NH_{Gal}	NH_{Int}	Z_{abs}	χ_r^2 (NDOF)
060115	177408	54.0158	17.3351	$139.1^{+15.2}_{-15.2}$	Long	3.5328	$1.48\ 10^{21}$	$7^{+10.0}_{-7.0}\ 10^{21}$	3.53	1.72 (228.0)
060116	177533	84.701	-5.4408	$104.8^{+27.3}_{-27.3}$	Long	6.6	$3.19\ 10^{21}$	$7.9^{+3.1}_{-2.6}\ 10^{21}$	0.0	1.24 (131.0)
060124	178750	77.1049	69.725	$13.42^{+1.29}_{-1.29}$	Long	2.3	$1.33\ 10^{21}$	$1.6^{+1.1}_{-1.1}\ 10^{21}$	2.297	2.93 (1014.0)
060206	180455	202.9263	35.0487	$7.552^{+2.193}_{-2.193}$	Long	4.0559	$9.62\ 10^{19}$	$0^{+3.97}_{-0}\ 10^{22}$	4.05	1.55 (272.0)
060210	180977	57.7255	27.0168	$288.0^{+151.8}_{-151.8}$	Long	3.9122	$8.64\ 10^{20}$	$2.6^{+0.4}_{-0.4}\ 10^{22}$	3.91	1.44 (751.0)
060223A	192059	55.1955	-17.135	$11.32^{+1.07}_{-1.07}$	Long	4.41	$9.9\ 10^{20}$	$2.8^{+3.6}_{-2.8}\ 10^{22}$	4.41	1.59 (103.0)
060418	205851	236.4307	-3.6397	$109.1^{+46.7}_{-46.7}$	Long	1.49	$1.59\ 10^{21}$	$5.6^{+0.9}_{-0.9}\ 10^{21}$	1.49	2.43 (513.0)
060502A	208169	240.9228	66.6032	$28.45^{+9.86}_{-9.86}$	Long	1.5026	$3.84\ 10^{20}$	$7.5^{+2.5}_{-2.2}\ 10^{21}$	1.51	1.03 (233.0)
060522	211117	322.9566	2.8915	$69.12^{+5.9}_{-5.9}$	Long	5.11	$4.9\ 10^{20}$	$1.4^{+5.0}_{-1.4}\ 10^{22}$	5.11	1.55 (107.0)
060526	211957	232.8338	0.2958	$298.0^{+22.9}_{-22.9}$	Long	3.2213	$6.32\ 10^{20}$	$5^{+2.5}_{-2.4}\ 10^{21}$	3.21	3.98 (289.0)
060604	213486	337.242	-10.905	$96.0^{+22.63}_{-22.63}$	Long	2.1357	$4.78\ 10^{20}$	$2.28^{+0.29}_{-0.27}\ 10^{22}$	2.68	4.39 (194.0)
060605	213630	322.1298	-6.0685	$79.84^{+6.63}_{-6.63}$	Long	3.773	$4.74\ 10^{20}$	$0^{+2.02}_{-0}\ 10^{22}$	3.8	1.01 (123.0)
060607A	213823	329.7078	-22.4963	$103.0^{+28.1}_{-28.1}$	Long	3.0749	$2.65\ 10^{20}$	$3.1^{+1.9}_{-1.8}\ 10^{21}$	3.082	2.0 (585.0)
060614	214805	320.8752	-53.0261	$109.1^{+3.4}_{-3.4}$	Unconst	0.1254	$1.99\ 10^{20}$	$3.2^{+0.8}_{-0.8}\ 10^{20}$	0.125	3.75 (818.0)
060707	217704	357.0736	-17.9079	$66.64^{+6.38}_{-6.38}$	Long	3.424	$1.54\ 10^{20}$	$0^{+1.26}_{-0}\ 10^{22}$	3.43	1.65 (108.0)
060714	219101	227.8538	-6.5434	$116.1^{+9.0}_{-9.0}$	Long	2.7108	$7.88\ 10^{20}$	$2^{+0.3}_{-0.3}\ 10^{22}$	2.71	4.7 (230.0)
060729	221755	95.3382	-62.3451	$113.0^{+22.1}_{-22.1}$	Long	0.5428	$5.4\ 10^{20}$	$2.66^{+0.24}_{-0.24}\ 10^{21}$	0.54	2.18 (716.0)
060801	222154	212.9847	16.987	$0.504^{+0.061}_{-0.061}$	Short	1.1304	$1.43\ 10^{20}$	$3.7^{+3.0}_{-2.6}\ 10^{21}$	1.13	0.95 (103.0)
060814	224552	221.3405	20.587	$145.1^{+4.8}_{-4.8}$	Long	1.9229	$2.58\ 10^{20}$	$2.48^{+0.16}_{-0.15}\ 10^{22}$	1.9229	2.19 (1131.0)
060904B	228006	58.219	-0.7201	$190.0^{+21.2}_{-21.2}$	Long	0.7029	$1.94\ 10^{21}$	$4.5^{+0.5}_{-0.5}\ 10^{21}$	0.7	3.73 (364.0)
060906	228316	40.712	30.3562	$44.59^{+2.59}_{-2.59}$	Long	3.6856	$1.61\ 10^{21}$	$1.8^{+4.9}_{-1.8}\ 10^{22}$	3.69	2.09 (114.0)
060908	228581	31.8254	0.3321	$19.3^{+1.3}_{-1.3}$	Long	1.8836	$2.55\ 10^{20}$	$4^{+4.0}_{-4.0}\ 10^{21}$	1.8836	1.69 (174.0)

GRB	ID	RA [°]	DEC [°]	T_{90} [s]	Type	z	NH_{Gal}	NH_{Int}	Z_{abs}	χ^2_r (NDOF)
060912A	229185	5.2808	20.9684	$5.028^{+0.581}_{-0.581}$	Long	0.937	$4.7\ 10^{20}$	$8^{+80.0}_{-8.0}\ 10^{20}$	0.94	1.52 (60.0)
060926	231231	263.9289	13.0423	$8.824^{+1.144}_{-1.144}$	Long	3.2086	$1.15\ 10^{21}$	$1.9^{+2.7}_{-1.9}\ 10^{22}$	3.2	1.84 (57.0)
060927	231362	329.5508	5.3684	$22.42^{+1.19}_{-1.19}$	Long	5.4636	$5.54\ 10^{20}$	$0^{+3.19}_{-0}\ 10^{22}$	5.467	1.78 (94.0)
061006	232585	111.0085	-79.199	$129.8^{+30.7}_{-30.7}$	Short w. EE	0.4377	$2.5\ 10^{21}$	$0^{+1.09}_{-0}\ 10^{21}$	0.0	4.01 (50.0)
061021	234905	145.1488	-21.9538	$47.82^{+5.63}_{-5.63}$	Long	0.3463	$5.53\ 10^{20}$	$0^{+4}_{-0}\ 10^{19}$	0.3463	1.88 (392.0)
061110A	238108	336.2859	-2.2597	$44.51^{+5.9}_{-5.9}$	Long	0.7578	$5.3\ 10^{20}$	$3.2^{+0.3}_{-0.3}\ 10^{21}$	0.757	2.58 (168.0)
061121	239899	147.2315	-13.1859	$81.22^{+46.4}_{-46.4}$	Long	1.3145	$4.63\ 10^{20}$	$5.7^{+0.9}_{-0.8}\ 10^{21}$	1.314	4.44 (607.0)
061222A	252588	358.2374	46.5158	$100.0^{+12.2}_{-12.2}$	Long	2.088	$1.26\ 10^{21}$	$6.5^{+0.7}_{-0.7}\ 10^{22}$	2.088	2.97 (674.0)
061222B	252593	105.3539	-25.8678	$37.25^{+6.06}_{-6.06}$	Long	3.355	$3.97\ 10^{21}$	$4.5^{+2.6}_{-2.3}\ 10^{22}$	3.36	1.58 (121.0)
070208	259714	197.92	61.9587	$64.0^{+22.63}_{-22.63}$	Long	1.165	$1.84\ 10^{20}$	$9.2^{+3.3}_{-2.9}\ 10^{21}$	1.17	1.34 (52.0)
070306	263361	148.082	10.4714	$209.2^{+64.6}_{-64.6}$	Long	1.49594	$3.13\ 10^{20}$	$4.3^{+0.3}_{-0.3}\ 10^{22}$	1.496	1.97 (475.0)
070318	271019	48.4859	-42.9423	$130.4^{+28.8}_{-28.8}$	Long	0.8397	$1.5\ 10^{20}$	$5.9^{+0.8}_{-0.8}\ 10^{21}$	0.84	1.44 (303.0)
070419A	276205	182.7518	39.8992	$160.0^{+50.6}_{-50.6}$	Long	0.9705	$2.63\ 10^{20}$	$6.2^{+0.8}_{-0.7}\ 10^{21}$	0.97	1.57 (155.0)
070506	278693	347.2197	10.7108	$5.992^{+1.407}_{-1.407}$	Long	2.309	$4.44\ 10^{20}$	$6^{+9.0}_{-6.0}\ 10^{21}$	2.31	1.39 (41.0)
070521	279935	242.6631	30.2617	$38.63^{+2.38}_{-2.38}$	Long	2.0865	$3.24\ 10^{20}$	$1.2^{+3.3}_{-1.0}\ 10^{23}$	2.0865	3.75 (175.0)
070529	280706	283.7106	20.6571	$108.9^{+20.7}_{-20.7}$	Long	2.4996	$3.03\ 10^{21}$	$7^{+9.0}_{-6.0}\ 10^{22}$	2.5	1.86 (72.0)
070721B	285654	33.1328	-2.2008	$336.9^{+22.5}_{-22.5}$	Long	3.6298	$2.56\ 10^{20}$	$5^{+7.0}_{-5.0}\ 10^{21}$	3.626	1.8 (268.0)
070802	286809	36.9042	-55.5177	$15.8^{+2.5}_{-2.5}$	Long	2.4541	$3.18\ 10^{20}$	$6^{+9.0}_{-6.0}\ 10^{21}$	2.45	1.17 (65.0)
070809	287344	203.7674	-22.1213	$1.28^{+0.373}_{-0.373}$	Short	0.2187	$8.59\ 10^{20}$	$0^{+3.37}_{-0}\ 10^{20}$	0.0	1.2 (139.0)
070810A	287364	189.9489	10.748	$9.04^{+2.682}_{-2.682}$	Long	2.17	$1.88\ 10^{20}$	$0^{+2.19}_{-0}\ 10^{22}$	2.17	1.02 (77.0)
071020	294835	119.6655	32.8565	$4.3^{+0.583}_{-0.583}$	Long	2.1462	$6.25\ 10^{20}$	$4.2^{+2.6}_{-2.4}\ 10^{21}$	2.146	3.69 (285.0)
071031	295670	6.3956	-58.0521	$180.6^{+30.3}_{-30.3}$	Long	2.6918	$1.25\ 10^{20}$	$1.14^{+0.13}_{-0.13}\ 10^{22}$	2.69	2.45 (378.0)

GRB	ID	RA [°]	DEC [°]	T_{90} [s]	Type	z	NH_{Gal}	NH_{Int}	Z_{abs}	χ_r^2 (NDOF)
071122	297114	276.5696	47.1044	$71.43^{+13.93}_{-13.93}$	Long	1.14	$5.59\ 10^{20}$	$1.8^{+1.7}_{-1.6}\ 10^{21}$	1.14	1.21 (77.0)
080210	302888	251.26	13.8247	$42.26^{+11.37}_{-11.37}$	Long	2.6419	$6.89\ 10^{20}$	$3.1^{+0.9}_{-0.9}\ 10^{22}$	2.64	1.65 (103.0)
080310	305288	220.0414	-0.1646	$363.2^{+16.9}_{-16.9}$	Long	2.42743	$3.75\ 10^{20}$	$5^{+0.8}_{-0.8}\ 10^{21}$	2.43	1.43 (1160.0)
080319B	306757	217.9192	36.2999	$124.9^{+3.1}_{-3.1}$	Ultralong	0.9382	$1.15\ 10^{20}$	$1.38^{+0.11}_{-0.11}\ 10^{21}$	0.94	5.29 (1975.0)
080319C	306778	259.0081	55.3913	$29.55^{+9.41}_{-9.41}$	Long	1.9492	$2.39\ 10^{20}$	$9^{+4.0}_{-3.0}\ 10^{21}$	1.95	1.51 (177.0)
080413A	309096	287.2992	-27.6778	$46.36^{+0.48}_{-0.48}$	Long	2.433	$1.34\ 10^{21}$	$1.9^{+0.6}_{-0.6}\ 10^{22}$	2.43	2.28 (162.0)
080413B	309111	326.1377	-19.9812	$8.0^{+2.0}_{-2.0}$	Long	1.1014	$3.43\ 10^{20}$	$2.6^{+1.2}_{-1.1}\ 10^{21}$	1.1	1.85 (219.0)
080430	310613	165.3286	51.6815	$13.87^{+1.9}_{-1.9}$	Long	0.767	$9.92\ 10^{19}$	$2.81^{+1.1}_{-1.0}\ 10^{21}$	0.767	1.66 (179.0)
080603B	313087	176.5514	68.062	$59.12^{+1.63}_{-1.63}$	Long	2.6892	$1.27\ 10^{20}$	$1.3^{+0.3}_{-0.3}\ 10^{22}$	2.69	2.55 (242.0)
080604	313116	236.9576	20.5593	$77.61^{+13.25}_{-13.25}$	Long	1.4171	$4.46\ 10^{20}$	$0^{+4.23}_{-0}\ 10^{20}$	1.42	1.87 (111.0)
080605	313299	262.13	4.0091	$18.06^{+0.89}_{-0.89}$	Long	1.6403	$1.02\ 10^{21}$	$8.2^{+1.3}_{-1.2}\ 10^{21}$	1.64	2.97 (471.0)
080607	313417	194.9636	15.9101	$78.97^{+3.04}_{-3.04}$	Long	3.0368	$1.82\ 10^{20}$	$6.1^{+0.4}_{-0.3}\ 10^{22}$	3.04	3.66 (516.0)
080707	316204	32.6304	33.0955	$30.16^{+2.4}_{-2.4}$	Long	1.2322	$9.32\ 10^{20}$	$0^{+6.59}_{-0}\ 10^{21}$	1.23	1.44 (60.0)
080721	317508	224.4774	-11.7086	$129.7^{+114.5}_{-114.5}$	Long	2.5914	$9.27\ 10^{20}$	$6.4^{+0.9}_{-0.9}\ 10^{21}$	2.6	1.14 (1290.0)
080804	319016	328.6731	-53.1895	$37.87^{+42.36}_{-42.36}$	Unconst	2.2045	$1.72\ 10^{20}$	$1^{+4.4}_{-1.0}\ 10^{21}$	2.2	1.05 (146.0)
080805	319036	314.223	-62.4366	$106.6^{+15.9}_{-15.9}$	Long	1.5042	$3.93\ 10^{20}$	$5.6^{+1.9}_{-1.8}\ 10^{21}$	1.51	2.1 (243.0)
080810	319584	356.783	0.3123	$107.7^{+3.5}_{-3.5}$	Long	3.3604	$3.62\ 10^{20}$	$0^{+1.62}_{-0}\ 10^{21}$	3.35	2.68 (328.0)
080905B	323898	301.7545	-62.5736	$120.9^{+28.1}_{-28.1}$	Long	2.3739	$4.05\ 10^{20}$	$2.09^{+1.18}_{-0.93}\ 10^{22}$	2.374	1.41 (221.0)
080913	324561	65.7457	-25.1297	$7.456^{+0.757}_{-0.757}$	Long	6.733	$3.66\ 10^{20}$	$4^{+9.0}_{-4.0}\ 10^{22}$	6.7	2.88 (32.0)
080916A	324895	336.2873	-57.0265	$61.35^{+6.68}_{-6.68}$	Long	0.6887	$1.95\ 10^{20}$	$1.02^{+0.11}_{-0.1}\ 10^{22}$	0.689	2.63 (261.0)
080928	326115	95.0586	-55.1722	$233.7^{+20.8}_{-20.8}$	Long	1.6919	$7.17\ 10^{20}$	$6.6^{+1.1}_{-1.0}\ 10^{21}$	1.69	2.57 (503.0)
081007	330856	339.9611	-40.1464	$9.728^{+4.874}_{-4.874}$	Long	0.5295	$1.44\ 10^{20}$	$8.6^{+1.5}_{-1.3}\ 10^{21}$	0.5295	1.28 (142.0)

GRB	ID	RA [°]	DEC [°]	T_{90} [s]	Type	z	NH_{Gal}	NH_{Int}	Z_{abs}	χ_r^2 (NDOF)
081008	331093	279.9682	-57.4376	$187.8^{+38.2}_{-38.2}$	Long	1.9683	$9.28\ 10^{20}$	$7.4^{+1.3}_{-1.2}\ 10^{21}$	1.967	3.21 (442.0)
081118	334877	82.5739	-43.3094	$53.4^{+12.09}_{-12.09}$	Long	2.58	$4.26\ 10^{20}$	$4^{+6.0}_{-4.0}\ 10^{21}$	2.58	1.89 (141.0)
081203A	336489	233.0711	63.5154	$223.0^{+90.0}_{-90.0}$	Long	2.05	$1.81\ 10^{20}$	$6.7^{+1.1}_{-1.0}\ 10^{21}$	2.1	2.04 (404.0)
081222	337914	22.7485	-34.0943	$33.0^{+4.0}_{-4.0}$	Long	2.77	$2.37\ 10^{20}$	$4.4^{+1.6}_{-1.6}\ 10^{21}$	2.77	2.38 (392.0)
081230	338633	37.3288	-25.1448	$60.69^{+13.43}_{-13.43}$	Long	2.03	$1.77\ 10^{20}$	$7^{+2.6}_{-2.4}\ 10^{20}$	0.0	3.16 (138.0)
090102	338895	128.2474	33.1078	$28.32^{+2.35}_{-2.35}$	Long	1.547	$4.69\ 10^{20}$	$6.2^{+2.8}_{-2.5}\ 10^{21}$	1.547	1.58 (191.0)
090205	342121	220.9165	-27.8492	$8.812^{+1.779}_{-1.779}$	Long	4.6497	$1.09\ 10^{21}$	$2.9^{+25.0}_{-2.9}\ 10^{21}$	4.65	1.35 (53.0)
090418A	349510	269.3233	33.4019	$56.3^{+4.06}_{-4.06}$	Long	1.608	$4.09\ 10^{20}$	$7^{+3.0}_{-3.0}\ 10^{21}$	1.608	1.63 (208.0)
090423	350184	148.8895	18.166	$10.3^{+1.06}_{-1.06}$	Long	8.26	$3.17\ 10^{20}$	$9^{+8.0}_{-7.0}\ 10^{22}$	8.2	1.3 (125.0)
090424	350311	189.5306	16.8294	$49.46^{+2.27}_{-2.27}$	Long	0.544	$2.02\ 10^{20}$	$5.12^{+0.25}_{-0.25}\ 10^{21}$	0.544	2.57 (806.0)
090426	350479	189.0834	32.9802	$1.236^{+0.253}_{-0.253}$	Short	2.609	$1.58\ 10^{20}$	$0^{+2.57}_{-0}\ 10^{22}$	2.609	1.21 (57.0)
090429B	350854	210.6739	32.171	$5.58^{+0.994}_{-0.994}$	Long	9.38	$1.25\ 10^{20}$	$1^{+0.6}_{-0.5}\ 10^{21}$	0.0	1.06 (78.0)
090510	351588	333.5699	-26.6012	$5.664^{+1.876}_{-1.876}$	Unconst	0.903	$1.77\ 10^{20}$	$1.3^{+1.3}_{-1.2}\ 10^{21}$	0.903	1.45 (189.0)
090516	352190	138.2544	-11.855	$181.0^{+41.3}_{-41.3}$	Long	4.109	$5.26\ 10^{20}$	$3.6^{+0.4}_{-0.4}\ 10^{22}$	4.109	3.28 (449.0)
090519	352648	142.3091	0.1852	$58.04^{+8.18}_{-8.18}$	Long	3.85	$3.34\ 10^{20}$	$1.57^{+2.07}_{-1.0}\ 10^{23}$	3.85	3.0 (60.0)
090529	353540	212.446	24.4544	$70.44^{+10.33}_{-10.33}$	Long	2.625	$1.7\ 10^{20}$	$3.9^{+3.1}_{-2.9}\ 10^{21}$	2.625	1.34 (78.0)
090530	353567	179.4026	26.5976	$40.46^{+7.87}_{-7.87}$	Unconst	1.266	$1.9\ 10^{20}$	$2.2^{+3.1}_{-2.2}\ 10^{21}$	1.266	1.75 (108.0)
090618	355083	294.0077	78.352	$113.3^{+0.6}_{-0.6}$	Long	0.54	$7.59\ 10^{20}$	$2.03^{+0.15}_{-0.15}\ 10^{21}$	0.54	3.55 (2131.0)
090715B	357512	251.3375	44.8384	$266.4^{+11.6}_{-11.6}$	Long	3.0	$1.4\ 10^{20}$	$2.03^{+0.17}_{-0.16}\ 10^{22}$	3.0	3.72 (623.0)
090812	359711	353.2006	-10.6103	$74.5^{+15.29}_{-15.29}$	Long	2.452	$2.47\ 10^{20}$	$1.07^{+0.12}_{-0.12}\ 10^{22}$	2.452	2.32 (548.0)
091018	373172	32.1911	-57.5462	$4.368^{+0.597}_{-0.597}$	Long	0.971	$3.07\ 10^{20}$	$8.1^{+13.0}_{-8.1}\ 10^{20}$	0.971	2.13 (201.0)
091020	373458	175.7268	50.9774	$38.92^{+4.89}_{-4.89}$	Long	1.71	$1.45\ 10^{20}$	$8^{+1.5}_{-1.4}\ 10^{21}$	1.71	1.57 (334.0)

GRB	ID	RA [°]	DEC [°]	T_{90} [s]	Type	z	NH_{Gal}	NH_{Int}	Z_{abs}	χ^2_r (NDOF)
091029	374210	60.1662	-55.9531	$39.18^{+4.86}_{-4.86}$	Long	2.752	$1.18\ 10^{20}$	$2.8^{+3.6}_{-2.8}\ 10^{21}$	2.752	1.48 (324.0)
091109A	375246	309.2525	-44.1774	$48.03^{+16.95}_{-16.95}$	Long	3.076	$3.34\ 10^{20}$	$1^{+3.8}_{-1.0}\ 10^{22}$	3.076	1.45 (87.0)
091208B	378559	29.4125	16.8794	$14.8^{+3.36}_{-3.36}$	Long	1.0633	$5.75\ 10^{20}$	$7^{+81.0}_{-7.0}\ 10^{20}$	1.063	1.17 (176.0)
100219A	412982	154.1858	-12.5637	$27.57^{+8.65}_{-8.65}$	Long	4.66723	$8.4\ 10^{20}$	$0^{+3.07}_{-0}\ 10^{22}$	4.6667	1.79 (99.0)
100316B	416103	163.5003	-45.4619	$3.836^{+0.426}_{-0.426}$	Long	1.18	$1.53\ 10^{21}$	$4^{+352.0}_{-4.0}\ 10^{22}$	1.18	1.15 (71.0)
100418A	419797	256.3586	11.457	$7.928^{+1.078}_{-1.078}$	Long	0.6239	$6.08\ 10^{20}$	$3.8^{+0.9}_{-0.8}\ 10^{21}$	0.6235	1.8 (77.0)
100425A	420398	299.1724	-26.4689	$38.97^{+2.31}_{-2.31}$	Long	1.755	$1.24\ 10^{21}$	$1.23^{+0.23}_{-0.22}\ 10^{22}$	1.755	1.96 (191.0)
100513A	421814	169.6002	3.6105	$83.5^{+21.63}_{-21.63}$	Long	4.772	$4.93\ 10^{20}$	$3.8^{+2.3}_{-2.1}\ 10^{22}$	4.772	1.14 (141.0)
100621A	425151	315.3091	-51.1024	$63.55^{+1.71}_{-1.71}$	Long	0.542	$3.19\ 10^{20}$	$2.49^{+0.13}_{-0.12}\ 10^{22}$	0.542	4.01 (757.0)
100724A	429868	194.5685	-11.0944	$1.388^{+0.156}_{-0.156}$	Short	1.288	$3.9\ 10^{20}$	$2.2^{+3.1}_{-2.2}\ 10^{21}$	1.288	1.13 (237.0)
100814A	431605	22.4792	-17.9908	$177.3^{+10.8}_{-10.8}$	Long	1.44	$1.85\ 10^{20}$	$1.3^{+0.5}_{-0.5}\ 10^{21}$	1.44	2.71 (771.0)
100816A	431764	351.7377	26.5679	$2.884^{+0.625}_{-0.625}$	Unconst	0.8049	$5.71\ 10^{20}$	$2.8^{+1.7}_{-1.5}\ 10^{21}$	0.8049	2.59 (147.0)
100901A	433065	27.2447	22.7443	$436.7^{+21.8}_{-21.8}$	Long	1.4084	$9.49\ 10^{20}$	$2.2^{+1.0}_{-0.9}\ 10^{21}$	1.408	2.11 (542.0)
100906A	433509	28.6976	55.634	$114.6^{+1.5}_{-1.5}$	Long	1.727	$3.53\ 10^{21}$	$0^{+1.65}_{-0}\ 10^{21}$	1.727	3.73 (490.0)
101219A	440606	74.587	-2.5267	$0.828^{+0.18}_{-0.18}$	Short	0.718	$5.79\ 10^{20}$	$2.1^{+13.6}_{-2.1}\ 10^{21}$	0.718	1.23 (126.0)
101219B	440635	12.2569	-34.5319	$41.86^{+5.84}_{-5.84}$	Long	0.55185	$3.32\ 10^{20}$	$0^{+1.39}_{-0}\ 10^{19}$	0.0	1.72 (160.0)
110106B	441676	134.1643	47.0096	$43.42^{+16.59}_{-16.59}$	Long	0.618	$2.55\ 10^{20}$	$0^{+6.38}_{-0}\ 10^{21}$	0.0	1.34 (115.0)
110205A	444643	164.604	67.5319	$249.4^{+15.0}_{-15.0}$	Long	2.22	$1.7\ 10^{20}$	$3.2^{+0.8}_{-0.8}\ 10^{21}$	2.22	3.04 (849.0)
110213A	445414	42.9725	49.2805	$48.0^{+16.0}_{-16.0}$	Long	1.4607	$3.44\ 10^{21}$	$1^{+0.9}_{-0.8}\ 10^{22}$	1.46	1.49 (262.0)
110422A	451901	112.0547	75.1	$25.78^{+0.6}_{-0.6}$	Long	1.77	$4.65\ 10^{20}$	$1.33^{+0.29}_{-0.27}\ 10^{22}$	1.77	2.37 (429.0)
110503A	452685	132.7995	52.2111	$58.7^{+47.01}_{-47.01}$	Long	1.613	$2.84\ 10^{20}$	$1.6^{+0.8}_{-0.8}\ 10^{21}$	1.613	1.32 (405.0)
110715A	457330	237.6658	-46.2376	$13.0^{+4.0}_{-4.0}$	Long	0.8224	$4.33\ 10^{21}$	$5.5^{+2.2}_{-2.1}\ 10^{21}$	0.82	2.69 (784.0)

GRB	ID	RA [°]	DEC [°]	T_{90} [s]	Type	z	NH_{Gal}	NH_{Int}	Z_{abs}	χ^2_r (NDOF)
110726A	458059	286.713	56.0697	$5.156^{+1.107}_{-1.107}$	Long	1.036	$7.02\ 10^{20}$	$8^{+6.0}_{-5.0}\ 10^{20}$	0.0	3.14 (44.0)
110808A	458918	57.3161	-44.1875	$40.7^{+9.03}_{-9.03}$	Long	1.348	$1.07\ 10^{20}$	$2.8^{+2.1}_{-1.9}\ 10^{21}$	1.348	1.76 (76.0)
110818A	500914	317.3749	-63.9818	$102.8^{+18.0}_{-18.0}$	Long	3.36	$2.93\ 10^{20}$	$3.6^{+13.2}_{-3.6}\ 10^{21}$	3.36	1.75 (152.0)
111008A	505054	60.4377	-32.7078	$62.85^{+2.26}_{-2.26}$	Long	4.99005	$9.92\ 10^{19}$	$2.8^{+0.9}_{-0.9}\ 10^{22}$	4.9898	3.42 (448.0)
111107A	507185	129.4852	-66.5197	$31.07^{+7.15}_{-7.15}$	Long	2.893	$1.32\ 10^{21}$	$0^{+1.63}_{-0}\ 10^{22}$	2.893	2.32 (128.0)
111228A	510649	150.0634	18.284	$101.2^{+5.4}_{-5.4}$	Long	0.71627	$3.26\ 10^{20}$	$6^{+0.3}_{-0.3}\ 10^{21}$	0.714	12.4 (446.0)
111229A	510736	76.6117	-84.7042	$25.37^{+5.58}_{-5.58}$	Long	1.3805	$1.6\ 10^{21}$	$1.8^{+5.1}_{-1.8}\ 10^{22}$	1.3805	1.79 (158.0)
120118B	512003	124.8656	-7.1825	$20.3^{+2.7}_{-2.7}$	Long	2.943	$9.36\ 10^{20}$	$0^{+2.7}_{-0}\ 10^{22}$	2.943	7.25 (178.0)
120211A	514586	87.7798	-24.7912	$64.32^{+8.83}_{-8.83}$	Long	2.4	$1.9\ 10^{20}$	$0^{+6.09}_{-0}\ 10^{20}$	0.0	1.22 (416.0)
120326A	518626	273.9026	69.2481	$69.48^{+8.18}_{-8.18}$	Long	1.798	$6.26\ 10^{20}$	$1.52^{+0.29}_{-0.27}\ 10^{22}$	1.798	9.21 (334.0)
120327A	518731	246.8536	-29.416	$63.53^{+7.03}_{-7.03}$	Long	2.8145	$2.66\ 10^{21}$	$0^{+3.4}_{-0}\ 10^{21}$	2.81	5.82 (296.0)
120404A	519380	235.0014	12.8824	$38.72^{+4.09}_{-4.09}$	Long	2.876	$3.98\ 10^{20}$	$0^{+5.48}_{-0}\ 10^{21}$	2.87	2.07 (134.0)
120422A	520658	136.929	14.0064	$60.35^{+5.73}_{-5.73}$	Long	0.28253	$4.25\ 10^{20}$	$2.6^{+0.6}_{-0.5}\ 10^{21}$	0.28	0.0 (66.0)
120521C	522656	214.2842	42.1443	$27.07^{+4.34}_{-4.34}$	Long	5.93	$1.08\ 10^{20}$	$8^{+4.0}_{-4.0}\ 10^{22}$	6.0	2.14 (164.0)
120712A	526351	169.5983	-20.0508	$14.81^{+3.24}_{-3.24}$	Long	4.1745	$4.12\ 10^{20}$	$0^{+2.9}_{-0}\ 10^{22}$	4.1745	2.43 (160.0)
120729A	529095	13.0789	49.9376	$93.93^{+36.64}_{-36.64}$	Long	0.8	$2.15\ 10^{21}$	$0^{+2.95}_{-0}\ 10^{20}$	0.8	2.41 (312.0)
120802A	529486	44.8326	13.762	$50.29^{+31.04}_{-31.04}$	Long	3.796	$1.46\ 10^{21}$	$0^{+2.74}_{-0}\ 10^{22}$	3.796	2.91 (154.0)
120804A	529686	233.9504	-28.7682	$0.808^{+0.083}_{-0.083}$	Short	1.3	$1.58\ 10^{21}$	$3.8^{+3.1}_{-2.4}\ 10^{21}$	0.0	5.05 (48.0)
120811C	530689	199.6916	62.2971	$24.34^{+3.06}_{-3.06}$	Long	2.671	$2.23\ 10^{20}$	$9^{+3.0}_{-3.0}\ 10^{21}$	2.671	9.78 (218.0)
120907A	532871	74.751	-9.3183	$6.08^{+0.785}_{-0.785}$	Long	0.97	$7.26\ 10^{20}$	$1.6^{+1.2}_{-1.1}\ 10^{21}$	0.97	1.3 (102.0)
121027A	536831	63.5952	-58.8334	$80.09^{+40.76}_{-40.76}$	Ultralong	1.773	$1.59\ 10^{20}$	$1.89^{+0.1}_{-0.09}\ 10^{22}$	1.773	2.31 (1407.0)
121128A	539866	300.5885	54.2997	$23.43^{+1.65}_{-1.65}$	Long	2.2	$3.32\ 10^{21}$	$2.8^{+6.7}_{-2.8}\ 10^{21}$	2.2	4.83 (284.0)

GRB	ID	RA [°]	DEC [°]	T_{90} [s]	Type	z	NH_{Gal}	NH_{Int}	Z_{abs}	χ^2_r (NDOF)
121201A	540178	13.4958	-42.935	$38.0^{+8.25}_{-8.25}$	Long	3.385	$2.05\ 10^{20}$	$0^{+3.03}_{-0}\ 10^{22}$	3.385	1.32 (106.0)
121209A	540964	326.7949	-8.2502	$42.92^{+1.43}_{-1.43}$	Long	2.1	$4.4\ 10^{20}$	$1.9^{+6.0}_{-1.9}\ 10^{22}$	2.1	1.87 (206.0)
130427B	554635	314.8975	-22.5368	$25.9^{+5.97}_{-5.97}$	Long	2.78	$5.35\ 10^{20}$	$8^{+39.0}_{-8.0}\ 10^{20}$	2.78	2.71 (114.0)
130610A	557845	224.4081	28.1904	$47.72^{+10.74}_{-10.74}$	Long	2.092	$2.07\ 10^{20}$	$0^{+1.52}_{-0}\ 10^{21}$	2.092	2.23 (190.0)
130831A	568849	358.6351	29.4305	$30.19^{+2.33}_{-2.33}$	Long	0.4791	$5.74\ 10^{20}$	$0^{+1.44}_{-0}\ 10^{20}$	0.4791	4.62 (300.0)
130925A	571830	41.1852	-26.1464	$160.3^{+3.4}_{-3.4}$	Ultralong	0.348	$1.75\ 10^{20}$	$2.54^{+0.04}_{-0.04}\ 10^{22}$	0.347	3.33 (3869.0)
131030A	576238	345.0743	-5.3791	$39.42^{+3.67}_{-3.67}$	Long	1.293	$5.62\ 10^{20}$	$2.8^{+0.4}_{-0.4}\ 10^{21}$	1.293	8.88 (788.0)
131227A	582184	67.366	28.8776	$17.99^{+1.55}_{-1.55}$	Long	5.3	$2.95\ 10^{21}$	$3.3^{+1.9}_{-1.6}\ 10^{21}$	0.0	1.71 (156.0)
140304A	590206	30.6491	33.473	$14.78^{+1.4}_{-1.4}$	Long	5.283	$7.68\ 10^{20}$	$4^{+8.0}_{-4.0}\ 10^{22}$	5.28	3.01 (146.0)
140430A	597722	102.9379	23.0365	$173.6^{+3.7}_{-3.7}$	Long	1.6	$2.13\ 10^{21}$	$4.4^{+1.5}_{-1.4}\ 10^{21}$	1.6	7.62 (332.0)
140506A	598284	276.8075	-55.5562	$111.1^{+9.5}_{-9.5}$	Long	0.889	$1.06\ 10^{21}$	$7.3^{+0.3}_{-0.3}\ 10^{21}$	0.889	6.82 (550.0)
140509A	598497	46.5638	-62.6615	$23.22^{+5.17}_{-5.17}$	Long	2.4	$2.23\ 10^{20}$	$1.7^{+4.4}_{-1.7}\ 10^{20}$	0.0	1.5 (144.0)
140629A	602884	249.011	41.8966	$38.27^{+11.62}_{-11.62}$	Long	2.275	$9.32\ 10^{19}$	$5^{+5.0}_{-5.0}\ 10^{21}$	2.275	2.49 (182.0)
140703A	603243	13.0103	45.1025	$68.64^{+66.46}_{-66.46}$	Long	3.14	$1.28\ 10^{21}$	$6.1^{+0.7}_{-0.7}\ 10^{22}$	3.14	5.55 (282.0)
140710A	603954	41.0866	35.4987	$3.0^{+2.236}_{-2.236}$	Unconst	0.558	$7.15\ 10^{20}$	$2.5^{+0.9}_{-0.8}\ 10^{21}$	0.0	1.45 (88.0)
141221A	622006	198.2827	8.1976	$36.82^{+4.1}_{-4.1}$	Long	1.452	$2.27\ 10^{20}$	$5.7^{+2130.0}_{-5.7}\ 10^{18}$	0.0	2.01 (178.0)
150301B	633180	89.1597	-57.9672	$17.14^{+4.64}_{-4.64}$	Long	1.5169	$6.15\ 10^{20}$	$0^{+3.78}_{-0}\ 10^{21}$	1.5169	2.13 (140.0)
150403A	637044	311.5048	-62.7061	$37.3^{+11.72}_{-11.72}$	Long	2.06	$5.35\ 10^{20}$	$6.1^{+0.6}_{-0.5}\ 10^{21}$	2.06	1.8 (2000.0)
151027A	661775	272.4971	61.3615	$129.6^{+5.5}_{-5.5}$	Long	0.81	$3.75\ 10^{20}$	$2.85^{+0.25}_{-0.24}\ 10^{21}$	0.81	3.87 (888.0)
151027B	661869	76.1894	-6.4284	$80.0^{+35.78}_{-35.78}$	Long	4.063	$9.43\ 10^{20}$	$2.7^{+2.9}_{-2.4}\ 10^{22}$	4.063	1.74 (126.0)
151111A	663074	56.8516	-44.1537	$76.04^{+12.75}_{-12.75}$	Long	3.5	$1.07\ 10^{20}$	$2.6^{+1.9}_{-1.7}\ 10^{20}$	0.0	2.49 (260.0)
151215A	667392	93.622	35.5312	$17.85^{+1.01}_{-1.01}$	Long	2.59	$4.02\ 10^{21}$	$0^{+1.21}_{-0}\ 10^{22}$	2.59	1.51 (54.0)

GRB	ID	RA [°]	DEC [°]	T_{90} [s]	Type	z	NH_{Gal}	NH_{Int}	Z_{abs}	χ^2_r (NDOF)
160104A	669319	76.8105	11.3326	$16.56^{+2.79}_{-2.79}$	Long	2.8	$2.71\ 10^{21}$	$1.2^{+3.1}_{-1.2}\ 10^{21}$	0.0	1.76 (72.0)
160117B	670800	132.1705	-16.3432	$11.54^{+2.61}_{-2.61}$	Long	0.87	$5.71\ 10^{20}$	$2.3^{+0.6}_{-0.5}\ 10^{21}$	0.87	6.4 (132.0)
160121A	671231	109.0798	-23.5894	$10.5^{+2.4}_{-2.4}$	Long	1.96	$5.26\ 10^{21}$	$0^{+2.68}_{-0}\ 10^{22}$	1.96	2.09 (92.0)
160314A	679120	112.7662	17.0234	$8.732^{+1.516}_{-1.516}$	Long	0.726	$6.19\ 10^{20}$	$0^{+9.23}_{-0}\ 10^{20}$	0.726	1.01 (28.0)
160327A	680655	146.699	54.0166	$33.74^{+9.37}_{-9.37}$	Long	4.99	$1.18\ 10^{20}$	$0^{+2.81}_{-0}\ 10^{20}$	0.0	2.45 (148.0)
160410A	682269	150.7096	3.4455	$96.0^{+50.6}_{-50.6}$	Long	1.717	$1.77\ 10^{20}$	$0^{+2.91}_{-0}\ 10^{21}$	1.717	3.18 (88.0)

Table 2: The GRBs, with observed redshifts, fitted in Chapter 2. The redshift, trigger ID, and duration data are extracted from Tables 39, and 9, respectively, of Lien et al. (2016b) (with references therein), along with GRB categories. The NH_{Gal}, NH_{Int} (in units of cm^{-2}), and z_{abs} data are taken from the Swift Burst Analyser site (Evans et al., 2009, 2007). The spectral fits used to derive the absorption columns are fitted assuming a particular redshift, which in some cases, is set at $z_{abs} = 0$. The reduced chi-square of the model fit, and the number of degrees of freedom are also given.

Pulse	T_{peak} [s]	T_{rise} [s]	T_f [s]	E_f [keV]	α	F_f [10^{-8} ergs s^{-1} cm^{-2}]	L_f [ergs s^{-1}]
GRB 050126							
1	4.8	4.8	$35.1^{+4.4}_{-3.8}$	218	$-1.95^{+0.21}_{-0.18}$	$10.21^{+1.77}_{-1.59}$	$(1.26^{+0.35}_{-0.27})10^{51}$
2	26.7	9.7	$24.6^{+16.7}_{-9.8}$	36	$-3.23^{+0.84}_{-0.77}$	$7.72^{+16.93}_{-7.64}$	$(6.59^{+17.37}_{-6.54})10^{50}$
GRB 050215B							
1	2.7	2.7	$10.3^{+9.6}_{-9.6}$	142	$-2.83^{+0.88}_{-0.89}$	$83.52^{+77.55}_{-77.82}$	$(4.36^{+4.02}_{-4.04})10^{52}$
GRB 050219A							
1	4.8	4.8	$4.54^{+3.74}_{-4.35}$	413	$-2.49^{+0.53}_{-0.59}$	$198.6^{+187.4}_{-182.9}$	$(3.22^{+2.94}_{-2.84})10^{50}$
2	13.6	8.1	$7.0^{+7.0}_{-7.0}$	413	$-2.17^{+0.18}_{-0.18}$	$444.6^{+437.5}_{-436.7}$	$(8.77^{+8.61}_{-8.59})10^{50}$
GRB 050315							
1	14.1	14.1	$31.1^{+9.4}_{-7.1}$	170	$-2.46^{+0.60}_{-0.62}$	$3.64^{+2.60}_{-0.93}$	$(1.05^{+0.99}_{-0.32})10^{51}$
2	56.2	5.0	$28.1^{+2.7}_{-2.1}$	170	$-2.39^{+0.14}_{-0.13}$	$18.60^{+1.76}_{-1.57}$	$(5.39^{+0.65}_{-0.55})10^{51}$
3	66.1	0.8	$18.9^{+5.0}_{-3.4}$	170	$-3.48^{+0.08}_{-0.29}$	$55.79^{+61.60}_{-46.50}$	$(1.41^{+1.58}_{-1.18})10^{52}$
4	81.5	6.6	$23.6^{+2.8}_{-4.0}$	61	$-3.09^{+0.22}_{-0.18}$	$26.05^{+13.21}_{-9.75}$	$(6.94^{+3.67}_{-2.66})10^{51}$
GRB 050319							
1	0.8	0.8	$31.5^{+1.9}_{-5.1}$	118	$-2.83^{+0.22}_{-0.21}$	$21.71^{+9.76}_{-4.44}$	$(2.12^{+1.02}_{-0.45})10^{52}$
GRB 050401							
1	1.7	1.7	$4.28^{+1.09}_{-0.52}$	128	$-2.12^{+0.26}_{-0.24}$	$100.6^{+16.7}_{-17.0}$	$(7.75^{+1.59}_{-1.44})10^{52}$
2	4.9	0.8	$3.95^{+2.84}_{-1.97}$	128	$-2.43^{+0.85}_{-1.00}$	$48.06^{+72.82}_{-47.58}$	$(3.58^{+6.46}_{-3.55})10^{52}$
3	7.1	1.6	$1.70^{+0.26}_{-0.23}$	128	$-1.82^{+0.26}_{-0.27}$	$134.9^{+30.2}_{-22.9}$	$(1.09^{+0.31}_{-0.22})10^{53}$
4	10.1	0.2	$3.08^{+3.37}_{-1.06}$	128	$-2.02^{+0.84}_{-0.83}$	$94.68^{+133.64}_{-31.55}$	$(7.44^{+13.65}_{-2.68})10^{52}$
5	17.9	5.2	$6.3^{+2.3}_{-3.2}$	128	$-1.67^{+1.17}_{-0.82}$	$29.37^{+24.34}_{-29.08}$	$(2.44^{+3.77}_{-2.42})10^{52}$
6	31.8	1.4	$3.77^{+0.06}_{-0.09}$	128	$-1.73^{+0.16}_{-0.19}$	$247.5^{+19.5}_{-28.0}$	$(2.03^{+0.22}_{-0.28})10^{53}$

Pulse	T_{peak} [s]	T_{rise} [s]	T_f [s]	E_f [keV]	α	F_f [10^{-8} ergs s^{-1} cm^{-2}]	L_f [ergs s^{-1}]
7	37.9	5.6	$11.2^{+2.2}_{-1.5}$	13	$-3.27^{+0.25}_{-0.77}$	$206.1^{+487.4}_{-191.0}$	$(1.65^{+4.51}_{-1.53})10^{53}$
GRB 050416A							
1	0.9	0.9	$7.8^{+0.8}_{-0.6}$	19	$-2.25^{+0.38}_{-0.28}$	$69.88^{+27.71}_{-28.22}$	$(1.20^{+0.52}_{-0.51})10^{51}$
GRB 050525A							
1	0.5	0.5	$1.25^{+0.02}_{-0.02}$	311	$-2.23^{+0.03}_{-0.03}$	$620.8^{+15.1}_{-15.4}$	$(1.22^{+0.05}_{-0.05})10^{52}$
2	1.2	0.4	$1.21^{+0.02}_{-0.03}$	311	$-2.10^{+0.02}_{-0.02}$	$767.9^{+31.3}_{-17.7}$	$(1.62^{+0.09}_{-0.06})10^{52}$
3	3.2	2.1	$6.3^{+0.4}_{-0.2}$	311	$-3.65^{+0.07}_{-0.03}$	$459.3^{+153.8}_{-204.9}$	$(4.29^{+1.71}_{-1.86})10^{51}$
4	5.5	1.2	$1.74^{+0.02}_{-0.02}$	311	$-2.30^{+0.02}_{-0.02}$	$506.0^{+8.4}_{-13.5}$	$(9.67^{+0.26}_{-0.36})10^{51}$
5	6.4	0.9	$0.92^{+0.05}_{-0.07}$	311	$-2.46^{+0.06}_{-0.06}$	$193.4^{+16.6}_{-8.5}$	$(3.54^{+0.41}_{-0.24})10^{51}$
6	6.7	0.3	$0.75^{+0.05}_{-0.05}$	311	$-2.14^{+0.08}_{-0.07}$	$276.7^{+22.9}_{-19.1}$	$(5.69^{+0.77}_{-0.59})10^{51}$
7	9.2	2.5	$3.01^{+0.05}_{-0.03}$	311	$-3.44^{+0.04}_{-0.02}$	$378.5^{+26.9}_{-374.7}$	$(5.91^{+0.60}_{-5.85})10^{51}$
GRB 050724							
1	1.1	1.1	$1.76^{+0.04}_{-0.02}$	397	$-2.57^{+0.27}_{-0.16}$	$76.42^{+33.02}_{-11.70}$	$(1.78^{+1.23}_{-0.41})10^{50}$
2	92.4	20.9	$34.4^{+1.8}_{-1.2}$	11	$-1.77^{+0.05}_{-0.05}$	$2.96^{+0.23}_{-0.23}$	$(5.80^{+0.47}_{-0.48})10^{48}$
3	140.5	39.7	$40.1^{+3.3}_{-3.1}$	12	$-2.19^{+0.10}_{-0.10}$	$0.536^{+0.081}_{-0.068}$	$(1.14^{+0.19}_{-0.16})10^{48}$
4	194.8	47.6	$49.5^{+3.0}_{-4.3}$	7.26	$-2.28^{+0.12}_{-0.12}$	$0.208^{+0.032}_{-0.023}$	$(4.50^{+0.84}_{-0.63})10^{47}$
5	286.4	46.4	$46.8^{+0.2}_{-0.2}$	22	$-3.14^{+0.17}_{-0.11}$	$0.0407^{+0.0098}_{-0.0087}$	$(1.70^{+0.62}_{-0.45})10^{47}$
6	50001.1	486.2	48618^{+15940}_{-48132}	7.95	$-2.52^{+0.48}_{-0.50}$	$0.0003^{+0.0001}_{-0.0001}$	$(4.49^{+2.12}_{-1.78})10^{44}$
GRB 050730							
1	29.2	29.2	$78.3^{+60.3}_{-12.1}$	101	$-1.91^{+0.28}_{-0.19}$	$2.82^{+0.60}_{-0.59}$	$(4.54^{+1.10}_{-0.99})10^{51}$
2	52.7	3.0	$7.7^{+3.1}_{-1.7}$	101	$-1.63^{+0.60}_{-0.54}$	$7.26^{+3.18}_{-2.62}$	$(1.20^{+0.67}_{-0.46})10^{52}$
3	58.4	2.5	$4.75^{+5.25}_{-4.70}$	101	$-1.43^{+0.93}_{-1.05}$	$7.54^{+3.83}_{-7.47}$	$(1.29^{+1.01}_{-1.27})10^{52}$

Pulse	T_{peak} [s]	T_{rise} [s]	T_f [s]	E_f [keV]	α	F_f [10^{-8} ergs s^{-1} cm^{-2}]	L_f [ergs s^{-1}]
4	66.4	3.0	$43.2^{+21.2}_{-10.6}$	101	$-1.79^{+0.47}_{-0.32}$	$3.75^{+1.53}_{-1.03}$	$(6.17^{+2.99}_{-1.78})10^{51}$
5	139.7	24.3	$55.4^{+22.4}_{-10.5}$	101	$-2.44^{+0.11}_{-0.12}$	$1.59^{+0.52}_{-0.57}$	$(2.52^{+0.83}_{-0.91})10^{51}$
6	280.2	13.8	$15.5^{+7.6}_{-3.8}$	101	$-2.22^{+0.24}_{-0.05}$	$0.547^{+0.555}_{-0.262}$	$(8.82^{+9.16}_{-4.23})10^{50}$
7	492.4	81.8	$82.6^{+5.5}_{-15.9}$	101	$-2.55^{+0.07}_{-0.09}$	$0.293^{+0.084}_{-0.065}$	$(5.23^{+1.54}_{-1.17})10^{50}$
8	724.1	28.4	$205.5^{+230.0}_{-203.5}$	74	$-3.17^{+0.15}_{-0.62}$	$0.0491^{+0.0133}_{-0.0275}$	$(8.38^{+4.73}_{-4.83})10^{49}$
GRB 050801							
1	0.3	0.3	$1.54^{+0.04}_{-0.12}$	195	$-2.18^{+0.28}_{-0.31}$	$32.46^{+6.91}_{-5.45}$	$(5.78^{+1.86}_{-1.30})10^{51}$
2	1.5	0.6	$19.8^{+10.2}_{-6.2}$	195	$-3.37^{+0.55}_{-0.58}$	$37.50^{+71.76}_{-37.13}$	$(5.08^{+11.44}_{-5.04})10^{51}$
GRB 050802							
1	3.0	3.0	$9.7^{+0.6}_{-1.5}$	185	$-2.08^{+0.24}_{-0.24}$	$34.10^{+6.23}_{-4.16}$	$(7.74^{+2.09}_{-1.31})10^{51}$
2	10.2	3.0	$2.98^{+1.16}_{-0.93}$	185	$-2.66^{+0.59}_{-0.50}$	$16.74^{+10.33}_{-5.55}$	$(3.90^{+3.20}_{-1.48})10^{51}$
3	15.6	3.7	$30.5^{+14.6}_{-7.6}$	185	$-3.19^{+0.62}_{-0.61}$	$18.75^{+36.95}_{-10.81}$	$(3.47^{+7.86}_{-2.16})10^{51}$
4	437.0	124.9	$649.6^{+323.3}_{-127.0}$	115	$-2.85^{+0.29}_{-0.32}$	$0.0238^{+0.0165}_{-0.0075}$	$(4.69^{+3.45}_{-1.60})10^{48}$
GRB 050803							
1	3.9	3.9	$7.7^{+7.4}_{-7.3}$	111	$-2.23^{+0.41}_{-0.36}$	$72.80^{+69.11}_{-69.58}$	$(8.69^{+8.24}_{-8.30})10^{52}$
2	11.7	2.7	$6.9^{+6.5}_{-6.5}$	111	$-1.66^{+0.15}_{-0.15}$	$81.24^{+73.66}_{-75.26}$	$(1.02^{+0.92}_{-0.95})10^{53}$
3	21.9	0.8	$2.99^{+1.08}_{-2.55}$	111	$-1.29^{+0.58}_{-0.56}$	$126.8^{+112.9}_{-90.9}$	$(1.67^{+1.50}_{-1.24})10^{53}$
4	87.8	1.7	$6.2^{+5.8}_{-5.8}$	111	$-1.63^{+0.29}_{-0.31}$	$88.59^{+81.34}_{-81.02}$	$(1.11^{+1.03}_{-1.02})10^{53}$
GRB 050814							
1	11.3	11.3	$18.5^{+4.0}_{-1.9}$	79	$-2.06^{+0.52}_{-0.53}$	$6.29^{+1.64}_{-1.66}$	$(1.98^{+0.56}_{-0.50})10^{52}$
2	72.0	56.8	$67.9^{+5.7}_{-3.4}$	79	$-3.06^{+0.06}_{-0.06}$	$4.76^{+0.61}_{-0.84}$	$(2.04^{+0.32}_{-0.40})10^{52}$
GRB 050820A							

Pulse	T_{peak} [s]	T_{rise} [s]	T_f [s]	E_f [keV]	α	F_f [10^{-8} ergs s^{-1} cm^{-2}]	L_f [ergs s^{-1}]
1	2.2	2.2	$17.0^{+1.3}_{-1.1}$	138	$-2.31^{+0.17}_{-0.16}$	$12.01^{+1.28}_{-1.27}$	$(7.09^{+0.92}_{-0.83})10^{51}$
2	12.3	0.9	$16.6^{+4.8}_{-3.0}$	138	$-2.24^{+0.31}_{-0.30}$	$8.22^{+2.24}_{-1.84}$	$(4.71^{+1.55}_{-1.15})10^{51}$
3	16.8	0.1	$12.9^{+4.3}_{-3.6}$	138	$-3.35^{+0.57}_{-0.65}$	$17.65^{+39.71}_{-17.47}$	$(1.04^{+2.51}_{-1.03})10^{52}$
4	232.5	6.2	$15.8^{+0.7}_{-0.5}$	138	$-1.84^{+0.03}_{-0.03}$	$34.12^{+2.77}_{-2.69}$	$(2.15^{+0.19}_{-0.18})10^{52}$
5	240.1	6.4	$65.8^{+12.7}_{-10.6}$	138	$-1.94^{+0.05}_{-0.05}$	$16.82^{+2.32}_{-2.49}$	$(1.01^{+0.15}_{-0.16})10^{52}$
GRB 050822							
1	2.0	2.0	$8.5^{+8.2}_{-8.1}$	205	$-2.74^{+0.80}_{-0.79}$	$186.7^{+163.8}_{-174.9}$	$(2.43^{+2.06}_{-2.24})10^{52}$
2	42.8	0.5	$4.26^{+3.88}_{-3.97}$	205	$-3.24^{+1.33}_{-1.29}$	$391.9^{+315.1}_{-310.0}$	$(4.52^{+3.29}_{-3.23})10^{52}$
3	49.0	2.2	$4.69^{+4.47}_{-4.51}$	205	$-2.88^{+0.92}_{-0.94}$	$244.2^{+228.1}_{-233.0}$	$(3.11^{+2.85}_{-2.93})10^{52}$
4	57.3	3.3	$5.7^{+5.5}_{-5.5}$	205	$-3.13^{+1.18}_{-1.17}$	$185.8^{+170.2}_{-167.7}$	$(2.25^{+1.99}_{-1.96})10^{52}$
5	60.5	0.7	$3.96^{+3.58}_{-3.69}$	205	$-2.96^{+1.03}_{-1.06}$	$153.0^{+121.9}_{-135.0}$	$(1.89^{+1.39}_{-1.61})10^{52}$
6	102.5	1.8	$10.0^{+9.3}_{-8.6}$	205	$-2.47^{+0.49}_{-0.50}$	$34.05^{+26.07}_{-30.07}$	$(4.63^{+3.38}_{-4.01})10^{51}$
7	131.0	17.8	$89.8^{+87.6}_{-87.6}$	205	$-3.27^{+1.30}_{-1.30}$	$1.54^{+1.49}_{-1.49}$	$(1.76^{+1.69}_{-1.70})10^{50}$
8	241.3	10.5	$30.9^{+22.6}_{-22.8}$	205	$-3.53^{+1.72}_{-1.88}$	$0.254^{+0.211}_{-0.225}$	$(2.75^{+1.98}_{-2.27})10^{49}$
9	446.1	36.6	$93.0^{+90.4}_{-90.4}$	205	$-4.38^{+2.42}_{-2.43}$	$0.657^{+0.628}_{-0.614}$	$(5.72^{+5.24}_{-5.01})10^{49}$
GRB 050908							
1	7.6	7.6	$20.9^{+1.9}_{-1.1}$	115	$-2.67^{+0.25}_{-0.27}$	$10.00^{+3.31}_{-1.84}$	$(1.06^{+0.38}_{-0.20})10^{52}$
GRB 050922C							
1	0.6	0.6	$4.12^{+0.64}_{-0.37}$	156	$-2.19^{+0.40}_{-0.45}$	$18.50^{+3.28}_{-4.65}$	$(7.45^{+2.07}_{-2.17})10^{51}$
2	3.2	1.4	$2.35^{+0.11}_{-0.08}$	156	$-1.95^{+0.07}_{-0.07}$	$107.8^{+6.2}_{-5.9}$	$(4.57^{+0.34}_{-0.32})10^{52}$
GRB 051016B							
1	0.6	0.6	$8.9^{+1.3}_{-1.4}$	258	$-3.04^{+0.25}_{-0.45}$	$34.02^{+39.76}_{-11.73}$	$(1.38^{+1.89}_{-0.64})10^{51}$

Pulse	T_{peak} [s]	T_{rise} [s]	T_f [s]	E_f [keV]	α	F_f [10^{-8} ergs s^{-1} cm^{-2}]	L_f [ergs s^{-1}]
GRB 051109A							
1	2.7	2.7	$7.3^{+1.6}_{-0.8}$	149	$-2.20^{+0.28}_{-0.28}$	$52.97^{+10.06}_{-9.52}$	$(2.46^{+0.61}_{-0.51})10^{52}$
2	30.9	6.0	$25.8^{+6.8}_{-5.5}$	149	$-2.92^{+0.21}_{-0.23}$	$13.84^{+9.19}_{-7.59}$	$(6.12^{+4.16}_{-3.37})10^{51}$
GRB 051221A							
1	0.1	0.1	$0.245^{+0.004}_{-0.003}$	323	$-2.01^{+0.05}_{-0.05}$	$745.5^{+42.9}_{-37.2}$	$(1.33^{+0.12}_{-0.10})10^{52}$
2	0.7	0.1	$2.67^{+0.69}_{-2.61}$	323	$-4.66^{+0.24}_{-0.16}$	$7176.9^{+3073.8}_{-5825.8}$	$(2.27^{+1.62}_{-1.79})10^{52}$
3	1.0	0.2	$0.77^{+0.19}_{-0.15}$	323	$-3.22^{+0.26}_{-0.09}$	$170.0^{+260.2}_{-71.4}$	$(1.59^{+3.07}_{-0.72})10^{51}$
4	121.4	372.0	$377.3^{+91.1}_{-69.1}$	323	$-2.96^{+0.18}_{-0.19}$	$0.0458^{+0.0205}_{-0.0136}$	$(7.21^{+4.18}_{-2.64})10^{47}$
GRB 060108							
1	1.4	1.4	$8.0^{+0.8}_{-0.5}$	165	$-2.57^{+0.27}_{-0.29}$	$12.25^{+3.62}_{-2.03}$	$(3.81^{+1.32}_{-0.72})10^{51}$
2	4.0	0.4	$4.11^{+5.03}_{-4.07}$	7.50	$-2.23^{+1.06}_{-2.27}$	$11.85^{+32.97}_{-10.06}$	$(3.52^{+9.89}_{-3.06})10^{51}$
3	6.0	1.1	$10.2^{+3.5}_{-2.6}$	165	$-2.93^{+0.49}_{-0.54}$	$10.81^{+15.70}_{-6.03}$	$(3.26^{+5.16}_{-1.88})10^{51}$
GRB 060115							
1	6.3	6.3	$48.1^{+4.4}_{-3.9}$	110	$-2.81^{+0.09}_{-0.10}$	$7.75^{+1.52}_{-1.34}$	$(9.49^{+1.98}_{-1.69})10^{51}$
2	91.6	5.8	$16.2^{+2.5}_{-2.2}$	110	$-2.50^{+0.22}_{-0.20}$	$4.87^{+1.15}_{-0.97}$	$(5.86^{+1.42}_{-1.15})10^{51}$
3	102.6	6.7	$11.4^{+1.6}_{-1.0}$	110	$-1.94^{+0.17}_{-0.15}$	$10.54^{+1.39}_{-1.25}$	$(1.31^{+0.20}_{-0.17})10^{52}$
4	403.6	42.8	$223.6^{+124.0}_{-49.7}$	15	$-3.80^{+0.48}_{-0.70}$	$0.0264^{+0.0130}_{-0.0090}$	$(4.10^{+3.39}_{-1.71})10^{49}$
GRB 060116							
1	4.1	4.1	$47.8^{+12.1}_{-9.6}$	66	$-1.59^{+0.30}_{-0.29}$	$8.60^{+2.41}_{-2.04}$	$(4.48^{+1.30}_{-1.07})10^{52}$
2	33.6	4.0	$6.1^{+0.9}_{-0.7}$	66	$-2.71^{+1.07}_{-0.57}$	$12.63^{+5.63}_{-7.57}$	$(7.00^{+5.92}_{-4.33})10^{52}$
3	79.9	1.3	$4.70^{+20.32}_{-1.62}$	66	$-3.51^{+0.44}_{-0.99}$	$43.91^{+52.16}_{-43.47}$	$(3.58^{+13.52}_{-3.55})10^{53}$
GRB 060124							

Pulse	T_{peak} [s]	T_{rise} [s]	T_f [s]	E_f [keV]	α	F_f [10^{-8} ergs s^{-1} cm^{-2}]	L_f [ergs s^{-1}]
1	2.2	2.2	$5.8^{+1.2}_{-0.9}$	152	$-2.10^{+0.53}_{-0.53}$	$9.70^{+2.73}_{-2.45}$	$(4.38^{+1.94}_{-1.31})10^{51}$
2	10.6	4.6	$4.61^{+0.01}_{-0.01}$	152	$-3.15^{+0.41}_{-0.17}$	$15.56^{+5.34}_{-5.56}$	$(1.49^{+0.54}_{-0.54})10^{52}$
3	15.9	0.5	$4.74^{+4.90}_{-4.69}$	152	$-3.81^{+2.63}_{-0.60}$	$100.3^{+234.3}_{-99.3}$	$(3.98^{+14.69}_{-3.94})10^{52}$
4	17.7	5.4	$544.6^{+488.3}_{-252.8}$	152	$-2.98^{+0.41}_{-0.39}$	$0.0295^{+0.0215}_{-0.0128}$	$(1.23^{+0.95}_{-0.54})10^{49}$
5	299.9	94.3	$212.3^{+168.1}_{-72.9}$	152	$-2.49^{+0.30}_{-0.31}$	$0.0881^{+0.0958}_{-0.0497}$	$(3.79^{+4.43}_{-2.18})10^{49}$
6	378.2	49.4	$129.2^{+8.2}_{-6.1}$	132	$-2.16^{+0.04}_{-0.05}$	$2.45^{+0.36}_{-0.33}$	$(1.07^{+0.17}_{-0.15})10^{51}$
7	453.2	51.8	$85.9^{+4.0}_{-4.3}$	6.96	$-1.78^{+0.09}_{-0.09}$	$0.719^{+0.086}_{-0.073}$	$(2.99^{+0.36}_{-0.30})10^{50}$
8	488.9	28.8	$58.0^{+5.3}_{-3.9}$	22	$-2.06^{+0.07}_{-0.08}$	$2.27^{+0.39}_{-0.39}$	$(9.39^{+1.62}_{-1.62})10^{50}$
9	523.5	15.3	$35.9^{+3.5}_{-3.0}$	95	$-2.27^{+0.05}_{-0.04}$	$9.01^{+0.76}_{-0.77}$	$(3.79^{+0.33}_{-0.33})10^{51}$
10	539.1	10.4	$17.8^{+1.3}_{-1.3}$	31	$-1.97^{+0.09}_{-0.06}$	$7.19^{+0.64}_{-0.64}$	$(2.99^{+0.27}_{-0.27})10^{51}$
11	562.9	5.6	$29.5^{+1.1}_{-0.9}$	182	$-2.34^{+0.03}_{-0.02}$	$29.61^{+1.14}_{-1.12}$	$(1.33^{+0.06}_{-0.06})10^{52}$
12	577.2	6.4	$8.7^{+0.4}_{-0.3}$	122	$-2.10^{+0.04}_{-0.03}$	$45.53^{+1.42}_{-1.40}$	$(1.99^{+0.07}_{-0.07})10^{52}$
13	671.5	12.2	$54.4^{+6.8}_{-4.5}$	3.00	$-1.54^{+0.15}_{-0.14}$	$1.24^{+0.16}_{-0.29}$	$(5.05^{+0.64}_{-1.19})10^{50}$
14	708.3	21.1	$28.8^{+0.5}_{-0.4}$	14	$-2.21^{+0.04}_{-0.04}$	$6.23^{+0.33}_{-0.33}$	$(2.61^{+0.14}_{-0.14})10^{51}$
15	758.0	23.3	$114.4^{+27.6}_{-21.3}$	14	$-4.25^{+0.36}_{-0.25}$	$0.340^{+0.064}_{-0.047}$	$(1.37^{+0.26}_{-0.19})10^{50}$
16	989.6	23.8	$51.6^{+6.2}_{-6.9}$	51	$-2.63^{+0.28}_{-0.28}$	$0.200^{+0.129}_{-0.067}$	$(8.31^{+5.37}_{-2.78})10^{49}$
GRB 060206							
1	2.9	2.9	$4.12^{+0.20}_{-0.12}$	99	$-2.23^{+0.08}_{-0.08}$	$35.82^{+1.74}_{-6.15}$	$(6.02^{+0.31}_{-1.04})10^{52}$
2	6.3	0.7	$3.01^{+11.73}_{-2.98}$	12	$-2.66^{+1.26}_{-1.02}$	$14.29^{+224.97}_{-11.59}$	$(2.45^{+51.31}_{-2.01})10^{52}$
GRB 060210							
1	6.7	6.7	$13.7^{+11.6}_{-3.4}$	102	$-2.06^{+0.57}_{-0.54}$	$9.65^{+3.40}_{-2.77}$	$(1.50^{+0.63}_{-0.44})10^{52}$
2	166.7	14.3	$19.8^{+4.7}_{-6.2}$	102	$-1.64^{+0.39}_{-0.47}$	$13.01^{+6.31}_{-2.53}$	$(2.10^{+1.18}_{-0.47})10^{52}$

Pulse	T_{peak} [s]	T_{rise} [s]	T_f [s]	E_f [keV]	α	F_f [10^{-8} ergs s^{-1} cm^{-2}]	L_f [ergs s^{-1}]
3	184.8	2.4	$36.5^{+6.1}_{-4.8}$	102	$-1.51^{+0.28}_{-0.23}$	$15.31^{+2.99}_{-2.60}$	$(2.48^{+0.60}_{-0.47})10^{52}$
4	191.4	3.8	$3.88^{+2.79}_{-2.22}$	102	$-0.50^{+0.00}_{-0.69}$	$28.79^{+23.52}_{-10.69}$	$(5.67^{+4.63}_{-2.57})10^{52}$
5	202.3	0.5	$15.3^{+6.6}_{-3.1}$	102	$-2.54^{+0.41}_{-0.45}$	$16.11^{+13.49}_{-4.90}$	$(2.37^{+2.20}_{-0.71})10^{52}$
6	213.2	2.7	$20.7^{+14.2}_{-8.0}$	102	$-2.36^{+0.95}_{-0.71}$	$6.85^{+7.19}_{-2.20}$	$(1.05^{+1.26}_{-0.29})10^{52}$
7	225.6	1.3	$8.8^{+0.9}_{-2.1}$	102	$-1.62^{+0.30}_{-0.27}$	$33.35^{+11.59}_{-4.56}$	$(5.25^{+2.09}_{-0.83})10^{52}$
8	318.4	8.2	$22.9^{+7.6}_{-4.1}$	102	$-2.40^{+0.11}_{-0.13}$	$2.55^{+0.84}_{-0.76}$	$(3.92^{+1.30}_{-1.16})10^{51}$
9	332.3	3.6	$31.3^{+8.6}_{-5.7}$	102	$-2.37^{+0.12}_{-0.14}$	$1.39^{+0.57}_{-0.45}$	$(2.07^{+0.85}_{-0.67})10^{51}$
10	370.4	26.3	$83.7^{+26.9}_{-20.4}$	102	$-4.15^{+0.45}_{-0.35}$	$0.0737^{+0.0220}_{-0.0151}$	$(1.74^{+0.85}_{-0.57})10^{50}$
11	397.7	5.3	$38.7^{+4.1}_{-4.9}$	102	$-2.46^{+0.10}_{-0.11}$	$1.33^{+0.37}_{-0.31}$	$(1.98^{+0.55}_{-0.46})10^{51}$
12	430.0	22.4	$22.6^{+1.8}_{-1.4}$	102	$-2.48^{+0.07}_{-0.07}$	$1.45^{+0.29}_{-0.26}$	$(2.42^{+0.48}_{-0.43})10^{51}$
13	453.1	20.9	$110.6^{+25.4}_{-20.6}$	13	$-4.28^{+0.39}_{-0.22}$	$0.131^{+0.030}_{-0.022}$	$(3.30^{+1.10}_{-0.92})10^{50}$
14	555.4	26.8	$352.3^{+104.0}_{-219.6}$	11	$-5.59^{+1.65}_{-1.09}$	$0.0757^{+0.0121}_{-0.0750}$	$(3.02^{+0.71}_{-3.01})10^{50}$
15	594.8	15.2	$181.1^{+21.6}_{-14.5}$	102	$-3.48^{+0.10}_{-0.12}$	$0.212^{+0.020}_{-0.020}$	$(3.85^{+0.54}_{-0.47})10^{50}$
GRB 060223A							
1	3.0	3.0	$6.4^{+0.3}_{-0.2}$	92	$-2.29^{+0.21}_{-0.22}$	$19.24^{+2.77}_{-2.15}$	$(3.94^{+0.59}_{-0.43})10^{52}$
2	7.1	0.2	$6.6^{+4.5}_{-2.3}$	92	$-2.01^{+0.74}_{-0.71}$	$10.22^{+19.54}_{-4.25}$	$(2.01^{+4.19}_{-0.82})10^{52}$
3	1476.3	285.4	$526.1^{+174.1}_{-174.1}$	34	$-2.57^{+0.42}_{-0.41}$	$0.0078^{+0.0065}_{-0.0033}$	$(1.62^{+1.56}_{-0.71})10^{49}$
GRB 060418							
1	5.6	5.6	$13.1^{+7.9}_{-1.4}$	201	$-2.47^{+0.17}_{-0.17}$	$29.25^{+3.35}_{-3.08}$	$(4.44^{+0.71}_{-0.60})10^{51}$
2	12.3	5.0	$17.0^{+1.0}_{-1.1}$	201	$-2.02^{+0.10}_{-0.10}$	$50.14^{+3.83}_{-4.18}$	$(8.59^{+0.97}_{-0.96})10^{51}$
3	17.4	1.8	$9.4^{+3.5}_{-2.2}$	201	$-2.68^{+0.29}_{-0.32}$	$28.45^{+11.59}_{-6.25}$	$(4.13^{+2.04}_{-1.10})10^{51}$
4	27.0	2.0	$5.3^{+2.6}_{-1.2}$	201	$-2.99^{+0.58}_{-0.18}$	$27.22^{+40.48}_{-14.82}$	$(3.73^{+6.69}_{-2.10})10^{51}$

Pulse	T_{peak} [s]	T_{rise} [s]	T_f [s]	E_f [keV]	α	F_f [10^{-8} ergs s^{-1} cm^{-2}]	L_f [ergs s^{-1}]
5	33.4	1.0	$9.7^{+2.0}_{-1.8}$	201	$-3.03^{+0.28}_{-0.25}$	$46.74^{+24.74}_{-17.93}$	$(6.21^{+3.83}_{-2.59})10^{51}$
6	36.2	0.2	$1.84^{+0.63}_{-0.32}$	201	$-2.34^{+0.13}_{-0.17}$	$118.2^{+18.4}_{-22.8}$	$(1.82^{+0.36}_{-0.41})10^{52}$
7	45.2	1.1	$16.4^{+5.8}_{-2.8}$	201	$-3.80^{+0.35}_{-0.59}$	$59.88^{+207.08}_{-53.98}$	$(6.71^{+26.18}_{-6.15})10^{51}$
8	68.7	3.8	$109.9^{+15.1}_{-14.3}$	201	$-3.83^{+0.16}_{-0.18}$	$2.09^{+0.40}_{-0.35}$	$(2.19^{+0.54}_{-0.46})10^{50}$
9	142.4	11.3	$23.7^{+1.5}_{-1.1}$	201	$-2.85^{+0.05}_{-0.05}$	$5.13^{+0.55}_{-0.54}$	$(7.21^{+0.85}_{-0.82})10^{50}$
GRB 060502A							
1	2.5	2.5	$8.7^{+1.5}_{-1.3}$	199	$-1.92^{+0.28}_{-0.27}$	$18.91^{+4.11}_{-3.17}$	$(3.39^{+1.20}_{-0.80})10^{51}$
2	6.7	3.3	$5.9^{+1.1}_{-1.0}$	199	$-1.55^{+0.22}_{-0.21}$	$32.16^{+7.83}_{-5.49}$	$(6.79^{+2.60}_{-1.63})10^{51}$
3	9.7	0.5	$5.1^{+4.3}_{-5.0}$	199	$-2.86^{+0.55}_{-0.64}$	$19.62^{+28.78}_{-6.64}$	$(2.75^{+4.84}_{-1.17})10^{51}$
4	12.5	1.8	$10.6^{+3.3}_{-2.1}$	199	$-2.01^{+0.32}_{-0.32}$	$15.43^{+3.70}_{-3.34}$	$(2.71^{+1.06}_{-0.77})10^{51}$
5	18.3	2.3	$7.6^{+2.9}_{-1.8}$	199	$-3.67^{+0.08}_{-0.56}$	$89.46^{+193.78}_{-88.56}$	$(1.08^{+2.40}_{-1.07})10^{52}$
6	44.3	6.0	$16.3^{+1.8}_{-2.4}$	199	$-4.68^{+0.33}_{-0.18}$	$133.8^{+79.9}_{-64.3}$	$(1.28^{+0.96}_{-0.58})10^{52}$
7	128.3	13.1	$355.4^{+229.3}_{-86.3}$	199	$-4.50^{+0.52}_{-0.00}$	$0.0321^{+0.0163}_{-0.0116}$	$(2.91^{+2.17}_{-1.06})10^{48}$
GRB 060522							
1	4.2	4.2	$22.7^{+5.4}_{-4.7}$	82	$-2.45^{+0.39}_{-0.37}$	$4.43^{+2.05}_{-1.18}$	$(1.26^{+0.67}_{-0.34})10^{52}$
2	33.5	1.1	$8.4^{+7.9}_{-3.0}$	82	$-1.44^{+0.94}_{-0.79}$	$6.77^{+9.27}_{-3.94}$	$(2.00^{+3.23}_{-1.19})10^{52}$
3	64.1	21.2	$26.6^{+8.2}_{-2.6}$	82	$-2.51^{+0.19}_{-0.19}$	$3.00^{+0.74}_{-0.94}$	$(8.84^{+2.43}_{-2.83})10^{51}$
GRB 060526							
1	3.0	3.0	$3.00^{+0.25}_{-0.06}$	119	$-2.17^{+0.29}_{-0.30}$	$19.81^{+4.15}_{-3.70}$	$(1.97^{+0.48}_{-0.39})10^{52}$
2	9.4	2.6	$14.8^{+2.7}_{-1.7}$	119	$-2.91^{+0.19}_{-0.20}$	$11.54^{+5.65}_{-4.25}$	$(1.11^{+0.58}_{-0.42})10^{52}$
3	248.7	10.0	$10.1^{+2.0}_{-0.9}$	119	$-2.33^{+0.05}_{-0.05}$	$4.10^{+0.70}_{-0.66}$	$(4.12^{+0.71}_{-0.67})10^{51}$
4	251.4	2.2	$23.0^{+2.7}_{-2.2}$	119	$-2.46^{+0.04}_{-0.04}$	$7.21^{+0.95}_{-0.91}$	$(6.67^{+0.89}_{-0.84})10^{51}$

Pulse	T_{peak} [s]	T_{rise} [s]	T_f [s]	E_f [keV]	α	F_f [10^{-8} ergs s^{-1} cm^{-2}]	L_f [ergs s^{-1}]
5	257.3	0.5	$50.7^{+6.4}_{-5.4}$	119	$-2.84^{+0.08}_{-0.09}$	$2.17^{+0.50}_{-0.45}$	$(2.06^{+0.49}_{-0.44})10^{51}$
6	304.6	13.8	$20.6^{+2.8}_{-1.3}$	119	$-2.48^{+0.09}_{-0.09}$	$4.11^{+1.20}_{-1.07}$	$(3.96^{+1.17}_{-1.04})10^{51}$
7	323.6	14.6	$83.3^{+15.0}_{-8.8}$	7.37	$-3.89^{+0.21}_{-0.34}$	$0.519^{+0.050}_{-0.051}$	$(6.15^{+1.10}_{-0.84})10^{50}$
GRB 060604							
1	11.5	11.5	$12.4^{+0.3}_{-0.2}$	136	$-3.18^{+0.52}_{-0.44}$	$5.36^{+2.76}_{-5.31}$	$(5.22^{+2.96}_{-5.17})10^{51}$
2	43.3	7.8	$11.7^{+0.7}_{-0.9}$	136	$-2.78^{+0.64}_{-0.77}$	$6.76^{+10.83}_{-2.12}$	$(4.19^{+7.19}_{-1.19})10^{51}$
3	168.6	19.1	$68.5^{+3.8}_{-2.6}$	136	$-3.20^{+0.06}_{-0.07}$	$0.674^{+0.056}_{-0.050}$	$(4.20^{+0.37}_{-0.32})10^{50}$
4	201.7	3.6	$31.5^{+19.3}_{-5.1}$	136	$-3.65^{+0.22}_{-0.43}$	$0.414^{+0.086}_{-0.065}$	$(2.64^{+0.68}_{-0.46})10^{50}$
GRB 060605							
1	15.8	15.8	$40.0^{+20.7}_{-12.9}$	104	$-2.19^{+0.60}_{-0.55}$	$1.44^{+0.54}_{-0.51}$	$(2.06^{+0.91}_{-0.73})10^{51}$
2	67.2	3.8	$22.1^{+2.7}_{-2.1}$	104	$-1.72^{+0.31}_{-0.26}$	$6.53^{+1.51}_{-1.22}$	$(9.74^{+2.72}_{-1.99})10^{51}$
3	73.1	0.7	$18.8^{+14.6}_{-7.1}$	104	$-2.24^{+0.81}_{-0.78}$	$2.90^{+2.99}_{-1.61}$	$(4.04^{+4.78}_{-2.16})10^{51}$
GRB 060607A							
1	5.8	5.8	$18.8^{+0.5}_{-0.4}$	122	$-1.80^{+0.09}_{-0.09}$	$21.24^{+1.32}_{-1.22}$	$(1.94^{+0.15}_{-0.13})10^{52}$
2	27.8	8.4	$32.0^{+4.3}_{-3.6}$	122	$-2.94^{+0.09}_{-0.09}$	$5.92^{+1.38}_{-1.34}$	$(5.14^{+1.25}_{-1.19})10^{51}$
3	103.2	2.1	$17.9^{+5.5}_{-1.9}$	122	$-2.16^{+0.12}_{-0.22}$	$4.17^{+1.74}_{-2.97}$	$(3.61^{+1.56}_{-2.58})10^{51}$
4	179.2	14.8	$181.5^{+64.0}_{-29.7}$	122	$-3.06^{+0.20}_{-0.30}$	$0.0918^{+0.0340}_{-0.0392}$	$(7.98^{+3.42}_{-3.48})10^{49}$
5	270.1	41.6	$67.8^{+2.5}_{-2.9}$	122	$-2.59^{+0.05}_{-0.05}$	$0.927^{+0.134}_{-0.120}$	$(8.09^{+1.18}_{-1.05})10^{50}$
GRB 060614							
1	0.0	0.04	$4.27^{+0.91}_{-0.65}$	444	$-2.28^{+0.16}_{-0.16}$	$135.4^{+20.0}_{-14.8}$	$(7.93^{+2.40}_{-1.65})10^{49}$
2	2.0	1.3	$2.47^{+0.58}_{-0.24}$	444	$-2.45^{+0.21}_{-0.19}$	$90.10^{+13.83}_{-12.79}$	$(4.65^{+1.59}_{-1.13})10^{49}$
3	3.9	0.9	$1.02^{+0.38}_{-1.01}$	444	$-2.17^{+0.48}_{-0.42}$	$73.11^{+39.91}_{-14.62}$	$(4.67^{+6.44}_{-1.92})10^{49}$

Pulse	T_{peak} [s]	T_{rise} [s]	T_f [s]	E_f [keV]	α	F_f [10^{-8} ergs s^{-1} cm^{-2}]	L_f [ergs s^{-1}]
4	13.4	4.0	$12.6^{+1.4}_{-1.5}$	444	$-2.64^{+0.17}_{-0.17}$	$43.92^{+6.80}_{-5.17}$	$(2.00^{+0.60}_{-0.43})10^{49}$
5	19.1	1.1	$3.94^{+1.05}_{-0.48}$	444	$-3.11^{+0.09}_{-0.33}$	$109.3^{+96.2}_{-36.4}$	$(3.46^{+3.53}_{-1.76})10^{49}$
6	22.3	2.1	$4.42^{+0.45}_{-1.16}$	444	$-2.75^{+0.22}_{-0.30}$	$53.58^{+25.22}_{-7.38}$	$(2.24^{+1.58}_{-0.69})10^{49}$
7	28.2	2.5	$12.7^{+1.6}_{-1.6}$	444	$-2.86^{+0.11}_{-0.25}$	$55.29^{+127.74}_{-6.42}$	$(2.13^{+5.50}_{-0.57})10^{49}$
8	33.4	3.1	$8.9^{+1.2}_{-0.6}$	444	$-3.10^{+0.12}_{-0.07}$	$98.72^{+27.57}_{-19.03}$	$(3.17^{+1.30}_{-0.75})10^{49}$
9	40.2	3.1	$15.1^{+0.8}_{-0.6}$	444	$-3.07^{+0.09}_{-0.05}$	$117.0^{+11.2}_{-19.5}$	$(3.83^{+0.69}_{-0.76})10^{49}$
10	46.6	1.9	$11.0^{+1.0}_{-0.7}$	444	$-3.10^{+0.14}_{-0.03}$	$94.31^{+14.02}_{-20.58}$	$(3.01^{+0.85}_{-0.72})10^{49}$
11	48.9	0.6	$24.9^{+1.7}_{-1.2}$	444	$-2.89^{+0.06}_{-0.04}$	$60.44^{+3.78}_{-7.00}$	$(2.28^{+0.25}_{-0.32})10^{49}$
12	64.6	2.5	$11.9^{+0.9}_{-0.7}$	444	$-3.11^{+0.08}_{-0.08}$	$57.39^{+10.95}_{-8.64}$	$(1.82^{+0.49}_{-0.38})10^{49}$
13	70.1	2.0	$6.7^{+1.4}_{-0.9}$	444	$-3.41^{+0.36}_{-0.19}$	$46.91^{+25.31}_{-46.44}$	$(1.15^{+1.28}_{-1.14})10^{49}$
14	78.2	3.5	$8.9^{+0.8}_{-0.8}$	444	$-2.99^{+0.09}_{-0.13}$	$30.88^{+9.28}_{-3.76}$	$(1.09^{+0.43}_{-0.23})10^{49}$
15	83.3	1.0	$4.39^{+1.42}_{-0.64}$	444	$-2.98^{+0.21}_{-0.24}$	$25.64^{+15.93}_{-6.67}$	$(9.15^{+8.14}_{-3.61})10^{48}$
16	86.6	1.6	$6.1^{+2.3}_{-1.0}$	444	$-2.85^{+0.18}_{-0.17}$	$18.19^{+6.46}_{-4.09}$	$(7.12^{+3.79}_{-2.24})10^{48}$
17	91.7	1.7	$3.08^{+1.06}_{-0.47}$	444	$-2.94^{+0.24}_{-0.21}$	$16.94^{+7.89}_{-4.16}$	$(6.25^{+4.56}_{-2.27})10^{48}$
18	97.2	1.5	$2.35^{+0.72}_{-0.30}$	444	$-2.50^{+0.15}_{-0.10}$	$17.21^{+3.06}_{-2.83}$	$(8.60^{+2.64}_{-1.90})10^{48}$
19	101.1	2.1	$14.6^{+2.2}_{-1.8}$	26	$-1.92^{+0.10}_{-0.07}$	$10.16^{+1.39}_{-1.04}$	$(3.92^{+0.56}_{-0.42})10^{48}$
20	106.9	1.9	$29.6^{+5.0}_{-4.0}$	26	$-2.15^{+0.10}_{-0.08}$	$5.78^{+0.93}_{-0.82}$	$(2.19^{+0.38}_{-0.33})10^{48}$
21	121.1	2.0	$28.7^{+6.3}_{-4.4}$	38	$-2.12^{+0.16}_{-0.10}$	$5.10^{+1.05}_{-0.96}$	$(1.99^{+0.44}_{-0.39})10^{48}$
22	145.6	20.7	$115.1^{+7.7}_{-6.6}$	1.29	$-1.04^{+0.12}_{-0.13}$	$1.70^{+0.16}_{-0.16}$	$(5.78^{+0.66}_{-0.66})10^{47}$
GRB 060707							
1	16.6	16.6	$44.6^{+10.8}_{-5.9}$	113	$-2.57^{+0.21}_{-0.20}$	$3.73^{+1.21}_{-1.13}$	$(4.15^{+1.40}_{-1.25})10^{51}$
2	46.6	5.2	$11.9^{+2.9}_{-1.3}$	113	$-2.05^{+0.33}_{-0.32}$	$12.41^{+2.51}_{-2.35}$	$(1.43^{+0.35}_{-0.29})10^{52}$

Pulse	T_{peak} [s]	T_{rise} [s]	T_f [s]	E_f [keV]	α	F_f [10^{-8} ergs s^{-1} cm^{-2}]	L_f [ergs s^{-1}]
3	50.6	1.0	$10.2^{+14.4}_{-10.1}$	113	$-2.86^{+1.60}_{-1.53}$	$9.90^{+9.50}_{-9.80}$	$(1.09^{+1.97}_{-1.07})10^{52}$
4	59.9	3.0	$18.0^{+17.6}_{-9.6}$	113	$-1.47^{+0.97}_{-0.94}$	$6.41^{+6.24}_{-6.34}$	$(7.86^{+11.62}_{-7.79})10^{51}$
GRB 060714							
1	6.3	6.3	$12.1^{+1.5}_{-1.7}$	135	$-2.26^{+0.60}_{-0.58}$	$7.75^{+2.38}_{-1.81}$	$(5.06^{+2.18}_{-1.28})10^{51}$
2	15.4	6.7	$14.3^{+4.1}_{-3.0}$	135	$-1.87^{+0.44}_{-0.42}$	$10.65^{+3.43}_{-2.39}$	$(7.31^{+3.28}_{-1.94})10^{51}$
3	25.6	4.6	$14.5^{+7.4}_{-8.7}$	135	$-2.89^{+0.95}_{-0.93}$	$7.88^{+19.93}_{-3.76}$	$(5.02^{+14.00}_{-2.21})10^{51}$
4	61.1	0.3	$7.7^{+1.5}_{-1.7}$	135	$-2.09^{+0.00}_{-0.94}$	$12.77^{+16.09}_{-8.00}$	$(8.25^{+10.39}_{-5.29})10^{51}$
5	90.2	4.1	$12.0^{+1.2}_{-0.8}$	135	$-2.40^{+0.11}_{-0.10}$	$15.19^{+1.47}_{-1.40}$	$(9.77^{+1.04}_{-0.96})10^{51}$
6	107.2	5.8	$6.6^{+0.2}_{-0.1}$	135	$-2.53^{+0.10}_{-0.09}$	$12.74^{+1.13}_{-1.13}$	$(8.37^{+0.80}_{-0.77})10^{51}$
7	113.3	0.2	$1.92^{+0.07}_{-0.05}$	135	$-1.61^{+0.31}_{-0.18}$	$64.02^{+30.49}_{-32.65}$	$(4.62^{+2.73}_{-2.44})10^{52}$
8	125.9	5.3	$19.3^{+3.1}_{-4.6}$	135	$-2.39^{+0.10}_{-0.11}$	$2.20^{+1.27}_{-0.61}$	$(1.42^{+0.84}_{-0.40})10^{51}$
9	150.3	13.3	$26.1^{+2.8}_{-1.8}$	135	$-2.95^{+0.07}_{-0.08}$	$1.17^{+0.17}_{-0.15}$	$(7.47^{+1.11}_{-0.95})10^{50}$
10	187.6	10.2	$22.9^{+1.2}_{-0.7}$	135	$-3.28^{+0.10}_{-0.11}$	$0.627^{+0.073}_{-0.063}$	$(4.07^{+0.51}_{-0.43})10^{50}$
GRB 060729							
1	8.2	8.2	$8.6^{+0.2}_{-2.0}$	325	$-2.56^{+0.94}_{-0.64}$	$14.49^{+6.10}_{-14.35}$	$(1.94^{+2.93}_{-1.92})10^{50}$
2	73.1	3.8	$20.3^{+3.0}_{-2.8}$	325	$-2.10^{+0.20}_{-0.21}$	$15.59^{+2.26}_{-2.19}$	$(2.53^{+0.76}_{-0.59})10^{50}$
3	79.8	4.0	$15.8^{+3.1}_{-2.6}$	325	$-2.87^{+0.28}_{-0.29}$	$14.51^{+7.91}_{-3.15}$	$(1.61^{+1.23}_{-0.54})10^{50}$
4	92.6	4.0	$16.7^{+1.5}_{-1.3}$	325	$-3.16^{+0.14}_{-0.30}$	$30.36^{+33.22}_{-7.29}$	$(2.86^{+3.62}_{-1.07})10^{50}$
5	127.0	4.7	$30.2^{+4.2}_{-3.3}$	325	$-3.58^{+0.11}_{-0.15}$	$11.26^{+1.49}_{-1.25}$	$(8.01^{+1.80}_{-1.64})10^{49}$
6	177.9	18.6	$112.2^{+8.9}_{-9.9}$	1.00	$-4.41^{+0.37}_{-0.09}$	$2.64^{+0.33}_{-0.42}$	$(5.70^{+2.51}_{-1.18})10^{48}$
GRB 060801							
1	0.4	0.4	$0.435^{+0.086}_{-0.068}$	235	$-1.31^{+0.32}_{-0.29}$	$68.24^{+33.12}_{-19.88}$	$(9.07^{+7.64}_{-3.64})10^{51}$

Pulse	T_{peak} [s]	T_{rise} [s]	T_f [s]	E_f [keV]	α	F_f [10^{-8} ergs s^{-1} cm^{-2}]	L_f [ergs s^{-1}]
GRB 060814							
1	15.8	15.8	$15.9^{+0.3}_{-0.3}$	272	$-2.27^{+0.04}_{-0.04}$	$47.92^{+1.56}_{-1.51}$	$(2.01^{+0.10}_{-0.09})10^{51}$
2	22.2	3.2	$9.6^{+0.4}_{-0.4}$	215	$-2.13^{+0.05}_{-0.05}$	$84.63^{+3.57}_{-3.92}$	$(3.37^{+0.20}_{-0.21})10^{51}$
3	75.4	8.9	$26.7^{+0.6}_{-0.5}$	205	$-2.38^{+0.02}_{-0.02}$	$43.24^{+1.06}_{-1.07}$	$(1.60^{+0.05}_{-0.05})10^{51}$
4	134.4	7.5	$35.2^{+4.0}_{-6.7}$	167	$-2.25^{+0.05}_{-0.05}$	$8.75^{+1.31}_{-0.83}$	$(3.21^{+0.52}_{-0.33})10^{50}$
5	155.8	77.4	$236.1^{+17.0}_{-17.3}$	2.90	$-2.58^{+0.10}_{-0.10}$	$0.433^{+0.031}_{-0.028}$	$(1.20^{+0.12}_{-0.11})10^{49}$
GRB 060904B							
1	2.3	2.3	$5.3^{+0.1}_{-0.2}$	294	$-2.06^{+0.12}_{-0.12}$	$47.03^{+4.76}_{-4.02}$	$(1.42^{+0.26}_{-0.20})10^{51}$
2	11.0	3.3	$14.7^{+5.2}_{-2.6}$	294	$-3.15^{+0.41}_{-0.47}$	$12.95^{+18.57}_{-7.33}$	$(2.37^{+4.56}_{-1.59})10^{50}$
3	159.2	18.0	$31.4^{+1.0}_{-0.6}$	294	$-2.66^{+0.04}_{-0.04}$	$4.17^{+0.47}_{-0.44}$	$(9.68^{+1.27}_{-1.18})10^{49}$
4	174.6	17.9	$81.0^{+3.5}_{-5.9}$	1.78	$-1.85^{+0.17}_{-0.14}$	$2.00^{+0.17}_{-0.10}$	$(3.79^{+0.44}_{-0.28})10^{49}$
GRB 060906							
1	15.3	15.3	$15.5^{+1.3}_{-0.6}$	107	$-2.63^{+0.12}_{-0.11}$	$16.89^{+2.02}_{-1.72}$	$(2.62^{+0.33}_{-0.27})10^{52}$
2	26.1	0.6	$3.86^{+3.84}_{-1.10}$	107	$-2.77^{+0.53}_{-0.62}$	$16.13^{+30.46}_{-6.03}$	$(2.13^{+4.81}_{-0.81})10^{52}$
3	44.7	5.4	$7.5^{+0.5}_{-0.2}$	107	$-3.18^{+0.84}_{-0.94}$	$16.73^{+49.32}_{-13.85}$	$(2.65^{+11.26}_{-2.22})10^{52}$
4	7208.5	1072.7	33155^{+14174}_{-9647}	6.97	$-2.39^{+0.31}_{-0.30}$	$0.0005^{+0.0001}_{-0.0001}$	$(6.44^{+1.44}_{-1.23})10^{47}$
GRB 060908							
1	2.8	2.8	$3.40^{+0.41}_{-0.13}$	173	$-2.21^{+0.20}_{-0.20}$	$25.13^{+3.94}_{-3.43}$	$(7.07^{+1.49}_{-1.19})10^{51}$
2	6.0	4.6	$4.91^{+0.64}_{-0.46}$	173	$-1.95^{+0.14}_{-0.14}$	$32.98^{+4.32}_{-3.81}$	$(9.88^{+1.74}_{-1.44})10^{51}$
3	9.9	2.9	$2.96^{+0.76}_{-0.42}$	173	$-1.85^{+0.15}_{-0.15}$	$43.36^{+6.87}_{-7.67}$	$(1.34^{+0.28}_{-0.28})10^{52}$
4	18.9	1.5	$2.83^{+0.37}_{-0.29}$	173	$-1.86^{+0.20}_{-0.20}$	$43.36^{+7.85}_{-6.67}$	$(1.33^{+0.34}_{-0.26})10^{52}$
GRB 060912A							

Pulse	T_{peak} [s]	T_{rise} [s]	T_f [s]	E_f [keV]	α	F_f [10^{-8} ergs s^{-1} cm^{-2}]	L_f [ergs s^{-1}]
1	1.0	1.0	$2.68^{+0.20}_{-0.30}$	258	$-2.60^{+0.10}_{-0.11}$	$147.7^{+14.9}_{-11.1}$	$(6.97^{+0.96}_{-0.74})10^{51}$
2	6.5	1.9	$16.9^{+10.5}_{-4.7}$	258	$-2.20^{+0.68}_{-0.64}$	$11.05^{+3.95}_{-4.49}$	$(5.98^{+5.58}_{-3.14})10^{50}$
GRB 060926							
1	1.3	1.3	$7.3^{+0.5}_{-0.5}$	119	$-3.06^{+0.58}_{-0.18}$	$31.18^{+12.53}_{-17.25}$	$(2.99^{+1.31}_{-1.69})10^{52}$
2	435.2	301.9	$4290.7^{+1029.4}_{-752.9}$	115	$-2.75^{+0.19}_{-0.24}$	$0.0078^{+0.0031}_{-0.0018}$	$(7.51^{+3.17}_{-1.74})10^{48}$
GRB 060927							
1	0.1	0.08	$5.3^{+0.7}_{-1.2}$	76	$-1.63^{+0.17}_{-0.13}$	$37.33^{+12.63}_{-3.30}$	$(1.29^{+0.45}_{-0.12})10^{53}$
2	5.2	0.06	$2.35^{+1.61}_{-0.33}$	76	$-2.44^{+0.42}_{-0.49}$	$20.16^{+41.17}_{-5.11}$	$(7.18^{+16.64}_{-1.86})10^{52}$
3	19.2	2.3	$6.1^{+1.2}_{-0.9}$	76	$-2.26^{+0.31}_{-0.33}$	$9.45^{+2.69}_{-1.57}$	$(3.39^{+1.06}_{-0.56})10^{52}$
4	24.1	0.3	$0.336^{+1.938}_{-0.326}$	76	$-1.27^{+0.77}_{-1.21}$	$7.45^{+43.19}_{-7.38}$	$(2.75^{+17.21}_{-2.72})10^{52}$
GRB 061006							
1	1.2	1.2	$3.31^{+0.16}_{-0.12}$	348	$-1.93^{+0.17}_{-0.08}$	$161.8^{+62.7}_{-12.1}$	$(1.83^{+1.05}_{-0.23})10^{51}$
2	35.7	15.8	$22.5^{+2.4}_{-5.3}$	348	$-2.38^{+0.44}_{-0.48}$	$4.13^{+1.56}_{-0.88}$	$(3.58^{+2.90}_{-1.38})10^{49}$
GRB 061021							
1	2.2	2.2	$5.3^{+0.2}_{-0.2}$	371	$-2.17^{+0.06}_{-0.06}$	$98.60^{+4.96}_{-4.73}$	$(5.63^{+0.52}_{-0.47})10^{50}$
2	10.8	0.5	$49.0^{+7.9}_{-7.2}$	371	$-2.92^{+0.09}_{-0.10}$	$5.12^{+1.58}_{-1.48}$	$(1.90^{+0.73}_{-0.63})10^{49}$
GRB 061110A							
1	21.9	21.9	$40.5^{+2.2}_{-1.5}$	284	$-2.78^{+0.08}_{-0.08}$	$8.15^{+0.74}_{-0.74}$	$(2.16^{+0.28}_{-0.26})10^{50}$
2	141.2	65.3	$172.6^{+9.2}_{-7.6}$	3.54	$-4.29^{+0.10}_{-0.10}$	$0.540^{+0.029}_{-0.027}$	$(5.71^{+0.65}_{-0.61})10^{48}$
GRB 061121							
1	3.4	3.4	$4.63^{+0.87}_{-0.52}$	216	$-2.47^{+0.10}_{-0.11}$	$26.34^{+2.36}_{-2.06}$	$(2.96^{+0.35}_{-0.30})10^{51}$
2	62.4	1.0	$9.2^{+0.4}_{-0.3}$	216	$-2.28^{+0.03}_{-0.03}$	$101.7^{+3.3}_{-3.3}$	$(1.20^{+0.05}_{-0.05})10^{52}$

Pulse	T_{peak} [s]	T_{rise} [s]	T_f [s]	E_f [keV]	α	F_f [10^{-8} ergs s^{-1} cm^{-2}]	L_f [ergs s^{-1}]
3	69.2	2.2	$6.8^{+0.2}_{-0.2}$	216	$-2.12^{+0.04}_{-0.03}$	$144.8^{+5.5}_{-3.7}$	$(1.77^{+0.09}_{-0.06})10^{52}$
4	73.9	2.3	$3.47^{+0.10}_{-0.09}$	216	$-2.20^{+0.03}_{-0.03}$	$152.8^{+5.8}_{-4.8}$	$(1.86^{+0.09}_{-0.07})10^{52}$
5	75.6	1.9	$1.96^{+0.07}_{-0.12}$	216	$-1.56^{+0.03}_{-0.03}$	$429.5^{+103.3}_{-15.5}$	$(3.16^{+0.81}_{-0.15})10^{53}$
6	93.4	3.1	$8.0^{+2.3}_{-3.3}$	216	$-2.58^{+0.19}_{-0.13}$	$6.26^{+2.13}_{-1.45}$	$(6.81^{+2.75}_{-1.74})10^{50}$
7	110.6	4.7	$22.6^{+2.7}_{-1.5}$	216	$-3.84^{+0.17}_{-0.19}$	$2.43^{+0.55}_{-0.53}$	$(1.81^{+0.54}_{-0.49})10^{50}$
GRB 061222A							
1	5.3	5.3	$11.7^{+1.6}_{-0.6}$	162	$-2.04^{+0.47}_{-0.49}$	$9.50^{+2.82}_{-2.77}$	$(3.49^{+1.64}_{-1.21})10^{51}$
2	30.0	1.0	$5.2^{+1.1}_{-0.9}$	162	$-2.28^{+0.19}_{-0.19}$	$35.49^{+4.78}_{-4.20}$	$(1.24^{+0.22}_{-0.18})10^{52}$
3	64.3	7.3	$12.2^{+0.6}_{-0.5}$	162	$-2.19^{+0.13}_{-0.13}$	$16.36^{+1.38}_{-1.24}$	$(5.85^{+0.65}_{-0.56})10^{51}$
4	78.3	4.9	$10.4^{+1.2}_{-0.8}$	162	$-1.95^{+0.12}_{-0.13}$	$21.00^{+2.19}_{-1.90}$	$(7.89^{+1.07}_{-0.92})10^{51}$
5	82.1	0.1	$14.2^{+1.7}_{-1.5}$	162	$-3.14^{+0.12}_{-0.13}$	$21.05^{+7.07}_{-5.50}$	$(6.83^{+2.37}_{-1.83})10^{51}$
6	86.1	0.2	$2.21^{+0.55}_{-0.37}$	162	$-1.20^{+0.15}_{-0.18}$	$116.8^{+20.8}_{-24.7}$	$(5.35^{+1.37}_{-1.40})10^{52}$
7	88.6	2.0	$4.73^{+0.44}_{-0.50}$	162	$-1.67^{+0.13}_{-0.13}$	$49.67^{+5.93}_{-5.39}$	$(2.00^{+0.33}_{-0.28})10^{52}$
8	91.4	1.2	$3.24^{+0.18}_{-0.16}$	162	$-1.67^{+0.06}_{-0.06}$	$159.9^{+9.7}_{-9.2}$	$(6.44^{+0.51}_{-0.46})10^{52}$
9	94.3	0.2	$2.60^{+1.39}_{-0.88}$	162	$-1.87^{+0.33}_{-0.39}$	$39.04^{+14.45}_{-12.85}$	$(1.50^{+0.76}_{-0.57})10^{52}$
10	124.3	5.8	$59.7^{+8.0}_{-9.9}$	162	$-3.65^{+0.20}_{-0.18}$	$0.646^{+0.075}_{-0.070}$	$(1.93^{+0.25}_{-0.23})10^{50}$
GRB 061222B							
1	5.6	5.6	$16.2^{+1.2}_{-0.9}$	115	$-2.27^{+0.27}_{-0.27}$	$19.82^{+2.58}_{-2.91}$	$(2.13^{+0.32}_{-0.33})10^{52}$
2	18.8	3.0	$12.2^{+2.3}_{-1.2}$	115	$-3.24^{+0.59}_{-0.58}$	$49.56^{+87.25}_{-48.41}$	$(5.57^{+12.06}_{-5.45})10^{52}$
3	30.2	0.5	$16.1^{+7.8}_{-6.6}$	115	$-2.09^{+0.32}_{-0.46}$	$20.55^{+17.41}_{-11.10}$	$(2.25^{+2.04}_{-1.24})10^{52}$
4	92.0	326.2	$329.5^{+95.9}_{-79.7}$	115	$-4.50^{+0.26}_{-0.00}$	$0.147^{+0.050}_{-0.042}$	$(7.18^{+2.41}_{-2.40})10^{52}$
GRB 070208							

Pulse	T_{peak} [s]	T_{rise} [s]	T_f [s]	E_f [keV]	α	F_f [10^{-8} ergs s^{-1} cm^{-2}]	L_f [ergs s^{-1}]
1	9.6	9.6	$15.9^{+1.5}_{-2.5}$	230	$-3.33^{+0.71}_{-1.17}$	$18.52^{+29.54}_{-18.34}$	$(1.26^{+2.78}_{-1.25})10^{51}$
2	46.8	4.0	$17.8^{+3.5}_{-2.7}$	230	$-2.55^{+0.46}_{-0.51}$	$10.75^{+7.27}_{-3.31}$	$(8.80^{+8.25}_{-3.50})10^{50}$
GRB 070306							
1	4.5	4.5	$15.0^{+5.1}_{-2.2}$	200	$-2.26^{+0.42}_{-0.43}$	$10.62^{+3.06}_{-2.69}$	$(1.70^{+0.80}_{-0.54})10^{51}$
2	15.3	4.6	$6.9^{+2.2}_{-2.2}$	200	$-1.92^{+0.91}_{-0.79}$	$12.14^{+9.20}_{-5.34}$	$(2.18^{+3.70}_{-1.18})10^{51}$
3	87.1	3.8	$16.6^{+2.4}_{-1.6}$	200	$-2.41^{+0.25}_{-0.25}$	$12.46^{+2.24}_{-1.85}$	$(1.92^{+0.50}_{-0.37})10^{51}$
4	95.5	1.8	$13.0^{+1.3}_{-1.0}$	200	$-2.50^{+0.11}_{-0.11}$	$34.19^{+2.97}_{-2.69}$	$(5.04^{+0.58}_{-0.50})10^{51}$
5	98.8	1.1	$12.2^{+0.9}_{-1.5}$	200	$-2.52^{+0.08}_{-0.11}$	$46.35^{+32.83}_{-2.55}$	$(6.92^{+5.12}_{-0.53})10^{51}$
6	121.8	0.3	$29.9^{+3.8}_{-3.5}$	200	$-3.28^{+0.09}_{-0.10}$	$13.05^{+3.90}_{-3.31}$	$(1.70^{+0.56}_{-0.46})10^{51}$
7	184.2	18.2	$45.7^{+3.7}_{-3.8}$	8.50	$-2.51^{+0.13}_{-0.13}$	$0.700^{+0.078}_{-0.067}$	$(9.68^{+1.19}_{-1.03})10^{49}$
GRB 070318							
1	3.8	3.8	$29.8^{+0.8}_{-1.0}$	272	$-2.24^{+0.07}_{-0.04}$	$23.31^{+12.41}_{-0.87}$	$(9.73^{+5.65}_{-0.52})10^{50}$
2	197.0	14.5	$34.4^{+30.4}_{-12.9}$	254	$-2.00^{+0.42}_{-0.40}$	$1.24^{+2.30}_{-1.23}$	$(5.67^{+14.53}_{-5.62})10^{49}$
3	271.6	43.3	$268.2^{+43.9}_{-25.6}$	184	$-3.04^{+0.12}_{-0.13}$	$0.155^{+0.031}_{-0.025}$	$(4.58^{+1.14}_{-0.94})10^{48}$
GRB 070419A							
1	13.6	13.6	$67.8^{+6.4}_{-6.4}$	254	$-3.52^{+0.08}_{-0.09}$	$10.55^{+3.35}_{-2.34}$	$(3.76^{+1.38}_{-0.96})10^{50}$
2	43.3	7.6	$39.1^{+6.4}_{-9.5}$	254	$-2.98^{+0.34}_{-0.37}$	$2.40^{+3.52}_{-0.92}$	$(1.09^{+1.92}_{-0.51})10^{50}$
3	95.6	36.1	$70.8^{+18.3}_{-13.7}$	254	$-2.64^{+0.14}_{-0.16}$	$0.994^{+0.390}_{-0.319}$	$(5.09^{+2.32}_{-1.81})10^{49}$
4	213.1	29.1	$211.2^{+45.9}_{-116.5}$	235	$-5.45^{+2.11}_{-0.95}$	$0.115^{+0.023}_{-0.062}$	$(1.52^{+3.84}_{-0.37})10^{48}$
GRB 070506							
1	2.8	2.8	$11.4^{+0.8}_{-1.1}$	151	$-2.42^{+0.27}_{-0.29}$	$11.67^{+2.55}_{-1.77}$	$(5.03^{+1.32}_{-0.87})10^{51}$
GRB 070521							

Pulse	T_{peak} [s]	T_{rise} [s]	T_f [s]	E_f [keV]	α	F_f [10^{-8} ergs s^{-1} cm^{-2}]	L_f [ergs s^{-1}]
1	3.3	3.3	$17.7^{+2.8}_{-2.7}$	322	$-2.90^{+0.28}_{-0.45}$	$19.14^{+24.95}_{-5.15}$	$(2.19^{+3.57}_{-0.95})10^{50}$
2	16.7	3.7	$6.0^{+0.2}_{-0.4}$	322	$-2.20^{+0.14}_{-0.15}$	$37.86^{+4.32}_{-3.65}$	$(6.20^{+1.29}_{-1.02})10^{50}$
3	33.7	6.7	$6.8^{+0.3}_{-0.3}$	322	$-1.97^{+0.06}_{-0.06}$	$85.64^{+5.24}_{-4.84}$	$(1.61^{+0.16}_{-0.15})10^{51}$
4	36.9	0.9	$1.41^{+0.24}_{-0.07}$	322	$-1.72^{+0.17}_{-0.18}$	$116.1^{+19.9}_{-20.6}$	$(2.57^{+0.87}_{-0.71})10^{51}$
5	39.6	1.3	$1.32^{+0.23}_{-0.13}$	322	$-1.86^{+0.10}_{-0.09}$	$137.9^{+20.4}_{-20.4}$	$(2.77^{+0.63}_{-0.55})10^{51}$
6	45.2	1.3	$1.83^{+0.13}_{-0.46}$	322	$-2.07^{+0.11}_{-0.11}$	$102.8^{+11.1}_{-7.5}$	$(1.80^{+0.34}_{-0.24})10^{51}$
7	50.2	1.7	$2.63^{+0.27}_{-0.13}$	322	$-2.60^{+0.08}_{-0.08}$	$73.52^{+5.17}_{-4.45}$	$(9.85^{+1.08}_{-0.93})10^{50}$
GRB 070529							
1	3.7	3.7	$5.1^{+0.6}_{-1.5}$	143	$-1.44^{+0.75}_{-0.55}$	$22.75^{+14.67}_{-7.08}$	$(1.45^{+1.64}_{-0.56})10^{52}$
2	12.4	4.6	$40.7^{+9.9}_{-7.7}$	143	$-1.18^{+0.22}_{-0.19}$	$21.04^{+6.24}_{-5.27}$	$(1.43^{+0.57}_{-0.42})10^{52}$
3	83.8	3.4	$4.97^{+5.65}_{-4.92}$	143	$-2.55^{+1.04}_{-1.22}$	$9.29^{+34.75}_{-4.91}$	$(4.90^{+22.53}_{-2.56})10^{51}$
4	127.2	11.1	$52.3^{+59.8}_{-51.8}$	143	$-4.50^{+0.75}_{-0.00}$	$0.184^{+0.413}_{-0.101}$	$(1.02^{+2.28}_{-0.58})10^{50}$
GRB 070721B							
1	8.5	8.5	$21.6^{+1.2}_{-0.9}$	108	$-1.52^{+0.16}_{-0.15}$	$23.28^{+2.95}_{-2.68}$	$(3.19^{+0.49}_{-0.42})10^{52}$
2	103.4	0.9	$49.5^{+12.6}_{-9.9}$	108	$-2.88^{+0.18}_{-0.19}$	$0.284^{+0.124}_{-0.099}$	$(3.62^{+1.74}_{-1.31})10^{50}$
3	282.3	22.4	$29.3^{+11.0}_{-10.7}$	108	$-2.03^{+0.13}_{-0.12}$	$1.57^{+0.53}_{-0.52}$	$(2.06^{+0.73}_{-0.70})10^{51}$
4	318.7	7.3	$9.7^{+0.3}_{-0.4}$	108	$-1.37^{+0.10}_{-0.09}$	$15.99^{+2.64}_{-2.40}$	$(2.27^{+0.42}_{-0.37})10^{52}$
5	351.6	13.9	$54.0^{+8.3}_{-15.0}$	108	$-2.49^{+0.23}_{-0.23}$	$0.254^{+0.222}_{-0.149}$	$(3.24^{+2.89}_{-1.90})10^{50}$
6	501.6	37.6	$227.9^{+192.3}_{-72.5}$	101	$-2.50^{+0.57}_{-0.45}$	$0.0964^{+0.4007}_{-0.0802}$	$(1.22^{+5.29}_{-1.01})10^{50}$
GRB 070802							
1	10.1	10.1	$24.0^{+4.6}_{-2.5}$	145	$-2.70^{+0.35}_{-0.35}$	$4.72^{+2.52}_{-1.43}$	$(2.35^{+1.35}_{-0.72})10^{51}$
GRB 070809							

Pulse	T_{peak} [s]	T_{rise} [s]	T_f [s]	E_f [keV]	α	F_f [10^{-8} ergs s^{-1} cm^{-2}]	L_f [ergs s^{-1}]
1	0.5	0.5	$1.33^{+0.11}_{-0.13}$	410	$-2.72^{+0.32}_{-0.36}$	$30.95^{+12.55}_{-6.15}$	$(4.56^{+3.30}_{-1.69})10^{49}$
GRB 070810A							
1	2.0	2.0	$12.9^{+1.2}_{-0.9}$	42	$-2.00^{+0.20}_{-0.20}$	$20.77^{+2.86}_{-2.33}$	$(7.43^{+1.03}_{-0.84})10^{51}$
GRB 071020							
1	0.9	0.9	$1.72^{+0.10}_{-0.08}$	147	$-1.86^{+0.08}_{-0.08}$	$132.7^{+9.1}_{-8.6}$	$(7.03^{+0.60}_{-0.55})10^{52}$
2	1.9	1.0	$0.99^{+0.12}_{-0.12}$	147	$-1.39^{+0.16}_{-0.19}$	$82.86^{+13.34}_{-14.85}$	$(4.96^{+1.10}_{-1.10})10^{52}$
3	3.1	0.7	$0.74^{+0.05}_{-0.05}$	147	$-1.58^{+0.10}_{-0.10}$	$148.5^{+16.4}_{-14.6}$	$(8.43^{+1.19}_{-1.01})10^{52}$
GRB 071031							
1	10.7	10.7	$32.0^{+7.5}_{-6.0}$	135	$-2.67^{+0.26}_{-0.27}$	$5.26^{+2.52}_{-1.45}$	$(3.30^{+1.65}_{-0.91})10^{51}$
2	125.7	22.7	$37.5^{+4.3}_{-3.2}$	135	$-2.52^{+0.05}_{-0.05}$	$2.59^{+0.43}_{-0.40}$	$(1.63^{+0.28}_{-0.25})10^{51}$
3	150.7	18.0	$76.7^{+6.0}_{-6.6}$	135	$-2.75^{+0.06}_{-0.06}$	$1.16^{+0.18}_{-0.15}$	$(7.21^{+1.13}_{-0.93})10^{50}$
4	200.7	14.9	$138.7^{+23.0}_{-15.3}$	135	$-3.61^{+0.15}_{-0.19}$	$0.178^{+0.023}_{-0.023}$	$(1.16^{+0.17}_{-0.17})10^{50}$
5	260.7	16.9	$98.3^{+22.1}_{-17.4}$	135	$-3.99^{+0.29}_{-0.44}$	$0.0926^{+0.0167}_{-0.0161}$	$(6.31^{+1.48}_{-1.24})10^{49}$
6	440.7	63.9	$435.6^{+29.6}_{-33.1}$	114	$-3.04^{+0.07}_{-0.07}$	$0.125^{+0.014}_{-0.012}$	$(7.78^{+0.93}_{-0.78})10^{49}$
GRB 071122							
1	17.7	17.7	$75.4^{+17.7}_{-14.4}$	234	$-2.97^{+0.10}_{-0.11}$	$2.56^{+1.20}_{-1.17}$	$(1.77^{+0.91}_{-0.84})10^{50}$
2	57.7	9.3	$15.3^{+132.8}_{-15.2}$	234	$-3.12^{+2.62}_{-1.38}$	$1.49^{+22.17}_{-1.48}$	$(9.95^{+571.54}_{-9.89})10^{49}$
GRB 080210							
1	5.4	5.4	$27.4^{+4.5}_{-2.5}$	137	$-2.73^{+0.23}_{-0.23}$	$13.74^{+4.91}_{-3.09}$	$(8.08^{+2.99}_{-1.81})10^{51}$
2	14.6	5.5	$20.4^{+2.9}_{-2.2}$	137	$-2.24^{+0.20}_{-0.21}$	$15.37^{+1.71}_{-1.70}$	$(9.41^{+1.32}_{-1.20})10^{51}$
3	197.4	15.4	$90.9^{+4.7}_{-4.1}$	3.23	$-3.47^{+0.28}_{-0.33}$	$0.211^{+0.039}_{-0.032}$	$(1.32^{+0.28}_{-0.22})10^{50}$
GRB 080310							

Pulse	T_{peak} [s]	T_{rise} [s]	T_f [s]	E_f [keV]	α	F_f [10^{-8} ergs s^{-1} cm^{-2}]	L_f [ergs s^{-1}]
1	8.8	8.8	$43.8^{+10.5}_{-7.4}$	146	$-3.45^{+0.23}_{-0.26}$	$13.20^{+11.87}_{-7.97}$	$(6.24^{+5.69}_{-3.78})10^{51}$
2	41.8	1.7	$8.3^{+5.6}_{-5.4}$	146	$-3.04^{+0.44}_{-1.04}$	$15.95^{+53.11}_{-15.79}$	$(7.50^{+25.69}_{-7.43})10^{51}$
3	57.0	4.5	$12.8^{+1.0}_{-1.8}$	146	$-2.28^{+0.23}_{-0.24}$	$12.38^{+1.96}_{-1.52}$	$(6.14^{+1.21}_{-0.88})10^{51}$
4	63.4	3.1	$17.0^{+3.0}_{-2.1}$	146	$-3.51^{+0.31}_{-0.23}$	$52.79^{+39.40}_{-36.62}$	$(2.48^{+1.87}_{-1.72})10^{52}$
5	220.6	25.8	$79.8^{+2.7}_{-2.9}$	12	$-2.29^{+0.08}_{-0.08}$	$0.713^{+0.073}_{-0.063}$	$(3.37^{+0.35}_{-0.30})10^{50}$
6	253.2	13.9	$48.3^{+5.0}_{-5.0}$	13	$-2.00^{+0.10}_{-0.10}$	$1.33^{+0.24}_{-0.20}$	$(6.20^{+1.12}_{-0.95})10^{50}$
7	271.6	16.8	$54.8^{+8.1}_{-6.8}$	21	$-2.17^{+0.10}_{-0.11}$	$1.25^{+0.27}_{-0.23}$	$(5.88^{+1.26}_{-1.07})10^{50}$
8	296.6	17.3	$37.9^{+7.3}_{-5.3}$	58	$-2.27^{+0.09}_{-0.10}$	$1.72^{+0.45}_{-0.35}$	$(8.16^{+2.14}_{-1.65})10^{50}$
9	313.4	15.4	$48.3^{+9.2}_{-8.5}$	42	$-2.12^{+0.10}_{-0.12}$	$1.31^{+0.38}_{-0.31}$	$(6.21^{+1.82}_{-1.48})10^{50}$
10	343.6	11.8	$39.7^{+7.2}_{-4.9}$	16	$-2.15^{+0.12}_{-0.13}$	$0.867^{+0.210}_{-0.172}$	$(4.13^{+1.00}_{-0.82})10^{50}$
11	370.3	21.7	$23.9^{+3.2}_{-3.1}$	16	$-1.76^{+0.11}_{-0.12}$	$1.22^{+0.26}_{-0.22}$	$(5.90^{+1.25}_{-1.06})10^{50}$
12	404.3	26.3	$29.0^{+2.6}_{-2.0}$	7.83	$-2.03^{+0.10}_{-0.10}$	$0.681^{+0.093}_{-0.082}$	$(3.49^{+0.48}_{-0.42})10^{50}$
13	427.6	20.8	$21.0^{+2.4}_{-1.9}$	34	$-2.55^{+0.13}_{-0.11}$	$0.573^{+0.158}_{-0.139}$	$(3.32^{+0.92}_{-0.81})10^{50}$
14	451.6	26.8	$55.7^{+5.5}_{-4.4}$	1.25	$-1.67^{+0.15}_{-0.16}$	$0.204^{+0.020}_{-0.018}$	$(9.80^{+0.98}_{-0.88})10^{49}$
15	575.4	31.5	$212.3^{+16.2}_{-10.0}$	3.80	$-3.37^{+0.12}_{-0.15}$	$0.164^{+0.011}_{-0.011}$	$(7.91^{+0.57}_{-0.56})10^{49}$
16	643.7	44.0	$60.7^{+2.0}_{-2.1}$	2.44	$-1.98^{+0.07}_{-0.07}$	$0.354^{+0.017}_{-0.017}$	$(1.84^{+0.09}_{-0.09})10^{50}$
GRB 080319B							
1	4.6	4.6	$5.2^{+0.1}_{-0.1}$	258	$-1.63^{+0.02}_{-0.05}$	$139.3^{+7.1}_{-7.0}$	$(1.03^{+0.06}_{-0.08})10^{52}$
2	8.5	3.7	$3.71^{+0.21}_{-0.19}$	258	$-1.00^{+0.05}_{-0.04}$	$303.1^{+18.8}_{-18.2}$	$(3.46^{+0.38}_{-0.30})10^{52}$
3	11.5	2.0	$4.59^{+0.12}_{-0.12}$	258	$-1.05^{+0.03}_{-0.04}$	$443.3^{+31.6}_{-14.0}$	$(4.83^{+0.46}_{-0.28})10^{52}$
4	14.1	1.6	$7.5^{+0.3}_{-0.3}$	258	$-2.38^{+0.05}_{-0.05}$	$177.6^{+9.3}_{-4.2}$	$(9.04^{+0.66}_{-0.36})10^{51}$
5	16.7	1.1	$5.4^{+0.3}_{-0.3}$	258	$-2.03^{+0.04}_{-0.05}$	$195.2^{+14.2}_{-9.1}$	$(1.14^{+0.11}_{-0.08})10^{52}$

Pulse	T_{peak} [s]	T_{rise} [s]	T_f [s]	E_f [keV]	α	F_f [10^{-8} ergs s^{-1} cm^{-2}]	L_f [ergs s^{-1}]
6	19.6	2.4	$4.20^{+0.13}_{-0.12}$	258	$-1.15^{+0.05}_{-0.05}$	$413.6^{+18.9}_{-19.4}$	$(4.18^{+0.35}_{-0.34})10^{52}$
7	21.9	1.7	$8.1^{+0.4}_{-0.2}$	258	$-2.14^{+0.04}_{-0.05}$	$217.3^{+6.7}_{-11.1}$	$(1.22^{+0.06}_{-0.09})10^{52}$
8	25.6	4.1	$4.17^{+0.17}_{-0.16}$	258	$-1.24^{+0.05}_{-0.06}$	$325.7^{+16.1}_{-21.1}$	$(3.09^{+0.26}_{-0.31})10^{52}$
9	28.6	2.1	$5.2^{+0.3}_{-0.1}$	258	$-1.70^{+0.03}_{-0.06}$	$299.2^{+10.1}_{-23.8}$	$(2.10^{+0.11}_{-0.23})10^{52}$
10	33.3	1.0	$2.15^{+0.09}_{-0.08}$	258	$-1.52^{+0.04}_{-0.04}$	$357.4^{+16.6}_{-27.5}$	$(2.82^{+0.20}_{-0.27})10^{52}$
11	37.2	2.2	$2.49^{+0.10}_{-0.09}$	258	$-1.34^{+0.07}_{-0.03}$	$333.0^{+29.4}_{-13.6}$	$(2.95^{+0.42}_{-0.18})10^{52}$
12	38.9	0.9	$2.85^{+0.19}_{-0.15}$	258	$-1.70^{+0.08}_{-0.08}$	$212.7^{+19.4}_{-18.0}$	$(1.50^{+0.21}_{-0.19})10^{52}$
13	40.6	0.6	$2.96^{+0.32}_{-0.30}$	258	$-1.74^{+0.09}_{-0.09}$	$215.8^{+27.3}_{-21.4}$	$(1.49^{+0.28}_{-0.21})10^{52}$
14	43.5	1.4	$2.13^{+0.10}_{-0.07}$	258	$-1.26^{+0.05}_{-0.04}$	$354.7^{+17.7}_{-27.6}$	$(3.33^{+0.31}_{-0.34})10^{52}$
15	46.7	3.1	$3.11^{+0.09}_{-0.09}$	258	$-1.69^{+0.04}_{-0.04}$	$268.3^{+11.5}_{-12.9}$	$(1.91^{+0.13}_{-0.13})10^{52}$
16	51.1	2.9	$2.89^{+0.06}_{-0.06}$	258	$-1.86^{+0.07}_{-0.02}$	$345.9^{+29.0}_{-7.8}$	$(2.24^{+0.28}_{-0.07})10^{52}$
17	53.9	0.9	$1.23^{+0.02}_{-0.01}$	258	$-2.33^{+0.04}_{-0.04}$	$300.0^{+11.1}_{-8.2}$	$(1.58^{+0.08}_{-0.06})10^{52}$
GRB 080319C							
1	1.2	1.2	$7.0^{+0.5}_{-0.7}$	169	$-1.95^{+0.11}_{-0.11}$	$90.14^{+9.35}_{-8.83}$	$(2.86^{+0.39}_{-0.35})10^{52}$
2	6.0	1.2	$8.5^{+3.4}_{-2.4}$	169	$-1.57^{+0.37}_{-0.34}$	$30.87^{+9.76}_{-8.03}$	$(1.09^{+0.56}_{-0.36})10^{52}$
3	9.4	1.5	$2.72^{+0.85}_{-0.49}$	169	$-2.20^{+0.32}_{-0.32}$	$32.02^{+7.42}_{-6.49}$	$(9.77^{+3.19}_{-2.38})10^{51}$
GRB 080413A							
1	2.2	2.2	$3.64^{+0.14}_{-0.10}$	146	$-2.00^{+0.06}_{-0.06}$	$89.18^{+4.10}_{-4.01}$	$(4.71^{+0.27}_{-0.26})10^{52}$
2	6.2	1.5	$8.1^{+1.6}_{-1.7}$	30	$-3.55^{+0.64}_{-0.95}$	$102.7^{+0.0}_{-101.7}$	$(5.00^{+0.14}_{-4.96})10^{52}$
3	16.0	2.9	$5.2^{+0.4}_{-0.3}$	146	$-2.13^{+0.10}_{-0.10}$	$43.58^{+3.27}_{-3.16}$	$(2.25^{+0.21}_{-0.19})10^{52}$
4	44.5	0.8	$5.7^{+1.3}_{-1.0}$	146	$-2.41^{+0.22}_{-0.22}$	$17.52^{+3.07}_{-2.47}$	$(8.57^{+1.77}_{-1.34})10^{51}$
5	47.7	1.7	$4.39^{+0.54}_{-0.32}$	146	$-3.04^{+0.21}_{-0.22}$	$36.94^{+17.69}_{-11.79}$	$(1.78^{+0.86}_{-0.57})10^{52}$

Pulse	T_{peak} [s]	T_{rise} [s]	T_f [s]	E_f [keV]	α	F_f [10^{-8} ergs s^{-1} cm^{-2}]	L_f [ergs s^{-1}]
6	73.9	4.9	$212.6^{+52.9}_{-41.3}$	0.63	$-4.50^{+0.71}_{-0.00}$	$0.347^{+0.070}_{-0.142}$	$(1.70^{+0.34}_{-0.72})10^{50}$
GRB 080413B							
1	1.5	1.5	$2.80^{+0.07}_{-0.07}$	238	$-2.53^{+0.06}_{-0.05}$	$281.6^{+23.9}_{-9.7}$	$(2.02^{+0.21}_{-0.10})10^{52}$
GRB 080430							
1	2.4	2.4	$11.7^{+0.6}_{-0.5}$	283	$-2.85^{+0.08}_{-0.08}$	$52.88^{+5.80}_{-4.85}$	$(1.39^{+0.20}_{-0.17})10^{51}$
GRB 080603B							
1	2.0	2.0	$3.61^{+0.23}_{-0.12}$	136	$-2.05^{+0.09}_{-0.09}$	$50.54^{+3.23}_{-3.30}$	$(3.33^{+0.26}_{-0.25})10^{52}$
2	9.9	1.9	$5.2^{+0.1}_{-0.1}$	136	$-2.25^{+0.10}_{-0.12}$	$35.50^{+2.01}_{-1.95}$	$(2.25^{+0.15}_{-0.15})10^{52}$
3	12.5	0.8	$1.00^{+0.19}_{-0.06}$	136	$-2.64^{+0.24}_{-0.15}$	$24.90^{+9.42}_{-4.47}$	$(1.57^{+0.62}_{-0.29})10^{52}$
4	47.1	3.6	$15.7^{+1.9}_{-1.4}$	136	$-2.53^{+0.08}_{-0.08}$	$10.29^{+1.35}_{-1.27}$	$(6.47^{+0.88}_{-0.82})10^{51}$
5	49.6	0.3	$30.2^{+11.1}_{-7.7}$	136	$-2.54^{+0.14}_{-0.18}$	$2.05^{+1.17}_{-0.97}$	$(1.29^{+0.75}_{-0.61})10^{51}$
6	56.6	2.3	$5.2^{+0.6}_{-0.7}$	136	$-2.46^{+0.16}_{-0.14}$	$14.67^{+2.21}_{-1.89}$	$(9.24^{+1.53}_{-1.25})10^{51}$
GRB 080604							
1	36.7	36.7	$57.4^{+5.4}_{-3.7}$	207	$-2.88^{+0.08}_{-0.08}$	$3.49^{+0.51}_{-0.57}$	$(4.32^{+0.71}_{-0.77})10^{50}$
GRB 080605							
1	1.0	1.0	$13.8^{+0.3}_{-0.8}$	189	$-2.30^{+0.10}_{-0.10}$	$58.04^{+4.27}_{-3.41}$	$(1.12^{+0.11}_{-0.09})10^{52}$
2	6.2	2.2	$4.42^{+0.21}_{-0.25}$	189	$-2.16^{+0.08}_{-0.09}$	$122.9^{+7.5}_{-6.9}$	$(2.52^{+0.21}_{-0.19})10^{52}$
3	7.7	0.04	$0.80^{+0.87}_{-0.18}$	189	$-1.79^{+0.01}_{-0.30}$	$297.6^{+66.3}_{-66.5}$	$(6.57^{+1.49}_{-1.92})10^{52}$
4	11.1	1.1	$3.99^{+0.29}_{-0.19}$	189	$-1.86^{+0.08}_{-0.08}$	$208.4^{+14.1}_{-14.5}$	$(4.58^{+0.44}_{-0.43})10^{52}$
5	13.7	1.0	$2.32^{+0.04}_{-0.15}$	189	$-1.79^{+0.30}_{-0.04}$	$350.1^{+63.6}_{-13.5}$	$(7.98^{+2.63}_{-0.19})10^{52}$
6	15.3	0.09	$0.296^{+0.236}_{-0.103}$	189	$-1.04^{+0.27}_{-0.21}$	$211.6^{+163.3}_{-76.7}$	$(6.74^{+7.21}_{-2.89})10^{52}$
7	19.5	1.1	$1.87^{+0.44}_{-0.35}$	189	$-3.63^{+0.10}_{-0.26}$	$153.7^{+240.5}_{-93.6}$	$(2.65^{+4.29}_{-1.67})10^{52}$

Pulse	T_{peak} [s]	T_{rise} [s]	T_f [s]	E_f [keV]	α	F_f [10^{-8} ergs s^{-1} cm^{-2}]	L_f [ergs s^{-1}]
8	22.3	0.4	$10.5^{+5.0}_{-4.3}$	25	$-3.58^{+1.43}_{-0.53}$	$89.18^{+68.30}_{-88.29}$	$(1.33^{+1.40}_{-1.31})10^{52}$
9	24.2	1.1	$7.1^{+7.9}_{-7.0}$	189	$-1.46^{+0.96}_{-0.99}$	$19.91^{+27.74}_{-19.71}$	$(5.05^{+15.55}_{-5.01})10^{51}$
GRB 080607							
1	3.3	3.3	$9.1^{+0.8}_{-0.5}$	124	$-1.73^{+0.14}_{-0.13}$	$117.4^{+14.5}_{-11.2}$	$(1.06^{+0.16}_{-0.12})10^{53}$
2	8.0	2.4	$4.54^{+0.16}_{-0.13}$	124	$-1.14^{+0.05}_{-0.04}$	$599.9^{+26.4}_{-75.5}$	$(6.14^{+0.35}_{-0.83})10^{53}$
3	12.8	1.4	$1.43^{+0.15}_{-0.76}$	124	$-1.33^{+0.23}_{-0.12}$	$348.6^{+101.2}_{-60.8}$	$(3.42^{+1.25}_{-0.67})10^{53}$
4	31.0	1.2	$3.84^{+0.61}_{-0.89}$	124	$-2.10^{+0.38}_{-0.34}$	$38.05^{+10.74}_{-7.67}$	$(3.23^{+1.12}_{-0.71})10^{52}$
5	38.7	3.1	$9.2^{+1.0}_{-0.6}$	124	$-2.24^{+0.13}_{-0.13}$	$44.57^{+3.83}_{-3.77}$	$(3.80^{+0.37}_{-0.35})10^{52}$
6	55.5	2.2	$12.7^{+2.0}_{-1.5}$	124	$-2.90^{+0.16}_{-0.14}$	$26.43^{+14.59}_{-5.14}$	$(2.24^{+1.28}_{-0.45})10^{52}$
7	63.2	3.0	$10.7^{+1.7}_{-1.2}$	124	$-2.84^{+0.20}_{-0.20}$	$22.09^{+8.22}_{-4.65}$	$(1.83^{+0.72}_{-0.39})10^{52}$
8	79.0	6.3	$16.7^{+1.3}_{-1.0}$	124	$-2.91^{+0.06}_{-0.06}$	$20.84^{+2.59}_{-2.23}$	$(1.77^{+0.23}_{-0.20})10^{52}$
9	86.3	4.9	$15.3^{+1.8}_{-9.2}$	124	$-2.23^{+0.02}_{-0.43}$	$8.10^{+1.55}_{-1.19}$	$(6.88^{+1.33}_{-1.12})10^{51}$
10	133.4	10.0	$54.4^{+3.4}_{-3.3}$	124	$-3.06^{+0.06}_{-0.06}$	$4.07^{+0.53}_{-0.40}$	$(3.40^{+0.47}_{-0.35})10^{51}$
GRB 080707							
1	3.9	3.9	$9.9^{+0.3}_{-0.6}$	224	$-3.04^{+0.21}_{-0.32}$	$29.18^{+20.81}_{-8.21}$	$(2.39^{+1.94}_{-0.84})10^{51}$
2	26.5	2.0	$8.6^{+1.3}_{-2.1}$	224	$-2.65^{+0.34}_{-0.48}$	$15.67^{+6.31}_{-4.20}$	$(1.43^{+0.77}_{-0.51})10^{51}$
GRB 080721							
1	3.3	3.3	$4.42^{+0.40}_{-0.26}$	139	$-1.82^{+0.40}_{-0.24}$	$97.22^{+26.07}_{-22.04}$	$(6.15^{+2.38}_{-1.58})10^{52}$
2	10.6	3.4	$5.8^{+0.5}_{-0.4}$	139	$-1.71^{+0.48}_{-0.11}$	$267.7^{+53.9}_{-26.5}$	$(1.73^{+0.62}_{-0.21})10^{53}$
3	15.5	0.9	$1.78^{+2.34}_{-0.43}$	139	$-1.03^{+0.47}_{-0.74}$	$345.1^{+149.2}_{-172.9}$	$(2.74^{+1.99}_{-1.63})10^{53}$
4	25.9	3.2	$15.4^{+8.3}_{-6.0}$	139	$-2.75^{+0.83}_{-0.86}$	$26.75^{+53.79}_{-26.49}$	$(1.53^{+3.47}_{-1.51})10^{52}$
GRB 080804							

Pulse	T_{peak} [s]	T_{rise} [s]	T_f [s]	E_f [keV]	α	F_f [10^{-8} ergs s^{-1} cm^{-2}]	L_f [ergs s^{-1}]
1	2.0	2.0	$11.1^{+0.7}_{-0.7}$	156	$-1.93^{+0.19}_{-0.18}$	$48.92^{+6.27}_{-5.67}$	$(2.02^{+0.37}_{-0.30})10^{52}$
2	5.8	0.6	$10.3^{+6.1}_{-4.4}$	156	$-1.66^{+0.75}_{-0.57}$	$21.53^{+14.52}_{-7.64}$	$(9.57^{+11.39}_{-4.11})10^{51}$
3	9.7	1.7	$15.3^{+15.4}_{-6.9}$	156	$-0.73^{+0.17}_{-0.60}$	$26.61^{+21.41}_{-13.65}$	$(1.74^{+1.68}_{-1.08})10^{52}$
4	18.2	0.04	$1.67^{+4.89}_{-1.01}$	156	$-1.01^{+0.49}_{-1.80}$	$55.20^{+53.20}_{-50.92}$	$(3.11^{+4.61}_{-2.95})10^{52}$
GRB 080805							
1	6.4	6.4	$34.5^{+2.7}_{-2.0}$	200	$-1.81^{+0.08}_{-0.07}$	$17.62^{+1.35}_{-1.29}$	$(3.26^{+0.36}_{-0.32})10^{51}$
2	24.9	4.6	$9.3^{+3.5}_{-1.2}$	200	$-3.23^{+0.38}_{-0.38}$	$9.58^{+11.45}_{-6.16}$	$(1.28^{+1.76}_{-0.87})10^{51}$
3	44.9	4.0	$4.67^{+0.03}_{-0.03}$	200	$-3.76^{+0.11}_{-0.74}$	$23.87^{+15.68}_{-14.53}$	$(6.74^{+4.77}_{-4.60})10^{51}$
4	72.7	14.1	$33.5^{+12.5}_{-7.0}$	6.11	$-0.40^{+0.10}_{-0.26}$	$1.16^{+0.30}_{-0.37}$	$(1.70^{+0.43}_{-0.54})10^{50}$
5	129.2	27.8	$60.7^{+4.0}_{-3.3}$	2.40	$-1.53^{+0.11}_{-0.11}$	$0.331^{+0.029}_{-0.029}$	$(4.74^{+0.44}_{-0.43})10^{49}$
GRB 080810							
1	2.5	2.5	$27.5^{+4.6}_{-3.5}$	115	$-1.10^{+0.21}_{-0.19}$	$21.57^{+3.86}_{-3.42}$	$(2.72^{+0.65}_{-0.52})10^{52}$
2	19.8	4.0	$10.8^{+2.3}_{-1.1}$	115	$-2.02^{+0.26}_{-0.26}$	$13.90^{+2.42}_{-2.19}$	$(1.50^{+0.31}_{-0.26})10^{52}$
3	27.8	1.5	$6.6^{+2.6}_{-1.6}$	115	$-1.96^{+0.34}_{-0.33}$	$16.55^{+3.92}_{-2.64}$	$(1.80^{+0.52}_{-0.33})10^{52}$
4	48.0	2.8	$5.5^{+0.8}_{-0.4}$	115	$-2.22^{+0.24}_{-0.25}$	$13.81^{+1.79}_{-1.78}$	$(1.49^{+0.23}_{-0.20})10^{52}$
5	54.7	1.5	$5.5^{+1.7}_{-1.9}$	115	$-2.34^{+0.33}_{-0.31}$	$12.49^{+2.71}_{-1.85}$	$(1.33^{+0.33}_{-0.20})10^{52}$
6	69.9	5.9	$10.6^{+1.9}_{-1.9}$	115	$-2.57^{+0.24}_{-0.26}$	$3.90^{+1.80}_{-1.13}$	$(4.15^{+1.98}_{-1.19})10^{51}$
7	92.6	6.3	$42.1^{+6.9}_{-4.4}$	115	$-2.63^{+0.10}_{-0.11}$	$1.02^{+0.33}_{-0.29}$	$(1.09^{+0.35}_{-0.31})10^{51}$
8	105.9	4.3	$10.9^{+0.9}_{-0.7}$	115	$-2.24^{+0.05}_{-0.05}$	$7.77^{+1.13}_{-1.10}$	$(8.33^{+1.24}_{-1.20})10^{51}$
9	211.8	14.9	$60.1^{+8.7}_{-5.0}$	115	$-3.02^{+0.12}_{-0.13}$	$0.257^{+0.059}_{-0.051}$	$(2.78^{+0.71}_{-0.59})10^{50}$
10	292.6	18.7	$95.1^{+62.2}_{-55.5}$	115	$-4.50^{+0.90}_{-0.00}$	$0.0192^{+0.0124}_{-0.0082}$	$(2.98^{+1.92}_{-1.63})10^{49}$
GRB 080905B							

Pulse	T_{peak} [s]	T_{rise} [s]	T_f [s]	E_f [keV]	α	F_f [10^{-8} ergs s^{-1} cm^{-2}]	L_f [ergs s^{-1}]
1	3.5	3.5	$17.0^{+0.9}_{-0.7}$	148	$-2.05^{+0.21}_{-0.20}$	$26.49^{+4.24}_{-3.91}$	$(1.28^{+0.27}_{-0.22})10^{52}$
2	61.3	1.3	$31.0^{+6.3}_{-5.2}$	148	$-1.71^{+0.17}_{-0.14}$	$7.86^{+1.47}_{-1.46}$	$(4.09^{+0.98}_{-0.86})10^{51}$
3	85.0	4.6	$8.9^{+0.7}_{-1.4}$	148	$-2.87^{+0.23}_{-0.29}$	$8.91^{+4.54}_{-1.85}$	$(4.06^{+2.14}_{-0.86})10^{51}$
GRB 080913							
1	0.8	0.8	$5.9^{+0.5}_{-2.4}$	65	$-0.95^{+0.35}_{-0.54}$	$18.70^{+9.88}_{-4.58}$	$(1.02^{+0.57}_{-0.27})10^{53}$
2	3.5	0.9	$5.1^{+3.4}_{-2.8}$	65	$-2.12^{+1.02}_{-1.12}$	$10.08^{+11.22}_{-4.34}$	$(5.45^{+9.71}_{-2.29})10^{52}$
GRB 080916A							
1	3.6	3.6	$12.6^{+0.1}_{-0.4}$	296	$-1.98^{+0.07}_{-0.04}$	$57.35^{+3.70}_{-1.85}$	$(1.72^{+0.19}_{-0.10})10^{51}$
2	19.2	4.5	$29.4^{+1.4}_{-1.4}$	296	$-3.01^{+0.05}_{-0.06}$	$30.30^{+3.60}_{-3.06}$	$(5.71^{+0.83}_{-0.71})10^{50}$
3	555.5	71.6	$468.9^{+275.2}_{-314.3}$	90	$-2.90^{+0.57}_{-0.64}$	$0.0195^{+0.0181}_{-0.0108}$	$(3.65^{+4.13}_{-2.44})10^{47}$
GRB 080928							
1	12.5	12.5	$22.8^{+17.5}_{-14.8}$	186	$-2.93^{+0.87}_{-0.80}$	$2.32^{+5.50}_{-1.14}$	$(4.46^{+13.26}_{-2.49})10^{50}$
2	74.8	8.2	$39.3^{+14.0}_{-9.7}$	186	$-2.73^{+0.46}_{-0.43}$	$3.71^{+2.62}_{-1.12}$	$(7.25^{+6.21}_{-2.52})10^{50}$
3	107.1	9.5	$52.9^{+17.7}_{-13.3}$	186	$-3.35^{+0.25}_{-0.27}$	$5.33^{+5.34}_{-3.12}$	$(9.31^{+10.14}_{-5.66})10^{50}$
4	197.1	17.8	$40.5^{+3.4}_{-2.0}$	186	$-2.84^{+0.05}_{-0.06}$	$3.15^{+0.42}_{-0.40}$	$(6.14^{+0.87}_{-0.83})10^{50}$
5	209.3	1.6	$18.6^{+2.0}_{-1.0}$	186	$-2.45^{+0.03}_{-0.04}$	$20.00^{+1.11}_{-2.20}$	$(4.14^{+0.26}_{-0.48})10^{51}$
6	219.0	2.8	$87.3^{+8.5}_{-7.6}$	186	$-2.75^{+0.05}_{-0.05}$	$3.51^{+0.55}_{-0.53}$	$(6.59^{+1.09}_{-1.03})10^{50}$
7	359.5	13.4	$31.6^{+2.4}_{-3.2}$	141	$-2.61^{+0.11}_{-0.10}$	$1.57^{+0.48}_{-0.36}$	$(3.09^{+1.00}_{-0.73})10^{50}$
GRB 081007							
1	2.0	2.0	$16.0^{+0.5}_{-0.6}$	327	$-3.73^{+0.18}_{-0.08}$	$375.0^{+183.5}_{-125.5}$	$(2.26^{+1.59}_{-0.85})10^{51}$
2	515.1	112.7	$284.9^{+321.2}_{-282.0}$	97	$-2.79^{+1.21}_{-1.25}$	$0.0081^{+0.0313}_{-0.0081}$	$(8.16^{+37.46}_{-8.12})10^{46}$
GRB 081008							

Pulse	T_{peak} [s]	T_{rise} [s]	T_f [s]	E_f [keV]	α	F_f [10^{-8} ergs s^{-1} cm^{-2}]	L_f [ergs s^{-1}]
1	11.2	11.2	$18.1^{+1.0}_{-1.0}$	169	$-1.86^{+0.13}_{-0.13}$	$16.40^{+1.83}_{-1.43}$	$(5.51^{+0.85}_{-0.64})10^{51}$
2	19.9	4.8	$18.2^{+4.1}_{-7.3}$	169	$-2.41^{+0.49}_{-0.19}$	$8.72^{+2.31}_{-1.39}$	$(2.58^{+1.03}_{-0.47})10^{51}$
3	75.4	6.1	$29.3^{+6.0}_{-3.6}$	169	$-2.98^{+0.09}_{-0.10}$	$7.06^{+2.03}_{-1.78}$	$(1.95^{+0.58}_{-0.51})10^{51}$
4	108.2	2.7	$17.6^{+4.6}_{-3.4}$	169	$-2.30^{+0.08}_{-0.08}$	$5.53^{+1.30}_{-1.15}$	$(1.68^{+0.43}_{-0.37})10^{51}$
5	116.5	4.4	$10.6^{+6.1}_{-1.6}$	169	$-2.19^{+0.07}_{-0.08}$	$8.45^{+1.76}_{-2.21}$	$(2.61^{+0.59}_{-0.71})10^{51}$
6	124.5	4.4	$10.5^{+1.9}_{-1.1}$	169	$-2.08^{+0.06}_{-0.06}$	$12.46^{+2.09}_{-1.90}$	$(3.97^{+0.73}_{-0.65})10^{51}$
7	131.9	5.4	$23.6^{+4.4}_{-3.5}$	169	$-2.50^{+0.07}_{-0.08}$	$4.05^{+0.90}_{-0.80}$	$(1.19^{+0.28}_{-0.24})10^{51}$
8	151.9	13.8	$28.3^{+5.0}_{-3.9}$	169	$-2.73^{+0.08}_{-0.09}$	$2.00^{+0.46}_{-0.45}$	$(5.75^{+1.39}_{-1.35})10^{50}$
9	170.9	13.6	$73.3^{+11.6}_{-8.6}$	169	$-3.46^{+0.15}_{-0.19}$	$0.626^{+0.110}_{-0.085}$	$(1.64^{+0.32}_{-0.25})10^{50}$
10	196.4	15.2	$16.8^{+1.7}_{-0.6}$	169	$-2.81^{+0.45}_{-0.17}$	$1.12^{+0.48}_{-1.11}$	$(3.54^{+1.82}_{-3.51})10^{50}$
11	208.8	12.0	$34.9^{+3.6}_{-3.6}$	169	$-3.25^{+0.11}_{-0.12}$	$0.915^{+0.151}_{-0.107}$	$(2.49^{+0.44}_{-0.32})10^{50}$
12	308.7	13.7	$85.9^{+8.1}_{-5.0}$	167	$-3.66^{+0.11}_{-0.13}$	$0.388^{+0.031}_{-0.031}$	$(9.90^{+0.91}_{-0.93})10^{49}$
GRB 081118							
1	9.5	9.5	$17.7^{+2.9}_{-3.4}$	140	$-2.76^{+0.26}_{-0.77}$	$7.07^{+18.01}_{-1.38}$	$(3.98^{+10.47}_{-0.74})10^{51}$
2	21.1	6.5	$20.5^{+3.9}_{-2.2}$	140	$-2.61^{+0.32}_{-0.31}$	$8.25^{+4.22}_{-2.06}$	$(4.65^{+2.55}_{-1.18})10^{51}$
3	31.7	2.8	$18.2^{+3.8}_{-3.7}$	140	$-3.93^{+0.31}_{-0.57}$	$113.8^{+124.1}_{-112.7}$	$(6.69^{+7.88}_{-6.62})10^{52}$
GRB 081203A							
1	12.4	12.4	$22.0^{+1.7}_{-2.1}$	161	$-2.11^{+0.42}_{-0.12}$	$13.28^{+1.68}_{-1.38}$	$(4.88^{+1.20}_{-0.61})10^{51}$
2	17.9	3.9	$48.3^{+5.8}_{-3.9}$	161	$-1.83^{+0.09}_{-0.08}$	$17.49^{+1.74}_{-1.62}$	$(6.70^{+0.84}_{-0.74})10^{51}$
3	30.3	0.2	$16.3^{+7.6}_{-5.7}$	161	$-3.30^{+0.59}_{-0.61}$	$14.90^{+34.16}_{-5.92}$	$(4.86^{+11.82}_{-2.05})10^{51}$
4	41.9	4.9	$19.3^{+1.8}_{-1.2}$	161	$-2.25^{+0.10}_{-0.10}$	$23.59^{+1.82}_{-1.80}$	$(8.49^{+0.82}_{-0.76})10^{51}$
5	75.0	4.2	$339.6^{+52.7}_{-60.0}$	161	$-3.17^{+0.18}_{-0.28}$	$0.226^{+0.073}_{-0.042}$	$(7.00^{+2.36}_{-1.39})10^{49}$

Pulse	T_{peak} [s]	T_{rise} [s]	T_f [s]	E_f [keV]	α	F_f [10^{-8} ergs s^{-1} cm^{-2}]	L_f [ergs s^{-1}]
6	101.6	10.7	$42.5^{+6.2}_{-4.9}$	161	$-3.53^{+0.14}_{-0.18}$	$1.10^{+0.17}_{-0.13}$	$(3.52^{+0.58}_{-0.46})10^{50}$
GRB 081222							
1	4.7	4.7	$7.3^{+0.1}_{-0.1}$	133	$-2.01^{+0.03}_{-0.03}$	$120.3^{+2.7}_{-2.6}$	$(8.52^{+0.22}_{-0.22})10^{52}$
2	37.4	3.7	$6.8^{+0.4}_{-0.3}$	133	$-3.37^{+0.19}_{-0.21}$	$22.23^{+4.83}_{-5.95}$	$(1.56^{+0.38}_{-0.44})10^{52}$
GRB 081230							
1	1.3	1.3	$12.3^{+4.8}_{-1.9}$	165	$-3.09^{+0.40}_{-0.40}$	$16.45^{+19.90}_{-11.12}$	$(4.92^{+6.34}_{-3.38})10^{51}$
2	9.0	2.7	$15.7^{+2.6}_{-3.9}$	165	$-2.34^{+0.34}_{-0.36}$	$6.87^{+1.86}_{-1.16}$	$(2.23^{+0.80}_{-0.46})10^{51}$
3	21.4	2.8	$11.0^{+2.8}_{-1.0}$	165	$-3.08^{+0.35}_{-0.31}$	$25.62^{+24.67}_{-16.71}$	$(7.72^{+7.91}_{-5.11})10^{51}$
4	94.5	8.2	$29.3^{+5.9}_{-4.7}$	165	$-2.65^{+0.11}_{-0.12}$	$1.22^{+0.46}_{-0.41}$	$(3.79^{+1.49}_{-1.29})10^{50}$
GRB 090102							
1	6.6	6.6	$9.8^{+1.4}_{-0.9}$	196	$-1.81^{+0.22}_{-0.30}$	$82.94^{+17.55}_{-21.45}$	$(1.67^{+0.54}_{-0.55})10^{52}$
2	13.1	1.0	$5.9^{+1.3}_{-0.4}$	196	$-1.86^{+0.25}_{-0.25}$	$134.8^{+33.0}_{-34.1}$	$(2.63^{+0.97}_{-0.82})10^{52}$
3	30.8	5.6	$11.6^{+0.6}_{-2.1}$	196	$-3.34^{+0.86}_{-1.16}$	$60.58^{+203.00}_{-56.23}$	$(8.54^{+35.38}_{-8.08})10^{51}$
GRB 090205							
1	5.1	5.1	$13.6^{+2.6}_{-1.1}$	88	$-2.60^{+0.28}_{-0.29}$	$6.98^{+2.86}_{-1.83}$	$(1.64^{+0.78}_{-0.45})10^{52}$
GRB 090418A							
1	6.9	6.9	$16.2^{+1.7}_{-1.1}$	192	$-1.84^{+0.21}_{-0.21}$	$26.16^{+4.71}_{-4.05}$	$(5.63^{+1.56}_{-1.18})10^{51}$
2	29.6	4.4	$12.1^{+3.6}_{-2.2}$	192	$-1.83^{+0.38}_{-0.37}$	$15.44^{+4.81}_{-3.79}$	$(3.32^{+1.74}_{-1.08})10^{51}$
3	44.7	10.9	$11.2^{+0.3}_{-0.7}$	192	$-2.22^{+0.13}_{-0.13}$	$19.58^{+2.06}_{-1.71}$	$(3.83^{+0.55}_{-0.44})10^{51}$
4	56.8	8.0	$12.1^{+0.6}_{-0.5}$	192	$-3.07^{+0.14}_{-0.16}$	$24.79^{+7.77}_{-4.93}$	$(4.16^{+1.43}_{-0.93})10^{51}$
GRB 090423							
1	1.4	1.4	$4.78^{+0.69}_{-0.80}$	54	$-2.08^{+0.39}_{-0.42}$	$9.19^{+3.14}_{-2.04}$	$(8.02^{+3.07}_{-1.79})10^{52}$

Pulse	T_{peak} [s]	T_{rise} [s]	T_f [s]	E_f [keV]	α	F_f [10^{-8} ergs s^{-1} cm^{-2}]	L_f [ergs s^{-1}]
2	5.0	2.0	$3.50^{+0.33}_{-0.41}$	54	$-2.13^{+0.23}_{-0.24}$	$15.88^{+2.26}_{-1.90}$	$(1.40^{+0.22}_{-0.17})10^{53}$
3	8.7	2.3	$20.5^{+3.1}_{-2.8}$	54	$-2.21^{+0.25}_{-0.24}$	$8.30^{+2.10}_{-1.49}$	$(7.28^{+2.02}_{-1.35})10^{52}$
GRB 090424							
1	1.3	1.3	$2.77^{+0.02}_{-0.02}$	324	$-2.37^{+0.04}_{-0.04}$	$1141.7^{+27.7}_{-29.4}$	$(1.63^{+0.07}_{-0.07})10^{52}$
2	3.2	0.2	$1.22^{+0.25}_{-0.17}$	324	$-2.22^{+0.18}_{-0.17}$	$365.3^{+57.3}_{-38.3}$	$(5.49^{+1.55}_{-0.99})10^{51}$
3	4.5	0.01	$0.62^{+0.15}_{-0.04}$	324	$-2.04^{+0.04}_{-0.17}$	$1122.7^{+176.7}_{-89.5}$	$(1.89^{+0.24}_{-0.32})10^{52}$
4	8.7	0.5	$1.84^{+1.33}_{-0.32}$	324	$-3.47^{+0.10}_{-0.28}$	$411.2^{+813.1}_{-346.7}$	$(3.23^{+7.07}_{-2.81})10^{51}$
5	16.8	1.5	$12.6^{+1.2}_{-1.3}$	324	$-4.07^{+0.05}_{-0.08}$	$1154.9^{+3171.6}_{-692.1}$	$(5.66^{+16.42}_{-3.53})10^{51}$
6	51.6	6.6	$21.4^{+1.9}_{-0.9}$	324	$-3.33^{+0.11}_{-0.06}$	$57.82^{+8.54}_{-18.89}$	$(4.97^{+1.13}_{-1.74})10^{50}$
GRB 090426							
1	0.8	0.8	$2.20^{+0.19}_{-0.16}$	139	$-2.57^{+0.31}_{-0.23}$	$85.58^{+37.24}_{-23.86}$	$(4.97^{+2.35}_{-1.41})10^{52}$
GRB 090429B							
1	0.6	0.6	$3.76^{+0.50}_{-0.25}$	48	$-1.81^{+0.34}_{-0.36}$	$14.71^{+2.94}_{-2.59}$	$(1.69^{+0.35}_{-0.30})10^{53}$
2	4.0	2.0	$3.07^{+0.23}_{-0.38}$	48	$-2.32^{+0.31}_{-0.33}$	$15.01^{+4.82}_{-2.87}$	$(1.80^{+0.70}_{-0.36})10^{53}$
GRB 090510							
1	0.2	0.2	$0.60^{+0.02}_{-0.04}$	263	$-1.60^{+0.23}_{-0.27}$	$288.2^{+95.0}_{-58.1}$	$(1.99^{+1.09}_{-0.63})10^{52}$
GRB 090516							
1	10.5	10.5	$17.5^{+10.4}_{-4.4}$	98	$-1.75^{+0.36}_{-0.47}$	$23.38^{+9.00}_{-6.23}$	$(4.16^{+1.82}_{-1.19})10^{52}$
2	22.8	4.1	$11.8^{+4.9}_{-11.6}$	98	$-1.71^{+1.19}_{-0.94}$	$28.09^{+9.75}_{-27.81}$	$(4.96^{+3.04}_{-4.91})10^{52}$
3	44.5	9.8	$14.2^{+3.7}_{-3.9}$	98	$-1.40^{+0.76}_{-0.67}$	$23.07^{+17.02}_{-7.25}$	$(4.25^{+4.12}_{-1.49})10^{52}$
4	96.3	5.4	$8.6^{+2.7}_{-1.8}$	98	$-1.90^{+0.60}_{-0.57}$	$23.92^{+10.66}_{-8.51}$	$(4.21^{+2.24}_{-1.54})10^{52}$
5	118.4	0.2	$12.1^{+23.7}_{-12.0}$	98	$-2.77^{+0.79}_{-0.65}$	$9.71^{+35.36}_{-9.61}$	$(1.67^{+7.46}_{-1.65})10^{52}$

Pulse	T_{peak} [s]	T_{rise} [s]	T_f [s]	E_f [keV]	α	F_f [10^{-8} ergs s^{-1} cm^{-2}]	L_f [ergs s^{-1}]
6	132.7	2.7	$21.1^{+3.3}_{-4.4}$	98	$-2.69^{+0.27}_{-0.23}$	$8.28^{+3.70}_{-1.87}$	$(1.44^{+0.71}_{-0.34})10^{52}$
7	177.5	13.3	$47.1^{+6.8}_{-5.0}$	98	$-2.68^{+0.06}_{-0.07}$	$3.08^{+0.50}_{-0.48}$	$(5.33^{+0.92}_{-0.84})10^{51}$
8	198.2	11.4	$15.6^{+6.0}_{-1.9}$	98	$-2.90^{+0.15}_{-0.12}$	$1.26^{+0.40}_{-0.38}$	$(2.35^{+0.82}_{-0.73})10^{51}$
9	218.6	21.8	$76.2^{+4.2}_{-4.3}$	98	$-2.91^{+0.06}_{-0.06}$	$2.14^{+0.24}_{-0.18}$	$(3.81^{+0.47}_{-0.36})10^{51}$
10	277.5	13.1	$47.7^{+3.4}_{-4.3}$	98	$-3.45^{+0.11}_{-0.06}$	$2.03^{+0.27}_{-0.17}$	$(4.27^{+0.68}_{-0.52})10^{51}$
11	403.5	25.6	$366.8^{+146.7}_{-88.8}$	0.78	$-5.44^{+1.50}_{-0.94}$	$0.183^{+0.014}_{-0.044}$	$(1.08^{+0.28}_{-0.62})10^{51}$
GRB 090519							
1	4.3	4.3	$29.1^{+5.7}_{-6.8}$	103	$-0.85^{+0.25}_{-0.43}$	$11.26^{+3.67}_{-2.78}$	$(2.01^{+0.82}_{-0.62})10^{52}$
2	21.2	5.1	$37.6^{+10.4}_{-7.5}$	103	$-2.64^{+0.22}_{-0.24}$	$2.64^{+1.46}_{-1.31}$	$(3.86^{+2.28}_{-1.93})10^{51}$
GRB 090529							
1	18.0	18.0	$68.9^{+9.7}_{-8.4}$	138	$-2.49^{+0.18}_{-0.18}$	$4.87^{+1.08}_{-0.90}$	$(2.85^{+0.69}_{-0.55})10^{51}$
2	35.1	6.7	$52.2^{+10.9}_{-8.0}$	138	$-4.18^{+0.11}_{-0.13}$	$108.3^{+87.2}_{-102.4}$	$(6.88^{+5.68}_{-6.50})10^{52}$
GRB 090530							
1	1.7	1.7	$7.4^{+0.3}_{-0.3}$	217	$-2.32^{+0.18}_{-0.19}$	$41.56^{+4.36}_{-4.14}$	$(4.66^{+0.79}_{-0.67})10^{51}$
2	45.5	7.6	$10.3^{+0.9}_{-0.4}$	217	$-3.54^{+0.22}_{-0.23}$	$17.89^{+3.30}_{-7.48}$	$(1.93^{+0.53}_{-0.89})10^{51}$
GRB 090618							
1	5.4	5.4	$16.1^{+0.1}_{-0.2}$	325	$-1.92^{+0.06}_{-0.03}$	$113.0^{+8.3}_{-2.8}$	$(2.07^{+0.24}_{-0.09})10^{51}$
2	15.2	8.4	$8.5^{+0.4}_{-0.4}$	325	$-2.26^{+0.05}_{-0.05}$	$68.08^{+3.53}_{-3.31}$	$(1.03^{+0.09}_{-0.08})10^{51}$
3	21.2	5.4	$24.4^{+1.0}_{-2.2}$	325	$-2.57^{+0.05}_{-0.06}$	$63.61^{+3.43}_{-2.10}$	$(7.96^{+0.64}_{-0.47})10^{50}$
4	55.6	5.0	$9.4^{+0.1}_{-0.2}$	325	$-2.59^{+0.04}_{-0.04}$	$130.1^{+3.2}_{-3.4}$	$(1.65^{+0.07}_{-0.07})10^{51}$
5	60.3	3.1	$12.1^{+0.8}_{-0.3}$	325	$-2.25^{+0.04}_{-0.04}$	$167.2^{+4.6}_{-8.1}$	$(2.52^{+0.12}_{-0.17})10^{51}$
6	65.8	3.2	$10.2^{+0.1}_{-0.1}$	325	$-2.13^{+0.01}_{-0.01}$	$607.1^{+11.7}_{-8.1}$	$(9.72^{+0.27}_{-0.21})10^{51}$

Pulse	T_{peak} [s]	T_{rise} [s]	T_f [s]	E_f [keV]	α	F_f [10^{-8} ergs s^{-1} cm^{-2}]	L_f [ergs s^{-1}]
7	68.3	2.0	$7.6^{+0.5}_{-0.3}$	325	$-2.47^{+0.06}_{-0.06}$	$207.6^{+9.4}_{-9.5}$	$(2.77^{+0.21}_{-0.21})10^{51}$
8	71.2	2.3	$3.23^{+0.15}_{-0.09}$	325	$-2.29^{+0.05}_{-0.05}$	$261.2^{+12.6}_{-10.4}$	$(3.83^{+0.30}_{-0.25})10^{51}$
9	73.2	1.8	$5.9^{+0.3}_{-0.3}$	325	$-2.74^{+0.05}_{-0.04}$	$239.8^{+17.9}_{-10.4}$	$(2.81^{+0.28}_{-0.17})10^{51}$
10	79.9	2.1	$9.1^{+0.4}_{-0.3}$	325	$-2.73^{+0.04}_{-0.03}$	$207.0^{+17.0}_{-7.1}$	$(2.46^{+0.25}_{-0.12})10^{51}$
11	82.7	2.1	$12.6^{+0.2}_{-0.2}$	325	$-2.47^{+0.03}_{-0.03}$	$302.1^{+4.6}_{-8.0}$	$(3.99^{+0.11}_{-0.15})10^{51}$
12	86.3	1.3	$6.3^{+0.3}_{-0.2}$	325	$-2.46^{+0.05}_{-0.05}$	$233.9^{+7.6}_{-9.4}$	$(3.16^{+0.18}_{-0.20})10^{51}$
13	89.0	1.4	$15.6^{+0.5}_{-0.4}$	325	$-2.66^{+0.03}_{-0.03}$	$178.9^{+6.3}_{-5.6}$	$(2.18^{+0.11}_{-0.10})10^{51}$
14	106.5	2.4	$15.1^{+1.3}_{-1.2}$	325	$-2.95^{+0.13}_{-0.07}$	$57.48^{+7.30}_{-9.42}$	$(6.03^{+1.21}_{-1.18})10^{50}$
15	112.5	3.4	$16.4^{+0.3}_{-0.3}$	325	$-2.93^{+0.05}_{-0.02}$	$206.3^{+6.6}_{-19.1}$	$(2.18^{+0.12}_{-0.22})10^{51}$
16	115.9	1.6	$18.6^{+0.5}_{-0.4}$	325	$-2.95^{+0.01}_{-0.04}$	$172.0^{+12.2}_{-6.7}$	$(1.82^{+0.14}_{-0.10})10^{51}$
17	155.4	5.1	$11.7^{+3.4}_{-2.0}$	325	$-3.27^{+0.13}_{-0.15}$	$9.09^{+2.67}_{-2.09}$	$(8.12^{+3.22}_{-2.45})10^{49}$
GRB 090715B							
1	2.6	2.6	$16.2^{+3.7}_{-1.6}$	125	$-2.20^{+0.22}_{-0.20}$	$10.58^{+1.65}_{-1.60}$	$(8.62^{+1.57}_{-1.41})10^{51}$
2	8.0	2.6	$12.7^{+0.8}_{-0.6}$	125	$-1.83^{+0.08}_{-0.08}$	$42.91^{+3.03}_{-2.43}$	$(3.65^{+0.31}_{-0.24})10^{52}$
3	12.1	1.6	$4.06^{+0.68}_{-0.28}$	125	$-2.07^{+0.15}_{-0.15}$	$33.31^{+3.91}_{-3.75}$	$(2.78^{+0.38}_{-0.35})10^{52}$
4	57.4	7.6	$20.1^{+3.4}_{-2.7}$	125	$-2.08^{+0.06}_{-0.07}$	$6.68^{+1.31}_{-1.28}$	$(5.62^{+1.15}_{-1.11})10^{51}$
5	66.4	0.8	$7.4^{+3.3}_{-1.2}$	125	$-2.09^{+0.09}_{-0.08}$	$9.61^{+2.83}_{-2.47}$	$(7.91^{+2.43}_{-2.08})10^{51}$
6	69.6	0.3	$12.4^{+5.0}_{-2.2}$	125	$-2.21^{+0.10}_{-0.09}$	$6.41^{+1.97}_{-1.53}$	$(5.21^{+1.66}_{-1.27})10^{51}$
7	72.7	0.1	$12.2^{+2.2}_{-1.9}$	125	$-2.13^{+0.06}_{-0.05}$	$16.12^{+3.04}_{-2.16}$	$(1.35^{+0.27}_{-0.19})10^{52}$
8	81.2	1.2	$20.8^{+4.9}_{-3.2}$	125	$-2.65^{+0.08}_{-0.10}$	$4.25^{+1.31}_{-1.16}$	$(3.36^{+1.04}_{-0.92})10^{51}$
9	113.3	11.9	$32.2^{+4.6}_{-5.1}$	125	$-2.70^{+0.11}_{-0.13}$	$1.12^{+0.38}_{-0.27}$	$(9.09^{+3.13}_{-2.17})10^{50}$
10	129.3	12.8	$69.6^{+14.2}_{-12.2}$	125	$-3.52^{+0.20}_{-0.30}$	$0.338^{+0.067}_{-0.047}$	$(2.90^{+0.76}_{-0.48})10^{50}$

Pulse	T_{peak} [s]	T_{rise} [s]	T_f [s]	E_f [keV]	α	F_f [10^{-8} ergs s^{-1} cm^{-2}]	L_f [ergs s^{-1}]
11	147.6	4.3	$28.9^{+30.7}_{-15.3}$	125	$-2.74^{+1.43}_{-0.30}$	$0.918^{+0.427}_{-0.312}$	$(7.46^{+5.39}_{-2.45})10^{50}$
12	163.2	8.8	$42.8^{+7.1}_{-5.8}$	125	$-2.86^{+0.10}_{-0.12}$	$1.23^{+0.29}_{-0.25}$	$(9.92^{+2.45}_{-2.08})10^{50}$
13	181.6	5.3	$50.4^{+10.2}_{-8.0}$	125	$-3.17^{+0.14}_{-0.16}$	$0.936^{+0.213}_{-0.163}$	$(7.77^{+1.96}_{-1.44})10^{50}$
14	199.2	6.3	$128.8^{+24.8}_{-19.2}$	125	$-4.50^{+0.25}_{-0.00}$	$0.590^{+0.071}_{-0.072}$	$(6.19^{+0.75}_{-1.00})10^{50}$
15	237.4	15.1	$145.6^{+34.3}_{-31.4}$	1.00	$-3.13^{+0.60}_{-0.66}$	$0.332^{+0.070}_{-0.046}$	$(3.01^{+0.99}_{-0.59})10^{50}$
16	260.0	13.7	$27.9^{+1.1}_{-2.9}$	125	$-2.87^{+0.07}_{-0.03}$	$4.18^{+0.43}_{-0.44}$	$(3.43^{+0.36}_{-0.37})10^{51}$
17	292.6	19.4	$27.7^{+2.2}_{-7.0}$	125	$-3.10^{+0.14}_{-0.04}$	$2.94^{+1.04}_{-0.27}$	$(2.58^{+0.93}_{-0.27})10^{51}$
GRB 090812							
1	10.5	10.5	$24.8^{+0.7}_{-0.7}$	145	$-1.87^{+0.08}_{-0.08}$	$26.71^{+1.64}_{-1.50}$	$(1.47^{+0.12}_{-0.10})10^{52}$
2	25.7	1.7	$12.7^{+5.1}_{-3.1}$	145	$-1.47^{+0.55}_{-0.47}$	$12.24^{+5.82}_{-3.87}$	$(7.30^{+5.63}_{-2.82})10^{51}$
3	33.7	4.7	$4.76^{+0.45}_{-0.32}$	145	$-1.73^{+0.10}_{-0.10}$	$44.38^{+4.50}_{-4.09}$	$(2.52^{+0.32}_{-0.28})10^{52}$
4	61.7	6.3	$27.0^{+1.7}_{-2.3}$	145	$-2.55^{+0.06}_{-0.07}$	$7.35^{+0.92}_{-0.79}$	$(3.68^{+0.48}_{-0.41})10^{51}$
5	140.9	43.8	$155.5^{+8.0}_{-10.6}$	145	$-2.96^{+0.05}_{-0.04}$	$0.813^{+0.085}_{-0.059}$	$(3.97^{+0.42}_{-0.29})10^{50}$
6	267.1	23.6	$139.0^{+14.8}_{-18.4}$	1.91	$-2.78^{+0.18}_{-0.20}$	$0.174^{+0.015}_{-0.015}$	$(8.61^{+0.80}_{-0.78})10^{49}$
GRB 091018							
1	1.5	1.5	$4.71^{+0.11}_{-0.09}$	254	$-3.24^{+0.01}_{-0.01}$	$347.1^{+46.4}_{-43.0}$	$(1.44^{+0.20}_{-0.18})10^{52}$
GRB 091020							
1	5.6	5.6	$11.6^{+0.3}_{-0.3}$	185	$-2.24^{+0.07}_{-0.07}$	$64.91^{+3.04}_{-2.95}$	$(1.44^{+0.09}_{-0.09})10^{52}$
2	34.8	3.5	$11.9^{+4.3}_{-2.4}$	185	$-2.74^{+0.44}_{-0.39}$	$9.50^{+7.13}_{-4.03}$	$(1.92^{+1.70}_{-0.88})10^{51}$
3	76.5	5.3	$10.2^{+5.4}_{-2.2}$	185	$-2.75^{+0.21}_{-0.28}$	$1.34^{+0.93}_{-0.70}$	$(2.72^{+2.05}_{-1.47})10^{50}$
4	89.5	0.8	$80.1^{+21.8}_{-17.0}$	185	$-3.41^{+0.24}_{-0.29}$	$0.227^{+0.060}_{-0.047}$	$(4.15^{+1.32}_{-1.03})10^{49}$
GRB 091029							

Pulse	T_{peak} [s]	T_{rise} [s]	T_f [s]	E_f [keV]	α	F_f [10^{-8} ergs s^{-1} cm^{-2}]	L_f [ergs s^{-1}]
1	2.0	2.0	$9.5^{+0.9}_{-0.7}$	133	$-2.25^{+0.24}_{-0.25}$	$12.08^{+2.00}_{-1.64}$	$(8.12^{+1.63}_{-1.24})10^{51}$
2	6.2	2.5	$9.4^{+4.2}_{-2.4}$	133	$-2.28^{+0.48}_{-0.50}$	$6.81^{+2.85}_{-1.63}$	$(4.56^{+2.35}_{-1.18})10^{51}$
3	11.1	0.3	$9.8^{+6.3}_{-3.5}$	133	$-2.74^{+0.62}_{-0.62}$	$7.45^{+11.62}_{-2.54}$	$(4.88^{+8.14}_{-1.56})10^{51}$
4	20.6	3.9	$10.6^{+0.9}_{-0.8}$	133	$-2.64^{+0.12}_{-0.11}$	$26.67^{+2.66}_{-2.52}$	$(1.74^{+0.18}_{-0.17})10^{52}$
5	25.7	2.9	$6.3^{+3.8}_{-2.2}$	133	$-2.68^{+0.40}_{-0.51}$	$10.35^{+4.13}_{-2.79}$	$(6.81^{+2.93}_{-1.76})10^{51}$
6	28.4	2.5	$11.0^{+2.0}_{-1.7}$	133	$-2.37^{+0.24}_{-0.24}$	$12.48^{+2.67}_{-1.74}$	$(8.34^{+2.03}_{-1.26})10^{51}$
7	32.6	3.7	$11.6^{+4.5}_{-3.0}$	133	$-2.58^{+0.61}_{-0.66}$	$5.52^{+6.11}_{-1.55}$	$(3.65^{+4.50}_{-0.98})10^{51}$
8	36.0	6.1	$48.7^{+4.6}_{-7.2}$	133	$-4.66^{+1.01}_{-0.16}$	$3.71^{+1.09}_{-3.67}$	$(2.86^{+0.77}_{-2.83})10^{51}$
GRB 091109A							
1	11.0	11.0	$23.5^{+3.5}_{-2.8}$	123	$-2.55^{+0.20}_{-0.20}$	$14.86^{+4.46}_{-4.21}$	$(1.29^{+0.40}_{-0.36})10^{52}$
GRB 091208B							
1	1.0	1.0	$8.5^{+0.5}_{-0.9}$	242	$-2.88^{+0.23}_{-0.10}$	$128.6^{+70.6}_{-34.2}$	$(7.50^{+4.92}_{-2.17})10^{51}$
2	8.8	1.1	$2.31^{+0.10}_{-0.49}$	242	$-2.41^{+0.16}_{-0.15}$	$214.1^{+34.6}_{-20.6}$	$(1.47^{+0.34}_{-0.20})10^{52}$
GRB 100219A							
1	24.0	24.0	$68.6^{+18.0}_{-12.6}$	88	$-2.46^{+0.20}_{-0.18}$	$2.36^{+0.69}_{-0.79}$	$(5.46^{+1.70}_{-1.85})10^{51}$
GRB 100316B							
1	1.5	1.5	$9.9^{+0.7}_{-3.1}$	229	$-3.20^{+0.65}_{-0.21}$	$37.71^{+19.84}_{-33.78}$	$(2.67^{+2.22}_{-2.41})10^{51}$
GRB 100418A							
1	0.3	0.3	$9.5^{+2.2}_{-1.5}$	308	$-3.26^{+0.47}_{-0.89}$	$57.50^{+51.11}_{-56.92}$	$(7.37^{+10.25}_{-7.33})10^{50}$
2	10.2	4.7	$6.8^{+11.2}_{-4.5}$	308	$-2.56^{+1.70}_{-1.94}$	$7.55^{+5.52}_{-7.48}$	$(1.37^{+6.41}_{-1.36})10^{50}$
3	23.0	6.7	$25.3^{+5.3}_{-2.8}$	1.13	$-1.59^{+0.73}_{-1.21}$	$17.90^{+10.28}_{-8.49}$	$(2.42^{+1.83}_{-1.57})10^{50}$
GRB 100425A							

Pulse	T_{peak} [s]	T_{rise} [s]	T_f [s]	E_f [keV]	α	F_f [10^{-8} ergs s^{-1} cm^{-2}]	L_f [ergs s^{-1}]
1	1.3	1.3	$6.0^{+1.7}_{-1.0}$	181	$-3.42^{+0.33}_{-0.44}$	$94.04^{+150.00}_{-58.63}$	$(1.81^{+3.14}_{-1.18})10^{52}$
2	4.6	1.2	$10.8^{+2.6}_{-2.5}$	181	$-4.50^{+0.08}_{-0.00}$	$1490.1^{+719.6}_{-160.0}$	$(2.39^{+1.21}_{-0.26})10^{53}$
3	38.5	0.8	$6.5^{+1.0}_{-0.6}$	181	$-4.25^{+0.30}_{-0.12}$	$1107.4^{+9135.4}_{-1096.3}$	$(1.86^{+16.31}_{-1.84})10^{53}$
4	69.1	0.7	$3.72^{+3.14}_{-1.83}$	181	$-3.34^{+0.52}_{-0.67}$	$11.47^{+10.11}_{-4.01}$	$(2.25^{+2.32}_{-0.95})10^{51}$
5	90.8	10.4	$151.5^{+6.8}_{-8.5}$	14	$-4.67^{+0.22}_{-0.17}$	$0.558^{+0.025}_{-0.035}$	$(8.60^{+0.75}_{-0.29})10^{49}$
GRB 100513A							
1	5.3	5.3	$12.7^{+4.3}_{-1.3}$	87	$-2.52^{+0.35}_{-0.28}$	$7.12^{+3.44}_{-1.98}$	$(1.75^{+0.93}_{-0.50})10^{52}$
2	9.7	1.4	$8.3^{+2.4}_{-4.8}$	87	$-1.20^{+0.70}_{-0.75}$	$8.00^{+7.67}_{-2.99}$	$(2.06^{+2.37}_{-0.83})10^{52}$
3	18.7	2.9	$16.1^{+10.7}_{-5.5}$	87	$-2.30^{+0.76}_{-0.80}$	$3.43^{+3.29}_{-1.41}$	$(8.19^{+9.87}_{-3.22})10^{51}$
4	28.4	2.0	$11.4^{+7.1}_{-4.6}$	87	$-2.40^{+0.73}_{-0.85}$	$6.03^{+5.72}_{-2.64}$	$(1.44^{+1.90}_{-0.62})10^{52}$
5	37.6	0.1	$14.6^{+10.9}_{-7.1}$	87	$-1.81^{+0.85}_{-0.69}$	$4.74^{+3.49}_{-1.95}$	$(1.18^{+1.02}_{-0.49})10^{52}$
6	51.8	4.9	$22.9^{+10.8}_{-7.9}$	87	$-3.41^{+0.40}_{-0.45}$	$7.34^{+13.31}_{-7.26}$	$(2.29^{+5.79}_{-2.27})10^{52}$
7	229.6	43.3	$216.9^{+51.8}_{-49.7}$	87	$-3.13^{+0.23}_{-0.26}$	$0.0320^{+0.0110}_{-0.0080}$	$(8.77^{+4.29}_{-2.60})10^{49}$
GRB 100621A							
1	6.7	6.7	$26.0^{+0.3}_{-0.6}$	324	$-2.44^{+0.04}_{-0.04}$	$57.21^{+1.46}_{-1.43}$	$(7.79^{+0.37}_{-0.35})10^{50}$
2	19.4	5.3	$17.0^{+0.7}_{-1.4}$	324	$-2.63^{+0.07}_{-0.07}$	$55.21^{+3.34}_{-2.35}$	$(6.89^{+0.66}_{-0.49})10^{50}$
3	24.6	3.7	$11.3^{+1.1}_{-0.7}$	324	$-2.25^{+0.07}_{-0.07}$	$60.13^{+3.23}_{-4.26}$	$(8.97^{+0.83}_{-0.95})10^{50}$
4	30.6	3.9	$20.5^{+0.4}_{-0.4}$	324	$-2.86^{+0.02}_{-0.05}$	$178.2^{+12.6}_{-4.5}$	$(1.99^{+0.16}_{-0.09})10^{51}$
5	55.2	3.8	$29.1^{+1.0}_{-0.8}$	55	$-4.02^{+0.01}_{-0.01}$	$1569.9^{+382.5}_{-213.0}$	$(8.07^{+2.05}_{-1.16})10^{51}$
6	57.6	1.5	$19.7^{+2.0}_{-1.6}$	74	$-3.79^{+0.03}_{-0.13}$	$454.5^{+222.9}_{-209.4}$	$(2.62^{+1.36}_{-1.34})10^{51}$
7	150.3	53.8	$103.8^{+9.6}_{-5.3}$	324	$-3.80^{+0.11}_{-0.11}$	$12.31^{+1.02}_{-1.08}$	$(8.08^{+1.43}_{-1.28})10^{49}$
GRB 100724A							

Pulse	T_{peak} [s]	T_{rise} [s]	T_f [s]	E_f [keV]	α	F_f [10^{-8} ergs s^{-1} cm^{-2}]	L_f [ergs s^{-1}]
1	0.1	0.1	$1.58^{+0.24}_{-0.21}$	219	$-2.75^{+0.23}_{-0.25}$	$119.3^{+120.0}_{-98.6}$	$(1.14^{+1.28}_{-0.95})10^{52}$
GRB 100814A							
1	4.7	4.7	$8.6^{+0.1}_{-0.2}$	205	$-1.41^{+0.06}_{-0.06}$	$78.70^{+3.95}_{-4.23}$	$(1.61^{+0.13}_{-0.13})10^{52}$
2	8.5	0.9	$20.7^{+3.5}_{-2.7}$	205	$-1.99^{+0.12}_{-0.11}$	$25.22^{+3.83}_{-3.03}$	$(3.97^{+0.80}_{-0.60})10^{51}$
3	23.6	1.5	$3.90^{+2.70}_{-3.86}$	205	$-3.89^{+0.46}_{-0.61}$	$85.71^{+450.62}_{-84.86}$	$(8.49^{+52.28}_{-8.42})10^{51}$
4	29.3	2.5	$5.9^{+4.3}_{-2.7}$	205	$-3.71^{+0.23}_{-0.79}$	$37.31^{+17.65}_{-36.94}$	$(3.90^{+2.24}_{-3.87})10^{51}$
5	45.6	2.5	$5.6^{+1.5}_{-1.5}$	205	$-3.33^{+0.22}_{-0.70}$	$11.77^{+6.39}_{-11.65}$	$(1.36^{+0.86}_{-1.35})10^{51}$
6	53.6	2.8	$11.9^{+10.8}_{-11.7}$	205	$-2.48^{+0.74}_{-0.88}$	$2.88^{+3.72}_{-2.86}$	$(3.98^{+7.50}_{-3.95})10^{50}$
7	68.0	5.3	$12.8^{+0.8}_{-1.0}$	205	$-2.16^{+0.10}_{-0.08}$	$15.93^{+1.75}_{-1.35}$	$(2.41^{+0.35}_{-0.25})10^{51}$
8	73.7	3.0	$20.0^{+5.2}_{-2.8}$	205	$-2.13^{+0.09}_{-0.07}$	$10.01^{+1.73}_{-1.54}$	$(1.53^{+0.32}_{-0.26})10^{51}$
9	83.1	3.7	$9.6^{+9.0}_{-3.3}$	205	$-1.98^{+0.26}_{-0.17}$	$4.75^{+2.64}_{-1.56}$	$(7.59^{+5.45}_{-2.76})10^{50}$
10	97.2	3.6	$43.7^{+12.3}_{-8.3}$	205	$-2.37^{+0.07}_{-0.07}$	$3.42^{+1.01}_{-0.80}$	$(4.79^{+1.51}_{-1.18})10^{50}$
11	107.8	5.5	$47.4^{+14.5}_{-11.1}$	205	$-2.44^{+0.12}_{-0.10}$	$2.20^{+1.45}_{-0.66}$	$(2.98^{+2.11}_{-0.95})10^{50}$
12	122.9	3.1	$29.8^{+10.7}_{-6.7}$	205	$-2.55^{+0.08}_{-0.09}$	$3.03^{+1.18}_{-0.71}$	$(4.10^{+1.70}_{-1.02})10^{50}$
13	132.4	3.0	$39.2^{+17.3}_{-8.7}$	205	$-2.50^{+0.10}_{-0.16}$	$2.55^{+0.90}_{-0.96}$	$(3.41^{+1.31}_{-1.35})10^{50}$
14	141.1	1.7	$64.8^{+15.0}_{-11.5}$	205	$-2.73^{+0.10}_{-0.14}$	$1.62^{+0.62}_{-0.49}$	$(2.12^{+0.88}_{-0.69})10^{50}$
15	149.1	1.9	$10.3^{+1.1}_{-1.7}$	205	$-2.20^{+0.06}_{-0.05}$	$18.35^{+2.53}_{-1.80}$	$(2.69^{+0.43}_{-0.30})10^{51}$
16	179.8	14.8	$54.6^{+6.5}_{-12.0}$	205	$-3.11^{+0.18}_{-0.02}$	$1.45^{+0.35}_{-0.24}$	$(1.76^{+0.52}_{-0.30})10^{50}$
17	224.5	21.5	$124.4^{+13.4}_{-10.2}$	5.61	$-3.10^{+0.12}_{-0.15}$	$0.468^{+0.041}_{-0.039}$	$(5.27^{+0.59}_{-0.58})10^{49}$
GRB 100816A							
1	1.2	1.2	$1.87^{+0.08}_{-0.08}$	277	$-2.12^{+0.10}_{-0.05}$	$227.1^{+84.6}_{-10.0}$	$(9.13^{+4.04}_{-0.62})10^{51}$
2	14.3	0.4	$35.4^{+28.2}_{-22.7}$	277	$-3.64^{+0.41}_{-0.50}$	$4.09^{+9.51}_{-4.05}$	$(8.36^{+26.38}_{-8.30})10^{49}$

Pulse	T_{peak} [s]	T_{rise} [s]	T_f [s]	E_f [keV]	α	F_f [10^{-8} ergs s^{-1} cm^{-2}]	L_f [ergs s^{-1}]
3	134.7	12.3	$87.4^{+39.2}_{-18.9}$	277	$-2.87^{+0.36}_{-0.36}$	$0.129^{+0.119}_{-0.065}$	$(3.75^{+4.46}_{-2.16})10^{48}$
GRB 100901A							
1	9.3	9.3	$37.9^{+4.9}_{-3.5}$	208	$-3.29^{+0.18}_{-0.18}$	$21.71^{+9.93}_{-8.83}$	$(2.34^{+1.23}_{-1.02})10^{51}$
2	221.2	19.6	$85.3^{+13.1}_{-14.3}$	208	$-2.34^{+0.13}_{-0.15}$	$0.869^{+0.375}_{-0.327}$	$(1.18^{+0.58}_{-0.47})10^{50}$
3	254.2	13.4	$534.1^{+177.9}_{-149.6}$	197	$-3.35^{+0.26}_{-0.33}$	$0.0574^{+0.0161}_{-0.0114}$	$(6.14^{+2.26}_{-1.67})10^{48}$
4	321.9	31.2	$309.8^{+47.1}_{-51.4}$	155	$-2.40^{+0.12}_{-0.13}$	$0.496^{+0.341}_{-0.150}$	$(6.22^{+4.48}_{-1.96})10^{49}$
5	391.0	21.9	$66.6^{+7.3}_{-5.3}$	128	$-2.22^{+0.05}_{-0.05}$	$2.92^{+0.43}_{-0.41}$	$(3.70^{+0.57}_{-0.53})10^{50}$
6	455.6	50.7	$220.6^{+48.2}_{-54.7}$	110	$-4.50^{+0.42}_{-0.00}$	$0.0812^{+0.0173}_{-0.0172}$	$(6.09^{+2.36}_{-1.29})10^{48}$
GRB 100906A							
1	2.1	2.1	$11.7^{+0.7}_{-0.5}$	183	$-1.95^{+0.05}_{-0.06}$	$111.5^{+4.9}_{-6.9}$	$(2.65^{+0.16}_{-0.21})10^{52}$
2	5.9	2.2	$14.2^{+3.8}_{-2.1}$	183	$-2.68^{+0.25}_{-0.25}$	$27.14^{+7.45}_{-4.50}$	$(5.65^{+1.85}_{-1.10})10^{51}$
3	11.0	3.8	$4.46^{+0.22}_{-0.27}$	183	$-2.07^{+0.07}_{-0.07}$	$101.0^{+6.1}_{-61.3}$	$(2.40^{+0.19}_{-1.47})10^{52}$
4	48.6	6.0	$18.4^{+1.9}_{-3.5}$	183	$-3.08^{+0.26}_{-0.25}$	$12.66^{+14.21}_{-4.77}$	$(2.49^{+2.99}_{-1.00})10^{51}$
5	53.2	1.5	$10.6^{+5.0}_{-5.6}$	183	$-2.88^{+0.55}_{-0.62}$	$8.37^{+10.86}_{-3.18}$	$(1.65^{+2.50}_{-0.72})10^{51}$
6	69.5	0.2	$12.1^{+8.8}_{-6.6}$	183	$-3.34^{+0.16}_{-0.17}$	$18.74^{+15.27}_{-7.67}$	$(3.37^{+2.91}_{-1.44})10^{51}$
7	79.9	4.3	$20.4^{+3.5}_{-2.5}$	183	$-3.23^{+0.13}_{-0.11}$	$15.92^{+4.60}_{-4.19}$	$(3.08^{+0.97}_{-0.85})10^{51}$
8	91.0	2.5	$19.0^{+5.7}_{-4.4}$	183	$-3.24^{+0.13}_{-0.11}$	$13.15^{+3.68}_{-3.82}$	$(2.53^{+0.78}_{-0.77})10^{51}$
9	100.9	3.3	$12.0^{+1.2}_{-1.2}$	183	$-2.92^{+0.07}_{-0.06}$	$24.00^{+2.57}_{-2.46}$	$(4.84^{+0.57}_{-0.53})10^{51}$
10	105.7	2.2	$5.8^{+0.8}_{-0.4}$	183	$-2.81^{+0.06}_{-0.05}$	$41.35^{+2.94}_{-4.13}$	$(8.52^{+0.68}_{-0.90})10^{51}$
11	112.0	1.6	$11.8^{+3.6}_{-3.1}$	183	$-3.30^{+0.09}_{-0.09}$	$19.73^{+3.94}_{-3.85}$	$(3.75^{+0.81}_{-0.78})10^{51}$
12	118.6	3.6	$9.8^{+1.3}_{-0.6}$	183	$-3.25^{+0.05}_{-0.05}$	$37.37^{+4.20}_{-4.92}$	$(7.18^{+0.88}_{-0.99})10^{51}$
13	124.8	3.1	$15.6^{+3.1}_{-2.1}$	183	$-3.50^{+0.10}_{-0.11}$	$22.65^{+6.33}_{-5.37}$	$(4.14^{+1.25}_{-1.05})10^{51}$

Pulse	T_{peak} [s]	T_{rise} [s]	T_f [s]	E_f [keV]	α	F_f [10^{-8} ergs s^{-1} cm^{-2}]	L_f [ergs s^{-1}]
14	134.7	6.9	$32.4^{+4.0}_{-3.3}$	183	$-3.88^{+0.13}_{-0.15}$	$15.17^{+2.77}_{-2.59}$	$(2.61^{+0.55}_{-0.51})10^{51}$
GRB 101219A							
1	0.0	0.02	$0.283^{+0.083}_{-0.068}$	291	$-1.30^{+0.23}_{-0.22}$	$417.9^{+122.2}_{-99.1}$	$(2.20^{+1.25}_{-0.78})10^{52}$
2	0.5	0.2	$0.283^{+0.110}_{-0.073}$	291	$-1.43^{+0.40}_{-0.38}$	$120.6^{+64.8}_{-45.1}$	$(5.78^{+6.52}_{-2.99})10^{51}$
3	127.2	120.1	$122.3^{+51.9}_{-36.4}$	291	$-2.87^{+0.41}_{-0.42}$	$0.0843^{+0.0859}_{-0.0491}$	$(2.41^{+3.32}_{-1.59})10^{48}$
GRB 101219B							
1	11.7	11.7	$53.4^{+8.2}_{-7.4}$	323	$-2.27^{+0.06}_{-0.06}$	$21.78^{+6.27}_{-6.01}$	$(3.32^{+1.09}_{-0.99})10^{50}$
2	326.6	123.4	$315.2^{+38.0}_{-23.7}$	143	$-3.27^{+0.12}_{-0.13}$	$0.0478^{+0.0073}_{-0.0070}$	$(4.33^{+1.00}_{-0.92})10^{47}$
GRB 110106B							
1	5.4	5.4	$6.0^{+0.4}_{-0.2}$	309	$-2.62^{+0.22}_{-0.24}$	$20.12^{+4.45}_{-2.75}$	$(3.58^{+1.24}_{-0.80})10^{50}$
2	9.7	1.3	$16.3^{+5.9}_{-4.0}$	309	$-2.79^{+0.26}_{-0.27}$	$27.58^{+9.99}_{-5.55}$	$(4.33^{+2.27}_{-1.29})10^{50}$
3	20.8	3.3	$9.3^{+1.7}_{-2.6}$	309	$-2.97^{+0.46}_{-0.55}$	$22.76^{+26.89}_{-8.23}$	$(3.36^{+5.66}_{-1.80})10^{50}$
4	825.6	586.6	$1017.6^{+679.1}_{-209.1}$	61	$-3.11^{+0.36}_{-0.53}$	$0.0351^{+0.0205}_{-0.0134}$	$(4.57^{+3.64}_{-2.48})10^{47}$
5	1959.9	122.5	$364.0^{+1072.9}_{-360.3}$	26	$-3.55^{+2.84}_{-0.95}$	$0.0068^{+0.0199}_{-0.0067}$	$(6.71^{+35.89}_{-6.67})10^{46}$
GRB 110205A							
1	14.5	14.5	$41.1^{+14.1}_{-7.5}$	155	$-2.10^{+0.29}_{-0.26}$	$6.13^{+1.64}_{-1.48}$	$(2.55^{+0.88}_{-0.69})10^{51}$
2	26.0	6.7	$27.1^{+17.9}_{-15.0}$	155	$-2.29^{+0.83}_{-0.63}$	$4.41^{+2.48}_{-2.06}$	$(1.77^{+1.58}_{-0.88})10^{51}$
3	53.1	5.3	$26.2^{+6.2}_{-3.2}$	155	$-2.16^{+0.23}_{-0.20}$	$11.05^{+2.17}_{-2.20}$	$(4.48^{+1.12}_{-1.00})10^{51}$
4	65.7	1.4	$5.8^{+13.2}_{-3.0}$	155	$-2.59^{+0.84}_{-1.17}$	$7.02^{+21.23}_{-3.56}$	$(2.70^{+9.81}_{-1.44})10^{51}$
5	86.4	14.3	$25.2^{+2.2}_{-1.6}$	155	$-2.42^{+0.11}_{-0.10}$	$10.37^{+0.88}_{-0.84}$	$(4.15^{+0.42}_{-0.38})10^{51}$
6	103.1	3.0	$14.6^{+2.5}_{-5.5}$	155	$-2.40^{+0.27}_{-0.22}$	$6.25^{+1.44}_{-1.11}$	$(2.45^{+0.69}_{-0.48})10^{51}$
7	114.1	5.5	$34.4^{+2.3}_{-1.8}$	155	$-2.31^{+0.04}_{-0.04}$	$19.80^{+1.05}_{-1.07}$	$(7.78^{+0.46}_{-0.45})10^{51}$

Pulse	T_{peak} [s]	T_{rise} [s]	T_f [s]	E_f [keV]	α	F_f [10^{-8} ergs s^{-1} cm^{-2}]	L_f [ergs s^{-1}]
8	133.6	2.5	$17.9^{+3.0}_{-2.0}$	155	$-2.14^{+0.05}_{-0.05}$	$16.78^{+2.08}_{-2.01}$	$(6.80^{+0.91}_{-0.86})10^{51}$
9	147.4	3.8	$23.0^{+4.5}_{-2.5}$	155	$-2.34^{+0.05}_{-0.05}$	$8.63^{+1.16}_{-1.15}$	$(3.41^{+0.49}_{-0.47})10^{51}$
10	155.5	2.4	$17.6^{+5.3}_{-5.3}$	155	$-2.43^{+0.07}_{-0.06}$	$7.28^{+2.05}_{-1.55}$	$(2.82^{+0.82}_{-0.61})10^{51}$
11	165.3	3.1	$43.1^{+6.8}_{-5.1}$	155	$-2.34^{+0.04}_{-0.04}$	$9.07^{+0.97}_{-1.06}$	$(3.63^{+0.41}_{-0.44})10^{51}$
12	188.3	13.8	$36.2^{+2.3}_{-1.6}$	155	$-2.16^{+0.02}_{-0.02}$	$22.67^{+0.94}_{-0.94}$	$(9.38^{+0.43}_{-0.42})10^{51}$
13	205.6	3.6	$27.7^{+10.0}_{-5.2}$	155	$-2.59^{+0.08}_{-0.08}$	$3.85^{+0.88}_{-0.91}$	$(1.51^{+0.36}_{-0.36})10^{51}$
14	222.3	3.8	$39.3^{+8.7}_{-6.8}$	155	$-2.72^{+0.09}_{-0.10}$	$3.41^{+0.80}_{-0.81}$	$(1.27^{+0.31}_{-0.31})10^{51}$
15	245.3	10.2	$170.4^{+13.5}_{-9.4}$	155	$-2.65^{+0.03}_{-0.04}$	$2.90^{+0.28}_{-0.38}$	$(1.10^{+0.11}_{-0.15})10^{51}$
16	443.5	26.6	$1993.8^{+319.7}_{-302.1}$	106	$-3.10^{+0.13}_{-0.15}$	$0.0520^{+0.0089}_{-0.0070}$	$(1.87^{+0.33}_{-0.26})10^{49}$
17	588.0	21.1	$93.3^{+11.7}_{-8.3}$	81	$-3.63^{+0.17}_{-0.22}$	$0.196^{+0.026}_{-0.024}$	$(7.16^{+1.00}_{-0.93})10^{49}$
GRB 110213A							
1	3.5	3.5	$10.2^{+1.1}_{-2.4}$	203	$-2.61^{+0.46}_{-0.80}$	$64.22^{+86.86}_{-11.13}$	$(9.03^{+14.76}_{-2.76})10^{51}$
2	5.3	0.5	$6.2^{+1.7}_{-1.2}$	203	$-2.96^{+0.26}_{-0.28}$	$208.5^{+122.1}_{-55.9}$	$(2.66^{+1.78}_{-0.83})10^{52}$
3	11.9	1.6	$9.2^{+12.5}_{-9.1}$	203	$-4.13^{+0.75}_{-0.37}$	$692.5^{+5900.2}_{-685.6}$	$(6.58^{+71.03}_{-6.52})10^{52}$
4	14.7	1.3	$3.42^{+9.62}_{-3.39}$	203	$-1.93^{+1.43}_{-2.57}$	$25.61^{+66.68}_{-25.35}$	$(4.28^{+29.38}_{-4.26})10^{51}$
5	21.8	0.3	$7.0^{+3.8}_{-1.7}$	203	$-2.97^{+0.23}_{-0.43}$	$107.1^{+48.4}_{-106.0}$	$(1.36^{+0.71}_{-1.35})10^{52}$
6	91.9	3.0	$41.4^{+69.0}_{-6.1}$	0.64	$-3.90^{+1.18}_{-0.60}$	$8.27^{+22.91}_{-8.19}$	$(6.32^{+24.74}_{-6.26})10^{50}$
GRB 110422A							
1	2.2	2.2	$12.8^{+0.4}_{-0.9}$	181	$-2.13^{+0.11}_{-0.12}$	$86.17^{+6.42}_{-6.43}$	$(2.13^{+0.22}_{-0.21})10^{52}$
2	8.6	2.3	$9.1^{+1.5}_{-0.6}$	181	$-1.88^{+0.09}_{-0.11}$	$134.5^{+10.1}_{-13.4}$	$(3.54^{+0.38}_{-0.46})10^{52}$
3	14.1	3.6	$7.3^{+0.1}_{-0.5}$	181	$-1.81^{+0.08}_{-0.04}$	$294.1^{+18.7}_{-13.4}$	$(7.96^{+0.72}_{-0.45})10^{52}$
4	19.1	4.5	$4.54^{+0.37}_{-0.16}$	181	$-1.96^{+0.04}_{-0.04}$	$372.9^{+17.2}_{-23.2}$	$(9.69^{+0.58}_{-0.71})10^{52}$

Pulse	T_{peak} [s]	T_{rise} [s]	T_f [s]	E_f [keV]	α	F_f [10^{-8} ergs s^{-1} cm^{-2}]	L_f [ergs s^{-1}]
5	23.2	1.2	$5.9^{+0.4}_{-0.3}$	181	$-2.28^{+0.09}_{-0.10}$	$204.6^{+12.7}_{-13.5}$	$(4.86^{+0.41}_{-0.41})10^{52}$
6	28.1	3.2	$3.20^{+0.37}_{-0.39}$	181	$-2.21^{+0.13}_{-0.04}$	$167.0^{+11.6}_{-13.7}$	$(4.11^{+0.42}_{-0.37})10^{52}$
7	31.0	1.4	$2.14^{+0.23}_{-0.11}$	181	$-2.87^{+0.18}_{-0.20}$	$125.9^{+45.0}_{-23.0}$	$(2.74^{+1.07}_{-0.56})10^{52}$
GRB 110503A							
1	2.4	2.4	$3.97^{+0.18}_{-0.14}$	191	$-2.05^{+0.05}_{-0.05}$	$496.7^{+27.3}_{-23.8}$	$(1.01^{+0.07}_{-0.06})10^{53}$
GRB 110715A							
1	0.9	0.9	$2.50^{+0.00}_{-0.10}$	275	$-2.48^{+0.07}_{-0.07}$	$211.0^{+11.0}_{-0.0}$	$(7.57^{+0.62}_{-0.21})10^{51}$
2	1.3	0.3	$1.35^{+0.06}_{-0.00}$	275	$-2.18^{+0.06}_{-0.06}$	$424.1^{+0.0}_{-15.4}$	$(1.73^{+0.05}_{-0.11})10^{52}$
3	2.2	0.6	$1.94^{+0.00}_{-0.08}$	275	$-3.14^{+0.03}_{-0.00}$	$732.6^{+37.9}_{-0.0}$	$(2.06^{+0.13}_{-0.00})10^{52}$
4	3.1	0.9	$0.92^{+0.00}_{-0.01}$	275	$-2.20^{+0.02}_{-0.02}$	$899.0^{+13.1}_{-0.0}$	$(3.68^{+0.10}_{-0.04})10^{52}$
5	14.2	0.4	$4.00^{+1.10}_{-1.04}$	275	$-2.62^{+0.22}_{-0.28}$	$50.21^{+19.25}_{-6.99}$	$(1.72^{+0.86}_{-0.39})10^{51}$
6	15.5	3.8	$120.9^{+47.0}_{-40.4}$	275	$-3.25^{+0.23}_{-0.27}$	$1.05^{+0.67}_{-0.53}$	$(2.71^{+2.21}_{-1.53})10^{49}$
7	50649.7	37085.0	$247338^{+232795}_{-233397}$	275	$-2.94^{+0.99}_{-1.03}$	$0.0013^{+0.0012}_{-0.0012}$	$(4.03^{+3.44}_{-3.38})10^{46}$
GRB 110726A							
1	3.0	3.0	$8.2^{+8.1}_{-8.1}$	246	$-3.14^{+1.17}_{-1.17}$	$151.0^{+138.4}_{-141.5}$	$(7.68^{+6.71}_{-6.95})10^{51}$
GRB 110808A							
1	0.3	0.3	$11.5^{+11.2}_{-11.2}$	213	$-3.60^{+1.63}_{-1.64}$	$533.4^{+469.7}_{-474.9}$	$(4.74^{+3.86}_{-3.93})10^{52}$
GRB 110818A							
1	9.9	9.9	$13.1^{+12.5}_{-12.6}$	115	$-2.17^{+0.24}_{-0.24}$	$99.06^{+95.63}_{-96.14}$	$(1.08^{+1.04}_{-1.05})10^{53}$
2	22.4	3.2	$3.45^{+2.83}_{-3.05}$	115	$-2.41^{+0.56}_{-0.51}$	$63.25^{+57.60}_{-58.30}$	$(6.98^{+6.33}_{-6.42})10^{52}$
3	30.2	5.3	$12.8^{+12.0}_{-12.0}$	115	$-2.09^{+0.15}_{-0.21}$	$103.0^{+98.0}_{-97.5}$	$(1.12^{+1.06}_{-1.06})10^{53}$
4	49.8	5.3	$14.1^{+13.3}_{-13.3}$	115	$-2.54^{+0.65}_{-0.64}$	$104.4^{+89.7}_{-95.6}$	$(1.12^{+0.96}_{-1.02})10^{53}$

Pulse	T_{peak} [s]	T_{rise} [s]	T_f [s]	E_f [keV]	α	F_f [10^{-8} ergs s^{-1} cm^{-2}]	L_f [ergs s^{-1}]
GRB 111008A							
1	0.9	0.9	$1.97^{+1.71}_{-1.82}$	83	$-2.05^{+0.20}_{-0.18}$	$329.4^{+305.6}_{-311.4}$	$(8.96^{+8.31}_{-8.47})10^{53}$
2	3.4	1.1	$2.62^{+2.52}_{-2.53}$	83	$-1.75^{+0.20}_{-0.18}$	$622.6^{+601.4}_{-600.7}$	$(1.71^{+1.65}_{-1.65})10^{54}$
3	6.2	0.7	$2.21^{+2.00}_{-2.07}$	83	$-1.69^{+0.13}_{-0.19}$	$433.1^{+395.9}_{-401.5}$	$(1.18^{+1.08}_{-1.09})10^{54}$
4	9.9	3.0	$3.49^{+3.09}_{-3.23}$	83	$-2.43^{+0.54}_{-0.76}$	$134.0^{+59.4}_{-120.4}$	$(3.75^{+1.64}_{-3.37})10^{53}$
5	31.7	0.7	$4.26^{+4.13}_{-4.12}$	83	$-2.19^{+0.25}_{-0.29}$	$250.5^{+241.1}_{-241.6}$	$(6.74^{+6.49}_{-6.50})10^{53}$
6	36.0	0.5	$1.78^{+1.65}_{-1.67}$	83	$-2.35^{+0.53}_{-0.44}$	$255.0^{+218.1}_{-235.3}$	$(6.87^{+5.87}_{-6.34})10^{53}$
7	64.8	3.8	$7.3^{+7.2}_{-7.2}$	83	$-2.77^{+0.78}_{-0.78}$	$130.4^{+127.6}_{-128.0}$	$(3.72^{+3.64}_{-3.65})10^{53}$
GRB 111107A							
1	4.0	4.0	$8.0^{+7.8}_{-7.8}$	128	$-2.01^{+0.06}_{-0.07}$	$106.6^{+103.5}_{-103.5}$	$(8.29^{+8.04}_{-8.05})10^{52}$
GRB 111228A							
1	3.4	3.4	$7.1^{+6.1}_{-6.7}$	291	$-3.22^{+1.26}_{-1.37}$	$373.8^{+263.8}_{-334.3}$	$(7.09^{+3.13}_{-5.76})10^{51}$
2	11.8	1.3	$3.53^{+3.11}_{-3.15}$	291	$-3.27^{+1.35}_{-1.35}$	$497.6^{+399.3}_{-362.2}$	$(9.15^{+5.77}_{-4.50})10^{51}$
3	36.2	2.6	$4.17^{+3.79}_{-3.84}$	291	$-3.48^{+1.56}_{-1.52}$	$633.5^{+573.8}_{-489.9}$	$(1.11^{+0.89}_{-0.59})10^{52}$
4	40.7	2.2	$6.3^{+5.1}_{-5.7}$	291	$-3.46^{+1.59}_{-1.60}$	$1148.6^{+743.5}_{-814.2}$	$(1.89^{+0.46}_{-0.71})10^{52}$
5	49.3	0.2	$1.80^{+1.67}_{-1.68}$	291	$-2.95^{+0.99}_{-0.99}$	$1459.2^{+1350.9}_{-1354.9}$	$(3.12^{+2.76}_{-2.77})10^{52}$
6	53.2	1.8	$3.12^{+3.05}_{-3.04}$	291	$-2.83^{+0.85}_{-0.85}$	$1087.1^{+1062.7}_{-1068.9}$	$(2.47^{+2.39}_{-2.41})10^{52}$
7	57.0	1.8	$2.65^{+2.61}_{-2.60}$	291	$-2.87^{+0.90}_{-0.89}$	$1237.0^{+1211.5}_{-1209.7}$	$(2.76^{+2.67}_{-2.67})10^{52}$
8	92.1	0.9	$2.37^{+2.27}_{-2.27}$	291	$-3.65^{+1.71}_{-1.69}$	$2225.8^{+1945.0}_{-1838.5}$	$(3.27^{+2.32}_{-1.98})10^{52}$
9	96.4	1.3	$9.5^{+9.5}_{-9.4}$	291	$-3.58^{+1.59}_{-1.59}$	$4669.7^{+4544.5}_{-4587.9}$	$(7.01^{+6.60}_{-6.75})10^{52}$
GRB 111229A							
1	4.6	4.6	$7.6^{+7.2}_{-7.3}$	210	$-2.68^{+0.79}_{-0.75}$	$84.91^{+75.10}_{-79.22}$	$(1.03^{+0.88}_{-0.94})10^{52}$

Pulse	T_{peak} [s]	T_{rise} [s]	T_f [s]	E_f [keV]	α	F_f [10^{-8} ergs s^{-1} cm^{-2}]	L_f [ergs s^{-1}]
GRB 120118B							
1	2.1	2.1	$4.32^{+4.12}_{-4.12}$	127	$-2.47^{+0.55}_{-0.55}$	$115.7^{+108.0}_{-109.0}$	$(9.02^{+8.40}_{-8.48})10^{52}$
2	7.4	1.8	$3.54^{+3.40}_{-3.39}$	127	$-2.56^{+0.62}_{-0.63}$	$199.7^{+183.3}_{-190.1}$	$(1.56^{+1.42}_{-1.48})10^{53}$
3	10.7	0.3	$0.55^{+0.40}_{-0.47}$	127	$-2.78^{+0.91}_{-0.89}$	$147.2^{+117.5}_{-122.8}$	$(1.15^{+0.90}_{-0.95})10^{53}$
4	13.4	2.3	$3.11^{+2.95}_{-2.97}$	127	$-2.91^{+1.00}_{-0.96}$	$176.5^{+156.0}_{-157.5}$	$(1.42^{+1.25}_{-1.26})10^{53}$
5	18.9	3.0	$7.2^{+7.0}_{-7.0}$	127	$-2.87^{+0.93}_{-0.93}$	$129.4^{+117.1}_{-119.0}$	$(1.00^{+0.90}_{-0.92})10^{53}$
GRB 120211A							
1	10.0	10.0	$10.9^{+10.4}_{-10.4}$	147	$-2.10^{+0.17}_{-0.40}$	$27.77^{+25.98}_{-26.01}$	$(1.40^{+1.30}_{-1.31})10^{52}$
GRB 120326A							
1	2.8	2.8	$5.9^{+5.9}_{-5.9}$	179	$-2.85^{+0.86}_{-0.86}$	$604.8^{+595.9}_{-595.8}$	$(1.37^{+1.34}_{-1.34})10^{53}$
GRB 120327A							
1	2.2	2.2	$3.64^{+3.45}_{-3.45}$	131	$-1.78^{+0.13}_{-0.12}$	$106.4^{+99.0}_{-100.5}$	$(8.09^{+7.54}_{-7.66})10^{52}$
2	19.0	0.8	$4.06^{+4.06}_{-4.02}$	131	$-2.50^{+0.50}_{-0.50}$	$178.2^{+178.2}_{-176.4}$	$(1.22^{+1.22}_{-1.21})10^{53}$
3	38.5	2.5	$2.87^{+2.70}_{-2.81}$	131	$-1.81^{+0.18}_{-0.19}$	$491.6^{+473.5}_{-482.8}$	$(3.73^{+3.59}_{-3.66})10^{53}$
4	44.1	1.2	$12.3^{+11.9}_{-11.9}$	131	$-2.37^{+0.39}_{-0.39}$	$70.72^{+65.48}_{-65.49}$	$(4.79^{+4.42}_{-4.43})10^{52}$
GRB 120404A							
1	4.4	4.4	$4.27^{+3.95}_{-3.96}$	129	$-2.58^{+0.64}_{-0.64}$	$96.89^{+92.37}_{-93.38}$	$(7.96^{+7.57}_{-7.66})10^{52}$
2	8.9	2.7	$5.7^{+5.5}_{-5.5}$	129	$-2.47^{+0.51}_{-0.51}$	$89.80^{+87.08}_{-86.21}$	$(6.63^{+6.42}_{-6.35})10^{52}$
3	18.9	5.2	$13.8^{+13.5}_{-13.5}$	129	$-2.62^{+0.66}_{-0.65}$	$78.81^{+74.94}_{-74.88}$	$(5.82^{+5.51}_{-5.51})10^{52}$
GRB 120422A							
1	6.2	6.2	$14.0^{+12.1}_{-12.3}$	390	$-2.49^{+0.49}_{-0.49}$	$44.82^{+43.78}_{-43.89}$	$(1.34^{+1.30}_{-1.31})10^{50}$
GRB 120521C							

Pulse	T_{peak} [s]	T_{rise} [s]	T_f [s]	E_f [keV]	α	F_f [10^{-8} ergs s^{-1} cm^{-2}]	L_f [ergs s^{-1}]
1	2.2	2.2	$4.05^{+3.93}_{-3.92}$	72	$-1.73^{+0.22}_{-0.21}$	$166.7^{+162.4}_{-162.4}$	$(6.84^{+6.66}_{-6.66})10^{53}$
2	8.5	2.5	$9.2^{+9.0}_{-9.0}$	72	$-3.36^{+1.40}_{-1.40}$	$250.2^{+213.3}_{-229.5}$	$(1.37^{+1.22}_{-1.29})10^{54}$
GRB 120712A							
1	2.9	2.9	$3.77^{+3.63}_{-3.62}$	97	$-1.60^{+0.35}_{-0.33}$	$173.9^{+165.2}_{-165.6}$	$(3.26^{+3.10}_{-3.11})10^{53}$
2	11.8	6.3	$6.5^{+6.4}_{-6.4}$	97	$-2.13^{+0.16}_{-0.17}$	$152.7^{+149.7}_{-149.6}$	$(2.80^{+2.74}_{-2.74})10^{53}$
GRB 120729A							
1	4.2	4.2	$11.4^{+11.3}_{-11.3}$	278	$-2.26^{+0.27}_{-0.28}$	$269.8^{+267.1}_{-267.0}$	$(9.89^{+9.78}_{-9.77})10^{51}$
GRB 120802A							
1	1.2	1.2	$3.84^{+3.74}_{-3.75}$	104	$-2.04^{+0.09}_{-0.09}$	$175.8^{+171.7}_{-171.7}$	$(2.56^{+2.50}_{-2.50})10^{53}$
2	8.7	2.5	$4.77^{+4.71}_{-4.71}$	104	$-2.37^{+0.40}_{-0.40}$	$251.8^{+247.8}_{-248.0}$	$(3.62^{+3.57}_{-3.57})10^{53}$
GRB 120804A							
1	3.4	3.4	$0.69^{+0.67}_{-0.67}$	217	$-2.22^{+0.25}_{-0.24}$	$1125.4^{+1103.1}_{-1106.3}$	$(1.34^{+1.31}_{-1.32})10^{53}$
GRB 120811C							
1	6.3	6.3	$12.8^{+11.2}_{-11.3}$	136	$-2.47^{+0.48}_{-0.47}$	$147.8^{+143.6}_{-145.2}$	$(9.14^{+8.87}_{-8.97})10^{52}$
2	9.7	2.4	$4.70^{+4.66}_{-4.64}$	136	$-2.68^{+0.69}_{-0.69}$	$376.7^{+373.3}_{-351.4}$	$(2.31^{+2.29}_{-2.15})10^{53}$
3	14.5	2.5	$3.56^{+3.44}_{-3.44}$	136	$-3.35^{+1.41}_{-1.40}$	$382.1^{+324.8}_{-332.0}$	$(2.72^{+2.29}_{-2.35})10^{53}$
GRB 120907A							
1	2.0	2.0	$3.02^{+2.81}_{-2.83}$	254	$-2.46^{+0.52}_{-0.52}$	$284.5^{+273.5}_{-273.7}$	$(1.55^{+1.47}_{-1.48})10^{52}$
GRB 121027A							
1	11.2	11.2	$36.3^{+2.9}_{-2.0}$	180	$-2.63^{+0.08}_{-0.07}$	$16.60^{+1.46}_{-1.35}$	$(3.70^{+0.37}_{-0.33})10^{51}$
2	59.8	7.7	$62.1^{+9.4}_{-7.6}$	180	$-2.89^{+0.06}_{-0.08}$	$3.65^{+0.78}_{-0.71}$	$(7.80^{+1.75}_{-1.58})10^{50}$
3	176.2	26.0	$215.0^{+91.8}_{-38.6}$	180	$-3.81^{+0.26}_{-0.69}$	$0.175^{+0.032}_{-0.031}$	$(3.19^{+0.76}_{-0.86})10^{49}$

Pulse	T_{peak} [s]	T_{rise} [s]	T_f [s]	E_f [keV]	α	F_f [10^{-8} ergs s^{-1} cm^{-2}]	L_f [ergs s^{-1}]
4	264.3	35.4	$232.9^{+13.5}_{-16.3}$	180	$-3.49^{+0.09}_{-0.10}$	$0.492^{+0.040}_{-0.031}$	$(9.80^{+0.95}_{-0.76})10^{49}$
5	1217.0	81.8	$1000.0^{+52.3}_{-114.4}$	180	$-2.36^{+0.06}_{-0.21}$	$1.91^{+0.38}_{-0.86}$	$(4.40^{+0.95}_{-2.06})10^{50}$
6	1754.9	306.8	$708.9^{+143.4}_{-93.2}$	180	$-2.90^{+0.18}_{-0.33}$	$5.71^{+4.14}_{-1.12}$	$(1.24^{+0.95}_{-0.29})10^{51}$
7	2078.7	5.1	$234.7^{+511.1}_{-232.4}$	180	$-3.25^{+1.12}_{-1.16}$	$6.97^{+29.69}_{-6.90}$	$(1.41^{+7.47}_{-1.40})10^{51}$
8	2439.9	124.4	$244.0^{+211.9}_{-58.7}$	180	$-2.91^{+0.49}_{-0.48}$	$5.58^{+6.22}_{-1.76}$	$(1.21^{+1.54}_{-0.44})10^{51}$
9	3123.7	122.1	$378.2^{+24.8}_{-17.8}$	180	$-2.49^{+0.08}_{-0.08}$	$20.90^{+1.28}_{-1.09}$	$(4.78^{+0.36}_{-0.31})10^{51}$
10	3720.5	64.4	$321.9^{+100.5}_{-68.1}$	180	$-3.18^{+0.42}_{-0.48}$	$8.00^{+11.73}_{-3.52}$	$(1.64^{+2.64}_{-0.79})10^{51}$
11	4428.2	101.1	$456.5^{+70.2}_{-51.9}$	180	$-2.89^{+0.11}_{-0.11}$	$5.99^{+1.46}_{-1.37}$	$(1.28^{+0.33}_{-0.31})10^{51}$
12	5143.5	1240.8	$1260.5^{+220.8}_{-176.7}$	180	$-2.34^{+0.10}_{-0.07}$	$1.25^{+0.39}_{-0.20}$	$(3.04^{+1.04}_{-0.52})10^{50}$
13	5757.8	173.4	$1873.8^{+92.7}_{-130.5}$	180	$-2.41^{+0.06}_{-0.01}$	$1.96^{+0.21}_{-0.20}$	$(4.50^{+0.55}_{-0.47})10^{50}$
14	11250.6	3060.0	$3090.9^{+403.4}_{-349.1}$	180	$-3.09^{+0.07}_{-0.07}$	$0.141^{+0.012}_{-0.010}$	$(5.91^{+0.58}_{-0.47})10^{49}$
15	17511.8	3124.5	17964^{+4068}_{-17785}	180	$-4.50^{+1.11}_{-0.00}$	$0.0085^{+0.0025}_{-0.0016}$	$(1.41^{+0.80}_{-0.27})10^{48}$
GRB 121128A							
1	1.0	1.0	$1.69^{+1.62}_{-1.63}$	156	$-2.70^{+0.72}_{-0.73}$	$423.7^{+411.3}_{-413.1}$	$(1.61^{+1.56}_{-1.57})10^{53}$
2	4.1	1.6	$1.77^{+1.77}_{-1.75}$	156	$-2.29^{+0.29}_{-0.29}$	$635.1^{+630.0}_{-627.0}$	$(2.55^{+2.53}_{-2.52})10^{53}$
3	6.5	1.1	$2.18^{+1.97}_{-2.05}$	156	$-2.45^{+0.45}_{-0.46}$	$607.0^{+518.7}_{-507.9}$	$(2.37^{+2.00}_{-1.96})10^{53}$
4	7.9	0.1	$2.05^{+1.84}_{-1.41}$	156	$-2.42^{+0.46}_{-0.49}$	$528.2^{+414.2}_{-468.3}$	$(2.03^{+1.56}_{-1.79})10^{53}$
5	9.5	1.0	$1.98^{+1.95}_{-1.94}$	156	$-2.02^{+0.03}_{-0.03}$	$1108.1^{+1093.6}_{-1094.8}$	$(4.64^{+4.58}_{-4.58})10^{53}$
6	15.6	1.0	$2.81^{+2.76}_{-2.76}$	156	$-2.64^{+0.67}_{-0.68}$	$369.2^{+358.9}_{-360.3}$	$(1.40^{+1.36}_{-1.36})10^{53}$
7	18.8	1.2	$2.42^{+2.35}_{-2.35}$	156	$-3.04^{+1.07}_{-1.07}$	$555.7^{+529.0}_{-529.1}$	$(2.07^{+1.96}_{-1.96})10^{53}$
8	26.4	1.1	$1.63^{+1.49}_{-1.57}$	156	$-2.96^{+0.97}_{-0.99}$	$246.4^{+243.2}_{-239.1}$	$(9.29^{+9.16}_{-8.98})10^{52}$
9	84.6	16.5	$66.0^{+62.9}_{-63.1}$	156	$-3.93^{+1.99}_{-2.00}$	$0.384^{+0.367}_{-0.368}$	$(1.37^{+1.30}_{-1.30})10^{50}$

Pulse	T_{peak} [s]	T_{rise} [s]	T_f [s]	E_f [keV]	α	F_f [10^{-8} ergs s^{-1} cm^{-2}]	L_f [ergs s^{-1}]
GRB 121201A							
1	0.2	0.2	$0.80^{+0.57}_{-0.70}$	114	$-1.92^{+0.07}_{-0.28}$	$77.44^{+67.39}_{-66.02}$	$(8.70^{+7.53}_{-7.41})10^{52}$
2	3.9	2.2	$5.9^{+5.4}_{-5.4}$	114	$-1.96^{+0.10}_{-0.10}$	$53.45^{+47.79}_{-48.80}$	$(5.95^{+5.32}_{-5.43})10^{52}$
3	13.9	1.5	$4.58^{+4.29}_{-4.32}$	114	$-2.39^{+0.47}_{-0.45}$	$84.55^{+79.61}_{-80.64}$	$(9.19^{+8.63}_{-8.75})10^{52}$
4	27.2	7.6	$14.4^{+13.7}_{-13.4}$	114	$-2.28^{+0.38}_{-0.37}$	$31.23^{+28.65}_{-29.06}$	$(3.44^{+3.15}_{-3.19})10^{52}$
GRB 121209A							
1	2.1	2.1	$6.9^{+6.5}_{-6.5}$	161	$-1.90^{+0.05}_{-0.00}$	$133.3^{+127.2}_{-127.0}$	$(5.11^{+4.88}_{-4.87})10^{52}$
2	20.9	3.6	$3.81^{+3.66}_{-3.72}$	161	$-2.09^{+0.12}_{-0.13}$	$264.0^{+256.5}_{-256.6}$	$(9.82^{+9.53}_{-9.54})10^{52}$
3	22.8	0.2	$0.494^{+0.410}_{-0.429}$	161	$-1.28^{+0.53}_{-0.60}$	$285.2^{+218.0}_{-246.3}$	$(1.33^{+1.06}_{-1.18})10^{53}$
4	24.2	0.03	$0.83^{+0.58}_{-0.68}$	161	$-2.02^{+0.18}_{-0.23}$	$151.5^{+124.5}_{-122.5}$	$(4.99^{+4.05}_{-3.99})10^{52}$
5	30.5	0.4	$0.90^{+0.80}_{-0.82}$	161	$-1.62^{+0.32}_{-0.31}$	$503.8^{+467.9}_{-460.1}$	$(2.09^{+1.95}_{-1.92})10^{53}$
6	39.3	2.3	$3.26^{+2.92}_{-2.96}$	161	$-2.44^{+0.55}_{-0.53}$	$80.79^{+72.77}_{-74.85}$	$(2.82^{+2.51}_{-2.60})10^{52}$
7	44.9	1.3	$5.3^{+5.0}_{-5.1}$	161	$-2.50^{+0.56}_{-0.57}$	$102.3^{+97.2}_{-97.0}$	$(3.53^{+3.34}_{-3.33})10^{52}$
GRB 130427B							
1	1.9	1.9	$2.90^{+2.75}_{-2.77}$	132	$-2.02^{+0.07}_{-0.12}$	$307.9^{+294.5}_{-294.7}$	$(2.20^{+2.10}_{-2.10})10^{53}$
2	6.7	3.3	$6.7^{+6.6}_{-6.6}$	132	$-3.24^{+1.33}_{-1.31}$	$276.1^{+210.6}_{-236.1}$	$(1.91^{+1.44}_{-1.62})10^{53}$
3	130.4	15.1	$15.8^{+15.0}_{-13.3}$	132	$-2.29^{+0.36}_{-0.38}$	$0.843^{+0.608}_{-0.615}$	$(5.94^{+4.20}_{-4.26})10^{50}$
GRB 130610A							
1	11.7	11.7	$10.5^{+10.4}_{-10.4}$	162	$-1.97^{+0.01}_{-0.01}$	$174.0^{+171.1}_{-171.2}$	$(6.58^{+6.47}_{-6.48})10^{52}$
GRB 130831A							
1	2.9	2.9	$4.61^{+4.57}_{-4.56}$	338	$-2.61^{+0.62}_{-0.62}$	$1502.6^{+1492.3}_{-1487.6}$	$(1.42^{+1.41}_{-1.40})10^{52}$
2	20.6	2.0	$4.04^{+3.92}_{-3.95}$	338	$-2.68^{+0.71}_{-0.69}$	$199.6^{+186.9}_{-191.4}$	$(1.83^{+1.66}_{-1.72})10^{51}$

Pulse	T_{peak} [s]	T_{rise} [s]	T_f [s]	E_f [keV]	α	F_f [10^{-8} ergs s^{-1} cm^{-2}]	L_f [ergs s^{-1}]
3	33.0	2.9	$8.7^{+8.6}_{-8.6}$	338	$-3.44^{+1.48}_{-1.48}$	$574.4^{+523.7}_{-515.8}$	$(3.35^{+2.66}_{-2.55})10^{51}$
4	755.2	328.6	$635.3^{+507.3}_{-536.9}$	338	$-2.55^{+0.62}_{-0.63}$	$0.0703^{+0.0551}_{-0.0532}$	$(6.81^{+4.70}_{-4.46})10^{47}$
GRB 130925A							
1	26.1	26.1	$33.0^{+3.9}_{-2.3}$	371	$-2.19^{+0.07}_{-0.08}$	$79.03^{+5.95}_{-5.87}$	$(4.55^{+0.59}_{-0.54})10^{50}$
2	44.9	17.4	$75.7^{+4.2}_{-3.7}$	371	$-2.71^{+0.08}_{-0.09}$	$63.77^{+6.02}_{-4.17}$	$(2.70^{+0.38}_{-0.30})10^{50}$
3	95.2	19.1	$50.5^{+2.4}_{-1.7}$	371	$-2.90^{+0.03}_{-0.03}$	$104.3^{+20.4}_{-7.0}$	$(4.00^{+0.88}_{-0.34})10^{50}$
4	119.4	3.2	$129.1^{+10.3}_{-11.1}$	371	$-2.95^{+0.18}_{-0.12}$	$28.09^{+6.45}_{-4.39}$	$(1.03^{+0.37}_{-0.22})10^{50}$
5	172.5	22.4	$106.1^{+8.7}_{-3.4}$	371	$-3.11^{+0.05}_{-0.03}$	$57.41^{+4.52}_{-18.17}$	$(1.91^{+0.22}_{-0.63})10^{50}$
6	227.2	8.6	$70.5^{+4.7}_{-3.5}$	371	$-3.07^{+0.05}_{-0.04}$	$34.31^{+3.56}_{-4.14}$	$(1.14^{+0.16}_{-0.17})10^{50}$
7	823.8	200.2	$217.4^{+7.2}_{-7.7}$	371	$-2.63^{+0.05}_{-0.05}$	$1.21^{+0.17}_{-0.15}$	$(5.57^{+0.95}_{-0.85})10^{48}$
8	1023.8	131.2	$132.5^{+1.3}_{-1.0}$	371	$-2.73^{+0.02}_{-0.02}$	$2.85^{+0.19}_{-0.18}$	$(1.34^{+0.11}_{-0.09})10^{49}$
9	1124.0	88.6	$131.4^{+3.2}_{-4.0}$	371	$-2.86^{+0.05}_{-0.05}$	$2.33^{+0.23}_{-0.19}$	$(9.14^{+1.21}_{-1.00})10^{48}$
10	1511.8	61.6	$207.1^{+7.7}_{-5.0}$	371	$-3.11^{+0.05}_{-0.05}$	$3.00^{+0.15}_{-0.12}$	$(10.00^{+0.90}_{-0.75})10^{48}$
11	2024.5	90.9	$286.6^{+28.9}_{-19.1}$	371	$-2.81^{+0.25}_{-0.11}$	$23.86^{+2.92}_{-3.29}$	$(9.56^{+2.77}_{-1.83})10^{49}$
12	2146.6	52.7	$177.9^{+13.3}_{-10.7}$	371	$-2.63^{+0.09}_{-0.09}$	$43.58^{+2.44}_{-2.36}$	$(1.94^{+0.21}_{-0.19})10^{50}$
13	2255.6	26.4	$127.3^{+11.6}_{-10.4}$	371	$-2.73^{+0.14}_{-0.12}$	$40.26^{+4.73}_{-3.81}$	$(1.67^{+0.35}_{-0.26})10^{50}$
14	2314.8	24.0	$51.0^{+7.1}_{-6.2}$	371	$-2.43^{+0.19}_{-0.20}$	$32.33^{+3.90}_{-3.29}$	$(1.60^{+0.41}_{-0.31})10^{50}$
15	2377.9	22.0	$167.4^{+30.6}_{-25.8}$	371	$-3.36^{+0.10}_{-0.07}$	$56.58^{+38.80}_{-36.39}$	$(1.58^{+1.28}_{-1.04})10^{50}$
16	2435.9	9.9	$33.7^{+10.6}_{-4.8}$	371	$-2.18^{+0.23}_{-0.29}$	$37.95^{+6.44}_{-7.41}$	$(2.20^{+0.83}_{-0.71})10^{50}$
17	2473.0	17.8	$57.6^{+9.2}_{-7.0}$	371	$-2.69^{+0.17}_{-0.22}$	$35.55^{+8.44}_{-3.95}$	$(1.51^{+0.55}_{-0.32})10^{50}$
18	2535.9	48.9	$152.5^{+5.9}_{-5.1}$	371	$-2.80^{+0.15}_{-0.05}$	$66.17^{+3.64}_{-6.33}$	$(2.66^{+0.39}_{-0.32})10^{50}$
19	2603.5	37.2	$131.6^{+7.7}_{-4.5}$	371	$-2.26^{+0.06}_{-0.06}$	$82.45^{+3.59}_{-3.18}$	$(4.47^{+0.38}_{-0.33})10^{50}$

Pulse	T_{peak} [s]	T_{rise} [s]	T_f [s]	E_f [keV]	α	F_f [10^{-8} ergs s^{-1} cm^{-2}]	L_f [ergs s^{-1}]
20	2662.5	30.6	$107.5^{+6.3}_{-4.5}$	371	$-2.92^{+0.11}_{-0.05}$	$89.49^{+8.42}_{-11.42}$	$(3.32^{+0.56}_{-0.52})10^{50}$
21	2723.0	17.9	$89.4^{+8.4}_{-6.1}$	371	$-3.24^{+0.15}_{-0.11}$	$83.89^{+51.90}_{-24.39}$	$(2.51^{+2.01}_{-0.87})10^{50}$
22	2764.1	26.8	$27.0^{+1.0}_{-0.5}$	371	$-2.49^{+0.06}_{-0.06}$	$87.30^{+3.92}_{-3.90}$	$(4.33^{+0.36}_{-0.33})10^{50}$
23	2799.2	23.4	$118.8^{+12.1}_{-10.9}$	371	$-2.95^{+0.16}_{-0.29}$	$37.71^{+19.09}_{-5.95}$	$(1.37^{+0.90}_{-0.42})10^{50}$
24	2846.2	15.8	$62.9^{+11.3}_{-4.1}$	371	$-2.19^{+0.10}_{-0.13}$	$63.87^{+4.87}_{-8.82}$	$(3.67^{+0.55}_{-0.77})10^{50}$
25	2899.2	50.4	$100.3^{+13.2}_{-10.2}$	371	$-3.78^{+0.35}_{-0.12}$	$134.3^{+176.5}_{-115.6}$	$(2.75^{+5.80}_{-2.32})10^{50}$
26	3359.7	18.8	$93.9^{+37.8}_{-21.4}$	371	$-2.96^{+0.49}_{-0.34}$	$24.18^{+13.91}_{-6.87}$	$(8.68^{+9.31}_{-3.76})10^{49}$
27	3520.7	97.3	$146.2^{+34.7}_{-24.0}$	371	$-3.34^{+0.58}_{-0.67}$	$14.35^{+12.63}_{-14.21}$	$(4.35^{+7.62}_{-4.32})10^{49}$
28	3947.2	39.3	$162.1^{+21.4}_{-11.8}$	371	$-2.28^{+0.21}_{-0.23}$	$18.22^{+2.93}_{-2.13}$	$(9.69^{+3.25}_{-2.22})10^{49}$
29	4054.1	23.9	$156.8^{+15.2}_{-13.9}$	371	$-3.25^{+0.35}_{-0.43}$	$27.28^{+30.20}_{-14.56}$	$(8.22^{+13.57}_{-5.51})10^{49}$
30	4265.3	12.1	$60.7^{+24.0}_{-18.9}$	371	$-1.69^{+0.47}_{-0.55}$	$24.00^{+10.63}_{-7.18}$	$(1.98^{+2.47}_{-1.06})10^{50}$
31	4312.9	22.8	$66.6^{+13.7}_{-7.0}$	371	$-3.02^{+0.43}_{-0.26}$	$29.90^{+18.36}_{-6.32}$	$(1.06^{+1.13}_{-0.36})10^{50}$
32	4343.2	17.9	$81.3^{+10.4}_{-13.6}$	371	$-3.22^{+0.46}_{-0.36}$	$36.77^{+35.94}_{-20.87}$	$(1.12^{+1.83}_{-0.75})10^{50}$
33	4400.4	16.8	$73.2^{+12.5}_{-11.6}$	371	$-3.31^{+0.47}_{-0.68}$	$33.60^{+86.54}_{-6.57}$	$(9.64^{+37.58}_{-5.26})10^{49}$
34	5123.8	124.4	$336.4^{+7.0}_{-11.1}$	371	$-3.37^{+0.04}_{-0.04}$	$1.83^{+0.06}_{-0.04}$	$(5.02^{+0.34}_{-0.26})10^{48}$
35	7263.2	360.3	$1304.6^{+18.5}_{-17.9}$	371	$-2.73^{+0.07}_{-0.03}$	$3.62^{+0.38}_{-0.26}$	$(1.52^{+0.22}_{-0.14})10^{49}$
36	10973.8	147.4	$618.9^{+211.0}_{-88.0}$	371	$-3.62^{+0.32}_{-0.31}$	$0.242^{+0.082}_{-0.057}$	$(5.41^{+4.01}_{-2.26})10^{47}$
37	11442.9	296.7	$551.3^{+22.4}_{-24.2}$	371	$-3.78^{+0.12}_{-0.12}$	$0.225^{+0.021}_{-0.017}$	$(4.74^{+1.02}_{-0.82})10^{47}$
38	12039.6	192.7	$988.9^{+475.3}_{-351.5}$	371	$-3.57^{+2.29}_{-0.93}$	$0.0981^{+0.1047}_{-0.0327}$	$(2.29^{+22.61}_{-1.62})10^{47}$
GRB 131030A							
1	9.3	9.3	$8.6^{+8.6}_{-8.5}$	218	$-1.89^{+0.10}_{-0.10}$	$1681.4^{+1669.7}_{-1664.5}$	$(2.21^{+2.19}_{-2.18})10^{53}$
2	12.8	0.9	$0.88^{+0.87}_{-0.87}$	218	$-2.00^{+0.01}_{-0.02}$	$3563.9^{+3516.3}_{-3513.3}$	$(4.48^{+4.42}_{-4.42})10^{53}$

Pulse	T_{peak} [s]	T_{rise} [s]	T_f [s]	E_f [keV]	α	F_f [10^{-8} ergs s^{-1} cm^{-2}]	L_f [ergs s^{-1}]
3	14.1	0.6	$4.39^{+4.35}_{-4.35}$	218	$-1.97^{+0.03}_{-0.02}$	$3637.7^{+3604.0}_{-3601.4}$	$(4.57^{+4.53}_{-4.52})10^{53}$
4	27.5	1.8	$11.8^{+11.7}_{-11.7}$	218	$-2.65^{+0.66}_{-0.67}$	$478.0^{+470.5}_{-469.8}$	$(4.94^{+4.85}_{-4.84})10^{52}$
5	123.1	48.7	$48.0^{+23.2}_{-47.6}$	218	$-2.90^{+0.90}_{-1.33}$	$28.21^{+27.99}_{-13.28}$	$(3.83^{+3.78}_{-1.23})10^{51}$
GRB 131227A							
1	1.4	1.4	$1.25^{+0.91}_{-0.97}$	79	$-2.22^{+0.39}_{-0.32}$	$109.6^{+87.4}_{-93.6}$	$(3.56^{+2.83}_{-3.04})10^{53}$
2	2.9	0.9	$4.16^{+3.97}_{-3.98}$	79	$-1.79^{+0.11}_{-0.08}$	$92.93^{+87.89}_{-88.41}$	$(2.94^{+2.78}_{-2.80})10^{53}$
3	7.8	0.4	$2.42^{+2.27}_{-2.26}$	79	$-2.04^{+0.25}_{-0.17}$	$104.1^{+87.0}_{-95.4}$	$(3.22^{+2.69}_{-2.95})10^{53}$
4	15.2	1.1	$3.20^{+2.92}_{-2.89}$	79	$-1.43^{+0.42}_{-0.05}$	$34.98^{+30.25}_{-31.81}$	$(1.12^{+0.96}_{-1.02})10^{53}$
GRB 140304A							
1	0.1	0.1	$2.89^{+2.63}_{-2.72}$	80	$-1.53^{+0.36}_{-0.38}$	$201.4^{+189.5}_{-189.8}$	$(6.34^{+5.97}_{-5.98})10^{53}$
2	3.1	0.9	$1.20^{+1.04}_{-1.07}$	80	$-1.98^{+0.09}_{-0.10}$	$89.75^{+83.37}_{-84.58}$	$(2.81^{+2.61}_{-2.65})10^{53}$
3	7.7	2.5	$3.60^{+3.38}_{-3.43}$	80	$-1.65^{+0.25}_{-0.26}$	$123.5^{+117.2}_{-117.9}$	$(3.91^{+3.72}_{-3.74})10^{53}$
4	10.9	1.9	$8.4^{+8.2}_{-8.2}$	80	$-3.08^{+1.15}_{-1.13}$	$131.3^{+117.6}_{-114.2}$	$(4.58^{+4.16}_{-4.05})10^{53}$
5	358.2	62.1	$70.9^{+61.5}_{-63.8}$	80	$-2.58^{+0.67}_{-0.70}$	$0.152^{+0.105}_{-0.116}$	$(5.05^{+3.51}_{-3.87})10^{50}$
6	813.4	18.7	$52.9^{+42.3}_{-40.7}$	80	$-2.58^{+0.68}_{-0.74}$	$0.213^{+0.152}_{-0.157}$	$(6.72^{+4.83}_{-4.98})10^{50}$
7	22222.3	3765.7	11324^{+7720}_{-9470}	80	$-2.59^{+0.70}_{-0.72}$	$0.0019^{+0.0013}_{-0.0014}$	$(5.92^{+4.26}_{-4.48})10^{48}$
GRB 140430A							
1	3.7	3.7	$3.50^{+3.45}_{-3.46}$	192	$-2.50^{+0.51}_{-0.52}$	$226.4^{+223.5}_{-223.3}$	$(4.31^{+4.25}_{-4.24})10^{52}$
2	30.0	3.4	$12.9^{+38.6}_{-6.9}$	192	$-3.45^{+1.57}_{-3.36}$	$74.19^{+229.89}_{-55.99}$	$(1.10^{+16.11}_{-0.72})10^{52}$
3	156.6	8.7	$13.4^{+11.9}_{-12.2}$	192	$-2.78^{+0.86}_{-0.88}$	$7.37^{+5.90}_{-5.96}$	$(1.26^{+0.95}_{-0.97})10^{51}$
4	173.2	3.0	$15.1^{+13.6}_{-14.3}$	192	$-2.31^{+0.32}_{-0.32}$	$64.40^{+62.06}_{-60.74}$	$(1.19^{+1.15}_{-1.12})10^{52}$
5	221.9	14.8	$27.1^{+26.3}_{-26.8}$	192	$-3.02^{+1.05}_{-1.05}$	$4.37^{+4.25}_{-4.32}$	$(7.19^{+6.94}_{-7.08})10^{50}$

Pulse	T_{peak} [s]	T_{rise} [s]	T_f [s]	E_f [keV]	α	F_f [10^{-8} ergs s^{-1} cm^{-2}]	L_f [ergs s^{-1}]
GRB 140506A							
1	0.7	0.7	$3.41^{+2.82}_{-3.31}$	265	$-2.53^{+0.54}_{-0.55}$	$353.6^{+348.9}_{-349.7}$	$(1.48^{+1.45}_{-1.46})10^{52}$
2	4.2	0.7	$2.15^{+2.10}_{-2.09}$	265	$-1.90^{+0.09}_{-0.09}$	$1353.2^{+1314.5}_{-1315.0}$	$(7.63^{+7.42}_{-7.42})10^{52}$
3	127.5	16.4	$23.5^{+22.8}_{-23.1}$	265	$-2.57^{+0.60}_{-0.60}$	$66.21^{+60.94}_{-62.55}$	$(2.81^{+2.52}_{-2.61})10^{51}$
4	251.2	33.9	$55.2^{+52.9}_{-53.3}$	265	$-2.76^{+0.77}_{-0.77}$	$6.95^{+6.50}_{-6.66}$	$(2.76^{+2.52}_{-2.60})10^{50}$
5	355.1	66.4	$171.6^{+156.3}_{-164.2}$	265	$-4.02^{+2.02}_{-2.02}$	$4.58^{+4.45}_{-4.31}$	$(1.01^{+0.94}_{-0.86})10^{50}$
GRB 140509A							
1	2.0	2.0	$2.68^{+2.27}_{-2.37}$	147	$-2.66^{+0.78}_{-0.75}$	$120.2^{+95.8}_{-103.1}$	$(5.71^{+4.43}_{-4.82})10^{52}$
2	6.0	3.3	$11.6^{+11.3}_{-11.3}$	147	$-2.13^{+0.17}_{-0.17}$	$122.5^{+114.6}_{-115.4}$	$(6.01^{+5.61}_{-5.65})10^{52}$
GRB 140629A							
1	1.0	1.0	$2.72^{+2.55}_{-2.57}$	153	$-2.25^{+0.34}_{-0.35}$	$186.3^{+177.5}_{-178.6}$	$(8.04^{+7.64}_{-7.69})10^{52}$
2	13.4	1.1	$3.21^{+3.14}_{-3.15}$	153	$-1.95^{+0.02}_{-0.01}$	$505.8^{+494.0}_{-493.5}$	$(2.31^{+2.26}_{-2.26})10^{53}$
3	19.1	1.4	$2.35^{+1.85}_{-2.15}$	153	$-2.90^{+0.90}_{-0.91}$	$299.8^{+291.6}_{-275.2}$	$(1.23^{+1.19}_{-1.12})10^{53}$
GRB 140703A							
1	3.0	3.0	$3.37^{+2.92}_{-3.08}$	121	$-2.22^{+0.38}_{-0.36}$	$206.8^{+190.0}_{-188.1}$	$(1.92^{+1.76}_{-1.74})10^{53}$
2	4.6	1.1	$3.80^{+3.52}_{-3.48}$	121	$-1.34^{+0.52}_{-0.49}$	$376.2^{+337.4}_{-341.4}$	$(3.96^{+3.58}_{-3.62})10^{53}$
3	31.0	3.9	$4.88^{+4.26}_{-4.50}$	121	$-2.64^{+0.75}_{-0.77}$	$131.5^{+75.7}_{-113.2}$	$(1.22^{+0.67}_{-1.04})10^{53}$
4	70.7	5.0	$14.6^{+14.4}_{-14.5}$	121	$-3.45^{+1.46}_{-1.46}$	$419.4^{+402.3}_{-402.7}$	$(4.15^{+3.99}_{-4.00})10^{53}$
5	122.8	7.4	$20.2^{+18.9}_{-19.7}$	121	$-4.01^{+2.03}_{-2.03}$	$3.40^{+3.33}_{-3.33}$	$(3.80^{+3.73}_{-3.73})10^{51}$
GRB 140710A							
1	0.9	0.9	$1.99^{+1.97}_{-1.96}$	315	$-2.52^{+0.54}_{-0.53}$	$242.0^{+232.5}_{-236.5}$	$(3.40^{+3.22}_{-3.29})10^{51}$
2	387.7	78.4	$236.5^{+219.6}_{-218.5}$	315	$-3.11^{+1.18}_{-1.23}$	$0.111^{+0.102}_{-0.099}$	$(1.17^{+0.97}_{-0.93})10^{48}$

Pulse	T_{peak} [s]	T_{rise} [s]	T_f [s]	E_f [keV]	α	F_f [10^{-8} ergs s^{-1} cm^{-2}]	L_f [ergs s^{-1}]
GRB 141221A							
1	2.5	2.5	$5.2^{+4.7}_{-4.6}$	204	$-2.59^{+0.72}_{-0.67}$	$58.17^{+50.27}_{-53.70}$	$(8.09^{+6.75}_{-7.35})10^{51}$
2	17.3	4.8	$7.2^{+6.7}_{-6.6}$	204	$-2.55^{+0.67}_{-0.61}$	$60.26^{+55.90}_{-56.76}$	$(8.49^{+7.75}_{-7.91})10^{51}$
3	25.2	1.8	$1.86^{+1.80}_{-1.81}$	204	$-2.36^{+0.39}_{-0.41}$	$283.4^{+277.3}_{-277.3}$	$(4.25^{+4.15}_{-4.15})10^{52}$
4	26.8	0.4	$4.87^{+4.52}_{-4.32}$	204	$-2.48^{+0.53}_{-0.53}$	$227.1^{+198.9}_{-216.8}$	$(3.20^{+2.74}_{-3.03})10^{52}$
5	38.9	3.2	$4.99^{+4.76}_{-4.75}$	204	$-2.77^{+0.80}_{-0.80}$	$171.9^{+165.1}_{-165.9}$	$(2.32^{+2.20}_{-2.22})10^{52}$
6	373.7	83.5	$118.9^{+108.4}_{-108.7}$	204	$-2.53^{+0.59}_{-0.64}$	$0.447^{+0.367}_{-0.315}$	$(6.32^{+4.96}_{-4.13})10^{49}$
GRB 150301B							
1	2.0	2.0	$3.26^{+3.19}_{-3.18}$	157	$-1.92^{+0.06}_{-0.06}$	$344.1^{+335.5}_{-335.9}$	$(5.85^{+5.71}_{-5.71})10^{52}$
2	5.0	1.6	$4.03^{+3.45}_{-3.64}$	199	$-2.13^{+0.14}_{-0.14}$	$243.7^{+233.8}_{-238.8}$	$(4.19^{+4.02}_{-4.11})10^{52}$
3	11.1	2.0	$6.2^{+5.9}_{-5.9}$	199	$-2.49^{+0.60}_{-0.57}$	$74.25^{+67.26}_{-69.38}$	$(1.16^{+1.03}_{-1.07})10^{52}$
GRB 150403A							
1	6.5	6.5	$8.4^{+8.3}_{-8.2}$	163	$-1.68^{+0.30}_{-0.30}$	$953.1^{+934.0}_{-919.2}$	$(3.74^{+3.67}_{-3.62})10^{53}$
2	11.5	3.4	$4.20^{+4.12}_{-4.12}$	163	$-1.63^{+0.35}_{-0.35}$	$2038.6^{+2008.2}_{-2005.2}$	$(8.12^{+8.01}_{-8.00})10^{53}$
GRB 151027A							
1	1.3	1.3	$4.16^{+3.93}_{-3.96}$	276	$-2.04^{+0.08}_{-0.08}$	$821.3^{+785.3}_{-787.8}$	$(3.45^{+3.30}_{-3.31})10^{52}$
2	19.2	2.77	$14.1^{+13.7}_{-13.7}$	276	$-2.98^{+1.01}_{-1.02}$	$163.3^{+149.9}_{-154.3}$	$(2.61^{+2.28}_{-2.39})10^{51}$
3	99.1	4.3	$28.9^{+28.3}_{-27.4}$	276	$-1.83^{+0.17}_{-0.17}$	$159.7^{+150.6}_{-155.0}$	$(7.60^{+7.20}_{-7.39})10^{51}$
4	109.6	3.1	$6.4^{+6.3}_{-6.3}$	276	$-1.82^{+0.17}_{-0.17}$	$375.6^{+370.5}_{-370.5}$	$(1.78^{+1.76}_{-1.76})10^{52}$
5	113.3	2.0	$3.38^{+3.26}_{-3.24}$	276	$-2.13^{+0.17}_{-0.15}$	$196.7^{+184.8}_{-189.3}$	$(7.99^{+7.46}_{-7.67})10^{51}$
6	119.3	4.1	$3.60^{+3.53}_{-3.52}$	276	$-2.31^{+0.33}_{-0.33}$	$46.05^{+43.21}_{-43.32}$	$(1.75^{+1.63}_{-1.63})10^{51}$
7	123.8	3.3	$3.40^{+3.20}_{-3.15}$	276	$-2.51^{+0.55}_{-0.54}$	$19.85^{+16.77}_{-17.24}$	$(7.17^{+5.74}_{-5.96})10^{50}$

Pulse	T_{peak} [s]	T_{rise} [s]	T_f [s]	E_f [keV]	α	F_f [10^{-8} ergs s^{-1} cm^{-2}]	L_f [ergs s^{-1}]
8	129.1	51.31	$99.1^{+80.4}_{-16.1}$	276	$-6.19^{+5.69}_{-4.92}$	$18.05^{+7.90}_{-12.28}$	$(5.86^{+94.71}_{-23.21})10^{48}$
9	335.6	91.4	$194.9^{+187.3}_{-188.2}$	276	$-3.96^{+2.00}_{-2.04}$	$0.143^{+0.141}_{-0.141}$	$(2.58^{+2.45}_{-2.45})10^{48}$
GRB 151027B							
1	2.3	2.3	$4.86^{+4.46}_{-4.35}$	99	$-2.40^{+0.57}_{-0.48}$	$109.7^{+97.0}_{-100.4}$	$(1.85^{+1.63}_{-1.69})10^{53}$
2	12.0	3.7	$7.6^{+7.2}_{-7.3}$	99	$-2.70^{+0.82}_{-0.77}$	$104.7^{+92.6}_{-92.5}$	$(1.79^{+1.58}_{-1.58})10^{53}$
3	51.5	4.6	$15.7^{+14.9}_{-15.1}$	99	$-3.57^{+1.63}_{-1.66}$	$147.5^{+125.1}_{-111.3}$	$(3.15^{+2.76}_{-2.53})10^{53}$
GRB 151111A							
1	10.4	10.4	$22.2^{+22.0}_{-21.9}$	111	$-1.72^{+0.27}_{-0.27}$	$96.02^{+93.80}_{-94.26}$	$(1.20^{+1.17}_{-1.17})10^{53}$
2	133.2	34.4	$29.8^{+28.8}_{-28.8}$	111	$-1.95^{+0.01}_{-0.01}$	$2.16^{+1.83}_{-1.86}$	$(2.65^{+2.24}_{-2.29})10^{51}$
3	182.7	52.5	$47.2^{+17.6}_{-39.1}$	111	$-2.42^{+0.50}_{-0.78}$	$0.247^{+0.173}_{-0.076}$	$(3.10^{+2.11}_{-0.88})10^{50}$
4	312.1	189.8	$251.0^{+239.8}_{-242.6}$	111	$-4.11^{+2.20}_{-2.26}$	$0.0178^{+0.0174}_{-0.0174}$	$(6.47^{+6.36}_{-6.36})10^{49}$
GRB 151215A							
1	0.9	0.9	$2.43^{+2.07}_{-2.13}$	139	$-2.03^{+0.12}_{-0.13}$	$193.7^{+177.9}_{-178.7}$	$(1.16^{+1.06}_{-1.07})10^{53}$
2	3.1	0.2	$0.426^{+0.295}_{-0.333}$	139	$-2.60^{+0.75}_{-0.79}$	$398.8^{+316.0}_{-308.8}$	$(2.28^{+1.76}_{-1.72})10^{53}$
GRB 160104A							
1	4.1	4.1	$9.7^{+9.5}_{-9.5}$	132	$-2.53^{+0.60}_{-0.65}$	$77.22^{+71.86}_{-73.48}$	$(5.33^{+4.94}_{-5.06})10^{52}$
2	265.1	48.0	$139.1^{+127.9}_{-135.3}$	132	$-3.48^{+1.49}_{-1.49}$	$0.0328^{+0.0325}_{-0.0321}$	$(2.36^{+2.34}_{-2.31})10^{49}$
3	854.4	280.1	$919.3^{+830.1}_{-837.2}$	132	$-3.59^{+1.73}_{-1.72}$	$0.0082^{+0.0075}_{-0.0077}$	$(5.98^{+5.48}_{-5.60})10^{48}$
GRB 160117B							
1	1.6	1.6	$6.9^{+6.8}_{-6.8}$	267	$-4.10^{+2.12}_{-2.12}$	$4380.6^{+3970.2}_{-4118.3}$	$(8.45^{+6.37}_{-7.12})10^{52}$
2	81.4	8.7	$54.2^{+53.1}_{-52.9}$	267	$-3.41^{+1.43}_{-1.43}$	$0.771^{+0.753}_{-0.755}$	$(2.14^{+2.05}_{-2.06})10^{49}$
GRB 160121A							

Pulse	T_{peak} [s]	T_{rise} [s]	T_f [s]	E_f [keV]	α	F_f [10^{-8} ergs s^{-1} cm^{-2}]	L_f [ergs s^{-1}]
1	4.4	4.4	$7.1^{+7.0}_{-7.0}$	169	$-2.53^{+0.57}_{-0.59}$	$110.3^{+106.9}_{-107.2}$	$(3.22^{+3.11}_{-3.12})10^{52}$
GRB 160314A							
1	2.5	2.5	$7.3^{+7.0}_{-7.1}$	290	$-2.64^{+0.71}_{-0.72}$	$87.03^{+81.27}_{-81.84}$	$(2.17^{+1.97}_{-1.99})10^{51}$
2	398.8	159.6	$220.5^{+189.5}_{-196.7}$	290	$-2.95^{+1.05}_{-1.16}$	$0.0065^{+0.0049}_{-0.0048}$	$(1.49^{+0.84}_{-0.84})10^{47}$
GRB 160327A							
1	2.5	2.5	$9.2^{+9.0}_{-9.0}$	83	$-2.50^{+0.52}_{-0.52}$	$89.39^{+86.32}_{-86.76}$	$(2.46^{+2.37}_{-2.39})10^{53}$
2	7.1	4.1	$4.05^{+3.96}_{-3.96}$	83	$-1.88^{+0.09}_{-0.08}$	$117.4^{+114.6}_{-114.5}$	$(3.26^{+3.18}_{-3.18})10^{53}$
3	14.5	1.2	$2.63^{+2.29}_{-2.37}$	83	$-2.63^{+0.76}_{-0.76}$	$59.99^{+43.80}_{-45.53}$	$(1.68^{+1.23}_{-1.28})10^{53}$
GRB 160410A							
1	2.8	2.8	$5.9^{+5.8}_{-5.8}$	184	$-1.99^{+0.03}_{-0.03}$	$277.9^{+266.6}_{-267.0}$	$(6.60^{+6.33}_{-6.34})10^{52}$

Table 3: Parameters of the fitted pulses, with the sequence of pulses for each bursts headed by the burst name. The temporal parameters include the rise time of the pulse, T_{rise}, the time of the peak, T_{peak}, and the arrival time of the last emitted photon, T_f. The spectral parameters at pulse peak are: the cut-off energy of the Band function, E_f, the low spectral index of the Band function, α, and the flux over the observed energy band 0.3-350 keV, F_f. The isotropic peak luminosity estimated over the bolometric band 1-10000 keV, L_f, is also shown. A single value indicates a parameter which was fixed during final fitting. The 90% range is indicated for parameters which were allowed to float in the final fitting. The 90% range of luminosity includes the uncertainty in the flux, F_f, and uncertainty in the k-correction which depends on redshift, z, and the spectral parameters, E_f and α.

GRB	T_{rise} [s]	T_{fall} [s]	α_c	T_{break} [s]	α_{break}
050126	100	$(1.62^{+126.73}_{-1.52})10^2$	$-0.77^{+0.50}_{-0.77}$	-	-
050215B	100	$(1.36^{+1.07}_{-0.10})10^4$	$-1.15^{+0.56}_{-0.41}$	-	-
050219A	100	$(1.44^{+10.25}_{-1.00})10^3$	$-0.77^{+0.30}_{-0.15}$	-	-
050315	100	$(1.20^{+1.61}_{-0.66})10^4$	$-0.68^{+0.06}_{-0.06}$	$1.67\ 10^5$	-1.36
050319	100	$(3.35^{+1.46}_{-1.10})10^4$	$-1.29^{+0.15}_{-0.09}$	-	-
050401	100	$(4.06^{+1.56}_{-3.58})10^2$	$-0.67^{+0.06}_{-0.05}$	$6.03\ 10^3$	-1.56
050416A	100	$(1.21^{+0.66}_{-0.49})10^3$	$-0.88^{+0.03}_{-0.03}$	-	-
050525A	100	$(7.99^{+6.63}_{-7.91})10^3$	$-1.60^{+0.11}_{-0.08}$	-	-
050724	100	$(9.03^{+0.97}_{-6.65})10^5$	$-10.00^{+0.00}_{-4.19}$	-	-
050730	100	$(1.66^{+0.12}_{-0.09})10^4$	$-2.62^{+0.05}_{-0.04}$	-	-
050801	100	$(1.09^{+1.18}_{-0.92})10^3$	$-1.52^{+0.12}_{-0.15}$	-	-
050802	100	$(8.41^{+1.48}_{-1.16})10^3$	$-1.59^{+0.06}_{-0.05}$	-	-
050803	100	$(2.03^{+0.54}_{-0.32})10^4$	$-1.53^{+0.07}_{-0.05}$	-	-
050814	100	$(1.38^{+0.98}_{-0.90})10^4$	$-0.83^{+0.12}_{-0.12}$	$9.04\ 10^4$	-1.98
050820A	100	$(1.34^{+0.21}_{-0.18})10^4$	$-1.27^{+0.03}_{-0.03}$	-	-
050822	100	$(2.25^{+1.61}_{-0.49})10^4$	$-1.03^{+0.06}_{-0.05}$	-	-
050908	100	$(2.46^{+3.67}_{-2.36})10^2$	$-1.40^{+0.14}_{-0.11}$	-	-
050922C	100	$(1.20^{+0.92}_{-1.10})10^2$	$-1.21^{+0.05}_{-0.04}$	$6.46\ 10^3$	-1.39
051016B	100	$(1.80^{+1.46}_{-1.46})10^4$	$-1.12^{+0.07}_{-0.06}$	-	-
051109A	100	$(8.09^{+2.12}_{-2.20})10^3$	$-1.23^{+0.04}_{-0.03}$	-	-
051221A	100	$(5.25^{+1.94}_{-1.43})10^4$	$-1.47^{+0.11}_{-0.09}$	-	-
060108	100	$(6.47^{+5.23}_{-3.69})10^3$	$-0.92^{+0.11}_{-0.11}$	-	-
060115	100	$(3.33^{+3.49}_{-3.30})10^4$	$-1.42^{+0.24}_{-0.18}$	-	-
060116	100	$(3.08^{+2.12}_{-2.08})10^3$	$-1.25^{+0.13}_{-0.10}$	-	-
060124	100	$(4.20^{+0.76}_{-1.29})10^4$	$-1.42^{+0.04}_{-0.04}$	-	-
060206	100	$(2.22^{+0.90}_{-0.60})10^3$	$-1.16^{+0.04}_{-0.04}$	-	-
060210	100	$(9.63^{+2.87}_{-4.40})10^3$	$-1.07^{+0.07}_{-0.07}$	$4.99\ 10^4$	-1.39
060223A	100	$(7.08^{+5.79}_{-3.79})10^2$	$-1.44^{+0.29}_{-0.18}$	-	-
060418	100	$(1.28^{+1.08}_{-0.24})10^3$	$-1.47^{+0.18}_{-0.06}$	-	-
060502A	100	$(2.30^{+0.95}_{-0.86})10^4$	$-1.11^{+0.06}_{-0.05}$	-	-
060522	100	$(4.10^{+2.51}_{-2.51})10^3$	$-1.39^{+0.20}_{-0.19}$	-	-
060526	100	$(1.67^{+1.00}_{-1.00})10^4$	$-1.16^{+0.16}_{-0.13}$	-	-
060604	100	$(2.66^{+1.06}_{-0.81})10^4$	$-1.23^{+0.11}_{-0.09}$	-	-
060605	100	$(1.52^{+0.48}_{-0.38})10^4$	$-2.13^{+0.15}_{-0.13}$	-	-

GRB	T_{rise} [s]	T_{fall} [s]	α_c	T_{break} [s]	α_{break}
060607A	100	$(2.11^{+0.00}_{-0.86})10^3$	$-0.44^{+0.05}_{-0.05}$	1.24 10^4	-3.44
060614	100	$(1.35^{+0.21}_{-0.16})10^5$	$-2.23^{+0.10}_{-0.08}$	-	-
060707	100	$(7.02^{+7.55}_{-2.69})10^3$	$-0.90^{+0.07}_{-0.05}$	-	-
060714	100	$(5.11^{+1.28}_{-1.27})10^3$	$-1.25^{+0.06}_{-0.05}$	-	-
060729	100	$(4.75^{+6.20}_{-3.36})10^3$	$-0.32^{+0.04}_{-0.04}$	8.45 10^4	-1.39
060801	100	$(9.37^{+1.02}_{-0.00})10^2$	$-10.00^{+0.00}_{-0.00}$	-	-
060814	100	$(1.86^{+0.39}_{-0.63})10^4$	$-1.40^{+0.05}_{-0.05}$	-	-
060904B	100	$(7.06^{+3.75}_{-2.30})10^3$	$-1.36^{+0.10}_{-0.08}$	-	-
060906	100	$(2.41^{+16.85}_{-2.39})10^4$	$-4.55^{+1.78}_{-1.00}$	-	-
060908	100	$(5.18^{+2.41}_{-2.09})10^2$	$-1.50^{+0.15}_{-0.13}$	-	-
060912A	100	$(7.57^{+5.82}_{-3.73})10^2$	$-1.15^{+0.10}_{-0.08}$	-	-
060926	100	$(1.00^{+-1.00}_{-0.99})10^1$	$-7.66^{+-7.66}_{-7.66}$	-	-
060927	100	$(1.92^{+3.49}_{-1.90})10^3$	$-1.36^{+0.24}_{-0.33}$	-	-
061006	100	$(2.02^{+5.28}_{-1.00})10^3$	$-0.81^{+0.25}_{-0.22}$	-	-
061021	100	$(3.43^{+2.41}_{-1.24})10^3$	$-0.97^{+0.05}_{-0.06}$	6.05 10^4	-1.14
061110A	100	$(9.98^{+16.50}_{-9.88})10^2$	$-0.78^{+0.14}_{-0.13}$	-	-
061121	100	$(2.89^{+1.16}_{-1.05})10^3$	$-0.85^{+0.05}_{-0.05}$	1.54 10^4	-1.51
061222A	100	$(4.17^{+0.63}_{-0.00})10^3$	$-1.06^{+0.04}_{-0.04}$	6.62 10^4	-1.71
061222B	100	$(1.27^{+0.00}_{-0.00})10^1$	$-2.76^{+-2.76}_{-2.76}$	-	-
070208	100	$(7.88^{+7.42}_{-2.74})10^3$	$-1.42^{+0.16}_{-0.14}$	-	-
070306	100	$(7.34^{+1.48}_{-0.93})10^4$	$-1.97^{+0.09}_{-0.08}$	-	-
070318	100	$(4.32^{+28.84}_{-3.32})10^1$	$-0.97^{+0.03}_{-0.03}$	-	-
070419A	100	$(1.43^{+-1.43}_{-1.43})10^5$	$-6.76^{+-6.76}_{-6.76}$	-	-
070506	100	$(3.59^{+45.78}_{-1.20})10^2$	$-0.60^{+0.22}_{-0.21}$	-	-
070521	100	$(3.76^{+0.94}_{-0.70})10^3$	$-1.57^{+0.08}_{-0.08}$	-	-
070529	100	$(2.38^{+1.29}_{-0.97})10^3$	$-1.31^{+0.15}_{-0.09}$	-	-
070721B	100	$(1.27^{+0.49}_{-0.25})10^4$	$-2.22^{+0.24}_{-0.17}$	-	-
070802	100	$(2.04^{+5.59}_{-1.39})10^4$	$-1.96^{+0.47}_{-0.31}$	-	-
070809	10	$(4.23^{+0.00}_{-0.00})10^4$	$-3.94^{+1.16}_{-0.87}$	-	-
070810A	100	$(2.21^{+1.11}_{-1.64})10^3$	$-1.27^{+0.15}_{-0.15}$	-	-
071020	100	$(1.00^{+47.53}_{-0.00})10^1$	$-1.29^{+0.03}_{-0.03}$	-	-
071031	100	$(2.07^{+2.57}_{-1.82})10^4$	$-1.29^{+0.23}_{-0.20}$	-	-
071122	100	$(2.60^{+0.00}_{-0.00})10^4$	$-1.23^{+-1.23}_{-1.23}$	-	-
080210	100	$(6.91^{+4.85}_{-6.84})10^3$	$-1.31^{+0.14}_{-0.13}$	-	-

GRB	T_{rise} [s]	T_{fall} [s]	α_c	T_{break} [s]	α_{break}
080310	100	$(2.10^{+0.57}_{-0.38})10^4$	$-1.58^{+0.11}_{-0.08}$	-	-
080319B	1	$(1.55^{+0.09}_{-0.19})10^2$	$-1.49^{+0.02}_{-0.02}$	-	-
080319C	100	$(1.30^{+0.32}_{-0.25})10^3$	$-1.43^{+0.07}_{-0.04}$	-	-
080413A	100	$(1.43^{+1.58}_{-1.22})10^3$	$-1.60^{+0.62}_{-0.20}$	-	-
080413B	100	$(3.74^{+70.65}_{-2.74})10^1$	$-0.95^{+0.03}_{-0.03}$	5.53 10^4	-1.44
080430	100	$(1.32^{+13.14}_{-0.53})10^2$	$-0.53^{+0.05}_{-0.06}$	3.67 10^4	-1.15
080603B	100	$(1.47^{+3.05}_{-1.04})10^3$	$-1.13^{+0.71}_{-0.10}$	-	-
080604	100	$(5.15^{+3.11}_{-2.84})10^2$	$-1.37^{+0.18}_{-0.14}$	-	-
080605	100	$(3.05^{+0.69}_{-0.69})10^2$	$-1.12^{+0.09}_{-0.07}$	6.37 10^3	-1.65
080607	100	$(1.93^{+0.64}_{-0.48})10^3$	$-1.62^{+0.14}_{-0.10}$	-	-
080707	100	$(1.79^{+1.92}_{-1.54})10^4$	$-1.06^{+0.21}_{-0.19}$	-	-
080721	100	$(3.17^{+14.40}_{-2.17})10^1$	$-1.08^{+0.02}_{-0.02}$	6.90 10^3	-1.70
080804	100	$(1.09^{+1.33}_{-0.08})10^2$	$-1.13^{+0.03}_{-0.03}$	-	-
080805	100	$(5.06^{+7.73}_{-0.00})10^2$	$-0.95^{+0.09}_{-0.09}$	-	-
080810	100	$(3.45^{+0.60}_{-0.56})10^3$	$-1.50^{+0.06}_{-0.06}$	-	-
080905B	100	$(6.47^{+1.47}_{-1.15})10^3$	$-1.45^{+0.09}_{-0.05}$	-	-
080913	100	$(3.40^{+4.14}_{-3.30})10^2$	$-1.25^{+0.13}_{-0.11}$	-	-
080916A	100	$(1.37^{+0.98}_{-0.63})10^4$	$-1.04^{+0.07}_{-0.06}$	-	-
080928	100	$(1.26^{+0.37}_{-0.29})10^4$	$-1.90^{+0.15}_{-0.13}$	-	-
081007	100	$(1.94^{+3.06}_{-1.00})10^3$	$-0.75^{+0.08}_{-0.10}$	4.13 10^4	-1.23
081008	100	$(2.89^{+3.09}_{-1.43})10^3$	$-0.98^{+0.13}_{-0.14}$	1.91 10^4	-2.13
081118	100	$(5.46^{+6.44}_{-5.40})10^4$	$-0.84^{+0.32}_{-0.17}$	-	-
081203A	100	$(3.68^{+0.52}_{-0.34})10^3$	$-1.83^{+0.10}_{-0.06}$	-	-
081222	10	$(3.86^{+0.86}_{-0.44})10^2$	$-1.10^{+0.03}_{-0.02}$	8.32 10^4	-2.03
081230	100	$(1.51^{+1.41}_{-0.63})10^4$	$-1.14^{+0.13}_{-0.12}$	-	-
090102	100	$(9.82^{+2.50}_{-2.95})10^2$	$-1.46^{+0.05}_{-0.05}$	-	-
090205	100	$(3.22^{+2.95}_{-2.51})10^3$	$-0.89^{+0.13}_{-0.12}$	-	-
090418A	100	$(3.89^{+0.64}_{-0.76})10^3$	$-1.60^{+0.07}_{-0.11}$	-	-
090423	100	$(1.01^{+0.31}_{-0.29})10^4$	$-1.54^{+0.15}_{-0.11}$	-	-
090424	100	$(1.61^{+0.42}_{-0.85})10^2$	$-0.96^{+0.03}_{-0.03}$	3.92 10^3	-1.20
090426	100	$(1.23^{+4.91}_{-0.24})10^2$	$-1.12^{+0.13}_{-0.13}$	-	-
090429B	491.084	$(9.30^{+8.70}_{-4.64})10^2$	$-1.42^{+0.18}_{-0.15}$	-	-
090510	100	$(8.22^{+629.76}_{-7.22})10^1$	$-1.04^{+0.10}_{-0.10}$	1.64 10^3	-2.19
090516	100	$(1.94^{+0.55}_{-0.32})10^4$	$-1.74^{+0.09}_{-0.07}$	-	-

GRB	T_{rise} [s]	T_{fall} [s]	α_c	T_{break} [s]	α_{break}
090519	100	$(1.43^{+0.00}_{-0.00})10^5$	$-10.00^{+0.00}_{-0.00}$	-	-
090529	100	$(9.76^{+7.29}_{-9.66})10^4$	$-1.06^{+0.35}_{-0.29}$	-	-
090530	100	$(9.03^{+17.96}_{-8.93})10^2$	$-0.64^{+0.09}_{-0.10}$	6.55 10^4	-1.49
090618	100	$(6.74^{+0.58}_{-0.67})10^3$	$-1.36^{+0.02}_{-0.02}$	3.08 10^5	-1.87
090715B	100	$(9.24^{+3.52}_{-3.08})10^3$	$-1.28^{+0.08}_{-0.08}$	-	-
090812	100	$(4.62^{+3.58}_{-2.15})10^3$	$-1.43^{+0.08}_{-0.07}$	-	-
091018	100	$(4.75^{+1.20}_{-1.15})10^2$	$-1.22^{+0.04}_{-0.04}$	-	-
091020	100	$(3.93^{+1.72}_{-1.38})10^2$	$-0.99^{+0.04}_{-0.04}$	6.84 10^3	-1.37
091029	100	$(1.77^{+0.59}_{-0.41})10^4$	$-1.08^{+0.07}_{-0.05}$	6.55 10^5	-3.02
091109A	100	$(3.71^{+4.06}_{-2.64})10^3$	$-0.98^{+0.15}_{-0.14}$	-	-
091208B	100	$(1.81^{+0.65}_{-0.54})10^3$	$-1.18^{+0.08}_{-0.05}$	-	-
100219A	100	$(2.58^{+1.27}_{-0.76})10^5$	$-10.00^{+0.00}_{-1.02}$	-	-
100316B	100	$(2.63^{+6.52}_{-1.09})10^3$	$-1.44^{+0.29}_{-0.11}$	-	-
100418A	100	$(3.51^{+1.72}_{-1.64})10^5$	$-1.95^{+0.30}_{-0.21}$	-	-
100425A	100	$(1.29^{+1.90}_{-0.74})10^4$	$-0.85^{+0.19}_{-0.15}$	-	-
100513A	100	$(5.63^{+4.75}_{-3.53})10^3$	$-1.01^{+0.14}_{-0.13}$	-	-
100621A	100	$(5.59^{+2.05}_{-1.86})10^3$	$-1.02^{+0.05}_{-0.05}$	9.36 10^4	-1.60
100724A	100	$(3.73^{+4.01}_{-3.63})10^2$	$-1.15^{+0.10}_{-0.09}$	-	-
100814A	100	$(1.39^{+0.95}_{-0.72})10^4$	$-0.58^{+0.05}_{-0.06}$	1.49 10^5	-2.07
100816A	100	$(7.43^{+272.41}_{-6.43})10^1$	$-1.13^{+0.06}_{-0.06}$	-	-
100901A	100	$(1.52^{+0.44}_{-0.24})10^5$	$-2.28^{+0.11}_{-0.10}$	-	-
100906A	100	$(1.33^{+0.95}_{-0.77})10^3$	$-0.84^{+0.07}_{-0.07}$	1.17 10^4	-1.97
101219A	10	$(2.09^{+59.15}_{-1.09})10^1$	$-2.47^{+-2.47}_{-2.47}$	-	-
101219B	100	$(8.67^{+8.37}_{-2.33})10^4$	$-0.78^{+0.10}_{-0.09}$	-	-
110106B	100	$(2.29^{+0.90}_{-0.83})10^4$	$-1.44^{+0.13}_{-0.11}$	-	-
110205A	100	$(1.30^{+0.74}_{-0.44})10^4$	$-1.56^{+0.11}_{-0.10}$	-	-
110213A	260.3788	$(6.25^{+0.75}_{-0.73})10^3$	$-1.88^{+0.08}_{-0.08}$	-	-
110422A	100	$(8.54^{+12.22}_{-8.44})10^2$	$-1.07^{+0.06}_{-0.06}$	7.51 10^3	-1.52
110503A	100	$(1.66^{+1.21}_{-1.56})10^2$	$-1.16^{+0.02}_{-0.02}$	3.06 10^4	-1.41
110715A	100	$(1.70^{+0.00}_{-0.43})10^3$	$-1.48^{+0.06}_{-0.11}$	-	-
110726A	100	$(2.14^{+2.34}_{-1.17})10^3$	$-1.21^{+0.13}_{-0.13}$	-	-
110808A	100	$(3.79^{+3.47}_{-3.75})10^4$	$-0.92^{+0.25}_{-0.19}$	-	-
110818A	100	$(8.59^{+224.74}_{-7.59})10^1$	$-1.17^{+0.08}_{-0.07}$	-	-
111008A	100	$(9.39^{+1.77}_{-1.88})10^3$	$-1.29^{+0.04}_{-0.04}$	-	-

GRB	T_{rise} [s]	T_{fall} [s]	α_c	T_{break} [s]	α_{break}
111107A	100	$(2.15^{+106.04}_{-1.15})10^1$	$-0.93^{+0.11}_{-0.11}$	-	-
111228A	100	$(1.29^{+0.82}_{-0.34})10^4$	$-1.15^{+0.05}_{-0.05}$	-	-
111229A	100	$(1.68^{+98.32}_{-0.53})10^4$	$-2.03^{+0.33}_{-0.30}$	-	-
120118B	100	$(1.80^{+1.36}_{-0.89})10^4$	$-1.70^{+0.24}_{-0.19}$	-	-
120211A	100	$(1.95^{+98.05}_{-1.93})10^4$	$-1.41^{+0.85}_{-0.84}$	-	-
120326A	100	$(3.07^{+6.93}_{-3.04})10^5$	$-3.31^{+0.25}_{-0.23}$	-	-
120327A	100	$(3.32^{+0.81}_{-1.78})10^3$	$-1.46^{+0.09}_{-0.08}$	-	-
120404A	100	$(6.74^{+4.79}_{-2.70})10^3$	$-1.89^{+0.25}_{-0.26}$	-	-
120422A	100	$(2.00^{+-2.00}_{-1.98})10^5$	$-1.50^{+-1.50}_{-1.50}$	-	-
120521C	100	$(6.84^{+115.62}_{-1.00})10^3$	$-0.77^{+0.32}_{-0.29}$	-	-
120712A	100	$(1.51^{+0.76}_{-1.16})10^3$	$-1.35^{+0.07}_{-0.07}$	-	-
120729A	100	$(4.01^{+1.57}_{-0.49})10^3$	$-2.35^{+0.12}_{-0.10}$	-	-
120802A	100	$(1.78^{+98.22}_{-1.76})10^4$	$-1.38^{+0.59}_{-0.57}$	-	-
120804A	100	$(8.04^{+514.05}_{-32.65})10^1$	$-1.24^{+0.12}_{-0.10}$	-	-
120811C	100	$(6.18^{+2.96}_{-2.66})10^3$	$-1.22^{+0.11}_{-0.12}$	-	-
120907A	100	$(8.18^{+13.35}_{-6.29})10^2$	$-0.99^{+0.11}_{-0.04}$	-	-
121027A	100	$(3.27^{+0.97}_{-0.62})10^5$	$-1.48^{+0.14}_{-0.12}$	-	-
121128A	100	$(1.74^{+0.42}_{-0.29})10^3$	$-1.54^{+0.07}_{-0.07}$	-	-
121201A	100	$(1.40^{+2.56}_{-1.15})10^3$	$-1.16^{+0.18}_{-0.17}$	-	-
121209A	100	$(4.24^{+1.57}_{-1.23})10^3$	$-1.24^{+0.08}_{-0.08}$	-	-
130427B	100	$(9.44^{+15.58}_{-8.44})10^1$	$-1.20^{+0.12}_{-0.09}$	-	-
130610A	100	$(2.49^{+1.77}_{-2.31})10^3$	$-1.22^{+0.14}_{-0.15}$	-	-
130831A	100	$(3.07^{+5.95}_{-0.93})10^3$	$-1.07^{+0.09}_{-0.09}$	-	-
130925A	100	$(1.89^{+0.96}_{-0.64})10^4$	$-0.59^{+0.17}_{-0.16}$	3.41 10^5	-1.36
131030A	100	$(3.53^{+0.40}_{-0.61})10^3$	$-1.28^{+0.03}_{-0.02}$	-	-
131227A	100	$(4.95^{+69.83}_{-3.95})10^1$	$-1.34^{+0.07}_{-0.05}$	-	-
140304A	100	$(3.03^{+1.38}_{-1.52})10^3$	$-2.78^{+0.74}_{-0.70}$	-	-
140430A	100	$(1.54^{+1.57}_{-0.78})10^4$	$-0.90^{+0.14}_{-0.14}$	-	-
140506A	100	$(6.37^{+33.02}_{-5.37})10^1$	$-0.85^{+0.03}_{-0.03}$	-	-
140509A	100	$(5.03^{+1.46}_{-1.78})10^3$	$-1.72^{+0.14}_{-0.12}$	-	-
140629A	100	$(6.44^{+127.76}_{-5.44})10^1$	$-0.98^{+0.03}_{-0.03}$	1.60 10^4	-2.12
140703A	100	$(1.93^{+0.40}_{-0.91})10^4$	$-1.89^{+0.13}_{-0.12}$	-	-
140710A	100	$(2.72^{+4.60}_{-1.00})10^3$	$-0.94^{+0.33}_{-0.32}$	-	-
141221A	100	$(6.02^{+7.36}_{-4.91})10^2$	$-1.21^{+0.18}_{-0.12}$	-	-

GRB	T_{rise} [s]	T_{fall} [s]	α_c	T_{break} [s]	α_{break}
150301B	100	$(6.09^{+993.91}_{-6.03})10^3$	$-3.62^{+0.58}_{-0.54}$	-	-
150403A	100	$(1.07^{+0.04}_{-0.25})10^3$	$-1.25^{+0.01}_{-0.01}$	5.37 10^5	-2.62
151027A	100	$(9.90^{+0.74}_{-1.90})10^3$	$-1.74^{+0.04}_{-0.03}$	-	-
151027B	100	$(1.47^{+0.55}_{-0.82})10^4$	$-1.15^{+0.10}_{-0.09}$	-	-
151111A	100	$(1.40^{+2.40}_{-0.74})10^4$	$-1.06^{+0.38}_{-0.30}$	-	-
151215A	100	$(7.29^{+13.13}_{-7.19})10^2$	$-1.06^{+0.17}_{-0.12}$	-	-
160104A	100	$(7.37^{+22.24}_{-7.30})10^4$	$-1.17^{+0.47}_{-0.29}$	-	-
160117B	100	$(1.88^{+0.94}_{-0.83})10^3$	$-0.97^{+0.09}_{-0.08}$	-	-
160121A	100	$(6.27^{+20.81}_{-1.00})10^3$	$-0.53^{+0.30}_{-0.53}$	-	-
160314A	100	$(8.81^{+111.06}_{-8.71})10^2$	$-0.55^{+0.21}_{-0.23}$	-	-
160327A	100	$(8.73^{+2.86}_{-6.89})10^3$	$-1.68^{+0.25}_{-0.20}$	-	-
160410A	100	$(1.00^{+1679.00}_{-0.00})10^1$	$-2.13^{+0.33}_{-0.35}$	-	-

Table 4: Temporal parameters of the fitted afterglow components. The rise time of the afterglow, T_{rise}, is typically fixed as the model fits are insensitive to the parameter. Smaller values are used for bursts which are particularly short. The time at which the afterglow plateau turns over, T_{fall}, and a late-time break, T_{break}, are also shown (where applicable). The afterglow model also contains the temporal index of the turnover: α_c; and, where a late-time break is observed, α_{break}. A single value indicates a parameter which was fixed during final fitting. The 90% range is indicated for parameters which were allowed to float in the final fitting.

GRB	α_{fall}	$E_{c,fall}$ [keV]	L_{aft} [ergs s^{-1}]	F_{aft} [10^{-8} ergs s^{-1} cm^{-2}]	E_{iso} [ergs]	$T_{90,aft}$ [s]
050126	$-1.06^{+0.75}_{-0.38}$	218	$(3.14^{+198.83}_{-3.13})10^{48}$	$161.5^{+822599.2}_{-161.5}$	$(7.04^{+446.17}_{-7.02})10^{51}$	$1.66\ 10^{5}$
050215B	$-1.73^{+0.85}_{-1.01}$	1000	$(5.07^{+294.17}_{-5.05})10^{47}$	$23.42^{+2456.19}_{-23.37}$	$(3.66^{+212.18}_{-3.65})10^{51}$	$6.26\ 10^{5}$
050219A	$-2.27^{+0.48}_{-0.59}$	1000	$(2.83^{+10.10}_{-1.86})10^{45}$	$11.91^{+430.39}_{-10.66}$	$(1.34^{+4.78}_{-0.88})10^{49}$	$2.56\ 10^{4}$
050315	$-2.08^{+0.12}_{-0.13}$	170	$(7.39^{+2.70}_{-1.85})10^{47}$	$123.5^{+270.3}_{-81.7}$	$(1.52^{+0.55}_{-0.38})10^{52}$	$7.10\ 10^{5}$
050319	$-2.13^{+0.12}_{-0.14}$	118	$(2.44^{+0.58}_{-0.42})10^{48}$	$76.37^{+59.45}_{-33.88}$	$(2.61^{+0.62}_{-0.45})10^{52}$	$1.02\ 10^{6}$
050401	$-1.83^{+0.07}_{-0.07}$	128	$(5.16^{+1.31}_{-0.80})10^{49}$	$246.9^{+181.6}_{-222.0}$	$(5.51^{+1.40}_{-0.85})10^{52}$	$1.63\ 10^{5}$
050416A	$-2.08^{+0.14}_{-0.14}$	302	$(9.74^{+4.40}_{-2.87})10^{46}$	$67.64^{+84.20}_{-39.32}$	$(8.44^{+3.81}_{-2.49})10^{50}$	$5.19\ 10^{6}$
050525A	$-2.14^{+0.24}_{-0.27}$	311	$(1.49^{+1.41}_{-0.64})10^{47}$	$71.06^{+181.76}_{-70.65}$	$(7.65^{+7.23}_{-3.29})10^{50}$	$1.85\ 10^{5}$
050724	$-1.26^{+0.80}_{-0.70}$	397	$(1.54^{+101.72}_{-1.44})10^{45}$	$72.41^{+5309.57}_{-71.23}$	$(1.16^{+76.53}_{-1.09})10^{50}$	$2.46\ 10^{5}$
050730	$-1.67^{+0.05}_{-0.05}$	101	$(1.44^{+0.20}_{-0.17})10^{50}$	$647.6^{+143.8}_{-106.9}$	$(2.32^{+0.32}_{-0.27})10^{53}$	$2.75\ 10^{4}$
050801	$-1.85^{+0.33}_{-0.37}$	195	$(8.49^{+23.86}_{-4.88})10^{48}$	$80.00^{+552.34}_{-74.70}$	$(5.62^{+15.81}_{-3.23})10^{51}$	$7.06\ 10^{4}$
050802	$-1.88^{+0.09}_{-0.10}$	185	$(2.69^{+0.90}_{-0.60})10^{48}$	$101.2^{+57.4}_{-33.2}$	$(8.61^{+2.86}_{-1.91})10^{51}$	$1.96\ 10^{5}$
050803	$-2.20^{+0.13}_{-0.14}$	1000	$(6.59^{+2.00}_{-1.23})10^{48}$	$79.20^{+51.30}_{-24.77}$	$(3.04^{+0.92}_{-0.57})10^{52}$	$4.45\ 10^{5}$
050814	$-2.03^{+0.18}_{-0.20}$	79	$(2.53^{+1.02}_{-0.65})10^{48}$	$18.64^{+26.07}_{-13.82}$	$(1.40^{+0.56}_{-0.36})10^{52}$	$3.37\ 10^{5}$
050820A	$-1.93^{+0.06}_{-0.06}$	138	$(1.49^{+0.25}_{-0.21})10^{49}$	$465.5^{+163.7}_{-119.3}$	$(9.07^{+1.51}_{-1.25})10^{52}$	$1.72\ 10^{6}$
050822	$-2.19^{+0.14}_{-0.16}$	1000	$(3.88^{+1.72}_{-1.06})10^{47}$	$146.7^{+216.0}_{-63.3}$	$(9.87^{+4.36}_{-2.69})10^{51}$	$3.36\ 10^{6}$
050908	$-2.73^{+0.33}_{-0.59}$	115	$(7.70^{+129.19}_{-4.94})10^{48}$	$1.81^{+78.39}_{-1.78}$	$(1.34^{+22.52}_{-0.86})10^{51}$	$7.61\ 10^{4}$
050922C	$-2.09^{+0.10}_{-0.10}$	156	$(3.13^{+0.98}_{-0.83})10^{49}$	$53.50^{+70.54}_{-50.22}$	$(8.38^{+2.64}_{-2.21})10^{51}$	$6.28\ 10^{4}$
051016B	$-2.01^{+0.16}_{-0.17}$	258	$(4.49^{+2.48}_{-1.47})10^{46}$	$29.98^{+54.45}_{-26.17}$	$(7.86^{+4.35}_{-2.57})10^{50}$	$6.67\ 10^{5}$
051109A	$-1.97^{+0.10}_{-0.10}$	149	$(5.80^{+1.43}_{-1.07})10^{48}$	$156.5^{+89.6}_{-63.6}$	$(2.56^{+0.63}_{-0.47})10^{52}$	$8.84\ 10^{5}$
051221A	$-1.98^{+0.19}_{-0.21}$	323	$(6.10^{+4.59}_{-2.45})10^{45}$	$24.60^{+34.45}_{-13.89}$	$(2.03^{+1.53}_{-0.82})10^{50}$	$5.17\ 10^{5}$
060108	$-1.96^{+0.25}_{-0.28}$	165	$(3.04^{+2.88}_{-1.35})10^{47}$	$17.64^{+44.43}_{-13.44}$	$(2.18^{+2.06}_{-0.97})10^{51}$	$3.89\ 10^{5}$

GRB	α_{fall}	$E_{c,fall}$ [keV]	L_{aft} [ergs s^{-1}]	F_{aft} [10^{-8} ergs s^{-1} cm^{-2}]	E_{iso} [ergs]	$T_{90,aft}$ [s]
060115	$-2.38^{+0.29}_{-0.34}$	110	$(5.35^{+2.06}_{-1.08})10^{47}$	$7.71^{+14.15}_{-7.65}$	$(4.07^{+1.57}_{-0.82})10^{51}$	$2.91\ 10^{5}$
060116	$-2.24^{+0.57}_{-0.51}$	66	$(3.62^{+3.40}_{-0.43})10^{49}$	$20.46^{+46.44}_{-14.58}$	$(2.97^{+2.78}_{-0.35})10^{52}$	$4.11\ 10^{5}$
060124	$-2.00^{+0.07}_{-0.08}$	152	$(3.27^{+0.59}_{-0.48})10^{48}$	$293.0^{+115.4}_{-119.8}$	$(4.68^{+0.84}_{-0.68})10^{52}$	$1.09\ 10^{6}$
060206	$-1.96^{+0.14}_{-0.16}$	99	$(3.58^{+1.31}_{-0.89})10^{49}$	$104.2^{+95.8}_{-47.3}$	$(4.60^{+1.69}_{-1.15})10^{52}$	$1.64\ 10^{6}$
060210	$-2.14^{+0.09}_{-0.10}$	102	$(1.68^{+0.31}_{-0.24})10^{49}$	$135.3^{+73.0}_{-72.5}$	$(6.62^{+1.23}_{-0.96})10^{52}$	$4.68\ 10^{5}$
060223A	$-2.36^{+0.47}_{-0.62}$	92	$(4.99^{+3.53}_{-1.37})10^{48}$	$1.52^{+3.20}_{-1.01}$	$(1.21^{+0.85}_{-0.33})10^{51}$	$3.29\ 10^{4}$
060418	$-1.95^{+0.14}_{-0.14}$	201	$(5.83^{+2.21}_{-1.45})10^{48}$	$72.18^{+111.12}_{-28.05}$	$(4.82^{+1.83}_{-1.20})10^{51}$	$1.03\ 10^{5}$
060502A	$-2.00^{+0.16}_{-0.18}$	199	$(3.35^{+1.58}_{-1.00})10^{47}$	$88.07^{+95.18}_{-49.46}$	$(6.18^{+2.91}_{-1.84})10^{51}$	$1.30\ 10^{6}$
060522	$-2.37^{+0.37}_{-0.53}$	82	$(4.35^{+1.80}_{-0.56})10^{48}$	$3.73^{+4.78}_{-2.47}$	$(4.04^{+1.67}_{-0.52})10^{51}$	$9.32\ 10^{4}$
060526	$-1.99^{+0.23}_{-0.24}$	119	$(1.06^{+0.63}_{-0.33})10^{48}$	$23.73^{+36.49}_{-17.06}$	$(7.04^{+4.15}_{-2.15})10^{51}$	$4.01\ 10^{5}$
060604	$-2.28^{+0.20}_{-0.24}$	136	$(5.06^{+1.85}_{-1.15})10^{47}$	$21.10^{+19.15}_{-9.77}$	$(5.70^{+2.09}_{-1.30})10^{51}$	$1.11\ 10^{6}$
060605	$-1.95^{+0.13}_{-0.14}$	104	$(5.53^{+1.70}_{-1.19})10^{48}$	$27.59^{+19.94}_{-11.34}$	$(1.08^{+0.33}_{-0.23})10^{52}$	$4.51\ 10^{4}$
060607A	$-1.69^{+0.10}_{-0.10}$	122	$(3.31^{+1.13}_{-0.81})10^{49}$	$322.2^{+109.7}_{-178.6}$	$(7.53^{+2.56}_{-1.85})10^{52}$	$2.16\ 10^{4}$
060614	$-1.88^{+0.09}_{-0.10}$	444	$(8.10^{+2.99}_{-2.17})10^{44}$	$140.8^{+82.0}_{-50.3}$	$(5.08^{+1.88}_{-1.36})10^{49}$	$3.44\ 10^{5}$
060707	$-1.97^{+0.21}_{-0.28}$	113	$(1.67^{+0.93}_{-0.52})10^{48}$	$36.65^{+81.87}_{-21.10}$	$(1.22^{+0.68}_{-0.38})10^{52}$	$1.52\ 10^{6}$
060714	$-2.22^{+0.18}_{-0.20}$	135	$(3.14^{+0.98}_{-0.65})10^{48}$	$31.39^{+20.03}_{-12.66}$	$(8.22^{+2.55}_{-1.70})10^{51}$	$7.66\ 10^{5}$
060729	$-2.17^{+0.06}_{-0.06}$	325	$(4.87^{+1.12}_{-0.92})10^{46}$	$399.4^{+732.2}_{-304.3}$	$(3.38^{+0.78}_{-0.64})10^{51}$	$5.95\ 10^{6}$
060801	$-1.98^{+0.36}_{-0.38}$	235	$(2.82^{+5.31}_{-1.53})10^{48}$	$6.77^{+14.85}_{-3.67}$	$(2.60^{+4.89}_{-1.41})10^{50}$	$3.33\ 10^{2}$
060814	$-2.12^{+0.10}_{-0.11}$	272	$(1.70^{+0.49}_{-0.36})10^{47}$	$97.56^{+54.44}_{-46.44}$	$(2.12^{+0.61}_{-0.44})10^{51}$	$6.68\ 10^{5}$
060904B	$-2.27^{+0.21}_{-0.22}$	294	$(6.09^{+3.75}_{-2.08})10^{46}$	$22.85^{+33.70}_{-12.73}$	$(3.56^{+2.19}_{-1.22})10^{50}$	$2.99\ 10^{5}$
060906	$-2.23^{+0.32}_{-0.41}$	107	$(1.88^{+1.23}_{-0.53})10^{48}$	$5.44^{+66.42}_{-5.41}$	$(2.60^{+1.69}_{-0.73})10^{51}$	$1.60\ 10^{4}$
060908	$-2.20^{+0.20}_{-0.23}$	173	$(7.81^{+3.41}_{-2.13})10^{48}$	$21.64^{+23.91}_{-12.24}$	$(2.70^{+1.18}_{-0.73})10^{51}$	$5.35\ 10^{4}$

GRB	α_{fall}	$E_{c,fall}$ [keV]	L_{aft} [ergs s^{-1}]	F_{aft} [10^{-8} ergs s^{-1} cm^{-2}]	E_{iso} [ergs]	$T_{90,aft}$ [s]
060912A	$-1.93^{+0.24}_{-0.27}$	258	$(3.50^{+4.97}_{-1.66})10^{47}$	$20.11^{+65.98}_{-14.74}$	$(5.14^{+7.29}_{-2.43})10^{50}$	$4.71\ 10^{5}$
060926	$0.00^{+-1.00}_{-1.00}$	119	$(1.23^{+-0.73}_{-1.23})10^{51}$	$17.82^{+-17.82}_{-17.82}$	$(3.98^{+-2.36}_{-3.98})10^{51}$	$2.36\ 10^{1}$
060927	$-2.16^{+0.40}_{-0.52}$	76	$(1.63^{+1.44}_{-0.50})10^{49}$	$8.33^{+35.89}_{-8.27}$	$(7.99^{+7.04}_{-2.44})10^{51}$	$8.33\ 10^{4}$
061006	$-2.02^{+0.78}_{-0.84}$	348	$(3.75^{+46.77}_{-3.74})10^{45}$	$4.72^{+225.34}_{-4.71}$	$(2.44^{+30.42}_{-2.43})10^{49}$	$8.34\ 10^{4}$
061021	$-1.91^{+0.09}_{-0.09}$	371	$(6.23^{+2.67}_{-1.90})10^{46}$	$228.5^{+327.3}_{-127.2}$	$(7.01^{+3.01}_{-2.14})10^{50}$	$3.86\ 10^{6}$
061110A	$-2.17^{+0.42}_{-0.45}$	284	$(1.31^{+3.45}_{-0.90})10^{46}$	$5.79^{+50.05}_{-5.77}$	$(1.02^{+2.70}_{-0.71})10^{50}$	$8.18\ 10^{5}$
061121	$-1.93^{+0.08}_{-0.08}$	216	$(4.53^{+1.11}_{-0.86})10^{48}$	$364.5^{+271.0}_{-176.8}$	$(1.87^{+0.46}_{-0.36})10^{52}$	$4.41\ 10^{5}$
061222A	$-2.11^{+0.09}_{-0.09}$	162	$(1.45^{+0.33}_{-0.26})10^{49}$	$335.0^{+138.6}_{-59.8}$	$(4.80^{+1.10}_{-0.86})10^{52}$	$2.77\ 10^{5}$
061222B	$-3.18^{+2.18}_{-2.18}$	115	$(NaN^{+NaN}_{NaN})10^{-Inf}$	$0.0000^{+0.0000}_{-0.0000}$	$(NaN^{+NaN}_{NaN})10^{-Inf}$	$NaN\ 10^{-Inf}$
070208	$-1.89^{+0.29}_{-0.34}$	230	$(7.95^{+12.46}_{-4.08})10^{48}$	$900.8^{+3589.8}_{-615.0}$	$(3.60^{+5.64}_{-1.85})10^{52}$	$1.71\ 10^{5}$
070306	$-1.81^{+0.13}_{-0.12}$	200	$(1.17^{+0.47}_{-0.30})10^{48}$	$340.3^{+232.0}_{-119.2}$	$(2.17^{+0.87}_{-0.55})10^{52}$	$3.17\ 10^{5}$
070318	$-1.84^{+0.13}_{-0.13}$	272	$(1.57^{+0.90}_{-0.55})10^{48}$	$116.3^{+1287.0}_{-98.8}$	$(2.31^{+1.32}_{-0.81})10^{51}$	$6.76\ 10^{5}$
070419A	$0.00^{+-1.00}_{-1.00}$	254	$(NaN^{+NaN}_{NaN})10^{-Inf}$	$0.0000^{+0.0000}_{-0.0000}$	$(NaN^{+NaN}_{-NaN})10^{-Inf}$	$NaN\ 10^{-Inf}$
070506	$-1.85^{+0.28}_{-0.33}$	151	$(1.80^{+3.04}_{-1.10})10^{48}$	$34.47^{+1239.73}_{-25.57}$	$(5.14^{+8.67}_{-3.14})10^{51}$	$8.77\ 10^{4}$
070521	$-1.97^{+0.20}_{-0.18}$	322	$(5.64^{+4.66}_{-2.16})10^{47}$	$185.4^{+237.5}_{-92.1}$	$(1.56^{+1.29}_{-0.60})10^{51}$	$8.57\ 10^{4}$
070529	$-2.17^{+0.28}_{-0.30}$	143	$(3.38^{+2.28}_{-1.10})10^{48}$	$19.67^{+31.10}_{-11.78}$	$(4.20^{+2.83}_{-1.36})10^{51}$	$2.15\ 10^{5}$
070721B	$-1.62^{+0.15}_{-0.16}$	108	$(1.22^{+0.73}_{-0.42})10^{49}$	$65.31^{+79.27}_{-30.94}$	$(1.96^{+1.17}_{-0.67})10^{52}$	$3.03\ 10^{4}$
070802	$-2.33^{+0.40}_{-0.48}$	145	$(3.01^{+2.61}_{-1.10})10^{47}$	$5.06^{+30.33}_{-4.04}$	$(1.20^{+1.04}_{-0.44})10^{51}$	$8.65\ 10^{4}$
070809	$-1.35^{+0.35}_{-0.33}$	410	$(6.50^{+25.35}_{-4.81})10^{45}$	$53.43^{+208.23}_{-39.54}$	$(6.08^{+23.68}_{-4.50})10^{49}$	$3.24\ 10^{4}$
070810A	$-2.00^{+0.20}_{-0.23}$	158	$(2.05^{+1.68}_{-0.92})10^{48}$	$16.41^{+28.43}_{-14.07}$	$(2.36^{+1.94}_{-1.06})10^{51}$	$3.28\ 10^{4}$
071020	$-1.79^{+0.08}_{-0.08}$	147	$(1.05^{+0.23}_{-0.18})10^{50}$	$146.5^{+8537.0}_{-25.2}$	$(2.30^{+0.51}_{-0.40})10^{52}$	$2.80\ 10^{5}$
071031	$-1.94^{+0.32}_{-0.37}$	135	$(2.13^{+2.78}_{-1.03})10^{47}$	$7.44^{+31.01}_{-6.98}$	$(1.54^{+2.01}_{-0.75})10^{51}$	$3.06\ 10^{5}$

GRB	α_{fall}	$E_{c,fall}$ [keV]	L_{aft} [ergs s^{-1}]	F_{aft} [10^{-8} ergs s^{-1} cm^{-2}]	E_{iso} [ergs]	$T_{90,aft}$ [s]
071122	$-2.29^{+1.29}_{-1.29}$	234	$(NaN^{+NaN}_{-NaN})10^{-Inf}$	$0.0000^{+0.0000}_{-0.0000}$	$(NaN^{+NaN}_{-NaN})10^{-Inf}$	$NaN\ 10^{-Inf}$
080210	$-2.31^{+0.20}_{-0.23}$	137	$(2.04^{+0.95}_{-0.62})10^{48}$	$19.88^{+29.63}_{-19.74}$	$(5.41^{+2.51}_{-1.64})10^{51}$	$1.17\ 10^{5}$
080310	$-1.77^{+0.15}_{-0.16}$	146	$(1.69^{+0.89}_{-0.53})10^{48}$	$62.16^{+58.53}_{-27.43}$	$(9.77^{+5.14}_{-3.09})10^{51}$	$2.57\ 10^{5}$
080319B	$-1.75^{+0.00}_{-0.03}$	28	$(1.26^{+0.14}_{-0.11})10^{51}$	$4292.0^{+765.1}_{-846.1}$	$(1.13^{+0.13}_{-0.09})10^{53}$	$6.41\ 10^{3}$
080319C	$-1.70^{+0.12}_{-0.12}$	169	$(4.50^{+2.27}_{-1.45})10^{49}$	$332.5^{+291.6}_{-150.6}$	$(3.40^{+1.72}_{-1.10})10^{52}$	$1.24\ 10^{5}$
080413A	$-2.17^{+0.45}_{-0.49}$	146	$(6.24^{+9.24}_{-2.98})10^{48}$	$16.11^{+68.18}_{-14.90}$	$(3.27^{+4.85}_{-1.56})10^{51}$	$2.33\ 10^{4}$
080413B	$-1.97^{+0.09}_{-0.09}$	238	$(3.71^{+1.07}_{-0.81})10^{48}$	$116.2^{+2863.2}_{-91.9}$	$(4.21^{+1.21}_{-0.91})10^{51}$	$3.02\ 10^{5}$
080430	$-2.08^{+0.12}_{-0.12}$	283	$(1.37^{+0.73}_{-0.50})10^{47}$	$88.49^{+1402.82}_{-55.06}$	$(1.56^{+0.84}_{-0.57})10^{51}$	$2.37\ 10^{6}$
080603B	$-1.93^{+0.25}_{-0.32}$	136	$(1.72^{+1.34}_{-0.65})10^{49}$	$65.21^{+291.46}_{-53.39}$	$(1.35^{+1.06}_{-0.51})10^{52}$	$1.53\ 10^{4}$
080604	$-1.67^{+0.33}_{-0.35}$	207	$(1.54^{+3.77}_{-1.01})10^{48}$	$14.32^{+64.72}_{-12.10}$	$(7.89^{+19.26}_{-5.17})10^{50}$	$8.76\ 10^{4}$
080605	$-1.79^{+0.06}_{-0.07}$	189	$(5.38^{+1.25}_{-0.90})10^{49}$	$349.7^{+178.8}_{-124.8}$	$(2.65^{+0.62}_{-0.44})10^{52}$	$4.18\ 10^{4}$
080607	$-2.33^{+0.11}_{-0.13}$	124	$(3.54^{+0.45}_{-0.36})10^{49}$	$55.13^{+27.46}_{-17.89}$	$(2.03^{+0.26}_{-0.21})10^{52}$	$4.41\ 10^{4}$
080707	$-2.34^{+0.24}_{-0.26}$	224	$(4.81^{+3.31}_{-1.87})10^{46}$	$12.63^{+31.54}_{-11.56}$	$(7.02^{+4.83}_{-2.73})10^{50}$	$3.00\ 10^{5}$
080721	$-1.85^{+0.03}_{-0.03}$	139	$(6.67^{+0.50}_{-0.45})10^{50}$	$1115.8^{+5531.4}_{-788.2}$	$(2.07^{+0.16}_{-0.14})10^{53}$	$6.09\ 10^{4}$
080804	$-1.79^{+0.12}_{-0.13}$	156	$(1.97^{+0.90}_{-0.57})10^{49}$	$60.80^{+135.97}_{-20.84}$	$(8.06^{+3.70}_{-2.34})10^{51}$	$3.00\ 10^{5}$
080805	$-2.03^{+0.26}_{-0.29}$	200	$(8.64^{+11.63}_{-4.80})10^{47}$	$22.75^{+112.05}_{-12.64}$	$(1.61^{+2.16}_{-0.89})10^{51}$	$7.07\ 10^{5}$
080810	$-2.19^{+0.12}_{-0.14}$	115	$(2.13^{+0.46}_{-0.35})10^{49}$	$55.97^{+23.78}_{-16.68}$	$(2.16^{+0.46}_{-0.35})10^{52}$	$1.19\ 10^{5}$
080905B	$-1.92^{+0.14}_{-0.15}$	148	$(1.14^{+0.46}_{-0.30})10^{49}$	$172.6^{+124.8}_{-68.1}$	$(2.80^{+1.13}_{-0.74})10^{52}$	$3.37\ 10^{5}$
080913	$-2.02^{+0.34}_{-0.39}$	65	$(1.81^{+3.04}_{-0.87})10^{49}$	$2.80^{+13.83}_{-2.76}$	$(3.12^{+5.24}_{-1.50})10^{51}$	$2.87\ 10^{5}$
080916A	$-2.11^{+0.21}_{-0.22}$	296	$(3.35^{+2.38}_{-1.25})10^{46}$	$49.53^{+95.88}_{-32.74}$	$(6.98^{+4.96}_{-2.60})10^{50}$	$1.35\ 10^{6}$
080928	$-2.09^{+0.15}_{-0.17}$	186	$(1.39^{+0.59}_{-0.38})10^{48}$	$51.01^{+42.84}_{-22.24}$	$(4.73^{+2.00}_{-1.28})10^{51}$	$5.64\ 10^{4}$
081007	$-2.04^{+0.28}_{-0.31}$	327	$(5.35^{+7.09}_{-2.77})10^{46}$	$67.81^{+338.49}_{-51.91}$	$(5.31^{+7.05}_{-2.75})10^{50}$	$1.09\ 10^{6}$

GRB	α_{fall}	$E_{c,fall}$ [keV]	L_{aft} [ergs s^{-1}]	F_{aft} [10^{-8} ergs s^{-1} cm^{-2}]	E_{iso} [ergs]	$T_{90,aft}$ [s]
081008	$-2.14^{+0.27}_{-0.34}$	169	$(1.95^{+1.48}_{-0.73})10^{48}$	$33.49^{+88.55}_{-22.87}$	$(4.34^{+3.31}_{-1.62})10^{51}$	$6.64\ 10^{4}$
081118	$-2.18^{+0.61}_{-0.99}$	140	$(3.10^{+7.95}_{-3.07})10^{46}$	$5.01^{+33.96}_{-5.01}$	$(1.15^{+2.95}_{-1.14})10^{51}$	$8.31\ 10^{5}$
081203A	$-1.96^{+0.11}_{-0.12}$	161	$(1.44^{+0.39}_{-0.29})10^{49}$	$115.5^{+51.7}_{-32.1}$	$(1.52^{+0.41}_{-0.31})10^{52}$	$3.34\ 10^{4}$
081222	$-2.04^{+0.06}_{-0.06}$	133	$(9.73^{+1.45}_{-1.54})10^{49}$	$122.4^{+49.5}_{-31.1}$	$(2.87^{+0.43}_{-0.46})10^{52}$	$1.29\ 10^{5}$
081230	$-1.96^{+0.21}_{-0.24}$	165	$(2.53^{+1.87}_{-1.01})10^{47}$	$19.06^{+45.07}_{-12.45}$	$(2.35^{+1.73}_{-0.94})10^{51}$	$6.40\ 10^{5}$
090102	$-1.78^{+0.10}_{-0.10}$	196	$(7.73^{+3.79}_{-2.05})10^{49}$	$768.0^{+667.2}_{-372.8}$	$(5.17^{+2.53}_{-1.37})10^{52}$	$9.71\ 10^{4}$
090205	$-1.73^{+0.19}_{-0.20}$	88	$(7.08^{+4.26}_{-2.46})10^{48}$	$37.56^{+77.68}_{-32.19}$	$(1.79^{+1.08}_{-0.62})10^{52}$	$3.15\ 10^{5}$
090418A	$-2.02^{+0.13}_{-0.14}$	192	$(9.62^{+3.48}_{-2.42})10^{48}$	$196.8^{+115.4}_{-78.4}$	$(1.58^{+0.57}_{-0.40})10^{52}$	$7.84\ 10^{4}$
090423	$-1.77^{+0.16}_{-0.17}$	54	$(3.03^{+1.10}_{-0.70})10^{49}$	$28.35^{+22.35}_{-12.86}$	$(3.50^{+1.27}_{-0.80})10^{52}$	$1.98\ 10^{5}$
090424	$-2.03^{+0.05}_{-0.05}$	324	$(1.01^{+0.16}_{-0.14})10^{49}$	$1759.4^{+816.6}_{-1043.3}$	$(1.45^{+0.23}_{-0.20})10^{52}$	$1.86\ 10^{6}$
090426	$-2.24^{+0.21}_{-0.26}$	139	$(4.72^{+2.94}_{-1.76})10^{48}$	$4.46^{+31.67}_{-2.19}$	$(1.10^{+0.69}_{-0.41})10^{51}$	$7.56\ 10^{3}$
090429B	$-2.17^{+0.30}_{-0.35}$	48	$(4.94^{+1.22}_{-0.22})10^{49}$	$6.00^{+8.49}_{-3.12}$	$(1.45^{+0.36}_{-0.06})10^{52}$	$1.39\ 10^{5}$
090510	$-1.70^{+0.14}_{-0.14}$	263	$(3.52^{+2.57}_{-1.43})10^{48}$	$63.62^{+8472.65}_{-59.03}$	$(1.43^{+1.04}_{-0.58})10^{51}$	$5.84\ 10^{3}$
090516	$-2.13^{+0.11}_{-0.13}$	98	$(9.91^{+1.81}_{-1.33})10^{48}$	$58.53^{+30.20}_{-16.21}$	$(3.10^{+0.57}_{-0.41})10^{52}$	$2.04\ 10^{5}$
090519	$0.00^{+0.00}_{-3.50}$	103	$(NaN^{+NaN}_{-NaN})10^{-Inf}$	$0.0000^{+0.0000}_{-0.0000}$	$(NaN^{+NaN}_{-NaN})10^{-Inf}$	$NaN\ 10^{-Inf}$
090529	$-1.88^{+0.45}_{-0.57}$	138	$(9.83^{+25.88}_{-5.73})10^{46}$	$23.02^{+123.03}_{-22.92}$	$(4.40^{+11.59}_{-2.56})10^{51}$	$1.50\ 10^{6}$
090530	$-2.07^{+0.22}_{-0.25}$	217	$(2.55^{+2.38}_{-1.21})10^{47}$	$30.70^{+146.55}_{-30.53}$	$(1.64^{+1.53}_{-0.78})10^{51}$	$5.29\ 10^{5}$
090618	$-2.12^{+0.04}_{-0.04}$	325	$(7.52^{+0.74}_{-0.68})10^{47}$	$567.5^{+109.4}_{-102.7}$	$(4.73^{+0.47}_{-0.43})10^{51}$	$3.57\ 10^{5}$
090715B	$-2.10^{+0.16}_{-0.20}$	125	$(4.39^{+1.81}_{-1.16})10^{48}$	$57.53^{+54.72}_{-29.28}$	$(1.64^{+0.68}_{-0.43})10^{52}$	$7.81\ 10^{5}$
090812	$-2.15^{+0.20}_{-0.23}$	145	$(6.20^{+2.54}_{-1.59})10^{48}$	$53.35^{+80.06}_{-32.17}$	$(1.08^{+0.44}_{-0.28})10^{52}$	$1.14\ 10^{5}$
091018	$-1.90^{+0.10}_{-0.11}$	254	$(3.80^{+1.45}_{-0.96})10^{48}$	$123.3^{+90.1}_{-53.4}$	$(3.36^{+1.28}_{-0.85})10^{51}$	$3.45\ 10^{5}$
091020	$-2.00^{+0.10}_{-0.10}$	185	$(1.22^{+0.33}_{-0.25})10^{49}$	$118.2^{+98.0}_{-57.5}$	$(1.07^{+0.29}_{-0.22})10^{52}$	$3.75\ 10^{5}$

GRB	α_{fall}	$E_{c,fall}$ [keV]	L_{aft} [ergs s^{-1}]	F_{aft} [10^{-8} ergs s^{-1} cm^{-2}]	E_{iso} [ergs]	$T_{90,aft}$ [s]
091029	$-2.03^{+0.12}_{-0.15}$	133	$(1.25^{+0.35}_{-0.26})10^{48}$	$52.57^{+37.32}_{-20.43}$	$(1.21^{+0.34}_{-0.25})10^{52}$	$7.36\ 10^{5}$
091109A	$-2.12^{+0.30}_{-0.35}$	123	$(8.34^{+7.95}_{-3.45})10^{47}$	$9.26^{+28.65}_{-7.70}$	$(2.82^{+2.69}_{-1.16})10^{51}$	$5.76\ 10^{5}$
091208B	$-1.96^{+0.18}_{-0.18}$	242	$(1.43^{+0.89}_{-0.50})10^{48}$	$103.7^{+125.7}_{-56.5}$	$(3.49^{+2.18}_{-1.23})10^{51}$	$8.32\ 10^{5}$
100219A	$-1.37^{+0.28}_{-0.28}$	88	$(9.21^{+12.34}_{-4.71})10^{48}$	$109.0^{+271.6}_{-71.6}$	$(4.64^{+6.23}_{-2.38})10^{52}$	$7.55\ 10^{4}$
100316B	$-2.22^{+0.37}_{-0.45}$	229	$(3.31^{+3.78}_{-1.48})10^{47}$	$12.35^{+79.64}_{-8.34}$	$(5.83^{+6.66}_{-2.61})10^{50}$	$1.69\ 10^{5}$
100418A	$-1.79^{+0.35}_{-0.36}$	308	$(7.53^{+18.32}_{-4.60})10^{45}$	$91.97^{+379.07}_{-72.88}$	$(9.66^{+23.51}_{-5.90})10^{50}$	$1.14\ 10^{6}$
100425A	$-2.42^{+0.36}_{-0.45}$	181	$(7.66^{+6.34}_{-2.73})10^{46}$	$9.91^{+34.91}_{-7.19}$	$(1.26^{+1.04}_{-0.45})10^{51}$	$5.70\ 10^{5}$
100513A	$-2.29^{+0.29}_{-0.36}$	87	$(1.60^{+0.67}_{-0.33})10^{48}$	$5.27^{+8.47}_{-3.71}$	$(4.45^{+1.85}_{-0.93})10^{51}$	$3.65\ 10^{5}$
100621A	$-2.13^{+0.15}_{-0.15}$	324	$(1.12^{+0.55}_{-0.36})10^{48}$	$1295.1^{+1345.6}_{-709.4}$	$(1.09^{+0.53}_{-0.35})10^{52}$	$6.77\ 10^{5}$
100724A	$-1.99^{+0.30}_{-0.35}$	219	$(4.11^{+11.38}_{-2.12})10^{48}$	$53.89^{+367.46}_{-53.19}$	$(2.73^{+7.55}_{-1.41})10^{51}$	$4.45\ 10^{4}$
100814A	$-1.88^{+0.08}_{-0.08}$	205	$(1.04^{+0.32}_{-0.24})10^{48}$	$486.1^{+582.5}_{-306.1}$	$(2.94^{+0.90}_{-0.69})10^{52}$	$7.11\ 10^{5}$
100816A	$-1.87^{+0.25}_{-0.26}$	277	$(8.87^{+11.79}_{-4.73})10^{47}$	$34.98^{+3035.48}_{-32.78}$	$(6.41^{+8.52}_{-3.42})10^{50}$	$4.54\ 10^{5}$
100901A	$-2.19^{+0.08}_{-0.09}$	208	$(2.43^{+0.42}_{-0.34})10^{47}$	$114.7^{+58.3}_{-31.8}$	$(7.73^{+1.33}_{-1.08})10^{51}$	$3.54\ 10^{5}$
100906A	$-1.89^{+0.14}_{-0.14}$	183	$(1.89^{+0.95}_{-0.60})10^{49}$	$385.1^{+608.7}_{-275.1}$	$(3.35^{+1.69}_{-1.07})10^{52}$	$5.87\ 10^{4}$
101219A	$-2.68^{+2.68}_{-0.82}$	291	$(7.27^{+250055.44}_{-7.24})10^{48}$	$4.65^{+4682891.42}_{-4.64}$	$(9.19^{+315717.56}_{-9.13})10^{49}$	$8.88\ 10^{1}$
101219B	$-2.02^{+0.23}_{-0.31}$	323	$(1.25^{+1.48}_{-0.67})10^{45}$	$27.71^{+91.39}_{-18.28}$	$(2.34^{+2.77}_{-1.25})10^{50}$	$2.52\ 10^{6}$
110106B	$-2.11^{+0.23}_{-0.24}$	309	$(1.29^{+1.01}_{-0.51})10^{47}$	$181.3^{+267.9}_{-111.7}$	$(2.02^{+1.58}_{-0.80})10^{51}$	$4.16\ 10^{5}$
110205A	$-2.08^{+0.17}_{-0.20}$	155	$(1.02^{+0.48}_{-0.30})10^{48}$	$25.81^{+33.85}_{-13.77}$	$(4.09^{+1.93}_{-1.20})10^{51}$	$1.51\ 10^{5}$
110213A	$-2.37^{+0.11}_{-0.11}$	203	$(1.46^{+0.30}_{-0.23})10^{49}$	$404.6^{+142.1}_{-102.7}$	$(3.33^{+0.69}_{-0.52})10^{52}$	$4.63\ 10^{4}$
110422A	$-1.89^{+0.09}_{-0.09}$	181	$(3.32^{+6.90}_{-1.81})10^{49}$	$357.7^{+2318.2}_{-355.8}$	$(3.27^{+6.80}_{-1.78})10^{52}$	$1.42\ 10^{5}$
110503A	$-1.89^{+0.06}_{-0.06}$	191	$(3.79^{+8.25}_{-1.17})10^{49}$	$224.9^{+1009.0}_{-215.6}$	$(1.72^{+3.73}_{-0.53})10^{52}$	$2.22\ 10^{5}$
110715A	$-1.96^{+0.13}_{-0.13}$	1000	$(6.12^{+3.40}_{-1.91})10^{48}$	$446.5^{+248.1}_{-218.0}$	$(8.56^{+4.76}_{-2.68})10^{51}$	$1.14\ 10^{5}$

GRB	α_{fall}	$E_{c,fall}$ [keV]	L_{aft} [ergs s^{-1}]	F_{aft} [10^{-8} ergs s^{-1} cm^{-2}]	E_{iso} [ergs]	$T_{90,aft}$ [s]
110726A	$-2.40^{+0.43}_{-0.59}$	1000	$(1.02^{+1.89}_{-0.55})10^{47}$	$5.95^{+29.51}_{-4.72}$	$(2.29^{+4.24}_{-1.24})10^{50}$	$1.16\ 10^{5}$
110808A	$-2.12^{+0.50}_{-0.69}$	1000	$(2.20^{+12.43}_{-2.19})10^{46}$	$14.73^{+172.63}_{-14.73}$	$(8.38^{+47.24}_{-8.34})10^{50}$	$8.01\ 10^{5}$
110818A	$-1.82^{+0.16}_{-0.18}$	1000	$(6.85^{+8.06}_{-3.38})10^{49}$	$61.50^{+3574.49}_{-57.87}$	$(1.62^{+1.91}_{-0.80})10^{52}$	$1.04\ 10^{5}$
111008A	$-1.98^{+0.10}_{-0.12}$	1000	$(3.53^{+1.21}_{-0.83})10^{49}$	$158.5^{+94.5}_{-61.7}$	$(8.89^{+3.06}_{-2.10})10^{52}$	$7.75\ 10^{5}$
111107A	$-2.32^{+0.38}_{-0.45}$	1000	$(2.83^{+4.27}_{-1.32})10^{48}$	$5.24^{+656.77}_{-3.94}$	$(1.61^{+2.43}_{-0.75})10^{51}$	$7.65\ 10^{4}$
111228A	$-2.34^{+0.06}_{-0.21}$	1000	$(2.06^{+0.41}_{-0.61})10^{47}$	$154.1^{+148.3}_{-74.1}$	$(2.54^{+0.50}_{-0.76})10^{51}$	$2.13\ 10^{5}$
111229A	$-2.71^{+0.28}_{-0.31}$	1000	$(9.02^{+5.28}_{-2.65})10^{47}$	$36.51^{+3403.46}_{-18.82}$	$(3.37^{+1.97}_{-0.99})10^{51}$	$1.61\ 10^{4}$
120118B	$-1.64^{+0.18}_{-0.29}$	1000	$(4.55^{+6.48}_{-2.90})10^{48}$	$81.19^{+264.39}_{-66.29}$	$(1.61^{+2.29}_{-1.03})10^{52}$	$6.02\ 10^{4}$
120211A	$-1.02^{+0.42}_{-0.36}$	1000	$(2.22^{+23.60}_{-1.91})10^{49}$	$932.6^{+554836.4}_{-931.3}$	$(1.21^{+12.85}_{-1.04})10^{53}$	$7.23\ 10^{4}$
120326A	$-2.20^{+0.10}_{-0.12}$	1000	$(4.53^{+1.12}_{-0.83})10^{47}$	$147.8^{+451.9}_{-146.6}$	$(1.59^{+0.39}_{-0.29})10^{52}$	$2.69\ 10^{5}$
120327A	$-1.82^{+0.15}_{-0.27}$	1000	$(2.80^{+2.30}_{-1.46})10^{49}$	$157.4^{+199.6}_{-122.6}$	$(3.08^{+2.53}_{-1.61})10^{52}$	$4.78\ 10^{4}$
120404A	$-1.77^{+0.20}_{-0.22}$	1000	$(8.09^{+11.69}_{-4.37})10^{48}$	$55.27^{+176.01}_{-40.03}$	$(1.10^{+1.59}_{-0.59})10^{52}$	$3.77\ 10^{4}$
120422A	$-1.60^{+0.60}_{-0.60}$	1000	$(1.27^{+-1.27}_{-1.08})10^{45}$	$81.79^{+-81.79}_{-81.67}$	$(1.59^{+-1.59}_{-1.35})10^{50}$	$6.91\ 10^{5}$
120521C	$-2.06^{+0.58}_{-0.71}$	1000	$(3.25^{+21.30}_{-1.19})10^{48}$	$9.49^{+1275.06}_{-4.36}$	$(7.62^{+50.00}_{-2.80})10^{51}$	$5.14\ 10^{4}$
120712A	$-2.04^{+0.16}_{-0.22}$	1000	$(2.01^{+1.29}_{-0.68})10^{49}$	$24.98^{+36.77}_{-21.22}$	$(1.11^{+0.71}_{-0.38})10^{52}$	$1.67\ 10^{5}$
120729A	$-1.94^{+0.22}_{-0.18}$	1000	$(1.08^{+1.38}_{-0.47})10^{48}$	$83.40^{+180.31}_{-41.98}$	$(1.50^{+1.91}_{-0.65})10^{51}$	$9.54\ 10^{3}$
120802A	$-1.98^{+0.30}_{-0.37}$	1000	$(2.81^{+5.28}_{-1.36})10^{48}$	$18.91^{+3045.69}_{-18.81}$	$(6.76^{+12.70}_{-3.28})10^{51}$	$1.70\ 10^{4}$
120804A	$-2.45^{+0.39}_{-0.33}$	1000	$(4.27^{+4.81}_{-2.17})10^{48}$	$23.85^{+3270.74}_{-35.52}$	$(1.57^{+1.76}_{-0.80})10^{51}$	$1.64\ 10^{5}$
120811C	$-2.12^{+0.22}_{-0.29}$	1000	$(3.55^{+3.23}_{-1.42})10^{48}$	$45.36^{+82.80}_{-29.82}$	$(9.82^{+8.94}_{-3.92})10^{51}$	$1.29\ 10^{5}$
120907A	$-1.76^{+0.14}_{-0.14}$	1000	$(2.30^{+3.12}_{-1.24})10^{48}$	$193.8^{+1008.5}_{-173.3}$	$(4.99^{+6.77}_{-2.69})10^{51}$	$2.13\ 10^{5}$
121027A	$-2.49^{+0.18}_{-0.27}$	1000	$(1.38^{+0.50}_{-0.35})10^{47}$	$108.0^{+83.1}_{-42.5}$	$(1.45^{+0.53}_{-0.36})10^{52}$	$2.28\ 10^{6}$
121128A	$-2.13^{+0.16}_{-0.16}$	1000	$(1.93^{+1.04}_{-0.50})10^{49}$	$90.26^{+82.38}_{-34.70}$	$(1.36^{+0.73}_{-0.36})10^{52}$	$3.25\ 10^{4}$

GRB	α_{fall}	$E_{c,fall}$ [keV]	L_{aft} [ergs s^{-1}]	F_{aft} [10^{-8} ergs s^{-1} cm^{-2}]	E_{iso} [ergs]	$T_{90,aft}$ [s]
121201A	$-1.70^{+0.37}_{-0.36}$	1000	$(9.19^{+45.46}_{-6.14})10^{48}$	$25.88^{+408.97}_{-24.33}$	$(6.58^{+32.54}_{-4.39})10^{51}$	$3.48\ 10^{4}$
121209A	$-1.41^{+0.16}_{-0.15}$	1000	$(1.26^{+1.85}_{-0.70})10^{50}$	$2495.8^{+5932.1}_{-1709.2}$	$(2.67^{+3.91}_{-1.49})10^{53}$	$5.45\ 10^{4}$
130427B	$-1.86^{+0.24}_{-0.28}$	1000	$(3.52^{+6.38}_{-1.96})10^{49}$	$44.83^{+289.44}_{-42.73}$	$(8.76^{+15.89}_{-4.88})10^{51}$	$9.59\ 10^{4}$
130610A	$-1.95^{+0.14}_{-0.45}$	1000	$(1.48^{+1.92}_{-1.47})10^{48}$	$20.19^{+59.33}_{-20.18}$	$(2.48^{+3.22}_{-2.46})10^{51}$	$1.63\ 10^{5}$
130831A	$-1.72^{+0.15}_{-0.18}$	1000	$(3.31^{+4.08}_{-1.83})10^{47}$	$384.4^{+2138.9}_{-264.6}$	$(2.28^{+2.81}_{-1.26})10^{51}$	$1.18\ 10^{6}$
130925A	$-3.12^{+0.52}_{-0.74}$	371	$(5.32^{+9.76}_{-3.62})10^{46}$	$848.1^{+2771.8}_{-668.1}$	$(3.55^{+6.51}_{-2.41})10^{51}$	$4.58\ 10^{6}$
131030A	$-2.08^{+0.06}_{-0.10}$	1000	$(7.95^{+1.63}_{-1.64})10^{48}$	$449.8^{+153.3}_{-154.5}$	$(2.30^{+0.47}_{-0.48})10^{52}$	$6.11\ 10^{5}$
131227A	$-2.33^{+0.25}_{-0.24}$	1000	$(2.83^{+1.34}_{-0.44})10^{50}$	$27.42^{+583.39}_{-22.73}$	$(2.67^{+1.26}_{-0.41})10^{52}$	$2.52\ 10^{4}$
140304A	$-2.32^{+0.23}_{-0.33}$	1000	$(1.42^{+0.55}_{-0.20})10^{50}$	$38.85^{+39.53}_{-22.24}$	$(3.67^{+1.41}_{-0.51})10^{52}$	$4.66\ 10^{3}$
140430A	$-2.26^{+0.25}_{-0.28}$	1000	$(3.83^{+3.44}_{-1.47})10^{47}$	$54.39^{+153.63}_{-37.80}$	$(4.81^{+4.32}_{-1.85})10^{51}$	$1.65\ 10^{5}$
140506A	$-2.16^{+0.12}_{-0.13}$	1000	$(5.11^{+2.47}_{-1.54})10^{48}$	$714.5^{+5839.0}_{-636.1}$	$(1.74^{+0.84}_{-0.52})10^{52}$	$2.29\ 10^{6}$
140509A	$-2.03^{+0.26}_{-0.22}$	1000	$(1.64^{+2.21}_{-0.64})10^{48}$	$13.32^{+27.04}_{-8.08}$	$(2.21^{+2.97}_{-0.86})10^{51}$	$3.50\ 10^{4}$
140629A	$-1.94^{+0.11}_{-0.13}$	1000	$(2.22^{+1.16}_{-0.72})10^{49}$	$72.81^{+2239.39}_{-65.17}$	$(1.04^{+0.54}_{-0.34})10^{52}$	$4.07\ 10^{4}$
140703A	$-2.43^{+0.08}_{-0.29}$	1000	$(1.66^{+0.39}_{-0.23})10^{49}$	$130.2^{+64.3}_{-70.7}$	$(5.40^{+1.28}_{-0.76})10^{52}$	$7.48\ 10^{4}$
140710A	$-2.18^{+0.80}_{-0.81}$	1000	$(3.72^{+89.71}_{-2.87})10^{46}$	$27.52^{+1832.68}_{-23.56}$	$(2.47^{+59.48}_{-1.91})10^{50}$	$2.29\ 10^{5}$
141221A	$-1.69^{+0.27}_{-0.31}$	1000	$(1.15^{+3.83}_{-0.89})10^{49}$	$155.4^{+1335.7}_{-148.8}$	$(8.76^{+29.08}_{-6.74})10^{51}$	$1.00\ 10^{5}$
150301B	$-2.10^{+0.47}_{-0.60}$	1000	$(1.04^{+3.98}_{-0.63})10^{48}$	$13.29^{+10533.73}_{-13.24}$	$(9.53^{+36.59}_{-5.79})10^{50}$	$5.51\ 10^{3}$
150403A	$-1.78^{+0.02}_{-0.02}$	1000	$(6.08^{+0.76}_{-0.53})10^{50}$	$4994.9^{+827.1}_{-1485.1}$	$(5.53^{+0.69}_{-0.48})10^{53}$	$3.41\ 10^{5}$
151027A	$-2.27^{+0.05}_{-0.06}$	1000	$(2.16^{+0.25}_{-0.23})10^{48}$	$487.8^{+98.1}_{-135.8}$	$(1.02^{+0.12}_{-0.11})10^{52}$	$1.05\ 10^{5}$
151027B	$-1.80^{+0.10}_{-0.35}$	1000	$(7.83^{+6.85}_{-7.79})10^{48}$	$110.9^{+175.3}_{-110.7}$	$(3.94^{+3.44}_{-3.92})10^{52}$	$3.99\ 10^{5}$
151111A	$-1.78^{+0.48}_{-0.60}$	1000	$(9.10^{+82.28}_{-9.07})10^{47}$	$18.87^{+494.81}_{-18.84}$	$(5.21^{+47.12}_{-5.19})10^{51}$	$2.26\ 10^{5}$
151215A	$-2.52^{+0.41}_{-0.49}$	1000	$(1.25^{+4.39}_{-0.31})10^{49}$	$35.81^{+417.39}_{-35.44}$	$(1.11^{+3.91}_{-0.28})10^{52}$	$1.93\ 10^{5}$

GRB	α_{fall}	$E_{c,fall}$ [keV]	L_{aft} [ergs s^{-1}]	F_{aft} [10^{-8} ergs s^{-1} cm^{-2}]	E_{iso} [ergs]	$T_{90,aft}$ [s]
160104A	$-2.30^{+0.81}_{-0.87}$	1000	$(2.48^{+28.80}_{-2.46})10^{47}$	$19.21^{+953.44}_{-19.21}$	$(5.42^{+62.93}_{-5.38})10^{51}$	$3.15\ 10^{5}$
160117B	$-1.94^{+0.25}_{-0.25}$	1000	$(1.63^{+2.58}_{-0.84})10^{47}$	$30.47^{+87.51}_{-22.27}$	$(6.55^{+10.36}_{-3.39})10^{50}$	$2.22\ 10^{5}$
160121A	$-2.40^{+0.41}_{-0.41}$	1000	$(4.28^{+6.64}_{-1.59})10^{47}$	$19.91^{+199.51}_{-9.39}$	$(3.04^{+4.71}_{-1.13})10^{51}$	$4.42\ 10^{4}$
160314A	$-1.74^{+0.75}_{-0.89}$	1000	$(3.10^{+123.19}_{-3.10})10^{46}$	$53.27^{+29434.87}_{-53.27}$	$(7.55^{+299.54}_{-7.54})10^{50}$	$8.84\ 10^{5}$
160327A	$-1.86^{+0.25}_{-0.21}$	1000	$(9.54^{+15.97}_{-4.30})10^{48}$	$24.42^{+62.30}_{-21.60}$	$(1.24^{+2.08}_{-0.56})10^{52}$	$6.81\ 10^{4}$
160410A	$-1.35^{+0.22}_{-0.22}$	1000	$(3.00^{+9.38}_{-2.21})10^{50}$	$233.2^{+1618072.5}_{-171.6}$	$(1.73^{+5.43}_{-1.28})10^{52}$	$1.23\ 10^{3}$

Table 5: The parameters of the fitted afterglow spectral components at $T = T_{fall}$ are: the cut-off energy of the Band functions, $E_{c,fall}$; the low-energy spectral index, α_{fall}; and the flux, $F_{aft,fall}$ over the observed bolometric energy band 1 keV - 1 MeV. The peak luminosity of the pulse, L_{aft}, is the isotropic peak luminosity and is also estimated over the bolometric band. E_{iso} ergs is the bolometric isotropic energy of the afterglow, and $T_{90,aft}$ is the 90% duration of the afterglow. A single value indicates a parameter which was fixed during final fitting. The 90% range is indicated for parameters which were allowed to float in the final fitting. The 90% range of luminosity includes the uncertainty in the flux, F_{aft}, and uncertainty in the k-correction which depends on redshift, z, and the spectral parameters, $E_{c,fall}$ and α_{fall}.

	Ultralong			Long			Short w. EE		
	IQR			IQR			IQR		
	25%	50%	75%	25%	50%	75%	25%	50%	75%
N_{pulses}	16	17	38	2	3	5	-	2	6
T_{peak}	47.8	2112.65	3480.45	8.0	30.85	111.65	27.08	116.45	217.7
T_{rise}	4.73	23.1	86.9	1.6	3.4	8.18	12.15	30.3	46.7
T_f	28.5	103.2	229.03	5.2	12.1	29.25	17.70	37.25	47.48
E_f	258	371	371	115	152	203	10.24	17	348
α	-3.10	-2.73	-2.19	-2.95	-2.50	-2.1	-2.53	-2.33	-2.13
F_f	5.61	34.93	126.8	5.12	20.14	108.18	0.17	1.75	22.20
L_f	0.097	0.27	4.5	1.1	6.4	27.5	0.00038	0.0035	0.071

	Short			Unconstrained		
	IQR			IQR		
	25%	50%	75%	25%	50%	75%
N_{pulses}	-	1	2	1	3	5
T_{peak}	0.325	0.6	1.6	13.63	47.75	95.83
T_{rise}	0.1	0.3	1.45	1.23	2.0	3.4
T_f	0.40	1.05	2.32	4.40	10.65	27.75
E_f	231	291	323	101	277	444
α	-2.90	-2.65	-1.87	-2.99	-2.51	-1.98
F_f	58.91	119.95	499.80	5.27	26.13	59.68
L_f	1.2	10.2	22.2	0.01	0.04	4.3

Table 6: *The summary table of the pulse fit parameters, for the different GRB categories. The temporal parameters, T_{peak} , T_{rise} , and T_f, are given in seconds; the cutoff energy of the Band function at $T = T_{peak}$, E_f, is given in keV; the flux at that time, observed over the 0.3 - 350 keV passband, F_f, is given in* units of 10^{-8} *ergs s^1 cm^2; and the bolometrically corrected peak luminosity, L f is given in* 10^{51} *ergs s^{-1}. The interquartile range (IQR) is between the 25%, and 75% percentiles, whilst the 50% percentile corresponds to the median of the distribution. See Fig 2.18 for a visual representation of the data.*

	Ultralong			Long			Short w. EE		
	IQR			IQR			IQR		
	25%	50%	75%	25%	50%	75%	25%	50%	75%
α_{fall}	-2.805	-2.49	-2.12	-2.17	-2.02	-1.87	-1.83	-1.64	-1.45
$E_{c,fall}$	139.5	371	685.5	139.5	208.0	1000	360.3	372.5	384.75
z	0.643	0.938	1.356	1.331	2.1	3.06	0.302	0.348	0.393
F_{aft}	4.78	8.48	25.7	0.20	0.58	1.55	0.22	0.39	0.55
L_{aft}	0.096	0.138	630	0.51	3.14	14.5	0.0002	0.00027	0.00032
E_{iso}	0.90	1.45	6.38	0.24	0.77	1.92	0.005	0.007	0.009
T_{fall}	9500	18900	173000	1150	4240	14400	227300	453000	677800
α_c	-1.49	-1.48	-1.04	-1.5	-1.25	-1.03	-7.7	-5.41	-3.11
T_{90}	11400	22800	34300	736	2040	6180	1241	1640	2050
T_{break}	3140	3410	3410	107	390	860			
α_{break}	-1.36	-1.36	-1.36	-1.99	-1.58	-1.39			

	Short			Unconstrained		
	IQR			IQR		
	25%	50%	75%	25%	50%	75%
α_{fall}	-2.35	-1.99	-1.98	-1.98	-1.87	-1.75
$E_{c,fall}$	227	291	366.5	186.5	263.0	360.5
z	0.632	1.130	1.294	0.681	0.903	1.735
F_{aft}	0.057	0.24	0.39	0.33	0.61	1.0
L_{aft}	1.41	4.11	4.50	0.146	0.887	11.61
E_{iso}	0.015	0.026	0.134	0.044	0.143	0.485
T_{fall}	101.7	373	21600	95.6	903	9700
α_c	-3.21	-1.47	-1.20	-1.68	-1.13	-0.99
T_{90}	39	324	1040	1280	3000	3990
T_{break}				176	336	495
α_{break}				-2.02	-1.84	-1.67

Table 7: *The summary table of the afterglow fit parameters, for the different GRB categories. The temporal parameters, T_{fall}, T_{break}, and T_{90}, are given in units of 10^2 seconds; the cutoff energy of the Band function at $T = T_{fall}$, $E_{c,fall}$, is given in keV; the flux at that time, observed over the 0.3 - 350 keV passband, F_{aft}, is given in units of 10^{-7} ergs s^1 cm^2; and the bolometrically corrected peak luminosity, L_{aft} is given in 10^{48} ergs s^{-1}. The isotropic energy of the afterglow, E_{iso}, is given in 10^{52} ergs s^{-1}. The interquartile range (IQR) is between the 25%, and 75% percentiles, whilst the 50% percentile corresponds to the median of the distribution. See Fig 2.24 for a visual representation of the data.*

III GRB Pulse Luminosity Function

III.1 K - Correction

The K - correction is a multiplicative factor that acts to correct for the redshifting of photon energies in the source-frame to those in the observer-frame, when observing over a finite passband width, $E_{pass,1} - E_{pass,2}$. This is typically applied when converting the observer-frame flux, $F_{E_{pass,1}-E_{pass,2}}$, into a bolometric luminosity, defined over the energy range $E_{bol,1} - E_{bol,2}$ (for gamma-ray bursts the bolometric passband is commonly defined as 1 keV to 10 MeV):

$$L_{E_{bol,1}-E_{bol,2}} = \frac{F_{E_{pass,1}-E_{pass,2}} K_{corr}}{4\pi(z+1)D_L^2}, \tag{1}$$

where D_L is the cosmological luminosity distance. The K - correction, K_{corr} is given by:

$$K_{corr} = \frac{\int_{E_{bol,1}/(z+1)}^{E_{bol,2}/(z+1)} EN(E)dE}{\int_{E_{pass,1}}^{E_{pass,2}} EN(E)dE}, \tag{2}$$

for a source with an arbitrary spectral shape defined as $N(E)$ (for GRBs, this is often the Band function, although power-laws, power-laws with exponential cutoffs, and broken power-laws are also popular).

III.2 Broadband Spectral Information

GRB	Indicator	Observatories	Reference
-	Black circles	Fermi, Swift	Heussaff, Atteia & Zolnierowski, 2013
-	Magenta diamonds	Suzaku, Swift	Krimm et al. 2009
-	Cyan squares	Fermi, Swift	Virgili et al. 2012
-	Green stars	Konus-Wind, Suzaku, Swift	Sakamoto et al. 2011c
-	Yellow pentagon	RHESSI, Swift	Bellm et al. 2008
110503A	Black cirle	Konus-Wind	Golenetskii et al., 2011a
110422A	Green square	Konus-Wind	Golenetskii et al., 2011b
110205A	Cyan square	Suzaku, Swift	Sakamoto et al., 2011a
100621A	Black star	Konus-Wind	Golenetskii et al., 2010
091020	Yellow pentagon	Fermi	Chaplin, 2009
091020	Red circle	Konus-Wind	Golenetskii et al., 2009b
091018	Blue circle	Konus-Wind	Golenetskii et al., 2009c
090812	Blue square	Konus-Wind, Swift	Pal'Shin et al., 2009b
090812	Red circle	Suzaku, Swift	Noda et al., 2009
090715B	Cyan square	Konus-Wind	Golenetskii et al., 2009a
090618	Green circle	Fermi	McBreen, 2009b
090618	green pentagon	Suzaku	Kono et al., 2009
090618	Green star	Konus-Wind	Golenetskii et al., 2009d
090516	Black square	Fermi	McBreen, 2009a
090423	Black pentagon	Fermi	von Kienlin, 2009
090418A	Magenta circle	Konus-Wind,Swift	Pal'Shin et al., 2009a
090102	Black diamond	Konus-Wind	Golenetskii et al., 2009e
081222	Green diamond	Fermi	Bissaldi & McBreen, 2008
081222	Magenta pentagon	Konus-Wind	Golenetskii et al., 2008f
081203A	Magenta star	Konus-Wind	Golenetskii et al., 2008c
080913	Red star	Konus-Wind, Swift	Pal'Shin et al., 2008
080810	Red diamond	Fermi	Meegan et al., 2008
080810	Magenta diamond	Konus-Wind, Swift	Sakamoto et al., 2008b
080804	Cyan pentagon	Fermi, Swift	Stamatikos, 2009
080721	Cyan star	Fermi	Golenetskii et al., 2008e
080607	Yellow diamond	Konus-Wind	Golenetskii et al., 2008d
080603B	Blue pentagon	Konus-Wind	Golenetskii et al., 2008b
080319B	Blue star	Konus-Wind	Golenetskii et al., 2008a
071020	Blue diamond	Konus-Wind	Golenetskii et al., 2007b
070521	Yellow square	Konus-Wind	Golenetskii et al., 2007a
061021	Yellow circle	Konus-Wind	Golenetskii et al., 2006
050401	Yellow star	Konus-Wind	Golenetskii et al., 2005

Table 1: *Broadband spectra references for observations collated in Figure 3.2, including the plot indicators, which observatories contibuted towards the broadband spectral data, and the references.*

III.3 BPL GRB pulse $L - z$ Distributions

The following figures are equivalent to the power-law with exponential cutoff distributions displayed in Figures 3.8, 3.9, 3.11, 3.12, 3.13, and 3.14 respectively, for a luminosity probability density function modelled by a broken power-law.

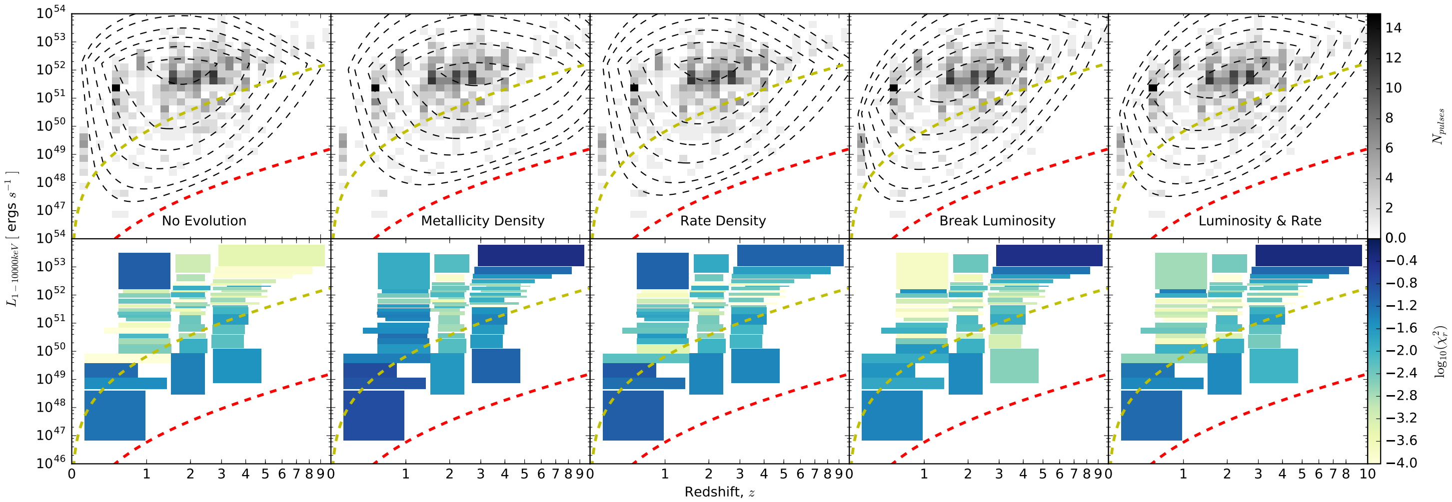

Figure 1: *The derived GRB pulse luminosity distribution for a Type I BPL LF (dashed contours) overlaying the observed pulse distribution, binned to an arbitrary 1/4 dex in luminosity and 1/32 dex in redshift (top row). The five models shown corresponds to: a non-evolving, I-1, model (column 1); a metallicity density I-4 model with metallicity density threshold, $Z/Z_{\odot}$ (column 2); a rate density evolution I-2 model, incorporating an additional $(z+1)^{\gamma}$ evolutionary factor (column 3); a break luminosity I-3 model evolving as $L_b = L_0(z+1)^{\delta}$ (column 4); and a bivariate break, and rate evolution I-5 model (column 5). The corresponding logarithm of the reduced χ^2 of the fits are shown for the data bins (bottom row). The upper (yellow) and lower (red) dashed lines denote the detection thresholds of the BAT and XRT respectively.*

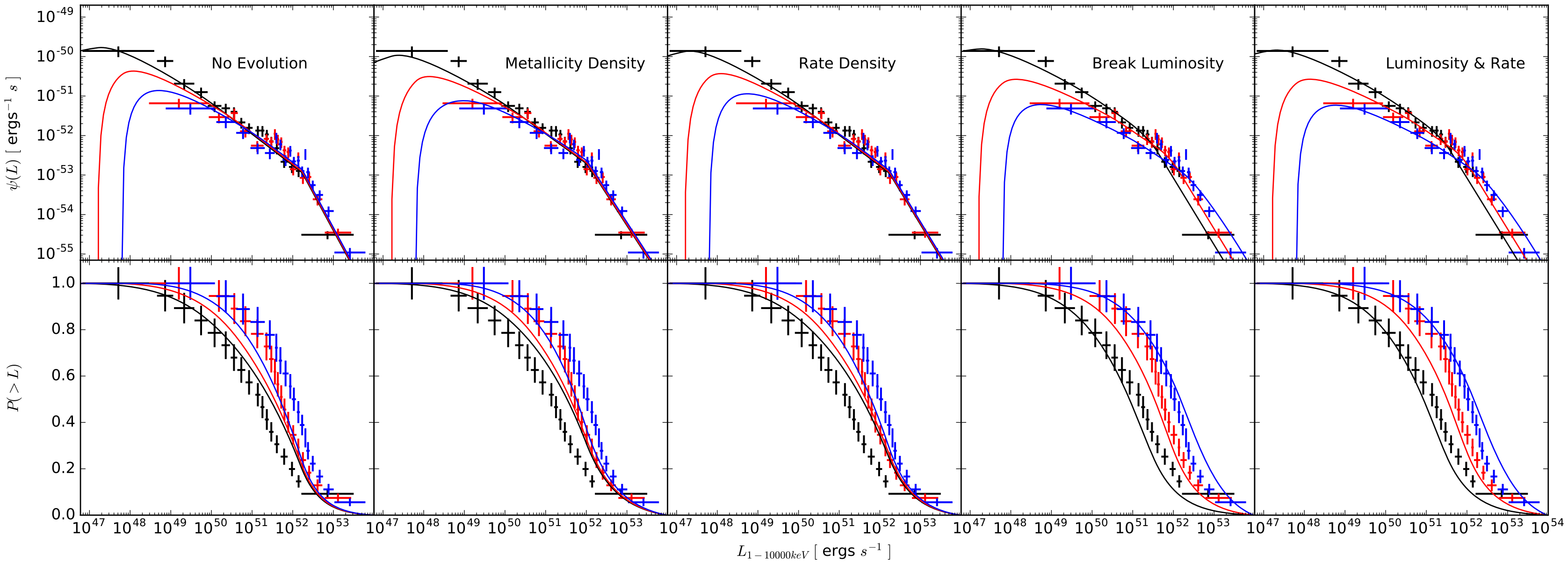

Figure 2: *The observed, and derived GRB pulse probability densities (top row) for the three redshift bins, and the equivalent cumulative probability densities (bottom row) for Type I GRB pulse formation models with a BPL LPDF. The five models shown corresponds to: a non-evolving, I-1, model (column 1); a metallicity density I-4 model with metallicity density threshold,* $Z/Z_\odot$ *(column 2); a rate density evolution I-2 model, incorporating an additional* $(z+1)^\gamma$ *evolutionary factor (column 3); a break luminosity I-3 model evolving as* $L_b = L_0(z+1)^\delta$ *(column 4); and a bivariate break, and rate evolution I-5 model (column 5). Black data, and lines correspond to the* $0.125 < z \leq 1.505$ *whilst red, and blue data correspond to the* $1.51 < z \leq 2.6$ *and* $2.612 < z \leq 9.4$ *bins respectively. The turn-off at low luminosities is due to the convolution to the Swift detection profile.*

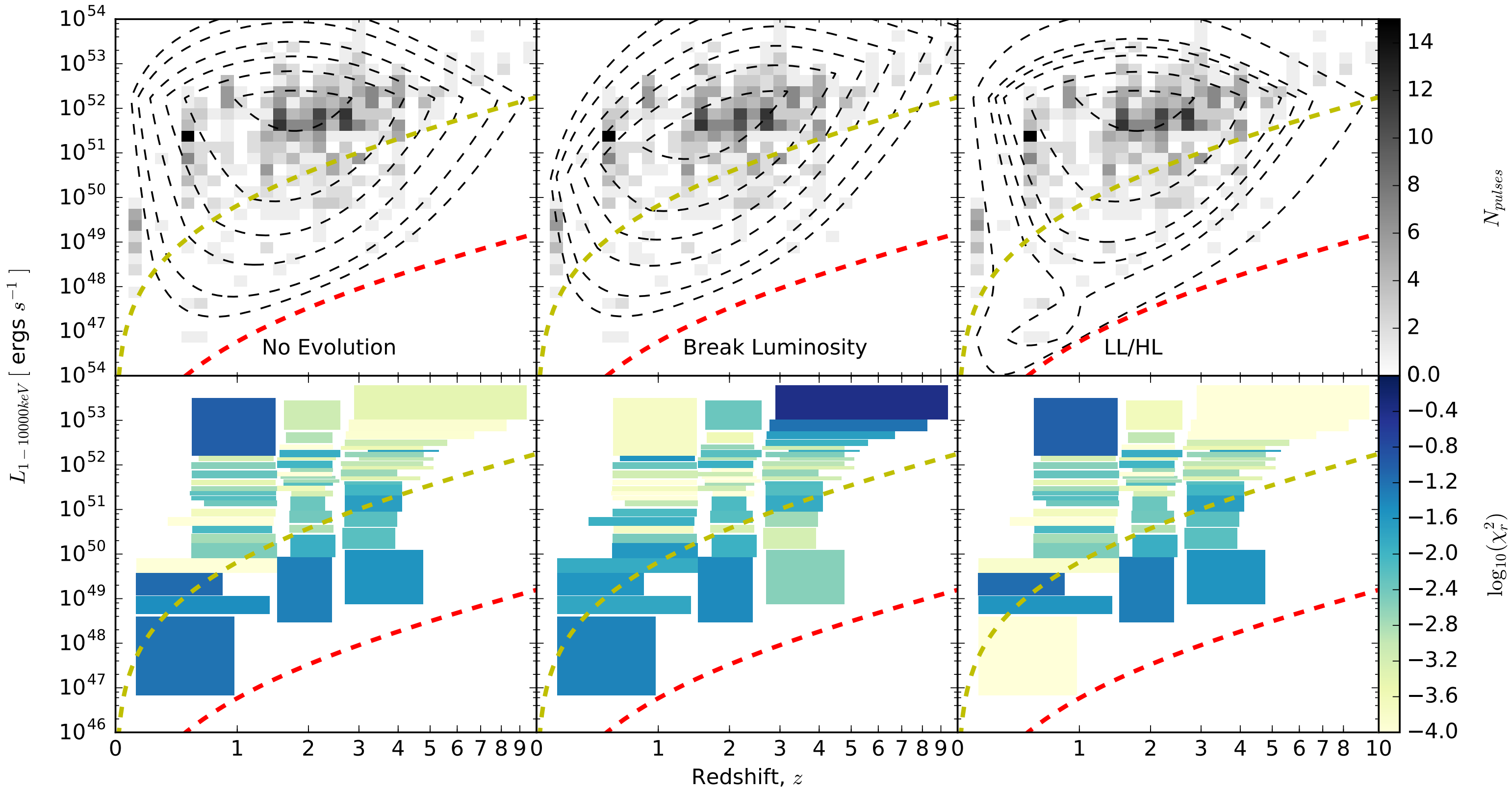

Figure 3: *The derived GRB pulse luminosity distribution for a Type II BPL LF (dashed contours) overlaying the observed pulse distribution, binned to an arbitrary 1/4 dex in luminosity and 1/32 dex in redshift (top row). The five models shown corresponds to: the non-evolving, I-1, model (column 1); the break luminosity I-3 model evolving as* $L_b = L_0(z+1)^\delta$ *(column 2); and the bimodal low-luminosity/high-luminosity GRB population Type II model (column 3). The corresponding logarithm of the reduced* χ^2 *of the fits are shown for the data bins (bottom row). The upper (yellow) and lower (red) dashed lines denote the detection thresholds of the BAT and XRT respectively.*

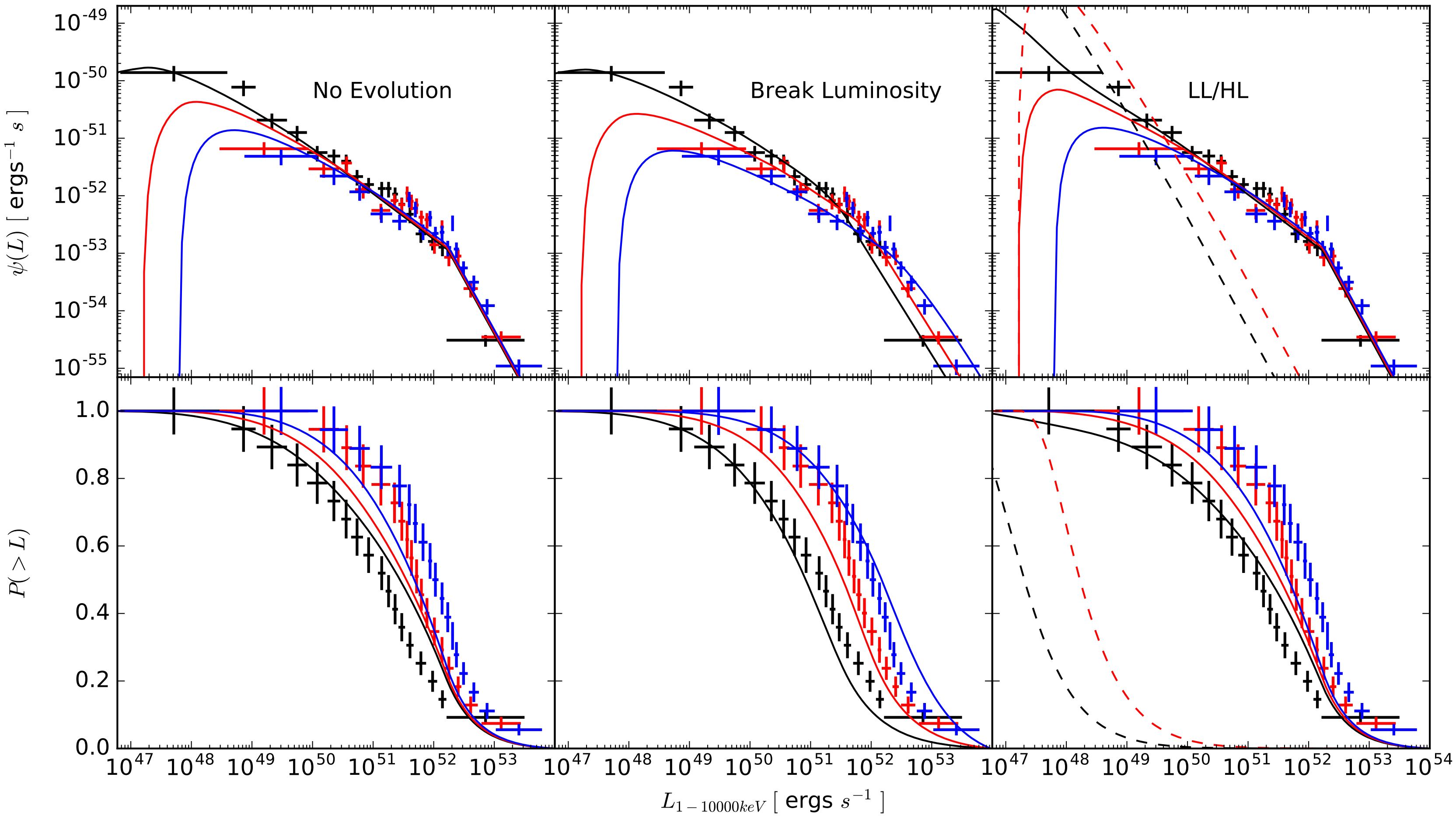

Figure 4: *The observed, and derived GRB pulse probability densities (top row) for the three redshift bins, and the equivalent cumulative probability densities (bottom row) for a Type II GRB pulse formation models with a BPL LPDF. The three models shown corresponds to: the non-evolving, I-1, model (column 1); the break luminosity I-3 model evolving as* $L_b = L_0(z+1)^\delta$ *(column 2); and the bimodal low-luminosity/high-luminosity GRB population Type II model (column 3). Black data, and solid lines correspond to the high-luminosity component of the LPDF* $0.125 < z \leq 1.505$ *redshift bin; whilst red, and blue data correspond to the* $1.51 < z \leq 2.6$ *and* $2.612 < z \leq 9.4$ *bins respectively. The dashed line, only displayed in the lowest redshift bin, is the low-luminosity component of the Type II distribution. The turn-off at low luminosities is due to the convolution to the Swift detection profile.*

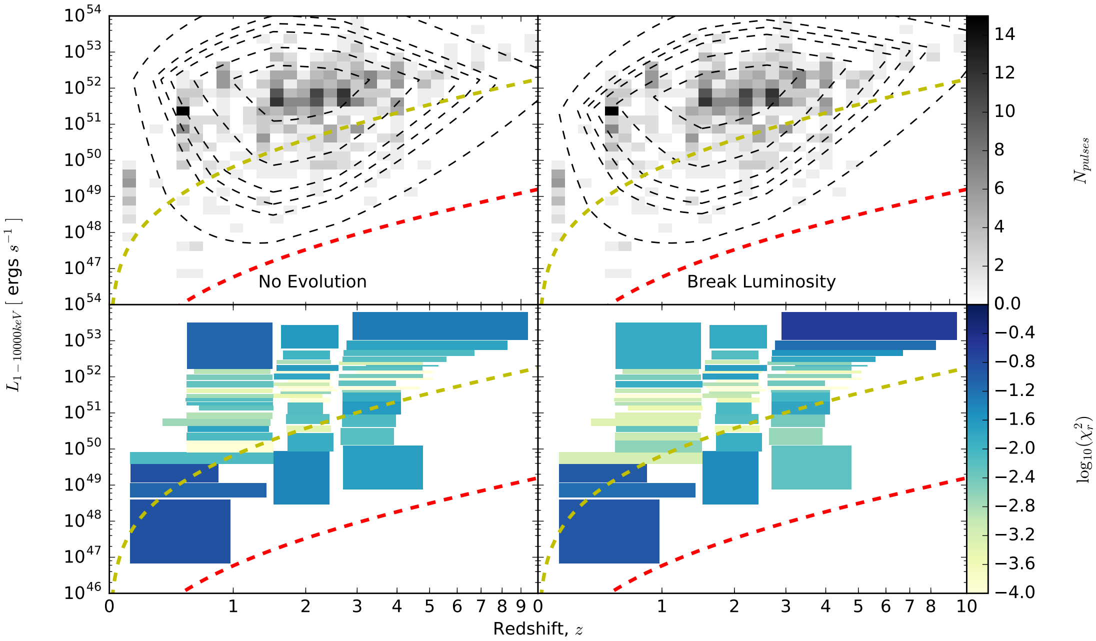

Figure 5: *The derived GRB pulse luminosity distribution for a Type III BPL LF (dashed contours) overlaying the observed pulse distribution, binned to an arbitrary 1/4 dex in luminosity and 1/32 dex in redshift (top row). The two models shown corresponds to: a non-evolving, III-1, model (column 1); and a break luminosity III-2 model evolving as* $L_b = L_0(z+1)^\delta$ *(column 2). The corresponding logarithm of the reduced* χ^2 *of the fits are shown for the data bins (bottom row). The upper (yellow) and lower (red) dashed lines denote the detection thresholds of the BAT and XRT respectively.*

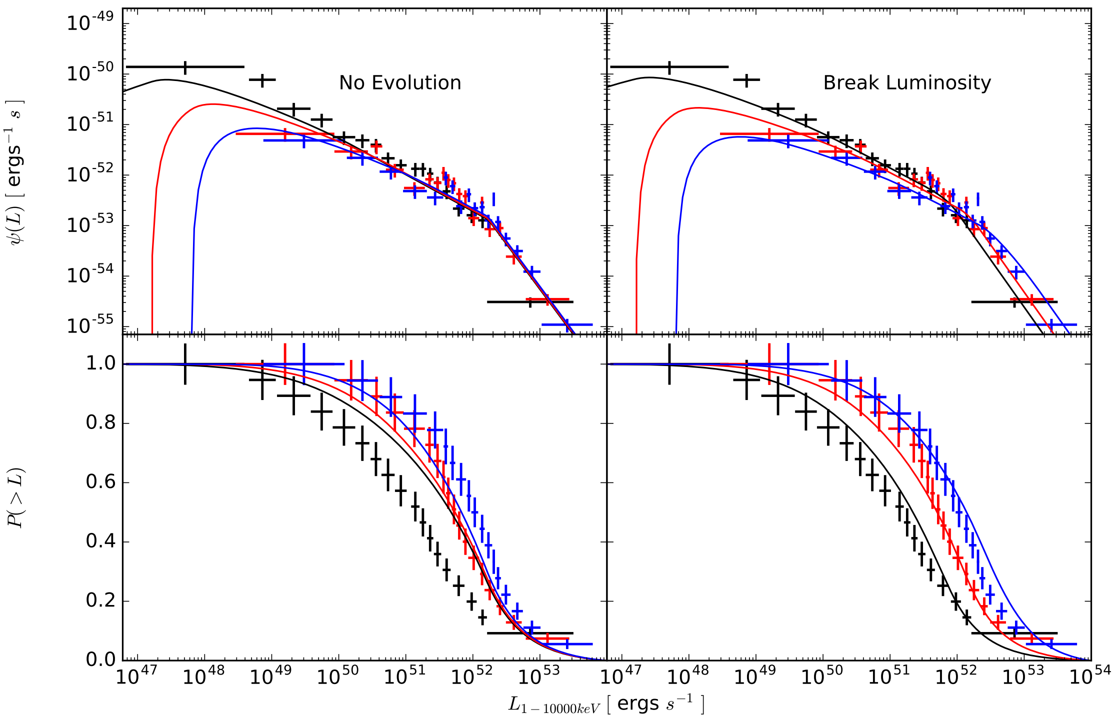

Figure 6: *The observed, and derived GRB pulse probability densities (top row) for the three redshift bins, and the equivalent cumulative probability densities (bottom row) for Type III GRB pulse formation models with a BPL LPDF. The two models shown corresponds to: a non-evolving, III-1, model (column 1); and a break luminosity III-2 model evolving as* $L_b = L_0(z+1)^\delta$ *(column 2). Black data, and lines correspond to the* $0.125 < z \leq 1.505$ *whilst red, and blue data correspond to the* $1.51 < z \leq 2.6$ *and* $2.612 < z \leq 9.4$ *bins respectively. The turn-off at low luminosities is due to the convolution to the Swift detection profile.*

References

Abbott B. P. et al., 2016, Physical Review Letters, 116, 061102

Achterberg A., Gallant Y. A., Kirk J. G., Guthmann A. W., 2001, MNRAS, 328, 393

Ackermann M. et al., 2013, ApJS, 209, 11

Akaike H., 1974, IEEE Transactions on Automatic Control, 19, 716

Akerlof C. et al., 1999, Nat, 398, 400

Amati L., 2006, MNRAS, 372, 233

Amati L. et al., 2002, A&A, 390, 81

Anders E., Grevesse N., 1989, GCA, 53, 197

Anderson K. A., Kane S. R., Primbsch J. H., Weitzmann R. H., Evans W. D., Klebesadel R. W., Aiello W. P., 1978, IEEE Transactions on Geoscience Electronics, 16, 157

Anderson T. W., Darling D. A., 1952, Ann. Math. Statist., 23, 193

Ando S., 2004, JCAP, 6, 007

Aptekar R. L. et al., 1995, SSR, 71, 265

Arnaud K. A., 1996, in Astronomical Society of the Pacific Conference Series, Vol. 101, Astronomical Data Analysis Software and Systems V, Jacoby G. H., Barnes J., eds., p. 17

Asplund M., Grevesse N., Sauval A. J., 2005, in Astronomical Society of the Pacific Conference Series, Vol. 336, Cosmic Abundances as Records of Stellar Evolution and Nucleosynthesis, Barnes III T. G., Bash F. N., eds., p. 25

Atteia J.-L., 2003, A&A, 407, L1

Atteia J.-L. et al., 1995, ApSS, 231, 471

Atwood W. B. et al., 2009, ApJ, 697, 1071

Bagoly Z. et al., 2006a, in KITP Conference: Supernova and Gamma-Ray Burst Remnants

Bagoly Z. et al., 2006b, A&A, 453, 797

Balazs L. G., Meszaros A., Horvath I., 1998, A&A, 339, 1

Balázs L. G., Mészáros A., Horváth I., Vavrek R., 1999, A&AS, 138, 417

Baldry I. K. et al., 2005, MNRAS, 358, 441

Band D. et al., 1993, ApJ, 413, 281

Barat C., Chambon G., Hurley K., Niel M., Vedrenne G., Estulin I. V., Kuznetsov A. V., Zenchenko V. M., 1981a, ApSS, 75, 83

Barat C., Chambon G., Hurley K., Niel M., Vedrenne G., Estulin I. V., Kuznetsov A. V., Zenchenko V. M., 1981b, Space Science Instrumentation, 5, 229

Barat C., Hurley K., Niel M., Vedrenne G., Mitrofanov I. G., Estulin I. V., Zenchenko V. M., Dolidze V. S., 1984, ApJL, 286, L11

Barraud C. et al., 2003, A&A, 400, 1021

Barret D. et al., 2001, in SF2A-2001: Semaine de l'Astrophysique Francaise, Combes F., Barret D., Thévenin F., eds., p. 411

Barthelmy S. D. et al., 2005a, SSR, 120, 143

Barthelmy S. D. et al., 2005b, ApJL, 635, L133

Barthelmy S. D. et al., 2005c, Nat, 438, 994

Basak R., Rao A. R., 2013, MNRAS, 436, 3082

Behar E., Dado S., Dar A., Laor A., 2011, ApJ, 734, 26

Belczynski K., Perna R., Bulik T., Kalogera V., Ivanova N., Lamb D. Q., 2006, ApJ, 648, 1110

Bellm E. C., Bandstra M. E., Boggs S. E., Hajdas W., Hurley K., Smith D. M., Wigger C., 2008, in American Institute of Physics Conference Series, Vol. 1000, American Institute of Physics Conference Series, Galassi M., Palmer D., Fenimore E., eds., pp. 154–157

Beloborodov A. M., 2000, ApJL, 539, L25

Beniamini P., Granot J., 2016, MNRAS, 459, 3635

Berger E., 2009, ApJ, 690, 231

Berger E., 2010, ApJ, 722, 1946

Berger E., 2014, ARAA, 52, 43

Berger E. et al., 2005, Nat, 438, 988

Bernardini M. G. et al., 2015, MNRAS, 446, 1129

Bhat P. N., Fishman G. J., Meegan C. A., Wilson R. B., Kouveliotou C., Paciesas W. S., Pendleton G. N., Schaefer B. E., 1994, ApJ, 426, 604

Bhattacharya D., 2001, Bulletin of the Astronomical Society of India, 29, 107

Bissaldi E., McBreen S., 2008, GRB Coordinates Network, 8715

Blanchard P. K., Berger E., Fong W.-f., 2016, ApJ, 817, 144

Blandford R., Eichler D., 1987, PhysRep, 154, 1

Blandford R. D., McKee C. F., 1976, Physics of Fluids, 19, 1130

Blinnikov S. I., Novikov I. D., Perevodchikova T. V., Polnarev A. G., 1984, Pisma v Astronomicheskii Zhurnal, 10, 422

Bloom J. S., Djorgovski S. G., Kulkarni S. R., Frail D. A., 1998, ApJL, 507, L25

Bloom J. S., Frail D. A., Kulkarni S. R., 2003, ApJ, 594, 674

Bloom J. S., Kulkarni S. R., Djorgovski S. G., 2002, AJ, 123, 1111

Bloom J. S. et al., 1999, Nat, 401, 453

Bloom J. S. et al., 2006, ApJ, 638, 354

Bloom J. S., Sigurdsson S., Pols O. R., 1999, MNRAS, 305, 763

Bloser P. F., Legere J. S., Bancroft C. M., Jablonski L. F., Wurtz J. R., Ertley C. D., McConnell M. L., Ryan J. M., 2014, Nuclear Instruments and Methods in Physics Research A, 763, 26

Boella G., Butler R. C., Perola G. C., Piro L., Scarsi L., Bleeker J. A. M., 1997, A&AS, 122

Boer M., Hurley K., Niel M., Vedrenne G., Kuznetsov A., 1986, Advances in Space Research, 6, 97

Böttcher M., Dermer C. D., 1998, ApJL, 499, L131

Bouwens R. J., Illingworth G. D., Franx M., Ford H., 2007, ApJ, 670, 928

Bouwens R. J., Illingworth G. D., Franx M., Ford H., 2008, ApJ, 686, 230

Bouwens R. J. et al., 2003, ApJ, 595, 589

Bošnjak Ž., Götz D., Bouchet L., Schanne S., Cordier B., 2014, A&A, 561, A25

Bradt H. V., Rothschild R. E., Swank J. H., 1993, A&AS, 97, 355

Briggs M. S., Band D. L., Preece R. D., Pendleton G. N., Paciesas W. S., Matteson J. L., 1998, in American Institute of Physics Conference Series, Vol. 428, Gamma-Ray Bursts, 4th Hunstville Symposium, Meegan C. A., Preece R. D., Koshut T. M., eds., pp. 299–303

Bromberg O., Nakar E., Piran T., 2011, ApJL, 739, L55

Bromberg O., Nakar E., Piran T., Sari R., 2013, ApJ, 764, 179

Burgess J. M. et al., 2014, ApJL, 784, L43

Burrows D. N. et al., 2006, ApJ, 653, 468

Burrows D. N. et al., 2005a, SSR, 120, 165

Burrows D. N. et al., 2005b, Science, 309, 1833

Butler N. et al., 2005, GRB Coordinates Network, 3570

Butler N. R., Bloom J. S., Poznanski D., 2010, ApJ, 711, 495

Butler N. R., Kocevski D., Bloom J. S., Curtis J. L., 2007, ApJ, 671, 656

Bykov A. M., Meszaros P., 1996, ApJL, 461, L37

Campana S. et al., 2005, ApJL, 625, L23

Campana S. et al., 2006a, Nat, 442, 1008

Campana S. et al., 2012, MNRAS, 421, 1697

Campana S. et al., 2006b, A&A, 454, 113

Campana S., Thöne C. C., de Ugarte Postigo A., Tagliaferri G., Moretti A., Covino S., 2010, MNRAS, 402, 2429

Campisi M. A., Li L.-X., Jakobsson P., 2010, MNRAS, 407, 1972

Cao X.-F., Yu Y.-W., Cheng K. S., Zheng X.-P., 2011, MNRAS, 416, 2174

Caroli E., Stephen J. B., Di Cocco G., Natalucci L., Spizzichino A., 1987, SSR, 45, 349

Cavallo G., Rees M. J., 1978, MNRAS, 183, 359

Cenko S. B. et al., 2010, ApJ, 711, 641

Chaplin V., 2009, GRB Coordinates Network, 10095

Chapman R., Levan A. J., Priddey R. S., Tanvir N. R., Wynn G. A., King A. R., Davies M. B., 2007a, in Astronomical Society of the Pacific Conference Series, Vol. 372, 15th European Workshop on White Dwarfs, Napiwotzki R., Burleigh M. R., eds., p. 415

Chapman R., Tanvir N. R., Priddey R. S., Levan A. J., 2007b, MNRAS, 382, L21

Chary R., Becklin E. E., Armus L., 2002, ApJ, 566, 229

Chen L., Lou Y.-Q., Wu M., Qu J.-L., Jia S.-M., Yang X.-J., 2005, ApJ, 619, 983

Cheng L. X., Ma Y. Q., Cheng K. S., Lu T., Zhou Y. Y., 1995, A&A, 300, 746

Chevalier R. A., Li Z.-Y., 2000, ApJ, 536, 195

Chincarini G. et al., 2010, MNRAS, 406, 2113

Chincarini G. et al., 2005, ArXiv Astrophysics e-prints

Chincarini G., Moretti A., Romano P., Falcone A. D., Morris D., Racusin J., et al., 2007, ApJ, 671, 1903

Chornock R. et al., 2010, ArXiv e-prints

Christensen L., Hjorth J., Gorosabel J., 2004, A&A, 425, 913

Christensen L., Vreeswijk P. M., Sollerman J., Thöne C. C., Le Floc'h E., Wiersema K., 2008, A&A, 490, 45

Chuang K.-W., 1990, PhD thesis, California Univ., Riverside.

Chuang K. W., White R. S., Klebesadel R. W., Laros J. G., 1992, ApJ, 391, 242

Church R. P., Levan A. J., Davies M. B., Tanvir N., 2011, MNRAS, 413, 2004

Cline T. L. et al., 2003, in American Institute of Physics Conference Series, Vol. 662, Gamma-Ray Burst and Afterglow Astronomy 2001: A Workshop Celebrating the First Year of the HETE Mission, Ricker G. R., Vanderspek R. K., eds., pp. 143–143

Cline T. L., Desai U. D., Klebesadel R. W., Strong I. B., 1973, ApJL, 185, L1

Cline T. L., Desai U. D., Trainor J. H., Pizzichini G., Spizzichino A., Klebesadel R. W., Helmken H., 1979, ApJL, 232, L1

Coe D. et al., 2013, ApJ, 762, 32

Cohen E., Piran T., 1995, ApJL, 444, L25

Cole S. et al., 2001, Monthly Notices of the Royal Astronomical Society, 326, 255

Colgate S. A., 1968, Canadian Journal of Physics, 46, 476

Colgate S. A., McKee C., 1969, ApJ, 157, 623

Costa E. et al., 1997, Nat, 387, 783

Coward D. M. et al., 2012, MNRAS, 425, 2668

Crider A., Liang E. P., Preece R. D., Briggs M. S., Pendleton G. N., Paciesas W. S., Band D. L., Matteson J. L., 1999a, ApJ, 519, 206

Crider A., Liang E. P., Preece R. D., Briggs M. S., Pendleton G. N., Paciesas W. S., Band D. L., Matteson J. L., 1999b, A&AS, 138, 401

Cucchiara A. et al., 2011, ApJ, 736, 7

D'Agostini G., 2005, ArXiv Physics e-prints

Dai Z. G., Cheng K. S., 2001, ApJL, 558, L109

Dai Z. G., Lu T., 1998, A&A, 333, L87

Dai Z. G., Wang X. Y., Wu X. F., Zhang B., 2006, Science, 311, 1127

Daigne F., 2004, in Accretion Discs, Jets and High Energy Phenomena in Astrophysics, Beskin V., Henri G., Menard F., et al., eds., pp. 251–312

Daigne F., Mochkovitch R., 2000, A&A, 358, 1157

Daigne F., Rossi E. M., Mochkovitch R., 2006, MNRAS, 372, 1034

Dainotti M., Petrosian V., Willingale R., O'Brien P., Ostrowski M., Nagataki S., 2015, MNRAS, 451, 3898

Dainotti M. G., Del Vecchio R., Shigehiro N., Capozziello S., 2014, ArXiv e-prints

Dainotti M. G., Willingale R., Capozziello S., Fabrizio Cardone V., Ostrowski M., 2010, ApJL, 722, L215

Darling D. A., 1957, Ann. Math. Statist., 28, 823

D'Avanzo P., Ghirlanda G., 2016, LPI Contributions, 1962, 4031

D'Avanzo P. et al., 2014, MNRAS, 442, 2342

D'Avanzo P. et al., 2012, MNRAS, 425, 506

Davé R., 2008, MNRAS, 385, 147

De Pasquale M. et al., 2003, ApJ, 592, 1018

D'Elia V. et al., 2015, A&A, 577, A116

Deng C.-M., Wang X.-G., Guo B.-B., Lu R.-J., Wang Y.-Z., Wei J.-J., Wu X.-F., Liang E.-W., 2016, ApJ, 820, 66

Deng J., Tominaga N., Mazzali P. A., Maeda K., Nomoto K., 2005, ApJ, 624, 898

Dingus B. L., 1995a, ApSS, 231, 187

Dingus B. L., 1995b, in Particle and Nuclear Astrophysics and Cosmology in the Next Millenium, Kolb E. W., Peccei R. D., eds., p. 99

Djorgovski S. G., Kulkarni S. R., Bloom J. S., Goodrich R., Frail D. A., Piro L., Palazzi E., 1998, ApJL, 508, L17

Doi H., Takami K., Yamazaki R., 2007, ApJL, 659, L95

Donato D., Angelini L., Padgett C. A., Reichard T., Gehrels N., Marshall F. E., Sakamoto T., 2012, ApJS, 203, 2

Dong Y., Wu B., Li Y., Zhang Y., Zhang S., 2010, Science China Physics, Mechanics, and Astronomy, 53, 40

Eichler D., Livio M., Piran T., Schramm D. N., 1989, Nat, 340, 126

Ellis R. S. et al., 2013, ApJL, 763, L7

Ellison D. C., Double G. P., 2002, Astroparticle Physics, 18, 213

Evans P. A. et al., 2009, MNRAS, 397, 1177

Evans P. A. et al., 2007, A&A, 469, 379

Evans P. A. et al., 2016, MNRAS

Evans P. A. et al., 2010, A&A, 519, A102

Evans P. A. et al., 2014, MNRAS, 444, 250

Evans W. D., Fenimore E. E., Klebesadel R. W., Laros J. G., Terrell N. J., 1981, ApSS, 75, 35

Falcone A. D. et al., 2006, ApJ, 641, 1010

Falcone A. D. et al., 2007, ApJ, 671, 1921

Fenimore E. E., Bloom J. S., 1995, ApJ, 453, 25

Fenimore E. E., Cannon T. M., 1978, AO, 17, 337

Fenimore E. E. et al., 1988, ApJL, 335, L71

Fenimore E. E. et al., 1993, Nat, 366, 40

Fenimore E. E., Ramirez-Ruiz E., 2000, ArXiv Astrophysics e-prints

Fermi E., 1949, Physical Review, 75, 1169

Feroci M. et al., 1997, in ProcSPIE, Vol. 3114, EUV, X-Ray, and Gamma-Ray Instrumentation for Astronomy VIII, Siegmund O. H., Gummin M. A., eds., pp. 186–197

Feroz F., Hobson M. P., Cameron E., Pettitt A. N., 2013, ArXiv e-prints

Fiore F., Guetta D., Piranomonte S., D'Elia V., Antonelli L. A., 2007, A&A, 470, 515

Firmani C., Avila-Reese V., Ghisellini G., Tutukov A. V., 2004, ApJ, 611, 1033

Firmani C., Ghisellini G., Avila-Reese V., Ghirlanda G., 2006, MNRAS, 370, 185

Fishman G. J., 1993, in American Institute of Physics Conference Series, Vol. 280, American Institute of Physics Conference Series, Friedlander M., Gehrels N., Macomb D. J., eds., pp. 669–680

Fishman G. J., Meegan C. A., 1995, ARAA, 33, 415

Fishman G. J., Meegan C. A., Parnell T. A., Wilson R. B., Paciesas W., Mateson J. L., Cline T. L., Teegarden B. J., 1985, International Cosmic Ray Conference, 3, 343

Fishman G. J., Meegan C. A., Watts, Jr. J. W., Derrickson J. H., 1978, ApJL, 223, L13

Fishman G. J. et al., 1994, ApJS, 92, 229

Fishman G. J. et al., 1989, in Developments in Observations and Theory for Solar Cycle 22, Winglee R. M., Dennis B. R., eds., pp. 96–106

Fong W., Berger E., Fox D. B., 2010, ApJ, 708, 9

Foreman-Mackey D., 2013, Corner: Make some beautiful corner plots. [Online; accessed 2016-08-16]

Fox D. B. et al., 2005, Nat, 437, 845

Frail D., 2004, Confirmation of the Fading Afterglow From the Short Burst GRB 050709. Chandra Proposal

Frail D. A., Kulkarni S. R., Nicastro L., Feroci M., Taylor G. B., 1997, Nat, 389, 261

Frail D. A. et al., 2001, ApJL, 562, L55

Frontera F., Costa E., dal Fiume D., Feroci M., Nicastro L., Orlandini M., Palazzi E., Zavattini G., 1997, A&AS, 122

Frontera F. et al., 2009, ApJS, 180, 192

Fruchter A. S. et al., 2006, Nat, 441, 463

Fruchter A. S. et al., 1999, ApJL, 519, L13

Fryer C. L. et al., 2007, PASP, 119, 1211

Fryer C. L., Woosley S. E., Hartmann D. H., 1999, ApJ, 526, 152

Fynbo J. P. U. et al., 2006, Nat, 444, 1047

Gal-Yam A. et al., 2006, Nat, 444, 1053

Galama T. J. et al., 2000, ApJ, 536, 185

Galama T. J. et al., 1998a, Nat, 395, 670

Galama T. J., Wijers R. A. M. J., 2001, ApJL, 549, L209

Galama T. J., Wijers R. A. M. J., Bremer M., Groot P. J., Strom R. G., Kouveliotou C., van Paradijs J., 1998b, ApJL, 500, L97

Garson, III A., Krawczynski H., Grindlay J., Fishman G. J., Wilson C. A., 2006, A&A, 456, 379

Gehrels N. et al., 2004, ApJ, 611, 1005

Gehrels N., Chipman E., Kniffen D. A., 1993, A&AS, 97, 5

Gehrels N. et al., 2006, Nat, 444, 1044

Gehrels N., Ramirez-Ruiz E., Fox D. B., 2009, ARAA, 47, 567

Gehrels N. et al., 2005, Nat, 437, 851

Gelman A., Rubin D. B., 1992, Statistical Science, 7, 457

Gendre B. et al., 2013, ApJ, 766, 30

Genet F., Granot J., 2009a, in American Institute of Physics Conference Series, Vol. 1133, American Institute of Physics Conference Series, Meegan C., Kouveliotou C., Gehrels N., eds., pp. 406–408

Genet F., Granot J., 2009b, MNRAS, 399, 1328

Georgy C., Meynet G., Walder R., Folini D., Maeder A., 2009, A&A, 502, 611

Ghirlanda G., Ghisellini G., Celotti A., 2004, in American Institute of Physics Conference Series, Vol. 727, Gamma-Ray Bursts: 30 Years of Discovery, Fenimore E., Galassi M., eds., pp. 69–72

Ghirlanda G., Ghisellini G., Lazzati D., 2004, ApJ, 616, 331

Ghirlanda G., Nava L., Ghisellini G., Celotti A., Burlon D., Covino S., Melandri A., 2012, MNRAS, 420, 483

Ghirlanda G., Nava L., Ghisellini G., Celotti A., Firmani C., 2009, A&A, 496, 585

Ghirlanda G. et al., 2016, ArXiv e-prints

Ghisellini G., Celotti A., 1999, ApJL, 511, L93

Giannios D., Spruit H. C., 2007, A&A, 469, 1

Goad M. R. et al., 2007, A&A, 476, 1401

Goldstein A., Preece R. D., Mallozzi R. S., Briggs M. S., Fishman G. J., Kouveliotou C., Paciesas W. S., Burgess J. M., 2013, ApJS, 208, 21

Golenetskii S. et al., 2009a, GRB Coordinates Network, 9679

Golenetskii S. et al., 2009b, GRB Coordinates Network, 10057

Golenetskii S. et al., 2010, GRB Coordinates Network, 10882

Golenetskii S. et al., 2011a, GRB Coordinates Network, 12008

Golenetskii S., Aptekar R., Mazets E., Pal'Shin V., Frederiks D., Cline T., 2005, GRB Coordinates Network, 3179

Golenetskii S., Aptekar R., Mazets E., Pal'Shin V., Frederiks D., Cline T., 2006, GRB Coordinates Network, 5748

Golenetskii S., Aptekar R., Mazets E., Pal'Shin V., Frederiks D., Cline T., 2007a, GRB Coordinates Network, 6459

Golenetskii S., Aptekar R., Mazets E., Pal'Shin V., Frederiks D., Cline T., 2007b, GRB Coordinates Network, 6960

Golenetskii S., Aptekar R., Mazets E., Pal'Shin V., Frederiks D., Cline T., 2008a, GRB Coordinates Network, 7482

Golenetskii S., Aptekar R., Mazets E., Pal'Shin V., Frederiks D., Cline T., 2008b, GRB Coordinates Network, 7812

Golenetskii S. et al., 2008c, GRB Coordinates Network, 8611

Golenetskii S., Aptekar R., Mazets E., Pal'Shin V., Frederiks D., Oleynik P., Ulanov M., Svinkin D., 2009c, GRB Coordinates Network, 10045

Golenetskii S. et al., 2008d, GRB Coordinates Network, 7862

Golenetskii S. et al., 2008e, GRB Coordinates Network, 7995

Golenetskii S. et al., 2008f, GRB Coordinates Network, 8721

Golenetskii S. et al., 2009d, GRB Coordinates Network, 9553

Golenetskii S. et al., 2009e, GRB Coordinates Network, 8776

Golenetskii S. et al., 2011b, GRB Coordinates Network, 11971

Gompertz B. P., Fruchter A. S., 2017, ArXiv e-prints

Gompertz B. P., O'Brien P. T., Wynn G. A., 2014, MNRAS, 438, 240

Goodman J., 1986, ApJL, 308, L47

Goodman J., 1997, NewAst, 2, 449

Goodman J., Dar A., Nussinov S., 1987, ApJL, 314, L7

Götz D. et al., 2014, in ProcSPIE, Vol. 9144, Space Telescopes and Instrumentation 2014: Ultraviolet to Gamma Ray, p. 914423

Gräfener G., Vink J. S., Harries T. J., Langer N., 2012, A&A, 547, A83

Graham J. F., Fruchter A. S., 2013, ApJ, 774, 119

Granot J., 2005, ApJ, 631, 1022

Granot J., Cohen-Tanugi J., Silva E. d. C. e., 2008, ApJ, 677, 92

Granot J., Piran T., Sari R., 1999, ApJ, 527, 236

Granot J., Piran T., Sari R., 2000, ApJL, 534, L163

Granot J., Ramirez-Ruiz E., Perna R., 2005, ApJ, 630, 1003

Granot J., Sari R., 2002, ApJ, 568, 820

Greiner J. et al., 2015, Nat, 523, 189

Grindlay J., Portegies Zwart S., McMillan S., 2006, Nature Physics, 2, 116

Gruber D. et al., 2014, ApJS, 211, 12

Gruber D. E. et al., 1992, Spectral evolution during a complex gamma ray burst observed with BATSE. Tech. rep.

Guetta D., Della Valle M., 2007, ApJL, 657, L73

Guetta D., Piran T., 2005, A&A, 435, 421

Guetta D., Piran T., Waxman E., 2005, ApJ, 619, 412

Guidorzi C., Lacapra M., Frontera F., Montanari E., Amati L., Calura F., Nicastro L., Orlandini M., 2011, A&A, 526, A49

Guiriec S. et al., 2011, ApJL, 727, L33

Guiriec S. et al., 2015, ApJ, 807, 148

Hakkila J., Giblin T. W., Norris J. P., Fragile P. C., Bonnell J. T., 2008, ApJL, 677, L81

Hakkila J., Preece R. D., 2011, ApJ, 740, 104

Harrison F. A. et al., 1999, ApJL, 523, L121

Hartmann D., Woosley S. E., Epstein R. I., 1990, ApJ, 348, 625

Hascoët R., Daigne F., Mochkovitch R., 2012, A&A, 542, L29

Hastings W. K., 1970, Biometrika, 57, 97

Heise J., Zand J. I., Kippen R. M., Woods P. M., 2001, in Gamma-ray Bursts in the Afterglow Era, Costa E., Frontera F., Hjorth J., eds., p. 16

Hjorth J. et al., 2012, ApJ, 756, 187

Hjorth J. et al., 2005, ApJL, 630, L117

Hjorth J. et al., 2003, Nat, 423, 847

Hogg D. W., 1999, ArXiv Astrophysics e-prints

Hogg D. W., Fruchter A. S., 1999, ApJ, 520, 54

Hopkins A. M., Beacom J. F., 2006, ApJ, 651, 142

Horváth I., 1998, ApJ, 508, 757

Howell E. J., Coward D. M., 2013, MNRAS, 428, 167

Hueter G. J., 1984, in American Institute of Physics Conference Series, Vol. 115, American Institute of Physics Conference Series, Woosley S. E., ed., pp. 373–377

Hurley K., 1991, in American Institute of Physics Conference Series, Vol. 265, American Institute of Physics Conference Series, pp. 3–12

Hurley K. et al., 2013, ApJS, 207, 39

Hurley K. et al., 1992, A&AS, 92, 401

Jager R. et al., 1997, A&AS, 125

Jakobsson P., Hjorth J., Fynbo J. P. U., Gorosabel J., Jaunsen A. O., 2006a, ArXiv Astrophysics e-prints

Jakobsson P. et al., 2012, ApJ, 752, 62

Jakobsson P. et al., 2006b, A&A, 447, 897

Johansson A., Beron B. L., Campbell L., Eichler R., Hofstadter R., Hughes E. B., Wilson S., Gorodetsky P., 1980, IEEE Transactions on Nuclear Science, 27, 375

Jones E., Oliphant T., Peterson P., 2001, SciPy: Open source scientific tools for Python. [Online; accessed 2016-07-04]

Kalberla P. M. W., Burton W. B., Hartmann D., Arnal E. M., Bajaja E., Morras R., Pöppel W. G. L., 2005, A&A, 440, 775

Kaneko Y., Preece R. D., Briggs M. S., Paciesas W. S., Meegan C. A., Band D. L., 2006, ApJS, 166, 298

Kann D. A. et al., 2011, ApJ, 734, 96

Katz J. I., 1994, ApJ, 422, 248

Katz J. I., Piran T., 1997, ApJ, 490, 772

Kawakubo Y., Sakamoto T., Yoshida A., Kazanas D., 2015, Advances in Astronomy, 2015, 341018

Kelley R. L. et al., 2007, PASJ, 59, 77

Kippen R. M., Woods P. M., Heise J., in't Zand J. J. M., Briggs M. S., Preece R. D., 2003, in American Institute of Physics Conference Series, Vol. 662, Gamma-Ray Burst and Afterglow Astronomy 2001: A Workshop Celebrating the First Year of the HETE Mission, Ricker G. R., Vanderspek R. K., eds., pp. 244–247

Kistler M. D., Yüksel H., Beacom J. F., Hopkins A. M., Wyithe J. S. B., 2009, ApJL, 705, L104

Kistler M. D., Yüksel H., Beacom J. F., Stanek K. Z., 2008, ApJL, 673, L119

Klebesadel R. W., Evans W. D., Glore J. P., Spalding R. E., Wymer F. J., 1980, IEEE Transactions on Geoscience and Remote Sensing, 18, 76

Klebesadel R. W., Evans W. D., Laros J. G., 1981, ApSS, 75, 5

Klebesadel R. W., Strong I. B., Olson R. A., 1973, ApJL, 182, L85

Knight F. K., Matteson J. L., Peterson L. E., 1981, ApSS, 75, 21

Kobayashi M. A. R., Inoue Y., Inoue A. K., 2013, ApJ, 763, 3

Kobayashi S., Piran T., Sari R., 1997, ApJ, 490, 92

Kobayashi S., Sari R., 2001, ApJ, 551, 934

Kocevski D., Liang E., 2006, ApJ, 642, 371

Kole M. et al., 2016, ArXiv e-prints

Kono K. et al., 2009, GRB Coordinates Network, 9568

Kouveliotou C., Meegan C. A., Fishman G. J., Bhat N. P., Briggs M. S., Koshut T. M., Paciesas W. S., Pendleton G. N., 1993, ApJL, 413, L101

Koyama K. et al., 2007, PASJ, 59, 23

Krimm H. A. et al., 2007, ApJ, 665, 554

Krimm H. A. et al., 2009, ApJ, 704, 1405

Kroupa P., 2001, in Astronomical Society of the Pacific Conference Series, Vol. 228, Dynamics of Star Clusters and the Milky Way, Deiters S., Fuchs B., Just A., Spurzem R., Wielen R., eds., p. 187

Kulkarni S. R. et al., 1998, ArXiv Astrophysics e-prints

Kumar P., Panaitescu A., 2000, ApJL, 541, L51

Kumar P., Panaitescu A., 2008, MNRAS, 391, L19

Langer N., Norman C. A., 2006, ApJL, 638, L63

Larson D. et al., 2011, ApJS, 192, 16

Lazzati D., Morsony B. J., Begelman M. C., 2009, ApJL, 700, L47

Lazzati D., Perna R., Begelman M. C., 2008, MNRAS, 388, L15

Le Floc'h E. et al., 2003, A&A, 400, 499

Leibler C. N., Berger E., 2010, ApJ, 725, 1202

Lemoine M., Pelletier G., 2003, ApJL, 589, L73

Levan A. J. et al., 2007, MNRAS, 378, 1439

Levan A. J. et al., 2014, ApJ, 781, 13

Levesque E., Chornock R., Kewley L., Bloom J. S., Prochaska J. X., Perley D. A., Cenko S. B., Modjaz M., 2009, GRB Coordinates Network, 9264

Levesque E. M., Berger E., Soderberg A. M., Chornock R., 2011, ApJ, 739, 23

Levesque E. M., Kewley L. J., Berger E., Zahid H. J., 2010a, AJ, 140, 1557

Levesque E. M., Kewley L. J., Graham J. F., Fruchter A. S., 2010b, ApJL, 712, L26

Li L.-X., 2008, MNRAS, 388, 1487

Liang E., Zhang B., Virgili F., Dai Z. G., 2007, ApJ, 662, 1111

Liang E. W. et al., 2006, ApJ, 646, 351

Lien A. et al., 2016a, ApJ, 829, 7

Lien A. et al., 2016b, ArXiv e-prints

Link B., Epstein R. I., Priedhorsky W. C., 1993, ApJL, 408, L81

Link W. A., Eaton M. J., 2012, Methods in Ecology and Evolution, 3, 112

Lithwick Y., Sari R., 2001, ApJ, 555, 540

Littlejohns O. M., Tanvir N. R., Willingale R., Evans P. A., O'Brien P. T., Levan A. J., 2013, MNRAS, 436, 3640

Littlejohns O. M. et al., 2012, MNRAS, 421, 2692

Litvin V. F., Matveev S. A., Mamedov S. V., Orlov V. V., 2001, Astronomy Letters, 27, 416

Lloyd-Ronning N. M., Fryer C. L., Ramirez-Ruiz E., 2002, ApJ, 574, 554

Lloyd-Ronning N. M., Ramirez-Ruiz E., 2002, ApJ, 576, 101

Lü H.-J., Zhang B., Liang E.-W., Zhang B.-B., Sakamoto T., 2014, MNRAS, 442, 1922

Lund N. et al., 2003, A&A, 411, L231

MacFadyen A. I., Woosley S. E., 1999, ApJ, 524, 262

Magliocchetti M., Ghirlanda G., Celotti A., 2003, MNRAS, 343, 255

Malesani D. et al., 2004, ApJL, 609, L5

Mao S., Paczynski B., 1992, ApJL, 389, L13

Margutti R. et al., 2007, A&A, 474, 815

Margutti R., Guidorzi C., Chincarini G., Bernardini M. G., Genet F., Mao J., Pasotti F., 2010, MNRAS, 406, 2149

Matsuoka M. et al., 2009, PASJ, 61, 999

Mazets E. P., Golenetskii S. V., 1981, ApSS, 75, 47

Mazets E. P., Golenetskii S. V., Aptekar R. L., Gurian I. A., Ilinskii V. N., 1981, Nat, 290, 378

Mazets E. P., Golenetskii S. V., Gurian I. A., Aptekar R. L., Ilinskii V. N., Panov V. N., 1983, in American Institute of Physics Conference Series, Vol. 101, Positron-Electron Pairs in Astrophysics, Burns M. L., Harding A. K., Ramaty R., eds., pp. 36–53

Mazets E. P., Golenetskii S. V., Il'Inskii V. N., 1974, Soviet Journal of Experimental and Theoretical Physics Letters, 19, 77

Mazets E. P. et al., 1979, Soviet Astronomy Letters, 5, 163

McBreen S., 2009a, GRB Coordinates Network, 9415

McBreen S., 2009b, GRB Coordinates Network, 9535

McBreen S. et al., 2008, ApJL, 677, L85

Meegan C., Fishman G., Wilson R., Paciesas W., 1993, in American Institute of Physics Conference Series, Vol. 280, American Institute of Physics Conference Series, Friedlander M., Gehrels N., Macomb D. J., eds., pp. 1117–1121

Meegan C. et al., 2009, ApJ, 702, 791

Meegan C. A., Fishman G. J., Wilson R. B., Horack J. M., Brock M. N., Paciesas W. S., Pendleton G. N., Kouveliotou C., 1992, Nat, 355, 143

Meegan C. A. et al., 2008, GRB Coordinates Network, 8100

Melandri A. et al., 2012, A&A, 547, A82

Mészáros A., Bagoly Z., Horváth I., Balázs L. G., Vavrek R., 2000, ApJ, 539, 98

Mészáros P., 2002, ARAA, 40, 137

Mészáros P., 2006, Reports on Progress in Physics, 69, 2259

Meszaros P., Rees M. J., 1993a, ApJL, 418, L59

Meszaros P., Rees M. J., 1993b, ApJ, 405, 278

Mészáros P., Rees M. J., 2000, ApJ, 530, 292

Mészáros P., Rees M. J., 2001, ApJL, 556, L37

Meszaros P., Rees M. J., Papathanassiou H., 1994, ApJ, 432, 181

Metropolis N., Rosenbluth A. W., Rosenbluth M. N., Teller A. H., Teller E., 1953, JCP, 21, 1087

Metzger A. E., Parker R. H., Gilman D., Peterson L. E., Trombka J. I., 1974, ApJL, 194, L19

Metzger B. D., Berger E., 2012, ApJ, 746, 48

Metzger B. D., Giannios D., Thompson T. A., Bucciantini N., Quataert E., 2011, MNRAS, 413, 2031

Metzger B. D., Quataert E., Thompson T. A., 2008, in AAS/High Energy Astrophysics Division, Vol. 10, AAS/High Energy Astrophysics Division #10, p. 5.05

Metzger M. R., Djorgovski S. G., Kulkarni S. R., Steidel C. C., Adelberger K. L., Frail D. A., Costa E., Frontera F., 1997, Nat, 387, 878

Mihara T. et al., 2011, PASJ, 63, S623

Miller N., Marka S., Bartos I., 2015, ArXiv e-prints

Mitsuda K. et al., 2007, PASJ, 59, 1

Mukherjee S., Feigelson E. D., Jogesh Babu G., Murtagh F., Fraley C., Raftery A., 1998, ApJ, 508, 314

Murakami T., Fujii M., Hayashida K., Itoh M., Nishimura J., 1988, Nat, 335, 234

Murakami T. et al., 1989, PASJ, 41, 405

Nakar E., 2007, PhysRep, 442, 166

Nakar E., 2015, ApJ, 807, 172

Nakar E., Sari R., 2012, ApJ, 747, 88

Nakauchi D., Kashiyama K., Suwa Y., Nakamura T., 2013, ApJ, 778, 67

Nappo F. et al., 2016, ArXiv e-prints

Narayan R., Paczynski B., Piran T., 1992, ApJL, 395, L83

Natarajan P., Albanna B., Hjorth J., Ramirez-Ruiz E., Tanvir N., Wijers R., 2005, MNRAS, 364, L8

Nava L., Ghirlanda G., Ghisellini G., Firmani C., 2008, MNRAS, 391, 639

Nava L. et al., 2012, MNRAS, 421, 1256

Nemiroff R. J., Norris J. P., Kouveliotou C., Fishman G. J., Meegan C. A., Paciesas W. S., 1994, ApJ, 423, 432

Nemiroff R. J. et al., 1993, ApJ, 414, 36

Noda K. et al., 2009, GRB Coordinates Network, 9816

Norris J., 1983, PhD thesis, National Aeronautics and Space Administration. Goddard Space Flight Center, Greenbelt, MD.

Norris J. P., 2002, ApJ, 579, 386

Norris J. P., Bonnell J. T., 2006, ApJ, 643, 266

Norris J. P., Bonnell J. T., Kazanas D., Scargle J. D., Hakkila J., Giblin T. W., 2005, ApJ, 627, 324

Norris J. P., Gehrels N., Scargle J. D., 2010, ApJ, 717, 411

Norris J. P., Marani G. F., Bonnell J. T., 2000, ApJ, 534, 248

Norris J. P., Nemiroff R. J., Bonnell J. T., Scargle J. D., Kouveliotou C., Paciesas W. S., Meegan C. A., Fishman G. J., 1996, ApJ, 459, 393

Norris J. P., Scargle J. D., Bonnell J. T., 2001, in American Institute of Physics Conference Series, Vol. 587, Gamma 2001: Gamma-Ray Astrophysics, Ritz S., Gehrels N., Shrader C. R., eds., pp. 176–180

Norris J. P., Share G. H., Messina D. C., Dennis B. R., Desai U. D., Cline T. L., Matz S. M., Chupp E. L., 1986, ApJ, 301, 213

Nousek J. A. et al., 2006, ApJ, 642, 389

Oates S. R. et al., 2009, MNRAS, 395, 490

O'Brien P., 2006, in COSPAR Meeting, Vol. 36, 36th COSPAR Scientific Assembly

O'Brien P. T. et al., 2006, ApJ, 647, 1213

Oesch P. A. et al., 2013, ApJ, 773, 75

Ohno M. et al., 2005, IEEE Transactions on Nuclear Science, 52, 2758

Ohno M. et al., 2012, in American Institute of Physics Conference Series, Vol. 1427, American Institute of Physics Conference Series, Petre R., Mitsuda K., Angelini L., eds., pp. 115–122

Owen A. B., 2015, ArXiv e-prints

Owens A. et al., 1995, SSR, 71, 273

Paciesas W. S. et al., 1999, ApJS, 122, 465

Paczynski B., 1986, ApJL, 308, L43

Paczynski B., 1990, ApJ, 363, 218

Paczynski B., 1991, ActA, 41, 257

Paczyński B., 1998a, ApJL, 494, L45

Paczyński B., 1998b, in American Institute of Physics Conference Series, Vol. 428, Gamma-Ray Bursts, 4th Hunstville Symposium, Meegan C. A., Preece R. D., Koshut T. M., eds., pp. 783–787

Paczynski B., Xu G., 1994, ApJ, 427, 708

Page K. L. et al., 2007, ApJ, 663, 1125

Palmer D. M. et al., 1994, ApJL, 433, L77

Pal'Shin V. et al., 2009a, GRB Coordinates Network, 9196

Pal'Shin V. et al., 2008, GRB Coordinates Network, 8256

Pal'Shin V. et al., 2009b, GRB Coordinates Network, 9821

Panaitescu A., Kumar P., 2001, ApJL, 560, L49

Panaitescu A., Mészáros P., 1999, ApJ, 526, 707

Parmar A. N. et al., 1997, A&AS, 122

Paul J. et al., 1991, Advances in Space Research, 11, 289

Paul J., Wei J., Basa S., Zhang S.-N., 2011, Comptes Rendus Physique, 12, 298

Pérez-González P. G. et al., 2005, ApJ, 630, 82

Perley D. A. et al., 2016a, ApJ, 817, 7

Perley D. A. et al., 2009, ApJ, 696, 1871

Perley D. A. et al., 2016b, ApJ, 817, 8

Pescalli A. et al., 2015, ArXiv e-prints

Peterson L. E., 1975, ARAA, 13, 423

Petrosian V., Kitanidis E., Kocevski D., 2015, ArXiv e-prints

Petrovic J., Langer N., Yoon S.-C., Heger A., 2005, A&A, 435, 247

Pian E. et al., 2006, Nat, 442, 1011

Piran T., 1992, ApJL, 389, L45

Piran T., 1999, PhysRep, 314, 575

Piran T., 2004, Reviews of Modern Physics, 76, 1143

Podsiadlowski P., Ivanova N., Justham S., Rappaport S., 2010, Monthly Notices of the Royal Astronomical Society, 406, 840

Popham R., Woosley S. E., Fryer C., 1999, ApJ, 518, 356

Porciani C., Madau P., 2001, ApJ, 548, 522

Poulsen J. M. et al., 2000, in ProcSPIE, Vol. 4140, X-Ray and Gamma-Ray Instrumentation for Astronomy XI, Flanagan K. A., Siegmund O. H., eds., pp. 293–303

Predehl P., Schmitt J. H. M. M., 1995, A&A, 293, 889

Preece R. D., Briggs M. S., Giblin T. W., Mallozzi R. S., Pendleton G. N., Paciesas W. S., Band D. L., 2002, ApJ, 581, 1248

Preece R. D., Briggs M. S., Mallozzi R. S., Pendleton G. N., Paciesas W. S., Band D. L., 2000, ApJS, 126, 19

Price P. A., Roth K., Fox D. W., 2005, GRB Coordinates Network, 3605

Prochaska J. X. et al., 2004, ApJ, 611, 200

Produit N. et al., 2005, Nuclear Instruments and Methods in Physics Research A, 550, 616

Qin S.-F., Liang E.-W., Lu R.-J., Wei J.-Y., Zhang S.-N., 2010, MNRAS, 406, 558

Qin Y. et al., 2013, ApJ, 763, 15

Racusin J. L. et al., 2009, ApJ, 698, 43

Ramirez-Ruiz E., Celotti A., Rees M. J., 2002, MNRAS, 337, 1349

Rau A., Kienlin A. V., Hurley K., Lichti G. G., 2005, A&A, 438, 1175

Rees M. J., 1966, Nat, 211, 468

Rees M. J., 1967, MNRAS, 135, 345

Rees M. J., Meszaros P., 1992, MNRAS, 258, 41P

Rees M. J., Meszaros P., 1994, ApJL, 430, L93

Reichart D. E., Lamb D. Q., Fenimore E. E., Ramirez-Ruiz E., Cline T. L., Hurley K., 2001, ApJ, 552, 57

Renaud M., Gros A., Lebrun F., Terrier R., Goldwurm A., Reynolds S., Kalemci E., 2006, A&A, 456, 389

Rhoads J. E., 1997, ApJL, 487, L1

Rhoads J. E., 1999, ApJ, 525, 737

Ricker G. R. et al., 2003, in American Institute of Physics Conference Series, Vol. 662, Gamma-Ray Burst and Afterglow Astronomy 2001: A Workshop Celebrating the First Year of the HETE Mission, Ricker G. R., Vanderspek R. K., eds., pp. 3–16

Robertson B. E., Ellis R. S., 2012, ApJ, 744, 95

Roming P. W. A. et al., 2005, SSR, 120, 95

Rosswog S., Ramirez-Ruiz E., 2003, ArXiv Astrophysics e-prints

Rowlinson A., O'Brien P. T., Metzger B. D., Tanvir N. R., Levan A. J., 2013, MNRAS, 430, 1061

Rowlinson A. et al., 2010, MNRAS, 408, 383

Ruderman M., 1975, in Annals of the New York Academy of Sciences, Vol. 262, Seventh Texas Symposium on Relativistic Astrophysics, Bergman P. G., Fenyves E. J., Motz L., eds., pp. 164–180

Ruderman M. A., Tao L., Kluźniak W., 2000, ApJ, 542, 243

Ruffini R., Bianco C. L., Fraschetti F., Xue S.-S., Chardonnet P., 2001, ApJL, 555, L117

Rujopakarn W. et al., 2010, ApJ, 718, 1171

Rybicki G. B., Lightman A. P., 1979, Radiative processes in astrophysics

Sacco B. et al., 1997, in Data Analysis in Astronomy, Di Gesu V., Duff M. J. B., Heck A., Maccarone M. C., Scarsi L., Zimmerman H. U., eds., pp. 133–141

Sakamoto T. et al., 2006, in American Institute of Physics Conference Series, Vol. 836, Gamma-Ray Bursts in the Swift Era, Holt S. S., Gehrels N., Nousek J. A., eds., pp. 43–47

Sakamoto T. et al., 2008a, ApJS, 175, 179

Sakamoto T. et al., 2008b, GRB Coordinates Network, 8101

Sakamoto T. et al., 2011a, GRB Coordinates Network, 11692

Sakamoto T. et al., 2011b, ApJS, 195, 2

Sakamoto T. et al., 2005, ApJ, 629, 311

Sakamoto T. et al., 2011c, PASJ, 63, 215

Salafia O. S., Ghisellini G., Pescalli A., Ghirlanda G., Nappo F., 2016, MNRAS, 461, 3607

Salvaterra R. et al., 2012, ApJ, 749, 68

Salvaterra R., Chincarini G., 2007, ApJL, 656, L49

Salvaterra R., Guidorzi C., Campana S., Chincarini G., Tagliaferri G., 2009, MNRAS, 396, 299

Sari R., Piran T., 1997, ApJ, 485, 270

Sari R., Piran T., Halpern J. P., 1999, ApJL, 519, L17

Sari R., Piran T., Narayan R., 1998, ApJL, 497, L17

Savaglio S., 2008, in IAU Symposium, Vol. 255, Low-Metallicity Star Formation: From the First Stars to Dwarf Galaxies, Hunt L. K., Madden S. C., Schneider R., eds., pp. 204–211

Schaefer B. E., 2006, ApJL, 642, L25

Schanne S., Cordier B., Atteia J.-L., Godet O., Lachaud C., Mercier K., 2015, ArXiv e-prints

Schmidt M., 1968, ApJ, 151, 393

Schmidt M., 1999, ApJL, 523, L117

Schmidt M., 2001, ApJ, 552, 36

Schmidt W. K. H., 1978, Nat, 271, 525

Schneid E. J. et al., 1992, A&A, 255, L13

Scholz F. W., Stephens M. A., 1987, Journal of the American Statistical Association, 82, 918

Segreto A., Piraino S., Santangelo A., Fazio G., Giarrusso S., 1997, in Data Analysis in Astronomy, Di Gesu V., Duff M. J. B., Heck A., Maccarone M. C., Scarsi L., Zimmerman H. U., eds., pp. 121–131

Serino M. et al., 2014, PASJ, 66, 87

Serino M. et al., 2013, in EAS Publications Series, Vol. 61, EAS Publications Series, Castro-Tirado A. J., Gorosabel J., Park I. H., eds., pp. 59–63

Shemi A., Piran T., 1990, ApJL, 365, L55

Shen R.-F., Song L.-M., Li Z., 2005, MNRAS, 362, 59

Shen R.-F., Zhang B., 2009, MNRAS, 398, 1936

Shirasaki Y. et al., 2000, Advances in Space Research, 25, 893

Siegmund O., Sanford P., Mason I., Culhane L., Kellock S., Cockshott R., 1981, IEEE Transactions on Nuclear Science, 28, 478

Skilling J., 2004, in American Institute of Physics Conference Series, Vol. 735, American Institute of Physics Conference Series, Fischer R., Preuss R., Toussaint U. V., eds., pp. 395–405

Soderberg A. M. et al., 2006a, Nat, 442, 1014

Soderberg A. M., Nakar E., Berger E., Kulkarni S. R., 2006b, ApJ, 638, 930

Spada M., Panaitescu A., Mészáros P., 2000, ApJ, 537, 824

Spitkovsky A., 2008, ApJL, 682, L5

Spruit H. C., 1999, A&A, 341, L1

Stamatikos M., 2009, ArXiv e-prints

Stanek K. Z. et al., 2006, ActA, 56, 333

Stanek K. Z. et al., 2003, ApJL, 591, L17

Starling R. L. C. et al., 2011, MNRAS, 411, 2792

Starling R. L. C., Willingale R., Tanvir N. R., Scott A. E., Wiersema K., O'Brien P. T., Levan A. J., Stewart G. C., 2013, MNRAS, 431, 3159

Sun H., Zhang B., Gao H., 2017, ApJ, 835, 7

Svensson K. M., Levan A. J., Tanvir N. R., Fruchter A. S., Strolger L.-G., 2010, MNRAS, 405, 57

T. W. Anderson D. A. D., 1954, Journal of the American Statistical Association, 49, 765

Tagliaferri G. et al., 2005, Nat, 436, 985

Takahashi T. et al., 2007, PASJ, 59, 35

Tang Q.-W., Peng F.-K., Wang X.-Y., Tam P.-H. T., 2015, ApJ, 806, 194

Teegarden B. J., Cline T. L., 1981, ApSS, 75, 181

Terekbov O. V. et al., 1995, Astronomy Letters, 21, 73

Terekhov O. V. et al., 1994, Astronomy Letters, 20, 265

Thompson C., 1994, MNRAS, 270, 480

Thöne C. C. et al., 2011, Nat, 480, 72

Tinney C. et al., 1998, IAUCirc, 6896

Tkachenko A. Y., Terekhov O. V., Sunyaev R. A., Kuznetsov A. V., Barat C., Dezalay J.-P., Vedrenne G., 2002, Astronomy Letters, 28, 353

Tkachenko A. Y., Terekhov O. V., Sunyaev R. A., Kuznetsov A. V., Barat C., Dezalay J.-P., Vedrenne G., Talon R., 1998, Astronomy Letters, 24, 722

Toy V. L. et al., 2016, ApJ, 818, 79

Troja E., King A. R., O'Brien P. T., Lyons N., Cusumano G., 2008, MNRAS, 385, L10

Tunnicliffe R. L. et al., 2014, MNRAS, 437, 1495

Ubertini P. et al., 2003, A&A, 411, L131

Usov V. V., 1992, Nat, 357, 472

van Dokkum P. G., 2008, ApJ, 674, 29

van Paradijs J. et al., 1997, Nat, 386, 686

Vavrek R., Balázs L. G., Mészáros A., Horváth I., Bagoly Z., 2008, MNRAS, 391, 1741

Vedrenne G., Atteia J.-L., 2009, Gamma-Ray Bursts

Vedrenne G. et al., 2003, A&A, 411, L63

Vietri M., 1997, Physical Review Letters, 78, 4328

Villasenor J. N. et al., 2003, in American Institute of Physics Conference Series, Vol. 662, Gamma-Ray Burst and Afterglow Astronomy 2001: A Workshop Celebrating the First Year of the HETE Mission, Ricker G. R., Vanderspek R. K., eds., pp. 33–37

Villasenor J. S. et al., 2005, Nat, 437, 855

Virgili F. J., Liang E.-W., Zhang B., 2009, MNRAS, 392, 91

Virgili F. J., Qin Y., Zhang B., Liang E., 2012, MNRAS, 424, 2821

Virgili F. J., Zhang B., Nagamine K., Choi J.-H., 2011a, MNRAS, 417, 3025

Virgili F. J., Zhang B., O'Brien P., Troja E., 2011b, ApJ, 727, 109

von Kienlin A., 2009, GRB Coordinates Network, 9229

von Kienlin A. et al., 2014, ApJS, 211, 13

Wainwright C., Berger E., Penprase B. E., 2007, ApJ, 657, 367

Wanderman D., Piran T., 2010, MNRAS, 406, 1944

Watson D., Jakobsson P., 2012, ApJ, 754, 89

Waxman E., 1997, ApJL, 485, L5

Wei D. M., Gao W. H., 2003, MNRAS, 345, 743

Wheaton W. A. et al., 1973, ApJL, 185, L57

Wiersema K. et al., 2012, GRB Coordinates Network, 13276

Wijers R. A. M. J., Galama T. J., 1999, ApJ, 523, 177

Wilkins S. M., Trentham N., Hopkins A. M., 2008, MNRAS, 385, 687

Willingale R., Genet F., Granot J., O'Brien P. T., 2010, MNRAS, 403, 1296

Willingale R. et al., 2007, ApJ, 662, 1093

Willingale R., Starling R. L. C., Beardmore A. P., Tanvir N. R., O'Brien P. T., 2013, MNRAS, 431, 394

Winkler C., Pace O., Volonté S., 1993, ESA Journal, 17, 207

Woosley S. E., 1993a, in Bulletin of the American Astronomical Society, Vol. 25, American Astronomical Society Meeting Abstracts #182, p. 894

Woosley S. E., 1993b, ApJ, 405, 273

Woosley S. E., Heger A., 2005, in Astronomical Society of the Pacific Conference Series, Vol. 332, The Fate of the Most Massive Stars, Humphreys R., Stanek K., eds., p. 407

Woosley S. E., Heger A., 2006, ApJ, 637, 914

Wu B., Fenimore E., 2000, ApJL, 535, L29

Wu C., Qiu Y. L., Cai H. B., 2012, in IAU Symposium, Vol. 279, Death of Massive Stars: Supernovae and Gamma-Ray Bursts, Roming P., Kawai N., Pian E., eds., pp. 421–422

Wu X. F., Dai Z. G., Liang E. W., 2004, ApJ, 615, 359

Yamaoka K. et al., 2005, IEEE Transactions on Nuclear Science, 52, 2765

Yamazaki R., Toma K., Ioka K., Nakamura T., 2006, MNRAS, 369, 311

Yonetoku D., Murakami T., Nakamura T., Yamazaki R., Inoue A. K., Ioka K., 2004, ApJ, 609, 935

Yoon S.-C., Langer N., 2005, A&A, 443, 643

Yoshida A. et al., 1989, pasj, 41, 509

Yu H., Wang F. Y., Dai Z. G., Cheng K. S., 2015a, ArXiv e-prints

Yu H.-F. et al., 2015b, A&A, 573, A81

Zhang B., 2006, Nat, 444, 1010

Zhang B., 2014, International Journal of Modern Physics D, 23, 1430002

Zhang B., Dai X., Lloyd-Ronning N. M., Mészáros P., 2004, ApJL, 601, L119

Zhang B., Mészáros P., 2004, International Journal of Modern Physics A, 19, 2385

Zhang B., Yan H., 2011, ApJ, 726, 90

Zhang B.-B., Liang E.-W., Zhang B., 2007, ApJ, 666, 1002

Zhang B.-B., van Eerten H., Burrows D. N., Ryan G. S., Evans P. A., Racusin J. L., Troja E., MacFadyen A., 2015, ApJ, 806, 15

Zhang B.-B., Zhang B., Liang E.-W., Wang X.-Y., 2008, in American Institute of Physics Conference Series, Vol. 1065, American Institute of Physics Conference Series, Huang Y.-F., Dai Z.-G., Zhang B., eds., pp. 169–172

Zheng W. et al., 2012, Nat, 489, 406

Zou Y.-C., Fan Y.-Z., Piran T., 2011, ApJL, 726, L2

Zou Y.-C., Piran T., 2010, MNRAS, 402, 1854